Dynamics of Type II Cepheids

by

Jennifer A. McSaveney

A thesis submitted
in partial fulfillment of the requirements
for the degree of
Doctor of Philosophy in Astronomy
in the University of Canterbury

University of Canterbury

2003

Dynamics of Type II Cepheids

Jennifer A. McSaveney

PhD THESIS 2003
Supervisors: Dr Karen Pollard and Assoc. Prof. Peter Cottrell

Abstract

To further understand the variations of Type II Cepheids, a selection of BL Her, W Vir and RV Tauri stars have been examined photometrically and spectroscopically, focusing on their dynamical variations. These three star types have been found to vary in a more similar fashion at the photospheric level, as traced by their spectral behaviour, than in their photometry.

A selection of twenty Type II Cepheids have been monitored from 1999–2002 at Mount John University Observatory. High resolution spectroscopic and $BVRI$ photometric observations have been made. The photometry has been used to monitor colour changes, long-term variations and establish periods for the stars. For the brighter stars, the photometry has been supplemented by visual estimates from a variety of sources. Period changes have been found for ST Pup and U Mon.

Changes of the phase of light minimum, depending on the photometric bandpass used, have necessitated an alternate zero-point for establishing phase. Mean Fe I radial velocity curves have been phased on the photometric periods and a spline curve fitted. The derivative of this curve has then been found and the resulting acceleration curve minimum associated with minimum photospheric radius used to rephase the data.

Under this phasing the shock-associated effects of line broadening, splitting, emission and the B magnitude peak occur around phase 0.0 for all the stars examined. The metallic lines velocities observed are also very similar for the W Vir and RV Tauri stars, despite the differences in the depths of the light minima. Where the differences enter is in the strength of the shock-related effects. In the W Virginis stars, the shock effects of line splitting, emission and strong peaks in B magnitude become more pronounced at longer periods and these same shock effects are observed in the RV Tauri stars. However, the strength of these effects in the RV Tauri stars, as seen by the emission and B magnitude peaks varies with the depths of the light curve minima. This does not however correlate overall with the occurrence of a deep or shallow minimum but varies depending on the star.

Line level effects are observed in all the Type II Cepheids examined, with the Hα absorption line velocities having a higher amplitude and reaching maximum velocity later in phase that the metallic lines. Within the metallic lines, velocity differences and phase lags are also observed between species. The magnitude of these differences increases in the longer-period stars.

Long-term photometric variations were observed in a selection of RVb stars. Reddening during the long-term minima was observed in SX Cen, AI Sco, U Mon and IW Car but not AR Pup. AI Sco and U Mon were found to show enhanced Hα emission during their long-term minima. RU Cen was found to show a strong blue absorption component in Hα over a single pulsational cycle, but this was not found to correlate with any photometric changes.

Oh give these clay feet wings to fly
To touch the face of the stars.

Dante's Prayer by Loreena McKennitt

Contents

Figures

Tables

Chapter 1

Introduction

The dynamics of Type II Cepheids have been well studied for individual stars and for various selections of period ranges (1–10 days, Vinkó et al., 1998), (64–~300 days, Pollard et al., 1996a), but apart from the occasional review (Wallerstein and Cox, 1984; Wallerstein, 2002), there has not been an analysis of the photometric and spectroscopic characteristics of a broad range of Type II Cepheids. The work presented here is an attempt to remedy this, as spectroscopic and photometric observations of a selection of Cepheids are investigated by focusing on the dynamical aspects.

The first section of this chapter (Section 1.1), gives a brief historical overview of the Type II Cepheids. Section 1.2 details the aims and structure of the thesis. This section refers the reader to more substantive overviews within the body of the thesis. Section 1.3 reviews the pulsational and evolutionary characteristics of the different Type II Cepheid subclasses and touches briefly on the period changes and stability (Section 1.3.4). Section 1.4 gives a general background on stellar radial pulsation followed by a review of shock waves (Section 1.5) and then some initial ideas related to line level effects (Section 1.6).

1.1 A brief historical overview of Type II Cepheids

Prior to 1920, the Cepheid classification included everything from RR Lyrae stars to W Virginis and RV Tauri stars. It was not until after this time, when more detailed spectral analysis occurred, that a better understanding of the stars arose.

The causes of the variability of these stars were widely debated, with an orbital theory appearing most popular in the first decade of the 1900s (See Albrecht (1907) for an example paper). In 1914 Shapley suggested a pulsational theory would be more appropriate but was not able to explain the full details of such a theory. Shapley (1918) gave the observational evidence for a period-luminosity relationship and then started explaining this relation based on the pulsational hypothesis (Shapley, 1919). The orbital hypothesis persisted into the 1920s (Hagan, 1920), but it proved difficult to explain the period-luminosity and period-colour relations based on binary stars.

By the 1940s, distinctions were being made between the Classical (Type I) Cepheids, Population II (Type II) Cepheids and Cluster-type Cepheids (RR Lyrae stars). The idea of a conceptual continuum with the Classical Cepheids at one extreme and the Cluster Cepheids at the other was being suggested (Payne-Gaposchkin, 1948). The Population II Cepheids and other intrinsic variables were thought to lie in between the Classical and Cluster extremes. Eventually it was established that all three of the types of Cepheids could not be directly used in the same period-luminosity relation (Baade, 1956). However they did fall in a particular area of the Hertzsprung-Russell diagram known as the Instability Strip (see Figure 1.1). Subsequent research has further refined our classifications so that they now reflect an understanding of the physical processes going on and the

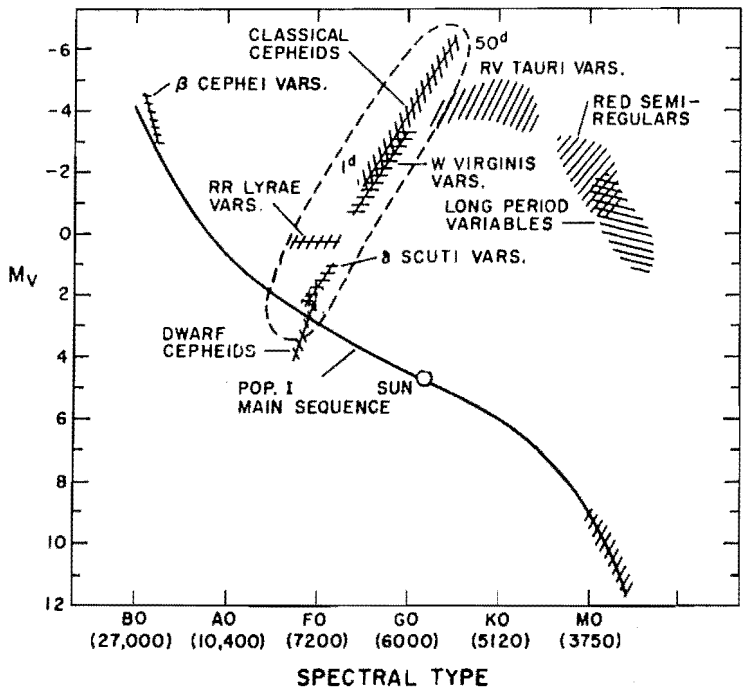

Figure 1.1: A Hertzsprung-Russell diagram showing the positions of some variable stars. The diagram is taken from Böhm-Vitense (1989), who adapted it from Cox (1980).

evolutionary state of the stars.

1.2 The aims and structure of this thesis

This PhD thesis is an effort to further understand the variations of the Type II Cepheids by examining a selection of BL Her, W Vir and RV Tauri stars, focusing on their dynamical variations and their place in the scheme of things.

Most variable stars tend to be categorised by the shape of their light curves. Within the Type II Cepheids, there is a distinction between the behaviour of the short period W Virginis stars (comprising the shortest period BL Her stars and the slightly longer period W Vir stars) and the long-period, double-peaked RV Tauri stars. However, are the stellar light curves fully reflective of the physical processes taking place? Are certain photometric features better understood by examining concurrent spectra and vice versa? To study this, it was decided to survey a selection of mainly Type II Cepheids of periods ranging from 1 to 150 days. Both photometric and spectroscopic data were acquired.

To this end, Chapter 2 details the observational and data reduction methods employed and the photometric analysis techniques used. Chapter 3 covers the spectroscopic analysis methods used, with particular attention to the techniques required for the lines with more complex structure.

Chapter 4 examines all of the photometric data of the stars observed. This consists of a detailed historical review, a Fourier analysis of the photometry establishing the pulsational periods and a comparison with historical photometry, particularly for the W Virginis stars.

As this chapter provides the individual photometric observing histories of the individual stars, these will not be repeated in detail in this introductory chapter.

The next three chapters deal with the spectroscopic observations, with the BL Herculis (Chapter 5), W Virginis (Chapter 6) and RV Tauri (Chapter 7) stars analysed using the photometrically-derived periods. Chapters 5 and 6 examine the mean radial velocity curves phased on the photometric periods and epochs which were then rephased based on the acceleration curves derived from the mean radial velocity curves. The various spectroscopic features are then compared with respect to this phasing. This is also done for some of the RV Tauri stars.

Chapter 8 summarises the results from the preceding four chapters and seeks the similarities and differences between the types of star and the regularity and long-term behaviour of the RV Tauri stars. Chapter 9 concludes the thesis and details possible future work which has arisen in the course of this research.

Before beginning the detailed research the overall defining characteristics of the Type II Cepheids need to be examined.

1.3 Type II Cepheids and their characteristics

Type II stars are older, often metal-poor stars. In our Galaxy they are found in the Galactic halo, often in globular clusters. They tend to be low mass, as the high-mass stars evolve faster and are no longer in a position on the Instability Strip. Thus, the Type II Cepheids are radially-pulsating, low-mass supergiants. They have evolved away from the main sequence, finished core helium burning on the horizontal branch (HB) and are now undergoing double shell burning associated with the asymptotic giant branch (AGB). This involves an interior shell of helium burning with an exterior shell of hydrogen burning. In terms of their evolution, these stars may be on the horizontal branch, moving red-ward through the instability strip, or evolving through the strip on a blue-ward loop from the asymptotic giant branch (AGB), or on a final blue-ward motion towards planetary nebulae and white dwarf status. The phase of evolution is generally related to the pulsational period of the star.

The Type II Cepheids are divided into three types – BL Her[1], W Vir and RV Tauri stars, covering the spectral range of late A to K with luminosity classes of I–II (Wahlgren, 1993).

1.3.1 BL Her stars

The BL Her stars are the faintest of the three types (V~1- -2, Figure 1.1) and have periods of about 1–10 days. The upper limits of the defining period can vary from paper to paper, with some giving an upper limit as low as 5 days (Wallerstein and Cox, 1984) or 8 days (Alcock et al., 1998). At the fainter end of the instability strip, these stars are thought to be moving red-ward into the instability strip along the horizontal branch towards the AGB (Wallerstein and Cox, 1984). Figure 1.2a shows the light curve of the typical BL Her star SW Tau. According to the General Catalogue of Variable Stars (Kholopov et al., 1990), the V magnitude changes for BL Her stars can be anywhere from 0.3 to 1.2 magnitudes with the amplitudes of the light curves decreasing in the R and I bandpasses. The stars

[1]The BL Her stars are also known as as short-period W Vir stars in some papers.

have bumps after maximum light for periods shorter than about 1.6 days and before maximum light for periods longer than 1.6 days. Petersen (1981) discussed the theory of a progression of bumps in the light curves of BL Her stars, specifically for those with periods from one to three days. Carsons and Stothers (1982) and King et al. (1981) also modeled BL Her type light curves, and described the bumps as being caused by a near resonance between the second overtone and fundamental pulsation modes. The position of the bump is also considered to be useful as an indication of the mass of the star(King et al., 1981). King et al. (1981) did warn that the resonance bump idea should not be extended to larger amplitude Cepheids, as at those amplitudes, shock waves were more likely to cause the bumps.

1.3.2 W Vir stars

The W Vir stars are intrinsically a little brighter than the BL Her stars (V~2- -3, Figure 1.1) and have periods of about 10 to 20 days (Cacciara, 1992). The upper limits of the periods overlap with the lower limits of the RV Tauri stars and some stars can be classified in both categories. For some long-period W Vir stars, the amplitude of the light variations can change from pulsation to pulsation. Thus you can get alternation of the depths of the minima, creating light curves in the characteristic shape of the RV Tauri stars. However, this is only for the long-period W Vir stars. The majority have light curves in the shape of Figures 1.2b and 1.2c. These are for κ Pav and W Vir respectively. As can be seen, the amplitude of the light curve variations is approximately the same as for the BL Her stars. It falls in the same amplitude range and shows the same lower-amplitude trends for shorter wavelength photometry. These are in the middle luminosity range of the instability strip and are crossing it as blue loops off the AGB. The blue loops are in response to helium-shell flashes (Cacciara, 1992).

1.3.3 RV Tauri stars

The RV Tauri stars are the most luminous Type II Cepheids (V~3- -5, Figure 1.1) and have the longest periods. They are the most evolved stars, being either in a final blue loop through the instability strip or evolving blue-ward towards possible planetary nebula and white dwarf status (Cacciara, 1992). They are generally thought to be at the end of their AGB evolution (Alcock et al., 1998) or are post-AGB stars (Jura, 1986).

As stated earlier, and as shown in Figure 1.2d for RU Cen, they show more complicated variations in their light curves with a deep minimum being followed by a shallow minimum. This can make statements about the period of these stars confusing. For the purposes of this work the formal period is the time between successive deep minima and will be used throughout this work. With respect to the phasing of the obsevations, the formal period results in the deep minimum defined as phase 0.0 and the shallow minimum as 0.5. The maximum following the deep minimum is referred to as the primary maximum, whereas the maximum following the shallow minimum is the secondary maximum. The convention of referring to the deep minimum as the primary minimum and the shallow minimum as the secondary minimum has generally been avoided here as for some stars a deep minimum is not automatically followed by a shallow minimum and vice versa (see, for example, Figures 1.3 and 4.72a for U Mon). There is no convention for referring to these breaks in the pattern of deep and shallow minima, but they are variously referred

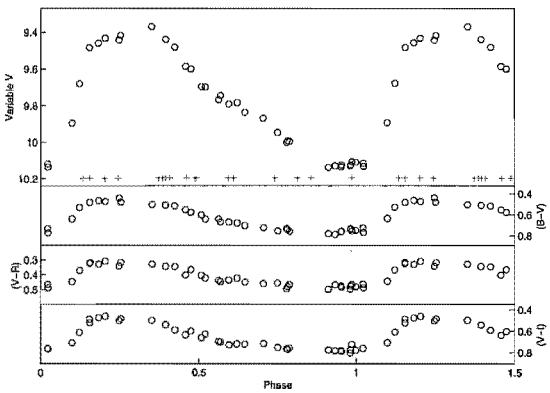

(a) MJUO photometry for SW Tau phased on a period of 1.5836 days.

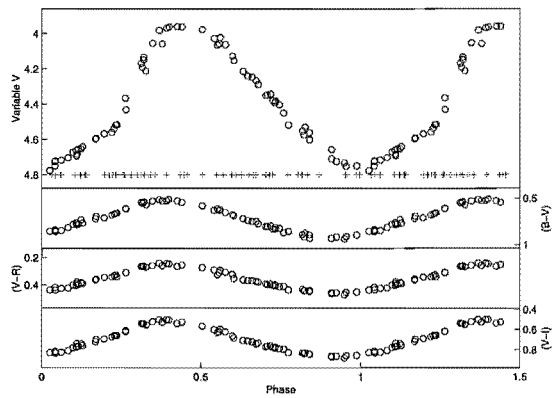

(b) MJUO photometry for κ Pav phased on a period of 9.0741 days.

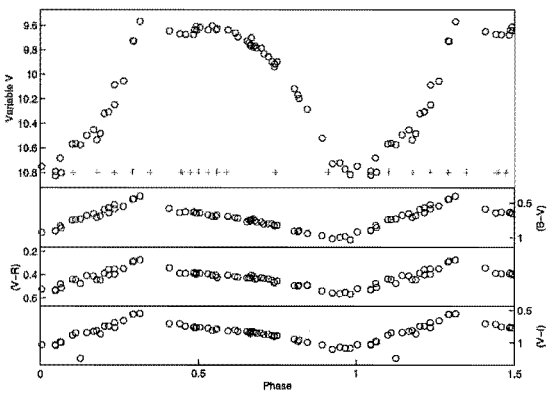

(c) MJUO photometry for W Vir phased on a period of 17.2768 days.

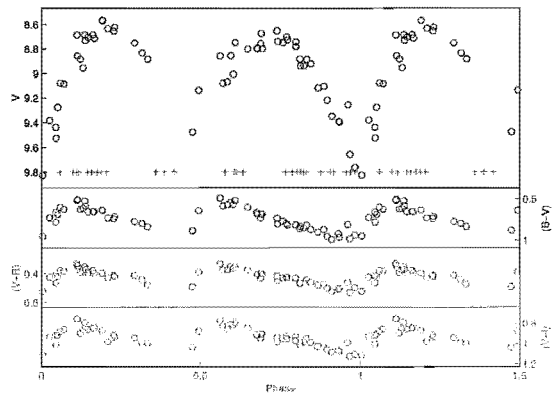

(d) MJUO photometry for RU Cen phased on a period of 64.57 days.

Figure 1.2: Sample phased photometry of Type II Cepheids. (+) indicate phases of spectral observation.

to as "variations", "alternations","switches" or "flips" in the pattern of deep and shallow minima.

Many of the RV Tauri stars show these variations to varying degrees. Some are quite stable in their deep/shallow pattern (eg. AC Her), while others (R Sct and to a lesser extent U Mon) go through phases when they have a stable pattern of deep and shallow minima and then become quite irregular. Percy et al. (2003) used self-correlation of RV Tauri light-curves to attempt to characterise the "RV Tauri-ness" of the stars in terms of the relative depths of adjacent minima and the persistence of the alternating minima with time. They argued that the relative strengths of the period between successive minima and the period between successive deep minima dictates the stability of the alternations. If the periods are in a 2:1 ratio such that the period between deep minima is twice that of the period between successive minima, then the alternating deep and shallow minima will persist, whereas if they are close to but not exactly in the 2:1 ratio

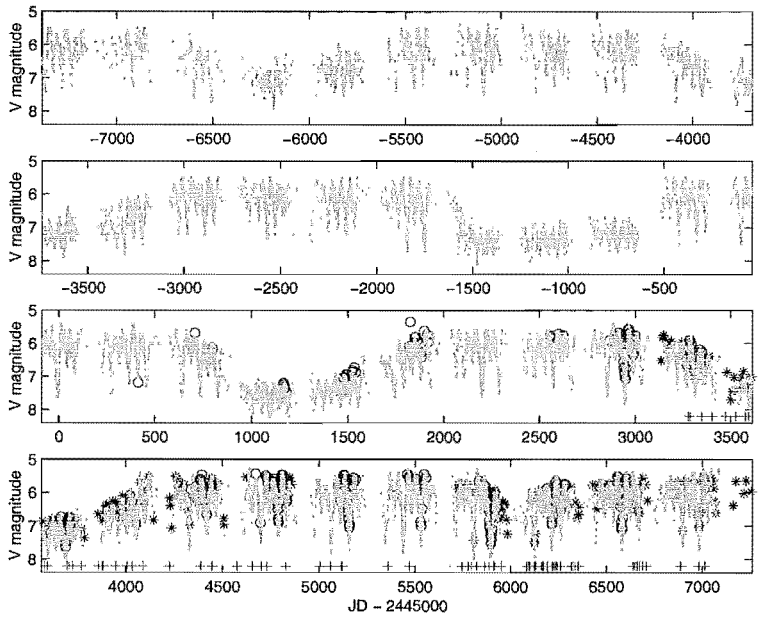

Figure 1.3: Photometry of the RV Tauri star U Mon. The photometry is a combination of Mount John University Observatory (MJUO) service photometry (o), American Association of Variable Star Observers (AAVSO) visual data (.) and AAVSO photoelectric data from JD 2437500 to 2452150. The AAVSO photoelectric data has been offset in magnitude to fit with the MJUO data.

the alternations will disappear after a few cycles. The exact cause of the deep-shallow minima is unknown, but it has been hypothesised that they are double mode pulsators with a 2:1 period ratio (Takeuti and Petersen, 1983) or that they show low-dimensional chaos (Buchler and Kovacs, 1987; Kovács and Buchler, 1988), especially R Sct (Buchler et al., 1995, 1996; Buchler and Kolláth, 2001, 2003).

The formal periods of the RV Tauri stars range from 40 to 150 days (Alcock et al., 1998). The visual magnitude variations are somewhat larger than the other Type II Cepheids with the GCVS giving ranges of 3 to 4 magnitudes. Unlike most other Cepheids, many of the RV Tauri stars show strong infrared excesses, often associated with large amounts of circumstellar material (Gehrz and Woolf, 1970; Gehrz and Ney, 1972; Lloyd Evans, 1985; Goldsmith et al., 1987). Photometrically, the RV Tauri stars can be classified into two subgroups: those with constant mean brightness (RVa) and those with long-term variations in this mean brightness (RVb). The causes of this long-term variation have been widely debated but suggested mechanisms include a single star which is periodically eclipsed by dust in an R Coronae Borealis-type outburst (Shenton et al., 1994b; Zsoldos, 1996), a binary star system (Percy, 1993) with such an outburst (Fokin, 1994) and a binary system in which the pulsating star is periodically eclipsed at certain phases in its orbit by a circumbinary dust torus (Waelkens and Waters, 1993), with occasional interaction between the stars depending on their separation (Pollard et al., 1996a; Van Winckel et al., 1999; Fokin, 2001; Maas et al., 2002).

The RV Tauri stars can also be subdivided into three categories based on their spectra. The classification scheme was devised by Preston et al. (1963) and subdivided into A, B, and C subtypes. Type A are G to K spectral type variables which occasionally showed

TiO bands around minimum light (R Sct, U Mon and AR Sgr: Pollard et al., 1997; Preston et al., 1963). Type B stars (RU Cen and AR Pup: Pollard et al., 1997), have peculiar spectra at all phases so are generally not assigned a particular spectral type (Preston et al., 1963) and show enhanced carbon (Pollard et al., 1997). Type C stars are the same as type B but do not show, or have only weak CN and CH bands at all phases (Preston et al., 1963) and are found in globular clusters.

1.3.4 Period changes and period stability

The Type II Cepheids spend a relatively short fraction of their lives in this phase, as they evolve out of the instability strip in several thousands of years (Gingold, 1976). This is especially true for those RV Tauri stars which are thought to be post-AGB stars, and are evolving to higher temperatures and radii (Percy et al., 1991). This evolution should be detectable as period changes, especially for the brighter stars which have been well observed. Percy et al. (1991) reported period changes in U Mon and R Sct. However, these proved to be quite abrupt with the period between adjacent minima decreasing from 46.117 to 45.814 days in 1957 for U Mon and for R Sct decreasing from 70.95 to 70 days in 1941. The abruptness of these changes is not predicted by post-AGB evolutionary models, but Percy et al. (1991) indicated that the amount of period change was consistent with the models. Matsuura et al. (2002) disputed this in the case of R Sct. They examined similar photometry by wavelet analysis and found that the period of R Sct fluctuated about a mean but did not show a consistent trend. They found this behaviour consistent with an AGB star rather than a post-AGB star. Prior to this, Percy et al. (1997), examining period changes in 15 RV Tauri stars, also found large fluctuations in period which were attributed to random cycle-to-cycle variations in period. These would make true evolutionary changes in period difficult to track (Percy et al., 1997).

The period changes are not confined to the RV Tauri stars. Gonzalez and Wallerstein (1996) found abrupt changes in the period of ST Pup. Prior to JD 244 1064, they found a period of 18.54694±0.00003 days, with a period of 18.4647±0.0002 days after that date. Overall, the observed trend in the Type II Cepheids appears to be for the periods to be more stable and regular for the shortest-period stars, with the degree of stability decreasing at longer periods, especially for the RV Tauri stars.

1.4 Stellar pulsations

As stated earlier, the current understanding is that the 1 to 150 day variations of the Type II Cepheids are caused by the radial movement of the star's outer layers. The pulsations are caused by instabilities occurring in areas of ionised hydrogen at $\sim$ 10 000 K and doubly ionised helium at $\sim$ 40 000 K. The areas where the stellar gases are in these states are known as the driving layers. It is the thermodynamical properties of these layers which drive the pulsations and the mechanisms by which this occurs are known as the kappa (κ) and gamma (γ) effects. Both mechanisms involve the blocking of light attempting to exit the star, with the blocking being due to a higher opacity (κ) of the gas for the κ effect and increased ionisation with respect to specific heat (γ) ratios for the γ effect. Both methods increase the amplitude of existing instabilities rather than creating them. In the κ effect the out-flowing light is blocked by the higher opacity gas, expanding the gas outward until the density decreases to the point where the opacity is lower and

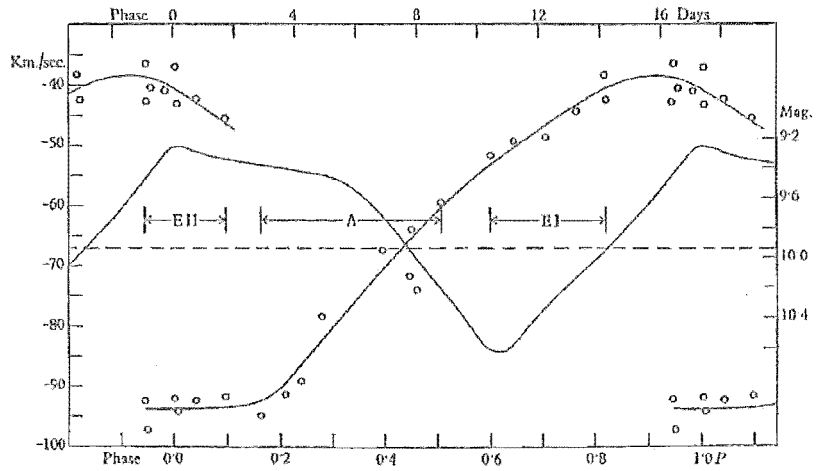

Figure 1.4: Historical radial velocity and light curve of W Vir from Sanford (1952).

the light is no longer absorbed by the gas (Cox, 1980). Energy flows more easily when the gas is expanded ,which reinforces the expansion (Cox, 1980). In the γ effect, when the gas is compressed the work done goes into ionizing the gas with only a small part raising the temperature. Later in the phase, when the gas is expanding, recombination recovers the ionisation energy and this energy reinforces the expansion (Cox, 1980).

1.5 Shock waves in Type II Cepheids

The understanding of the processes inside the stars is further complicated by the presence of shock waves propagating out through the stellar envelope. The chief evidence for this is in the appearance of emission lines and line doubling at certain pulsational phases. One of the earliest descriptions of this was by Schwarzschild (1954) to explain the observations in W Vir (Figure 1 of Sanford, 1952, repeated here in Figure 1.4). The line splitting is due to the velocity difference on either side of the shock, with material on one side falling inward (red-shifted), and on the other side being pushed outward (blue-shifted) by the pulsations. An approximate representation of the shock propagation and line effects is shown in Figure 1.5, reprinted from Alvarez et al. (2000).

The emission observed by Sanford is thought to be associated with material de-exciting and emitting photons after being excited by the shock. The shock wave rushes through faster than the speed of sound in the medium it is traveling in and compresses, heats and accelerates the gas it is in. The shock itself is divided into several zones, as shown in Figure 1.6, reprinted from Gillet and Lafon (1983). The first is the precursor. It is in front of the shock front and is where radiation heats and possibly dissociates and ionises the gas. Next is the actual shock front or discontinuity where the gas is accelerated, heated and compressed by already shocked material. The following layer is the relaxation layer where the shocked gas can cool by emitting radiation. The gas in this layer can also change its state as it can be ionised by collisions behind the shock or recombine further behind the shock. The final layer is the thermalisation layer where the radiation from the relaxation layer is absorbed and re-radiated (Gillet and Lafon, 1983; Hollenbach and

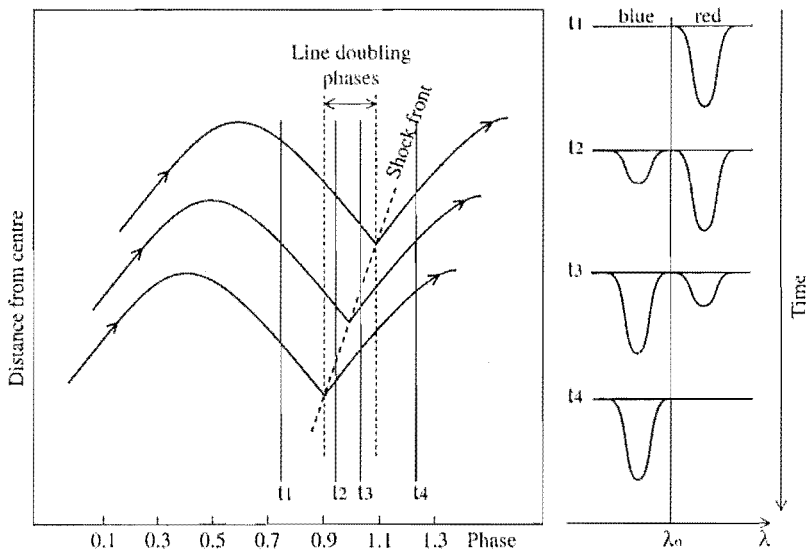

Figure 1.5: Schwarzschild line doubling mechanism (from Figure 1, Alvarez et al., 2000)

McKee, 1992).

Shock waves have been studied in the context of various Type II Cepheids: BL Her (Gillet et al., 1994; Fokin and Gillet, 1994); W Vir (Wallerstein, 1959a,b; Lèbre and Gillet, 1992); R Sct (Lèbre and Gillet, 1991a,b). However, a great deal of the work has been undertaken with respect to modelling and the observations have yet to achieve the level of detail described by the modelers, in order to test their models. A major part of testing these is getting a greater spatial resolution of the behaviour at different depths of the star as a function of time. One way of examining this is through the different line level effects observed in the stars.

1.6 Line level effects in Cepheids

Line level effects have been observed in both Classical Cepheids and Type II Cepheids. More detailed work has been undertaken on the Classical Cepheids. These line level effects are defined as phase-dependent velocity differences between lines of different excitation and ionisation potentials (Kiss and Vinkó, 2000). These are due to the fact that different lines are formed in different regions of the star, influenced by their intrinsic line strength, species abundance, excitation potential and the temperature of the star at various depths.

The largest differences are generally observed between the visual and infrared layers, due to the fact that the continuous opacity varies as a function of wavelength in Cepheids (Sasselov and Lester, 1990). At 1.2 microns there is a continuous opacity minimum due to the H− ion, so certain infrared atomic lines which are formed deeper in the star geometrically, are visible. This cannot be taken as a general statement however, as certain molecular lines observed at infrared wavelengths form under much cooler conditions and so may be formed much further out. The line level differences are especially noticeable in R Sct where the optical wavelength atomic lines vary on the period between successive

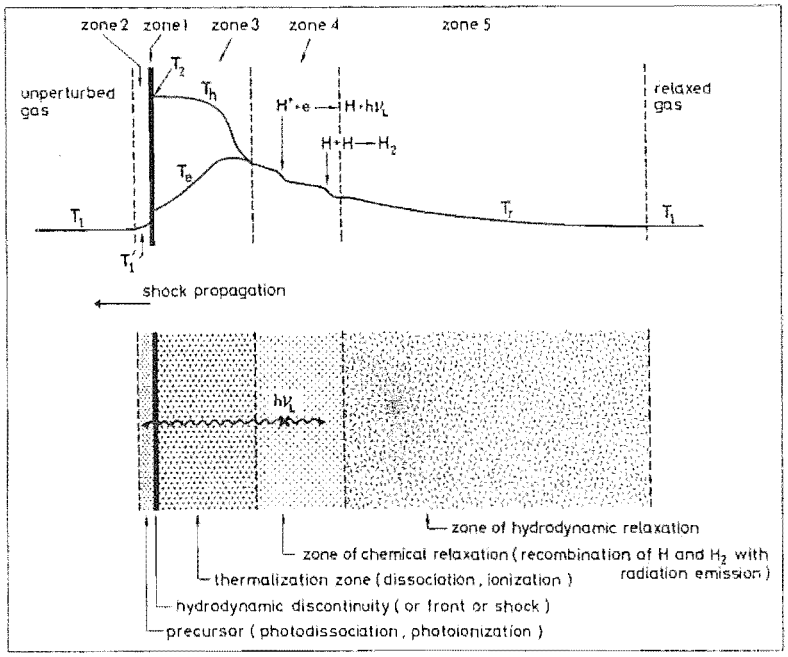

Figure 1.6: Shock structure from Figure 1, Gillet and Lafon (1983).

minima whereas the infrared atomic lines vary on the longer period between successive deep minima (Mozurkewich et al., 1987; Hinkle et al., 1996; Pollard et al., 1996b).

Smaller differences are observed in the atomic optical lines. These reflect a velocity gradient across the line forming regions of the star. This has been observed in Classical Cepheids by Butler et al. (1996) and Petterson (2002), who found the general trend that the shallower the line was formed in the atmosphere, the greater the amplitude of the velocity variations and the later in phase the peak velocity occurred. To a certain extent this has been observed in Type II Cepheids, but it has been mainly studied as a difference between the mean metallic line velocities and the Hα line velocities (Wallerstein et al., 1992; Vinkó et al., 1998). This is not exactly the same as the differences observed between various metallic lines as the line forming regions are much narrower for the metallic lines observed, in comparison to the Hα line which can form over a greater range of optical depths.

If different lines can be associated with different regions of the star, then by monitoring these different lines, velocity gradients and, at the extreme end, the passage of shock waves can be tracked through the star as a function of time. This has already been done for Long-Period-Variables (LPV), where numerical masks have been created to model the different depths of Miras. These masks are then cross-correlated with spectra to investigate line splitting due to shocks in the different levels of the stars (Alvarez et al., 2000). However Miras have the advantages of long periods and large atmospheres so differences are easily resolved. The more compact Type II Cepheids do not have this advantage but, as will be seen from Chapters 5, 6 and 7, different line behaviours can be observed.

Chapter 2

Observation and reduction procedure

In this chapter, the data-gathering and reduction techniques are examined. We give the reasoning behind choosing the selected stars and then detail the observing techniques used, including the equipment and software used. Following this is an exposition of the data reduction methods employed, both for the spectroscopic and the photometric observations obtained.

Table 2.1: Observing program Cepheids in order of increasing period.

Star	Type	Period[a] (days)	V range	Spectral Type [b]
VY Pyx	BL Her	1.239938	7.15–7.4	F3/F5III
SW Tau	BL Her	1.583560	9.4–10.2	A7
V381 Cen	Classical Cepheid	5.07878	7.2–8.0	F8Ib/II
TX Del	BL Her?	6.1634	8.9–9.6	F8
κ Pav	W Vir	9.0741	4.0–4.8	F5Ib/II
AL Vir	W Vir	10.2950	9.2–10.0	F3/F5III
W Vir	W Vir	17.2768	9.6–10.8	F0Ib
ST Pup	W Vir	18.6204	9.6–10.8	G2Iab
SX Cen	RVb Tauri	32.82	9.1–11.4	G3/G5Vp
TT Oph	RVa Tauri	60.97	9.4–10.7	F5pe
RU Cen	RVa Tauri	64.57	8.5–9.8	G2w
CT Ori	RVa Tauri	67.42	10.3–11.2	F9
AI Sco	RVb Tauri	71.45	8.8–11.2	G4
AR Pup	RVb Tauri	76.47	9.1–10.1	F0Iab
AR Sgr	RVa Tauri	87.13	9.1–10.4	G4
UZ Oph	RVa Tauri	88.90	10.2–12.5	G2
U Mon	RVb Tauri	91.79	5.5–7.8	K0Ibpvar
R Sct	RVa Tauri	134.87	4.9–6.7	K0Ibpvar
TX Oph	RVa Tauri	135.81	9.7–10.7	G0
IW Car	RVb Tauri?	142.73	7.8–9.2	A4Ib/II

[a]Between successive deep minima for RV Tauris and successive minima for the rest.
[b]Classification from SIMBAD.

2.1 Selection of stars for study

The twenty stars chosen for study are listed in Table 2.1. They were initially selected on the basis of their classification in the General Catalogue of Variable Stars (GCVS)

(Kholopov et al., 1990). Of these, four were listed as BL Her stars and four as W Vir stars. Of the remaining twelve RV Tauri stars, six were listed as RVa stars, five as RVb stars and one was simply classified as RV Tauri. Further selection criteria were their brightness (spending at least part of their time brighter than 10th magnitude in the visual wavelengths), and location in the sky, so as to be observable at least part of the time using the Mount John University Observatory (MJUO) 1m telescope and equipment. The stars were also selected so as to cover a wide range of periods and thus get the maximum range of behavioral patterns for the three types of Type II Cepheids.

Later research and observation has changed the status of several of the stars on this list. V381 Cen was found to be a classical Cepheid but was included as a comparison to the other stars. TX Del was found to possibly be a classical Cepheid but was continued due to it being in a binary system and thus being useful to test several of the methods used on the RV Tauri binaries. In addition, ST Pup is chemically peculiar and κ Pav behaves in an atypical fashion, as does VY Pyx.

2.2 Data collection

Two main sources of data collection were employed for this research. The first was spectroscopic observations, undertaken using an échelle spectrograph with a red cross-grating mounted on the 1m telescope at MJUO. Details of the equipment and settings used are given in the following section. These were gathered at (on average) monthly intervals with approximately one-week-long observing runs, from March 1999 to June 2001. Also included in this thesis were spectroscopic observations of the listed stars (mainly U Mon) obtained by various University of Canterbury staff and students from October 1997 onward. These earlier observations were made using the same spectrograph and telescope as later observations but with a smaller CCD chip (Thomson CSF TH7882 CDA). For details of this system, see Pollard (1994), Tobin (1990) and Tobin (1992).

Concurrent with these spectroscopic observations, the stars were also monitored photometrically as part of the service photometry program undertaken at MJUO by Alan Gilmore and Pam Kilmartin. All the stars in Table 2.1 (except U Mon and R Sct) were observed in the *BVRI* bands, with these two exceptions being observed in the *UBVRI* bands. This was ongoing, with the frequency of observation dictated by the weather and the availability of the Optical Craftsmen (OC) 0.61m telescope at MJUO. The RV Tauri and less regular W Vir stars were monitored as often as possible to keep track of their less predictable photometric variability. The remaining, more regular, stars were observed often enough to establish regular light curves and then reduced in priority for observation on the service photometry schedule such that only occasional observations were made to confirm the continuing light curve patterns. These observations were made between April 1999 and May 2002.

2.2.1 Spectroscopic observation methods

Spectroscopic observations consisted of five or so flat field images taken at the beginning and/or end of the night, and then a sequence of Th-Ar calibration image, stellar image, and another Th-Ar calibration image. As well as the Cepheids on the observing program, a selection of radial velocity standard stars (listed in Table 3.1) were also observed for calibration purposes.

The telescope used for these observations was the McLellan 1m telescope. It had an échelle spectrograph directly mounted at the Cassegrain focus. The telescope was used in the f/13.5 configuration, that is to say a Dall-Kirkham optical setup with an ellipsoidal primary mirror and spherical secondary mirror (Nankivell and Rumsey, 1986).

The échelle spectrograph used a grating with 79 groove mm^{-1} and a blaze angle of $\theta_B = \arctan 2 = 36°26'$ (Pollard, 1994). Reciprocal dispersion of the spectrograph as of 1994 was 2 Å mm^{-1} at Hα, giving a resolving power R of approximately 30 000 (Pollard, 1994). However, in early 1998 a focal reducer was installed in the spectrograph which changed this to a reciprocal dispersion of 2.6 Å mm^{-1} on average (Tobin et al., 1998). This meant there was a considerable increase in the wavelength coverage. Further details on the échelle spectrograph can be found in Hearnshaw (1977, 1978).

The spectrograph was used with a yellow OG530 glass filter to block out second order light and thus contamination of the intended orders.

The size of the CCD chip meant that 16 orders (orders 42–27) of the spectrogram were recorded, ranging from 5430 Å to 8550 Å with some gaps in the wavelength coverage.

The CCD used was a Photometric Series 200 CCD system with 1024 pixels by 1024 pixels with the option of a 100 pixel bias strip. The chip itself was a SITe 003 thinned CCD chip with 23 micron square pixels over-coated with Metachrome II to enhance sensitivity in the blue (Barnes et al., 2000).

Initially observations were controlled using a *Windows* setup with "V for Windows" providing an interface for data acquisition and recording. However, in mid-1999 John Pritchard (and Andrew Richards) wrote and installed a Linux-based program to serve the same purpose. This was called MOJO and proved to be far more stable and less prone to errors than the previous system (Barnes et al., 2000). Under both systems, data was saved to a large central directory for MJUO archiving and to personal directories for general work. In some cases, initial data reduction was done at MJUO (often on cloudy nights), using the same reduction procedure as on the Departmental computers, but for the most part, observations were written to CD using *Easy CD Creator* (under *Windows*) and taken back to Christchurch to be reduced.

2.2.2 Spectroscopic reduction methods

The spectra were reduced using scripts written for the FIGARO and ECHOMOP Starlink reduction packages.

Images were recorded at the mountain in FITS format. However before they could be worked with under FIGARO, they had to be converted to the Starlink internal format. At the same time, a bias strip at the side was averaged and removed, and the value subtracted from the image to remove the average bias offset.

The images then had their cosmic rays removed. This process consisted of an algorithm which removed isolated signals from pixels which were five times greater than the square root of the average number of counts in the surrounding four pixels, greater than 0.4 times the average of the neighbours, and at least 50 more than the neighbourhood average. The process was repeated three times until the number of cosmic rays detected each time was sufficiently reduced. A limit of three cycles of the process was chosen to decrease the likelihood of stellar signal being removed.

Once the cosmic rays were removed, the images needed to be flat fielded to remove pixel to pixel variations across the CCD chip. The flat field images were created each

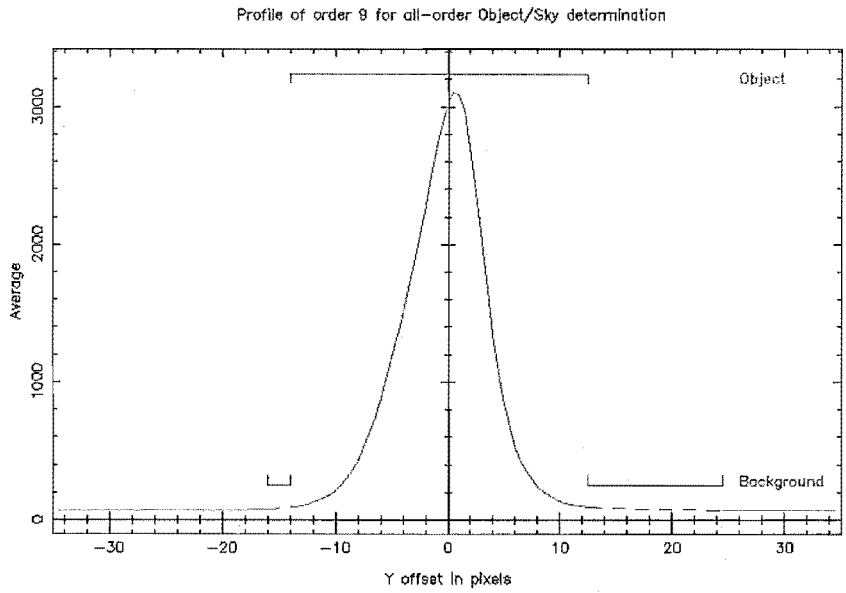

Figure 2.1: Example of object selection within dekker limits from reduction routine.

night by recording the image created by illuminating the spectrograph slit with a white light source. This mapped out the variations across the chip. A series of these images were taken each night and then, during reduction, the total for the night were averaged, thus recording the mean variations, while reducing cosmic ray strike contamination. This averaged flat field image was then used to remove the CCD chip irregularities from all the stellar images. The flat field image was also used to define the dekker limits which dictated what signal was defined as sky and star along each order and what was inter-order signal, to be classed as part of the global background. Then a trace template was made which used a typical star image to place objects within the dekker limits as shown in Figure 2.1.

To speed up the reduction process, a template of identified Th-Ar lines was used in the wavelength calibration. Once these lines were identified on a representative image, the wavelength solutions and any additional information were stored and this wave-template used for observations with similar dekker slopes and wavelength coverage. This reduced the need for repeated manual line identification, a process both labour intensive and time consuming.

The wave-template was then used on the stellar observation to obtain a preliminary wavelength fit. Subsequently, a two dimensional fitting routine was used to optimise the wavelength fit over the observed orders before the stellar spectrum for each order was extracted. This corrected any anomalies in the initial fitting and also provided an opportunity to correct for some second-order effects — see Petterson (2002) for details. Then the sixteen individual spectral orders were extracted from the wavelength-calibrated stellar image.

Next, the continuum was fitted to each order and the observations normalised by dividing by this fitted continuum. This gave a continuum height of one with zero being complete absorption (Pollard, 1994). This was mainly done by an automated routine

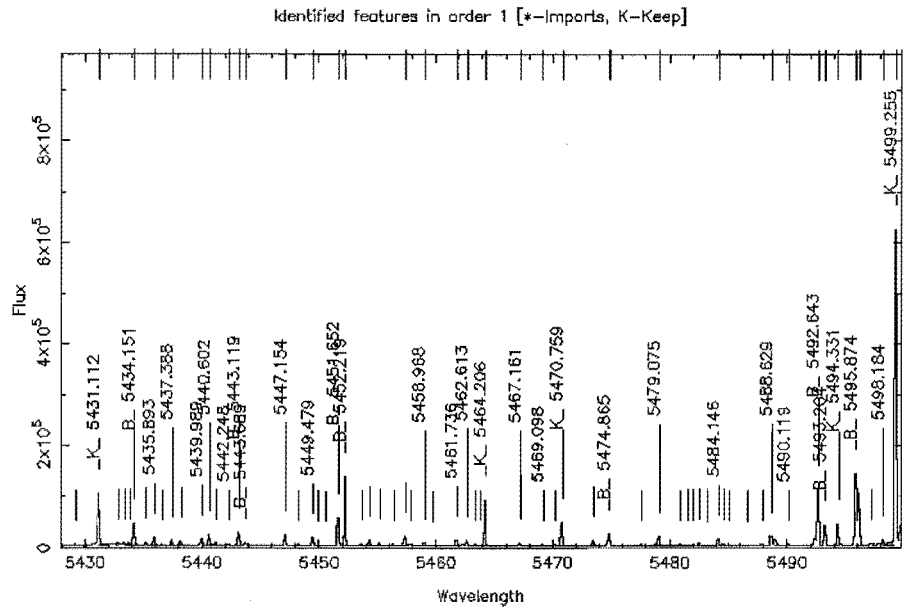

Figure 2.2: Example of wavelength calibration. Image of single order (~5425–5500 Å) showing arc lines and wavelengths.

written by Michael Albrow, which employed MATLAB scripts to fit a continuum to the orders. For orders 1–12 and 14 and 15, this involved spline fitting to the mean signal. However different techniques were required for order 13, which was dominated by atmospheric lines which lowered the mean level, and 16 where two very strong Ca II lines also lowered the mean level. These were then manually inspected to confirm a reasonable continuum fit. Any badly fitted orders, often order 8, where many of the RV Tauri and W Vir stars show a strong emission line, which could upset the automatic fitting routine, were redone manually.

Before heliocentric corrections were applied, velocities from a selection of telluric lines (O_2 and H_2O) were obtained to fine-tune the zero point in velocity space and allow an offset to be applied to velocities obtained later. This was possible as the telluric lines were assumed to be created in an atmospheric layer having a rest velocity of 0 kms^{-1}. The lines were also used to give an indication of the precision of wavelength calibration, and to check for systematic trends such as velocities sloping across orders. This was done, by plotting the telluric line velocities obtained for all the lines of the spectrum in order of wavelength. An example of a correctly-fitted wavelength solution is shown in Figure 2.3a. Any scatter in the points is random and the standard deviation small. In contrast, Figure 2.3b shows a greater variation and scatter in the velocities, indicating the wavelength scale has been distorted and any velocities obtained for stellar lines would be wrong by varying amounts. The standard deviation is large and so the spectrum from which these velocities were obtained was either re-reduced or discarded. A numerical cut off of a standard deviation of 2.5 kms^{-1} was used to cull out data which were too scattered. Additional culling of some observations took place when the velocity slopes across orders were too extreme.

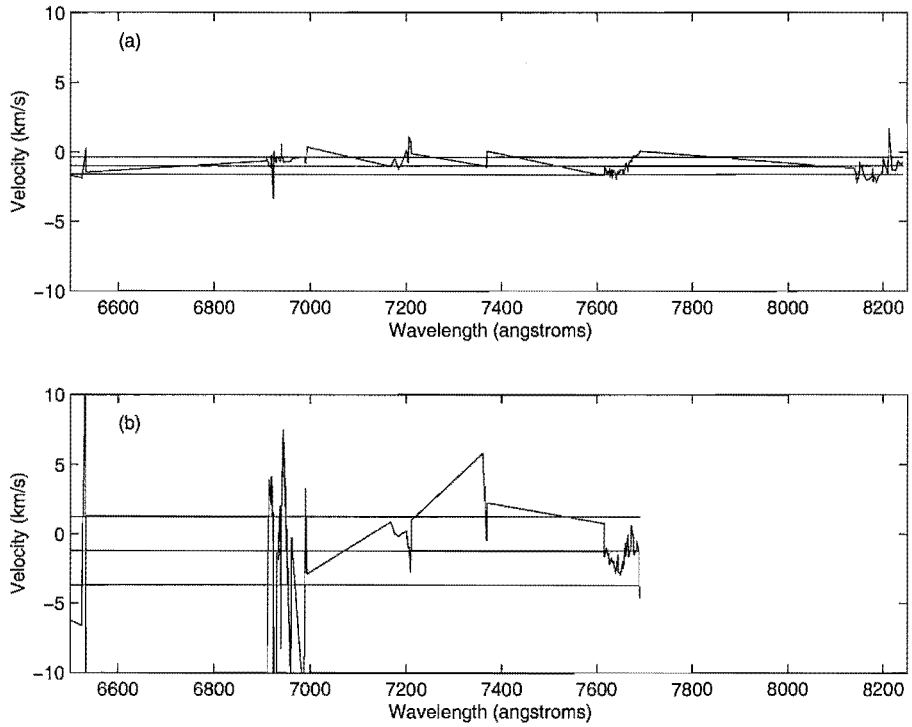

Figure 2.3: Telluric line velocities occuring in the range of 6500–8250 Å. Horizontal lines indicate mean velocity and one standard deviation either side.
(a) Example showing velocity variation from good wavelength calibration of an observation.
(b) Example showing velocity variation from bad wavelength calibration of an observation. Wavelength coverage does not extend beyond 7700 Å due to filter problems (Section 2.2.3).

Heliocentric corrections were applied to account for the motion of the Earth around the Sun, then the spectra were re-linearised in wavelength space to correct for the non-linear effects of the heliocentric correction. After this, a smoothing routine was applied and the spectra were then ready for analysis.

2.2.3 Spectroscopic reduction problems encountered

Over the course of observing, several problems were encountered from which important lessons were learned, particularly with respect to checking instrumentation thoroughly while observing. Some of those affecting the reduction in particular are detailed below.

Filter problems: A rather major problem occurring over the course of several months (March and April 2001), was the use of an incorrect yellow filter in the beam (immediately behind the spectrograph slit). This allowed inter-order light to contaminate the orders, particularly the two longest wavelength ones. Several solutions were attempted. However the contamination of the Th-Ar lines used for identification proved too great for both automated and manual template fitting. The final solution was to only calibrate and work with the 14 shortest wavelength orders. This meant important information on such lines as the Ca II lines at 8498 Å and 8542 Å was lost, but did mean that the information was still available from the other orders.

Further problems were discovered in this subset of observations, when several of the radial velocity standard stars were examined. It was found that the 14-order-observation radial velocities show systematic curves across their orders. This was traced back to a problem with the two dimensional fitting in the wavelength calibration. Petterson (2002) (whose reduction routines had been used) applied an additional quadratic correction to his data to remove systematic residuals in his velocities. This quadratic was found to be systematically increasing the scatter of the 14-order-observation radial velocities and the observations were re-reduced with the quadratic correction removed.

Dekker limit shifts: Another problem encountered was that of the dekker limits shifting by up to 5–10 pixels down the chip during the night, such that the star fell outside the original dekker limits. As long as flat field images were taken at the beginning AND end of the night in the two main different dekker positions, then this was not a problem. Since the dekker limits were defined by the averaged flat field, the average was wide enough to include the star signal from either position.[1] Unfortunately on a number of occasions (six nights in April and May 2000) flats were only recorded at the start or at the end of the night and several of the stars on these nights were shifted. For reduction purposes, the easiest solution was to shift the position of the orders on the averaged flat image by subtracting a strip of pixels from the bottom of the image and adding it to the top. This shifted the orders down by 5–10 pixels and allowed the automated reduction sequence to detect the signal from the star in a usable fashion, enabling reduction to continue as usual.

Missing bias strip: The final example which upset the usual reduction sequence, is a problem with bias measurements. Incorrect use of the MOJO program initially meant that for two runs at the start of April 2000, no bias strip (100 x 1024 pixels at the side of the image) was recorded. To remedy this, on later observing runs, bias images were taken and these images were subtracted from the earlier observations. While this did work on the assumption that the bias amount was relatively constant over the years, all indications were that this was not a problem. Any slight changes in bias would only result in a slight zero point offset, which would affect relative intensities only, and not the radial velocities.

2.3 Photometric observation collection and analysis

As stated earlier in section 2.2, photometric observations were also collected over the same time-span as the spectroscopic ones. The main source of these were service photometry from MJUO. The methods of observation and reduction were those described in Section 2.3.1 and also in Pollard (1994). Other data was obtained from the American Association of Variable Star Observers (AAVSO), Association Française des Observateurs d'Etoiles Variables (AFOEV) and from Albert Jones (private communications). The latter three were a mixture of photoelectric data and visual estimates detailed in Section 2.3.2.

[1] Usually two distinct star positions were observed, indicating that a significant abrupt shift had occurred at some point during the night.

2.3.1 MJUO photometry

The photometric observations were undertaken by Alan Gilmore and Pam Kilmartin using the Optical Craftsman (OC) telescope at MJUO, as part of a larger programme of service photometry. A single-channel photometer with a EMI 9202B photomultiplier tube was used. Details of the method used are as described in Pollard (1994).

The stars were observed by measuring first the sky (S), comparison star (C), variable star (V), and check star (K). Then, measurements were made working back through V-C-S. Sky counts were then calculated and removed from the star observations. By using the number of counts for the comparison star, a differential V magnitude and colours of the variable star could be found which was then added to the V and colours on file for the comparison star. This transformed the observation to standard V magnitudes and colours and was calibrated using observations of E-region standard stars. To confirm this, the check star was reduced in the same way (Pollard, 1994). Thus, constant check and comparison stars were required, and these were selected from the literature or from stars previously used by Pollard (1994).

Since each observation of a star resulted in two magnitudes at two times of observation, these were averaged to give a single measure and then the associated errors in the magnitudes calculated. The lists of these observations were then sorted and those observations for which the V magnitude errors were greater than 0.03 mag, whose check star values were greater than two standard deviations from the mean, whose comparison error magnitudes were greater than 0.03 mag, or whose B-V and V-I errors were both greater than 0.02, were discarded. The photometry from this reduced dataset was then plotted, giving graphs such as Figure 2.4. This shows the light curve of AR Sgr with its comparison and check star photometry.

2.3.2 Other photometry and visual estimates

AAVSO and AFOEV

The AAVSO[2] is a society devoted to collating observations of various variable stars obtained by both amateur and professional astronomers. Organised in 1911 (Saladyga, 1999), it has observations dating from this time and has large datasets on a wide selection of variable stars. Of particular relevance to this thesis were the visual estimates and photoelectric observations of U Mon. This data is available by request from the organization. They also have various computer programs for display and analysis of the data, including the wavelet analysis program used on the U Mon AAVSO visual estimates. The AFOEV is a similar style organisation based in France who supply data from mainly European observers.

The estimates (and photoelectric observations) were provided by various individuals to a central database from which discrepant data points were culled, and the resulting datasets were archived. The visual estimates had a large degree of scatter due to the nature of the observations, but had no seasonal gaps in coverage, and in the case of U Mon, extended back to 1961. An example of how the visual estimates are gathered is detailed later in this section. However the observations refered to there, were obtained from Albert Jones directly and covered all the RV Tauri stars on the program list for a slightly shorter period of time, from 2000 May to 2002 June.

[2] www.aavso.org

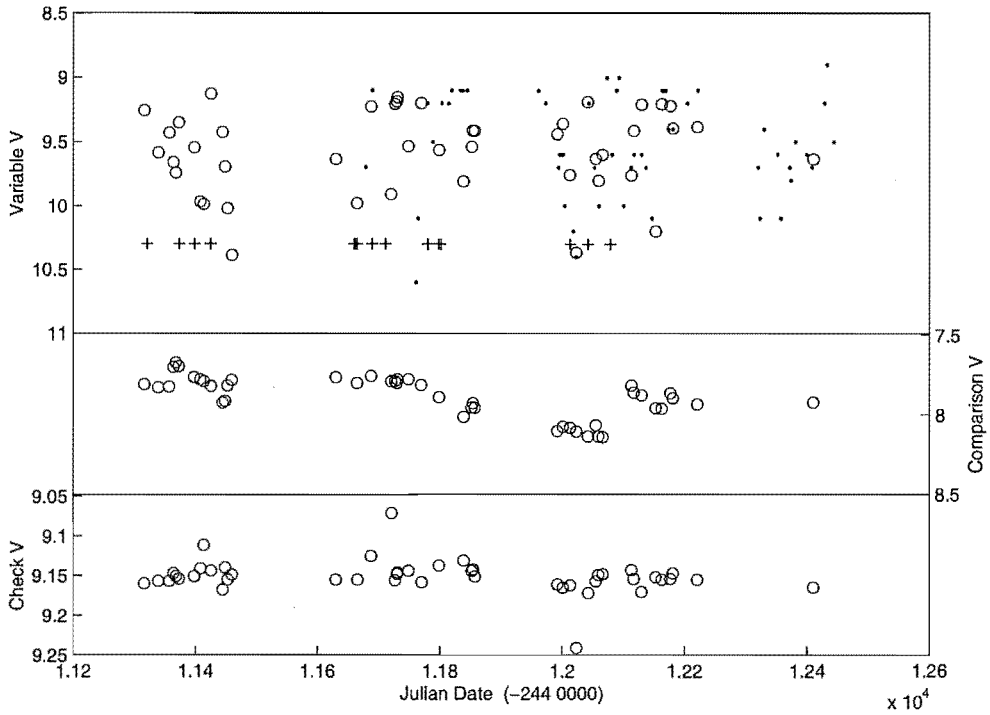

Figure 2.4: Photometry of the RV Tauri star AR Sgr showing variable, comparison and check star photometry. (o) were obtained as part of the MJUO service photometry; (.) were Jones visual estimates; (+) indicate times of spectral observation of the star at MJUO.

Albert Jones visual estimates

The magnitude of the star being observed was obtained by visually comparing it with nearby bright standard stars of known visual magnitude. Care had to be taken with the colour of the star as redder stars could appear brighter if gazed on for too long, and the moonlight conditions also had an effect, making it inadvisable to observe the red stars in bright moonlight. This information and further details of the visual estimate techniques used by Jones are detailed in Bedding et al. (1998).

2.4 Photometric analysis techniques

Two main methods of photometric period analysis have been applied in the course of this thesis: Fourier analysis and wavelet analysis. Each has their advantages and disadvantages and have have been included with the observation and reduction material as they are not in this case part of the tools used in the spectral analysis.

2.4.1 Fourier analysis

The program used was the STAR package created by Lois Balona of the South African Astronomical Observatory (SAAO). This included a variety of Fourier analysis programs ranging from full least-squares periodogram analysis to single-period and multi-periodic Fourier curve fitting. Both the Fourier-type periodogram analysis and the full least-

squares periodogram analysis were trialed on the BL Her and W Vir stars. A Fourier curve was then fitted using each of the derived periods and the residuals of the fit to the observations found. The two periodogram methods were found to produce similar residuals (Appendix C) with the least squares residuals being lower for 5 out of the 8 stars. However the Fourier-type periodogram method proved simpler to operate and so was used for the RV Tauri stars.

The Fourier curve fitted took the form of Equation 2.1 below.

$$\begin{aligned} y = c_o + c_1 \cos 2\pi\phi_{rel} + c_2 \sin 2\pi\phi_{rel} + c_3 \cos 4\pi\phi_{rel} + c_4 \sin 4\pi\phi_{rel} \\ + c_5 \cos 6\pi\phi_{rel} + c_6 \sin 6\pi\phi_{rel} + c_7 \cos 8\pi\phi_{rel} + c_8 \sin 8\pi\phi_{rel} \\ + c_9 \cos 10\pi\phi_{rel} + c_{10} \sin 10\pi\phi_{rel} \end{aligned} \tag{2.1}$$

where: y = V magnitude, c_n = Fourier coefficient, ϕ_{rel} = relative phase = $\frac{remainder\left(\frac{HJD-\phi_{op}}{p}\right)}{p}$ and p and ϕ_o are defined in Table 4.1 and HJD is the Heliocentric Julian Date (i.e. JD - 244 0000).

The Fourier curves were trialed with greater and lesser order Fourier components, but 5 was found to be optimal. This is discussed further with respect to SW Tau in Section 4.1, as are the results of the Fourier analysis of the photometry, in Chapter 4.

2.5 Wavelet analysis

The other photometric analysis technique to be employed was wavelet analysis. This used the AAVSO WWZ program[3]. In this, a Morelet wavelet is fitted to the data in a series of time steps for a range of frequencies with the best fit in the frequency range producing the maximum WWZ value. This allows three free parameters, the frequency being looked at, the time of observation being centred on, and the rate of decay of the wavelet which is a function of the frequency being looked at and the c value correlating to a decay constant. The process is made more complicated by the fact that the data needs to be projected and weighted to get around the uneven sampling. A full mathematical description along with discussion of the advantages and disadvantages of the method are detailed in Foster (1996). For the purposes of this study, three c values were examined using model data to select the c value to apply to the visual data. Figure 2.5 shows a schematic view of the three wavelets generated by the three c values and Figure 2.6 shows the results of using the three different wavelets on the same model dataset. The model RV Tauri light curve was created by adding two sine waves of periods 45 and 90 days, with the data sampling spacing based on the AAVSO visual estimate sampling rate for U Mon, to reflect seasonal gaps and the irregular spacing of the data.

From Figure 2.6, it is clear that the lowest c value gave the most accurate data, with the larger c values obtaining more scattered results for the period and amplitude. This was due to the higher c value wavelet fits being more easily influenced by the seasonal gaps in the data, producing a spurious reading. However the lowest c value was also the longest to run with running times of up to 5 hours over 4000 data points.

[3]for more information on the program see http://www.aavso.org/cdata/software.stm and Foster (1996)

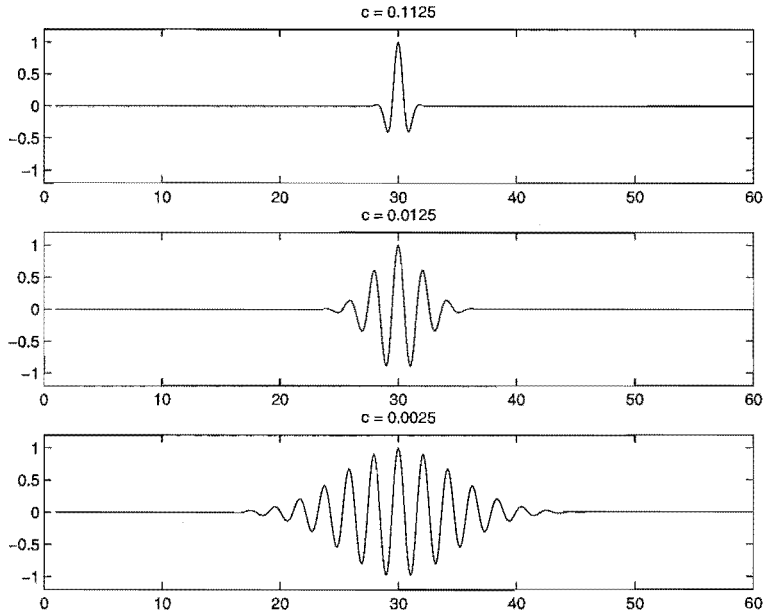

Figure 2.5: Schematic shape of wavelets produced by various c values which govern the decay rate of the wavelets.

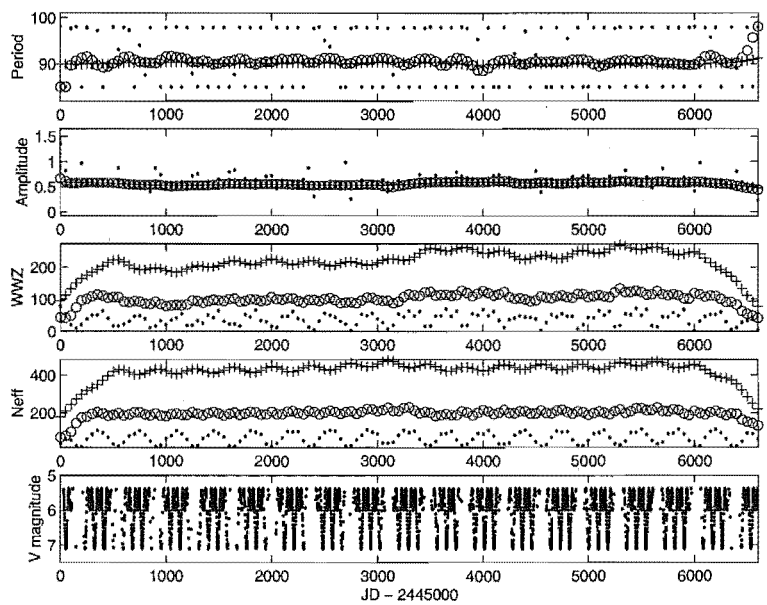

Figure 2.6: Wavelet responses obtained using various c values for the wavelet. (.) c = 0.1125, (o) c = 0.0125, (+) c = 0.0025. Panel 1 (top) shows the period to which the peak wavelet response was found. Panel 2 shows the amplitude of the wavelet fitted at that period, normalized to 1. Panel 3 shows the peak WWZ response which is the equivalent of the peak amplitude on a Fourier power spectrum. Panel 4 shows N_{eff} which gives an indication of the goodness of fit. Panel 5 (bottom) shows the model photometry used.

The wavelet program worked well and allowed time resolution of period changes, but required a high density of data points such that the light curve had to be well defined for each pulsation. In contrast, while not giving the time resolution, the Fourier program could handle one or two data points per pulsation cycle. Thus, the Fourier program was found to be more applicable to the MJUO photometry analysis, whereas the wavelet program could only be used on the high-density observation sets, such as the AAVSO U Mon visual estimate set.

Chapter 3

Spectral line analysis methods

3.1 Introduction

This chapter examines the physics of line formation associated with hydrodynamical motion and how this affects the data-analysis methods used. It then goes on to detail the references used for line identification. The line-analysis methods used are then explained in detail, examining both those used in extracting radial velocities (line bisection and Gaussian profile fitting) and equivalent widths for some of the more complicated lines.

3.2 The effects of mass motion on physics of line formation

The formation of spectral lines is a complicated process, too long to be fully described in the space available here (see Gray, 1992, for full details). Of the various line shaping production mechanisms that act on the continuum to produce the lines present, the one of most concern here is the effect of mass motion of the region over which the line forms. While in most cases, this will produce a relatively clean line profile with a single central core, the presence of shock waves in the stars (as discussed in Section 1.5) can complicate matters.

Material on either side of the shock can be traveling at very different velocities, and if the velocity disparity is large enough, the line may appear split. Material excited by the shock wave, de-excitates behind it, and may create an emission line. Figure 3.1 demonstrates this in terms of the elements of a line formed in different regions of the star at a given pulsational phase. For ease of modelling, the line profile elements have been taken to follow a Gaussian distribution in shape. At the lowest level of the atmosphere (region A), the continuum is approximately flat as conditions are not appropriate for the line to form. Region B however, has the correct temperatures, pressures, and species number densities for light to be absorbed around a wavelength centered on λ_b, a wavelength shifted to the blue from the rest-frame wavelength due to the outward motion of that layer of the star. Region C also has these same temperatures, pressures and species number densities, however it is still falling inward, red-shifting the mean wavelength (λ_r) from its rest position. Marking the border between these two regions is the shock wave, which will propagate outwards over the course of a pulsation cycle. A detailed description of the structure of the shock structure can be found in Gillet and Lafon (1983). The main area of concern here within the shock is the thermal-relaxation zone behind the initial shock, where the de-excitation of shock-heated material can lead to emission line production.

The line can be further altered by absorption from circumstellar material outside the atmosphere of the star, and from interstellar material between the star and us. While these last two factors are not critical to the majority of lines examined here, they are important in the case of such lines as Na D and Hα.

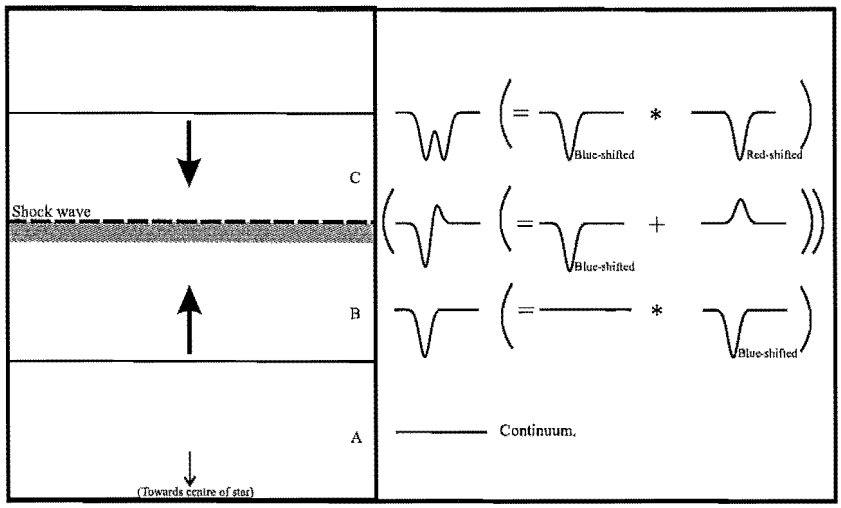

Figure 3.1: Schematic line formation diagram showing line profile combinations. Left panel shows line forming regions in the star. Right panel shows line profiles associated with the light traveling through each region. The profiles associated with emission from the shock are in brackets as they are not always observed to be present.

This is a simplistic view of the situation, and ignores various nuances of the situation. However it does indicate where, and how, different components of the lines are formed, which in turn dictates how the lines are analysed. In the case of the simpler, single component lines (the majority of lines examined), formed either in regions of the star not affected by the shock wave or during phases when the shock wave is absent from the regions where they are forming, the line bisection method of Section 3.4.1 is used. For lines split in two, which may or may not have an emission component, Gaussian profile fitting (Section 3.4.2) has been used. For the more complicated lines, such as Hα, in many of the stars studied here there were too many components to the line which changed position and amplitude. In several cases, no single component could be tracked in a systematic and logical manner. This required a quite different approach, so the equivalent width of the line was used instead (Section 3.4.3). While this method did not give the same hydrodynamical information of the velocity work, it did give correlations between line equivalent width and pulsation which lead to further understanding of the pulsations and motions of these stars.

3.3 Line identification

Before any velocities can be measured, a reliable set of rest wavelengths for spectral lines must be obtained. The final atomic line data used (listed in Appendix E), were obtained from the Vienna Atomic Line Database (VALD)[1]. More information on this database is available at the website footnoted and in Piskunov et al. (1995) and Kupka et al. (2000). Initially, line rest wavelengths from Petterson (2002) were used to find line positions and then measure wavelengths. However, while internally consistent, these are based on only one source. In comparison, the VALD data is an average of the data

[1] http://www.astro.universitie.ac.at/~vald/

available in the literature, with a quantified system of quality control. Using the VALD data resulted in an internally consistent and up-to-date set of wavelengths, log(gf) values, and excitation potentials, with which to determine stellar velocities, compare species, and better understand variations in line strength and depth of line formation.

Rather than re-measure the lines with the VALD wavelengths, a correction to the earlier measurements was applied, which was based on the difference between the Petterson (2002) wavelengths and the VALD wavelengths. This correction was applied at the same time as the telluric line correction, and the resulting velocities sorted and graphed.

3.4 Methods of line analysis

3.4.1 Line bisector method

For the majority of lines measured, the line bisector method (Gray, 1992; Wallerstein et al., 1992) was used. This involved the calculation of a line connecting the midpoints of line segments running horizontally between the sides of the line profile (Gray, 1992). An example of such a fitted line is shown in Figure 3.2. The line bisector method as used here, set the continuum to be at depth 0.0 and the deepest part of the line to be 1.0. The deviation of the bisector line from the rest wavelength was then used to calculate the velocities for line depths of 0.7, 0.8 and 0.9. The final velocity was then a mean of the velocities at these different depths. Other uses of the line bisector method include allowing line asymmetries to be quantified (Gray, 1992), and using the difference in velocities at the different depths to investigate the range of motions of the line-formation regions (Albrow and Cottrell, 1994).

The line bisector method has the advantage that it is easily automated and a standard set of lines can be used for each star. However, the automated method is only effective for clean lines with a single component. It may be applied to two very distinct separate components of a line, but this requires careful selection and placement of limits to ensure the correct positions are found. As such, it works well for determining velocities for standard stars and for the majority of lines in the Cepheids. Different approaches were required for the more complicated cases.

One different approach allowed by the line bisector method, was to parametrize the line into its velocity at depths 0.9 and 0.5, and the line widths at these levels (Figure 3.3). While this did not give clear velocities for separate components, it did allow quantification of the degree of line broadening/splitting. Unsplit unbroadened lines would appear symmetrical, with similar line widths at 0.9 and 0.5, whereas split lines would have broader line widths, and/or greater asymmetry and a greater difference in the velocities at the different depths. When stacked as a function of phase, lines connecting the 0.9 and 0.5 depth velocities gave a vector diagram mapping the asymmetry of the line changing over time. Added to this, line widths could indicate where broadening occurs which in turn could be indicative of the passage of shock waves through the line-forming region.

3.4.2 Gaussian profile fitting

In order to examine the more complicated cases, a program for fitting various combinations of Gaussian profiles was created. This MATLAB script optimised the fit of one or more Gaussians to the observed line profile. Initial parameters of the line depth, position of

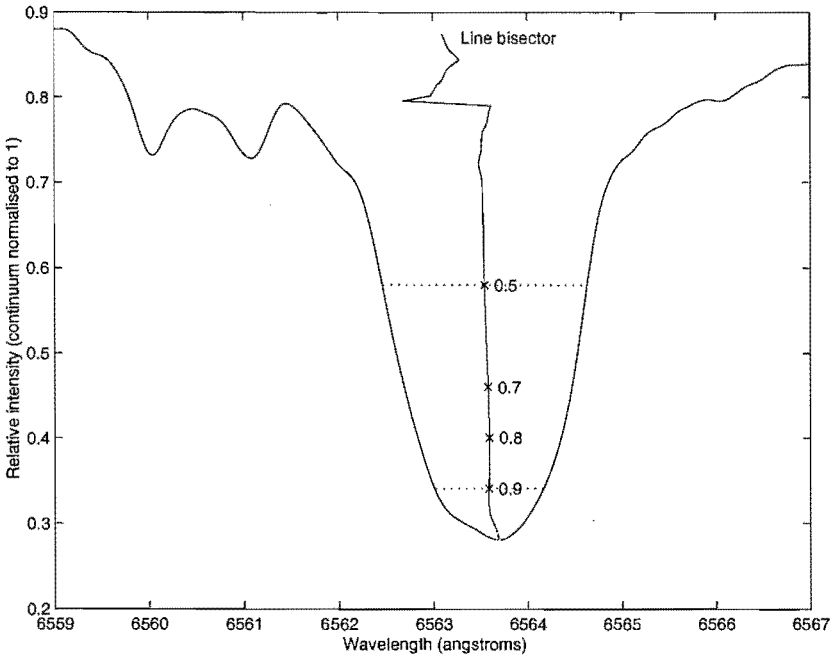

Figure 3.2: Line bisector using the example of an Hα line profile from VY Pyx. The numbers indicate the relative depths of the line bisector. Depths 0.7, 0.8 and 0.9 indicate the line depths used for velocity calculations. Depths 0.5 and 0.9 show the levels and line widths (dotted lines) used when stacking the line parameters.

the peak, and full width at half maximum of the line were used. The equation for the Gaussian distribution used was:

$$y = 1 + A \exp\left(-4 \log 2 \frac{(x - x_0)^2}{f^2}\right) \tag{3.1}$$

where

$y =$ line depth as a function of wavelength x.
$A =$ amplitude of Gaussian.[2]
$x_0 =$ central wavelength position of Gaussian.
$f =$ wavelength full width at half maximum of Gaussian.

All wavelengths used were in angstroms. The shift in the peak position of the Gaussian from the rest wavelength was then used to obtain the radial velocity of the component of the line.

The maximum number of profiles fitted was two, as that gave a total of six parameters to be optimised. Further profiles would only have increased the number of degrees of freedom of possible solutions, and complicated any attempts to relate such solutions to the physical mechanisms responsible.

The physical mechanisms of line formation also affected this method, in that they dictated how the Gaussian profiles were combined. While this was a simple additive process for the emission lines, the absorption lines were more complicated. Each absorption component was the convolution of a Gaussian profile with whatever the line profile of the light

[2]The convention adopted was that absorption was negative and emission positive.

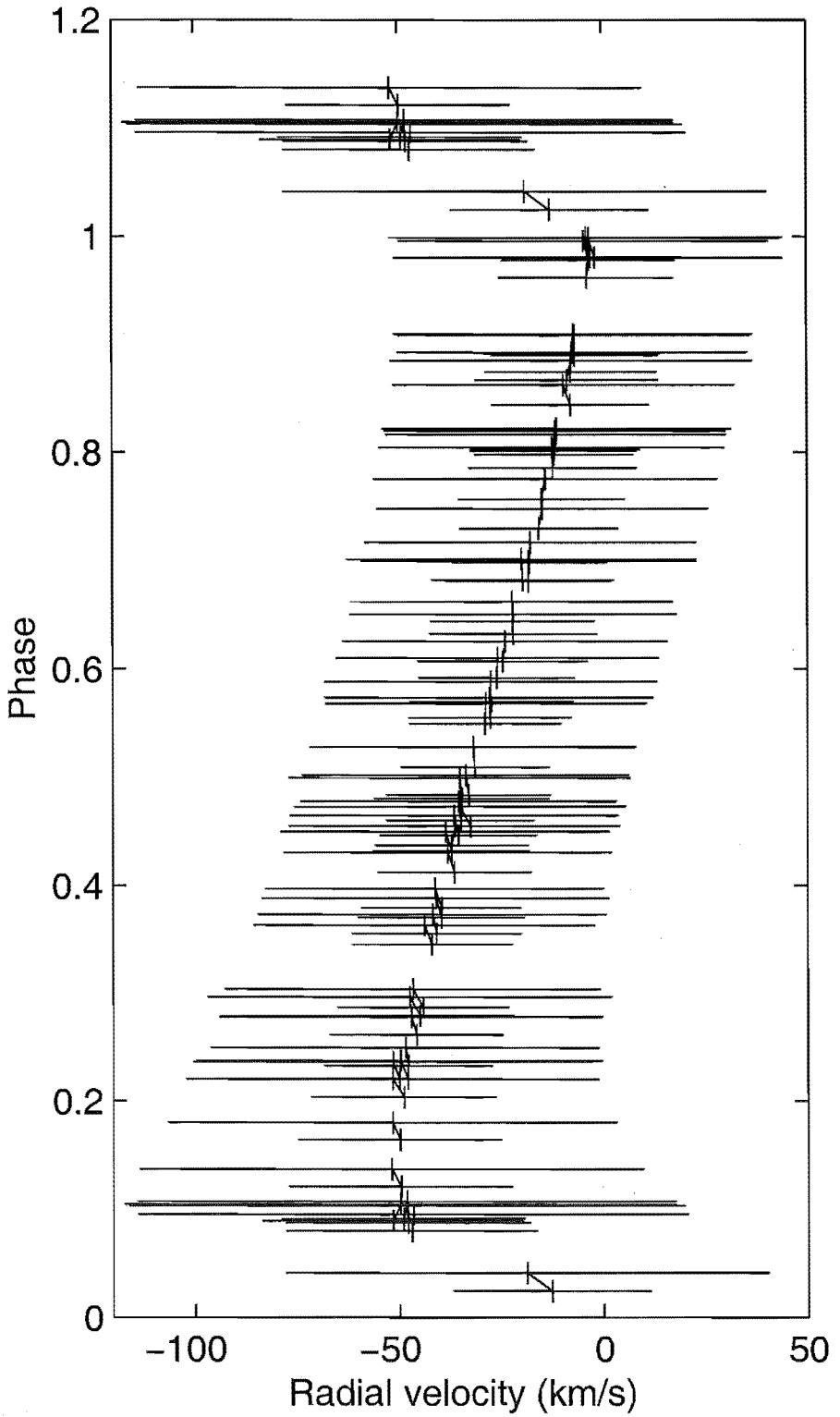

Figure 3.3: Example of line widths and velocities at line depths 0.9 and 0.5 stacked as a function of phase. This example shows the line bisector parameters for V381 Cen for the Hα line (Section 5.3.1).

entering the particular line forming region was. This was straight forward when the line formation region was unaffected by shocks as the profile emerging was the convolution of a flat continuum with a Gaussian profile. The case of a line such as formed in Figure 3.1, Section 3.2, was far more complicated as where the emission occurred changed the shape of the emerging profile. As with the earlier example, the light emerging from region A was the convolution of a Gaussian profile with a flat continuum. The light entering region C however, was the profile emerging from region A which may or may not have an emission line added to it from the passage of the shock front. This resulting profile then had to be convolved with the Gaussian profile which is characteristic of absorption formed in region C. If the particular characteristics of the line-forming region were such that 60% of the light centered on the appropriate wavelengths was absorbed, then on one side of the shock 60% of the light arriving would be absorbed, at a blue-shifted wavelength appropriate to the mean velocity of the line-forming material. On the other side of the shock 60% of that light would be absorbed at an appropriately red-shifted wavelength. This is of course a gross simplification with respect to the line formation, but does give a very basic idea of what is going on with respect to the line formation due to the bulk motions observed in the star.

The end application of this with respect to the Gaussian profile fitting using MATLAB, was the addition of emission profiles and the multiplication of absorption profiles, to fit the given line profiles.

Fitting Gaussian profiles was used more sparingly than the line bisector method as it proved more labour intensive and the velocity derived was more dependent on the line portion selected from which to fit the Gaussian curve. It should also be noted that the two methods of velocity measurement can and will give different velocities for the same line, depending on the line asymmetry. The greater the asymmetry of the line is, the greater the difference between the mean bisector velocity and the velocity of the minimum of the fitted Gaussian. This does however assume that the profile has been fitted to the base of the line. If the degree of line fit is greater to the sides than to the base, the velocity found may be shifted from the true line base velocity. More details of the implications of the differences can be found in Butler (1993) and Sabbey et al. (1995). This does mean that care should be taken in looking for line level effects between lines measured by different methods.

3.4.3 Equivalent width measurement

Where the line line profiles became too complicated for individual fitting, equivalent widths were calculated using the FIGARO program ABLINE. The program required a continuum level to be established from either manual fitting or a previously fitted continuum. The limits of the line were then inputted and the program integrated to find the area bounded by the line and the continuum. If the total area above the continuum was greater than the total area below the continuum, the program treated the line as an emission line. This resulted in the area above the continuum being assigned a positive value, while the area below the continuum was counted as negative and so was subtracted from the total area. However, if the program found the total area below the continuum to be greater, it treated the line as an absorption line, and treated *below* the continuum as positive and *above* the continuum as negative. This resulted in the problem of the program outputting positive values for the equivalent widths regardless of the type of

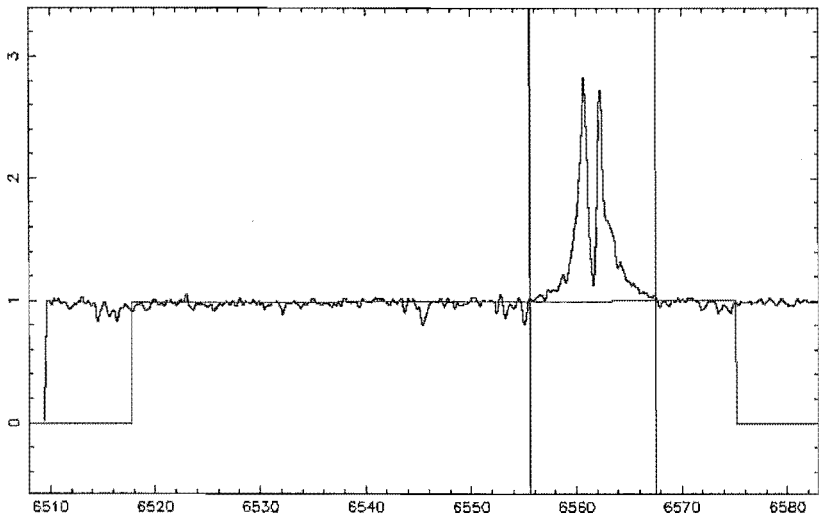

Figure 3.4: Example of ABLINE line fitting. This particular line is the Hα line for TT Oph.

line. To solve this, the convention of the equivalent width being negative for overall emission and positive for overall absorption was adopted for this project.

An additional problem was the definition of the line limits for the equivalent widths. For lines such as Hα, where there could be broad wings in either absorption, emission, or a combination thereof, a standard wavelength limit definition was used for all observations of a particular star. For stars such as W Vir and ST Pup, a wide limit of 6550–6570Å worked well, due to a lack of other lines contaminating that region of the spectrum. The same limit was less successful in the case of U Mon, where it was unclear whether the absorption lines present within the limits assigned were associated with the Hα line production or due to other line species.

3.5 Radial velocity standard stars

Over the course of gathering spectral observations, a selection of radial velocity standard stars were observed, with a minimum of one, or preferably two observed per night. Of these, the stars in Table 3.1 were observed sufficiently often to be able to establish their mean radial velocities to a reasonable degree of accuracy. Also shown in this table are the mean velocities measured, and the velocities of the stars as stated in the Astronomical Almanac 2002. All the velocities agree within the stated uncertainties, with the majority of the measured uncertainties falling under 0.5 kms^{-1}. Of the two exceptions, α TrA was found to show long-term variability by Petterson (2002), and δ Sgr was observed the least of the standard stars. This is shown in Figure 3.5, where a greater degree of scatter is observable in the α TrA and δ Sgr velocities.

Table 3.1: Table of radial velocity standard stars used. Standard velocities are taken from Astronomical Almanac 2002. α TrA has since been discovered to be a long-term variable (Petterson, 2002).

Star	# of observations	Standard velocity (kms^{-1})	Mean observed velocity (kms^{-1})
β Cet	18	13.1±0.1	13.4±0.2
β Lep	13	-13.5±0.1	-13.9±0.4
α Hya	12	-4.4±0.2	-4.3±0.2
β Crv	29	-7.0±0.0	-7.3±0.4
α TrA	15	-3.7±0.2	-4.1±0.6
δ Sgr	6	-20.0±0.0	-19.8±0.8
β Aqr	23	6.7±0.1	6.7±0.3

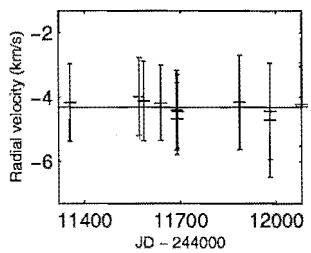

(a) α Hya

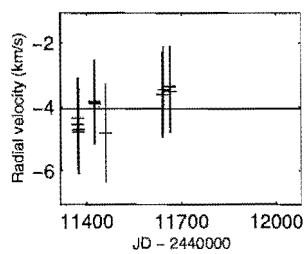

(b) α TrA

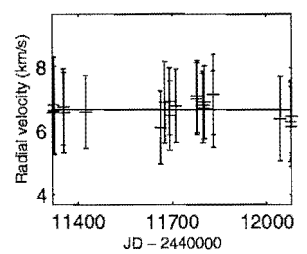

(c) β Aqr

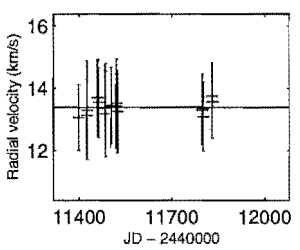

(d) β Cet

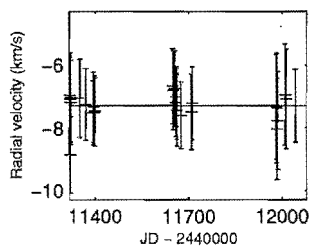

(e) β Crv

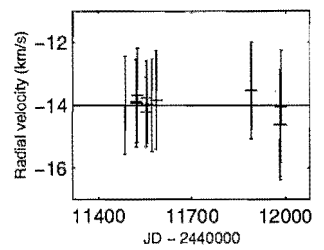

(f) β Lep

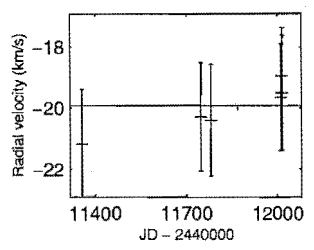

(g) δ Sgr

Figure 3.5: Radial velocities of the standard stars.

Chapter 4

Photometry

In order to interpret the radial velocity data and to understand the motion of the stars studied here, a clear grasp of the pulsation period is required. The simplest means of determining this is by studying the photometric observations of the stars. Hence, photometry was obtained over the same time period as the spectroscopic observations. Photometric phases needed to be mathematically defined and, in the case of the less regular stars, visually confirmed, for phasing the radial velocity data. Possible recent period changes also needed to be identified. In addition, it was necessary to know how regular the pulsations were. While this is trivial for the Cepheids, it is far less so for the RV Tauri stars.

The photometry also provides further information about the evolution of characteristics of the light curves as a function of period, both qualitatively and quantitatively. This is used to look at further links between the stars and examine global characteristics.

To this end, in this chapter the photometry for each of the stars is presented, compared to historical data and the periods determined.

4.1 Photometry and period analysis

Photometric observations of the stars on this program were obtained at MJUO using the Optical Craftsmen (OC) 60cm telescope by Alan Gilmore and Pam Kilmartin. The reduction is as detailed in Chapter 2.

Period finding and fitting problems

In order to establish reliable periods for these stars, a variety of sources of information and techniques were used. In addition to running the MJUO photometric data through a Fourier period-finding program and a least squares version of the same, historical periods were fitted to the data. The optimal period was defined to be the period for which the fitted curve provided the smallest residuals to the V magnitude observations. This period was then used for phasing the other magnitudes and fitting curves to them. The raw Fourier coefficients, phases and periods trialled are found in Appendix C. The program used and the methods employed are found in Section 2.4.1.

An inherent problem with the Fourier fitting for all the stars was finding the appropriate order for the fit. For SW Tau (Figure 4.1), 5th order Fourier components produced the observed double bump at maximum, but failed to fit the side bump at phase 0.75 or the minimum well. A fit with 3rd order Fourier components matched the minimum better, but failed to fit either the side bump and maximum well, and gave greater residuals. A 7th order fit was better at the peaks, but introduced too many variations to the side bump. Hence, a compromise of a 5th order fit was decided upon, as it seemed to fit the inherent scatter of the data better.

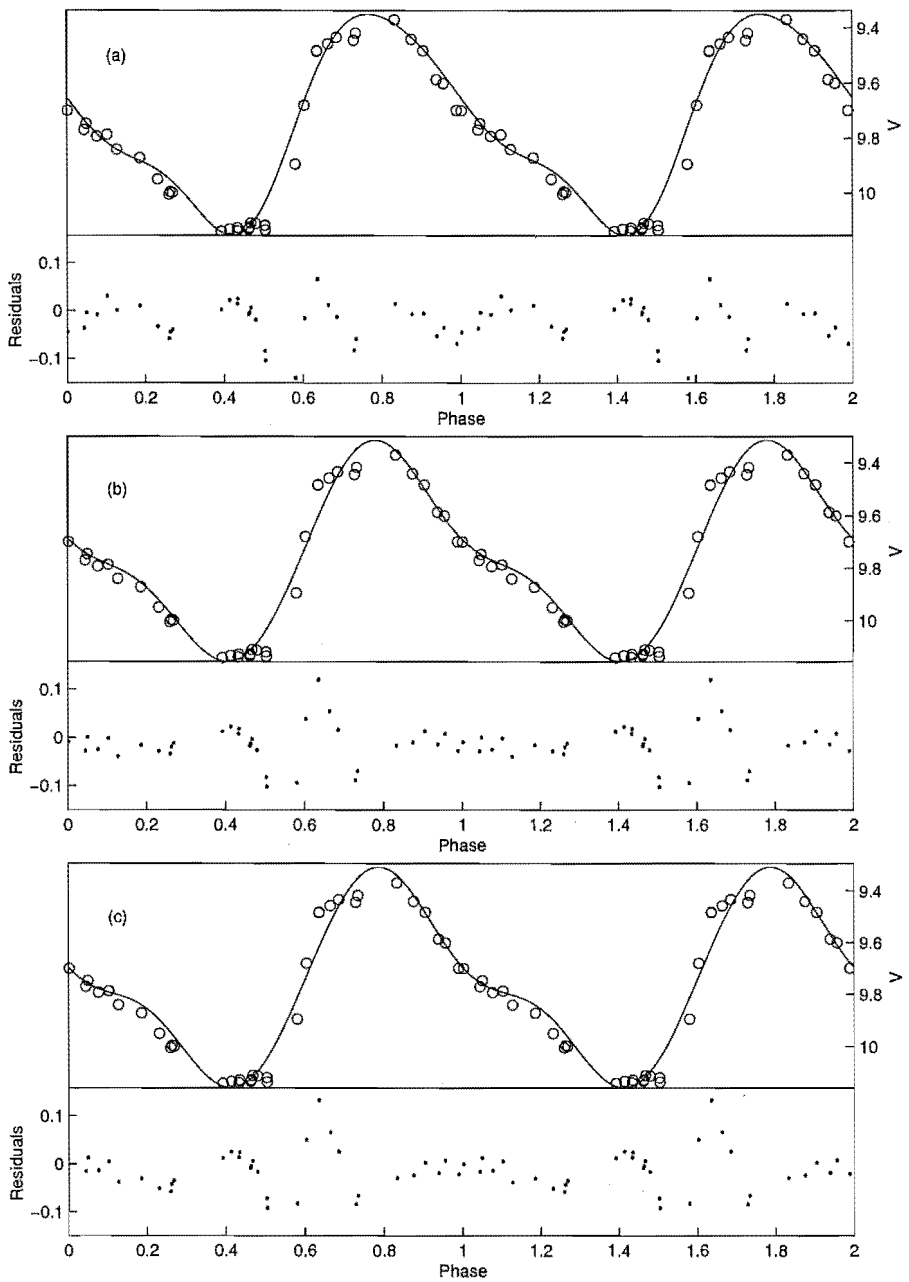

Figure 4.1: Fourier fits to SW Tau V photometry, phased on a 1.58356 day period.
(a) 3rd order Fourier components, mean residuals of 0.0352.
(b) 5th order Fourier components, mean residuals of 0.0346.
(c) 7th order Fourier components, mean residuals of 0.0377.

4.2 BL Her stars

As stated in Chapter 1, the BL Herculis stars are the shortest period Type II Cepheids, with periods between 1 and ~7 days. Numerous comprehensive studies of most of these stars exist, so much of this work will include comparison to the available historical data. The parameters found for phasing the data are summarized in Table 4.1, with the full Fourier parameters in Appendix C.

Table 4.1: Phasing parameters for BL Her stars.

		ϕ_0 [a]	ϕ_{max} [b]	period (p) (days)	RMS Fit (magnitude)
SW Tau	B	-0.128	0.206		0.0269
	V	0.000	0.351	1.583560	0.0281
	R	-0.12	0.358		0.0144
	I	-0.006	0.374		0.0178
VY Pyx	B	-0.003	0.377		0.0109
	V	0.000	0.387	1.2399380	0.0065
	R	-0.007	0.391		0.0084
	I	0.021	0.406		0.0066
V381 Cen	B	-0.018	0.280		0.0047
	V	0.000	0.283	5.07878	0.0042
	R	-0.002	0.284		0.0072
	I	0.012	0.289		0.0084
TX Del	B	-0.036	0.367		0.0109
	V	0.000	0.358	6.1634	0.0090
	R	-0.003	0.376		0.0099
	I	0.003	0.362		0.0118

[a]phase of minimum brightness — defined to be 0.00 for V.
[b]phase of maximum brightness

4.2.1 SW Tau

Historical data

SW Tau has been well studied historically due to it being a reasonably bright northern object. It is a well established Type II Cepheid (see Schaltenbrand and Tammann, 1971). Its period is 1.5836±0.0005 days (see Table 4.2) in some recent studies, with only Hipparcos (of those whose period is sufficiently accurately determined) falling outside this range due to its poor phase coverage. Hipparcos also gave a parallax of 3.04±1.45 milliarcseconds, placing the star 329±106 pc away. The photometric coverage from MJUO observations is far more comprehensive than the Hipparcos data, as can be seen in Figure 4.2. The MJUO photometry is listed in Table B.2 in Section B.1.2.

Table 4.2: Periods for SW Tau.

	Period (days)	Epoch JD - 2440000
Joy (1937)	1.58	—
Schaltenbrand and Tammann (1971)	1.583648	5953.488
Stobie and Balona (1979)	1.583586	—
Henden (1980)	1.583584	1687.773
Moffett and Barnes (1984)	1.583584	1687.770
Meakes et al. (1991)	1.583	—
Hipparcos	1.58368	—
Barnes et al. (1997)	1.583561	5013.249
Arellano Ferro et al. (1998)	1.583584	1761.963
This work	1.58356	11394.477

Period finding and phasing

As seen from Figure 4.3a, the MJUO data phased well on the Moffett and Barnes (1984) period. However, there was a systematic shift between the two data sets. To a first approximation, the phase shift appeared of the order of 0.1 of one pulsational cycle over approximately 20 years. Assuming a period of 1.583584 days, this gave a shift of approximately 2 seconds per year. To test this, the photometric *BVRI* data from Barnes et al. (1997) was included with the MJUO data and the Moffett and Barnes (1984) data. This gave coverage for 1980–82, 1988 and 1999–2002. These data were analyzed together, giving a period of 1.583566 $\pm$ 0.000006 days. This still did not quite phase all the historical data, so the period was stepped through the range 1.583584–1.583538 days in 0.000002 day increments to see if the curves crossed, indicating a common period. The phased curves crossed in the region of 1.583562 to 1.583558 days, with the lowest RMS residuals attributed to 1.583560 days. This indicated a period of 1.583560$\pm$0.000002 days as shown in Figure 4.3c. However, when the RMS residuals of this period are examined for only the MJUO photometry, they are larger than for many of the other periods examined (see Table C.3). Hence, while in this case a common period does exist for the different data sets (which can be found to a high precision), it does not necessarily follow that it is the best period for the current time period. In this case, the period has been taken as 1.58356$\pm$0.00002 days, but the uncertainty in it has been increased to reflect the differing results depending on the data sets used. The finalized curve is plotted in Figure 4.5.

This gives an ephemeris of[1] :

$$\phi = \frac{JD - 2451394.477}{1.58356} \tag{4.1}$$

Fourier fitting accuracy

The different periods found here raised the issue of the accuracy of the STAR Fourier fitting program. The Fourier amplitude as a function of frequency for the full frequency

[1]See also Table 4.2.

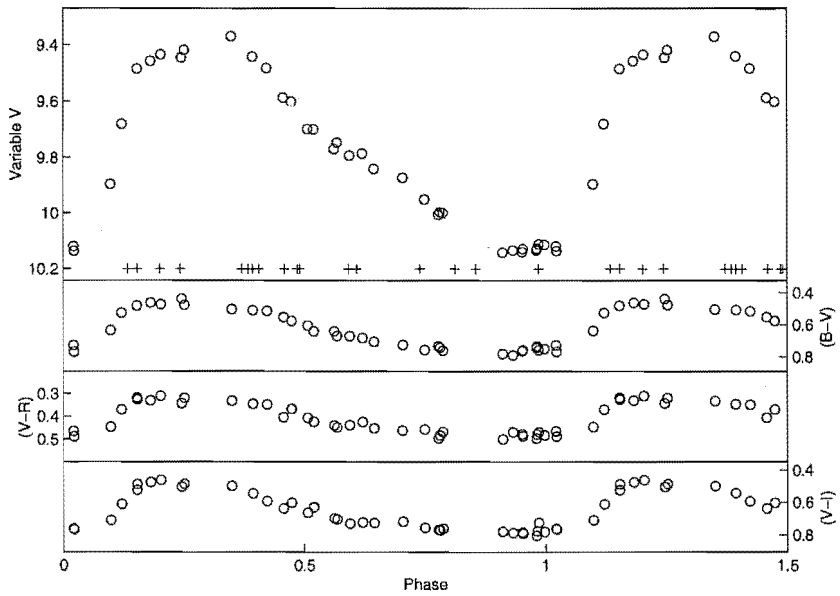

Figure 4.2: MJUO colour photometry of SW Tau phased on a period of 1.58360±0.000002 days from stepping through periods. (+) indicate phases of MJUO spectral observation.

range searched by the STAR package is shown in Figure 4.4. It should be noted that if this figure is scaled such that the range of frequencies stepped through in Figure 4.3 are used as the x–axis limits, it appears as a straight line. Hence, the STAR package periods found are far less accurately determined than those found by comparing to historical data and stepping through it. This should be taken into account before assuming that the period has changed. However, there are not always historical data able to be used in comparison, and in some cases, the period of the star has physically changed since the historical data was obtained.

Photometry curves

As can be seen from Figure 4.5, the light curves of the star are not completely symmetrical or sinusoidal in phase space. The V curve rises rapidly from minimum to maximum light in 0.2 of a pulsational cycle. The curve then becomes less steep towards maximum light for about 0.2 of a cycle. The star then dims more gradually over approximately 0.4 of a cycle, with changes in the slope occurring at phases 0.5 and 0.75. Qualitatively there appears to be a dip around phase 0.5 and a bump around phase 0.75. Minimum light then lasts from phase 0.8 to 1.0. Unfortunately, the phase coverage means that at maximum light, the data points are relatively sparse, whereas minimum light has a high density of observations but only over part of this time period. Hence neither maximum nor minimum light are particularly well defined in the blue and the double peaks at maximum and minimum light does not fit the data well. The fit improves for the redder filters.

This problem with the fitting extends to the times of maximum and minimum in Table 4.1, as for the B filter, the observations show the time of maximum light to be the second "peak", whereas the Fourier fit gives the first "peak" maximum amplitude. The problem is exacerbated for minimum light due to the poor data coverage. For the V

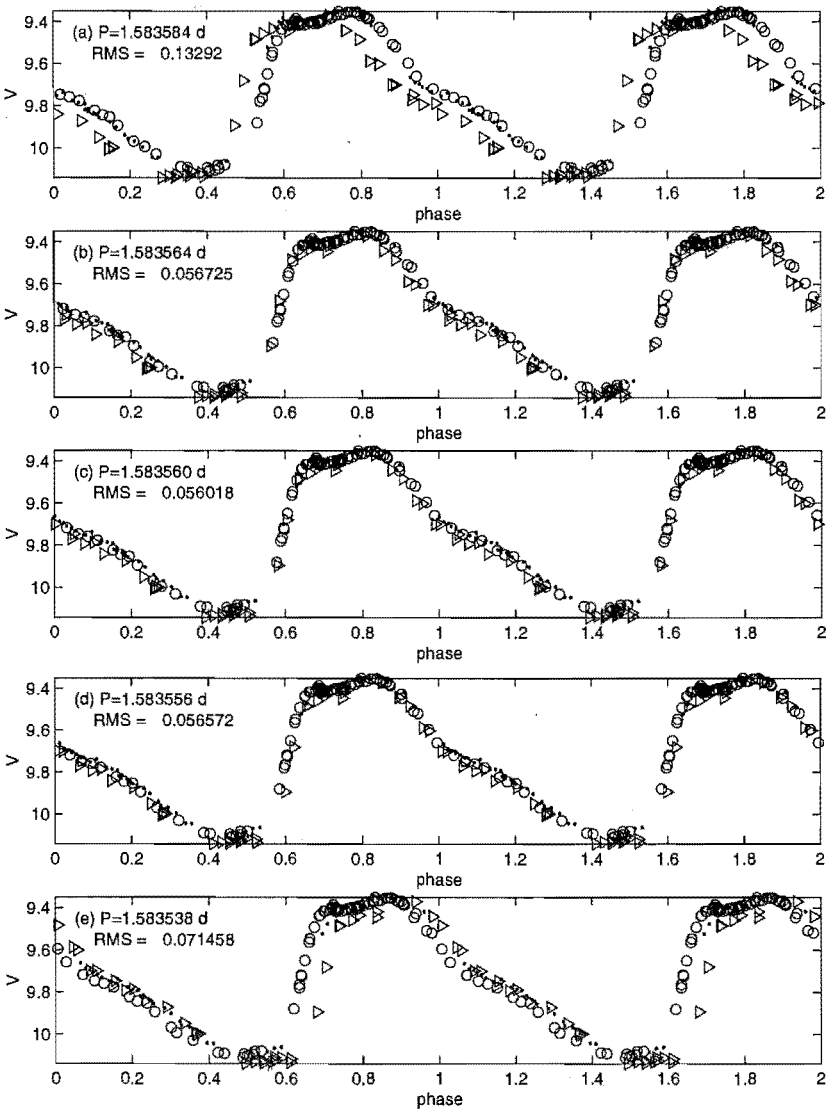

Figure 4.3: Period used for phasing V photometry of SW Tau to test accuracy of periods. (▷) are from Moffett and Barnes (1984), (.) are from Barnes et al. (1997), and (○) are MJUO data. (c) shows the period with minimum residuals.

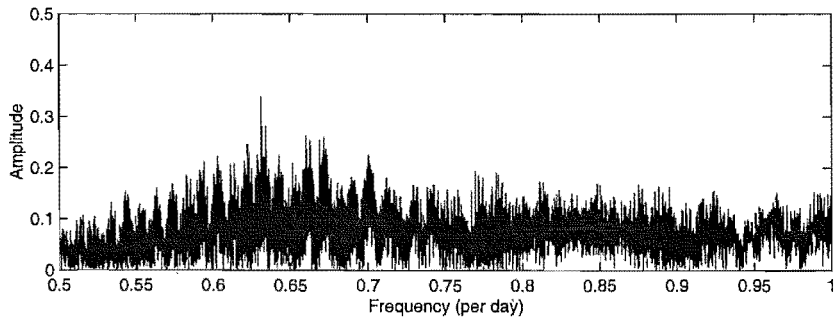

Figure 4.4: SW Tau Fourier amplitude as a function of frequency showing the range of frequencies searched using the STAR package.

photometry (used to provide the phasing zero-point), minimum light occurs at the second "dip", rather than the first, which is where it had occurred in the other filters. Assuming a reflectional symmetry along median light levels and through phase 0.65, it would be expected that the first dip would be deepest, but there is insufficient evidence for that here.

Extending the data set by looking at the historical data from Moffett and Barnes (1984) and Barnes et al. (1997), helped to clarify the shape of the maximum light curve which, as shown in Figure 4.3, was well covered. However, it did not help with the minimum light problem, as they lacked data in similar parts of the curve. There were also problems with different effective wavelengths for the R and I filters, introducing an offset in magnitude to the R and I data. The data could still be compared in terms of their relative amplitude and shape, as shown in Figure 4.6. The change in magnitude was greatest in the B band, and the amplitude became smaller in magnitude for the redder filters. This trend continued into the infrared, with the I and K bands having even smaller amplitudes. The amplitude of the first maximum light "peak" followed a similar trend, decreasing in significance towards the redder wavelengths, until it was barely noticeable in the K band. Unfortunately, possible motions of the second "peak" could not be tracked far into the infrared due to gaps in the Barnes et al. (1997) JHK data, of which only the K band is shown here.

Table 4.3: Periods for VY Pyx.

	Period (days)	Epoch JD - 2440000
Hipparcos	1.239948	—
Sarnwal and Sarma (1991)	1.2400	—
This work	1.239938	11310.187

4.2.2 VY Pyx

VY Pyx (P$\simeq$1.24 days) proved to be quite a contrast to SW Tau (P$\simeq$1.58 days), with no double peaks at maximum nor any prolonged time at minimum light.

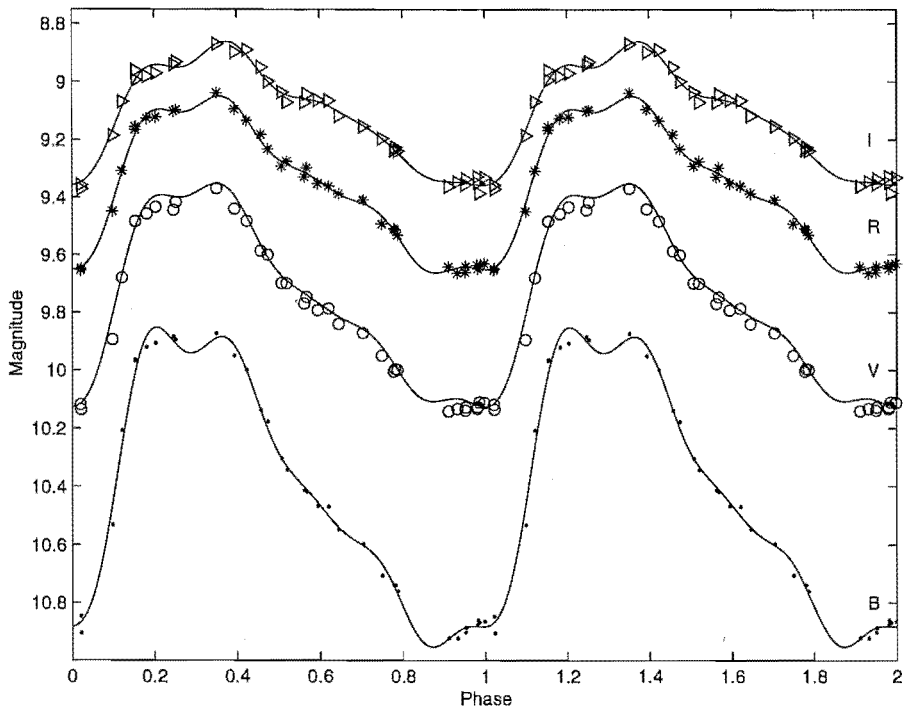

Figure 4.5: *BVRI* magnitudes of SW Tau phased on a period of 1.583560±0.000002 days, the best period for the complete data set 1980–2002.

Historical data

VY Pyx has been studied far less often than SW Tau, which is a little surprising given its relative brightness (V=7.1–7.4), although its southern declination (-23°) may have discouraged many observers. Only Hipparcos and Sarnwal and Sarma (1991) have examined it photometrically. Sarnwal and Sarma were endeavouring to determine whether it was a Type I or Type II Cepheid. By using the Hipparcos data, luminosity arguments and its position in the Galactic disk Sarnwal and Sarma concluded that it was a Type II Cepheid. With a parallax of 5.74±0.66 milliarcseconds from Hipparcos, the star is at a distance of 174±14 pc and its height above the Galactic plane is 41±3 pc.

Period

The high frequency of data from Hipparcos gives a period (P=1.239948 d), which is close to that (P= 1.239938 d) derived from the MJUO data. This lack of historical data meant that little could be compared to the MJUO results. The MJUO photometric observations are listed in Section B.1.1 (Table B.1) and the Fourier parameters used to obtain the period found in Table C.1 of Section C.1.1.

This gave an ephemeris of[2]:

$$\phi = \frac{JD - 2451310.187}{1.239938} \tag{4.2}$$

[2]See also Table 4.3.

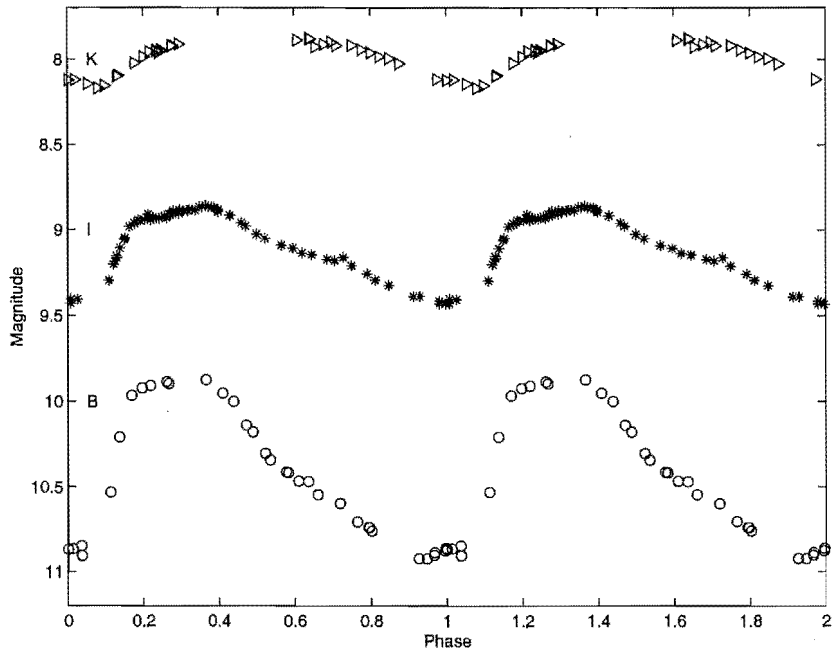

Figure 4.6: *BIK* magnitudes of SW Tau phased on a period of 1.583560 days. (o) are MJUO B data, while (*) are I data from Moffett and Barnes (1984) and (▷) are from Barnes et al. (1997) K data.

Fourier analysis

The period of 1.239938 days (frequency $\sim$0.8 day^{-1}) appears as the primary peak of the periodogram, as shown in Figure 4.8a. However, there is also a strong signal present at a frequency of approximately 0.2 day^{-1} (P$\simeq$5 d). To determine if this is a feature of the star or of the data sampling, a model data set has been generated. This uses the period, amplitude and phase derived from the MJUO V data, but with a pure sinusoidal signal. As Figure 4.8b shows, the same major peaks are present, indicating that the 0.2 day^{-1} peak is purely a result of the data sampling. This is most likely due to observations being made at approximately 5 day intervals (or some integer multiple), which would emerge as a strong signal in the data.

Photometry curves

As shown in Figure 4.7 and 4.9, the shape of the VY Pyx light curve is simpler than that of SW Tau, and has no bump in brightness following light maximum.

As with SW Tau, VY Pyx brightens faster than it fades, but it does this in $\tilde{0}.4$ of a cycle (see Table 4.1), making it a far more symmetrical light curve. The star also does not linger at maximum or minimum light, nor is there a bump as the star grows fainter. Again, as with SW Tau, the amplitude of the pulsations decreases towards the redder wavelengths and the peak at maximum light grows broader.

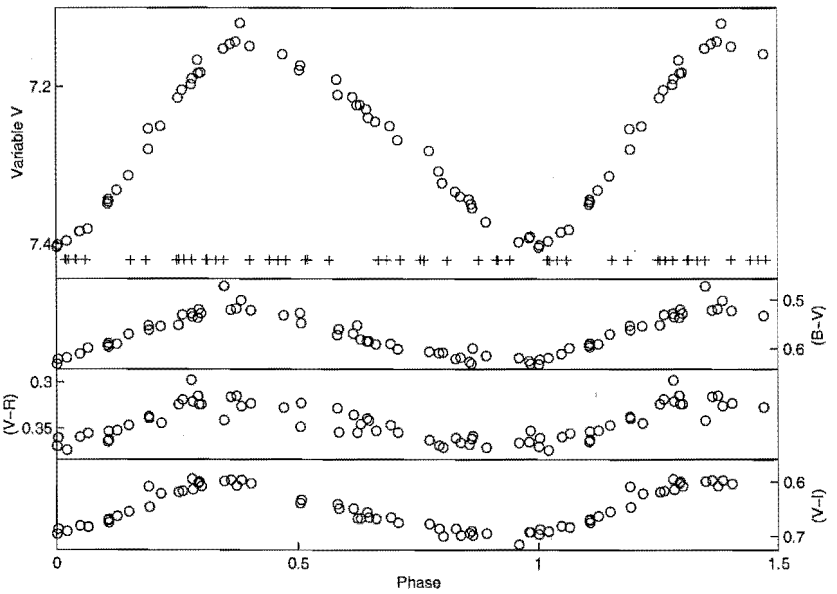

Figure 4.7: MJUO colour photometry of VY Pyx phased on a period of 1.239938 days. (+) indicate phases of MJUO spectral observation.

A brief digression: bump progression in Type II Cepheids

As stated in Section 1.3.1, a progression of bumps in the light curves of BL Her stars is predicted in those stars with periods 1–3 days. In the case of the stars studied here that fall in the predicted bump range, SW Tau (P=1.58 d) shows signs of a bump whereas VY Pyx (P=1.24 d) does not. Based on the model predictions, it is not clear whether the bump for SW Tau is before or after maximum light, as there were two possible candidates for the resonance bump. Carsons and Stothers (1982) found the bump on the descending branch of the light curve, which was at 0.75 with respect to the MJUO phasing. However, they also reported a bump visible on the radial velocity curve. The radial velocity details of SW Tau are covered more thoroughly in Section 5.2.1, but it should be noted that the radial velocity curve from an average of the Fe I lines does not appear to show anything at phase 0.75, although the data coverage is not comprehensive at that phase. It does, however, show a substantial bump at phase 0.2, corresponding to the bump on the ascending part of the light curve.

4.2.3 V381 Cen

V381 Cen shows no bumps on its light curve. It is misclassified as a Type II Cepheid in Kholopov et al. (1990), but is clearly a Type I Cepheid from the literature.

Historical periods

The regularity of the star made it easy to accurately determine the period of the star, as shown in Table 4.4. The Hipparcos data has far better coverage for V381 Cen than for SW Tau. Its parallax of 1.13±0.91 milliarcseconds puts V381 Cen at a distance of 900±400 pc. This compares to a distance of 1131 pc from the Database of Galactic

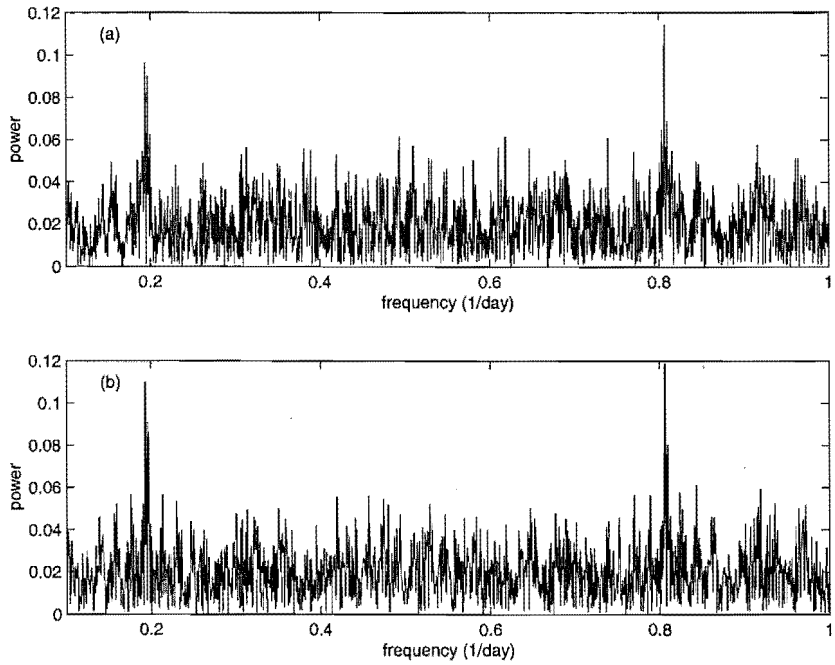

Figure 4.8: Fourier analysis of VY Pyx photometry.
(a) Analysis of the MJUO V photometry.
(b) Analysis of a model light curve using a pure sinusoid with the same sampling as the observational data set and the same period, amplitude and phase.

Classical Cepheids [3] (Fernie et al., 1995).

Period

The period which best fits (minimum RMS residuals) the MJUO observations is 5.07878 days, based on the period found in Fernie et al. (1995) and not on that found by the Fourier fitting routine (see Table C.5).

[3] http://ddo.astro.utoronto.ca/cepheids.html

Table 4.4: Periods for V381 Cen.

	Period (days)	Epoch JD - 2440000
Schaltenbrand and Tammann (1971)	5.07878	6201.953
Opotaki (1984)	$\log(p) = 0.706$	—
Fernie et al. (1995)	5.07878	–
Hipparcos	5.0787	—
This work	5.07878	11310.088

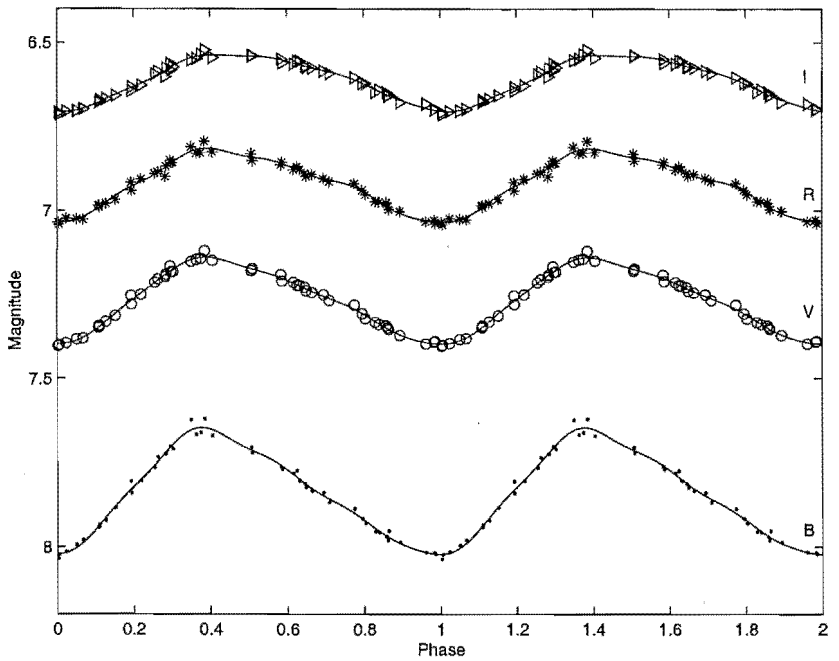

Figure 4.9: MJUO *BVRI* photometry of VY Pyx phased on a period of 1.239938 days from the Fourier fitting to the V data.

This gave an ephemeris of[4]:

$$\phi = \frac{JD - 2451310.088}{5.07878} \tag{4.3}$$

Photometry curves

Figures 4.10 and 4.11 show that the light curves of V381 Cen are far more regular than any of the other stars studied here. In the V band, the star rose rapidly from minimum to maximum light (in $\tilde{0}.3$ of a cycle — Table 4.1) and then gently returned to minimum light. Unfortunately the lack of MJUO data at maximum light means that approximately 0.1 of a cycle is missing between ϕ=0.2 and 0.35. Again, the amplitude of the pulsations decreased towards the red.

4.2.4 TX Del

In contrast to the sawtooth light curve shown by V381 Cen, TX Del has a much more rounded light curve. However, its classification as to the type of Cepheid is far more ambiguous.

Historical data

Harris and Welch (1989) stated that TX Del is a Type II Cepheid, based on its distance ($|z|$) of 450 pc from the Galactic plane (Harris, 1981, 1985) and its distance of 1.1 kpc from the Sun. They assumed a Type II Cepheid period-luminosity and period-colour

[4]See also Table 4.4.

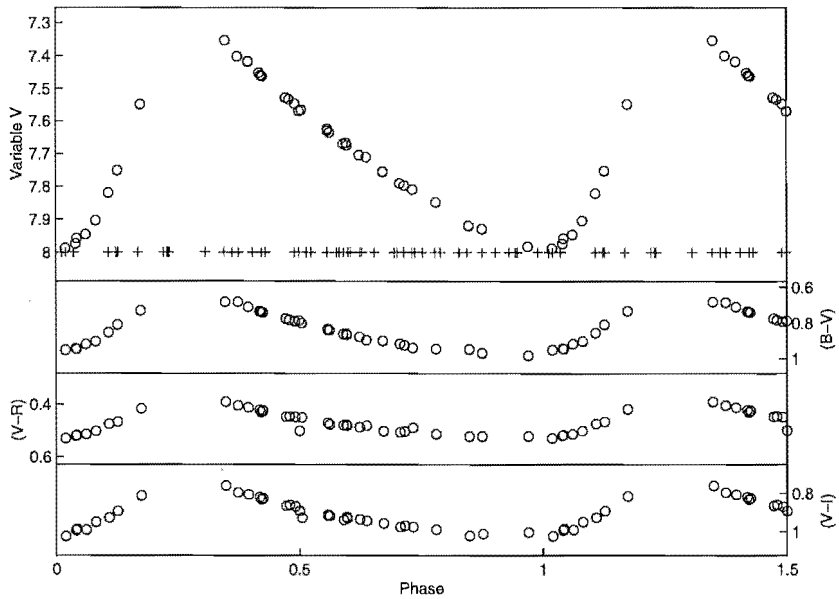

Figure 4.10: MJUO colour photometry of V381 Cen phased on a period of 5.07878 days. (+) indicate phases of MJUO spectral observation.

relationship. This result compared to a $|z|$ of 1200 pc and distance from the Sun of 4 kpc assuming Classical Cepheid relations of a similar nature (Feast and Walker, 1987). As it was far larger than the Classical Cepheid scale height of 70 pc found by Harris (1985) and Fernie (1968), Harris and Welch (1989) inferred it to be of Type II. The Hipparcos parallax is -0.33±1.25 milliarcseconds, from which a distance cannot be derived.

With respect to other research, as discussed further in Section 5.4, Galazutdinov (1995) found TX Del to be Type I, based on its chemical composition. Vinkó and Balzog (1995) also though it to be Type I, based on its large Baade-Wesselink radius, despite its large distance from the Galactic plane. They also cited the infrared photometry of Laney (1995) to be more typical of a Type I Cepheid. Laney (1995) himself seemed more ambivalent to its Type I or II status, but was partially of a mind to have it in a category of its own as it seemed too large and too bright to be a Type II Cepheid. TX Del also had a larger J-K amplitude than K amplitude which ill matched either type.

In terms of the period itself, the historical papers listed in Table 4.5 appear fairly consistent, with a period of around 6.166 days.

Period

Figure 4.12 shows the MJUO data phasing well on a period of 6.1634 days (determined from the Fourier fitting technique with the Fourier response of Figure 4.13), which is a little different from the historical periods listed. However, as seen in Table C.7, this gives the lowest residuals. As with SW Tau, the accuracy of the STAR program is insufficient to resolve period differences of the kind shown between the MJUO period and the historical period of Moffett and Barnes (1985). When the power spectrum (Figure 4.13) is scaled such that the axis limits are the MJUO period and the historical period, only a straight line is visible. To test the 6.1634 day period (Figure 4.14a), the Moffett and Barnes

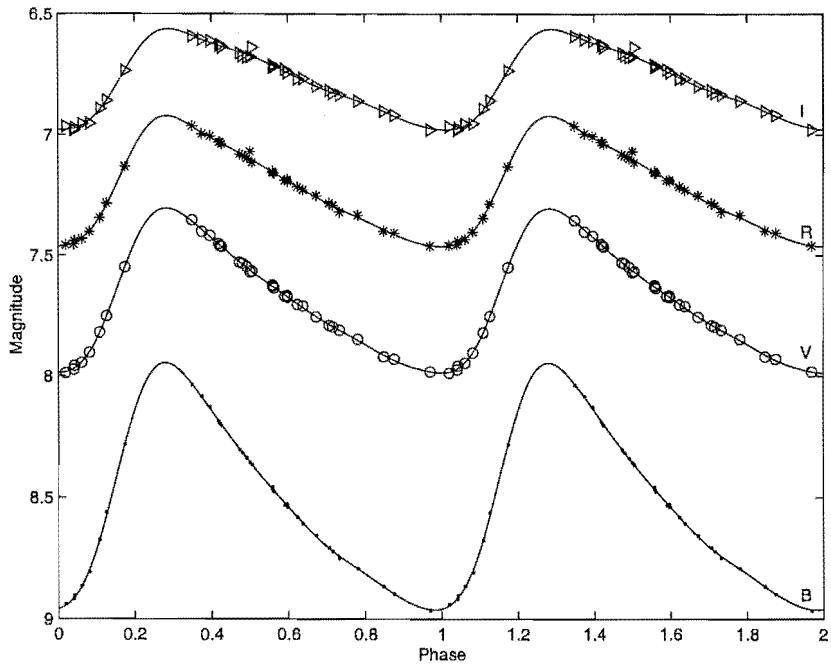

Figure 4.11: MJUO *BVRI* magnitudes of V381 Cen phased on a period of 5.07878 days.

(1984) data has been phased on that period, along with the MJUO data. A phase shift of approximately 0.5 of a pulsational cycle is observed between the two data sets. Stepping through a range of periods towards the Moffett and Barnes (1984) period (example of 6.1645 days shown in Figure 4.14b), the light curves move toward each other but do not cross. By the Moffett and Barnes (1984) period (6.165806 d, Figure 4.14c), the light curves have yet to cross, indicating no common period in that range. The RMS residuals of the fit to the MJUO data also increase as the period increases, indicating that increasing the period is moving away from the most accurate period for the MJUO data set (that found by Fourier analysis in this case).

Table 4.5: Periods for TX Del.

	Period (days)	Epoch JD - 2440000
Schaltenbrand and Tammann (1971)	6.16654	6448.348
Harris (1980)	6.1660	4081.81
Szabados (1980)	6.165907	2947.033
Moffett and Barnes (1984)	6.165806	-3551.652 (2436448.348)
Moffett and Barnes (1985)	6.165981	4501.119
Meakes et al. (1991)	6.166	—
Hipparcos	6.1657	—
This work	6.1634	11312.483

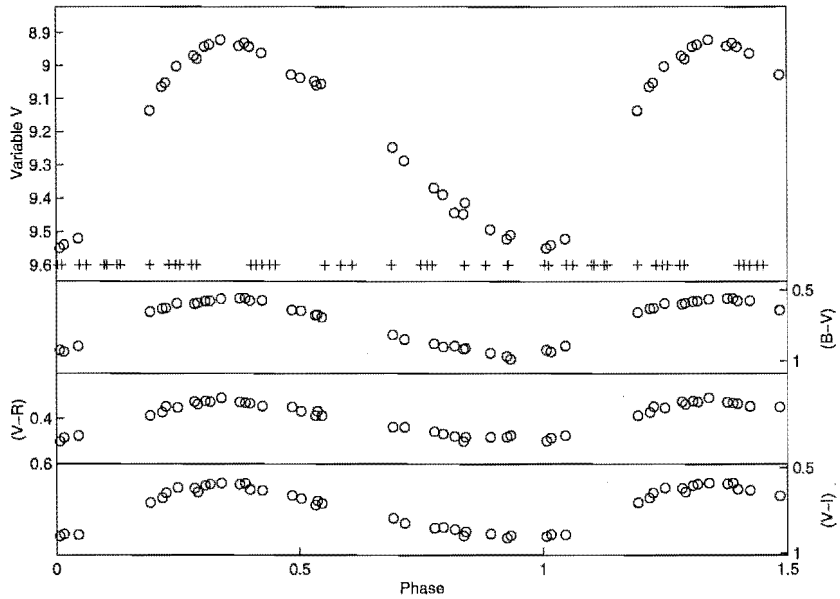

Figure 4.12: MJUO colour photometry of TX Del phased on a period of 6.1634 days from Fourier fitting to the V photometry. (+) indicate phases of MJUO spectroscopic observation.

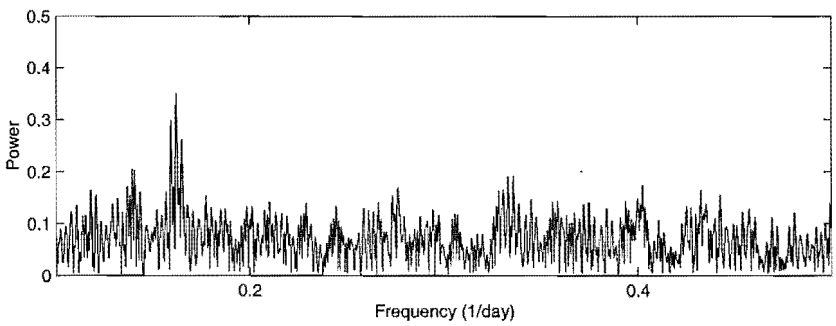

Figure 4.13: TX Del Fourier amplitude as a function of frequency.

The MJUO period gives an ephemeris of[5]:

$$\phi = \frac{JD - 2451312.483}{6.1634} \tag{4.4}$$

Photometric light curves

Using the MJUO period for TX Del, the V light curve is a far more rounded curve than for the previous stars. Again, it rises to maximum light in $\tilde{0}.4$ of a cycle (see Table 4.1) and quite gently curves around at maximum light. As it declines, it does show a bump around phase 0.5–0.7. Unfortunately, due to poor data sampling between ϕ=0.55 and 0.65, it is not possible to define the bump clearly. Based on the the Fourier fitted curves, it does appear to grow in relative amplitude towards redder wavelengths. However, the

[5]See also Table 4.5.

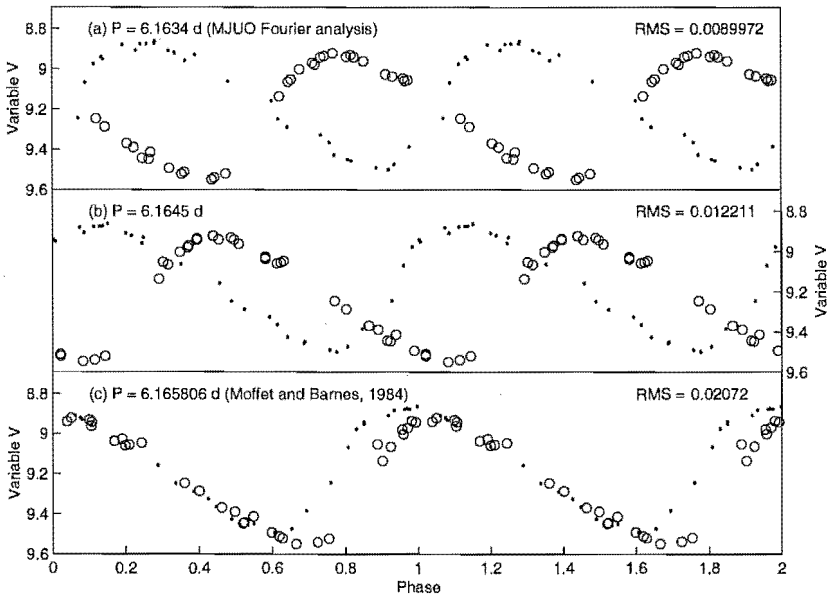

Figure 4.14: Testing the accuracy of periods using V photometry of TX Del from MJUO (o) and Moffett and Barnes (1984) data (.).
(a) Phased on MJUO 6.1634 d period.
(b) Phased on intermediate 6.1645 d period.
(c) Phased on Moffett and Barnes (1984) 6.165806 d period.
RMS is from fitting to the MJUO data only. Phasing epoch is 0 for all panels.

overall pattern of a decreasing amplitude towards longer wavelengths continues in a similar manner to the other stars.

4.3 W Vir stars

Moving to the longer period Type II Cepheids, the W Virginis stars have periods of 7 to ~20 days (Table 4.6). Many of these have also been studied in great detail, so historical comparisons are possible (especially with AL Vir and ST Pup) to confirm period changes in the recent past.

4.3.1 κ Pav

The transition to the longer period stars is quite apparent when examining the regularity of the light curves, as the scatter of the curves becomes larger and the reliability of the periods less certain. κ Pav is an interesting example of this. While bright it is a southern object, so little published photometry on it exists. This makes investigation of any period changes difficult.

Historical periods

κ Pav is definitely not classed as a Type I Cepheid. Laney (1995) analyzed *JHK* observations of it through Baade-Wesselink methods and found it to have about half the radius

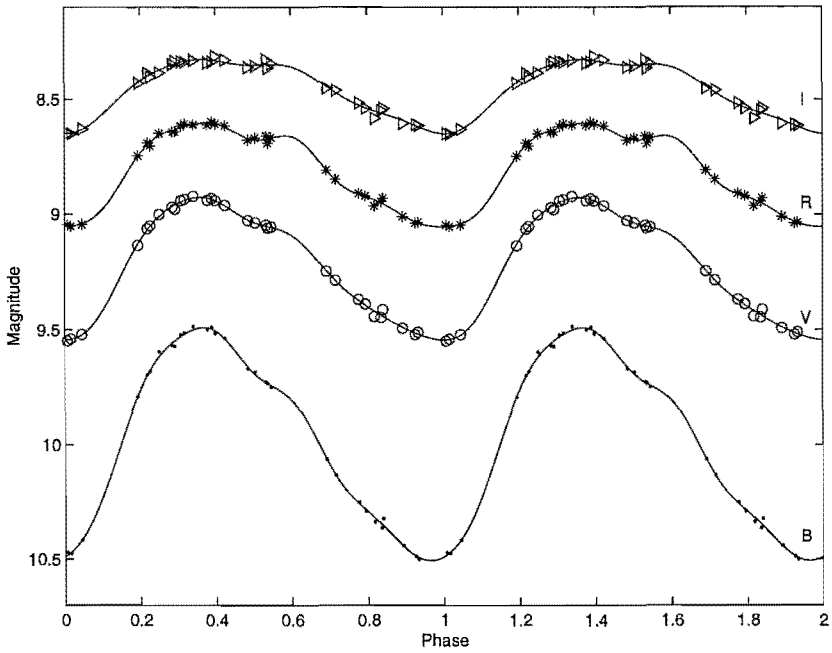

Figure 4.15: MJUO magnitudes for TX Del phased on a period of 6.1634 days from Fourier fits to the V photometry.

of a Type I Cepheid of its period. It does however have some spectral features that made it atypical of the Type II Cepheids — features which will be discussed in Section 6.2.

Historically, κ Pav has a changeable period, as indicated by Table 4.7. The Hipparcos data does show a curious scatter on descending light and around minimum light (Figure 4.16). which makes their period determination unreliable. The Hipparcos parallax for κ Pav of 6.00±0.67 milliarcseconds implies a distance of 167±17 pc.

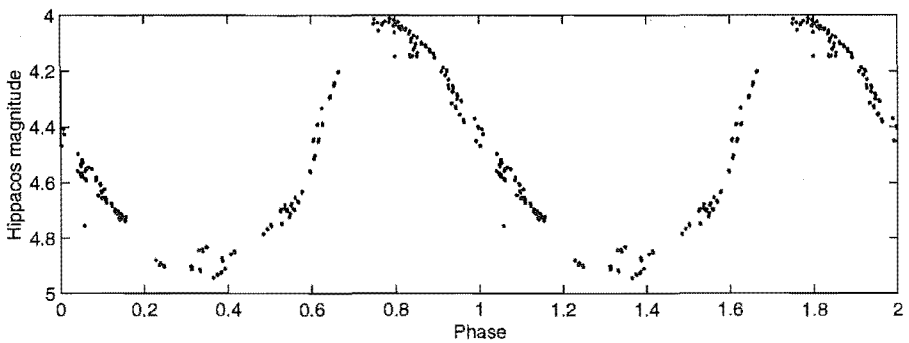

Figure 4.16: Hipparcos photometry of κ Pav phased on the Hipparcos period of 9.0944 days.

Table 4.6: Phasing parameters for W Vir stars.

		ϕ_0 [a]	ϕ_{max} [b]	period (p)	RMS fit
κ Pav	B	-0.024	0.416		0.0280
	V	0.000	0.439	9.0741	0.0214
	R	0.015	0.464		0.0194
	I	0.025	0.495		0.0182
AL Vir	B	-0.177	0.287		0.0453
	V	0.000	0.330	10.2950	0.0348
	R	0.018	0.360		0.0326
	I	0.017	0.379		0.0330
W Vir	B	-0.013	0.344		0.0538
	V	0.000	0.356	17.2768	0.0372
	R	0.010	0.555		0.0287
	I	0.015	0.559		0.0500
ST Pup	B	-0.014	0.273		0.1024
	V	0.000	0.245	18.6204	0.0723
	R	0.005	0.251		0.0605
	I	0.049	0.243		0.0892

[a]phase of minimum brightness — defined to be 0.00 for V.
[b]phase of maximum brightness

Table 4.7: Periods for κ Pav.

	Period (days)	Epoch JD - 2440000
Schaltenbrand and Tammann (1971)	9.0741	(243?)6616.629
Shobbrook (1992)	9.0694 ± 0.0019	—
Hipparcos	9.0944	—
This work	9.0741	11315.176

Period

Fourier analysis of the MJUO photometry gives a fit with lowest residuals to the period found by Schaltenbrand and Tammann (1971), although the STAR package Fourier fitting and least-squares Fourier fitting all produced similar size residuals (see Table C.9) and are around the 9.07 day period range. As seen from Figure 4.17, this phases up quite cleanly with no large gaps in phase coverage.

The period analysis results in an ephemeris of[6]:

$$\phi = \frac{JD - 2451315.176}{9.0741} \tag{4.5}$$

[6]See also Table 4.7.

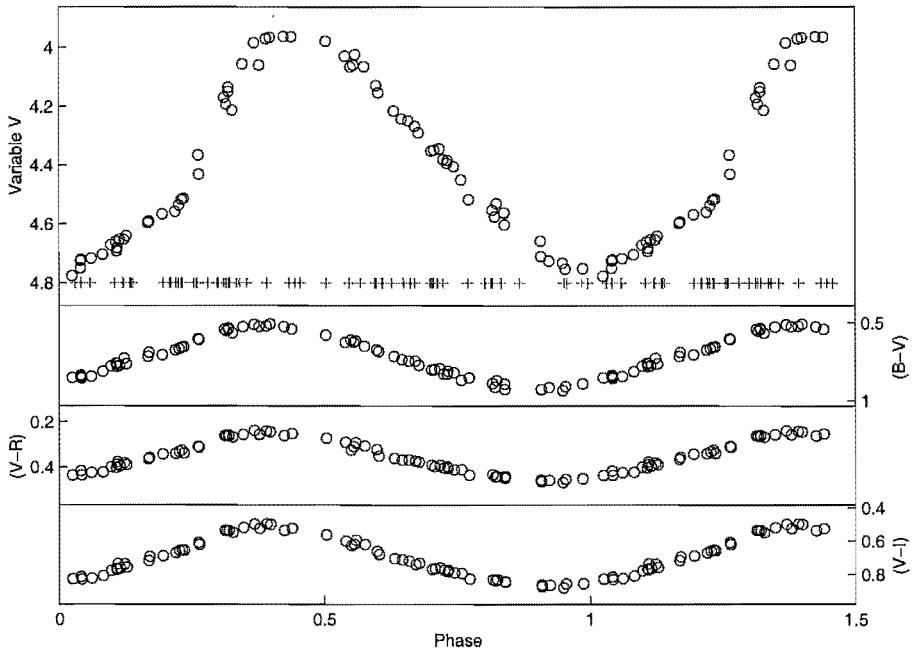

Figure 4.17: MJUO colour photometry of κ Pav phased on a period of 9.0741 days from Fourier fits to the V photometry. (+) represent phases of MJUO spectral observations.

Photometry curves

While having a four-day-longer period than TX Del, κ Pav's light curve is more similar to that of TX Del than to the shapes of the other stars. κ Pav has a very rounded light curve (Figure 4.18) with no distinct bumps of the scale of SW Tau (Figure 4.5). However, it does have a slight bump on rising light at phase 0.1. Unlike the one on TX Del, this bump is most distinct in the blue and becomes less prominent in the redder filters.

As shown in Table 4.6, the star takes $\tilde{0}.4$ of a phase to go from minimum to maximum light and has a relatively rounded peak at maximum light. The descent to minimum light has a similar but shallower slope ending in a slightly broader minimum. Again, the amplitude of the pulsations decreases to the red.

4.3.2 AL Vir

Despite an extremely similar light curve to κ Pav, AL Vir is unequivocally a Type II Cepheid. For instance, Laney (1995) was quite clear from its Baade-Wesselink radius that it was a Type II Cepheid. He did, however, state that he thought the available data strongly suggested that AL Vir was a binary with an orbital period of less than 1900 days, but did not cite data, references, or give any other reasons.

Historical periods

While noted in the GCVS to have a variable light curve, the periods listed in Table 4.8 appear to be reasonably stable at around 10.3 days. Hipparcos obtained a parallax of

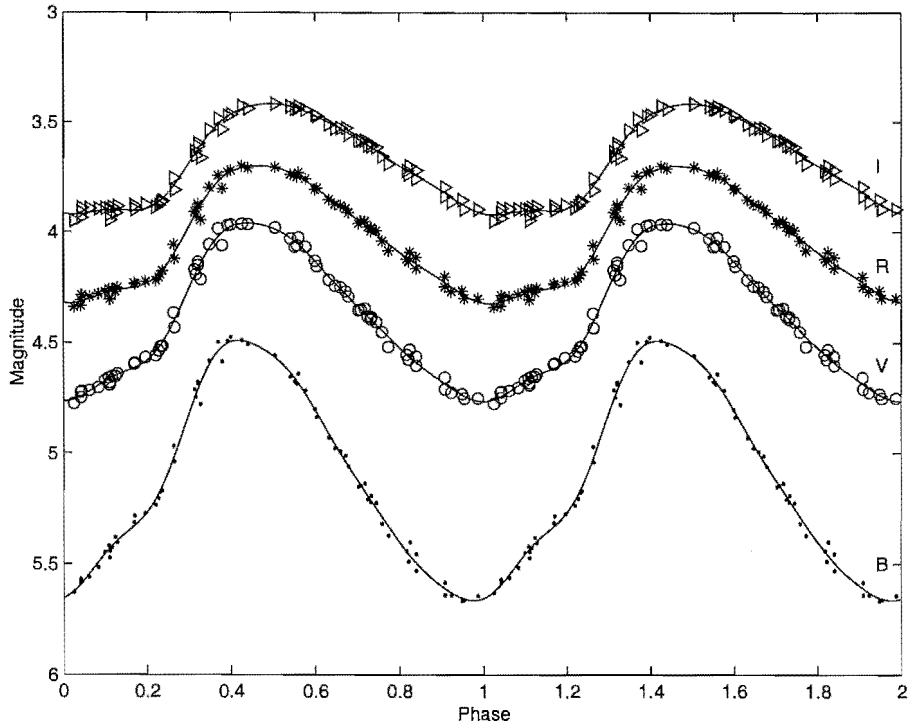

Figure 4.18: MJUO *BVRI* magnitudes of κ Pav phased on a period of 9.0741 days from the Fourier fits to the *V* photometry.

0.38±1.63 milliarcseconds, giving a distance of about 2600±2100 pc (as an lower limit on the uncertainty).

Period

From Fourier analysis, an initial period of 10.2950 days is found and, when this is compared to the historical periods, it gives lowest RMS residuals to the MJUO data (Table C.11). As with SW Tau (Figure 4.3) and TX Del (Figure 4.14), data from Moffett and Barnes (1984) has been plotted up on the 10.2950 day period with the MJUO data (Figure 4.19a). This results in a phase difference of ~0.2 of a pulsation cycle. Stepping though a series of periods (exemplified by Figure 4.19b, p = 10.2985 d) towards the Moffett and Barnes (1984) period of 10.302323 d (Figure 4.19c), the light curves move towards each other, but as seen for TX Del, do not cross within the period range examined, indicating no common period in this range. The RMS residuals also increase as the period increases, indicating the MJUO fourier analysis period is the most suitable period to apply over the MJUO observations.

This results in an ephemeris of:

$$\phi = \frac{JD - 2451309.037}{10.2950} \tag{4.6}$$

Table 4.8: Periods for AL Vir.

	Period (days)	Epoch JD - 2440000
Joy (1937)	10.30	—
Schaltenbrand and Tammann (1971)	10.299971	7988.648
Moffett and Barnes (1984)	10.302323	-2011.352
Barnes et al. (1988)	10.302323	4406.913
Hipparcos	10.3113	–
Fernie and Ehlers (1999)	10.302	—
This work	10.2950	11309.037

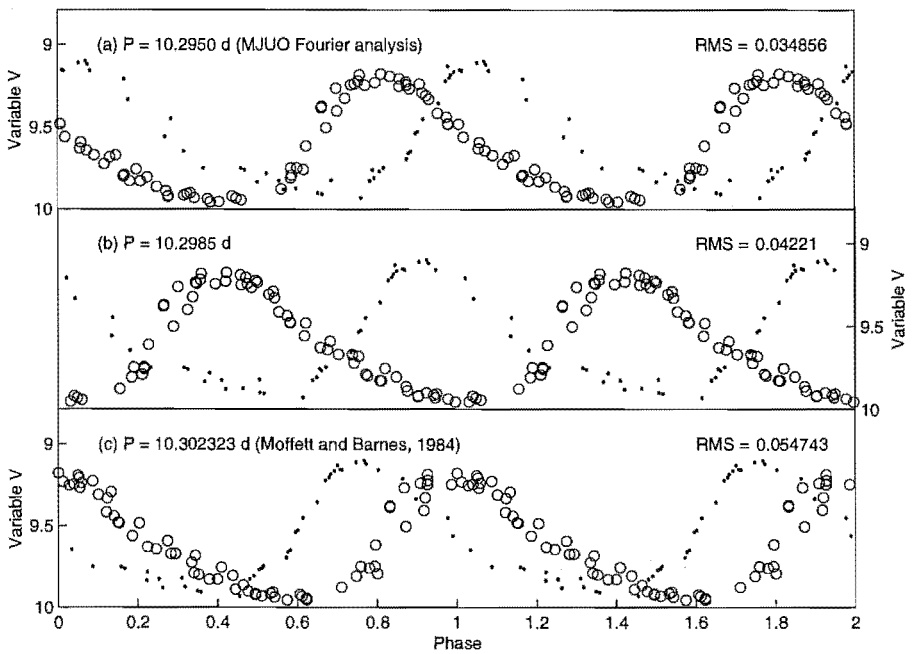

Figure 4.19: Testing the accuracy of periods using V photometry of AL Vir from MJUO (o) and Moffett and Barnes (1984) (.) data.
(a) Phased on MJUO 10.2950 d period.
(b) Phased on intermediate 10.2985 d period.
(c) Phased on Moffett and Barnes (1984) 10.302323 d period.
RMS relates to MJUO data only. Phasing epoch is 0 for all panels.

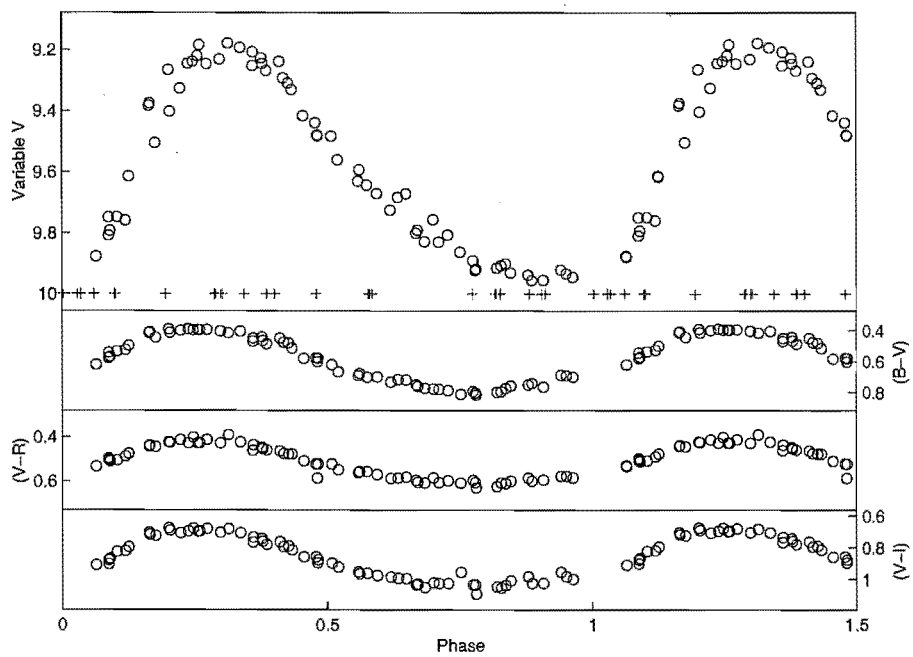

Figure 4.20: MJUO colour photometry of AL Vir phased on a period of 10.2950 days from Fourier fits. (+) indicates phases of MJUO spectral observation.

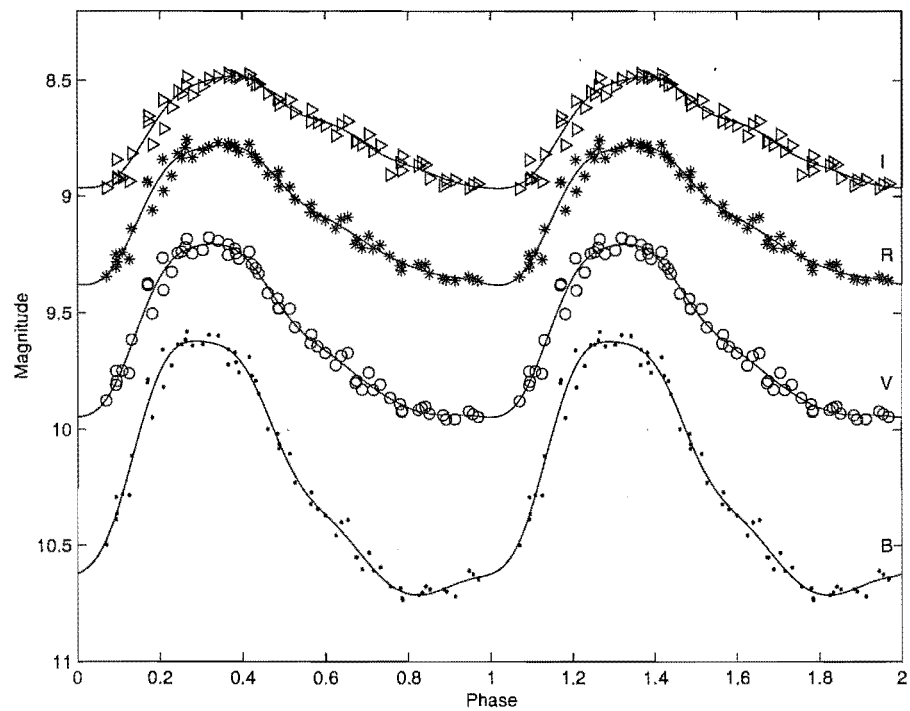

Figure 4.21: MJUO *BVRI* magnitudes of AL Vir phased on a period of 10.2950 days from the Fourier fit to the V photometry.

Table 4.9: Periods for W Vir.

	Period (days)	Epoch JD - 2440000
Joy (1937)	17.27	—
Schaltenbrand and Tammann (1971)	17.2768	6576.687
Meakes et al. (1991)	17.273	—
Hipparcos	17.267	—
Fernie and Ehlers (1999)	17.242	—
This work	17.2768	11300.651

Photometry curves

The light curve of AL Vir is very similar to κ Pav, although it lacks the possible bump around phase 0.1. Unfortunately the scatter on the data points and the data gap around minimum light did not help the analysis and interpretation.

The star takes $\tilde{0}.3$ of a cycle to go from minimum to maximum light in the visual, with a more gradual curve back to minimum light. Both maximum and minimum light are quite rounded, though minimum light is the broader of the two. As with the other stars, the amplitude of the pulsations decreases to the red.

4.3.3 W Vir

The shape of the light curve changed markedly from AL Vir, with its period around 10 days, to W Vir, the prototype of its class, which has a period of about 17 days.

Historical periods

Schaltenbrand and Tammann (1971) noted the period of W Vir to be variable, however they did not state by how much it varied. As seen in Table 4.9, the period is stable over the times given to within 0.3 days, but is variable on the digits after that. Again, as with SW Tau and AL Vir, the Hipparcos data were insufficient to give good phase coverage,and hence there is some uncertainty in the reliability of its period determination. Hipparcos also gave a negative parallax, from which no distance could be extracted.

Period

As shown in Figure 4.22, the MJUO data phased well on a 17.2768 day period, the same as that found by Schaltenbrand and Tammann (1971). This produced the lowest residuals to the fit of all the periods trialled in Table C.13.

This gives rise to an ephemeris of[7]:

$$\phi = \frac{JD - 2451300.651}{17.2768} \tag{4.7}$$

[7]See also Table 4.9.

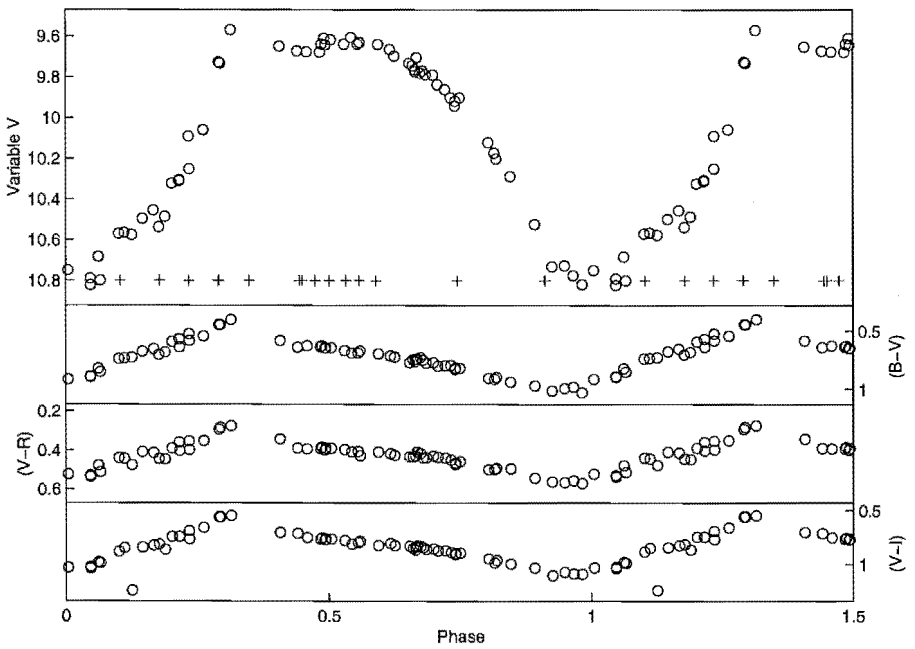

Figure 4.22: MJUO colour photometry of W Vir phased on a period of 17.2768 days from the Fourier parameters for the V photometry. (+) indicates the phase of MJUO spectral observation.

Photometric curves

The shape of the light curve of W Vir is quite different to the shape of those Type II Cepheids with shorter periods. A distinct double peak is apparent at maximum light, but it decreases markedly towards redder wavelengths. Unfortunately the phase coverage is lacking around maximum light, but the change in amplitude of the data points leading up to it gives a good indication of the relative change in height of the peak.

In terms of the V curve, the star rises from minimum to maximum light on the primary peak in $\tilde{0}.36$ of a cycle, and then rapidly declines briefly for 0.05 of a cycle, before rising more slowly to the second maximum at around phase $\sim$0.6. It then declines smoothly to minimum light. A small bump in the light curve was observable around phase 0.1, but the scatter on the data points around minimum light and leading up to it made it difficult to identify this clearly. It is quite noticeable that the scatter in the phased data is a great deal less around the secondary maximum compared to the minimum.

The light minimum is also quite narrow, though this varies as a function of wavelength, being narrowest in B, and getting broader in the redder filters. As with the other stars, the amplitude of the variations decreases towards the redder wavelengths. The relative amplitude of the primary maximum light peak also decreases towards the red.

4.3.4 ST Pup

ST Pup shares a similar light curve shape to W Vir, with a distinctive initial peak in the light curve. It proved a little more interesting in terms of its period, and the variability of that period.

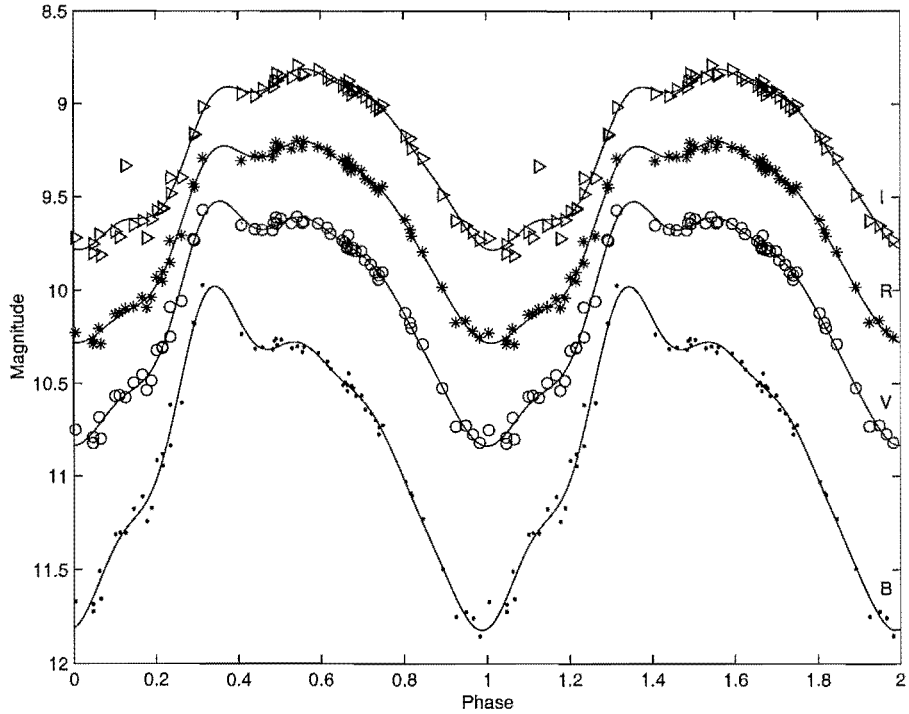

Figure 4.23: MJUO *BVRI* Magnitudes of W Vir phased on a period of 17.2768 days from the *V* magnitude Fourier analysis.

Historical periods

ST Pup had historically shown definite evidence of period changes, as can be seen from the range of periods shown in Table 4.10. Gonzalez and Wallerstein (1996) cited Payne-Gaposchkin (1950) as finding numerous unpredictable period changes of the star in the first half of the century, with a period varying between 17.4 to 19.2 days. In the second half of the century, Gonzalez and Wallerstein (1996) found only one distinct period change at around JD = 244 1064 (April, 1971). Prior to JD 244 1064, they found a period of 18.54694±0.00003 days, with a period of 18.4647±0.0002 days after that date. Analyzing Kilkenny et al. (1993) only, a period of 18.4622±0.0006 days was found. On the other hand, Hipparcos found a period of 18.46 days and a negative parallax.

Period

As shown in Figure 4.24, the MJUO data phases up on a period of 18.6204 days. When the historical periods are used to phase the MJUO data, scatter diagrams appear. To investigate this further, the Kilkenny et al. (1993) data has been examined in greater detail. A light curve has been Fourier fitted to it, and the fit to the data as a function of JD plotted up (Figure 4.25a–d). The same has been done to the MJUO data using the MJUO period derived (Figure 4.25e–h). As can be seen from this figure, both datasets fit the curves well (RMS residuals 0.038073 Kilkenny et al. (1993)), though the scatter on the MJUO data is slightly greater overall (RMS residuals 0.072471). Also, it is clear from the fits that the periods have not changed during the individual times observed. Unfortunately there is no data available here for when the period change took place, but

Table 4.10: Periods for ST Pup.

	Period (days)	Epoch JD - 2440000
Schaltenbrand and Tammann (1971)	18.559	5395.430
Harris (1980)	17.4	4023.96
Kilkenny et al. (1993)	18.462 ± 0.001	8363.26
Gonzalez and Wallerstein (1996)	18.54694±0.00003	(prior to JD 2441064)
	18.4647±0.0002	(after JD 2441064)
(reanalyzing Kilkenny et al. (1993))	18.4622±0.0006	—
Hipparcos	18.46	—
This work	18.6204	11388.125

it did not appear to be a gradual one but appeared quite suddenly. The data of Gonzalez and Wallerstein (1996) support this, with their abrupt change of period discussed earlier.

For the MJUO data, this results in an ephemeris of[8]:

$$\phi = \frac{JD - 2451388.125}{18.6204} \tag{4.8}$$

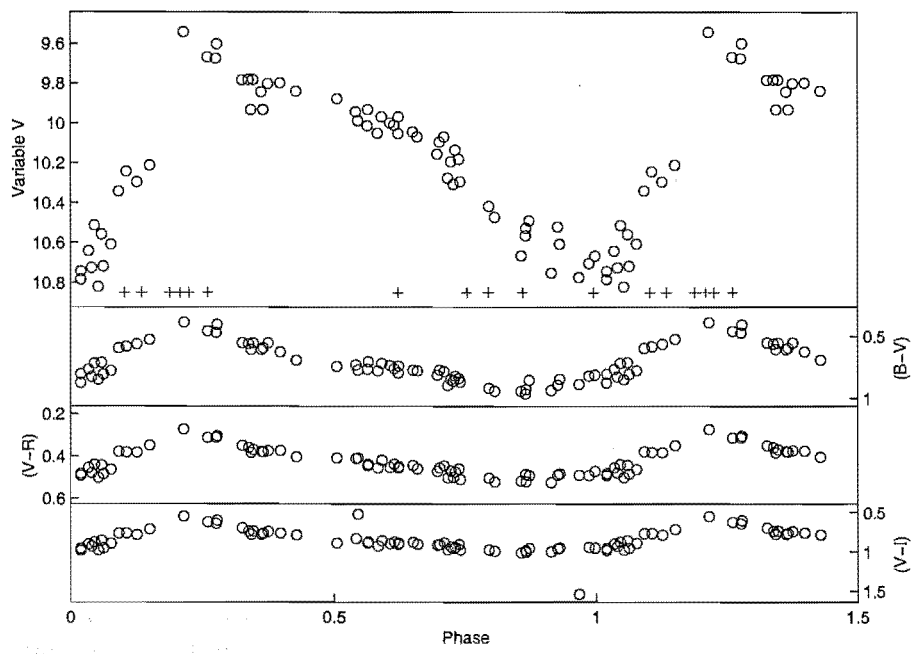

Figure 4.24: MJUO colour photometry of ST Pup phased on a period of 18.6204 days from V Fourier fitting.

[8]See also Table 4.10.

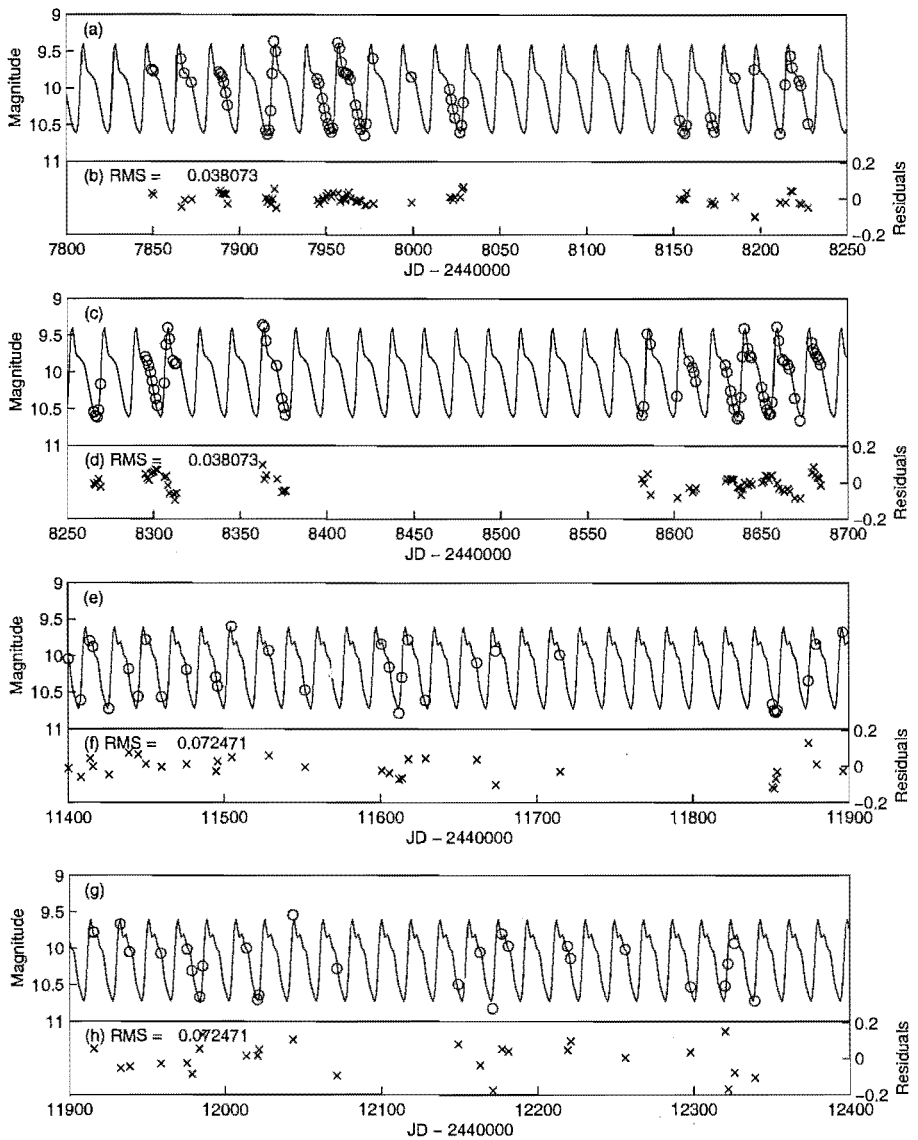

Figure 4.25: SAAO and MJUO photometry of ST Pup with fitted curves.
(a)–(d) SAAO V photometry of ST Pup and residuals to a fitted curve of period 18.462 days (Kilkenny et al., 1993).
(e)–(h) MJUO V photometry and residuals to a fitted curve of period 18.6204 days.

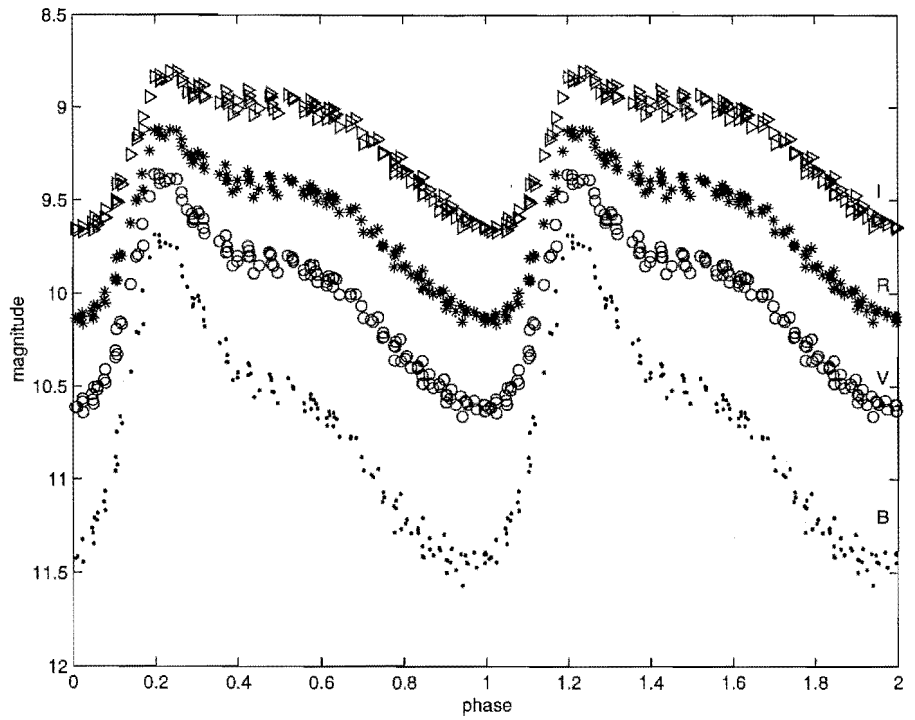

Figure 4.26: SAAO *BVRI* magnitudes of ST Pup phased on a period of 18.462 days from Kilkenny et al. (1993).

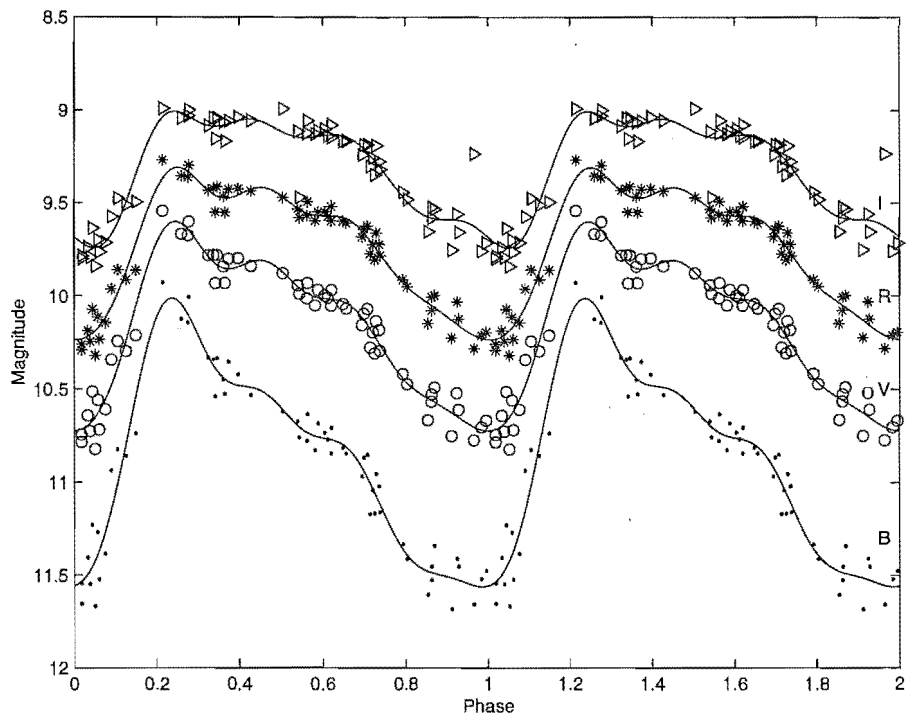

Figure 4.27: MJUO *BVRI* magnitudes of ST Pup phased on a period of 18.6204 days from *V* Fourier fitting.

Photometric curves

In terms of the light curve itself, and its changes over time, the Kilkenny et al. (1993) data phases up extremely well on its period of 18.462 days. The shape of the light curve is quite similar to W Vir. However the secondary maximum is more of a bump than the distinct one for W Vir. Better phase coverage from the SAAO data gives a far better defined primary maximum at around a phase of 0.25, which very clearly decreases in relative amplitude to the redder wavelengths. In contrast to W Vir, the scatter on the data points is fairly evenly distributed in phase. Minimum light is also much wider than for W Vir and does not appear to change shape as a function of wavelength, although the phase of minimum light does shift to later in the cycle for the redder filters. Again, the amplitude of the magnitude variations decreased towards the red, though it was far less pronounced for ST Pup.

The MJUO curves showed similar features for a period of 18.6204 days, but with a great deal more scatter. Extra bumps were visible from around phases 0.4–0.6, and possibly around phase 0.9, but the scatter of the data makes these less well defined. In terms of the main features, primary light maximum still occurs at around phase 0.25, as with the SAAO curves. As with the SAAO data, the width of light minimum does not seem to change as a function of wavelength, though the bump at phase 0.9 may emerge more at the redder wavelengths. The trend of decreasing amplitude variations towards the red is definitely present.

4.4 RV Tauri stars

It is not the intent of this thesis to examine the RV Tauri stars in the same detail as the W Vir stars. They will be examined less thoroughly and historical photometry will not be included. The less regular nature of these stars has been reported widely in the literature and will not be examined in detail here. In the cases where the stars have been recently studied in depth (Pollard, 1994), these studies should be referred to for historical background. More recent studies or changes from the earlier results will be discussed here.

4.4.1 SX Cen

While having one of the shortest pulsational periods (32.86 d) of the RV Tauri stars (Table 4.13 and Khopolov et al., 1985), very little has been done to photometrically study the pulsations of SX Cen. Most work on it has been in the context of spectroscopic abundance studies (Maas et al., 2002) and various infrared (Gehrz and Ney, 1972; Lloyd Evans, 1985; Raveendran, 1989) and multi-wavelength studies (Goldsmith et al., 1987; Shenton et al., 1994a). Most of these, if they mention a period, use the period listed in the appropriate edition of the General Catalogue of Variable Stars.

Table 4.11: Phasing parameters for RVa stars.

		ϕ_0 [a]	ϕ_{max} [b]	period (p) (days)	RMS Fit (magnitude)
TT Oph	B	-0.018	0.198		0.1265
	V	0.000	0.714	60.97	0.0963
	R	0.007	0.234		0.0835
	I	0.018	0.243		0.0737
RU Cen	B	0.430	0.158		0.1286
	V	0.000	0.266	64.57	0.0936
	R	0.006	0.263		0.0803
	I	0.011	0.266		0.0701
CT Ori	B	-0.008	0.167		0.0789
	V	0.000	0.172	67.42	0.0522
	R	0.005	0.181		0.0437
	I	0.006	0.196		0.0402
AR Sgr	B	-0.006	0.685		0.2789
	V	0.000	0.699	87.13	0.1959
	R	0.004	0.708		0.1645
	I	0.011	0.716		0.1413
UZ Oph	B	-0.013	0.217		0.2304
	V	0.000	0.221	88.90	0.2186
	R	0.003	0.291		0.2203
	I	0.014	0.267		0.1316
R Sct	B	-0.011	0.708		0.2770
	V	0.000	0.710	134.87	0.2805
	R	0.004	0.710		0.2930
	I	0.008	0.715		0.1677
TX Oph	B	0.416	0.160		0.1569
	V	0.000	0.189	135.81	0.1289
	R	-0.002	0.218		0.1177
	I	-0.002	0.224		0.1034

[a] phase of minimum brightness — defined to be 0.00 for V.
[b] phase of maximum brightness

Table 4.12: Phasing parameters for RVb stars.

		ϕ_0 [a]	ϕ_{max} [b]	period (p) (days)	RMS Fit (magnitude)
SX Cen	B	0.475	0.182		0.1480
	V	0.000	0.699	32.82	0.0914
	R	0.000	0.705		0.1024
	I	0.000	0.836		0.1383
AI Sco	B	-0.030	0.680		0.2749
	V	0.000	0.714	71.45	0.1916
	R	0.010	0.722		0.1785
	I	0.013	0.729		0.1777
AR Pup	B	-0.015	0.215		0.1054
	V	0.000	0.810	76.47	0.0775
	R	0.008	0.815		0.0664
	I	0.538	0.821		0.0616
U Mon	B	-0.011	0.677		0.5113
	V	0.000	0.274	91.79	0.3359
	R	0.019	0.786		0.3462
	I	0.042	0.758		0.4031
IW Car	B	-0.003	0.752		0.0672
	V	0.000	0.755	142.73	0.0531
	R	0.000	0.759		0.0503
	I	0.470	0.774		0.0447

[a]phase of minimum brightness — defined to be 0.00 for V.
[b]phase of maximum brightness

Table 4.13: Periods between successive deep minima for SX Cen.

	Period (days)	Epoch JD - 2440000	long term period (days)
Khopolov et al. (1985)	32.8682	—	—
Lloyd Evans (1985)	32.8642	—	615
This work	32.82	11292.410	—

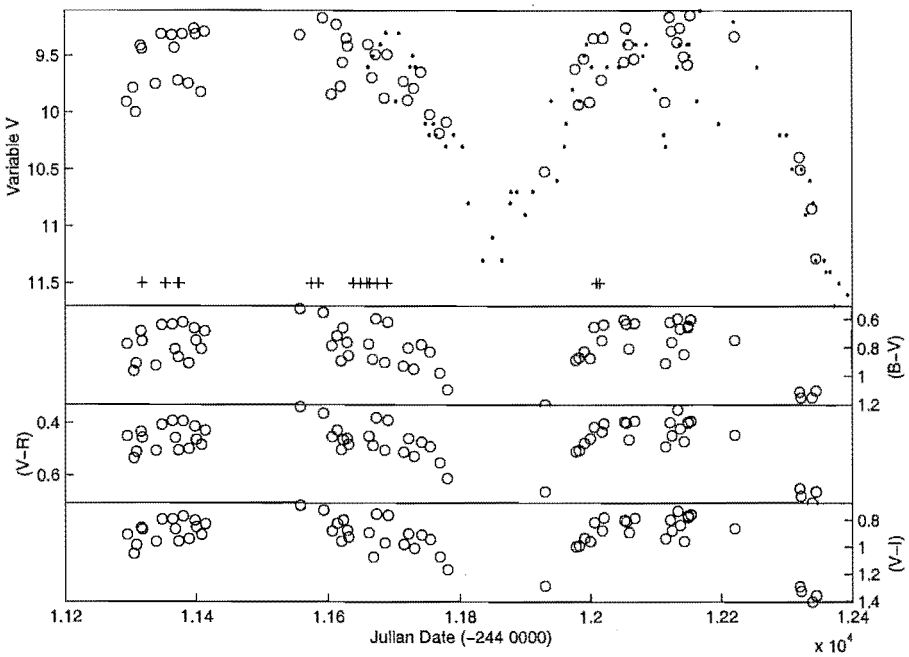

Figure 4.28: MJUO colour photometry of SX Cen. (+) indicate when MJUO spectral observations were made. (.) are Albert Jones visual estimates.

Classified as an RVb star, SX Cen exhibits long-term variations (Figure 4.28) where the magnitude achieved at maximum light decreases from $V = 9.0$ to 10.7. To supplement the MJUO photometry, and provide greater coverage in terms of overall variation, visual estimates from Albert Jones have been included in Figure 4.28. However these have not been included in the period analysis. These visual estimates provide an idea of how the star is varying during the seasonal gaps in the MJUO data. Hence we can see that SX Cen was at $V \simeq 10.7$–11.3 during the first long-term minimum ($\sim$ JD 2451900) presented here and appears to have been even fainter ($V = 11.3$–11.8) during the second long-term minimum ($\sim$ JD 2452350). The duration between long-term minima also appears to have changed over time. Lloyd Evans (1985) reported a long-term period of 615 days (Table 4.13), based on observations from the 1930s. Figure 4.28 indicates a changing time between long-term minima. There are approximately 450 days between the first and second long-term minima, but the previous long-term minimum is more than 600 days before that.

To find the pulsational period a spline curve has been fitted to the maxima of the V data (see Figure 4.29) to remove these long term variations. That spline curve was then subtracted from the data. The light maxima have been used as the RV Tauri stars spend a greater percentage of their pulsational cycle near maximum light as opposed to minimum light. Also the maxima are far more consistent in amplitude than the light minima as they lack the deep and shallow alternations. In order to keep the same scale, the minimum spline value has been added as a constant offset, once the spline curve has been removed. This restores the photometry to a scale at which it would (in theory) be if the star were permanently at long-term light maximum. It does ignore the possibility of decreased amplitude of pulsational variation over the long-term minima, as witnessed

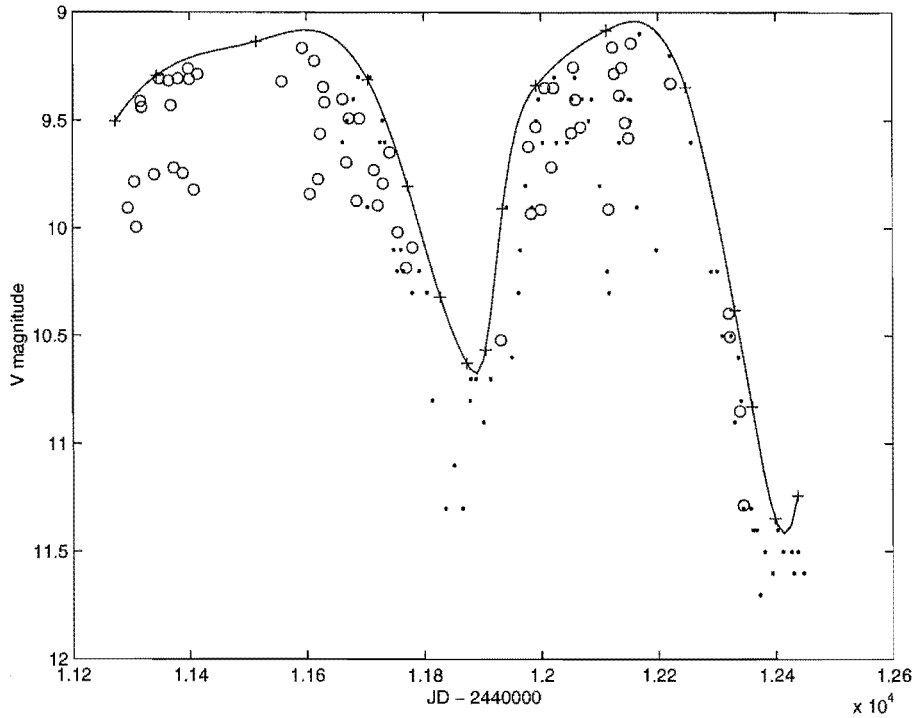

Figure 4.29: MJUO V photometry of SX Cen showing the spline curve fitted to remove the long-term variation.

in U Mon (see Section 4.5).

From Fourier analysis, a period of 32.82 days has been derived. As can be seen from Figures 4.30 and 4.31, this gives a good fit in the V, with the scatter becoming greater towards the redder wavelengths (see Table C.17 for Fourier parameters and residuals). This increased scatter is due to the long-term minima having different amplitude variations at different wavelengths, as the amplitude of the long-term variations is greater at the redder wavelengths. While the long-term variations have been removed from V, removing the same amplitude variations from B, R and I removes most but not all of the variations at the other wavelengths. Thus part of the scatter from the long-term variations is still present.

In terms of the pulsational light curves (Figure 4.30), the curves are quite sinusoidal, with little difference between the depths of the deep (phase 0.0) and shallow minima. In fact minimum light in B occurred ~0.5 of a cycle after minimum light in V, R and I (Table C.17), but this is more likely a result of the Fourier fit than a physical difference and should not be relied upon. A slight similarity to the longer period W Vir stars (W Vir, Figure 4.23 and ST Pup, Figure 4.27) is noticeable in that the position of maximum light shifts to later phases towards the redder wavelengths. This may be due to a shock effect at those phases increasing flux at the bluer wavelengths. The colour curves (Figure 4.31) also lead the V curve in phase as *(B-V)*, *(V-R)* and *(V-I)* all reach minimum and maximum before V.

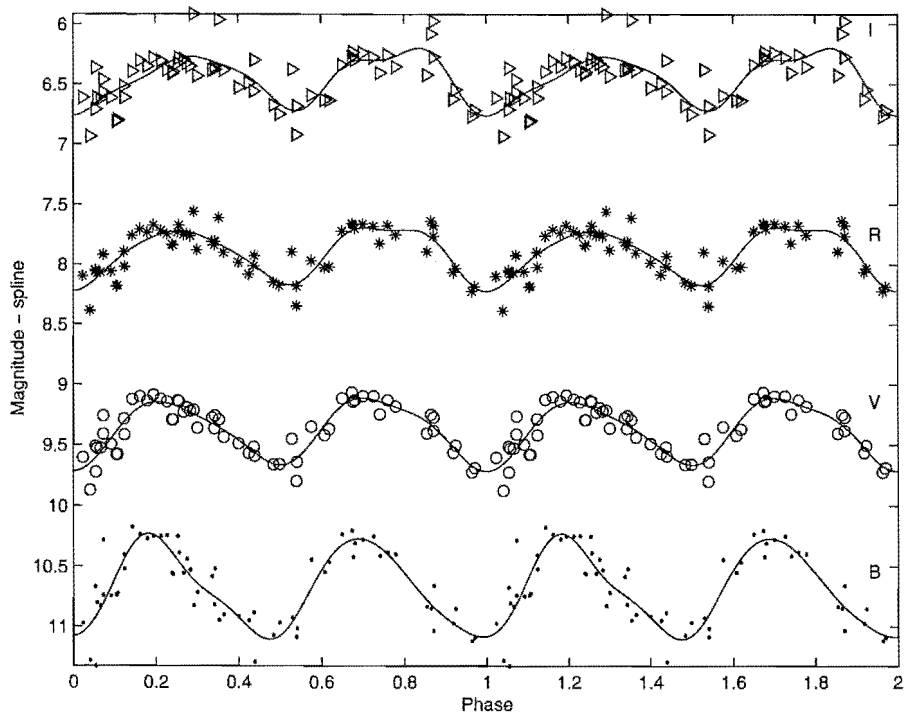

Figure 4.30: MJUO *BVRI* magnitudes of SX Cen phased on a period of 32.82 days from Fourier fitting to the V data with the spline curve fit to the V photometry removed. B magnitudes have been offset by +0.5 magnitudes, R by -1 and I by -2.

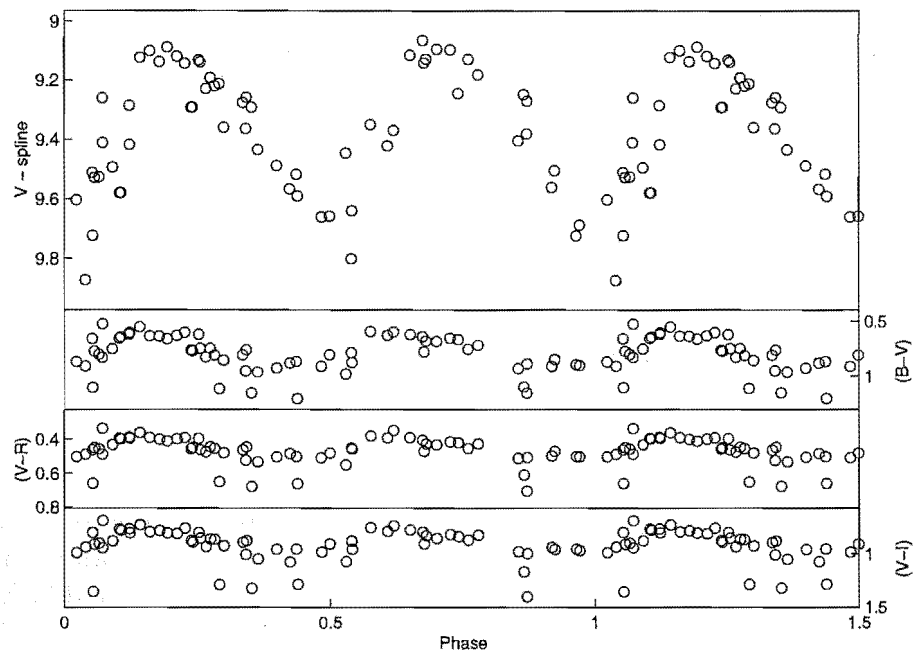

Figure 4.31: MJUO colour photometry of SX Cen phased on a period of 32.82 days from Fourier fitting to the V data.

Table 4.14: Periods between successive deep minima for TT Oph.

	Period (days)	Epoch JD - 2440000
Kukarkin et al. (1958)	61.08	—
DuPuy (1973)	61.08	(242)8723
This work	60.97	11251.709

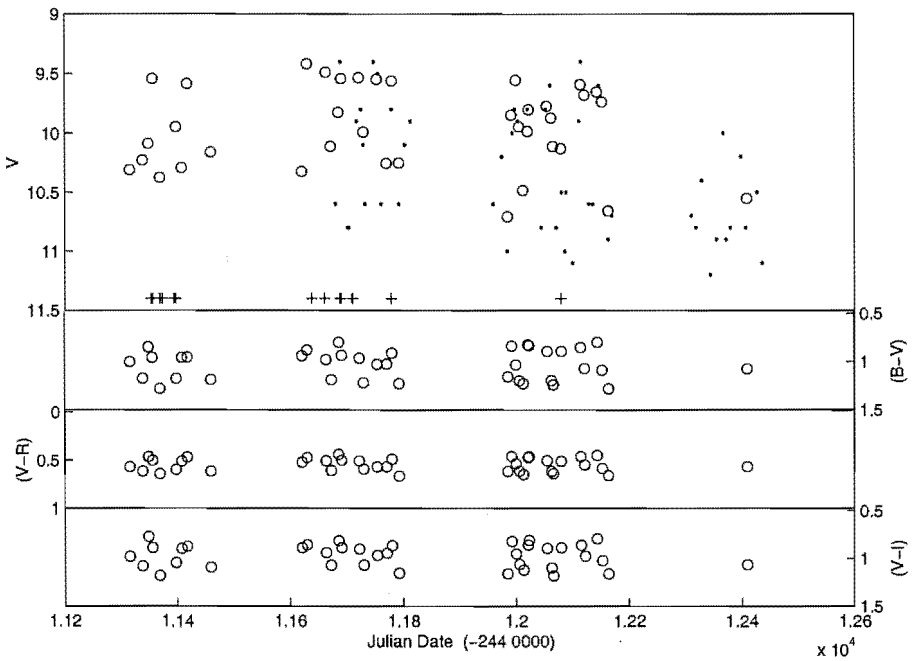

Figure 4.32: MJUO colour photometry of TT Oph.(+) indicate times of MJUO spectral observation. (.) indicate Albert Jones visual estimates.

4.4.2 TT Oph

TT Oph is simpler than SX Cen in that it is an RVa star and so does not show long-term variations in average light level. It has a longer period (~61 days; Table 4.14 and Khopolov et al., 1985), but still has not had its photometry studied to the same degree as many of the W Vir stars. Percy et al. (1997) contains a good summary of early photometric studies of TT Oph. The major studies include Preston et al. (1963); DuPuy (1973); Dawson (1979); Lloyd Evans (1985); Goldsmith et al. (1987); Horowitz (1987); Cardelli and Howell (1989). However these all use a period of 61.08 days from the General Catalogue of Variable Stars.

From Figure 4.32, there is very little to indicate long-term variations in the photometry. While the visual estimates decline in value (mean of V $\simeq$ 10.6 compared to ~10.2 when they started), this is unconfirmed by the MJUO photometry as there is only one data point in the relevant time period.

By Fourier fitting, the photometry phases well on a period of 60.97 days. Figure 4.33 (and Table C.18) show the *BVRI* magnitudes and Fourier fits to the photometry. The

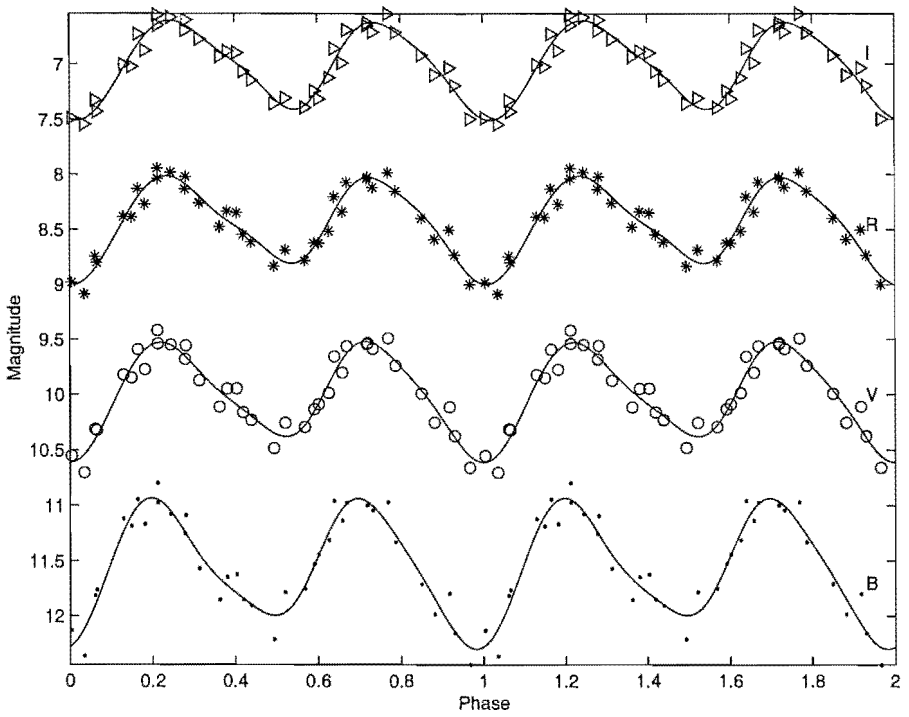

Figure 4.33: MJUO *BVRI* magnitudes of TT Oph phased on a period of 60.97 days from Fourier fitting to the *V* data. *B* magnitudes have been offset by +0.5 magnitudes, *R* by -1 and *I* by -2.

Table 4.15: Periods between successive deep minima for RU Cen.

	Period (days)	Epoch JD - 2440000
Pollard (1994) & Pollard et al. (1996a)	64.60	8124.570
This work	64.57	11295.618

light curves are smooth and repeat well, showing a small difference in depth between deep and shallow minima. As with the W Vir stars and SX Cen, the minimum position depends on wavelength as the redder the wavelengths, the later in the pulsational cycle the minimum occurs. Such a shift between the filters is also visible in the colour curves (Figure 4.34), as the *(B-V)*, *(V-R)* and *(V-I)* curves peak earlier in the pulsation cycle than the *V* curve.

4.4.3 RU Cen

RU Cen is also an RVa star, with a slightly longer period of 64 days (Table 4.15). It is considered to be one of the more regular RV Tauri stars. Pollard (1994) and specifically Pollard et al. (1996a) have studied the star recently and offer a comprehensive historical review of the star. Since then, the main work has been a spectroscopic analysis (Maas et al., 2002) who used the period of 64.6 days from Pollard et al. (1996a).

The mean amplitude of the *V* variations is constant (Figure 4.35). The colour curves

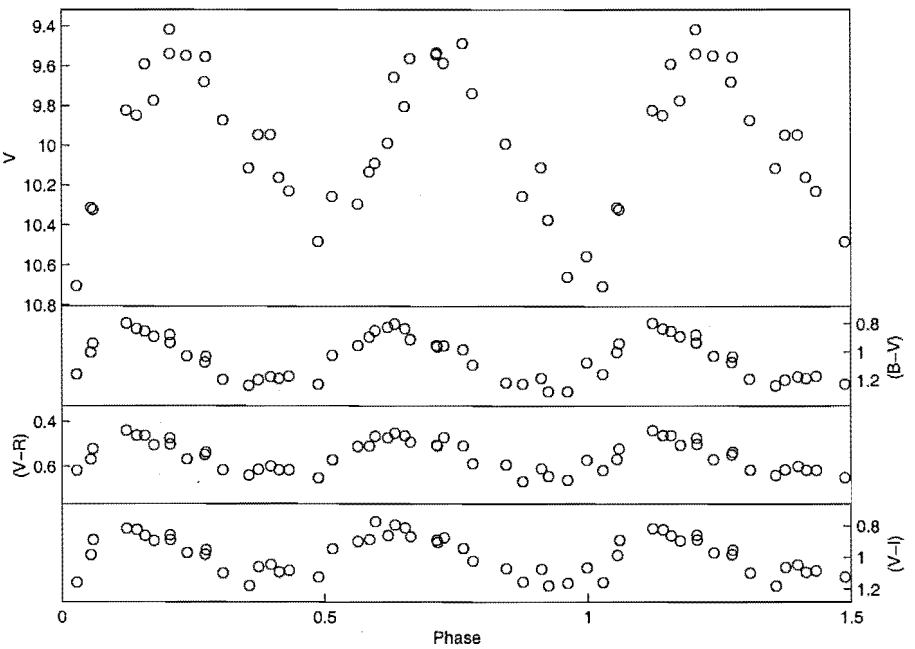

Figure 4.34: MJUO colour photometry of TT Oph phased on a period of 60.97 days from Fourier fitting to the V data.

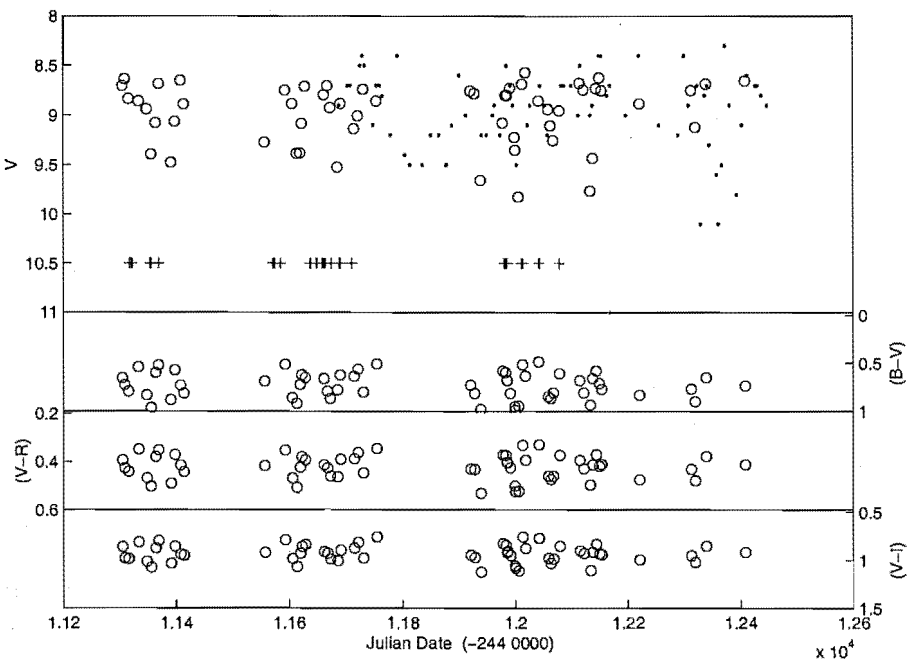

Figure 4.35: MJUO colour photometry of RU Cen. (+) indicate times of spectral observation. (.) indicate Albert Jones visual estimates.

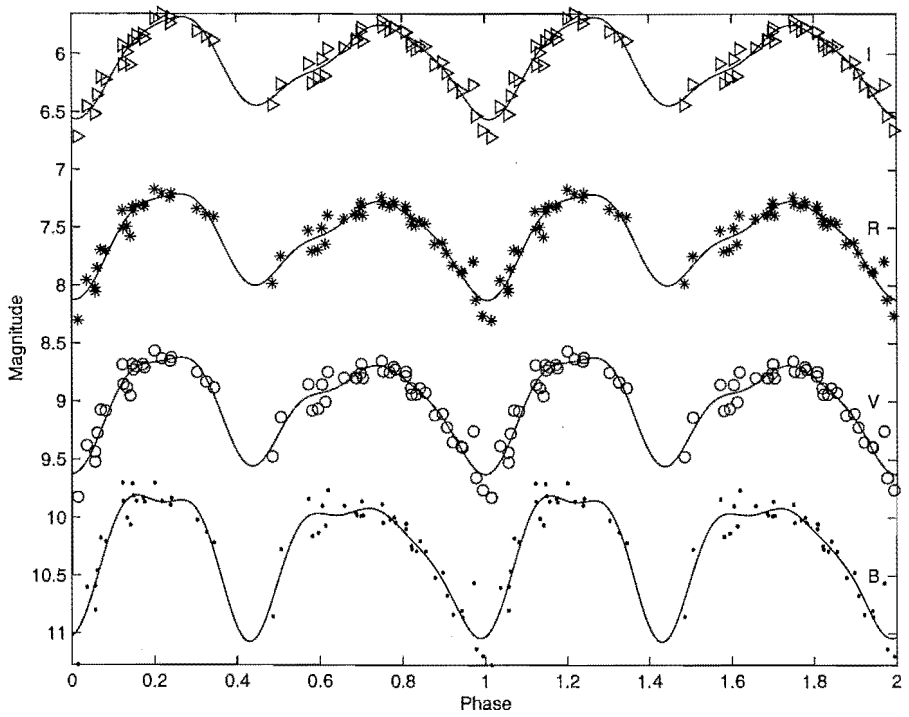

Figure 4.36: MJUO *BVRI* magnitudes of RU Cen phased on a period of 64.57 days from Fourier fitting to the *V* data. *B* magnitudes have been offset by +0.5 magnitudes, *R* offset by -1, *I* offset by -2.

are a little more complex in that they appear to show that the amplitude of the maxima in the colours varies. However it is not clear if this is real or an artifact of the data sampling. Such variations are not observed in the historical *(B-V)*, *(V-R)*, and *(V-I)* curves of Pollard et al. (1996a).

Fourier fitting to the *V* data gives a period of 64.57 days (Figures 4.36 and 4.37), giving minimal residuals (Table C.19). The lack of phase coverage between 0.35 and 0.45 means that the shallow minimum is not fitted as precisely as it might have been. This has truncated the time between deep and shallow minimum and lengthened the time between shallow and deep minimum, as measured by the Fourier fitted curve. The difference in the depths of the deep-shallow alternations is still clear, although it makes the overall shape of the curves a little more difficult to interpret.

Overall, both the primary maximum (the one following deep minimum) and the secondary maximum show the same pattern observed in the longer period W Vir stars (W Vir and ST Pup) and in SX Cen. There is an initial bump/peak after deep minimum, as the star reaches maximum light, but this bump decreases in magnitude as we move to redder wavelengths. The same phase lag is visible at the different wavelengths. *B* reaches its minimum light first, followed by *V* then *R* and *I*. These colour effects are also seen in the phased colour photometry (Figure 4.37), as *(B-V)*, *(V-R)* and *(V-I)* are all slightly ahead of *V* in phase, and reach maximum ~0.2 of a pulsational cycle before *V*.

The colour curves themselves rise from minimum to maximum in approximately 0.1 of a cycle but take approximately 0.4 of a cycle to return to minimum. This is similar to the behaviour observed in TT Oph (Figure 4.34).

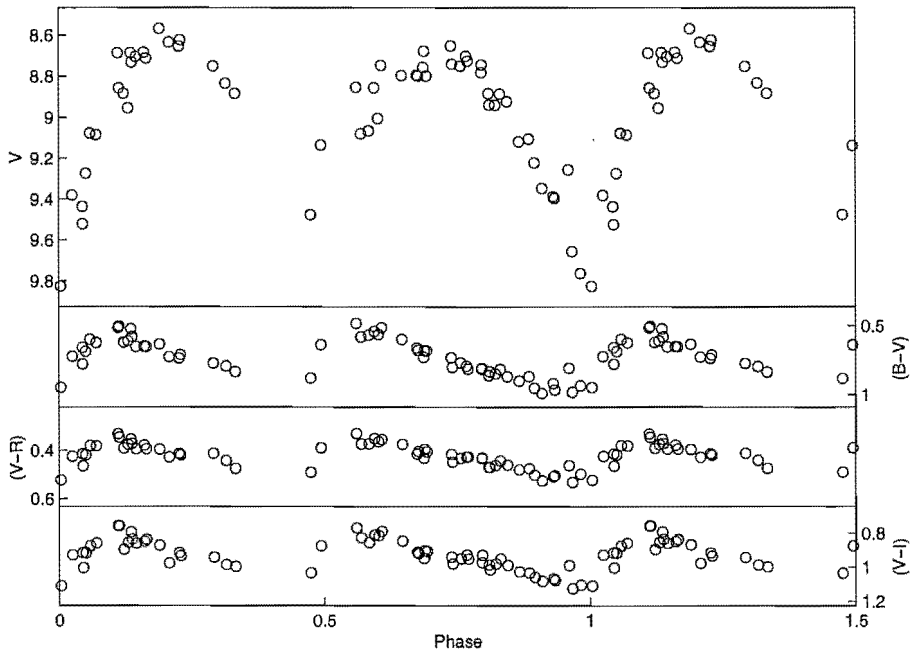

Figure 4.37: MJUO colour photometry of RU Cen phased on a period of 64.57 days from Fourier fitting to the V data.

Table 4.16: Periods between successive deep minima for CT Ori.

	Period (days)	Epoch JD - 2440000
Kukarkin et al. (1958)	135.52	(242)5649
Horowitz (1986)	66	—
This work	67.42	11370.181

4.4.4 CT Ori

CT Ori is more enigmatic than the previous stars in that it has not been determined if the star is an RVa or RVb. Also the period is not well established, as Kukarkin et al. (1958) give a period of 135.52 days but more recent visual estimates (Horowitz, 1986) give a period of 66 days between successive deep minima (Table 4.16).

There appear to be very few photometric studies examining the pulsations of CT Ori. While there has been some spectroscopic (DuPuy, 1973; Mantegazza, 1991), infrared (Lloyd Evans, 1985; Raveendran, 1989), molecular (Alcolea and Bujarrabal, 1991) and abundance analysis work (Gonzalez et al., 1997), the period does not appear to have been analysed at all. People either take the Kukarkin et al. (1958) period of 135.52 days, or the Horowitz (1986) period of 66 days from his visual estimates.

The mean magnitude appears quite constant (Figure 4.38), indicating CT Ori is an RVa star, at least over the time period examined. Neither the V, nor the colour photometry, appear to vary on a longer time span than the pulsational period.

CT Ori phases well on a 67.42 day period from Fourier fitting (Table C.20). In

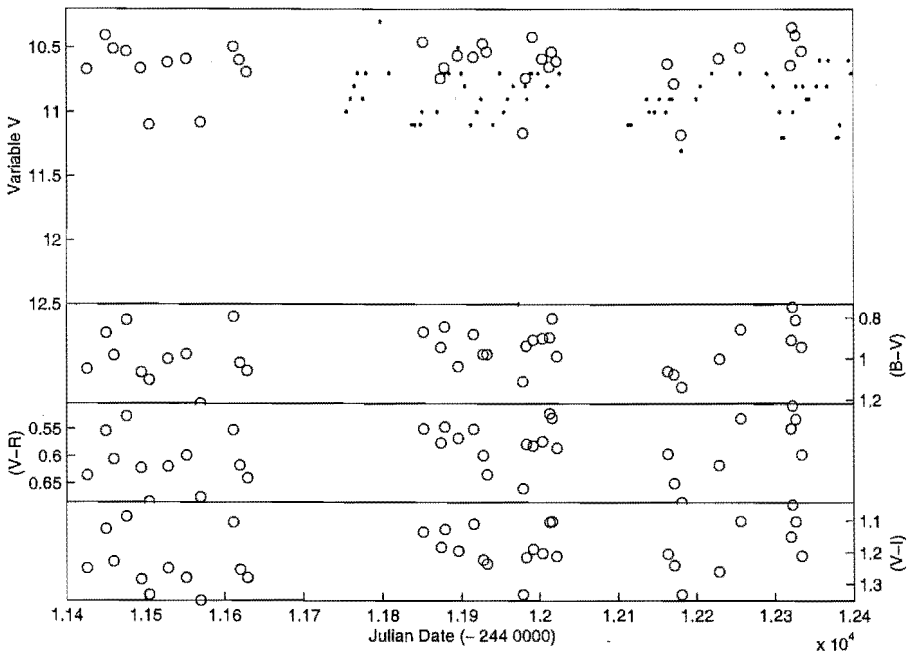

Figure 4.38: MJUO colour photometry of CT Ori. (.) are Albert Jones visual estimates. No MJUO spectral observations were made of this star.

comparison to the previous RV Tauri stars, the shallow minimum is much shallower than the deep minimum (Figure 4.39). Insufficient photometry to distinguish this shallow minimum may be the reason behind the 135.52 day period from Kukarkin et al. (1958).

The light curves (Figure 4.39) show that the primary maximum is brighter than the secondary maximum. Both the primary and secondary maxima in B show a strong initial peak (ϕ=0.2 and 0.6) directly after the deep minimum, with an irregular curve declining in light after (ϕ=0.4 and 0.8). This initial peak is weaker on the secondary maximum, but still clearly present. From the pattern observed in the W Vir stars (W Vir and ST Pup), this would indicate a strong shock in the star at those phases, especially since the amplitude of the initial maximum decreases at redder wavelengths for both the primary and secondary maximum. The same trend of phase lag with pulsational phase occurs at redder wavelengths, which is observed in the all other stars.

Similar phase shifts in colour are observed in the phased colour photometry for CT Ori (Figure 4.40). Both the primary minimum and maximum in the *(B-V)*, *(V-R)* and *V-I* curves are ahead of the V deep minimum. However the colour maximum occurs much earlier. That is to say $\delta\phi$=0.05 for the minimum compared to $\delta\phi$=0.1 for the maximum. The secondary minimum is far less clear in the colour curves, so it is difficult to calculate any phase shift. The secondary minimum is much smoother and more gently curved than primary minimum. Also, the bump after the initial light peak on the secondary light maximum is far more pronounced in *(V-R)* and *(V-I)* than *(B-V)*, indicating the star is much bluer at that phase. It is unclear why this is and more investigation is recommended at a later date.

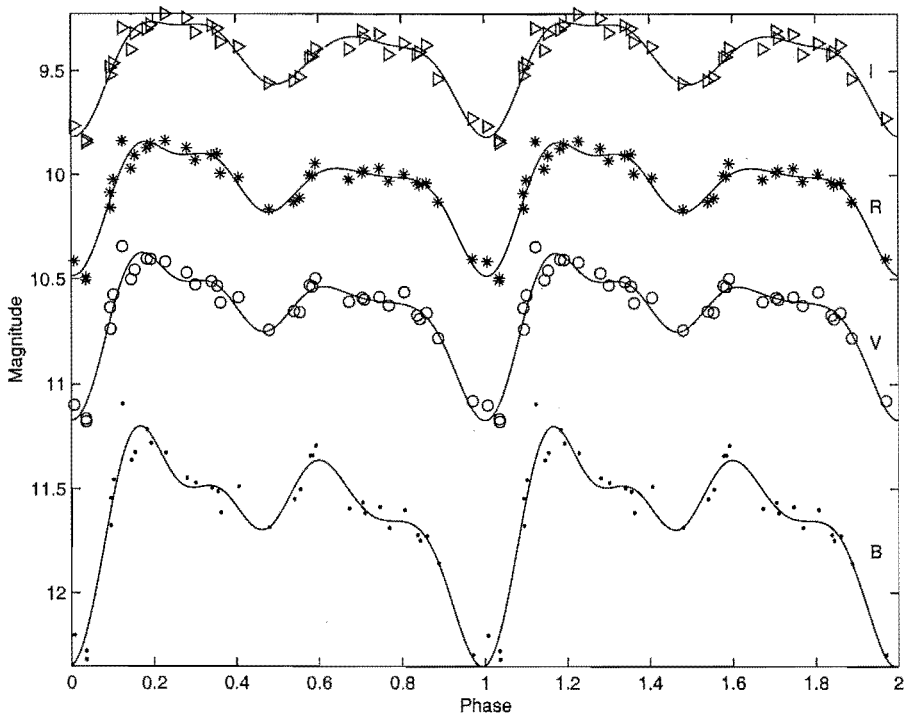

Figure 4.39: MJUO *BVRI* magnitudes of CT Ori phased on a period of 67.42 days from the Fourier fitting to the V data. No offsets have been applied.

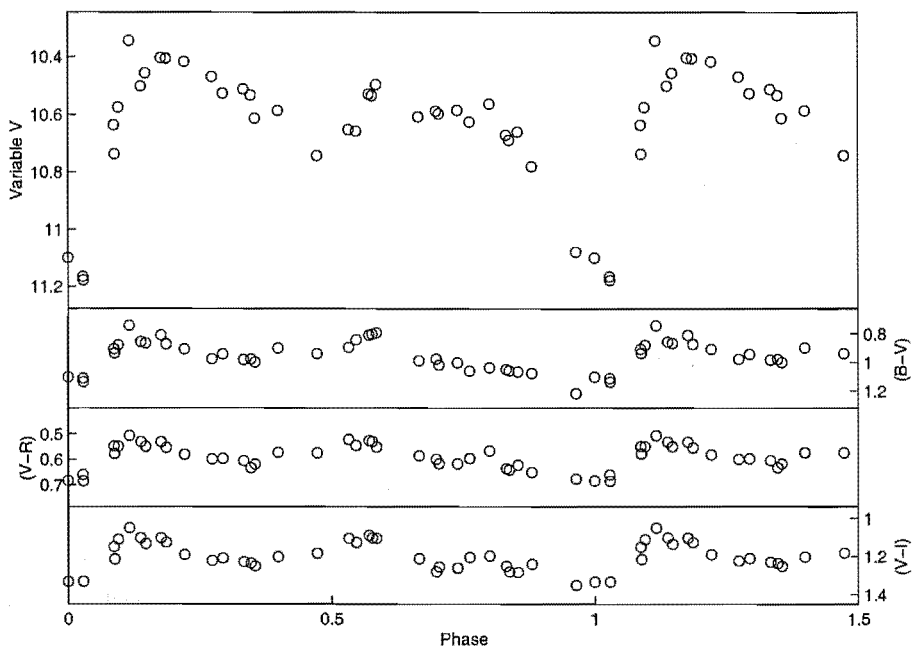

Figure 4.40: MJUO colour photometry of CT Ori phased on a 67.42 day period from Fourier fitting to V data.

Table 4.17: Periods between successive deep minima for AI Sco.

	Period (days)	Epoch JD - 2440000	Long-term period (days)
Pollard (1994) & Pollard et al. (1996a)	71.0	8373.93	940
This work	71.45	11263.092	—

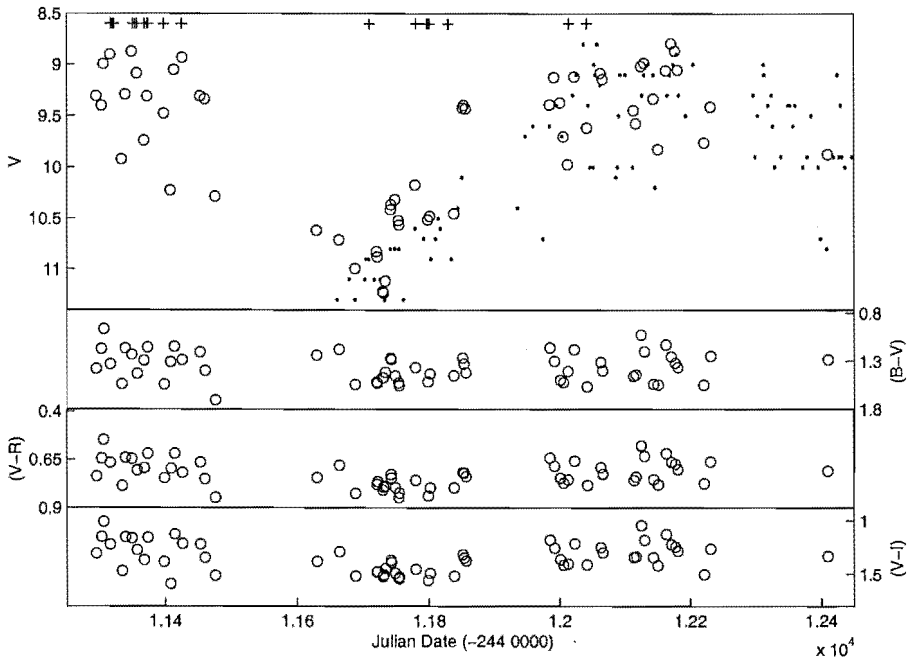

Figure 4.41: MJUO colour photometry of AI Sco. (+) indicate when MJUO spectral observations were made. (.) are Albert Jones visual estimates.

4.4.5 AI Sco

The RVb star AI Sco (P = 71 d), has been more intensively studied than CT Ori, but still without any great detail. The best and most recent review and study has been by Pollard et al. (1996a), who found a period of 71.0 days (Table 4.17) and provide a good historical review.

Long-term variations in magnitude are clearly visible in Figure 4.41. Between the end of the first observing season and the beginning of the next, the star goes very rapidly into a long-term minimum and takes a little over one observing season to recover. This is in contrast to the observations presented by Pollard et al. (1996a), who managed to observe either side and in the middle of a long-term minimum, but not during the transition. From the colour curves, and as observed by Pollard et al. (1996a), AI Sco becomes much redder over the long-term minimum. This has also been observed in SX Cen (Figure 4.28).

In order to find a pulsational period, the long-term variations have been removed by fitting a spline curve (Figure 4.42) to the V photometry, and subtracting that curve. The

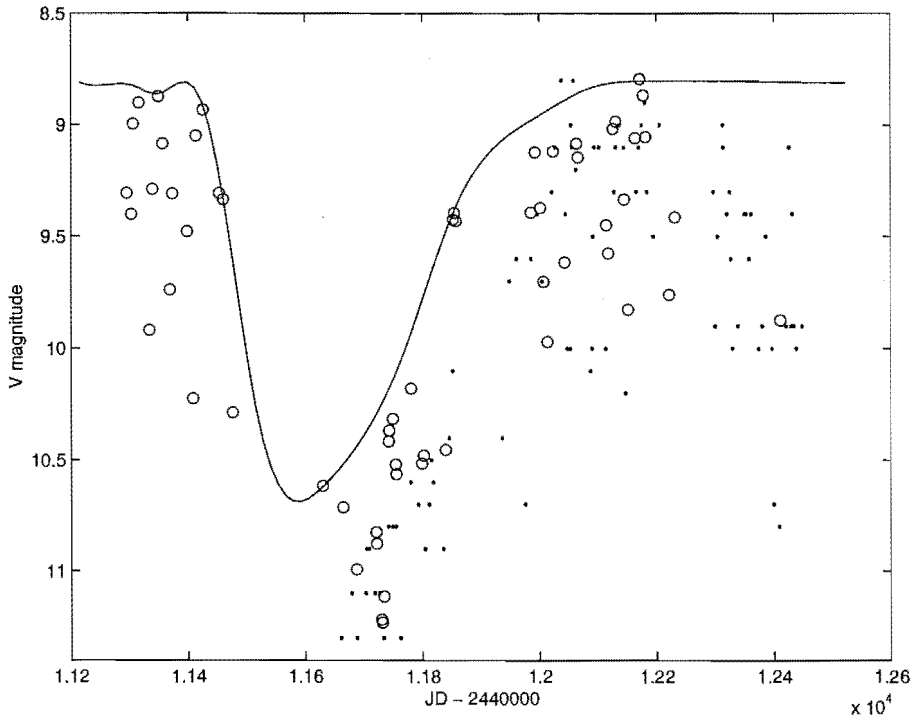

Figure 4.42: MJUO V photometry of AI Sco showing spline curve fitted to remove the long-term variation. (.) are Albert Jones visual estimates.

photometry has then been rescaled to model the amplitude of the star without the presence of the long-term variations by adding a constant offset of the amplitude of maximum light (see Table C.21). A period of 71.45 days was then found by Fourier fitting (see Table C.21).

As can be seen from Figure 4.43 and 4.44, the photometry phases well on the period of 71.45 days with minimal residuals (Tables 4.12 and C.21). The light curves are quite smooth, with a rounded shallow minimum. The deep and shallow minima are distinct, declining in brightness down to 10.2 in V for the deep minimum and ~9.8 in V for the shallow minimum. The light maxima are not completely symmetrical, but show a slight peak following the light minimum, which decreases in amplitude for the redder wavelengths. This is much less distinct than observed in RU Cen (Figure 4.36) and CT Ori (Figure 4.39).

The phased colour data (Figure 4.44) appears more scattered in *(V-R)* and *(V-I)*, but this is due to the long-term variations, where as mentioned with respect to the unphased colour photometry (Figure 4.41), the star appears much redder when it is in long-term minimum.

4.4.6 AR Pup

Another RVb star, AR Pup (P = 77 days) shows more sinusoidal variations over the long-term than the previously examined RVb stars. Again, Pollard et al. (1996a) offers the most comprehensive presentation of $BVRI$ photometry and historical review, finding a period of 77.79 days (Table 4.18). Since then, Raveendran (1999) has also examined

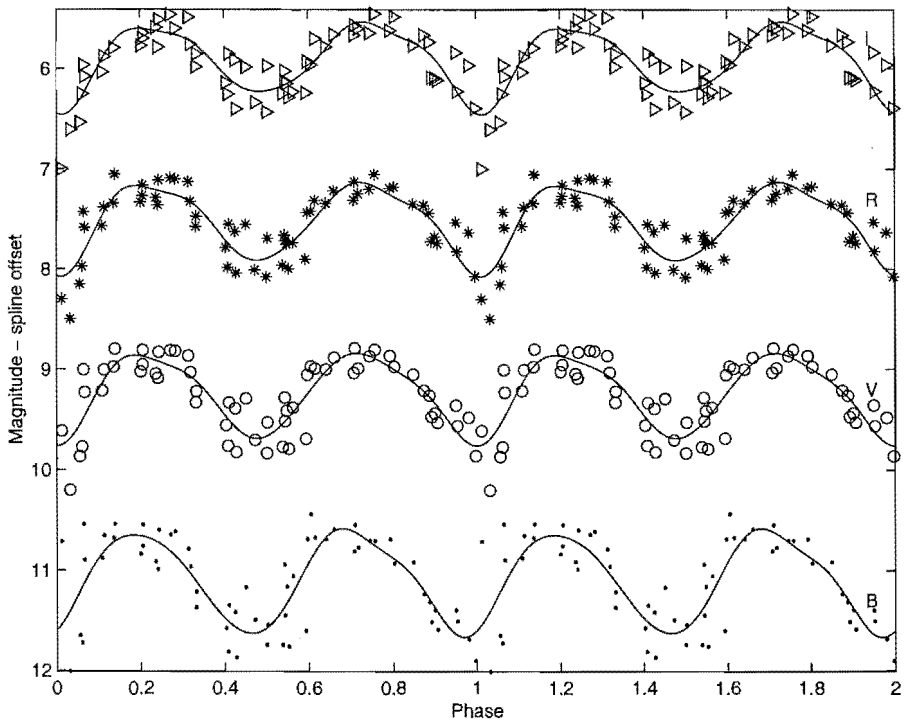

Figure 4.43: MJUO *BVRI* magnitudes of AI Sco phased on a period of 71.45 days from Fourier fitting to the V data with the spline curve fit to the V photometry removed. B magnitudes have been offset by +0.5 magnitudes, R by -1 and I by -2.

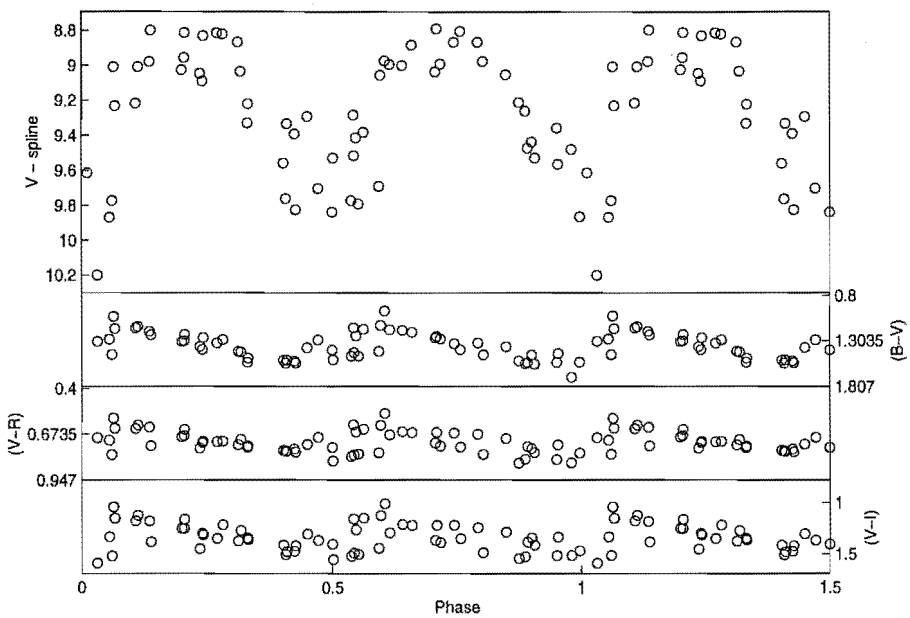

Figure 4.44: MJUO colour photometry of AI Sco phased on a period of 71.45 days from Fourier fitting to the V data.

Table 4.18: Periods between successive deep minima for AR Pup.

	Period (days)	Epoch JD - 2440000	Long-term period (days)
Pollard (1994) & Pollard et al. (1996a)	77.79±0.01	8071.09	1389±30
Raveendran (1999)	—	—	1165±4
This work	76.47	11226.331	—

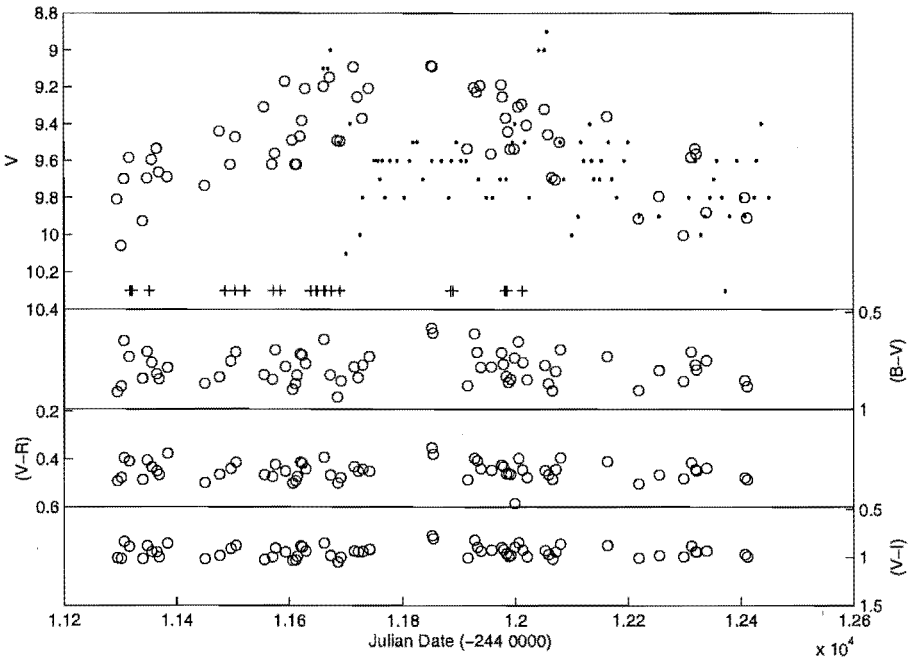

Figure 4.45: MJUO colour photometry of AR Pup. (+) indicate times of spectral observation. (.) indicate Albert Jones visual estimates.

AR Pup photometrically, specifically concentrating on the long-term variations and degree of polarization of the light of the star. They found a nearly sinusoidal long-term period of 1165 days.

This long-term trend is clearly visible in Figure 4.45. In contrast to the other RVb stars so far examined (SX Cen and AI Sco), AR Pup spends minimal time at long-term maximum light, which illustrates the sinusoidal shape (Pollard et al., 1996a; Raveendran, 1999). AR Pup also shows no variation of colour as a function of the long-term variation as seen in Figure 4.45 and Pollard et al. (1996a, Figure 20), unlike SX Cen and AI Sco which get redder during long-term minimum.

To remove the long-term variations for subsequent Fourier analysis, a spline curve has been fitted to the V photometry (Figure 4.46) and subtracted from the data. A constant offset has then been applied to re-scale the data to the maximum light brightness. From the Fourier analysis, a period of 76.47 days has been obtained (see Table C.22 for offset, Fourier coefficients and RMS residuals). This phases well (Figure 4.47) but does show more scattered light curves than the shorter period stars SX Cen, TT Oph, RU Cen and

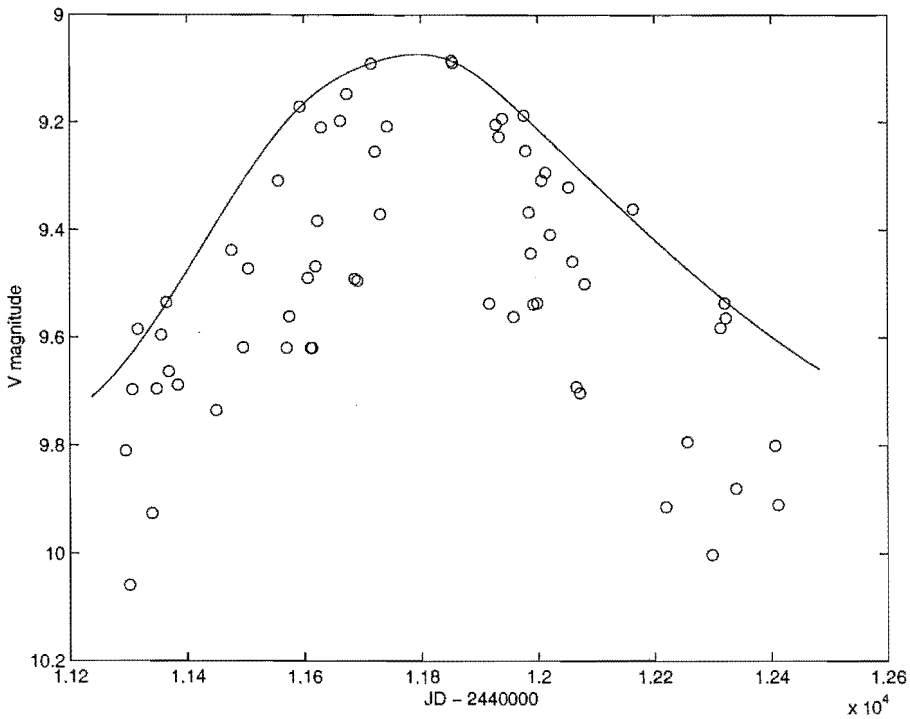

Figure 4.46: MJUO V photometry of AR Pup showing the spline curve fitted to remove the long-term variation.

CT Ori. The degree of scatter does not appear to get greater at the redder wavelengths (RMS = 0.0616 in I compared to 0.1054 in B). This confirms that there is no reddening as a function of long-term phase.

In terms of the light curves, there are similarities to the previous stars in that to the blue, there is a distinct initial maximum light peak, with a bump thereafter. This initial bump decreases in amplitude at redder wavelengths and is visible at both primary and secondary maximum, although the peak is far less pronounced in association with the secondary maximum. Association of the initial blue peak with a shock wave would imply a weaker shock being associated with the secondary maximum. Investigation of spectral shock features such as emission lines and line splitting would be needed to investigate this further.

Differences between the depths of the deep and shallow minima in AR Pup are reasonably clear although not as distinct as in TT Oph or RU Cen. Deep minimum occurs around V=9.6 for AR Pup, whereas shallow minimum is around V=9.5. The phase of minimum light lags behind at redder wavelengths. A similar colour offset is visible when we examine the phased colour photometry (Figure 4.48). Minimum *(B-V)*, *(V-R)* and *(V-I)* occurs shortly before minimum V light. The phased colour curves show little scatter, indicating that there is little or no change in colour due to the long-term variations.

4.4.7 AR Sgr

As an RVa star, AR Sgr (P = 88 days) is far simpler to examine. The most recent and comprehensive photometric study has been by Pollard et al. (1996a) and it should be

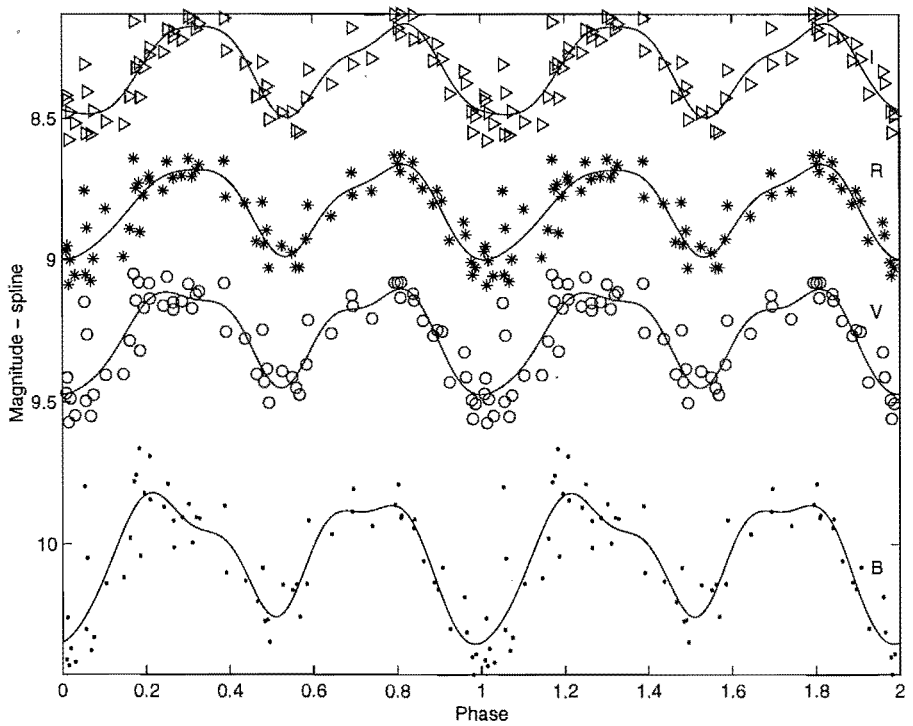

Figure 4.47: MJUO *BVRI* magnitudes of AR Pup phased on a period of 76.47 days from the Fourier fitting to the *V* data. Long-term variations (Figure 4.46) have been removed and a constant offset applied. No additional offsets have been applied to the photometry.

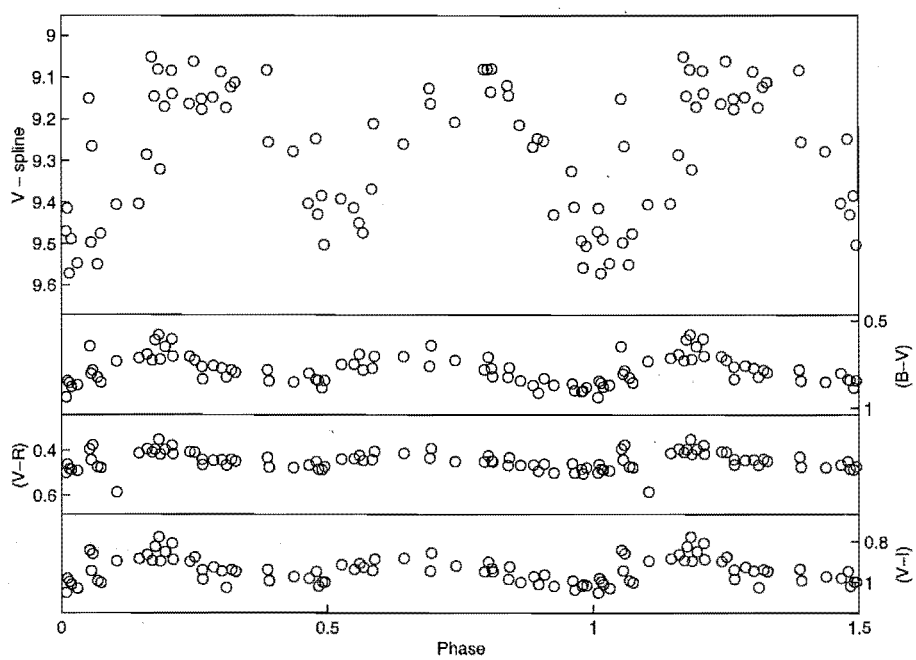

Figure 4.48: MJUO colour photometry of AR Pup phased on a period of 76.47 days from Fourier fitting to the *V* data. Long-term variations have been removed from the *V* photometry, but not the *(B-V)*, *(V-R)* and *(V-I)* colours.

Table 4.19: Periods between successive deep minima for AR Sgr.

	Period (days)	Epoch JD - 2440000
Pollard (1994) & Pollard et al. (1996a)	88.86±0.03	8362.57
This work	87.13	11236.023

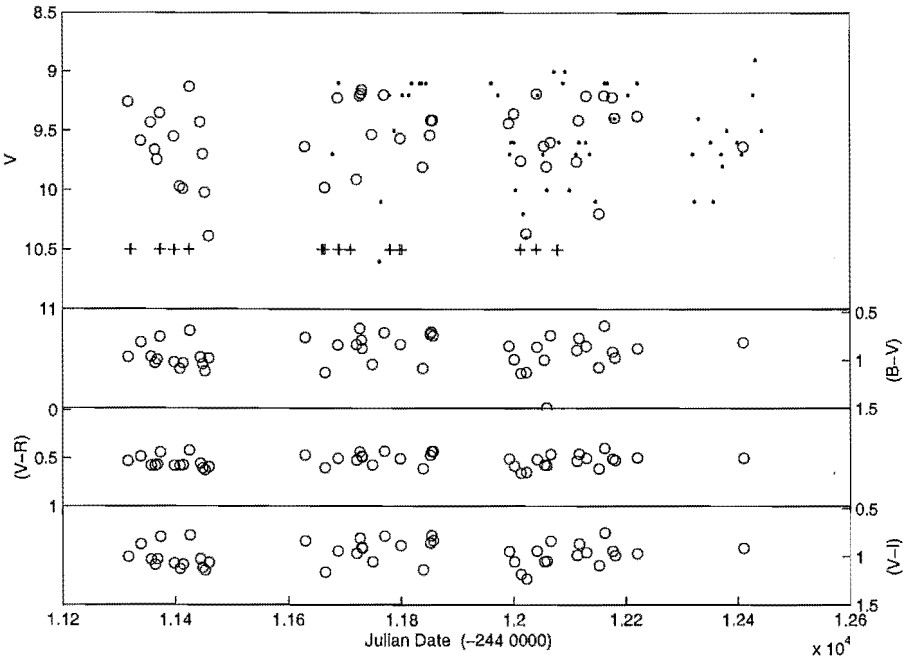

Figure 4.49: MJUO colour photometry of AR Sgr.(+) indicate times of spectral observation. (.) indicate Albert Jones visual estimates.

consulted for historical references. Pollard et al. (1996a) found a period of 88.86 days (Table 4.19) and a star with clear alternations between deep and shallow minima. Figure 4.49 shows no changes in mean magnitude or colour over the time period examined. However, the clear deep and shallow minima and repeatable light curve do not seem to be supported by the phased photometry.

Fourier analysis of AR Sgr results in a period of 87.13 days (see Table C.23 for Fourier coefficients and residuals). As seen from Figure 4.50, this results in a curve with no apparent difference between the depths of the two minima. This is in contrast to the regular behaviour examined by Pollard et al. (1996a) who found the deep minima to be down to V=10.8 and the shallow minima to be a magnitude higher at V=9.8. From this it would appear that during the time of observation examined here, the star has "flipped" such that a deep minimum has followed a deep minimum or a shallow minimum has followed a shallow minimum, and the usual pattern has been reversed. Unfortunately the scattered data coverage means that it is not possible to tell when the flip occurred, or if there were more than one of them. The density of data around phase 0.5 suggests that this is usually the shallow minimum as there is a cluster of data at V=9.7, whereas the deep minimum level appears to be around V=10.3.

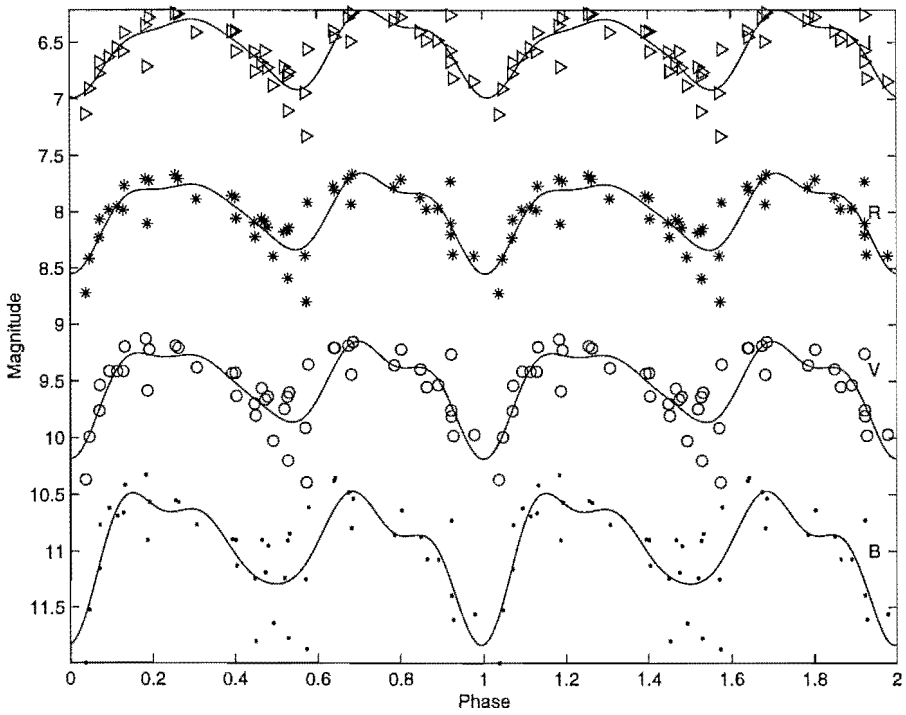

Figure 4.50: MJUO *BVRI* magnitudes of AR Sgr phased on a period of 87.13 days from the Fourier fitting to the *V* data. *B* magnitudes have been offset by +0.5 magnitudes, *R* by -1 and *I* by -2.

With respect to the light curves similar trends are observed to those in the earlier stars. In the blue, there is an initial peak which is followed by a bump, and the amplitude of that peak decreases as we move to redder wavelengths. This is true of both the primary maximum and the secondary maximum. However the secondary maximum peak persists much further into the red. This may indicate a stronger shock in the secondary maximum compared to the primary one[9].

With respect to the phased colour photometry (Figure 4.51), the minimum at phase 0.5 (nominally the shallow one) is of interest in that *(B-V)*, *(V-R)* and *(V-I)* all show more scatter towards the red at that phase. Moreover, as observed by Pollard (1994), the rise from deep minimum in *(B-V)*, *(V-R)* and *(V-I)* is quite steep and abrupt compared to that observed for the secondary minimum.

4.4.8 UZ Oph

Another RVa star, UZ Oph (P = ~88 days) has also been somewhat neglected with respect to an historical pulsational study. As with many of the RV Tauri stars, rather than actually examine the period, most authors have taken the period from the General Catalogue of Variable Stars edition with the closest date to their observations. The only authors who appear to have reviewed the period are DuPuy (1973) and Horowitz (1986) (see Table 4.20), but neither appear to have done a full Fourier analysis. Since 1950 historical photometry has been obtained by Preston et al. (1963); DuPuy (1973); Dawson

[9]Or it may reflect the relatively large scatter in the data points.

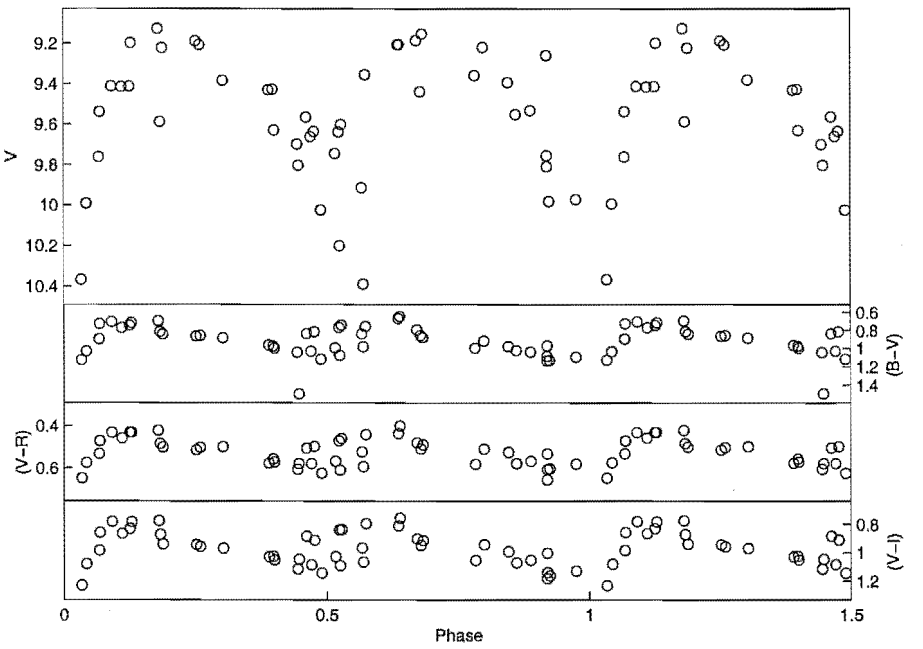

Figure 4.51: MJUO colour photometry of AR Sgr phased on a period of 87.13 days from Fourier fitting to the V data.

Table 4.20: Periods between successive deep minima for UZ Oph.

	Period (days)	Epoch JD - 2440000
Kukarkin et al. (1958)	87.44	(242)2230.2
DuPuy (1973)	87.3	—
Horowitz (1986)	87	—
This work	88.90	11277.410

(1979), infrared photometry by Lloyd Evans (1985) and a combination of both and/or other measurements by Goldsmith et al. (1987); Cardelli and Howell (1989). Horowitz (1987) examined visual estimates and showed that the star was capable of a variety of behaviour, with one observing season (JD ~2446500) showing a series of deep minima followed by a series of shallow minima, and the following season (JD ~ 2447000) showing clear alternations of deep and shallow minima in a classical RV Tauri shaped light curve.

From the MJUO photometry (Figure 4.52), the star is clearly an RVa star as it shows no signs of varying in mean magnitude over the time period examined.

UZ Oph phases well on a period of 88.90 days from Fourier fitting (see Table C.24 for Fourier parameters and RMS residuals). As seen in Figure 4.53, UZ Oph shows a clear deep and shallow minimum pattern, with the deep minimum reaching V ~12.5 and the shallow minimum reaching V ~11.4. Once again, minimum light lags further behind in phase at redder wavelengths. Also, the initial blue peak ($\phi \sim 0.2$ and 0.65) with the gradual bumpy decline is present, and this initial peak declines in prominence at redder wavelengths. Like AI Sco (Figure 4.43), the initial peak appears slightly stronger after

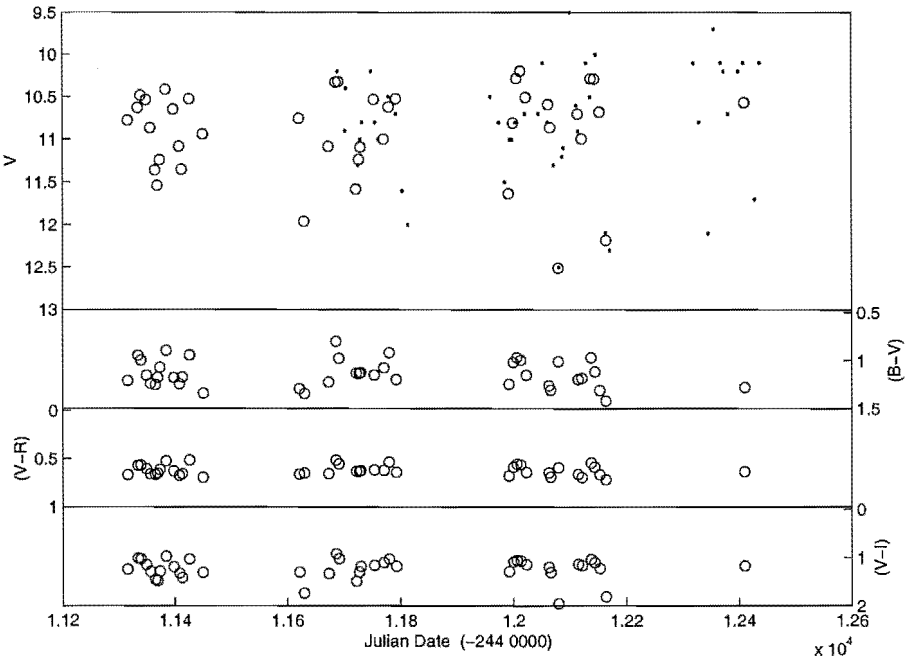

Figure 4.52: MJUO colour photometry of UZ Oph. (.) indicate Albert Jones visual estimates. No MJUO spectral observations were made of this star.

Table 4.21: Periods between successive deep minima for TX Oph.

	Period (days)	Epoch JD - 2440000
Kukarkin et al. (1958)	135	—
DuPuy (1973)	135.33	—
This work	135.81	11210.029

the shallow minimum from the fitted curve, however this may be an artifact of the scatter in the data. The blue peak is supported by the phased MJUO colour photometry (Figure 4.54), as there is a distinct blue peak in the colours at phases 0.2 and 0.6. This indicates that a shock is present in the star at those phases, as the the temperature of the star is increased by the shock passage and appears bluer. None of the colours show much scatter, indicating there is no long-term colour change in the star.

4.4.9 TX Oph

The next three stars (TX Oph, R Sct and IW Car) are more complicated as they show far more variation in magnitude and in the stability of their period than the other stars. This has made finding a period and adequately fitting a curve to the data quite difficult.

For instance, TX Oph is listed in Kukarkin et al. (1958) as having a period of 135 days (Table 4.21). Unfortunately the only historical work to check this period has been DuPuy (1973) who suggested a revision to 135.33 days. Photometrically, TX Oph has been studied even less than UZ Oph, with the only photometric studies in the past 40

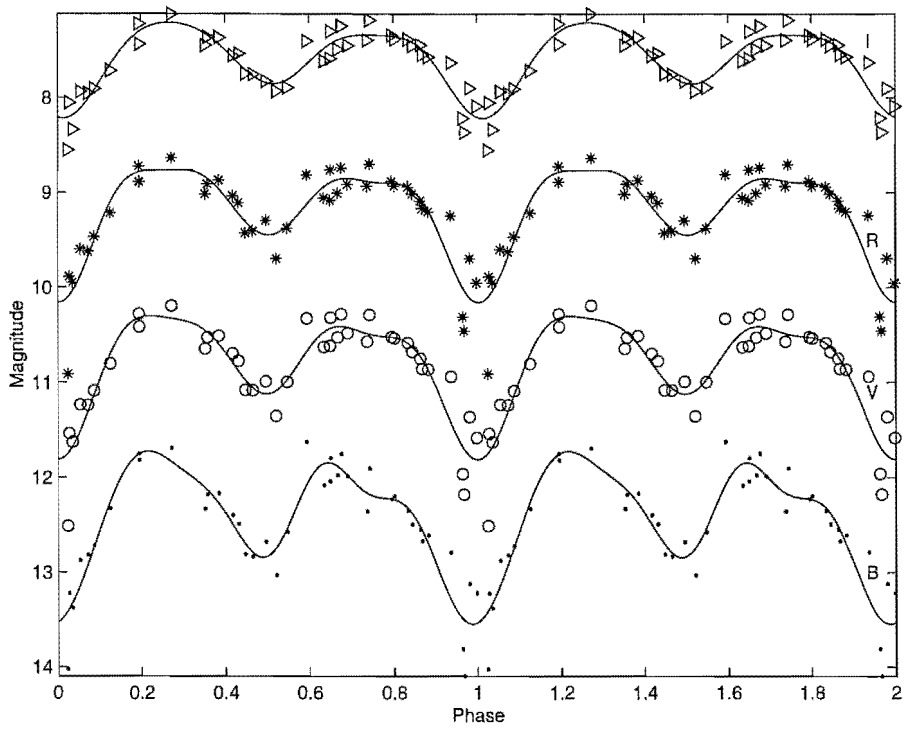

Figure 4.53: MJUO *BVRI* magnitudes of UZ Oph phased on a period of 88.90 days from the Fourier fitting to the V data. B magnitudes have been offset by +0.5 magnitudes, R by -1 and I by -2.

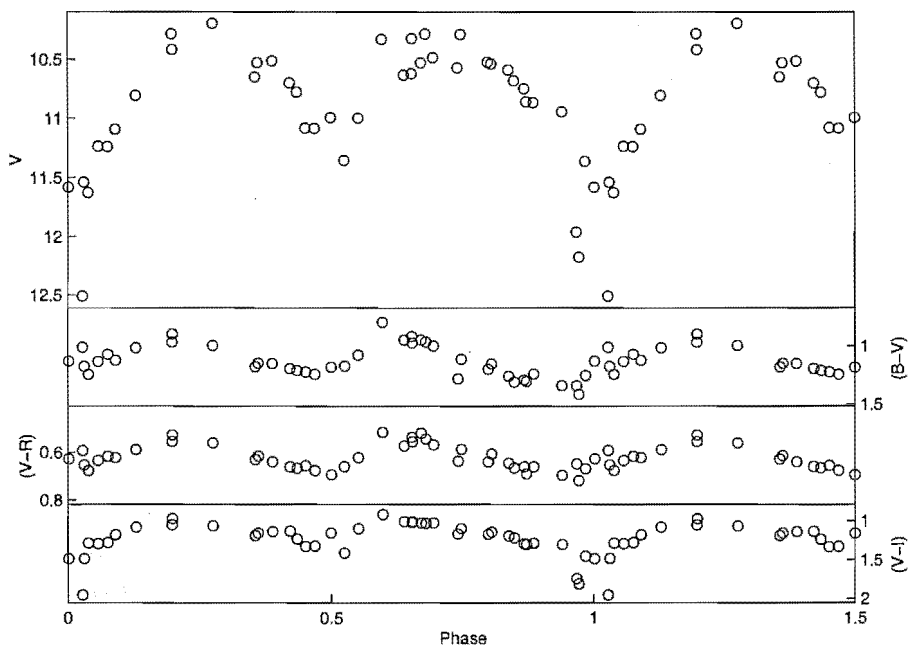

Figure 4.54: MJUO colour photometry of UZ Oph phased on a period of 88.90 days from Fourier analysis of the V data.

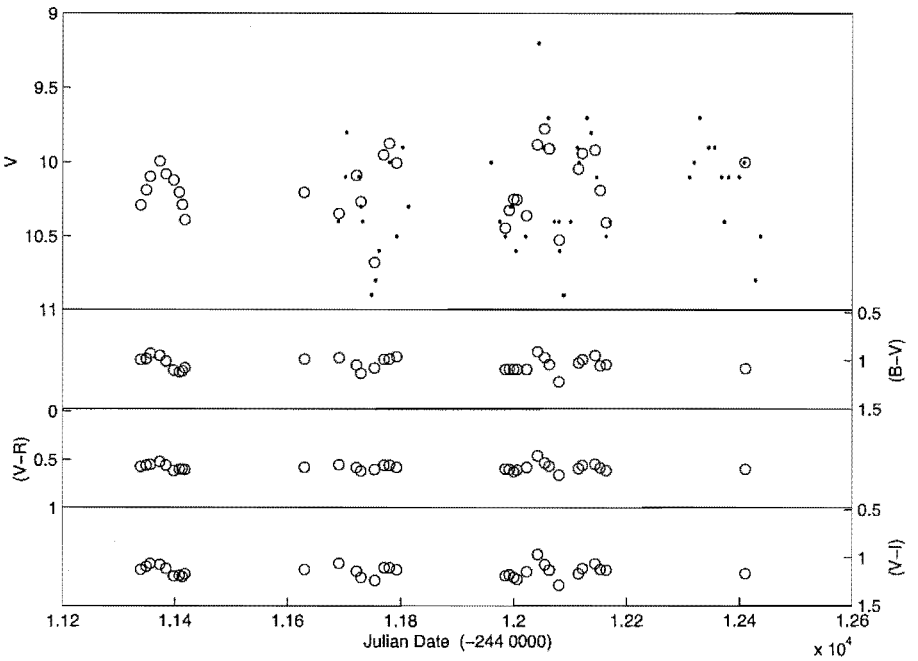

Figure 4.55: MJUO colour photometry of TX Oph. (.) indicate Albert Jones visual estimates. No MJUO spectral observations were made of this star.

years being Preston et al. (1963); DuPuy (1973); Dawson (1979); Goldsmith et al. (1987); Cardelli and Howell (1989).

Examining the MJUO photometry (Figure 4.55), there is very little sign of long-term variation in magnitude, indicating that the star is an RVa star.

By Fourier analysis, a period of 135.81 days is derived (see Table C.27 for Fourier parameters and RMS residuals). However this period results in a relatively irregular curve which shows several maxima (Figure 4.56). If we ignore the Fourier fitted curve, we can see approximately 2 maxima and 2 minima between phases 0.0 and 1.0. The primary maximum following the deep minimum by the phasing convention occurs around phase 0.2. The shallow minimum appears to occur around phase 0.5. The secondary maximum following that is a little more ambiguous, given the double peak between phases 0.6 and 0.9. The scattered points make it difficult to determine if the trend of phase lag towards redder wavelengths is present. This also means that it is difficult to determine if there is an initial shock-related peak in the light curves at the bluer wavelengths.

From the phased colour curves (Figure 4.57), this shock feature may be present, as the colours are marginally bluer just after the deep minimum. However, the scatter and the lack of phase coverage means that it is inconclusive as to whether or not there is a shock wave present just after the shallow minimum.

4.4.10 R Sct

Being the brightest RV Tauri star (V=5.0-6.8), R Sct (P $\simeq$140 days) has been studied extensively. However it is also one of the most irregular RV Tauri stars, which has made these studies difficult to interpret. Photometric studies of R Sct since 1950 are listed in Table 4.23.

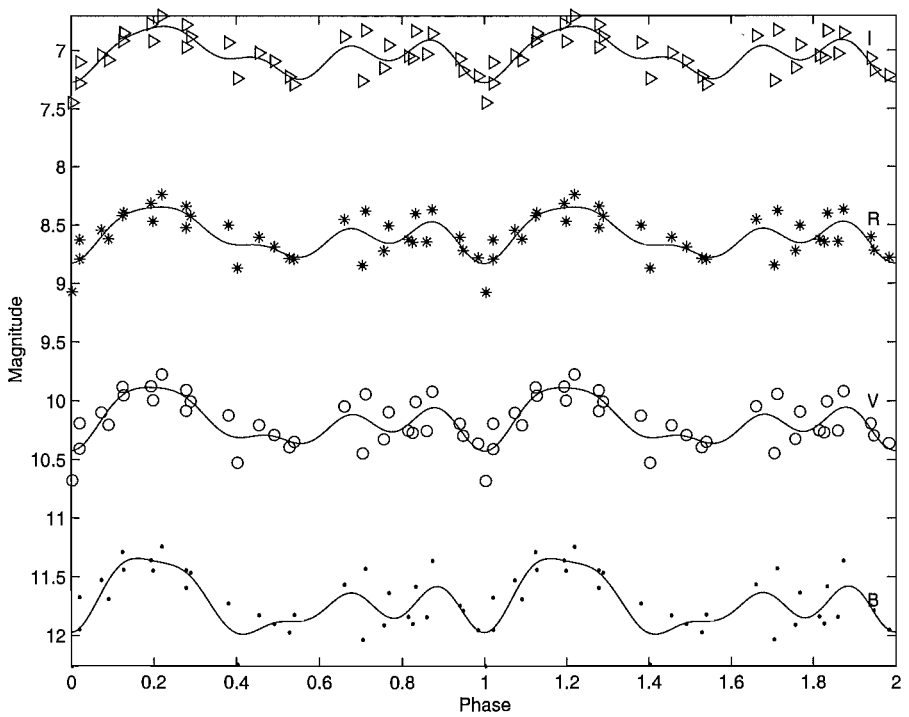

Figure 4.56: MJUO *BVRI* magnitudes of TX Oph phased on a period of 135.81 days from the Fourier fitting to the V data. B magnitudes have been offset by +0.5 magnitudes, R by -1 and I by -2.

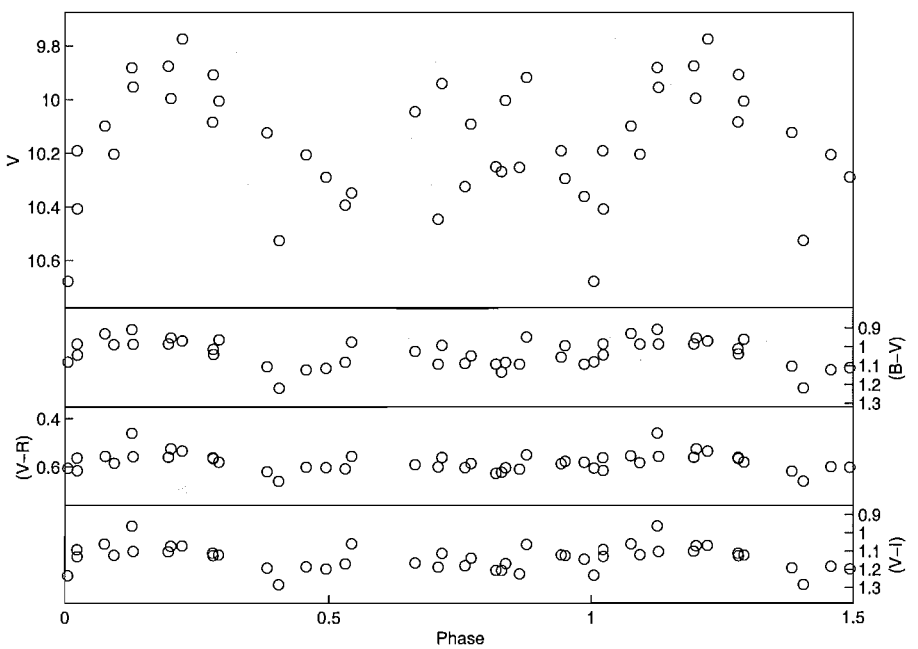

Figure 4.57: MJUO colour photometry of TX Oph phased on a period of 135.81 days from Fourier fitting to the V data.

Table 4.22: Periods between successive deep minima for R Sct.

	Period (days)	Epoch JD - 2440000
Percy et al. (1991)	141.90 (prior to 1941)	—
	140.0 (after 1941)	—
Pollard (1994) & Pollard et al. (1996a)	140.30	8073.05
Matsuura et al. (2002)	132-150[a]	—
This work	134.87	11075.524

[a]Range from wavelet analysis of visual estimates from a range of sources.

Table 4.23: R Sct historical photometry.

Colour photometry	Rosino (1951); Preston et al. (1963); Serkowski (1970); DuPuy (1973); Wisse and Wisse (1973); Dawson (1979); Cardelli (1985); Cardelli and Howell (1989)
Infrared	Gehrz and Woolf (1970); Lloyd Evans (1985); Goldsmith et al. (1987); Raveendran (1989)
Others	Horowitz (1987); Shenton et al. (1994c)

Percy et al. (1991) studied the period changes in the star (Table 4.22). As well as finding a period of 141.90 days prior to 1941 and 140.0 days after 1941, they summarise the literature discussing historical photometry and period changes of R Sct. Since then, Pollard et al. (1996a) found a period of 140.30 days. Most recently, several authors have examined historical visual estimates of R Sct in order to determine nonlinear pulsational properties (Buchler et al., 1996; Buchler and Kolláth, 2003) and evolutionary changes (Matsuura et al., 2002). Unfortunately the extreme irregularity of the star has meant that the light curve characteristics cannot be described simply. This chaotic behaviour of the light curve of R Sct has lead some to argue that it should be classed as an RVb star (Howell et al., 1983; Cardelli, 1985; Cardelli and Howell, 1989) in that its light curve shows variations, especially with respect to the depths of its minima, on a time-scale greater than that of the pulsation cycle.

From Figure 4.58, R Sct does not show any change in maximum mean brightness. The variable depths of the light minima are more of note, as R Sct shows a far deeper than usual minimum just after JD 2452000. During this minimum, the *(B-V)* and *(V-R)* colours become bluer, whereas the *(V-I)* colours are redder. This same effect has been observed by Pollard et al. (1996a) for R Sct around JD 2449200 and the subsequent deep minimum at $\sim$ JD 2449200, when the star experienced a very deep minimum and the *(B-V)* and *(V-R)* colours went bluer while the *(V-I)* colours were redder. The mechanism behind this is not known but spectroscopy of such a decline is reminiscent of R Coronae Borealis decline behaviour and a similar mechanism may be involved (Pollard et al., 1996a).

Fourier analysis of the MJUO V photometry results in a period of 134.87 days (see Table C.26 for Fourier coefficients and RMS residuals). This does not phase up nearly

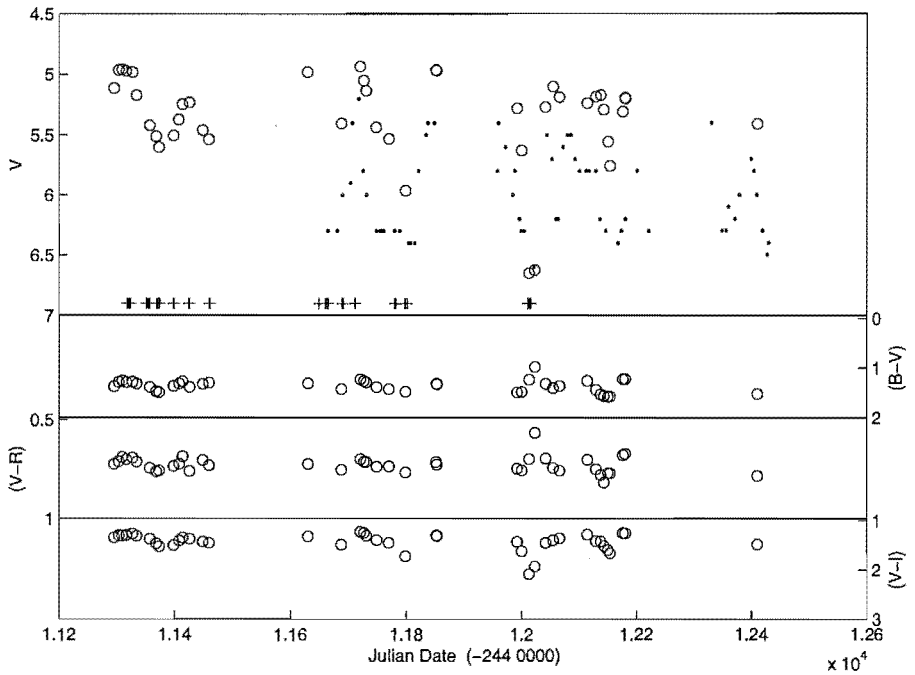

Figure 4.58: MJUO colour photometry of R Sct.(+) indicate times of spectral observation. (.) indicate Albert Jones visual estimates.

as cleanly as the other RV Tauri stars (Figure 4.59). The Fourier fitted curve shows no distinct maxima, and the only distinct minimum is in association with the data points from the very deep minimum of JD 2452000.

The phased colour curves (Figure 4.60) show similar degrees of scatter. There does appear to be a relatively clean maximum at phase 0.75, but the data becomes quite scattered at phases after that, with some of the data becoming redder. The anomalously blue data from the very deep minimum is visible at phase 0.05.

Based on a comparison with the equivalent *BVRI* curves from Pollard (1994, Figure 3.34) and phased colour curves (Pollard et al., 1996a, Figure 11), R Sct is in an irregular phase as the minima are not prominent apart from the one deeper one. This becomes even more apparent when Association Française des Observateurs d'Etoiles Variables (AFOEV) photometry and visual estimates are examined. JD 2451300–2451800 are quite irregular, with very little difference in minima depth. After this, the minima become deeper on occasion, until the deep minimum around JD 2452000, where a regular pattern of deep and shallow minima is established for at least the following three cycles.

4.4.11 IW Car

Unlike R Sct, IW Car is an RVb star which shows mean magnitude variations of a similar style to AR Pup (Figure 4.45), but with larger scale and less sinusoidal variations. As with AR Pup, the most recent photometric analysis and historical review has been by Pollard et al. (1996a). Unfortunately the large long-term variation, complicated by irregular pulsations meant that Pollard et al. (1996a) could only find an approximate period between successive minima of 72 days with the long-term period even less precisely known due to

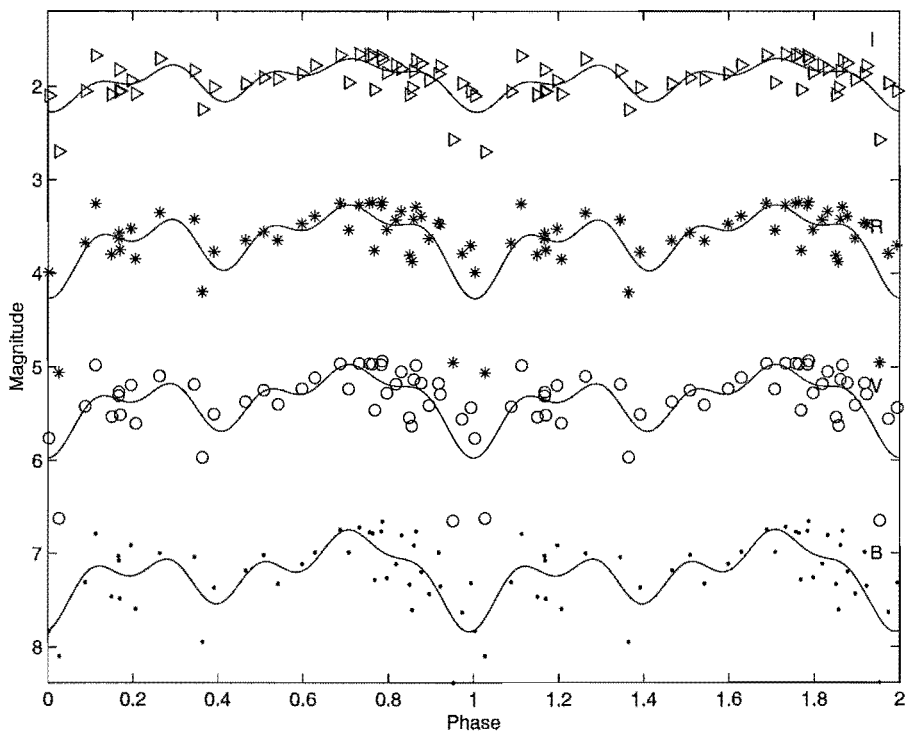

Figure 4.59: MJUO *BVRI* magnitudes of R Sct phased on a period of 134.87 days from Fourier fitting to the V data. B magnitudes have been offset by +0.5 magnitudes, R by -1 and I by -2.

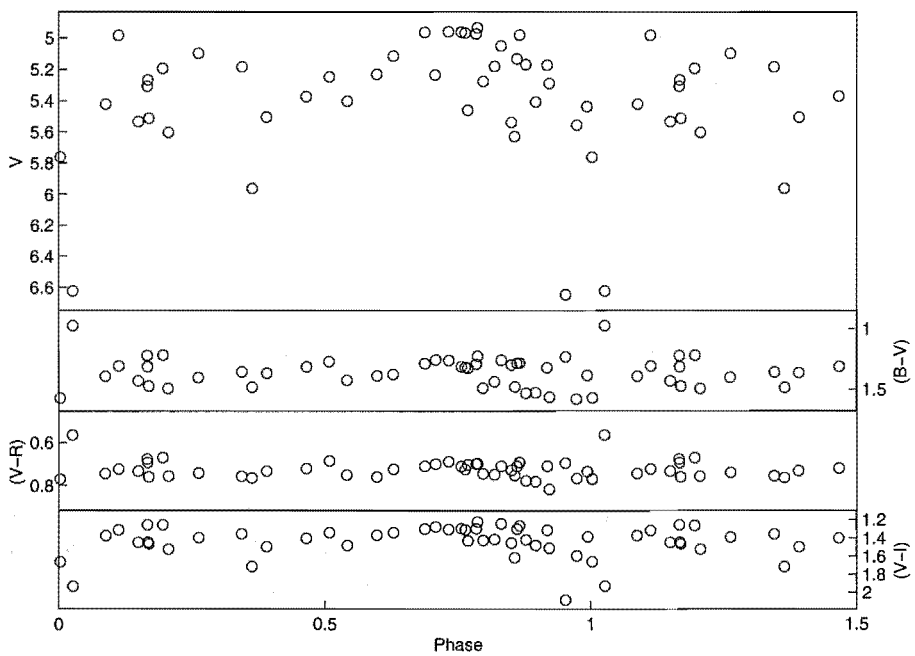

Figure 4.60: MJUO colour photometry of R Sct phased on a period of 134.87 days from Fourier fitting to the V data.

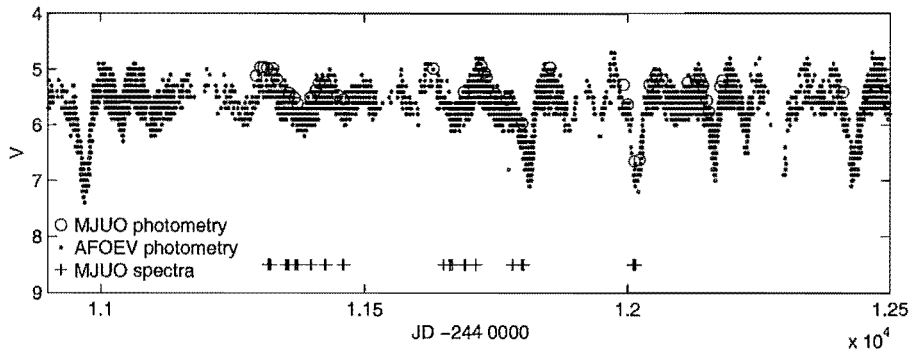

Figure 4.61: AFOEV photometry of R Sct from JD 2450900–2452500. Also displayed are MJUO V magnitudes and times of spectral observation presented in this work.

Table 4.24: Periods between successive deep minima for IW Car.

	Period (days)	Epoch JD - 2440000	Long-term period (days)
Pollard (1994) & Pollard et al. (1996a)	72 [a]	8123.0	730 or 1444
This work	142.73	11204.448	—
	73.865 [a]	—	—

[a]successive minima

sporadic historical photometry (see Table 4.24, and Pollard et al. (1996a) and references therein).

As can be see from Figure 4.62, IW Car shows very distinct long-term variations, both in V and in the various colours, with the colours getting redder as the star goes into long-term minimum.

In order to find the pulsational period, splines have been fitted to the photometric data and the resulting curves subtracted from the photometry. A constant offset of the maximum light level of the spline has been applied to re-scale the data to what it might appear if the long-term variations were not present (see Table C.28 for offsets). In the case of IW Car, separate spline curves were fitted to the B, V, R and I curves as the variations between the colours were too great to be adequately approximated by removal of just the V variations.

Once the long-term variations are removed the MJUO data phases well on a period of 142.73 days from Fourier analysis (see Figure 4.64 and Table C.28 for Fourier coefficients and RMS residuals). IW Car shows very little if any alternations in the depths of the minima. Only the scatter of the data points gives any indication that it would not phase well on the period between successive minima. The maximum at ϕ=0.75 ("secondary maximum" by phasing convention) is much better defined than the primary minimum ($\phi \simeq$0.2) and agrees much better with the fitted curve. Also the maxima are not the same shape, as one appears to be a mirror image of the other, rather than a repeat. The

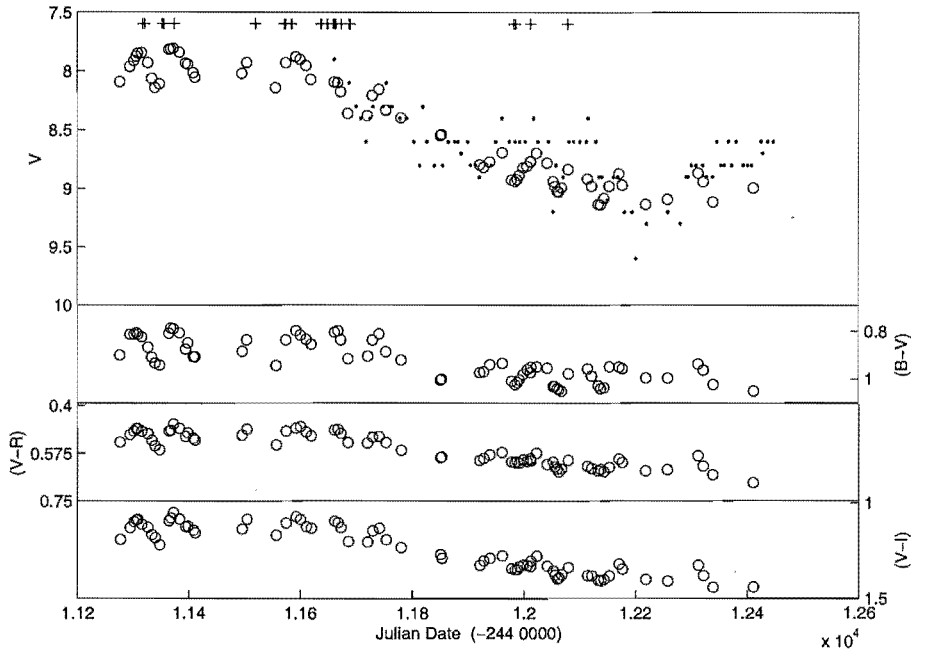

Figure 4.62: MJUO colour photometry of IW Car. (+) indicate times of spectral observation. (.) indicate Albert Jones visual estimates.

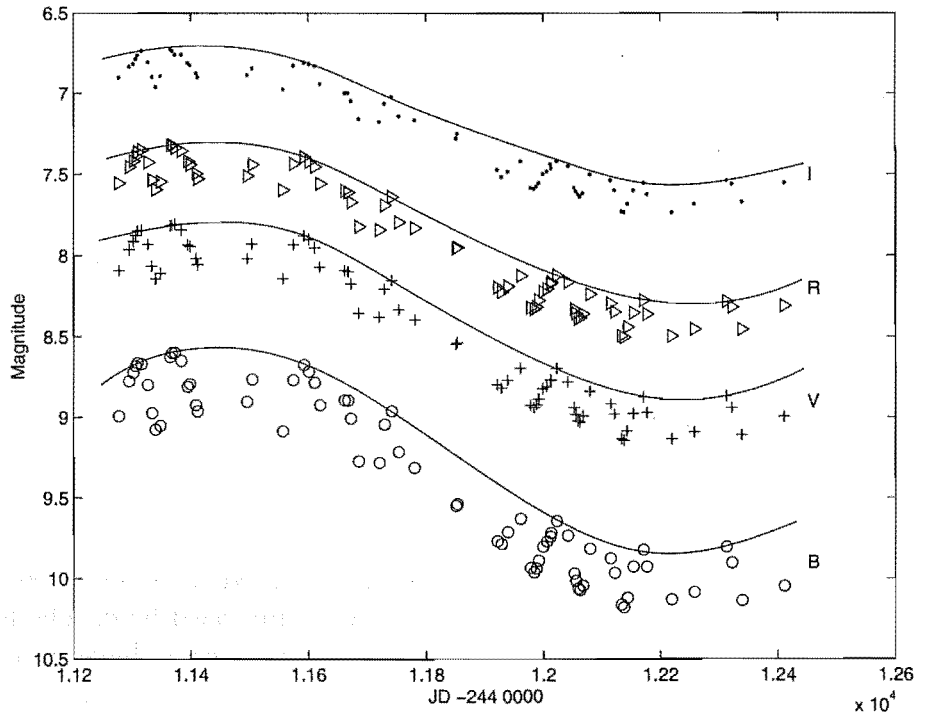

Figure 4.63: MJUO *BVRI* photometry of IW Car showing the spline curves fitted to remove the long-term variation.

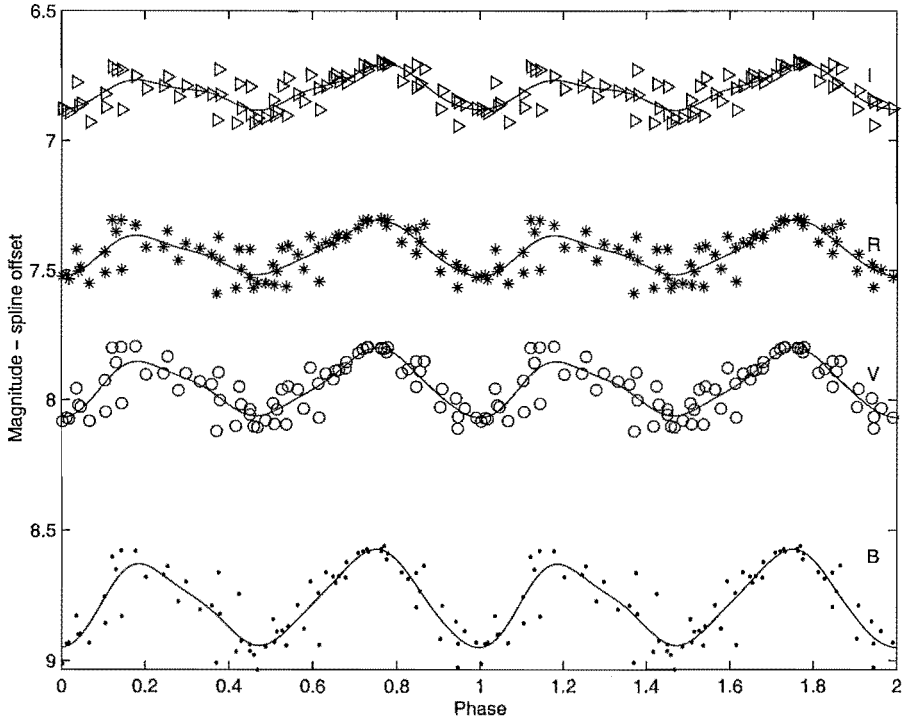

Figure 4.64: MJUO *BVRI* magnitudes of IW Car phased on a period of 142.73 days from Fourier fitting to the V data with the spline curves from Figure 4.63 removed and a constant offset applied. No additional offsets have been applied to the photometry..

difference to the other RV Tauri stars is that there is no phase lag in the time of minimum light at redder wavelengths.

The same trends are observable in the phased colour curves (Figure 4.65), which have also had the long-term variations removed and been rescaled to light maximum values. IW Car does get bluer at maximum light but there is little or no phase shift between minimum V and the colour minima.

4.5 Case study: Analysis of U Mon

U Mon (P = 92 days) is being analysed last because of the large amount of data available on it and which will be examined as part of this thesis. Not only are there long continuous MJUO *BVRI* photometric observations (photometry from Pollard (1994) included), but there are AAVSO visual estimates from 1961–2001. The MJUO *BVRI* photometry has been analyzed by Fourier analysis and the AAVSO data by wavelet techniques. The wavelet analysis component of this has been presented as a poster at IAU Colloquium 185 (McSaveney et al., 2002) and will be briefly summarized here. The longer baselines of these observations have meant that fluctuations in the period have been observed, and so additional AAVSO visual estimates have been examined via Fourier analysis to confirm instantaneous periods at the times of the spectral observations.

U Mon is the second brightest RV Tauri star (V=5.5–7.7) and the brightest RVb star and as a consequence has been observed for many years. It is considered to be one of the more stable of the RV Tauri stars with clear alternations in deep and shallow minima

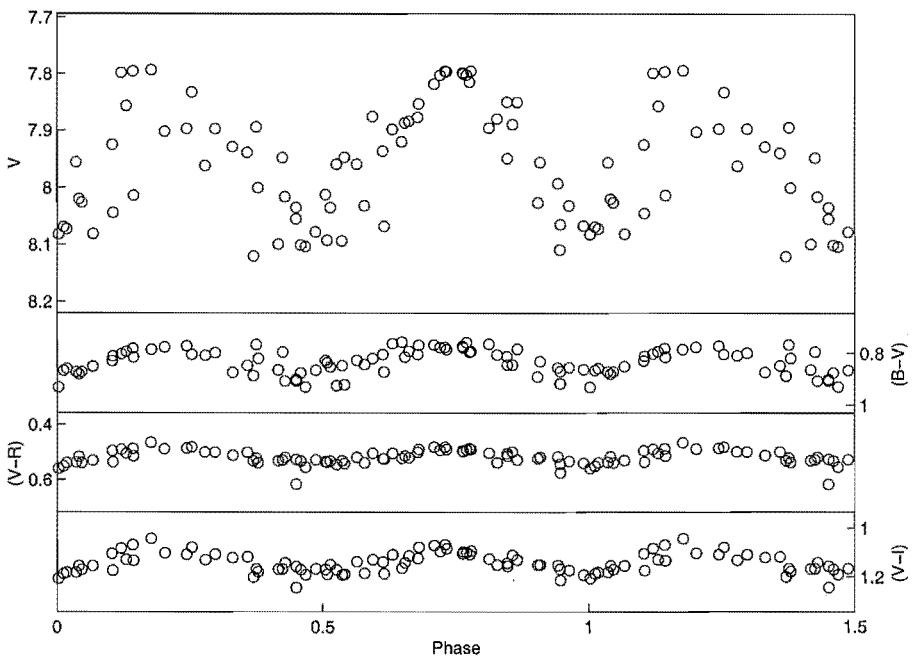

Figure 4.65: MJUO colour photometry of IW Car phased on a period of 142.73 days from Fourier fitting to the V data with the long-term variations removed.

Table 4.25: Periods for U Mon.

Author	single period (d)	formal period [a] (d)	long-term period (d)
Gerasimovič (1929)	—	92.26	—
Sanford (1933)	—	92.26	2300 [b]
Loreta (1939)	—	—	2320 [c]
Abt (1955)	46	—	1980/2640 [b]
Preston (1964)	46.1	—	1560 [b]
Percy et al. (1991)	46.117 ± 0.003 (pre1957)	—	2475 [c]
	45.814 ± 0.005 (post1957)	—	—
Pollard (1994)	46.16	92.32 ± 0.04	2597 ± 6 [b]
McSaveney (1998)	—	—	2595 ± 5 [b]
McSaveney et al. (2002)	45.81 ± 1.9	90.70 ± 2.0	2498 ± 72 [c]
	46.07 ± 0.7	92.40 ± 1.4	—
This work	45.90±0.03	91.79±0.05	—

[a] between successive deep minima
[b] From radial velocity data
[c] From photometric data

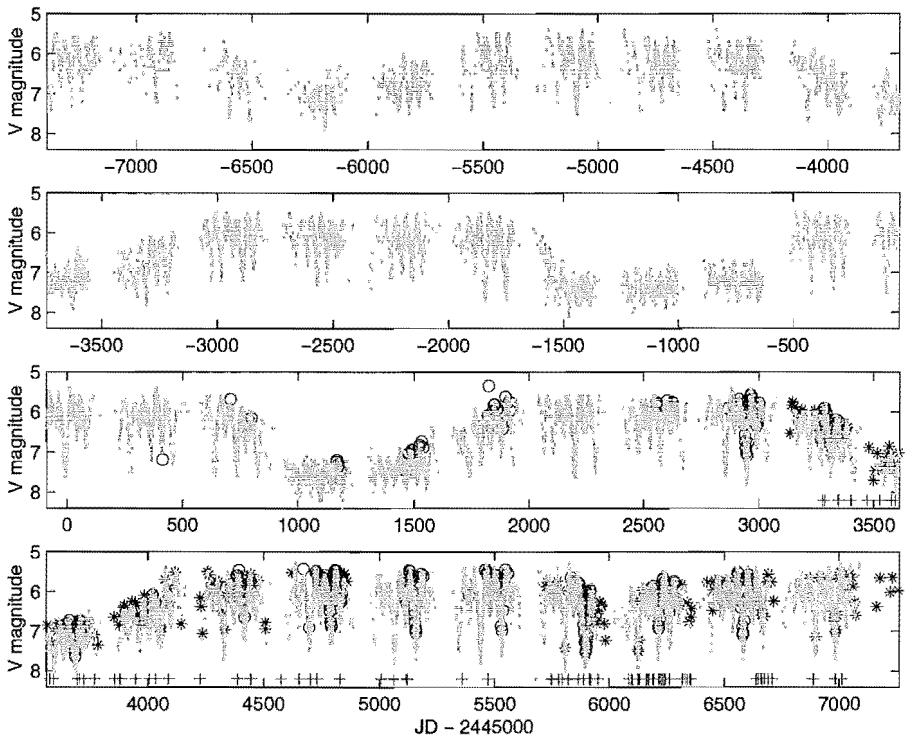

Figure 4.66: Photometry of the RV Tauri star U Mon. (.) are AAVSO visual estimates, (o) are AAVSO photoelectric photometry, (*) are MJUO photoelectric photometry. (+) indicate times of MJUO spectral observation.

and generally distinct long-term fluctuations in mean magnitude with a period of $\sim$ 2500 days. It has a formal period between successive deep minima of 92.32 days (Pollard et al., 1996a, and references therein). Historically, the period has been known to change (see Table 4.25 for details). For instance, Percy et al. (1991) found a period between successive deep and shallow minima of 46.117 $\pm$ 0.003 days prior to 1957 and 45.814 $\pm$ 0.005 days after that time.

Wavelet analysis of AAVSO visual estimates

There is a large amount of AAVSO visual estimate data available (Figure 4.66), and a subset of this data was analysed via the wavelet analysis technique. This was used to see if the period shows discrete changes or whether it shows a gradual evolution in a particular direction. There are three main periods found in the U Mon data (Figure 4.67). The first is the period between successive minima centered on 46 days (Figure 4.67b), the second is the period between successive deep minima centered on 92 days (Figure 4.67c), and the third is the $\sim$2500 day period associated with the long-term variations (Figure 4.67d). While the 46 day period is constantly present, the 92 day period is far less distinct. It is only detected sporadically in the initial half of the data set but is clearly present for much of the later half, only to be lost again during parts of the most recent long-term minimum. The presence of the 92 day period shows less correlation with the long-term minima than with the stability of the deep shallow alternation pattern in the pulsations. On the occasions when flips occur in the alternation pattern, the 92 day period is lost or

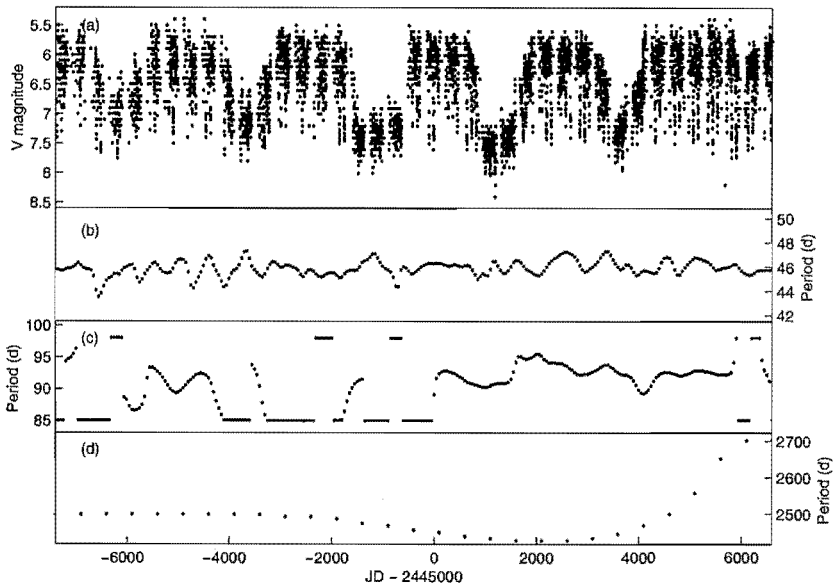

Figure 4.67: Dominant periods derived from the wavelet analysis of the AAVSO visual estimates. (a) AAVSO visual estimates. (b) Period between successive minima. (c) Period between successive deep minima. (d) Period between long-term minima.

at least becomes difficult to find. This can be seen in more detail in Figure 4.66 around JD 245 1000 and later, where several flips are present during the latest long-term minimum which corresponds to the time when the 92 day period is not easily detected.

In terms of the nature of the pulsational period changes, no constant change is apparent. The ~45 day period is always present, but there is no clear trend to longer or shorter periods. Instead the period oscillates in an apparent irregular fashion. Based on the observed rate of period change of 0.003 days per year (Percy et al., 1991), the expected period change over the observational data set should be 0.12 days, which is below the uncertainty limits of this work (see Table 4.25 for mean periods found for two sections of the AAVSO data set and associated uncertainties). The observed fluctuations in period are far larger than those found by the Percy et al. (1991) rate. These fluctuations in period are similar in scale to those observed in R Sct (68–73 days between successive minima) by Matsuura et al. (2002), using similar wavelet techniques.

The amplitudes associated with the observed pulsational periods are also not constant (Figure 4.68). Both the 46 day and 92 day periods decrease in amplitude over the long-term minima. The ratio of the 90 day to 46 day periods is approximately 0.6 in both inside and outside of long-term minimum, except for the initial long-term minimum shown, where the ratio is 0.3. This particular minimum is also the deepest minimum in the time period examined.

MJUO photometry

The MJUO photometry of U Mon (Figure 4.69), shows a number of effects. The photometry covers two long-term minima, but they are quite different in shape. The second long-term minimum is far more shallow that the first one, with light maximum going down to around V=6 compared to V=6.8 in the first long-term minimum and V~5.5 outside

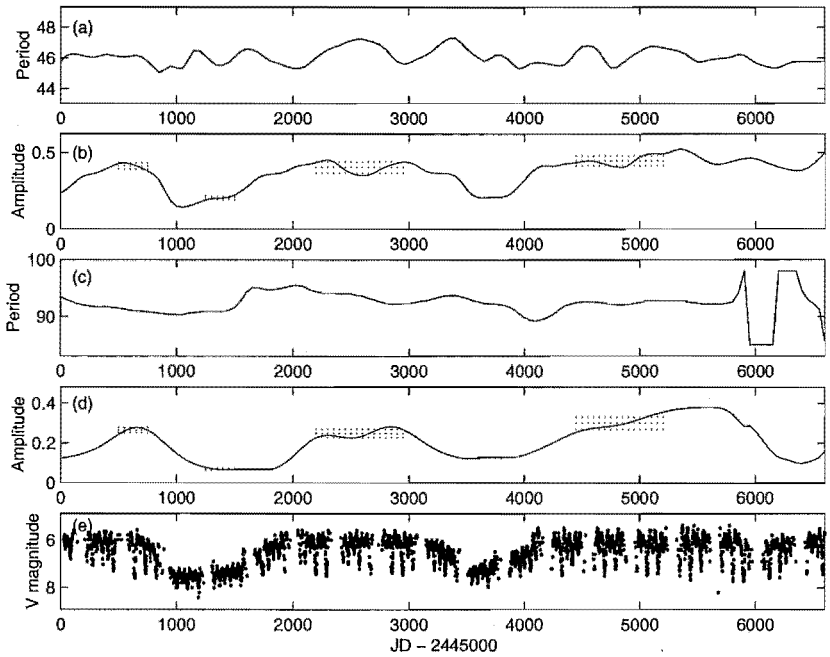

Figure 4.68: Wavelet amplitudes for the two pulsational periods observed in U Mon. (a) 46 day period between successive minima. (b) Amplitude of the wavelet for the 46 day period. (c) 92 day period between successive deep minima. (d) Amplitude of the wavelet for the 92 day period. (e) AAVSO visual estimates. Dotted lines indicate mean amplitudes and standard deviations for the duration of the time periods shown by the lines.

the long-term minima. The light minima stay at around the same level (V=7.6) for both long-term minima, indicating the amplitude of pulsation as indicated by the photometry is larger in the second minimum, compared to the first. The long-term minima are easily seen in the colours as U Mon becomes redder just after both long-term minima, confirming the colour changes and time lag observed by Pollard et al. (1996a). The magnitude of the colour change is still much smaller following the second long-term minimum, compared to the first.

A spline curve has been fitted to the MJUO photometry, removed and a constant magnitude offset applied (V offset = 5.4), to remove the long-term variations and to re-scale the data as though the long-term variations were not present. Fourier analysis of this adjusted photometry resulted in a period of 91.79 days (see Table C.25 for Fourier coefficients and residuals). This resulting period phases up quite well (Figure 4.71), although there is still scatter in the data and the Fourier curves fitted are somewhat variable. There are clear alternations in the depths of the minima, with the deep minimum reaching V=7.0 on average compared to V=6.5–6.6 for the shallow minimum. There is still more scatter in the points than observed by Pollard (1994), whose data makes up a subset of the data discussed here. This is due to the "flips" observed in U Mon since the last long-term minimum. If more recent AAVSO data is examined (Figure 4.72a, JD 2451000–2452200), several such flips are seen. In the first season a deep minimum is followed by a deep minimum, and the second season shows a shallow minimum followed by another shallow minimum. These become evident when the data for each season is phased on the same period (see Figure 4.72b-d). The second season shows evidence of the

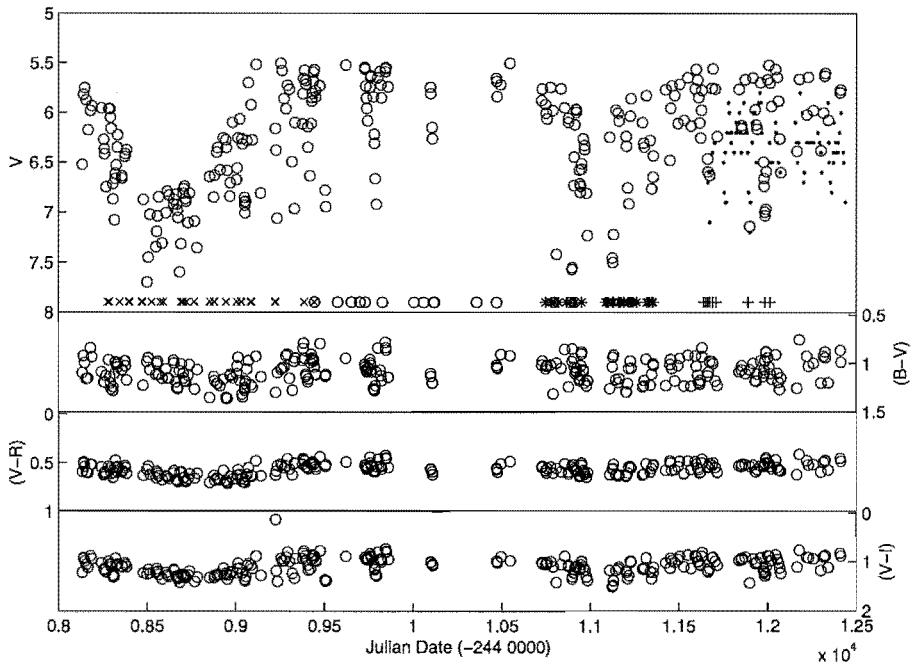

Figure 4.69: MJUO photometry of U Mon, including photometry from Pollard et al. (1996a). (.) are Albert Jones visual estimates; (x) indicate Pollard et al. (1997) spectral observations; (o) indicate McSaveney (1998) spectral observations (see Table D.15); (*) indicate intermediate spectral analysis (see Table D.16 for details and explanation); (+) indicate spectral observations of this work.

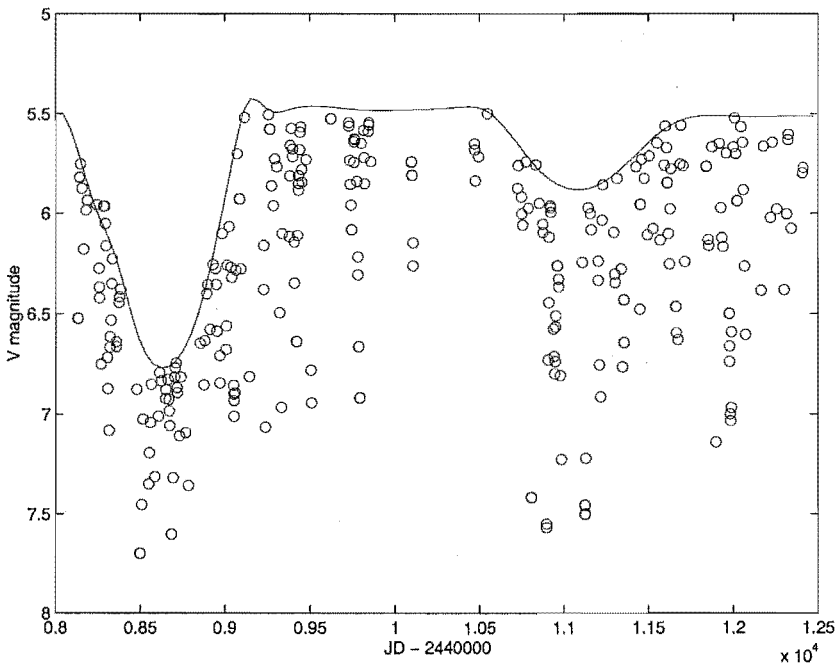

Figure 4.70: MJUO V photometry of U Mon showing the spline curve fitted to remove the long-term variation.

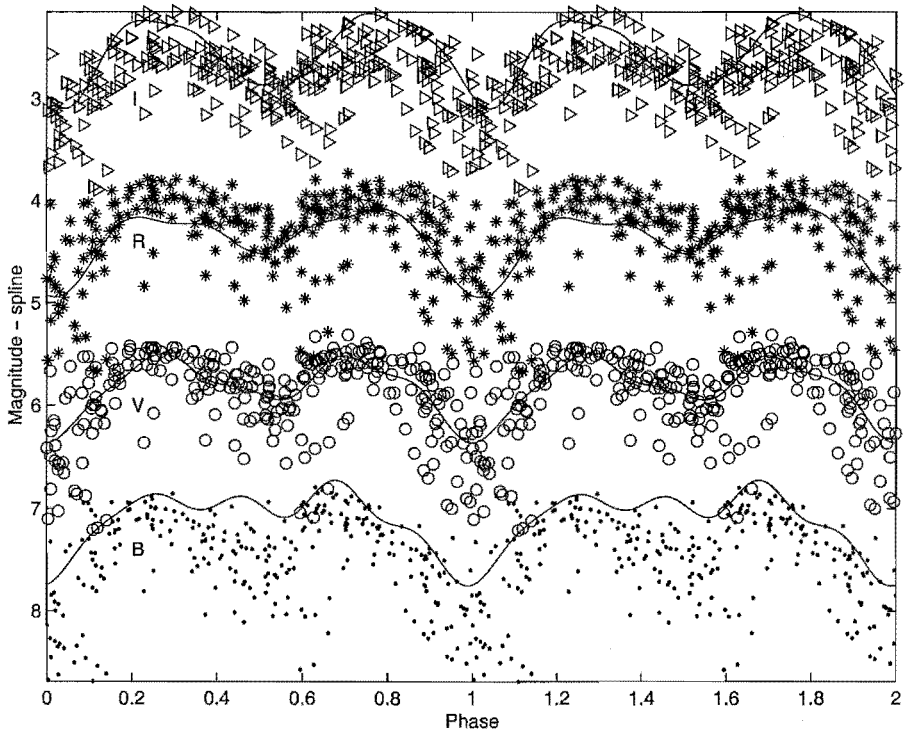

Figure 4.71: MJUO *BVRI* magnitudes of U Mon phased on a period of 91.79 days from Fourier fitting to the *V* data with the spline curves from Figure 4.70 removed and a constant offset applied. *B* magniutudes have been offset by +0.5 magnitudes, *R* by -1 and *I* by -2.

flip part way through the observing season as there is a partial deep minimum present at phase 0.0 (and 1.0) as well as a shallow minimum, whereas the first season has a shallow minimum at 0.0. The third season has a deep minimum at 0.0, returning to the conventional phasing. This data is also marked by the fact that Fourier analysis of only these three seasons results in a 45.14±0.02 day period between successive minima. This will be discussed further in Section 7.3.3.

In terms of looking for shock wave characteristics (a blue initial peak which declines in amplitude as we move to redder wavelengths), the scatter introduced by the flips and the residuals from the removal of the long-term variations, means that any possible peaks are obscured. This also means any phase lags between *B*, *V*, *R* and *I* are obscured by the scatter, although a shift in the position of the deep minimum as a function of wavelength is visible from the fitted curves.

The phased colour curves (Figure 4.73) do show a clear phase lag between the colours and the *V* photometry. This is strongest around the shallow minimum for all colours, and in the deep minimum, but only for *(B-V)* and *(V-R)*. *(V-I)* shows little, if no phase lag.

Table 4.26: Type II Cepheids photometric characteristics.

Star	Type	Period[a] (days)	V range	Pulsational amplitude in V^b	ϕ_{min} shifts between B and I
VY Pyx	BL Her	1.239938	7.15–7.4	0.25	0.024
SW Tau	BL Her	1.583560	9.4–10.2	0.8	0.122
V381 Cen	Classical Cepheid	5.07878	7.2–8.0	0.8	0.03
TX Del	BL Her?	6.1634	8.9–9.6	0.7	0.039
κ Pav	W Vir	9.0741	4.0–4.8	0.8	0.049
AL Vir	W Vir	10.2950	9.2–10.0	0.8	0.194
W Vir	W Vir	17.2768	9.6–10.8	1.2	0.028
ST Pup	W Vir	18.6204	9.6–10.8	1.2	0.063
SX Cen	RVb Tauri	32.82	9.1–11.4	0.8	0.475
TT Oph	RVa Tauri	60.97	9.4–10.7	1.5	0.036
RU Cen	RVa Tauri	64.57	8.5–9.8	1.3	0.419
CT Ori	RVa Tauri	67.42	10.3–11.2	0.9	0.014
AI Sco	RVb Tauri	71.45	8.8–11.2	1.4	0.043
AR Pup	RVb Tauri	76.47	9.1–10.1	0.55	0.553
AR Sgr	RVa Tauri	87.13	9.1–10.4	1.3	0.017
UZ Oph	RVa Tauri	88.90	10.2–12.5	2.3	0.027
U Mon	RVb Tauri	90.29	5.5–7.8	2.0	0.053
R Sct	RVa Tauri	134.87	4.9–6.7	1.8	0.019
TX Oph	RVa Tauri	135.81	9.7–10.7	1.0	0.418
IW Car	RVb Tauri?	142.73	7.8–9.2	0.35	0.473

[a]Between successive deep minima for RV Tauri's and successive minima for the rest.
[b]Long-term variations removed.

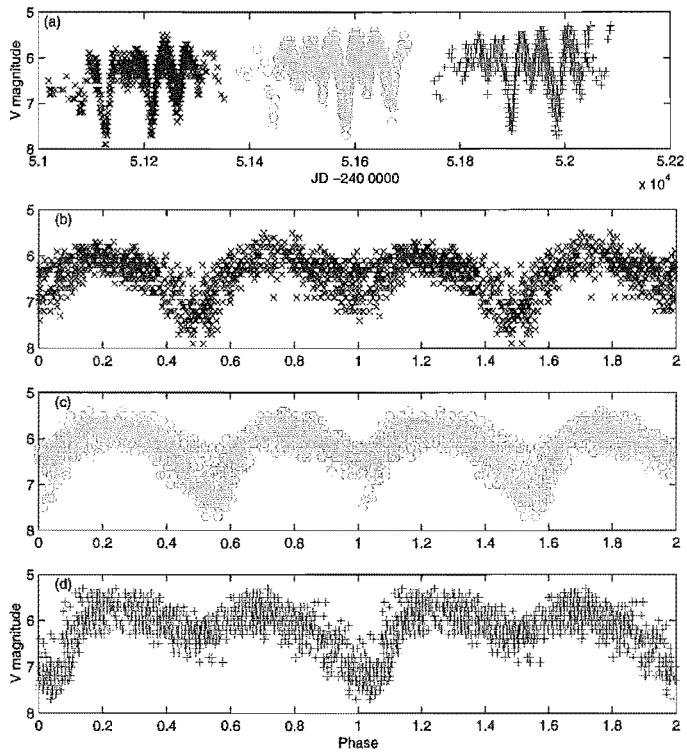

Figure 4.72: Visual estimates estimates of U Mon from the AAVSO measurements. (b)–(d) Phased on 90.29 day period from Fourier analysis of these AAVSO visual estimates. (b) Covers JD 2451000–2451380. (c) Covers JD 2451380–2451750. (d) Covers JD 2451750–2452100.

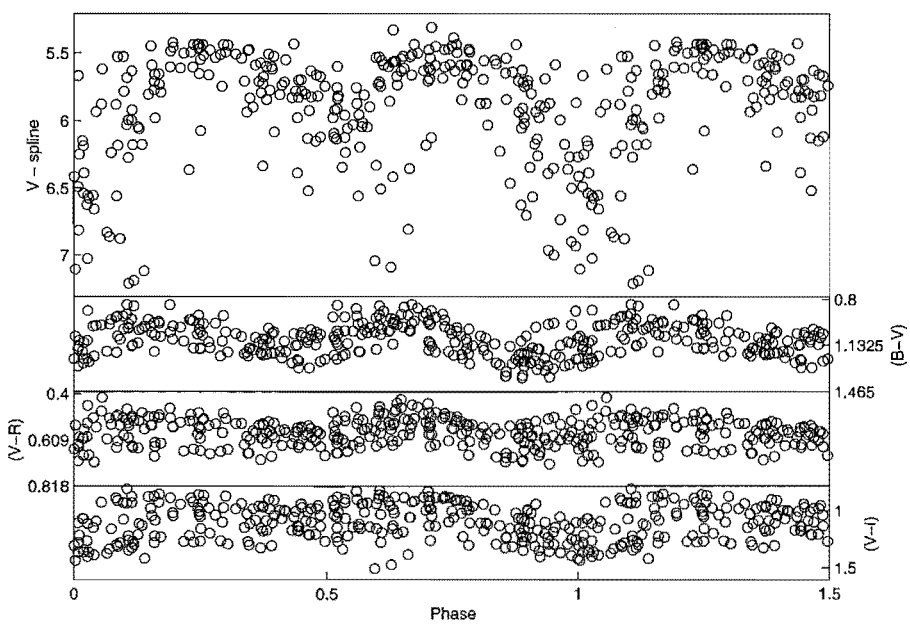

Figure 4.73: MJUO colour photometry of U Mon phased on a period of 91.79 days from Fourier fitting to V data with the spline curves from Figure 4.70 removed from the V.

Chapter 5

BL Herculis Stars

BL Herculis-type stars are recognized as low-mass radially pulsating giants ($M \approx 0.6\,M_\odot$, $L \approx 100\,L_\odot$) with periods ranging from 1 to ~7 days[1]. Their general properties were reviewed in Wallerstein and Cox (1984) and Wallerstein (2002), and their evolutionary status was studied by Gingold (1976), who found they were "undergoing blueward noses from the asymptotic giant branch". In recent years the pulsation of the BL Her stars has been studied theoretically by many workers (King et al., 1981; Carsons et al., 1981; Carsons and Stothers, 1982; Hodson et al., 1982; Fokin, 1986; Buchler and Moskalik, 1992; Fokin and Gillet, 1994). Some would say that these authors have shown that the main pulsational characteristics and features of BL Her stars — their periods, amplitudes, bump progression and shock-induced Balmer emission and line doubling — can be well explained by current hydrodynamical models, using generally accepted stellar parameters (the aforementioned $M \approx 0.6\,M_\odot$, $L \approx 100\,L_\odot$). This appears to be true in terms of some specific stars, such as BL Her (Gillet et al., 1994; Fokin and Gillet, 1994), but seems less clear with respect to stars of the overall BL Her group.

What appears to have been lacking is an in-depth spectroscopic study of the stars as a group, against which the general W Vir type spectroscopic models could be tested. This has been started by Vinkó et al. (1998), who briefly reviewed a selection of field Type II Cepheids of period 1–10 days, including SW Tau and TX Del. While an excellent review, this lacked the detail attained by various individual studies due to poor phase coverage of several of the stars.

What is apparent from this review, and from a brief overview of the MJUO radial velocities, is that the phasing of the velocity curves using photometric maxima is inadequate for comparison of the occurrence of various spectral features in the pulsation cycle. It is unclear whether the variations in when line-splitting and broadening occur are a reflection of the physical differences in characteristics of the stars themselves, or an artifact of the difficulty in phasing the stars based on the different shaped light curves. For instance, as the MJUO *BVRI* curves for SW Tau show (Figure 4.5), the phase of minimum light varies depending on the photometric bandpass viewed. The phase of maximum light is also problematic to determine for the longer period stars such as W Vir (Figure 4.23),especially in the bluer filter regions, as shock related emission features become more prominent. Even in the case of Vinkó et al. (1998), where well-established epochs from the literature are used, it is clear that minimum radial velocity occurs at different phases in the various stars.

An alternative approach is called for. In the process of examining rudimentary acceleration curves derived from the radial velocity curves of the stars, it was noted that a distinct acceleration minimum was present during each pulsation cycle. It was decided to

[1]Initially BL Her stars were defined by period from 1 to 3 days but later papers indicate periods up to 7 days.

Table 5.1: Starting parameters for BL Her stars.

	VY Pyx	SW Tau	V381 Cen	TX Del
period (days)	1.2399	1.5836	5.0788	6.1634
epoch[a]	11310.187	11394.477	11310.088	11312.483
Minimum V magnitude	7.15	9.4	7.2	8.9
Maximum V magnitude	7.4	10.2	8.0	9.6

[a]From photometric phasing. Epoch = JD - 2440000.

phase the data based on where this minimum occurred, rather than the more commonly used photometric approach. The results of this shift in approach are presented in this and the following chapter. However before this can be done, we need starting parameters for examining the stars (Table 5.1). These have been based on the photometric analysis of Chapter 4.

5.1 VY Pyx

As was stated in Section 4.2.2, VY Pyx has been studied very little, and principally only photometrically. While this means no historical data for comparison, it also means that there are no preconceived ideas about the star's behaviour. As such, it proves an excellent example to examine the new approach in analyzing the velocity and acceleration curves, and their implications in the motions of the pulsating layers of the star.

Figure 5.1 presents the photometric and Fe I radial velocity curves for VY Pyx. The Fe I velocity curve was chosen as iron is a representative metal which shows behaviour typical of the metal lines (as shown and discussed further in Figure 5.2 and Section 5.1.1), and is the average of the velocities of over one hundred Fe I lines (with excitation potentials ranging from 0.8 to 5 eV as listed in Section E.6). While any line level effects are of interest in later parts of the thesis, for this current analysis, a clean smooth average with as little scatter as possible is required.

A spline curve has been fitted to this radial velocity curve (Figure 5.1b), and a derivative with respect to time has been found (Figure 5.1c). It should be noted that that this is not the true acceleration curve with respect to the star for two reasons: the Fe I velocity curve has not been converted to the rest frame of the star; the velocities have not been converted to a pulsational velocity curve, as is required for a numerically accurate acceleration curve (as shown by Lèbre and Gillet, 1992), or for Baade-Wesselink radius measurements such as in Sasselov and Lester (1990). Lèbre and Gillet (1992) defined the pulsational velocity curve to be:

$$\dot{\mathrm{R}}(t) = -\beta(V_r(t) - V_*) \tag{5.1}$$

while Sasselov and Lester (1990) used:

$$v_p = pv_r \tag{5.2}$$

In these, β and p both refer to the projection factor, which is a function of the geometric effects of the projection of the stellar sphere and effects due to limb darkening.

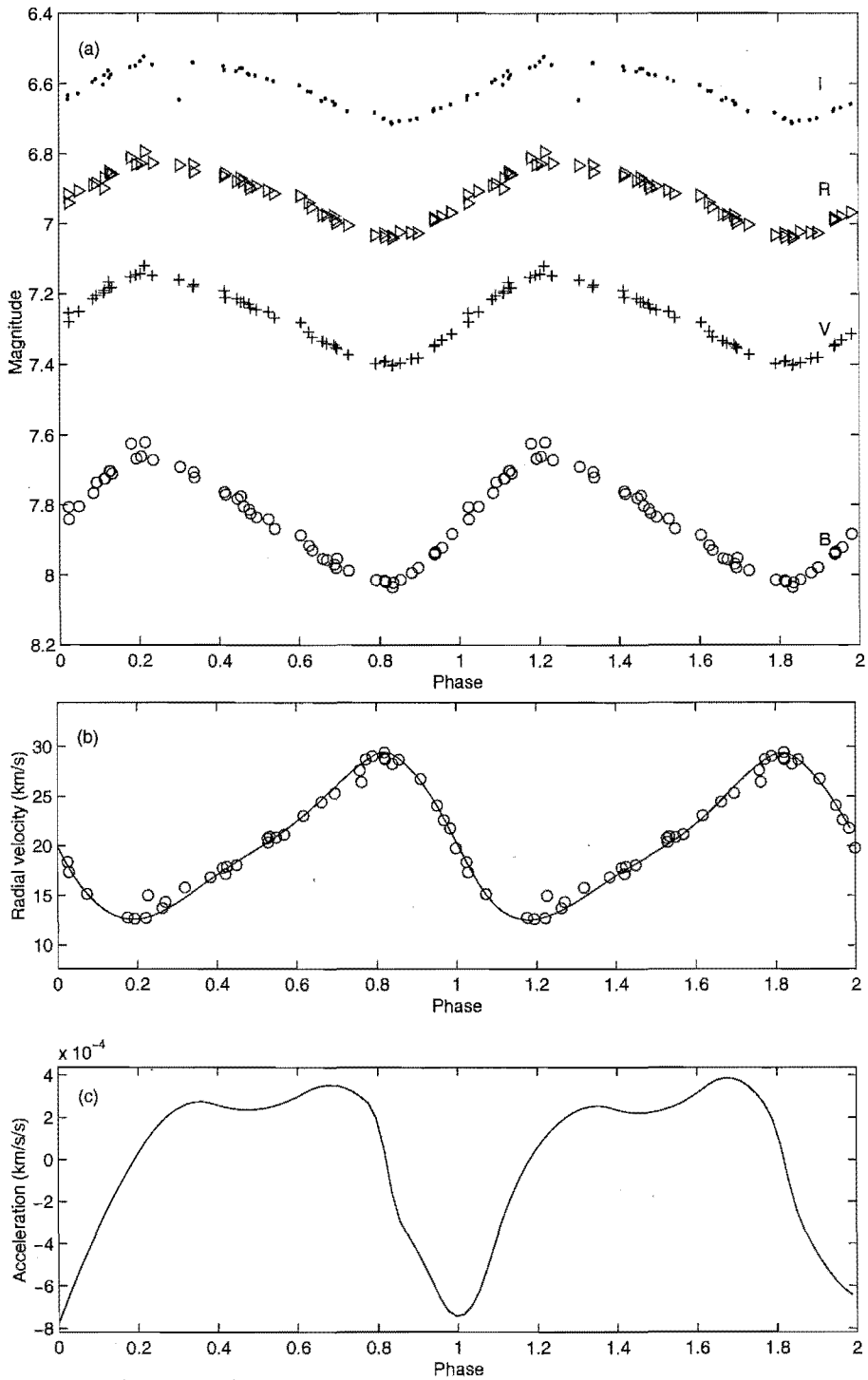

Figure 5.1: (a) *BVRI* photometry, (b) Fe I radial velocity and (c) acceleration curves for VY Pyx. The solid line in (b) is a spline fit to the Fe I velocity data, which is differentiated to give the curve in (c).

However, for the purpose of the curves presented here, the projection factor is not included as it is a scalar[2] which only affects the magnitude of the acceleration, not the position of the minimum.

As can be seen from Figure 5.1, the light curve for VY Pyx is strongly correlated with the radial velocity curve, with minimum light coinciding with maximum radial velocity at phase 0.8, and maximum light with minimum radial velocity at phase 0.2 (and repeated at phase 1.2). While this means that for this star phasing based on acceleration is not perhaps the most obvious option, the variations of others makes such rethinking necessary. It also ties the phasing into a dynamical rather than observational perspective and gives closer links to the physical processes in the stars.

In terms of how these velocity curves and their derivatives relate to the physical motions of the layers of the star, the acceleration minimum occurs when the line formation layer being tracked is at its minimum displacement from the centre of the star. The material falls inwards until it can fall no further and is then rapidly thrust outwards. In the case of VY Pyx this is a fairly smooth, almost gentle, transition. Deceleration commences around phase 0.8 (with maximum radial velocity away from the observer, towards the centre of the star), reaches the turning point at 0.0 (where the material stops falling into the star and is forced outwards), and increases up to phase 0.2 (with maximum radial velocity towards the observer, away from the centre of the star). As shall be seen in subsequent sections, this gentle transition is not always the case for other BL Her and W Vir stars. The smooth motion is, however, supported by the motions of other line species.

5.1.1 Spectroscopy

If we extend the range of species examined, as stated earlier, VY Pyx still shows smooth radial velocity curves for the metallic lines. Figure 5.2 demonstrates this, repeating the Fe I curve, and including Fe II (an average of 2 lines), Ca II (averaging 2 lines), Na I (averaging 2 lines), and the Hα line. Fe II follows Fe I almost exactly, with very little deviation from its path. This is unsurprising in that, for the shorter period and therefore more compact Cepheids, the lines are forming in very similar, if not the same, regions of the star. Within a particular line species, there is little scatter in velocity between lines of different excitation potential and log(gf) values, as shown by the small mean error bar ($<2 \mathrm{kms}^{-1}$) for Fe I (Figure 5.2). Both the Fe I and Fe II lines share a velocity amplitude of approximately 17 kms^{-1}, and reach maximum velocity around phase 0.8 and minimum velocity around phase 0.2.

While Na I (as measured from the Na D lines), shares this phasing of minimum velocity around 0.2 and has a similar minimum velocity of 11–12 kms^{-1}, it behaves differently as it heads towards maximum velocity. It too reaches peak velocity around phase 0.8, possibly even around phase 0.85. However the amplitude of this peak is much lower. This gives an amplitude of 11 kms^{-1}, and a systemic velocity difference of approximately 3 kms^{-1}. The Na D lines are formed in quite different regions, high up in the stellar atmosphere, compared to the Fe lines, which may explain the difference in amplitude, but it is unclear where this systemic velocity difference could arise. The Na D lines appear split between

[2]Although some papers have started suggesting a possible phase dependence, at least with respect to Classical Cepheids (Kiss, 1998) and different projection factors based on the velocity measurement method used (Sasselov and Lester, 1990; Hindsley and Bell, 1986).

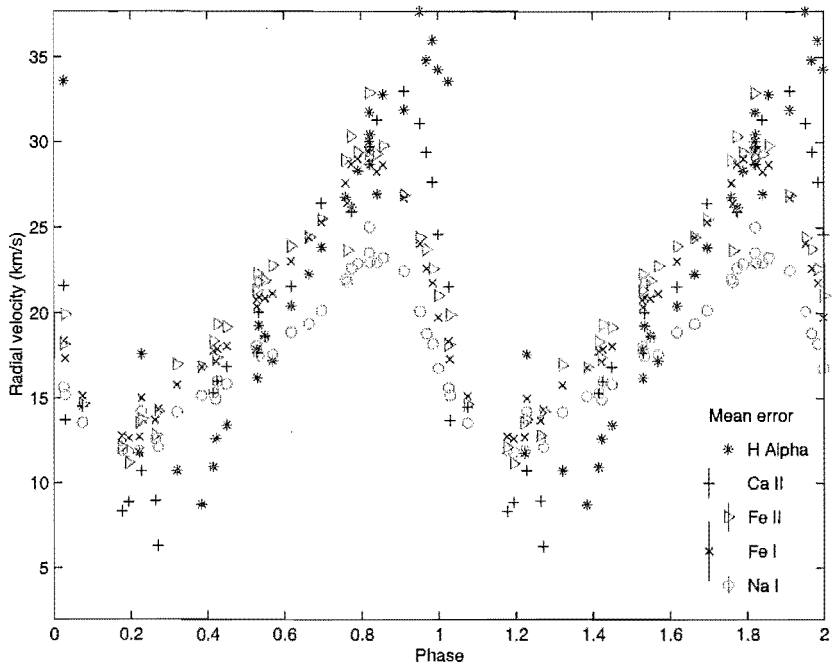

Figure 5.2: Radial velocity curves for VY Pyx, measured from averaged Fe I, Fe II, Ca II, Na I and Hα lines.

phases 0.77–0.96, yet none of the other spectral lines in VY Pyx show evidence of splitting, which indicates a shock wave is not observed in the star. If this is the case, the "splitting" at phases 0.77–0.96 may be due to the pulsational component of the Na D lines shifting far enough to the red that an underlying interstellar Na D line component becomes visible at those phases. This may shift the line centre, and thus reduce the velocity measured.

In contrast to the Na D lines, the Ca II line velocities show a larger amplitude variation than the Fe lines, but they do not share the systemic velocity shift. Their amplitude is approximately 27 kms^{-1}. Their maximum velocity is also shifted in phase from the Fe (and Na) lines and occurs around phase 0.9. Unfortunately, while the maximum velocity peak is well defined and easily discerned, the minimum velocity peak is far less clear, with a greater scatter in the velocities around and just after phase 0.2. Therefore it is difficult to determine if the phase of minimum velocity has shifted as well. The Ca II velocity curve crosses the Fe velocity curves around phase 0.0 indicating that, while the magnitudes of the acceleration curves derived would be different, the phasing obtained from minimum acceleration would not be.

This is quite different to the velocity curve from the Hα line, which would produce quite different phasing based on its acceleration curve. Its peak velocity occurs at phase 0.0, with minimum velocity occurring around phase 0.4. Not only is the curve shifted in phase from the Ca II line, its amplitude is different (30 kms^{-1}), and its systemic velocity appears to be a little higher than the rest.

The greater amplitude of velocity variation of Ca II and Hα can be understood more clearly when it is realized that their excitation potentials and log(gf) values mean that they are capable of being formed over a much greater range of depths in the star. Thus they reflect the behaviour of a larger percentage of the stellar atmosphere. More details

are observable by examining the line features themselves in the following three sections.

Hα line

By stacking the Hα lines in order of pulsational phase (Figure 5.3), more details of the changes in the line over a pulsational cycle are observable. Phases 0.0 to 0.5 have been repeated so as to make the line behaviour around the acceleration turning point more clear. Around phase 0.9 to 0.2, the lines are definitely broadened, with possibly a few extra bumps visible. There is, however, no clear sign of line splitting such that a unique solution of two velocity components can be obtained. This means that fitting two Gaussian components to the line and interpreting the velocities derived from their line cores becomes problematical, as the uniqueness of the solutions is questionable.

An alternate approach is to look at the line bisector itself and use it, and the line widths, at particular line depths to parametrize the line profile. Figure 5.4 shows the velocities of the line bisector at depths of 0.5 and 0.9, along with the width of the line at these levels. This characterizes the line asymmetry through the shift in 0.9 and 0.5 velocities and allows examination of the change of line widths at different depths. While some of the fine detail is lost in this approach, it still allows knowledge of whether the line is broadened/split below the 0.9 level or between the 0.5 and 0.9 level. This is something which is lost when only looking at the mean bisector velocity. The lines have been displayed as a function of phase, so that phase coverage and line motion can be seen.

Figure 5.4 shows that the line widths at level 0.5 (the top line of each pair) do not change much with phase. However the 0.9 depth widths do change, and approximately as a function of phase. It is also apparent that the line symmetry changes greatly, with a slope to the blue from phase 0.0 until approximately 0.3. The lines are more vertical around phase 0.3–0.4, then they slope to the red until phase 1.0. This is more clearly noticeable in Figure 5.5, where the velocities of the two line levels are plotted as a function of phase. The velocity difference is least around phase 0.4 and often, though not necessarily always, larger at the other phases.

Ca II lines

From the radial velocity curves of Figure 5.2, the lines most similar in behaviour to the Hα line are the Ca II lines. The stacked spectra of the 8498 Å (Figure 5.6a) and 8542 Å (Figure 5.6b) Ca II lines show that the behaviour is similar to Hα in that the line broadening is apparent around phase 0.0. It is, however, not as distinct as Hα. This is due to the Ca II lines being formed over a wider range of depths than Fe I and such metal lines, but not as large a range as Hα. What is also noticeable, is that the 8542 Å line behaviour is definitely not the same as the 8498 Å line behaviour. As the 8498 Å line has a smaller log(gf) value than the 8542 Å line, the lines form in slightly different layers of the atmosphere and so track slightly different mean motions, but the differences would not be expected to be large.

The behavioural difference is unusual in that the Ca II 8542 Å line shows clear line splitting but at no particular phases. Figure 5.6 demonstrates this as double components on several of the Ca II 8542 Å line are distinctly present to the red, but are not present on the slightly weaker Ca II 8498 Å line. To examine this further, Gaussian profiles have been fitted to the different components of the 8542 Å line and compared to velocities from

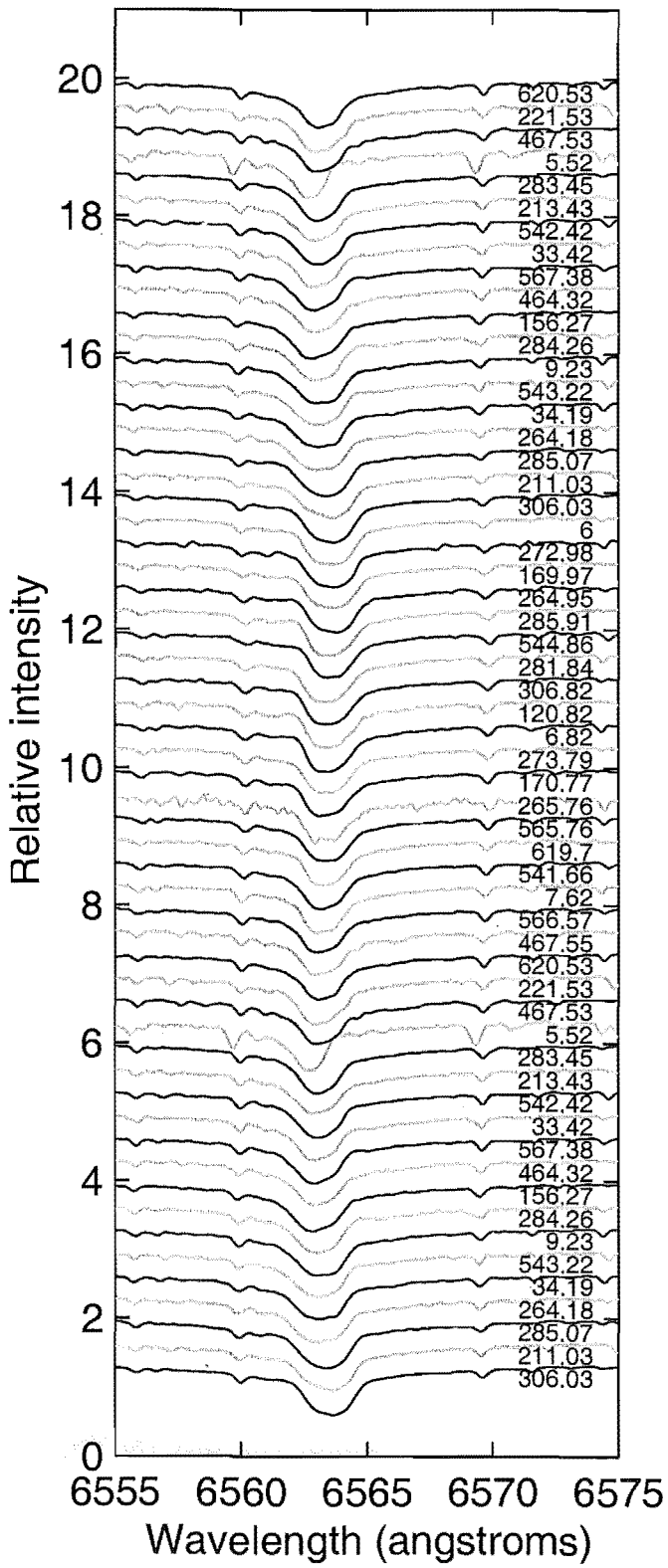

Figure 5.3: The Hα line of VY Pyx stacked in order of phase. Phases 0.0 to 0.5 are repeated to clarify the line behaviour around the acceleration turning point.

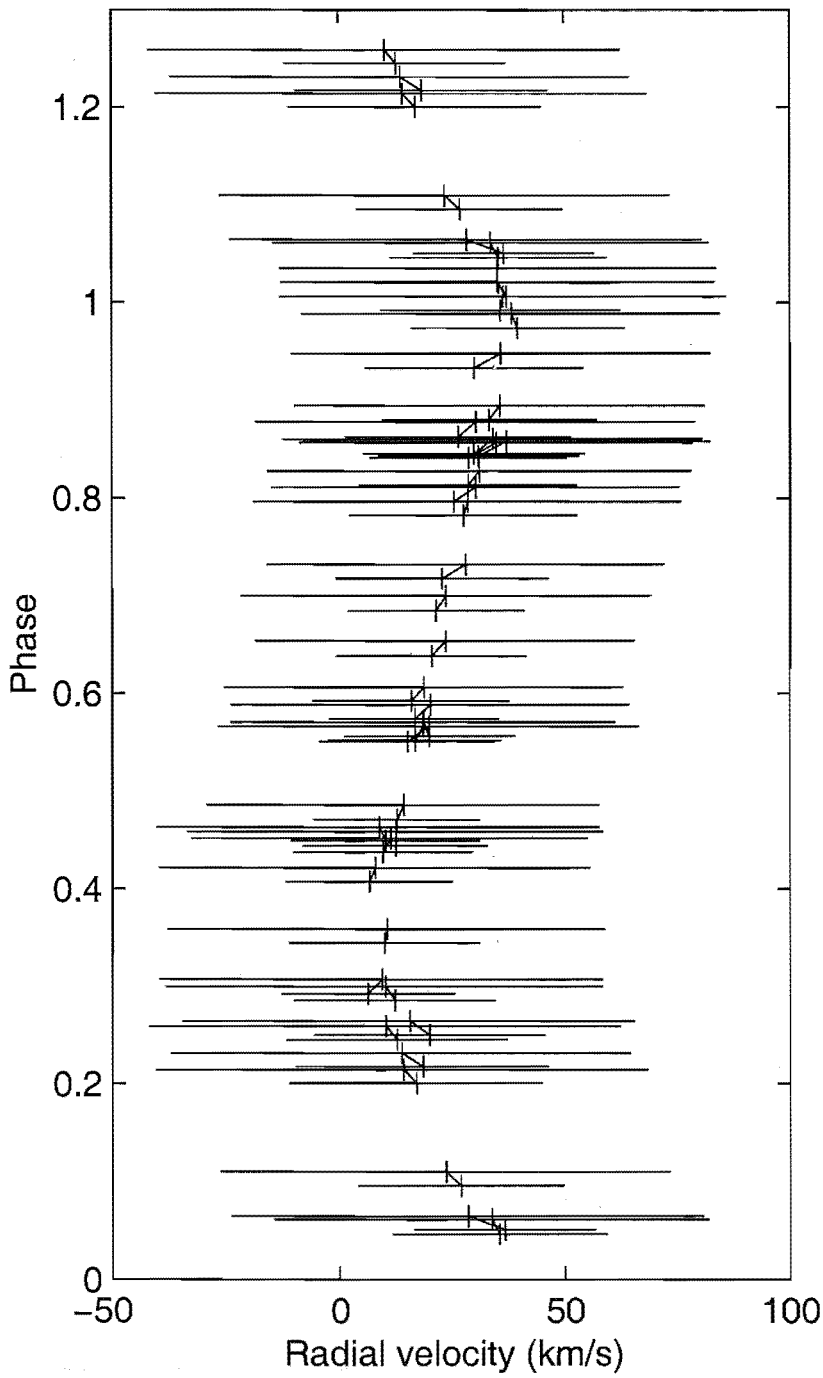

Figure 5.4: VY Pyx stacked Hα line bisectors, showing line bisector velocities at line depths 0.5 and 0.9, and the associated line width in velocity space for each depth.

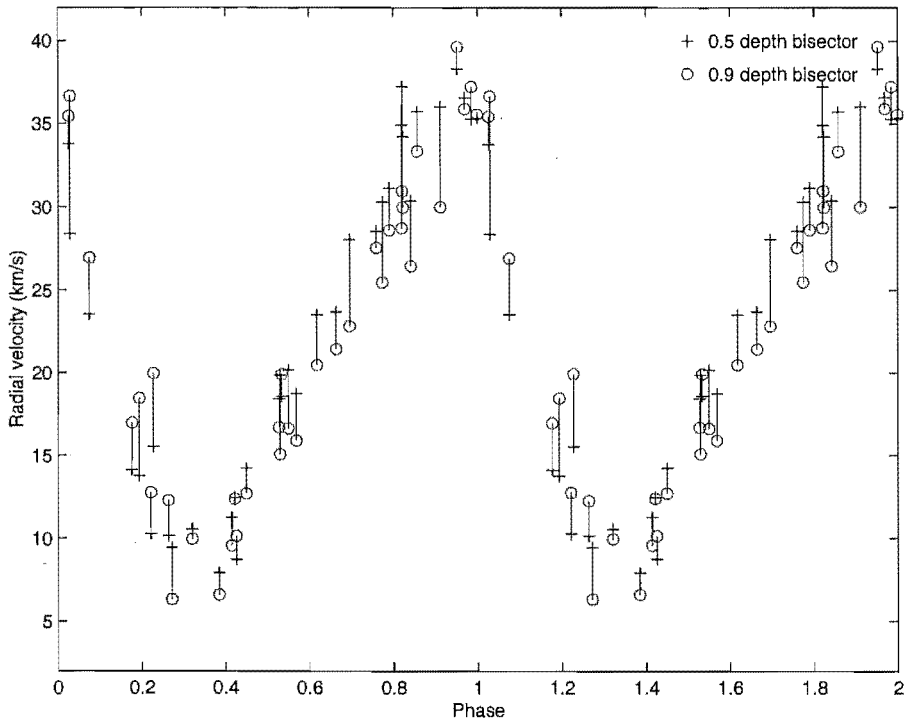

Figure 5.5: Radial velocity curves for VY Pyx plotted as a function of phase, measured from the Hα line using line bisector velocities at line depths 0.5 and 0.9.

the Gaussian fit to the Ca II 8498 Å line and the Ca II average velocities from the line bisectors.

When the radial velocities of these components are plotted up as a function of phase (Figure 5.7), there is still no obvious correlation of the phase of line splitting. It is clear that, when not split, the 8542 Å line follows the velocity of the 8498 Å line, however the velocities of both line components do not follow the same trend. This has nothing in common with the shock-produced line doubling of Schwarzschild (1954) (Section 3.2). In fact, as shown in Table 5.2, the variations are of a longer term nature.

It is not clear where or how such a long-term variation in only a select spectral line would originate in VY Pyx. A possible similar phenomenon is observed in RR Lyrae stars, where a secondary periodicity of the order of tens of days is observed (Smith, 1995). Known as the Blazhko effect, the phenomenon can change the character of the line doubling for hydrogen and metallic lines, and also affect the observed photometric variations. Unfortunately the effect is observed to be quite irregular for the RR Lyrae stars, and the mechanism behind it is not clearly understood. Also, it is clear that for VY Pyx, only the Ca II 8542 Å line is affected. The remainder of the lines examined vary smoothly and regularly, with a gentle transition from falling inward to being pushed away from the star. This regularity and smoothness is in stark contrast to the next star, SW Tau.

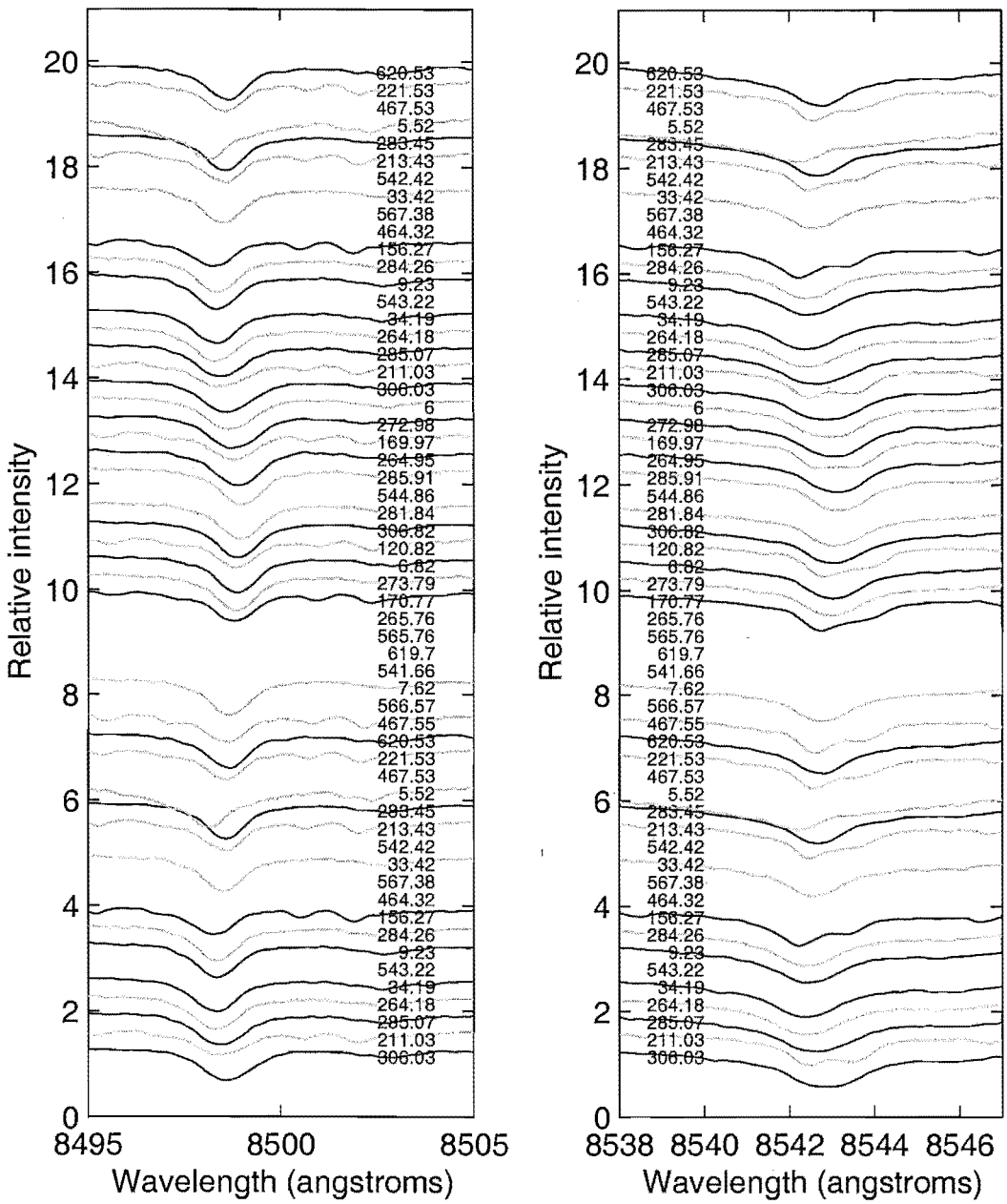

(a) 8498 Å

(b) 8542 Å

Figure 5.6: VY Pyx Ca II lines stacked in order of phase. Gaps indicate observations for which wavelength coverage does not extend to 8000 Å due to filter problems (Section 2.2.3).

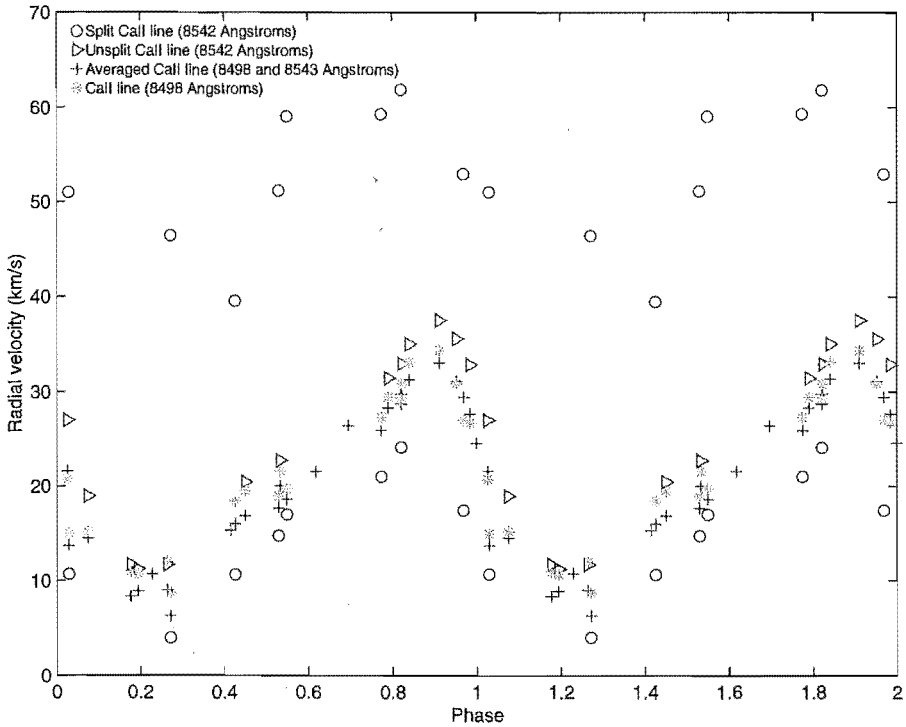

Figure 5.7: VY Pyx phased radial velocity curves for Ca II showing split and unsplit lines. Circles indicate the two components of the 8542 Å line measured by fitting Gaussian profiles, whereas the triangles indicate the single component measured by fitting a Gaussian profile to the unsplit 8542 Å lines. Asterisks indicate the 8498 Å lines also measured by fitting a Gaussian profile and plusses indicate the mean Ca II velocities measured from the line bisectors.

5.2 SW Tau

From Section 4.2.1, and from Figure 4.5, it is clear that the irregular bumps in the photometry at light maximum and minimum of SW Tau could make phasing difficult. The variation in bump prominence depending on the photometric filter used also make phasing problematic, in that there appears to be no dominant physical reason to base the phasing on one particular bandpass. Thus the use of the acceleration curve in phasing is more obvious and it makes the comparisons of the spectral features far easier, both within the star and between it and the other stars.

In comparison to the previous star (VY Pyx), many more observations of SW Tau have been made historically (Joy, 1937; Barnes et al., 1988; Bersier et al., 1994; Vinkó et al., 1998). Of these, the most recent is of most interest as it contains the most useful comparison data. They found that, in comparison to BL Her, the prototype of the class, SW Tau exhibited simpler variations in terms of Hα profile variations, with less of a difference in velocity between the hydrogen and metallic lines. It was, however, noted that SW Tau has a lower metal content than BL Her. Looking in detail at their velocity curve for SW Tau (Figure 7, Vinkó et al., 1998, repeated in Figure 5.8 here)), it is clear their velocity curve is slightly different to the one obtained here (Figure 5.9).

Table 5.2: VY Pyx spectral observations

JD - 2400000	phase	Ca II line unsplit	Ca II line split
51352.795	0.20	o	
51460.206	0.82		o
51504.163	0.28		o
51521.147	0.97		o
51522.145	0.78		o
51572.059	0.04		o
51575.031	0.43		o
51585.079	0.54		o
51637.959	0.19	o	
51638.920	0.96	o	
51648.880	0.99	o	
51649.879	0.80	o	
51659.861	0.85	o	
51661.857	0.46	o	
51662.866	0.27	o	
51663.871	0.08	o	
51664.908	0.92	o	
51689.849	0.04	o	
51690.837	0.83	o	
51890.129	0.56		o
52079.819	0.55	o	

5.2.1 Spectroscopy

As with VY Pyx, the radial velocities of the set of averaged Fe I lines have been plotted initially using the photometric phasing from Equation 4.2.1. A spline curve has then been fitted and its derivative taken to find the acceleration minimum. This has then been used to rephase the acceleration, velocity and photometric curves.

In terms of how this differs from the velocity curve of Vinkó et al. (1998), the clearest difference here (apart from the increase in phase coverage) is a decrease in the velocities measured between phases 0.4–0.7. This corresponds in phase to a bump in the photometry, which is most noticeable in I. It is unclear what the origin of the photometric and velocity variation is. Most shock-related features tend to be associated with a more prominent increase in B rather than I, however, this is not observed here. The momentary decrease in velocity is not confined to the Fe I line velocities, as when a wider array of lines are examined (Figure 5.10), the same pattern is followed by the Fe II lines. Both share an amplitude of 35 kms^{-1} and reach a maximum velocity around phase 0.9, although the lack of phase coverage in this region makes this ambiguous.

In contrast to the Fe lines, the behaviour of the Na I, Ca II and Hα lines is quite different. The Na I velocity curve is quite scattered and erratic, with an amplitude of 12 kms^{-1}, a much higher average systemic velocity, and no distinct velocity maximum or minimum. The Hα and Ca II velocity curves are more distinct, with amplitudes of

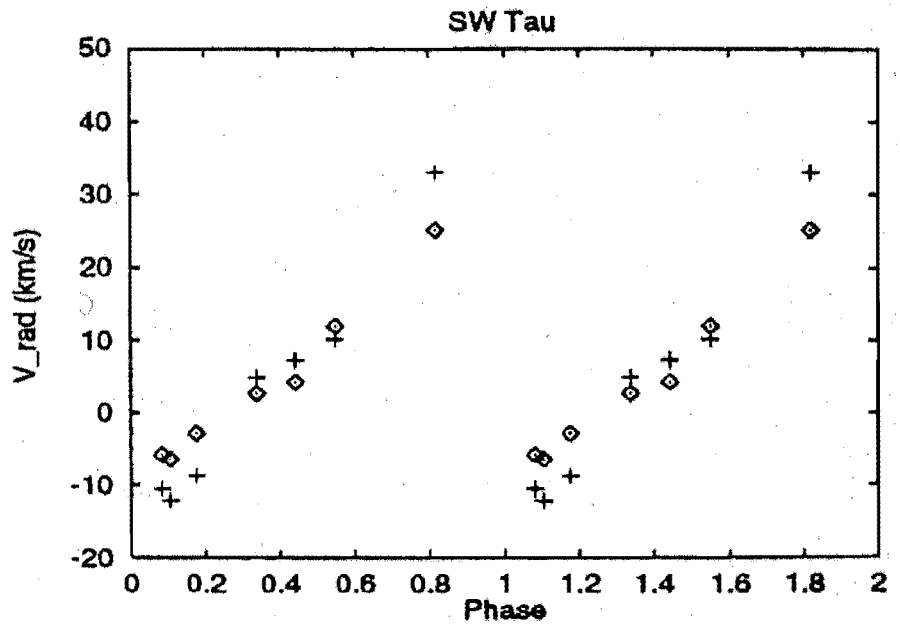

Figure 5.8: Vinkó et al. (1998) radial velocity curve for SW Tau. Plusses show Hα velocities while diamonds show metallic line velocities (reproduced from Figure 7, Vinkó et al., 1998).

32 kms^{-1} for Ca II and 39 kms^{-1} for Hα. They also have different systemic velocities, with 10 kms^{-1} for Hα and around 2 kms^{-1} for Ca II. It is curious then that they share very similar velocities from phases 0.3 to 0.6, with the Hα velocities being far larger from phases 0.6 to 1.3. In fact, where the Hα velocities are greater than the Ca II velocities, they agree far more closely with the Fe velocities. The reason for this becomes clear when the method of line measurement is taken into account.

Hα line

Figure 5.11 shows the parameters of the lines based on their widths and velocities for the 0.9 and 0.5 depths of the line bisector. When examined like this, the Hα line is clearly of fairly constant width between phases 0.3 and 0.8 and strongly broadened between phases 0 and 0.2[3]. In the broadened phases, there is a far greater difference between the velocities at the two different depths, a feature more clearly illustrated in Figure 5.12. The velocity curve of Figure 5.12 from the 0.9 bisector level lacks the bump where the velocities are around 0 kms^{-1} (phases 0.0–0.2) which is observed in the Hα curve of Figure 5.10. The 0.9 bisector level velocity curve also has a greater maximum velocity compared to the earlier curve. The 0.5 level velocity has a similar amplitude to that of Figure 5.10. This becomes clearer when it is remembered that for Figure 5.10 not only are the velocities an average of various lines, but also various depths of the lines. The velocity is taken from an average of the velocity at line depths of 0.7, 0.8 and 0.9. Hence line splitting and the depth of the

[3]The exact phasing here is of higher uncertainty, due to the offset created by the finite width of each bisector plot

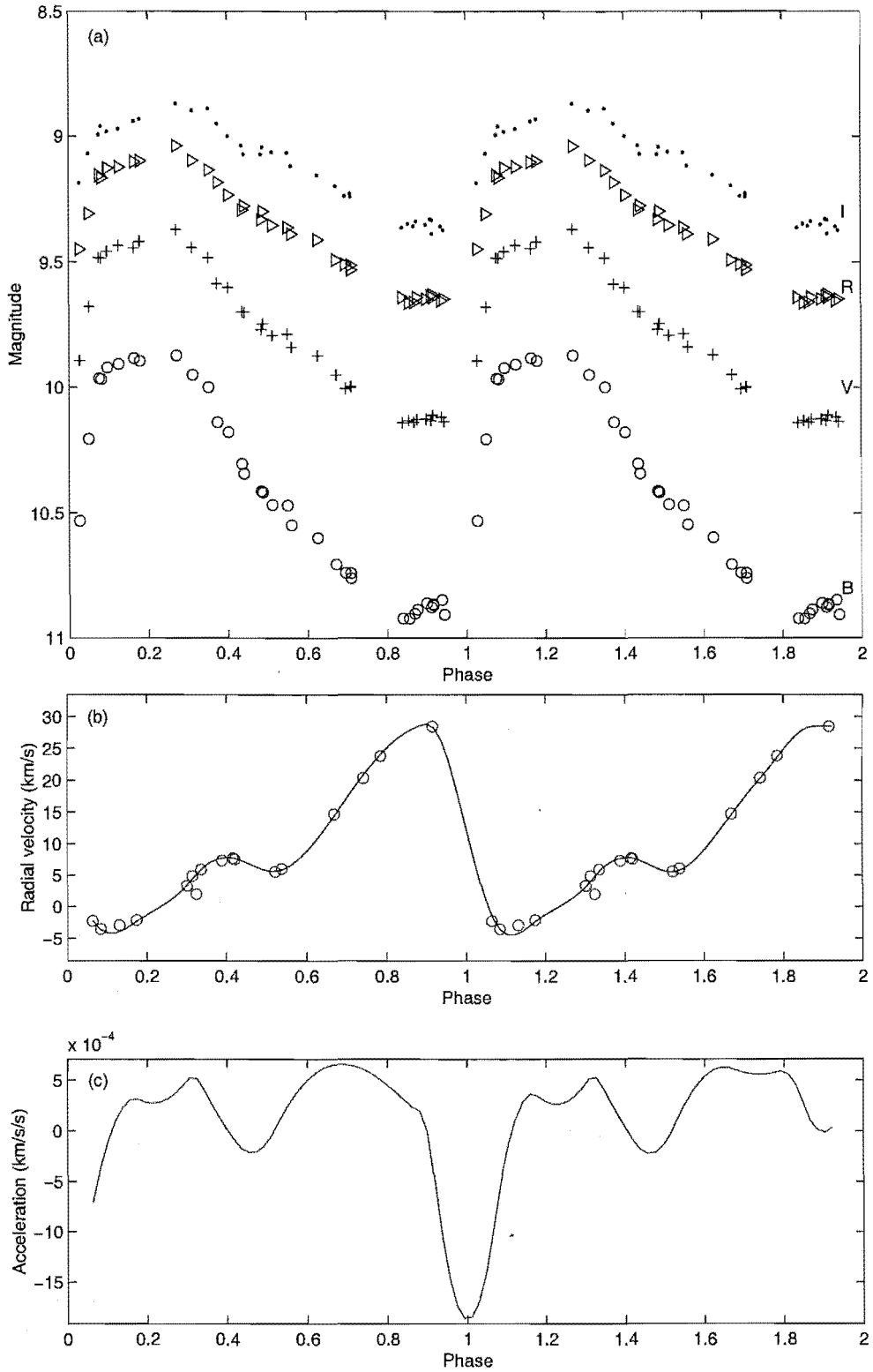

Figure 5.9: (a) *BVRI* photometry, (b) Fe I radial velocity and (c) acceleration curves for SW Tau.

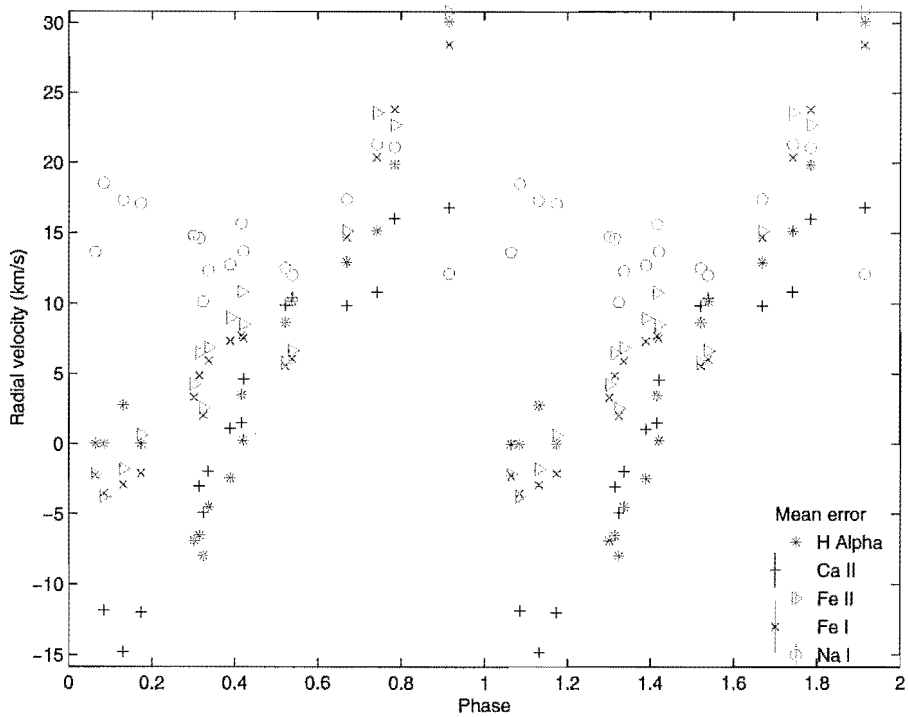

Figure 5.10: Radial velocity curves for SW Tau, measured from averaged Fe I, Fe II, Ca II, Na I and Hα lines.

line at which this occurs can have major effects on the velocity curve seen, which can be hidden if only the one average velocity value is examined. If the line splits between the 0.7 and 0.8 level, the mean velocity will be closer to the deepest line core velocity, whereas if it splits between the 0.8 and 0.9 levels, the velocity will reflect the centre of the split line. This is easily seen in Figure 5.13, where the actual Hα lines are stacked in order of phase. Phases 0.0–0.1 will favour the 0.9 level velocity with the broadening at the higher level reducing the velocity slightly, whereas for phases 0.1–0.2, the split occurs much lower down so the velocity will be higher than the 0.9 level line bisector velocity. Hence, based on the 0.9 level velocities, the amplitude of the Hα line is greater than that previously obtained, around 55 kms^{-1}, with a systemic velocity of around 13 kms^{-1}, which is closer to the Fe systemic velocity. Also, based on this, maximum velocity for Hα occurs around phase 0.05, rather than at phase 0.9.

Ca II lines

The behaviour of the Ca II lines agrees more with that of Hα than with the Fe lines. The agreement of these lines between phases 0.3 and 0.6 was clearly shown in Figure 5.10, and extended to just after phase 0.15 for the 0.9 level bisector in the previous discussion. An inspection of the Ca II lines themselves (Figure 5.14a and b) shows similar patterns, in that the lines broaden around phase 0.0 to 0.1, although to a lesser degree. This is most noticeable in the 8498 Å line (Figure 5.14a), whereas the 8542 Å line (Figure 5.14b) shows an irregularly occurring red-ward component at various phases, similar to VY Pyx.

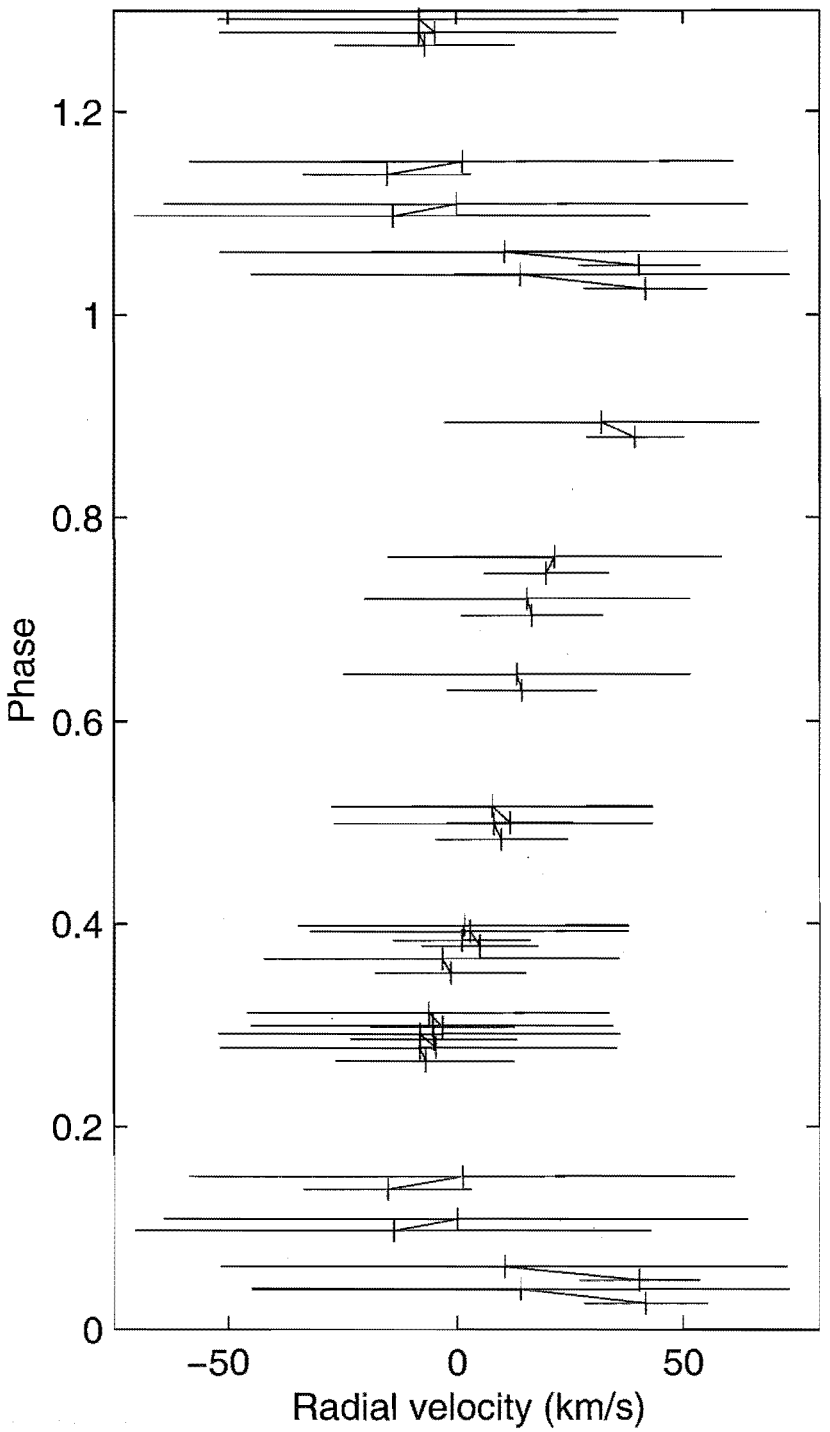

Figure 5.11: SW Tau stacked Hα line bisectors, showing line bisector velocities at line depths 0.5 and 0.9, and the associated line width in velocity space for each depth.

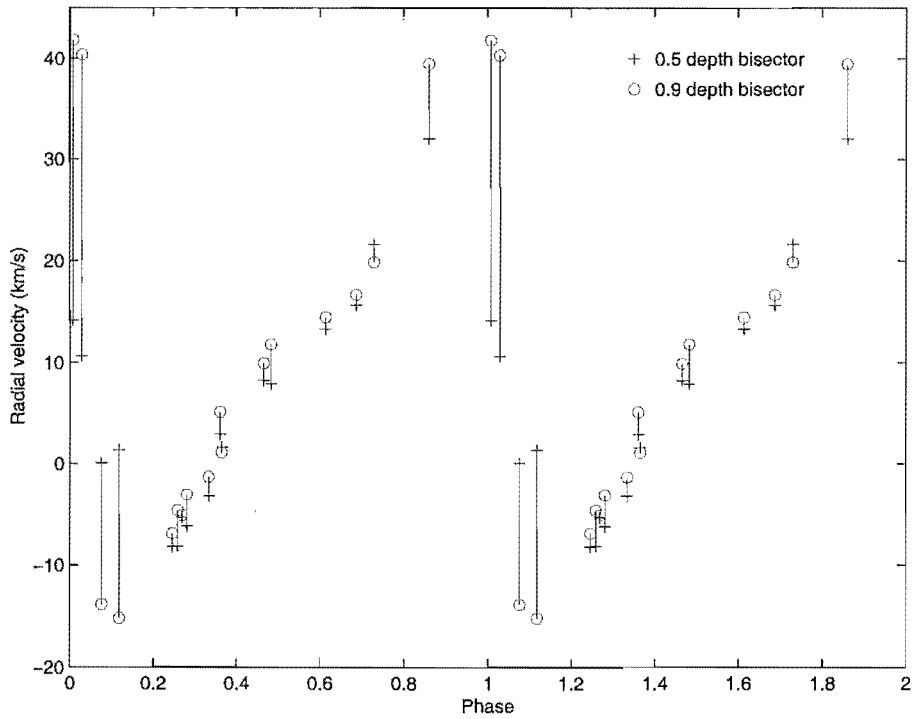

Figure 5.12: Radial velocity curves for SW Tau, measured from the Hα line using line bisector velocities at line depths 0.5 and 0.9.

Na D lines

The species which behaves most differently in Figure 5.10 is Na I, as measured from the Na D lines. These lines are stacked in Figure 5.15. There appears to be a single centrally unmoving core to the Na line, with a smaller moving component which occurs on the blue side around phase 0 to 0.1. The main unmoving component is most likely to be interstellar in nature, and, lying where it is, obscures any pulsational motion from the star itself which contributes to the lines. Thus the velocity tracked in the velocity curves was mainly that of the interstellar component, hence the very low amplitude and lack of distinct maximum and minimum. Also present are two emission components on the spectrum of cycle 242.93. The cause of this is unclear[4], but they have not been investigated further due to their isolated occurrence. As phase coverage in that region is somewhat lacking, further future observation of this phase is warranted, both to clarify the matter of the emission lines, and to fine-tune our knowledge of the star's behaviour in the very rapid transition from maximum velocity to minimum velocity.

Overall, SW Tau shows a similar velocity curve to VY Pyx in that its transition from maximum to minimum velocity is far faster than its transition from minimum velocity to maximum velocity. The duration of these transitions is rather different however, as where VY Pyx took 0.4 of a pulsational cycle to travel from maximum velocity through minimum radius out to minimum velocity with respect to the observer, SW Tau took less that 0.1 of a pulsation cycle to do the same. This more rapid change in acceleration was also accompanied by far more distinct line broadening at those phases, as shown in

[4]They may be night sky emission.

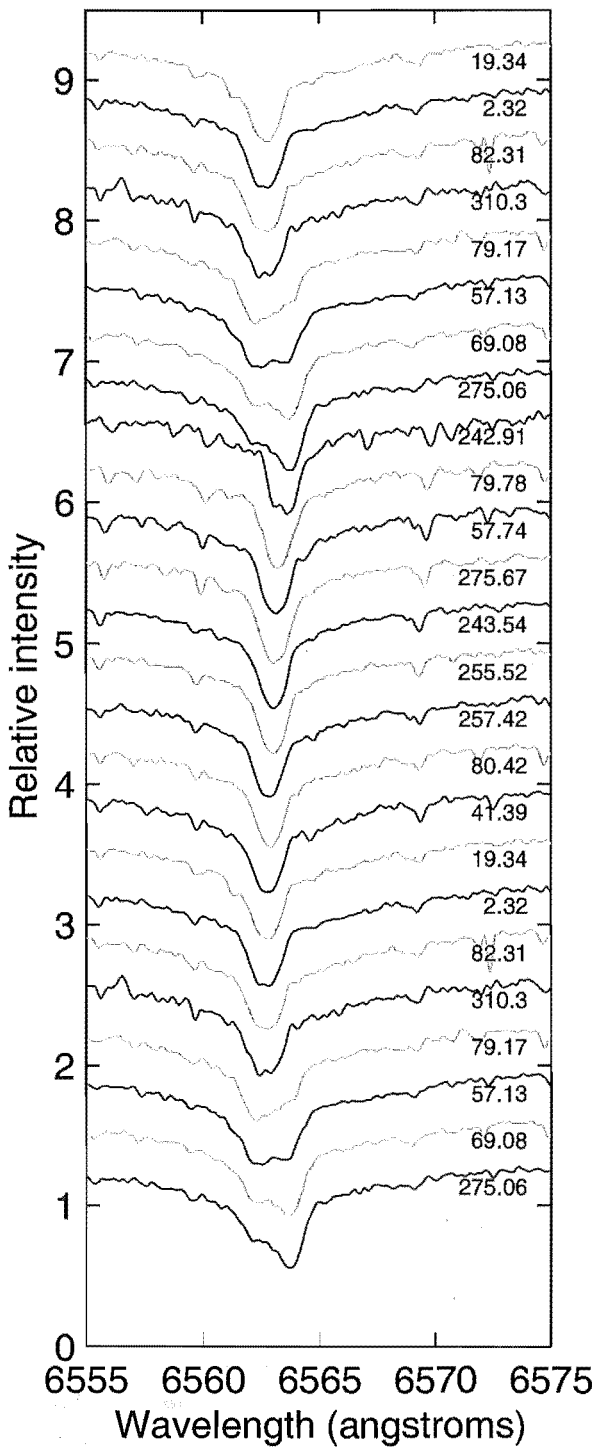

Figure 5.13: SW Tau stacked Hα lines.

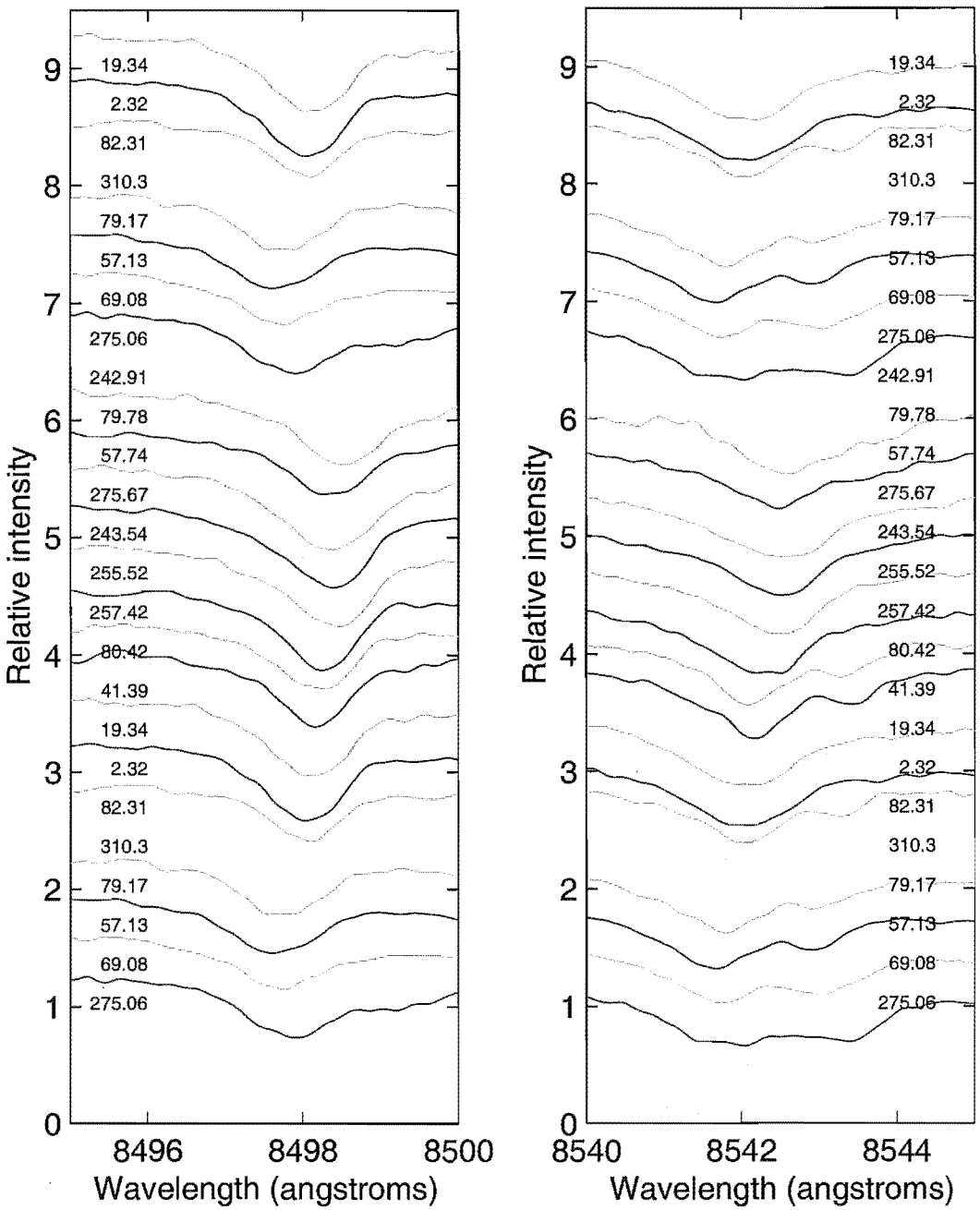

(a) 8498 Å

(b) 8542 Å

Figure 5.14: SW Tau stacked Ca II lines. Gaps indicate observations for which wavelength coverage does not extend to 8000 Å due to filter problems (Section 2.2.3).

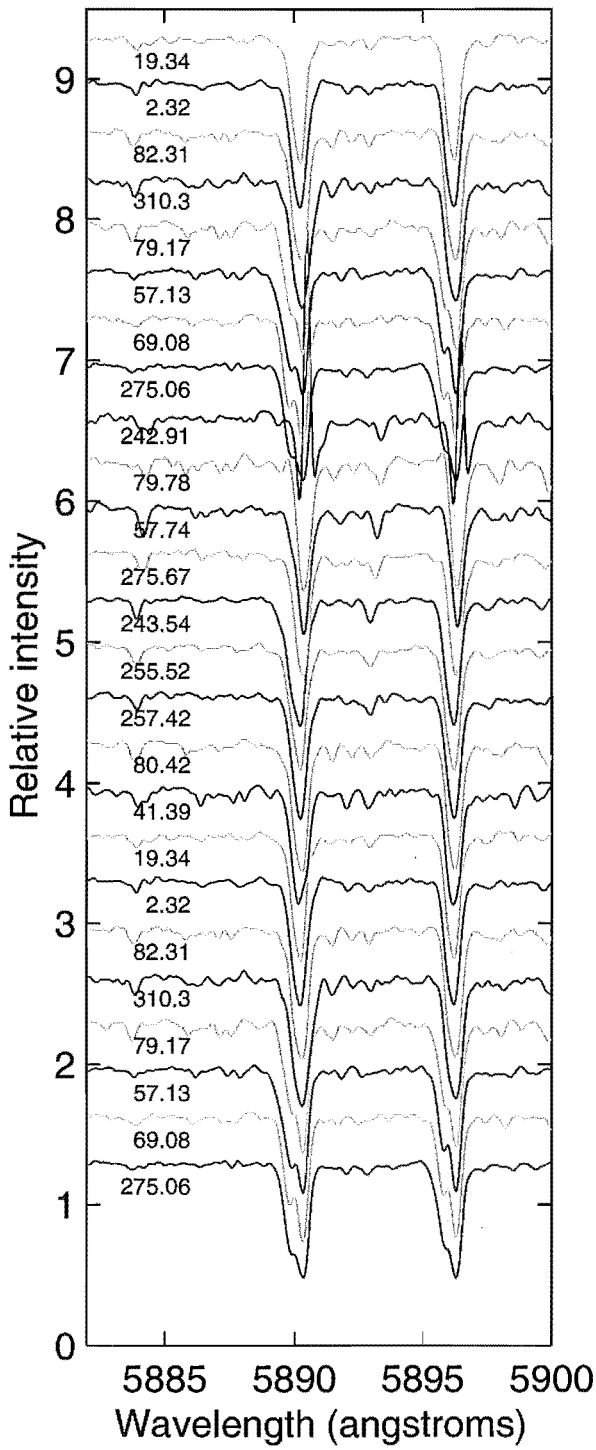

Figure 5.15: SW Tau stacked Na D lines.

Figures 5.11 and 5.12. This indicates the presence of a shock wave traveling through those regions of SW Tau at those phases.

This is most easily observed in SW Tau in the Hα line as it is formed over a larger region of the star compared to the metallic lines observed. As the shock enters the Hα line forming region it creates a velocity discontinuity as the material on one side of the shock is falling inwards whereas the material behind the shock is now flowing outwards. This becomes visible in the line, first as a line broadening to the blue which strengthens into a separate line component. This occurs when there is enough material moving in outwards with enough of a mean velocity separation from the still inward falling material that a separate absorption peak is visible. As the shock propagates further through the line forming region, there is now more material moving outwards, so the component of the line formed by that motion becomes stronger and increases in depth, As there is now less of the material falling inwards in the line forming region, the red-ward line component decreases in strength until it can no longer be observed as a separate component and merely broadens the absorption line profile to the red. This broadening disappears completely once the shock has exited the line forming region.

This behaviour is traceable though the bisector velocities at different line depths in that the 0.9 line level bisector velocity will reflect the dominant motion in the line forming region. The 0.5 level bisector velocity will be shifted in the direction of the auxiliary motion in the region, reflecting a compromise between the two velocity regimes, with the velocity difference between these two levels directly showing the line asymmetry. Hence as the shock enters the line forming region, and starts broadening the line, the 0.5 level velocity will be shifted to the blue. The line widths at the different levels also show the shock presence, as the 0.5 level width is widest with multiple line components and asymmetry, whereas the 0.9 level line width is widest when there are similar amounts of material traveling inwards and outwards such that the line is broader/doubles in the core. The difference in velocities either side of the shock will affect this, as if there is too great a velocity difference, two distinct lines of equal depth are formed. SW Tau (and the BL Her stars) is compact enough that the line forming regions are small enough and the shock weak enough that the lines are not completely separated like this, so the line widths measured will still reflect the line broadening.

So when examining the 0.5 and 0.9 level line bisector velocities, the transition of the shock though the line forming region shows itself first the 0.5 level velocity being blue-shifted, with a greater line width. This will become further and further blue-shifted to a lower velocity as the outward motion becomes more dominant and the blue-ward component becomes stronger. As the material becomes approximately equally divided into material falling inwards and material being forced outwards, the 0.9 level line width will increase and the 0.9 level bisector velocity shifts from tracing the red-ward in-falling component to the now dominant blue-ward outward moving component. The 0.5 level bisector velocity itself is still in the same place with respect to the line but is now red-ward of the 0.9 level bisector velocity. As the outward motion dominates more of the motion in the line forming region, the asymmetry decreases and the 0.5 level bisector velocity comes into closer agreement with the 0.9 level velocity. This will be the case as the shock wave leaves the line forming region[5].

[5]Once this is no longer the dominant mechanism governing the line profile, asymmetries may still be present from causes such as line projection effects and localized turbulence in the line forming region. These appear to have been studied for Type I Cepheids, but not really Type II Cepheids, although there

Such a shock wave is not as distinctively observed in VY Pyx, at least in the Hα line. The line width stays comparatively constant at all phases (Figure 5.4), although there is some broadening observed around phase 0.0. This may indicate the passage of a very weak shock wave which does not give a velocity difference across the shock wave large enough to show distinct components, but merely broaden the line very slightly.

5.3 V381 Cen

Line broadening is noticeable in V381 Cen, although to a lesser extent that in SW Tau, and a greater extent than VY Pyx. This is interesting in that V381 Cen is not actually a Type II Cepheid (as reported in Kholopov et al., 1990), but is actually a Type I Cepheid. As such, it is considered to be a larger star, giving it a brighter luminosity for the same period, in comparison to the Type II Cepheids. It is also considered to belong to a younger population of stars which are more metal rich. More work has been done on Type I Cepheids in general as they are far more numerous to observe, being intrinsically brighter, so their behaviour is better established than the Type II Cepheids. The observed line level effects are better established (Petterson, 2002), though work on this is still quite recent.

The majority of velocity work on V381 Cen itself is older. Stibbs (1955) presented an early radial velocity curve, established a period of 5.0789 days and a spectral type range of F6-G7 over its pulsation cycle. Apart from that paper, most of the work on this star has been part of larger studies (Caldwell and Coulson, 1987; Pont et al., 1994; Feast and Whitelock, 1997), attempting to get kinematic and/or distance parameters for the Milky Way, by studying Cepheids around the centre of the Galaxy.

Even though it was discovered relatively early on in this study, that the star is a Type I Cepheid, it was decided to include the star in this chapter and to analyze it using the phasing technique of the acceleration minimum method. It is hoped to examine if the method is applicable to such stars, and if so, see what it can tell about the differences between Type I and Type II Cepheids in this period range[6].

5.3.1 Spectroscopy

As can be seen from Figure 5.16, the radial velocity curve of V381 Cen, as measured from averaged Fe I lines, is smooth and continuous, similar to its light curve. Consequently it is similar to VY Pyx. The smooth acceleration curve implies that the acceleration minimum technique is directly applicable to at least this Type I Cepheid. The regularity in both smoothness and repeatability from cycle to cycle is far more marked in V381 Cen and VY Pyx, in comparison to SW Tau. The overall shape and amplitude of the velocity curve for V381 Cen is far closer to SW Tau though, as ignoring SW Tau's bump in velocity around phase 0.4, they both show a larger amplitude and a far more rapid return to minimum radial velocity, than VY Pyx.

The Fe II velocity curve tracks the Fe I velocity curve well (Figure 5.17), as in SW Tau. Both species share maximum velocity around phase 0.9 and minimum velocity around

is little indication that the effects should not be present for the Type II.

[6]Particularly in how this relates to what is known about line level effects in Type I Cepheids, especially in recent work such as Petterson (2002).

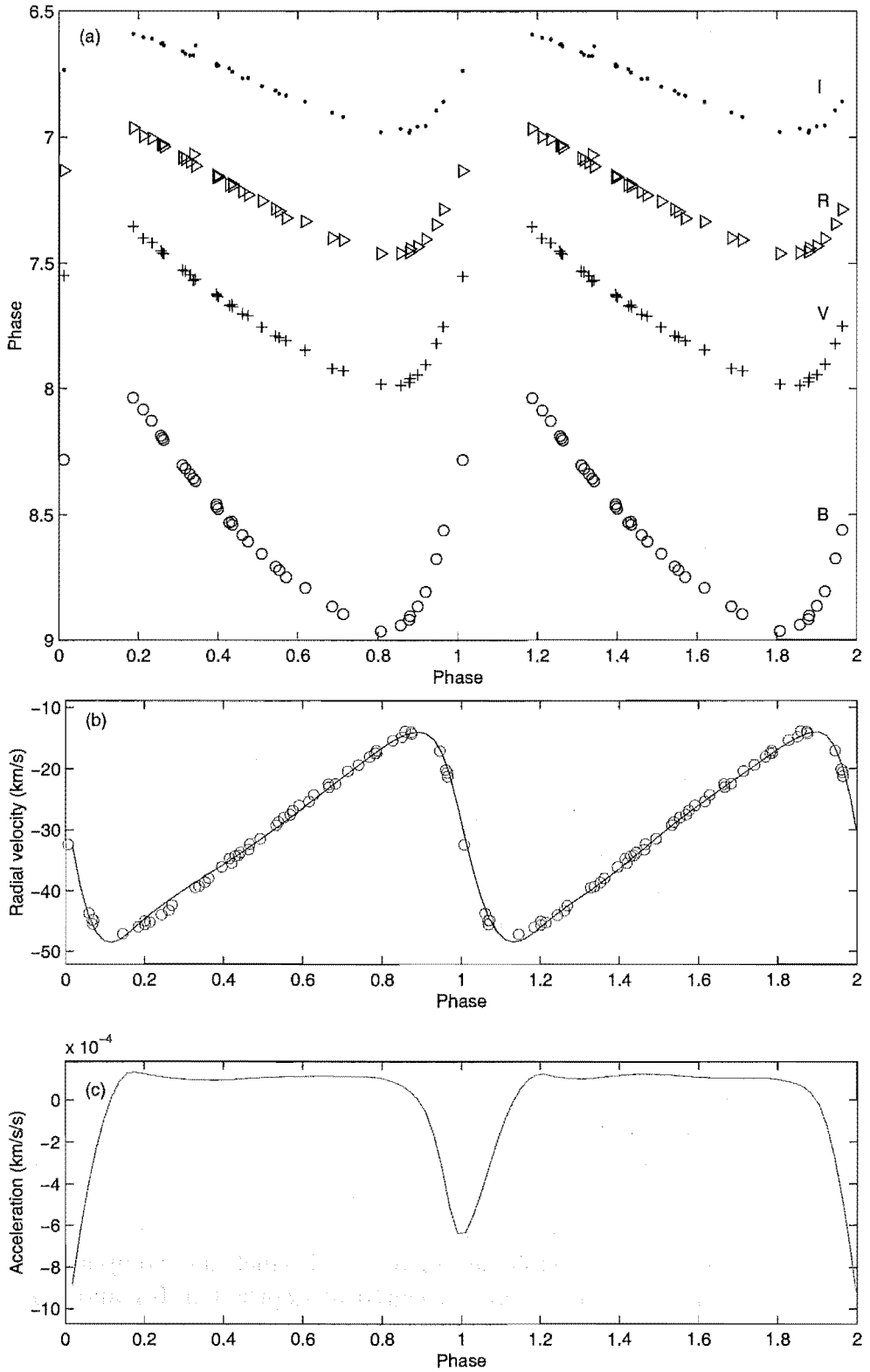

Figure 5.16: (a) *BVRI* photometry, (b) Fe I radial velocity and (c) acceleration curves for V381 Cen.

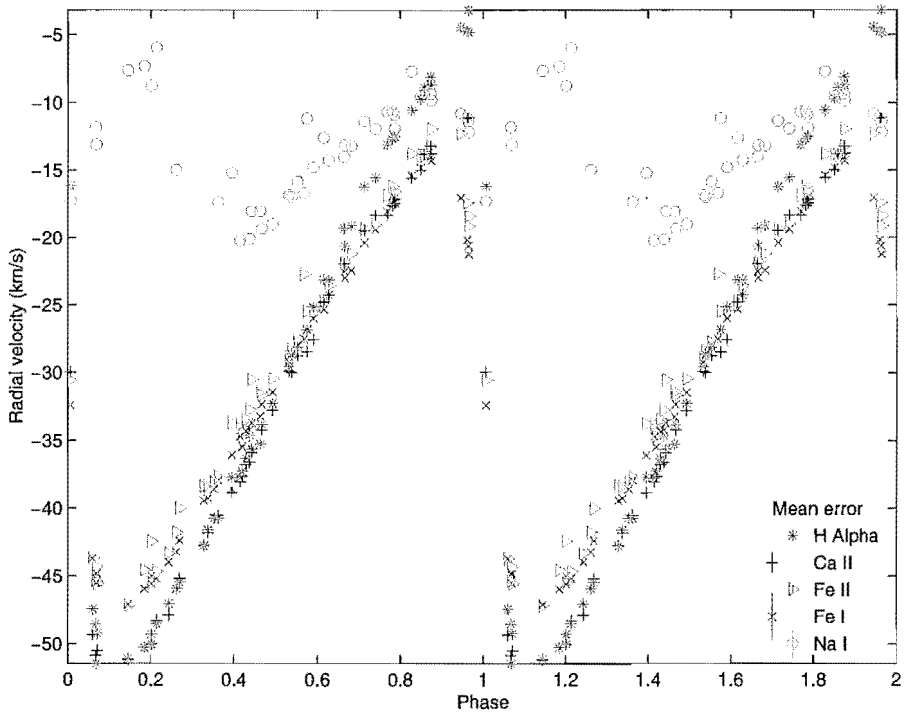

Figure 5.17: Radial velocity curves for V381 Cen, measured from averaged Fe I, Fe II, Ca II, Hα and Na I lines.

phase 0.1, with an amplitude of approximately 35 kms^{-1}. They also share a systemic velocity of around -30 kms^{-1}.

The Hα line is far larger in velocity amplitude, and it attains a velocity amplitude of 49 kms^{-1}. The curve reaches maximum velocity around phase 0.95 and minimum velocity around phase 0.05, phases which are later than those for the Fe maximum velocity and earlier than those for Fe minimum velocity. Its systemic velocity is also higher, at approximately -27 kms^{-1}.

In contrast, the Ca II velocity behaviour is somewhere in between these two extremes. Its peak velocity is only slightly higher than that of the Fe maximum velocity, velocities with which it has agreed fairly closely since around phase 0.5. However the Ca II peak phase position is far closer to that of Hα, and from around phase 0.0 to phase 0.5, the velocities track the Hα line very closely, sharing a minimum velocity at phase 0.05. Hence the systemic velocity is less than both the Fe and Hα velocities, at approximately -31 kms^{-1} and the amplitude is between Fe and Hα, at 41 kms^{-1}.

In SW Tau, some of these variations, in terms of which lines had similar velocities to which and when, could be explained in terms of which line component was dominating the velocity as averaged from that measured at depths 0.5, 0.7 and 0.9. Unfortunately, this is less easily done with V381 Cen.

Hα line

Unlike SW Tau, very little asymmetry occurs in the Hα line for V381 Cen. This is easily seen by looking at the bisector summaries in Figure 5.18. The line clearly broadens

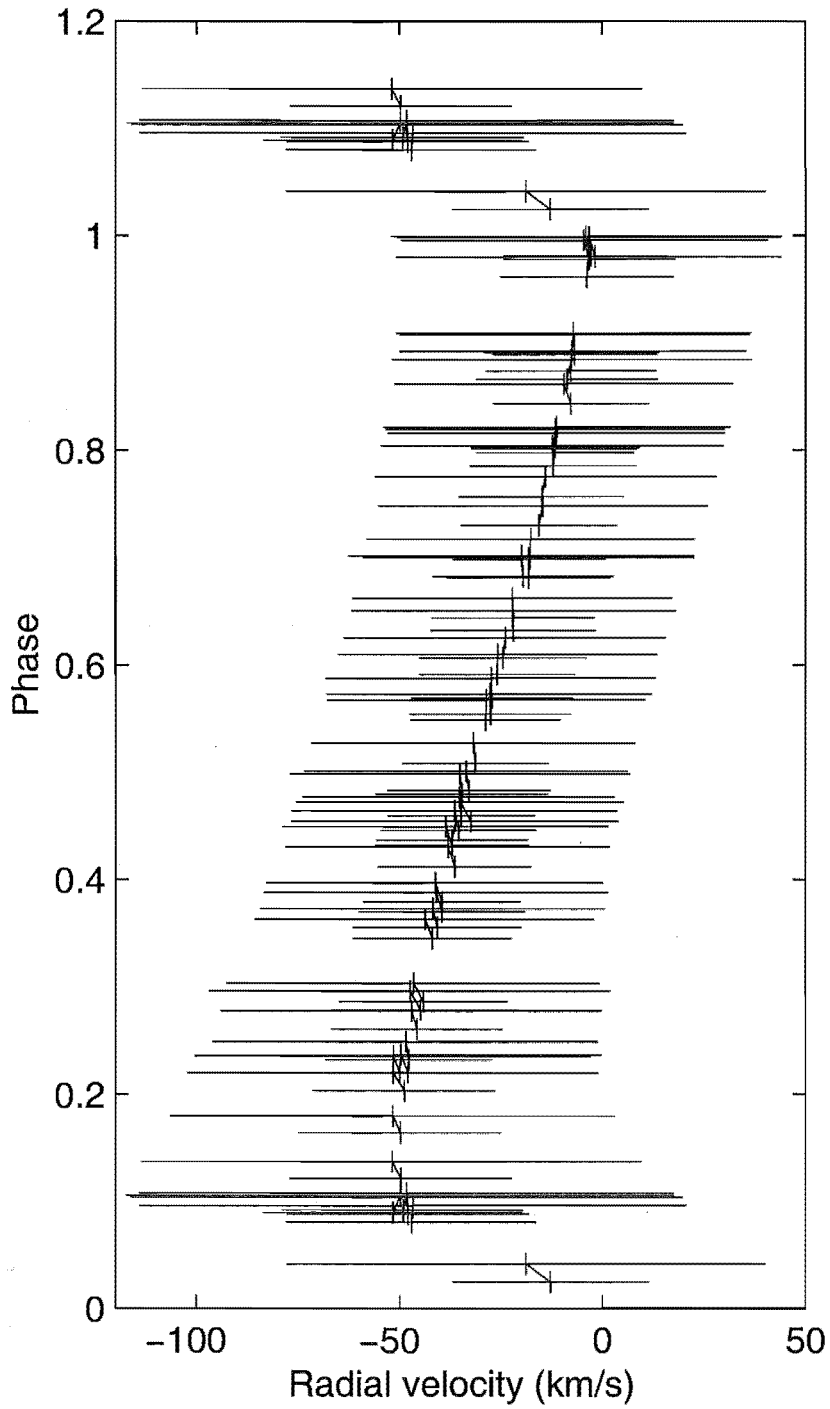

Figure 5.18: V381 Cen stacked Hα line bisectors, showing line bisector velocities at line depths 0.5 and 0.9, and the associated line width in velocity space for each depth.

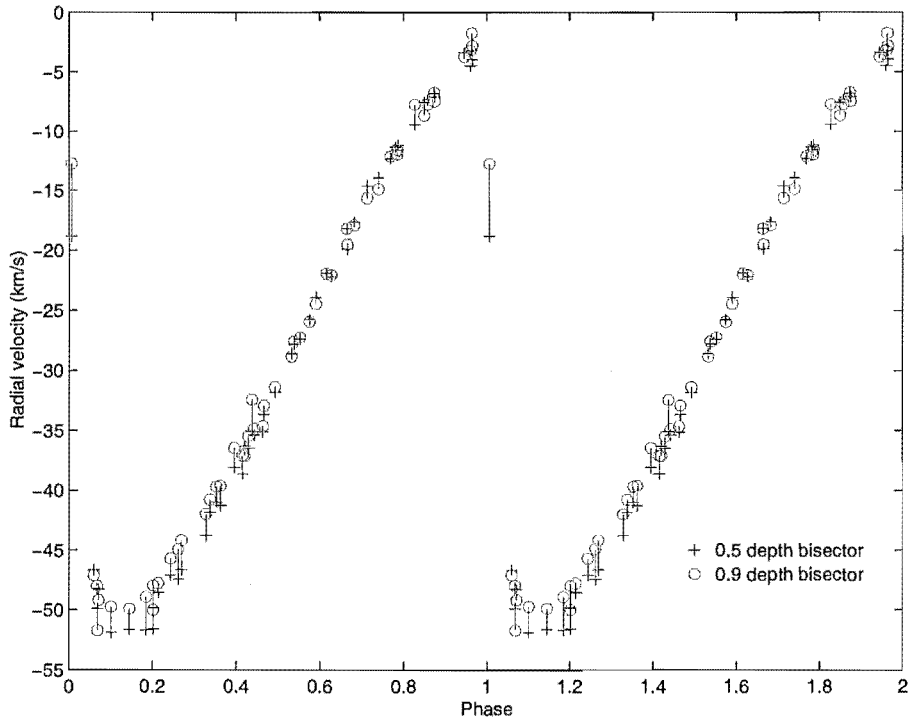

Figure 5.19: Radial velocity curves for V381 Cen, measured from Hα line using line bisector velocities at line depths 0.5 and 0.9.

in width but there is little slope on the lines connecting the 0.9 and 0.5 level bisector velocities. This is even more clearly visible in Figure 5.19, where only these velocities are plotted. A very slight asymmetry is noticeable from phases 0.0 to approximately 0.4, but it is of a far lower amplitude than that observed in previous stars. Clearly, there is an effect which is broadening these lines, but it is not producing the far more distinct asymmetry observed in the previous two stars.

When the profiles of the Hα lines are examined (Figure 5.20), it is clear that the lines are very smooth and are definitely broadened rather than split. It is unclear whether this is a feature of the Type I Cepheids in this period range, as opposed to the Type II Cepheids. However studies of line asymmetries in Hα profiles for southern Cepheids (Wallerstein et al., 1992) indicate that such line asymmetries as seen in SW Tau around phase 0.0, have been observed in Type I Cepheids. Unfortunately their period range is from approximately 7 to 39 days, which makes comparison difficult with these shorter period Type II objects.

Ca II lines

The smoothness of the Hα lines is repeated when we examine the stacked Ca II line profiles (Figure 5.21). No splitting is visible in either of the lines. A slight degree of broadening is visible around phase 0.0, but it is much less pronounced than in the Hα line. The Ca II lines are far more regularly behaved than in SW Tau and VY Pyx. While the lines of 8542 Å are slightly broader than those of 8498 Å they do not show the same irregular non-phase related splitting which was a curious feature of VY Pyx and, to a

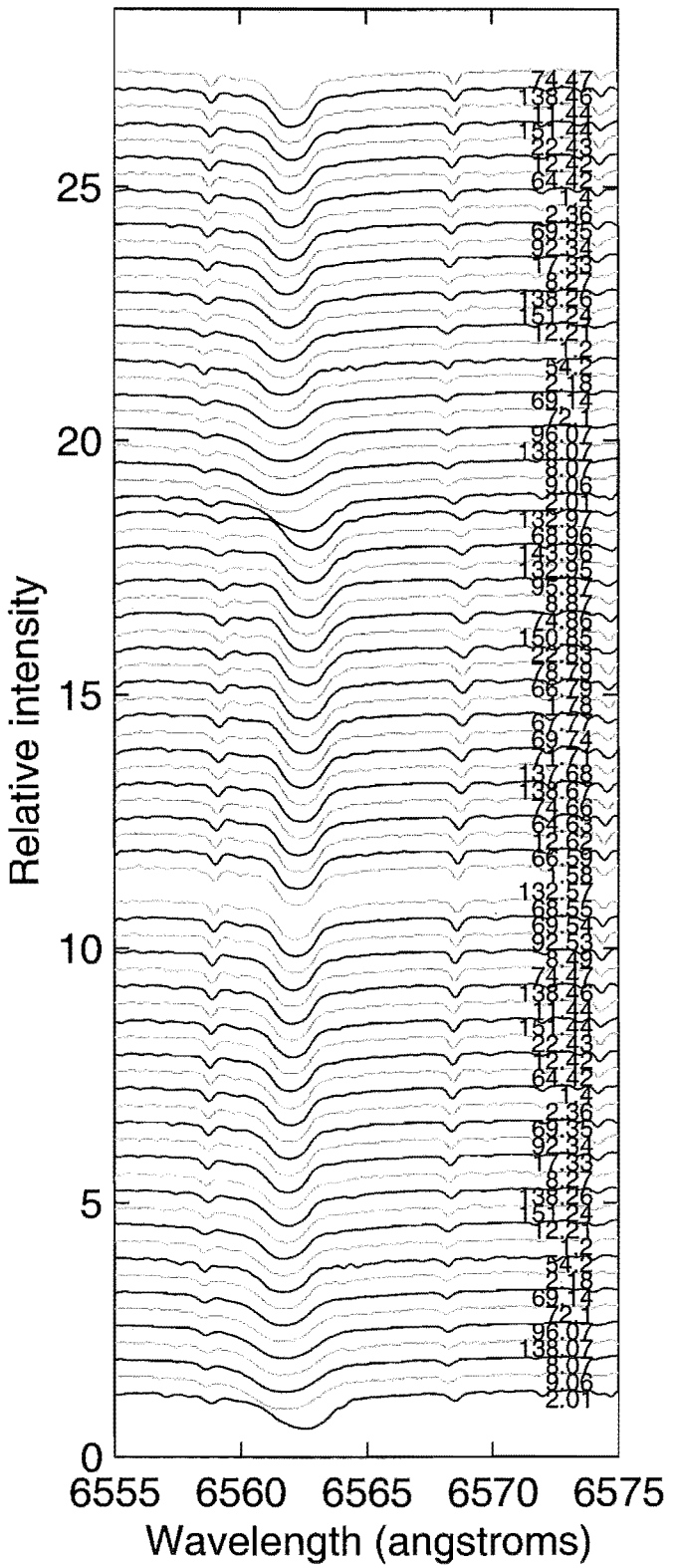

Figure 5.20: V381 Cen stacked Hα line.

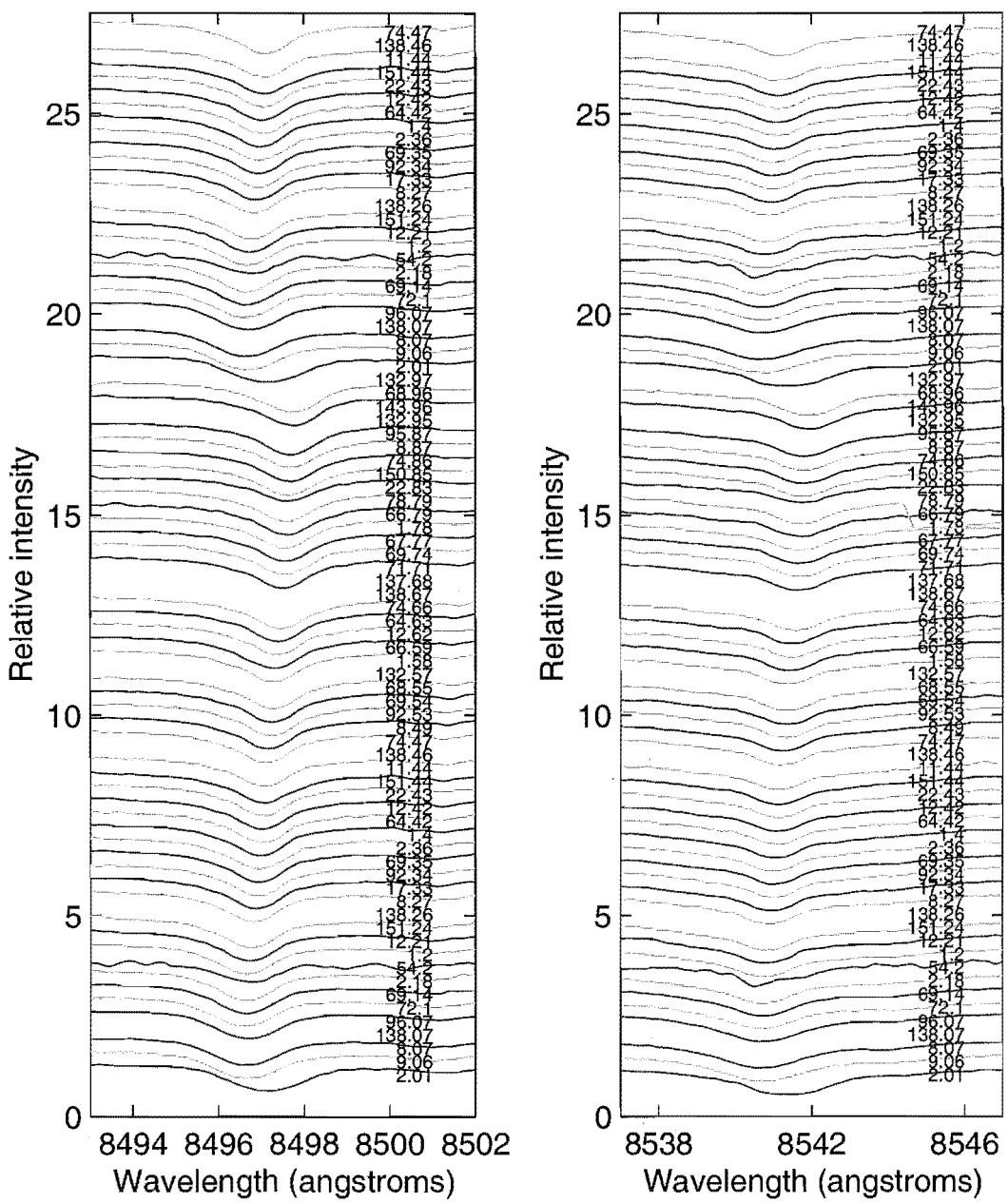

(a) 8498 Å

(b) 8542 Å

Figure 5.21: V381 Cen stacked Ca II lines. Gaps indicate observations for which wavelength coverage does not extend to 8000 Å due to filter problems (Section 2.2.3).

lesser extent SW Tau.

Na D lines

The Na I curve in Figure 5.17 is less regular than the other curves shown, with greater scatter and a lower amplitude, centred around approximately 13 kms^{-1}. The stacked spectra (Figure 5.22) illustrate why the lines give such a different result as it is clear that the lines are made of multiple components. The redder and deepest component appears to be interstellar in origin, in that it stays at a constant wavelength, whereas the components to the blue change shape radically over the course of a pulsation cycle. A third component, red-shifted to the main pulsational component and blue-shifted from the interstellar component, appears from phases 0.0 to 0.4. It is difficult to tell whether or not it is associated with the pulsations, as while it shifts position very slightly over time, its changes are not of the same magnitude nor in the same direction as those of the pulsational component. Observation of the various components explains why the large difference in velocity curve behaviours exist. As the velocities in Figure 5.17 were obtained via averaging velocities at various line depths through the line bisector method, the velocity of the deeper, interstellar component would have contributed most to the mean velocity obtained. While some slight pulsational variations are apparent, they are distorted by the impact of the interstellar line.

Comparison to other Classical Cepheids

Apart from those of Na I, the line level effects observed here are comparable to and consistent with those found for various Classical Cepheids by Butler et al. (1996) and Petterson (2002). The later examined a selection of lines (Hα, Ca II, Ba II, Fe I, Fe II, Si I and Si II) in a number of Cepheids and found similar trends to those observed here. He found that the shallower the line was formed in the atmosphere, the greater the amplitude of the velocity variations was, and the peaks in the curve occurred later in the pulsation cycle. As such, Hα has the highest amplitude and the latest peak velocity phase, decreasing in the order stated, to Si II having the lowest amplitude and earliest peak velocity phase.

The same trend is observable here. The lines of Hα, Ca II, Fe I and Fe II, all show the same amplitude and peak velocity phase trends. As all the stars examined so far show such trends, it is of interest to see if the same is true for the next star. However it is a little more complicated than those examined so far.

5.4 TX Del

TX Del has two complications compared to the previous stars. The first is that it is a single–lined spectroscopic binary with an orbital period of approximately 133 days (Harris and Welch, 1989; Szatmáry, 1990, see Table 5.3 herein,). The second is that it has not been clearly established as to whether the star is a Type I or Type II Cepheid.

This problem over the classification of the star has resulted from the various classification criteria used by different authors. Several of the photometric arguments have been discussed in Section 4.2.4. A summary of various authors and their arguments is

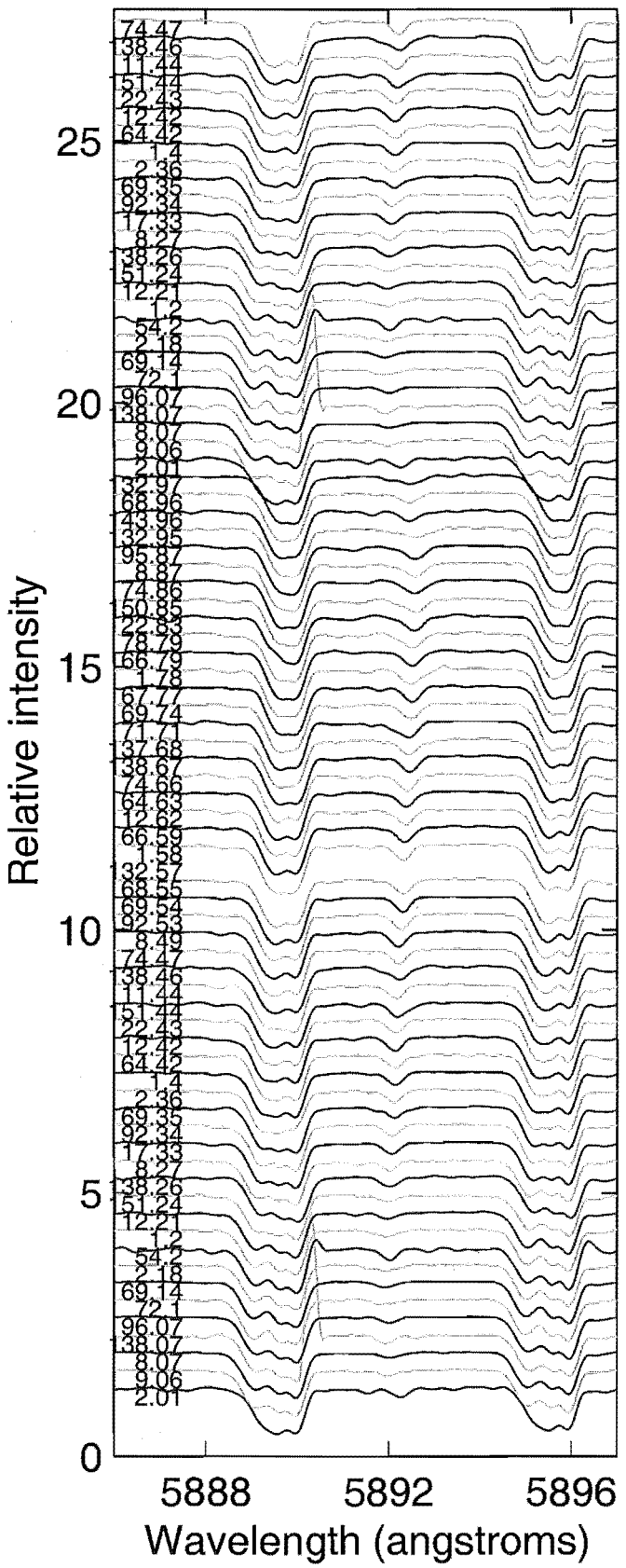

Figure 5.22: V381 Cen stacked Na D lines.

Table 5.3: Orbital parameters for TX Del.

	Harris and Welch (1989)	MJUO (Fe I line averages)[a]
P (days)	133.15 ± 0.29	133.71989 ± 0.00003
γ (kms^{-1})	13.9 ± 0.3	0.394 ± 0.003
K_1 (kms^{-1})	14.4 ± 0.3	14.3046 ± 0.0002
e	0.068 ± 0.022	0.02408 ± 0.00001
ω (^{o})	159 ± 18	127.228 ± 0.006
T_0 (JD)	2443956 ± 8	2443923.51848 ± 0.00009
σ (kms^{-1})	0.84	—
$a \sin i$ (km)	$(2.63 \pm 0.06)x10^7$	—
$f(m)$ (solar masses)	0.041 ± 0.003	—

[a]Errors given are the difference between the final iteration value and the previous iteration value,

given in Table 5.4. For the current discussion, and with respect to the pulsations and hydrodynamics involved, the type of Cepheid does not matter.

What it is necessary to know for this discussion are the parameters of the orbital motion of the star. Table 5.3 lists the orbital parameters from Harris and Welch (1989) and those derived using the MJUO data. These parameters were found by interpolation, least squares fitting and iterating on that process. Initially, the radial velocity data was plotted as a function of phase, and from that systemic velocity and amplitudes were found. The Harris and Welch (1989) parameters were then used as starting orbital parameters to interpolate with the residuals of the initial pulsational fit. This interpolation was then least squares fitted to the orbit and the pulsations recalculated. This process was repeated until the pulsational and orbital fits were either reasonable or obviously implausible. More details of this method are described by Petterson (2002). The results of this are presented in Figure 5.23, where quite reasonable fits have been obtained which agree well with those obtained by Harris and Welch (1989). Due to problems with the iterating program, the MJUO γ value was incorrectly calculated, so the Harris and Welch (1989) value has been adopted instead. For the rest of the discussion, unless specifically stated, orbital motions based on these parameters have been removed from the velocities and spectra shown.

5.4.1 Spectroscopy

Once the orbital motion component has been removed, the resulting velocity curve is shown in Figure 5.24. As with the previous stars, a spline curve has been fitted and from that, an acceleration curve derived. Unfortunately, the error introduced in the fitting of the orbital motion and its removal will introduce a certain degree of scatter. Hence the acceleration minimum found for TX Del is possibly a little less accurate than for the earlier stars.

This scatter from the orbital fitting also leads to greater uncertainty when looking for line level effects in the pulsations. As can be seen in Figure 5.25, the curves are far less distinct, and the phases of maximum and minimum velocity far less easily discernible

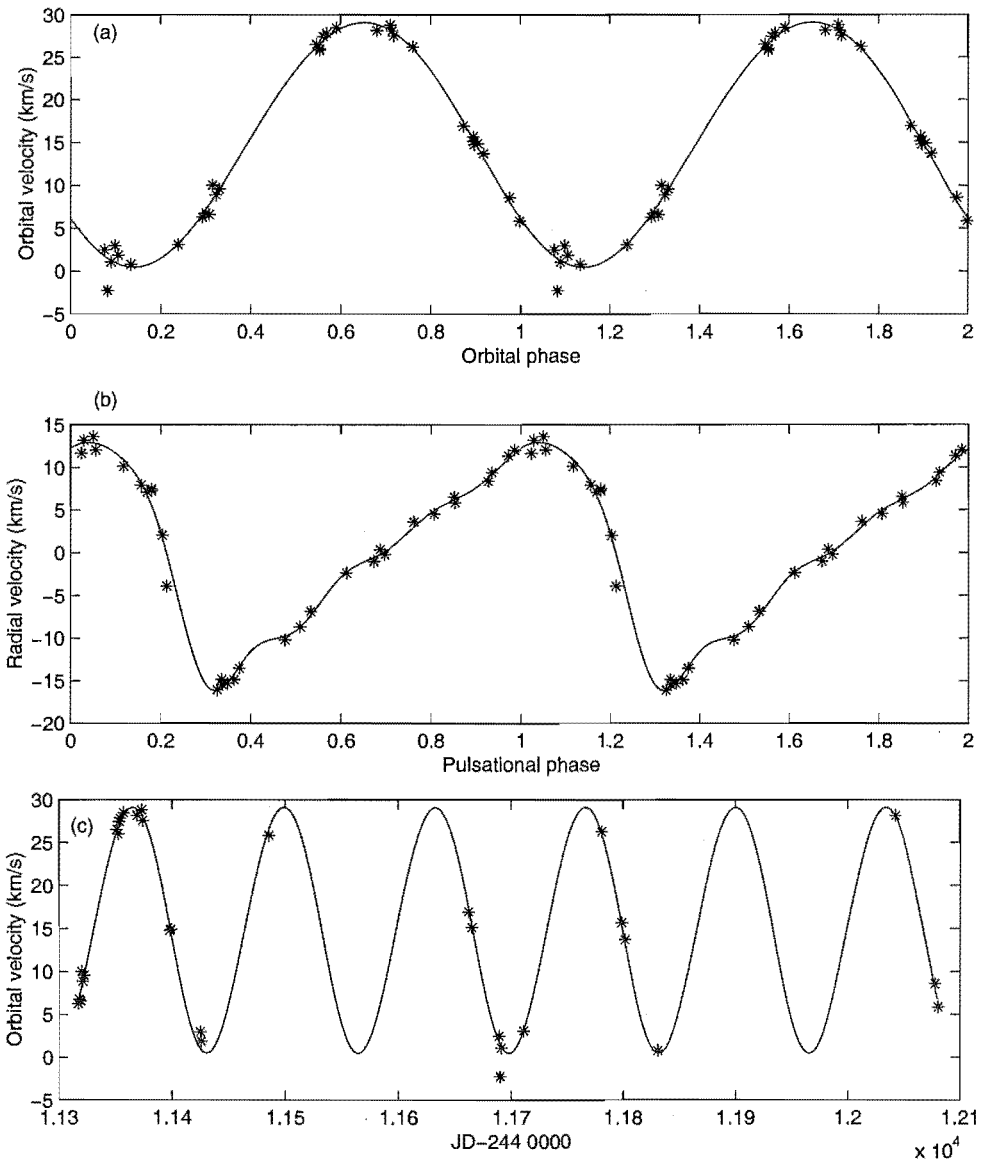

Figure 5.23: Velocity curves for TX Del, from average Fe I line velocities, separated into (a) orbital phase components, (b) pulsational phase components and (c) orbital components as a function of JD.

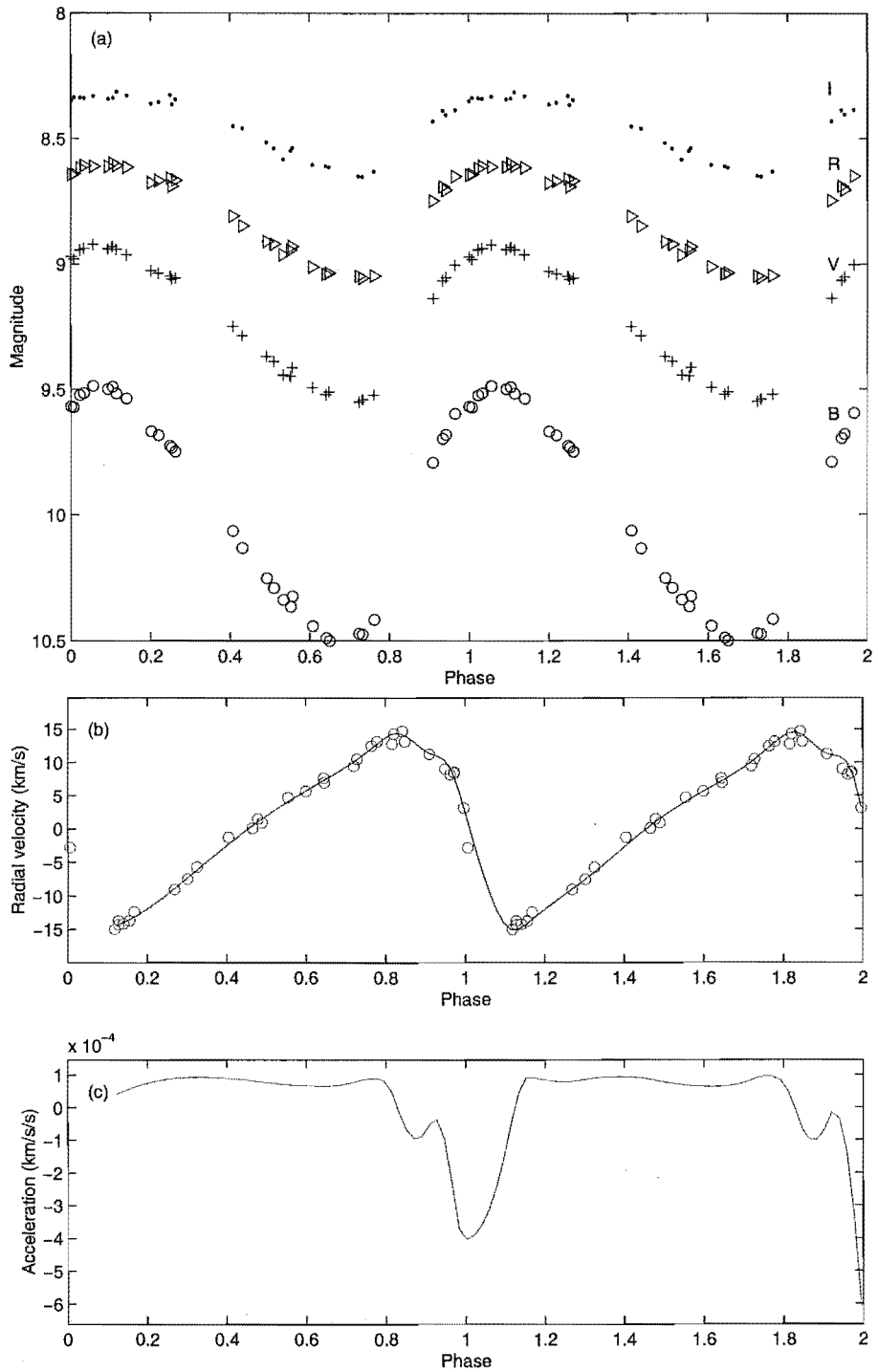

Figure 5.24: (a) *BVRI* photometry, (b) Fe I radial velocity and (c) acceleration curves for TX Del.

Table 5.4: Classification of TX Del

Author	Type	Reasons
Harris and Welch (1989)	II	Photometry and position (Section 4.2.4)
Szatmáry (1990)	II	
Balog and Vinkó (1995)	I	Baade-Wesselink and surface-brightness measurements. Radius too large for Type II Cepheid. Agrees with period-radius relation for Classical Cepheids. Also other arguments based on photometry (Section 4.2.4).
Galazutdinov (1995)	I	Based on chemical composition. Most elements have solar-type abundances. CNO distribution is typical of Classical Cepheids. Slight deficiency in s-process elements. Some possibility of Type II based on possibility of mass transfer in the binary system (Harris and Welch, 1989).
Balog et al. (1997)	II	Type II Cepheid but member of a sub-set of Type-I-like Type II Cepheids in terms of their radii and luminosities (along with DQ Aql, KL Aql, V733 Aql and BB Her).

than for the earlier stars. The trends observable are still broadly similar to those observed in the earlier stars.

From Figure 5.25, Fe I and Fe II share the same velocity curve, with maximum radial velocity occurring around phase 0.8. Unfortunately, the paucity of data around velocity minimum makes it difficult to determine the exact phase of the minimum. However it occurs a little before phase 0.1. This also affects the derived amplitude. A lower limit amplitude of 30 kms^{-1} is observed, with a systemic velocity of approximately 0 kms^{-1}. It should be noted that removal of the orbital motion has shifted the velocities such that the systemic velocity will be centred around 0 kms^{-1}.

As is the pattern with the other stars, the Ca II velocity curve is of higher amplitude and reaches maximum velocity at a slightly later phase. It peaks around phase 0.9, but has the same minimum velocity phase coverage problem so that the latest at which minimum velocity can occur, is phase 0.1. This same problem means that the amplitude of the velocity curve has a lower limit of 40 kms^{-1}.

Based on the behaviour of the previous stars, it would be expected that Hα would have a even larger amplitude, with a later phase peak velocity. While the peak velocity is higher, at approximately 19 kms^{-1}, the phase at which this occurs is approximately the same as Ca II, at 0.9. The positioning of the minimum velocity is even more ambiguous, for the same reasons as mentioned above. However the minimum velocity at phase 0.1 is approximately -18 kms^{-1}, a value far closer to the minimum Fe I and Fe II velocities of around -16 kms^{-1}. This leads to an amplitude of 37 kms^{-1}, which is somewhat lower than that found for Ca II, and a systemic velocity of approximately 1 kms^{-1}.

The Na I velocity curve returns to patterns observed previously around maximum

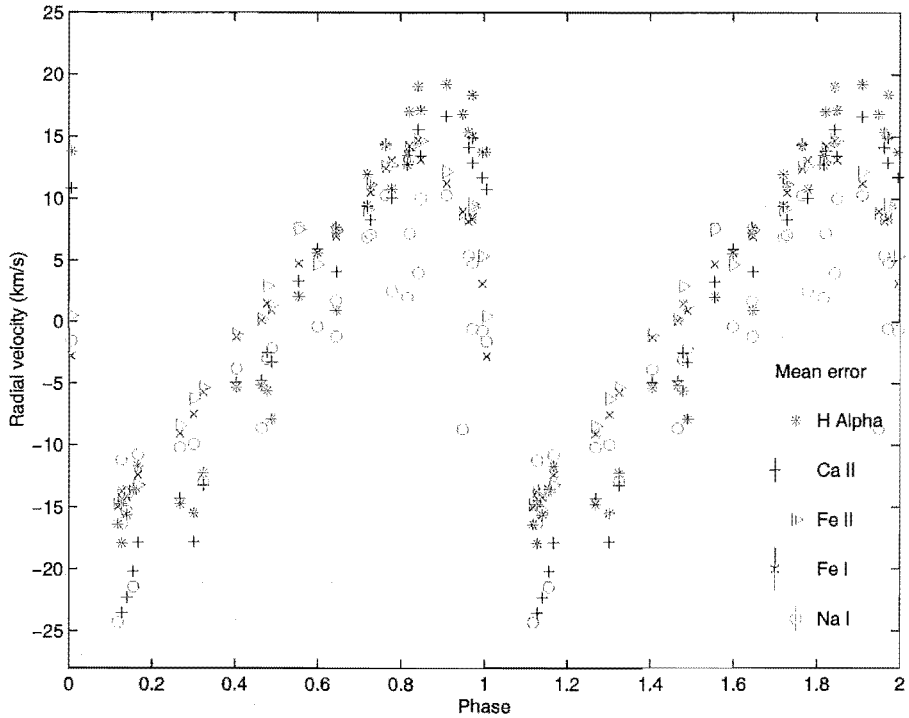

Figure 5.25: Radial velocity curves for TX Del, measured from averaged Hα, Fe I, Fe II, Ca II and Na I lines.

velocity, in that it has a lower amplitude than the rest of the lines examined here. Like VY Pyx, the pulsations of TX Del are readily visible in the velocity curve. However there is a great deal more scatter in the velocities. It is greater than that shown in the other lines studied and is more than can be accounted for by errors introduced in the removal of the orbital motion. From what can be seen, the peak velocity occurs around phase 0.8, at a similar phase to Fe, and has a slightly lower velocity (12 kms^{-1}). The major difference is around the minimum velocity, where the Na I minimum velocity ($\sim$ -25 kms^{-1}) is actually lower than all the other lines shown here. This gives a minimum amplitude of 37 kms^{-1}, a value far closer to the Hα amplitude.

Na D lines

The reason for this strange scatter and curious behaviour becomes apparent when the Na D lines, from which these velocities are derived, are examined in more detail (Figure 5.26a). A secondary (blue-ward) component to the line is clearly visible at all phases. Due to the presence of this component, the line variations appear far less regular, and were it not for the regular smooth variations of the Ni I line at 5893 Å the phasing of the star might be called into question. What is clear from this line irregularity, is that the secondary component is not circumstellar in origin, as it is not co-moving with the pulsating member of the TX Del system. This can be inferred from the fact that the variations of the secondary component are not in phase with those of the main pulsational component. To further examine the origin of this secondary component, the lines have been stacked in order of pulsational phase without the orbital motion being removed

(Figure 5.26b). The blue-ward component is clearly a little more stationary with respect to the binary system, but it is still variable. This indicates that it is unlikely to be circumbinary in nature. It may be that this is evidence of the pulsating star's stellar companion, however there is no evidence of such a blue-ward secondary component in the Ca II and Hα lines. More investigation is warranted at a future date, preferably examining a greater range of wavelengths.

Ca II lines

As stated, there is little sign of extra components in the Ca II lines in TX Del. When the lines are stacked in order of phase (Figure 5.27), there is no observable line splitting or irregularity. In fact, the lines are remarkably smooth, with definite broadening observable between phases 0.95 and 0.15.

Hα line

Line broadening is also observed in the Hα lines, as can be seen when the line widths at bisector levels 0.9 and 0.5 are plotted as a function of phase (Figure 5.28). While the widths of the lines are not as regular or as smoothly changing as for the preceding stars (VY Pyx, SW Tau and V381 Cen), the lines are definitely broader around phases 0.1 to 0.2. This is also reflected in the asymmetry of the lines, as shown by the lines linking the 0.9 and 0.5 depth velocities. From the slopes of these lines (Figure 5.28), and from the large velocity differences observable (Figure 5.29), the lines are far more asymmetric from phase 0.9 to approximately phase 0.3.

This is supported by Figure 5.30, where the lines are stacked in order of phase. The broadening occurs very low down in the line from phase 0.1 to 0.15. This is dissimilar to SW Tau and V381 Cen, as they don't seem to broaden in such a smooth way. It is a little more similar to VY Pyx, however VY Pyx only broadens slightly over the course of a pulsation cycle, being already quite broad.

The line broadening may be enough to explain why the minimum velocity of the Hα line was greater than the Ca II minimum velocity. The Hα line broadens, but the deepest part of the line is still the red-ward component until around phase 0.15. Thus the averaged velocity from the mean of the 0.9, 0.8 and 0.7 depth velocities of the bisector, will only be slightly blue-shifted by the shallower blue edge, and the velocity will be greater than if the blue-ward edge had been the deepest. This is also seen in SW Tau (Figure 5.12), where the velocity from the mean of the different bisector depths is around that of the Fe lines, whereas the 0.9 level bisector was at a lower velocity than the Ca II minimum velocity.

Type I or Type II Cepheid?

It becomes clear upon examining this star that there is nothing in its pulsational behaviour which distinguishes it as being either a Type I or Type II Cepheid. It shares similarities in behaviour with VY Pyx, SW Tau and V381 Cen, and also shows differences from each. In order to investigate this further, a larger sample of stars should be observed to seek out any distinguishing characteristics between Type I and Type II Cepheids.

The inability to classify TX Del as a Type I or Type II Cepheid reflects the similarity in pulsational behaviour between the Type I and Type II Cepheids. This has been partially

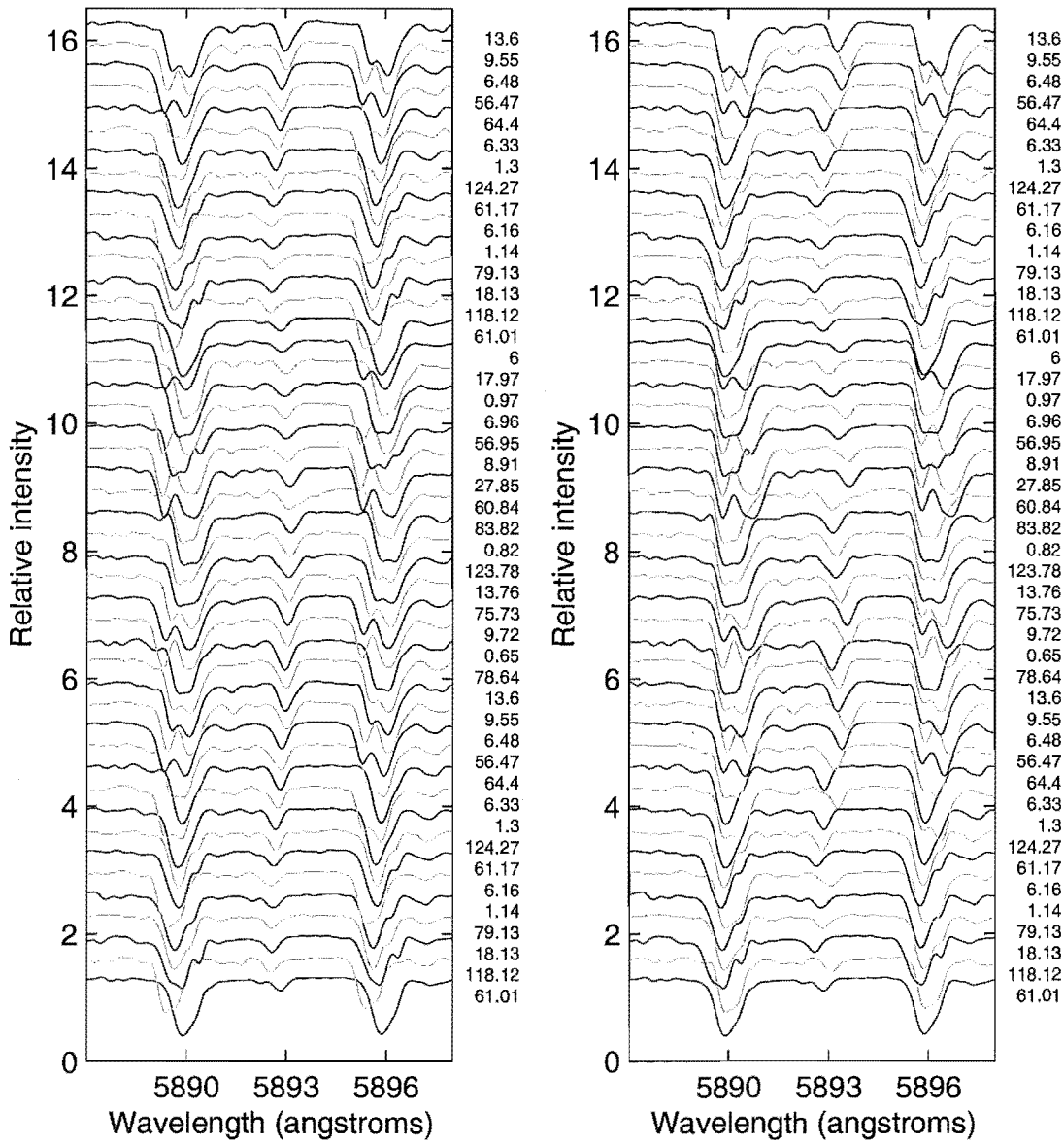

(a) Orbital motion removed.

(b) Orbital motion present.

Figure 5.26: TX Del stacked Na D lines.

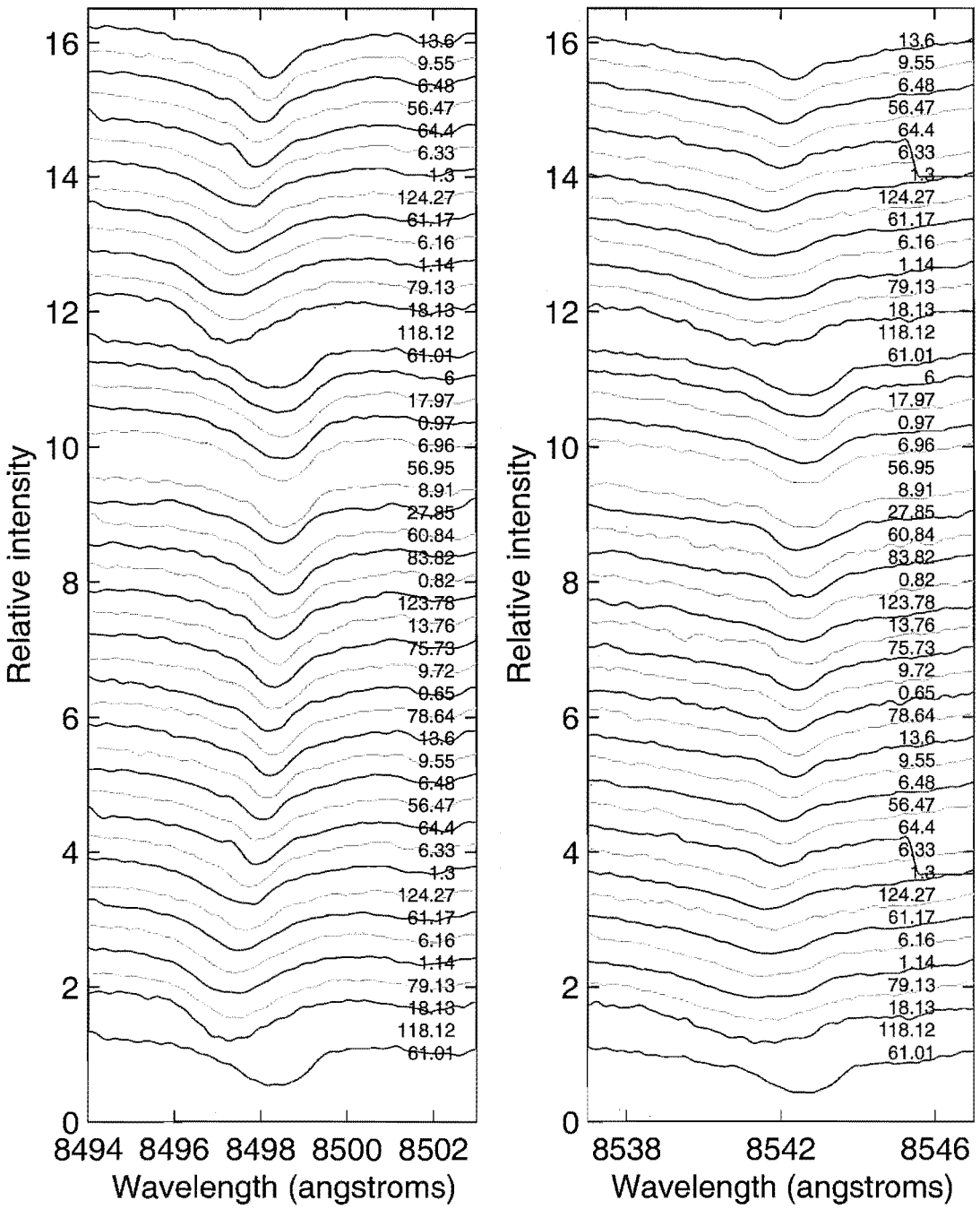

(a) 8498 Å (b) 8542 Å

Figure 5.27: TX Del stacked Ca II lines with orbital motion removed. Gaps indicate observations for which wavelength coverage does not extend to 8000 Å due to filter problems (Section 2.2.3).

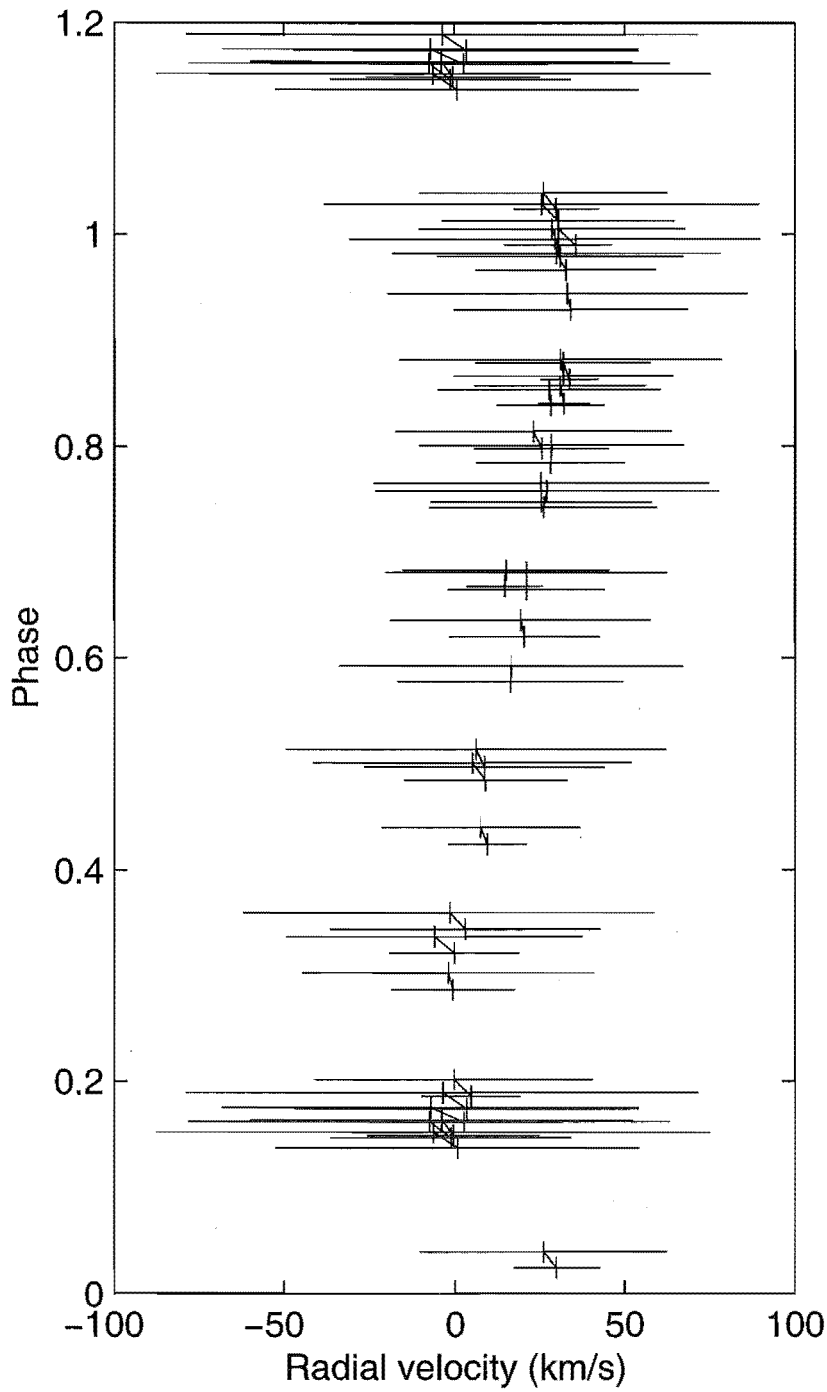

Figure 5.28: TX Del stacked Hα line bisectors, showing line bisector velocities at line depths 0.5 and 0.9, and the associated line width in velocity space for each depth.

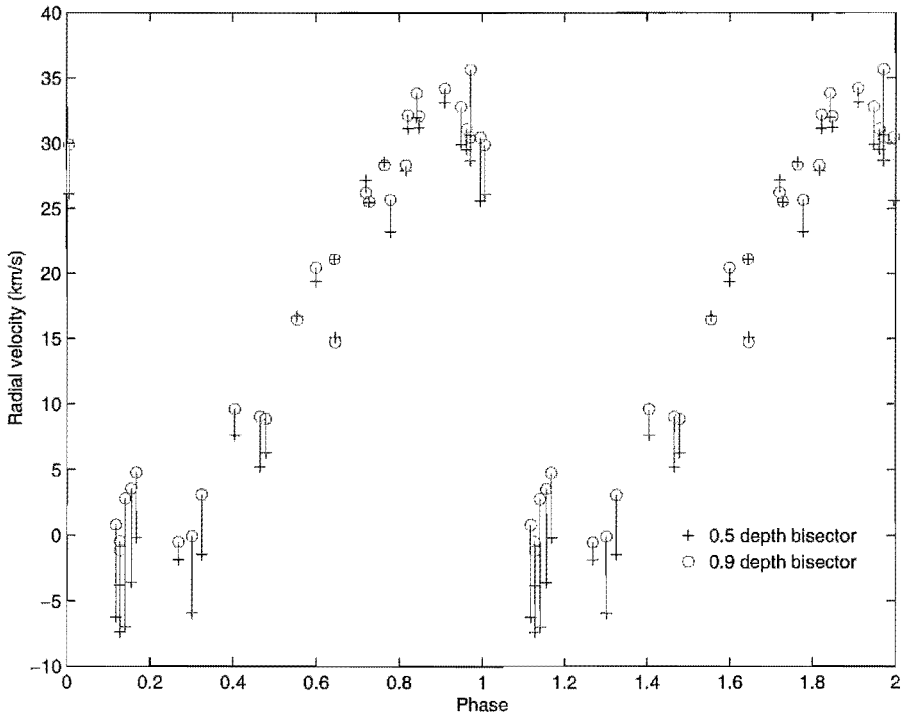

Figure 5.29: Radial velocity curves for TX Del, measured from the Hα line using line bisector velocities at line depths 0.5 and 0.9.

studied by Vinkó et al. (1998), when they looked at the maximum velocity difference between the 0.9 level bisector velocity for Hα and the metallic line velocity as derived by cross correlation (a value they found to agree with the 0.9 level bisector velocity for the stars) as a function of period, velocity amplitude and V light curve amplitude for a large selection of Type I and Type II Cepheids. They found both types of stars share similar regions of various parameter spaces.

This inability to note clear differences between the star types means it is relatively easy to characterize these stars in terms of their radial velocities. On average, they show the trends reported in Petterson (2002) in that those lines formed deeper in the atmosphere give lower amplitude velocity curves (Table 5.5), which peak earlier in the pulsation cycle.

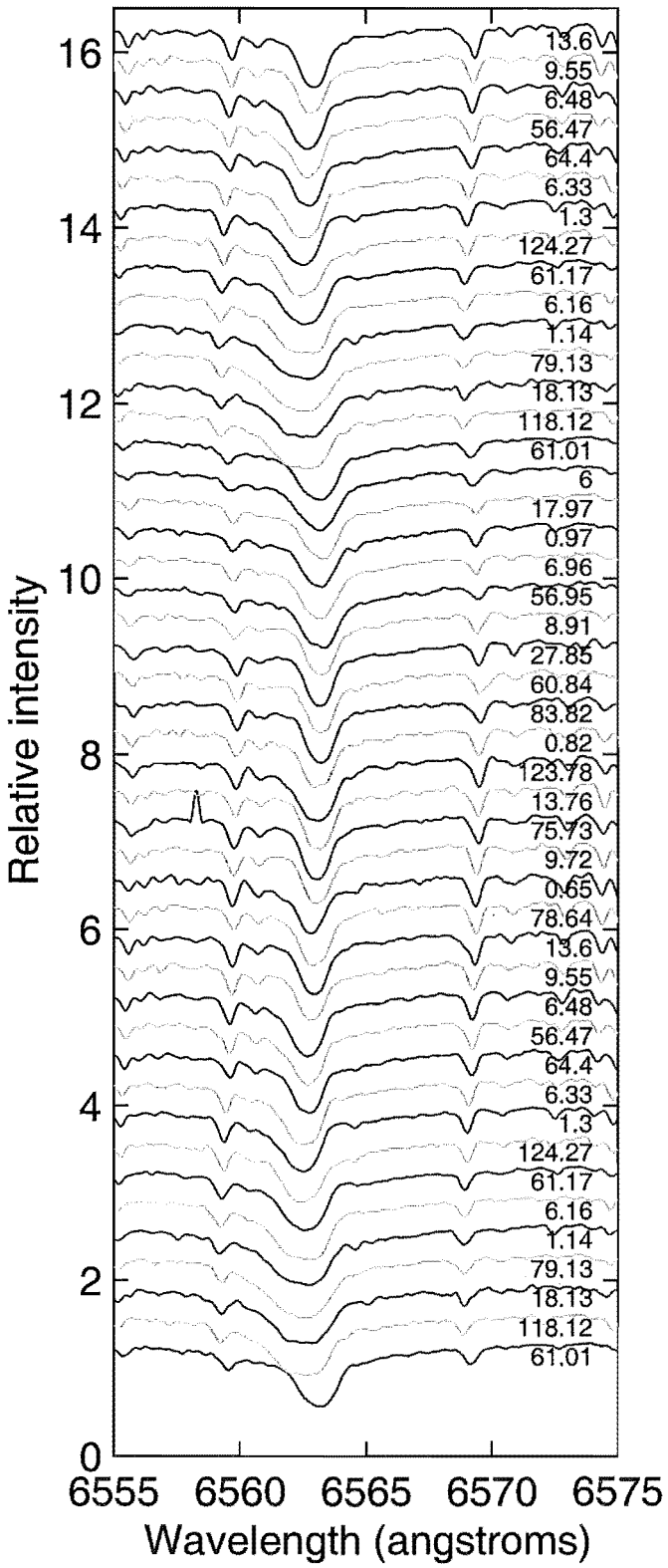

Figure 5.30: TX Del stacked Hα lines with orbital motion removed.

Table 5.5: BL Her star summary.

	VY Pyx	SW Tau	V381 Cen	TX Del
period (days)	1.2399	1.5836	5.0788	6.1634
epoch[a]	11310.396	11394.589	11310.913	11314.228
radii (in solar radii)[b]	—	8.3±0.8[c]	—	38.8[d]
		12.3±3[b]		47.6±5.4[c]
				43±7[b]
Hα velocity amplitude	30	55[e]	49	>40[e]
phase max	0.0	>0.9	0.95	0.9
phase min	0.4	0.15	0.05	<0.1
Ca II velocity amplitude	27	32	41	>40
phase max	0.9	>0.9	0.95	0.9
phase min	0.2	0.15	0.15	<0.1
Fe I velocity amplitude	17	35	35	>30
phase max	0.8	>0.9	0.9	0.8
phase min	0.2	0.1	0.1	<0.1
Na I velocity amplitude	11	—	—	—
phase max	0.85	—	—	—
phase min	0.2	—	—	—
	Type II	Type II	Type I	Type ?

[a]From acceleration phasing. Epoch = JD -2440000.
[b]Balog et al. (1997)
[c]Laney (1995)
[d]Balona (1977)
[e]From 0.9 level bisector.

Chapter 6

W Virginis Stars

As with the BL Herculis stars, the W Virginis stars are low-mass, radially-pulsating giants ($M \approx 0.6\,M_\odot$, $L \approx 100\,L_\odot$). However their periods range from where the BL Herculis periods stop (3–7 days, Wallerstein and Cox, 1984; Wallerstein, 2002) to somewhat longer than where the RV Tauri periods start (~20 days, Wallerstein, 2002). In reality there is a great deal of overlap in period. This overlap exists in light curve behaviour as well as period, as incipient RV Tauri-like alternations in the light curves can be observed in some W Vir stars of periods greater than 20 days in some globular clusters and in the LMC (Arp, 1955; Alcock et al., 1998). This inability to distinguish between the two types of stars can introduce problems when looking at period-luminosity relations, as the question of whether the fundamental period for the RV Tauri stars is that between successive minima or successive deep minima has not been resolved yet. Examining this issue with respect to the pulsations of the stars is one of the areas of investigation of this thesis.

6.1 Analysis techniques

In order to investigate the behaviour of the W Virginis stars, and to see how the stars fit in the context of the pulsation patterns of the BL Herculis stars, the spectral lines of a selection of W Vir stars were examined (Table 6.1). Spline curves were fitted to the phased Fe I line bisector average velocities, and from the derivatives of these spline curves, acceleration curves were derived. The minima of these were then used to define the zero point in phase. As with the BL Herculis stars, the same provisos exist on the acceleration curves (Section 5.1). Projection factors have been ignored, as they do not affect the position of minimum acceleration, and thus minimum radius.

As was seen for the BL Her stars, and will be shown in the course of this chapter, this makes the shock effects more easily compared from star to star. However, moving to the longer period stars, the pulsations become that much more irregular, and emission lines become far more prominent. This reaches an extreme for W Vir and ST Pup,

Table 6.1: Starting parameters for W Vir stars.

	κ Pav	AL Vir	W Vir	ST Pup
period (days)	9.0741	10.295	17.2768	18.6204
epoch[a]	11315.176	11309.037	11300.651	11388.125
Minimum V magnitude	4.0	9.2	9.6	9.6
Maximum V magnitude	4.8	10.0	10.8	10.8

[a]From photometric phasing. Epoch = JD - 2440000.

where velocities can no longer be derived from the Hα line due to a complicated emission structure. At this point, equivalent widths must be used instead. Before starting on such complications, we must first examine the shortest period star of this type: κ Pav.

6.2 κ Pav

As seen from the MJUO photometry and radial velocity curve (Figure 6.1), κ Pav exhibits quite a smooth velocity curve of a similar shape to V381 Cen. As such, one would expect that it would show very similar behaviour to V381 Cen, and for the most part it does. However, it does exhibit certain curiosities in behaviour.

Historically, κ Pav has been known to vary for a very long time. Roberts (1901) established it to be a variable star and Roberts (1911) used the radial velocity variations found by Wright (1904) to justify its examination as a spectroscopic binary. Once it was established that the velocity and light variations were due to pulsations of the star, rather than orbital motions, the next major examination of its radial velocity variations was by Stibbs (1955). A flurry of research appears in the late 1950's and 1960's (Rogers, 1957; Rogers and Bell, 1963; Bell and Rogers, 1953; Rogers and Bell, 1968), examining metal abundances and line profiles. κ Pav was found to be generally metal deficient ([Fe/H]=-0.42), and specifically deficient in s-process elements ([s/Fe]=-0.9$\pm$0.3). The period was also found to vary between 9.04 and 9.10 days between 1962 and 1966.

While these variations helped establish the star's classification as a Type II Cepheid and irregularities with respect to that category, of more interest for the pulsational study of the Type II Cepheids is the more recent work of Wallerstein et al. (1992) and Albrow and Cottrell (1994). The former establishes the use of the line bisector method in analyzing the line profiles and presents a comparison of the metallic line and Hα line velocities for a selection of Cepheids, including κ Pav. The latter, while focusing on modelling to examine projection factors and asymmetries, used comparison of observations with theory to examine how the line depth at which the line velocity measurement is made affects the derived velocity. It is the asymmetry features and differences in line behaviour between line species that are of interest here. However, before examining these in detail, phasing of the data with respect to the acceleration curve is required.

6.2.1 Spectroscopy

As can be seen in Figure 6.1, a spline curve has been fitted to the averaged Fe I line bisector velocities plotted as a function of phase, and from that, an acceleration curve has been derived. The acceleration curve itself is quite smooth, with a very clear minimum. In this, it is quite similar to V381 Cen (Figure 5.16), with a very smooth flat acceleration curve when the radial velocity is increasing, whereas VY Pyx and SW Tau (Figures 5.1 and 5.9) show greater variation.

This similarity in acceleration curve is also apparent in the averaged velocity curves for the various line species (Figure 6.2). Both the Fe I and Fe II velocities are quite smooth with a very close agreement in behaviour, as it was with V381 Cen (Figure 5.17). A peak radial velocity of 54 kms^{-1} is reached around phase 0.9, with minimum velocity occurring around phase 0.15 at 26 kms^{-1}. This results in an amplitude of 28 kms^{-1}, which is only slightly smaller than that for the same species in V381 Cen. The Ca II lines also behave smoothly, in a similar manner to V381 Cen, although there is slightly more scatter

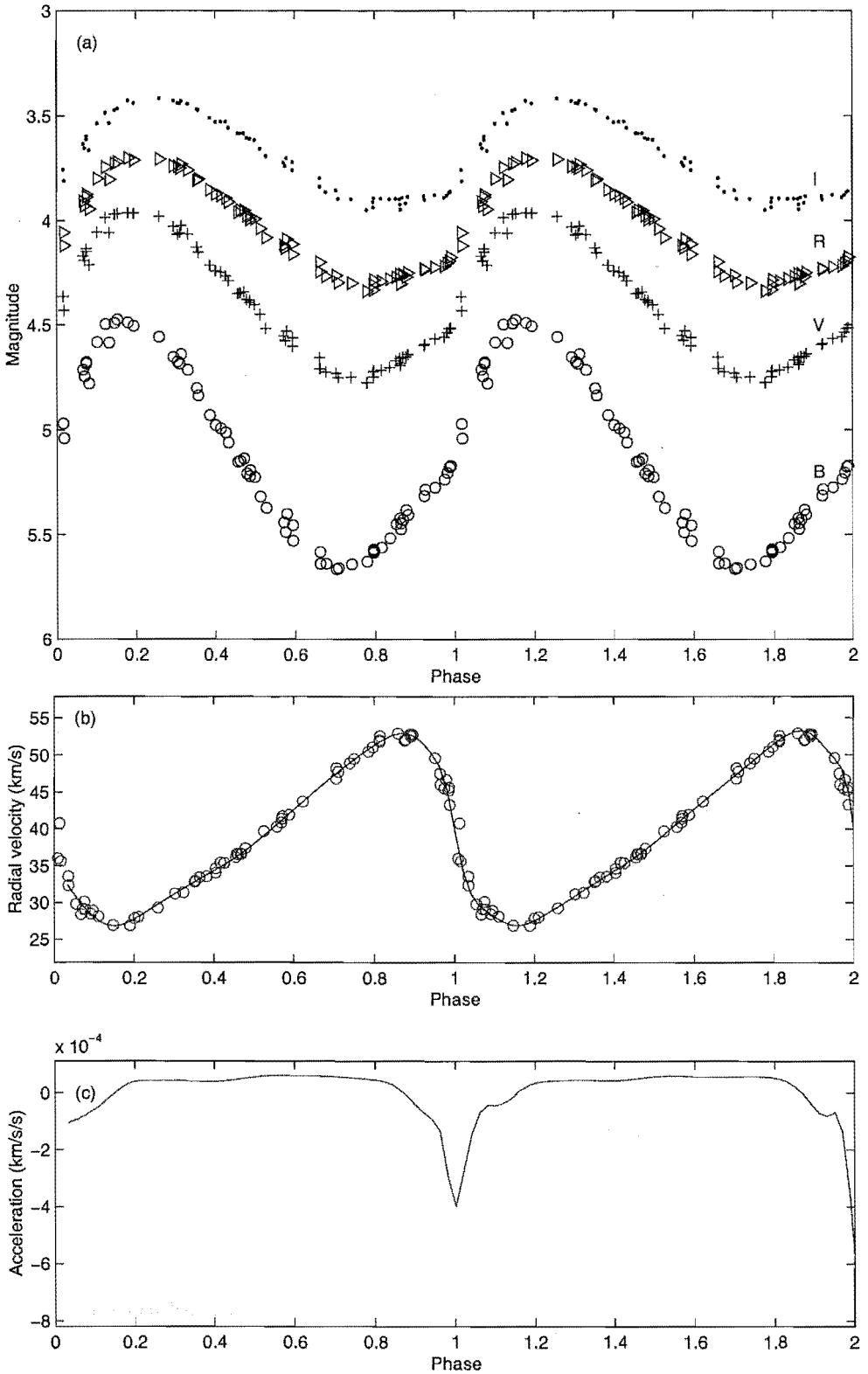

Figure 6.1: (a) *BVRI* magnitudes, (b) Fe I radial velocity and (c) acceleration curves for κ Pav.

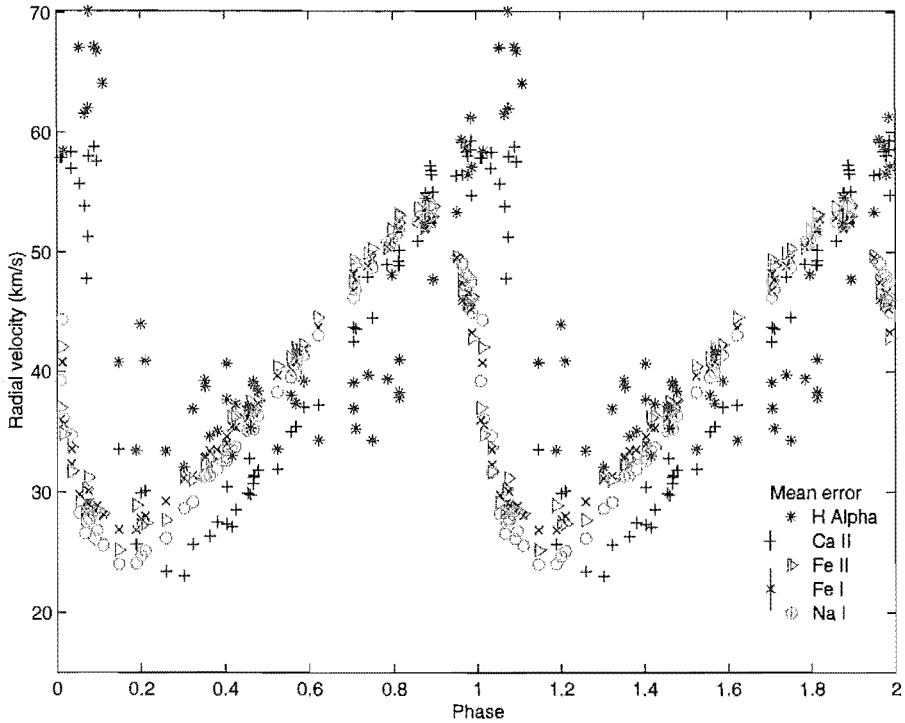

Figure 6.2: Radial velocity curves for κ Pav, measured from averaged Hα, Fe I, Fe II, Ca II and Na I lines.

around maximum velocity. A maximum velocity of 59 kms^{-1} is found in the region of phase 0.00–0.05. The minimum velocity is less ambiguous and occurs at a velocity of 23 kms^{-1} at phase 0.3. Thus it has a slightly higher amplitude of 36 kms^{-1}, which is still lower than the 41 kms^{-1} of V381 Cen's Ca II lines.

The behaviour of the Na I and Hα lines in κ Pav is different to that observed in V381 Cen. Whereas V381 Cen showed quite irregular Na I velocities overall due to an interstellar component to the Na D lines, the Na I velocities of κ Pav are very regular and behave similarly to the Fe velocities. As with the Fe lines, a peak velocity of $\sim$54 kms^{-1} occurs at phase $\sim$0.9. Minimum velocity for the Na I lines occurs at a phase of 0.15, similar to that of iron. However it is a slightly lower velocity at 24 kms^{-1}. This gives a larger velocity amplitude than for iron, of 30 kms^{-1}.

In contrast to the regularity displayed by Na I, the Hα velocities are greatly scattered. While a maximum velocity of 70 kms^{-1} is easily observed at phase 0.1, minimum velocity is scattered between phase 0.2–0.8, with the lowest velocity point occurring at 32 kms^{-1} at phase 0.3. This gives a velocity amplitude of 38 kms^{-1} which, while greater than that observed for the other species, is lower than what would have been expected if the velocity maximum behaviour was similar to the velocity minimum behaviour.

Astrophysically, this translates to less regular behaviour for the Hα line forming regions at maximum velocity falling inwards and for a while after, than for minimum velocity and for $\sim$0.3 of a pulsation cycle leading up to this point. This behaviour is in contrast to that evidenced by those regions of the star as traced by the Fe I, Fe II, Na I and to some extent Ca II line motions which are formed closer to the centre of the star, and are forced outward earlier in the pulsation cycle. These regions are regular at all phases of

the pulsational cycle and show smoothly varying curves. It should be noted that what differences there are between the various line behaviours of these four line species manifest themselves most noticeably at minimum velocity rather that maximum velocity. This is when the star is expanding out towards maximum radius. Unfortunately this does not explain the extreme irregularity of the Hα velocities as the duration of the irregularity is approximately 0.6 of a pulsation cycle, whereas the differences in the iron and sodium velocities while lasting approximately 0.8 cycles are more consistent and regular and far smaller in comparison to the Hα variations.

In order to understand the range of velocity behaviours and better understand the mechanisms behind them, the line profiles need to be examined, starting with what is in this case the most uncomplicated velocity curve: Na I.

Na I lines

As can be seen from Figure 6.3, the Na D lines vary quite smoothly. While they do not show distinct line splitting, they do appear to broaden markedly from phase 0.95 to 0.05 and is also more asymmetric at those phases.

Ca II lines

The two Ca II lines investigated show similar behaviour to the Na D lines in that they vary smoothly (Figure 6.4). In the case of the 8498 Å line (Figure 6.4a), line splitting occurs between phases 0.05 and 0.15, whereas it is more difficult to tell with the 8542 Å line (Figure 6.4b) as the line is intrinsically much broader. There appears to be a double component to the line at many of the phases between 0.8 and 0.3, although it is not distinct. This indistinct transition between line components as the majority of the line moves from being formed by the in-falling material at minimum radius, to being formed by the material that has been pushed out to maximum radius, may be why the maximum velocity measurements for the Ca II averaged velocities were so scattered. The lack of clear minimum to the 8542 Å line during the split phases may have reduced the mean velocity obtained as it would have reduced the mean velocity of the 8542 Å line. While this explains why the velocity measured is higher than expected, it does not explain the difference in line behaviour with respect to splitting for the Ca II lines examined here. Of the two Ca II lines, the 8542 Å line has the higher excitation potential (χ = 1.700 eV) and lower log(gf) value (-0.463), so is intrinsically stronger. Being stronger, it is formed over a greater range of optical depth of the star. The variations it shows may be due to variations in the regions of the star which the Ca II line at 8498 Å is not formed in. Certainly, VY Pyx showed variations in the Ca II 8542 Å line which were not evident in the 8498 Å line (Figures 5.6 and 5.7.) However these were not found to correlate with the pulsations of the star (Table 5.2).

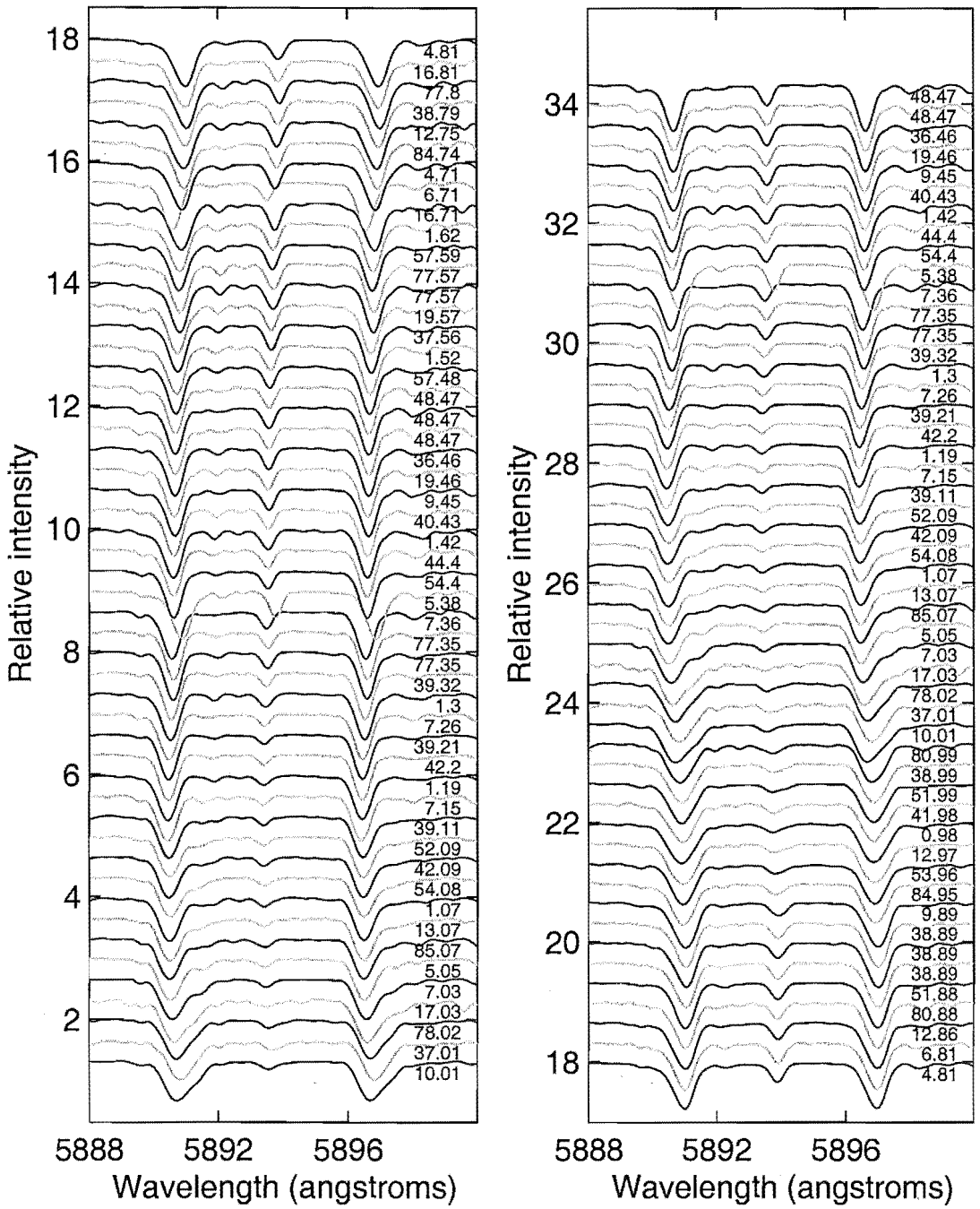

(a) $\phi = 0.00$–0.81.

(b) $\phi = 0.81$–0.47.

Figure 6.3: κ Pav stacked Na D lines.

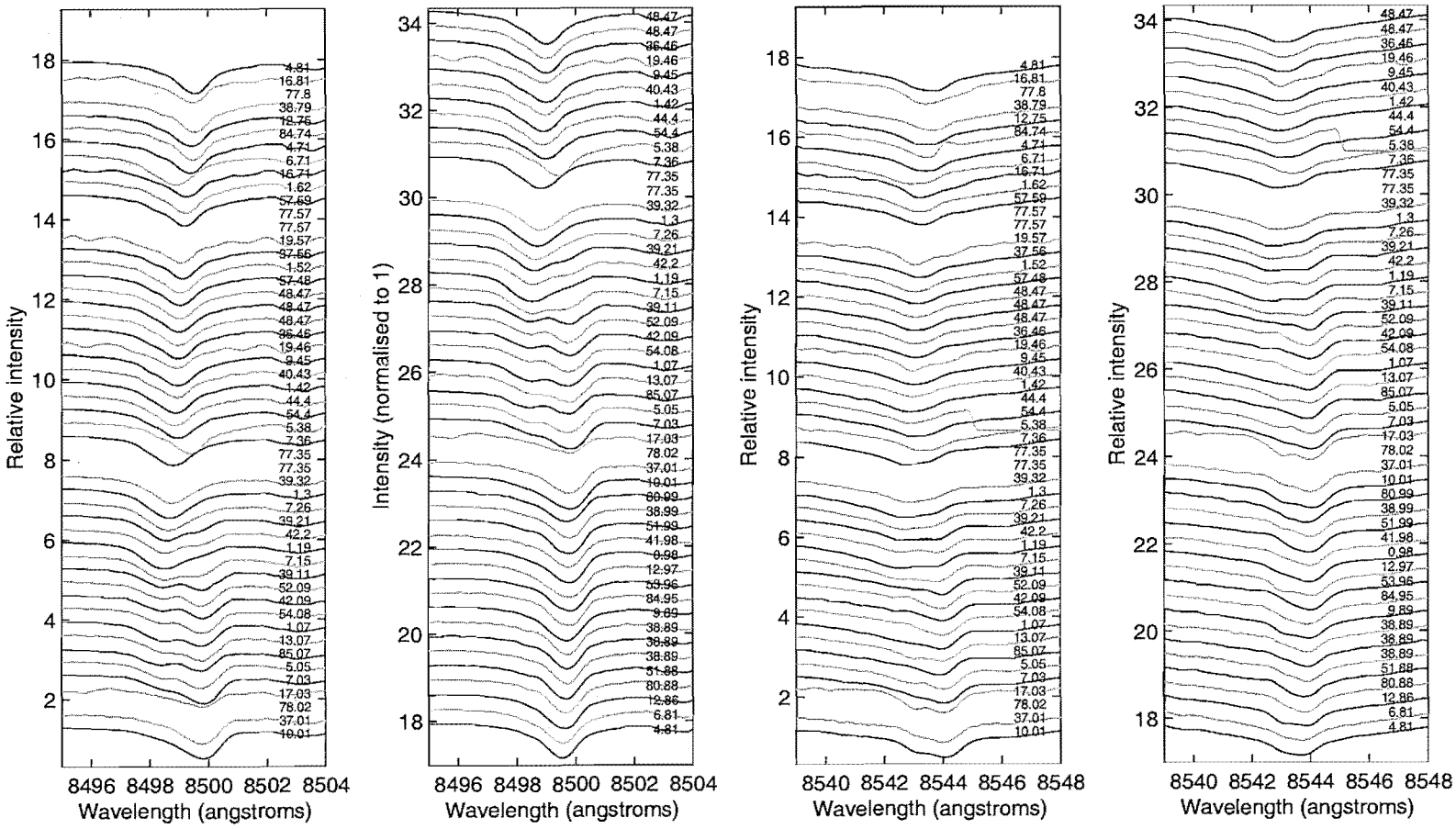

(a) 8498 Å. ϕ=0.00–0.81. (b) 8498 Å. ϕ=0.81–0.47. (c) 8542 Å. ϕ=0.00–0.81. (d) 8542 Å. ϕ=0.81–0.47.

Figure 6.4: κ Pav stacked Ca II lines. Gaps indicate observations for which wavelength coverage does not extend to 8000 Å due to filter problems (Section 2.2.3).

Hα line

The Hα line behaviour is more complicated than the Ca II line behaviour (Figure 6.2). A view of the Hα line stacked in order of phase (Figure 6.5) does not clarify the issue of why the velocities are so scattered around minimum velocity nor why this scatter is maintained for such a large percentage of the pulsation cycle. The Hα line maintains a relatively constant red-ward wing profile while the blue-ward side varies markedly, with multiple components from phases 0.85 to approximately 0.10 and extreme broadening of the blue-ward wing around phase 0.15–0.3. This is not dependent on cycle as the pulsation cycles range from 1 to 42, with very similar broad blue-ward wings in all cycles.

In order to simplify what we are looking at, the line widths and line bisector velocities at line depths of 0.9 and 0.5 (Figure 6.6) were examined. This technique is as introduced in Section 3.4.1 and first used in Section 5.1.1. From this, it is clear that the Hα line is far less regular in κ Pav than in the preceding BL Her stars and, for that matter, than the other lines examined in κ Pav. From the line connecting the 0.9 and 0.5 level velocities to map out a vector map of the direction of line asymmetry, the Hα line is asymmetric towards the blue for most phases and is asymmetric towards the red from approximately phases 0.8 to 0.0. The line widths do not vary in a smooth manner, as is observed in V381 Cen (Figure 5.18) and to a lesser extent in TX Del (Figure 5.28). In order to see if the blue-ward asymmetry is seasonal, the velocities of Figure 6.7 have been plotted up into three separate observing seasons covering cycles 0–20, 36–57, and 77–85. It is clear from this that the scatter in velocities and near constant blue-ward asymmetry is present in all of these seasons, so any variations must be cycle to cycle rather than season to season.

While this Hα variation has been found by other authors for κ Pav, it appears to be more extreme with these observations. The clearest comparison is with Wallerstein et al. (1992) who show the bisector velocities for Hα at the 0.9 and 0.5 levels (Figure 13, Wallerstein et al. (1992)). These were obtained using the same telescope, with the same spectrograph[1] and the same line analysis technique for admittedly less observations (29 compared to 67) over a 3 year time period. They found that maximum line asymmetry occurred between phases 0.8 and 1.0. Their phase 0.8 occurs approximately 0.2 of a pulsation cycle after their maximum velocity, which places the maximum asymmetry at 0.2–0.4 using the new minimum acceleration phasing technique. They also observed an asymmetry minimum from phases 0.3–0.8, which corresponds to phases 0.5–0.2 from the acceleration phasing. No such phase asymmetry correspondence is observable with the more recent observations presented here. While Wallerstein et al. (1992) did comment on the erratic variability of the Hα line, the variations they observed were not of the magnitude presented here[2].

The line asymmetry maximum as observed between phases 0.2 and 0.4 in the Wallerstein et al. (1992) velocities is consistent with a shock wave splitting and broadening the Hα line. The shock splits the line forming region into areas where the material is still falling inwards while below that, and behind the shock wave, the remainder of the material in the region is now moving outwards. This follows the pattern observed in the BL Herculis stars, especially TX Del (Figure 5.29), where maximum Hα line asymmetry

[1] although different CCD detector

[2] They raised the possibility that κ Pav is a spectroscopic binary, but found their velocities to be inconclusive with respect to that.

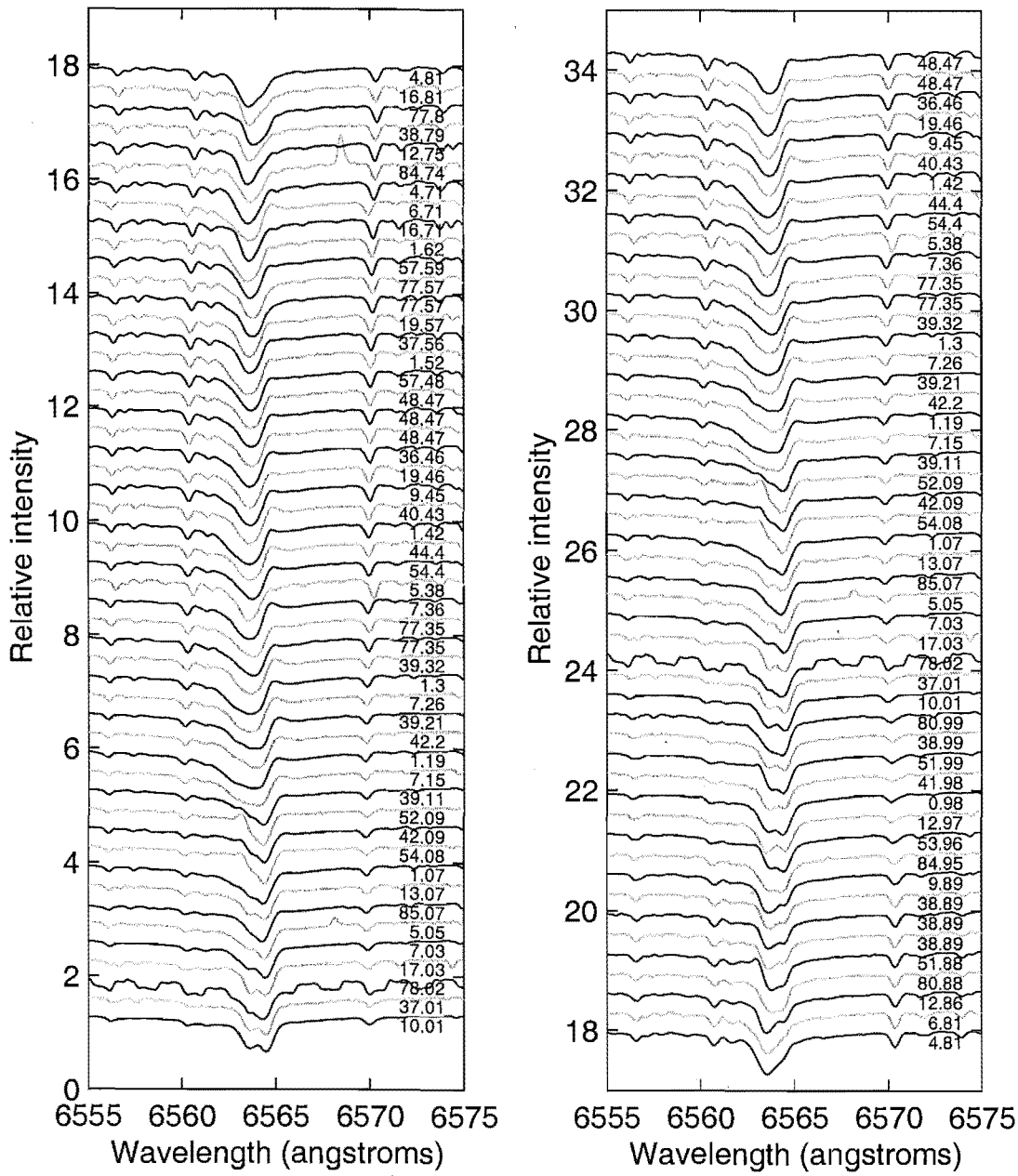

(a) ϕ=0.00–0.81 (b) ϕ=0.81–0.47

Figure 6.5: κ Pav stacked Hα lines.

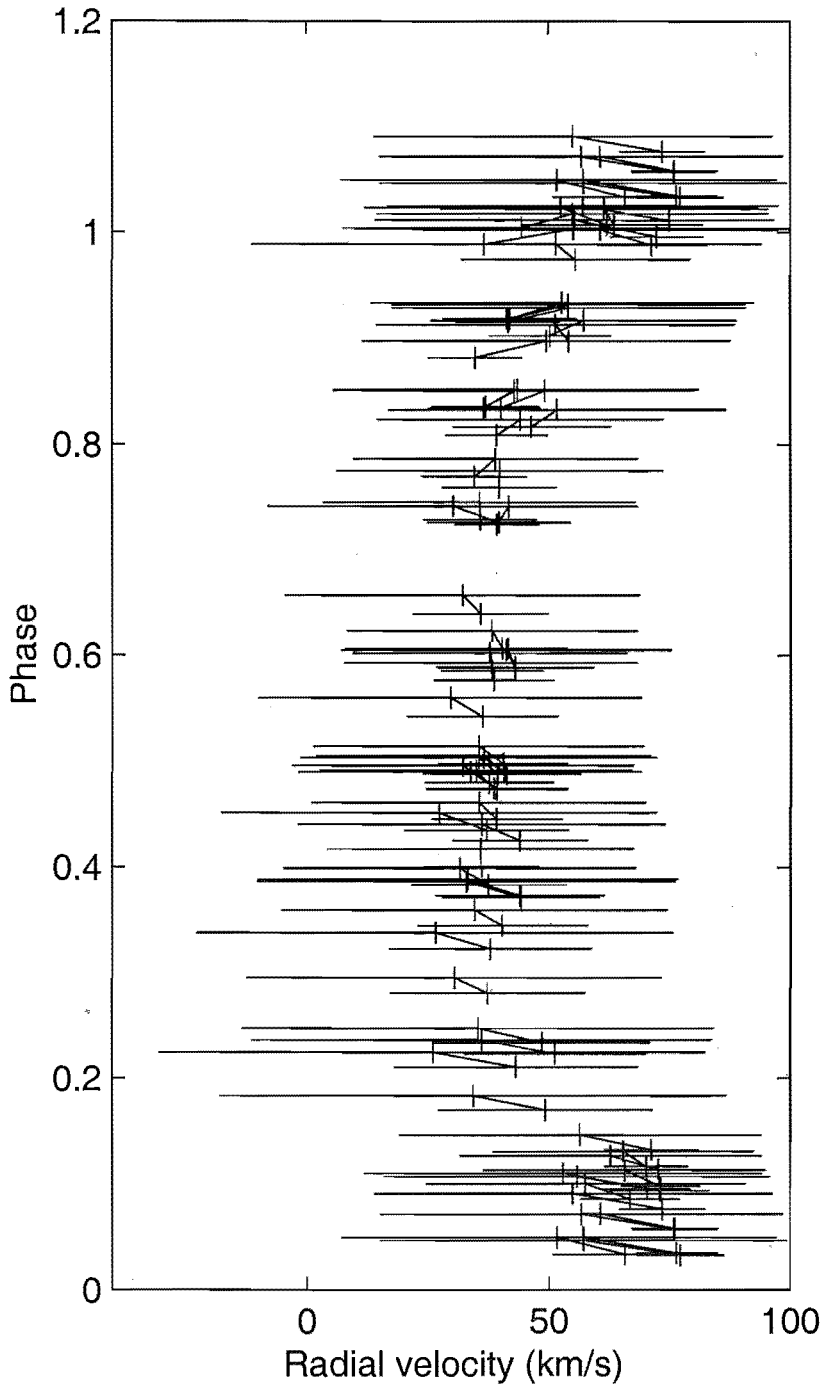

Figure 6.6: κ Pav phased Hα line bisector velocities for line depths 0.5 and 0.9, showing line widths (in velocity space) at these depths. Lines connect the 0.5 and 0.9 level bisector velocities for each observation.

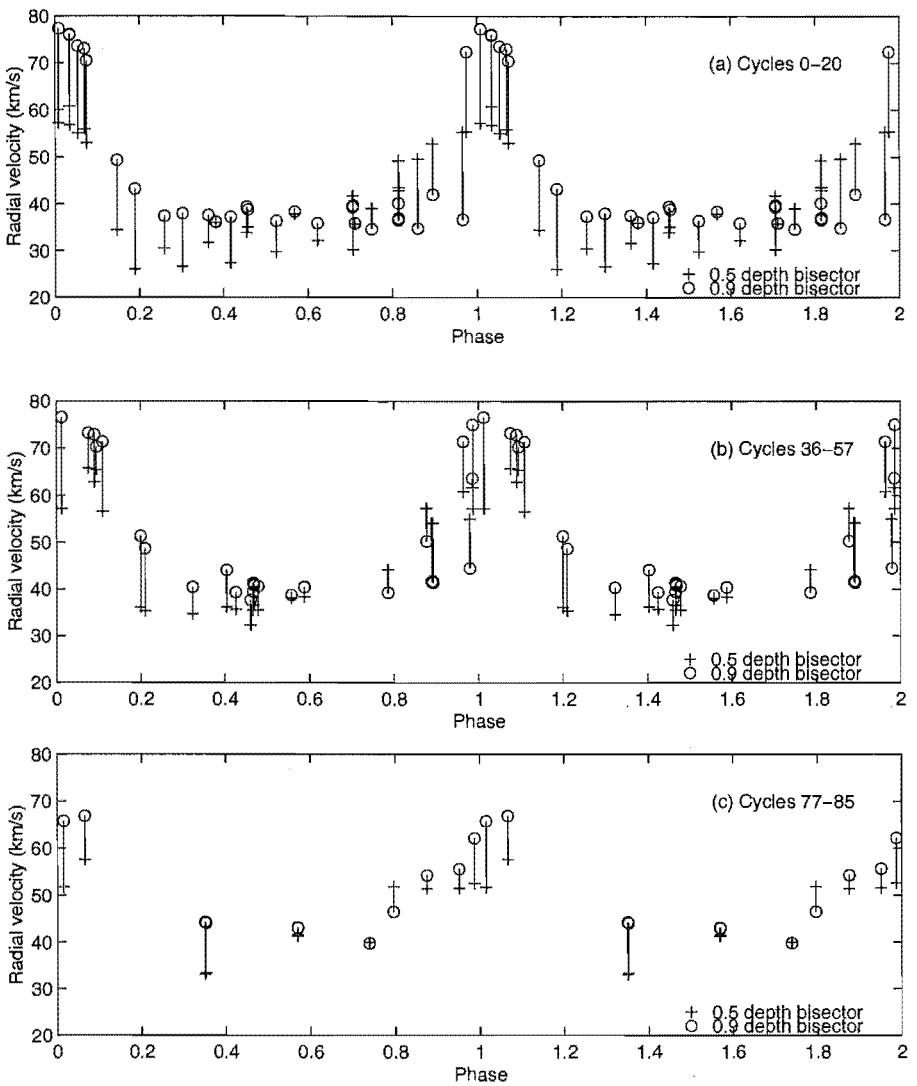

Figure 6.7: Radial velocity curves of κ Pav, measured from the Hα line using the line bisector velocities at line depths 0.5 and 0.9. Panels are divided into observing seasons to examine long-term trends.

occurred around, or just after minimum velocity. This is when the average velocity direction of the majority of the material in the line forming region is now outwards towards the edge of the star, but there is still enough of the material in the region falling inwards to absorb a significant enough amount of light from the star to make the line broader and asymmetric. The phase delay in when the shock asymmetry is observed is consistent with a continuation of the pattern observed in the BL Her stars: the Hα line forming regions encounter the shock (which reverses the average motion in them) after the inner layers of the photosphere where the metallic lines are formed.

Unfortunately when this concept is extended to examine which is the dominant average motion in the line forming region, which is inferred from seeing which line component associated with a particular average motion dominates the line and is deepest, problems are encountered. Of the BL Her stars studied, SW Tau illustrates the classical expected pattern most clearly in its Hα profile variations (Figures 5.11, 5.12, and 5.13 and Section 5.2.1). κ Pav, and to a lesser extent TX Del, do not show this. In both the Wallerstein et al. (1992) data and the data presented here for κ Pav, the 0.9 level bisector velocity tracks the red-ward component, except for briefly around phase 0.8 by the acceleration minimum phasing. This would indicate that the dominant motion of the material in the Hα line forming region is towards the centre of the star (falling inwards) and for the majority of the pulsational cycle there is always a substantive amount of material moving towards the star. Also in the data presented here, the lines are asymmetric well before the shock is expected to enter the line-forming region.

This time before the expected main shock is of interest as it is where the atypical asymmetry behaviour is found. If we examine the Hα lines between phases 0.81 and 0.08 (Figure 6.5 and 6.7), we can see this is where the main difference to the Wallerstein et al. (1992) velocities occurs. At these phases, from the pattern seen in SW Tau, the blue-ward component would be observed to be moving towards the red as the material in the line forming region accelerates inwards and falls back in towards the star. While the blue-ward component does appear to do this, a red-ward component develops and grows in strength such that it becomes the dominant motion of the line. This is seen in the way the line asymmetry shifts towards the red (the 0.9 level bisector velocity is lower than the 0.5 level bisector velocity) until around phase 0.95, when the red component becomes dominant (the 0.9 level bisector velocity is much higher than the 0.5 level bisector velocity). This indicates that, at these pulsational phases, the average velocity of the material in the line-forming region can be divided into two main components with one falling into the star far faster than the other. The distinct velocity difference may indicate another shock briefly propagating back into the star.

While this may go some way to explaining the currently observed κ Pav behaviour, it is unclear why the Hα velocities have behaved so differently over the two time periods examined, especially when the metallic lines behave in much the same way with the same amplitudes and velocities. This would appear to indicate that the inner layers of the photosphere are still behaving the same, but something may be perturbing the outer layers that was not there previously. As stated earlier, the possibility of κ Pav being a spectroscopic binary has been raised (Wallerstein et al., 1992), but the results were inconclusive. A peak Fe I velocity of 54 kms^{-1} was observed which is similar to those in the 50–55 kms^{-1} range historically found (Wallerstein et al., 1992) so orbital velocity variations may be possible on that scale. However, the previous authors did not specify which lines and species were used and, as seen from the results presented here, it is possible

to get such a scatter from examining different line species, let alone observations from different time periods. Thus the option of orbital motions or orbital perturbations of the outer layers causing shock waves in the star is merely speculation at present.

What can be stated is that, for the most part, κ Pav behaves regularly in a manner comparable to the stars examined earlier in the inner absorbing layers of the stellar photosphere, as indicated by similar radial velocity curves for the Fe I, Fe II, Ca II and Na I line averages. However the Hα line behaviour (both historically and especially currently) is radically different and it is unclear why.

6.3 AL Vir

AL Vir behaves very similarly to κ Pav, although it does not show the same extremes of Hα behaviour. Both stars share similar shaped light curves and similar line behaviours. As it is somewhat fainter than κ Pav, varying from 9.2-10.0 magnitudes in V, AL Vir has been studied far less. The earliest radial velocity measurements appear to date from Joy (1937), with the only other radial velocity measurements in Barnes et al. (1988). Balog et al. (1997) put these velocities to use in determining Baade-Wesselink radii for AL Vir, but made no new measurements. Hence the addition of the velocities presented here is timely.

6.3.1 Spectroscopy

As with the previous stars, the Fe I line velocity averages have been plotted as a function of phase and a spline curve fitted. From this curve, an acceleration curve was then derived and the data rephased based on the position of the acceleration minimum. The Fe I line velocity and acceleration curves are shown in Figure 6.8. Possessing a larger amplitude Fe I curve and a smaller amplitude acceleration curve, the AL Vir acceleration curve is of a very similar shape to that of VY Pyx (Figure 5.1).

When the velocity curves for a wider selection of line species are examined (Figure 6.9), the similarity to VY Pyx holds for the Fe I velocity curve and for the Fe II curve, but not for the other velocity curves. In general, all the curves appear more scattered in velocity than for the equivalent species in VY Pyx (Figure 5.2), and for the equivalent species of κ Pav (Figure 6.2), indicating the star is more variable on a cycle to cycle basis.

Examining the least complicated velocity curve first, the Fe I lines reach their peak velocity of 33 kms^{-1} at phase 0.85. Fe II reaches a similar maximum velocity of 33 kms^{-1} at approximately the same phase of 0.85, although the velocity curve maximum is less clearly defined. This is also the case for the velocity minima, as minimum velocity occurs around the same phase of approximately 0.2 for both the iron species, but the minimum velocity of Fe II (4 kms^{-1}) is lower than the 8 kms^{-1} of Fe I. The velocities around the minimum vary from cycle to cycle for Fe II, so an upper limit may be as high as 7 kms^{-1} during certain pulsational cycles. This gives an amplitude of 25 kms^{-1} for Fe I and an upper limit on the amplitude of Fe II $\sim$29 kms^{-1}.

The Na I velocities agree quite closely with the iron velocities between phases 0.4 and 0.8. They share a maximum velocity value of 33 kms^{-1}, although this is reached by the Na I at phase 0.9, which is slightly later than the maxima for the Fe I and Fe II line velocity curves. Again, it is around velocity minimum where they differ quite markedly, with the Na I minimum velocity occurring just before phase 0.2, at a velocity of -2 kms^{-1},

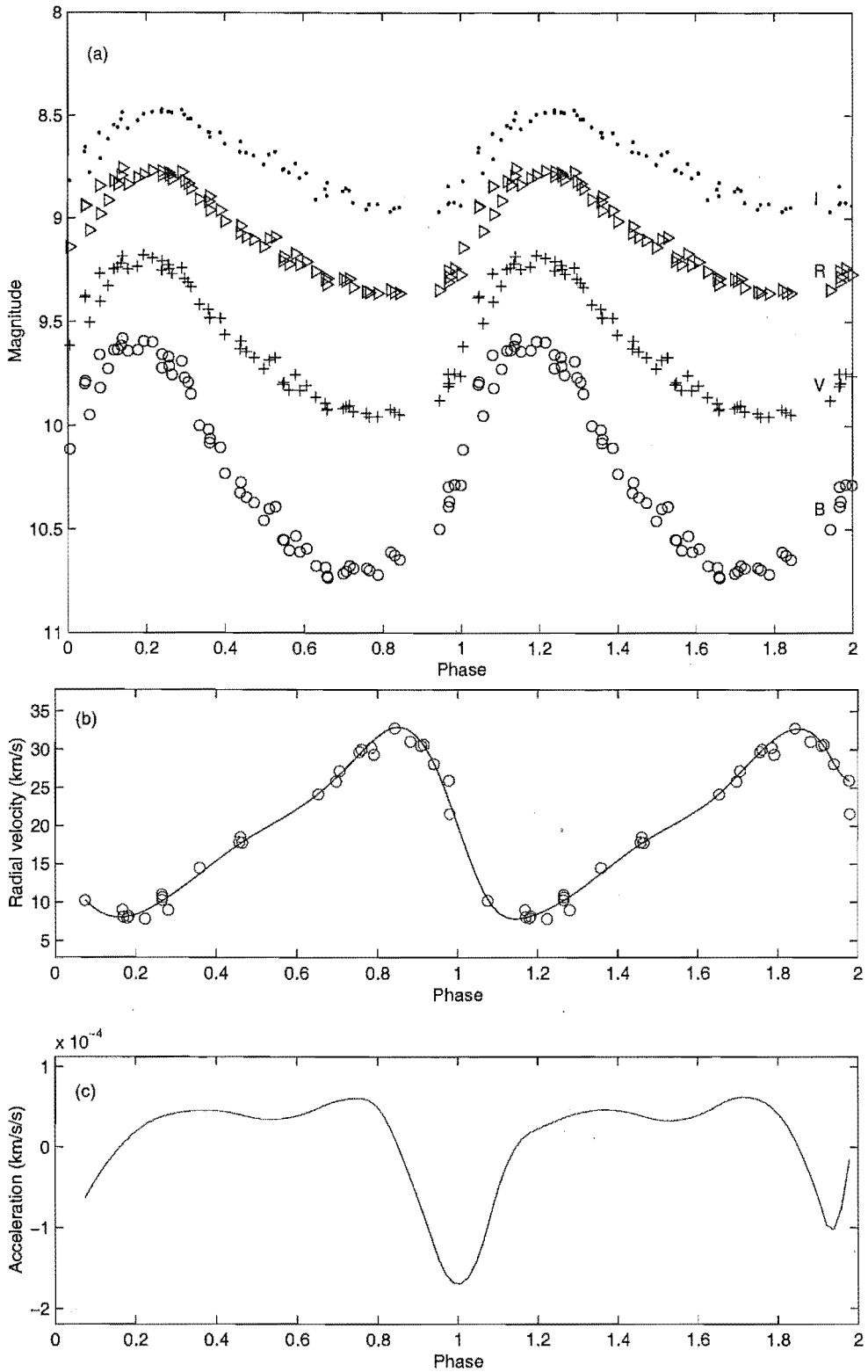

Figure 6.8: (a) *BVRI* magnitudes, (b) Fe I radial velocity and (c) acceleration curves for AL Vir.

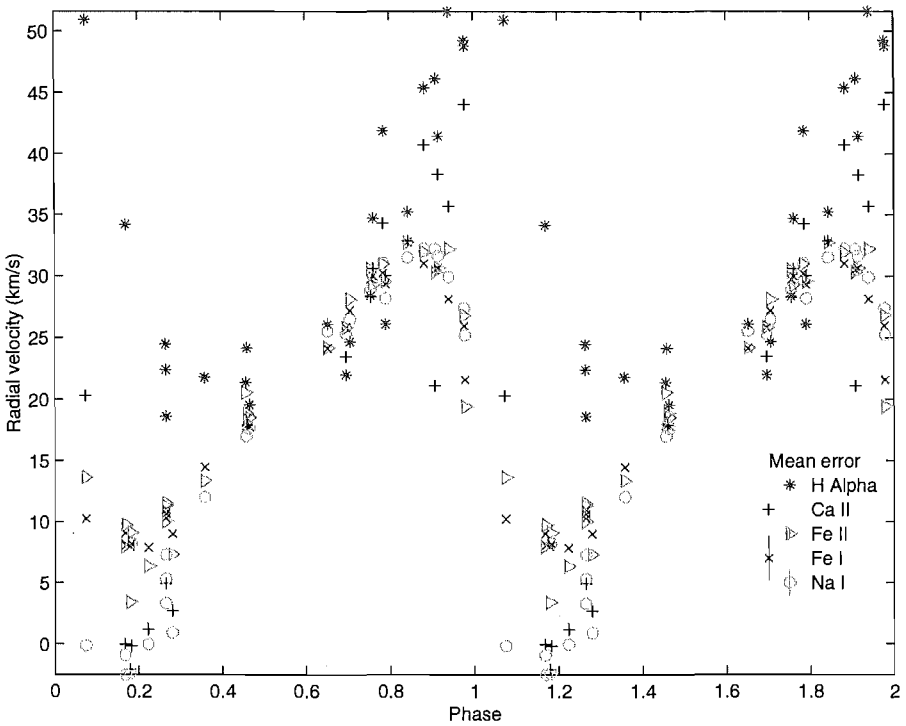

Figure 6.9: Radial velocity curves for AL Vir, measured from averaged Hα, Fe I , Fe II, Ca II and Na I lines.

well below the 8 kms^{-1} of the Fe I line velocity curve. This gives an amplitude of 35 kms^{-1} which is well above the amplitude of 25 kms^{-1} for Fe I.

As with κ Pav, the Ca II velocities are more regular than the Hα velocities. Ca II reaches a clear velocity minimum of approximately -2 kms^{-1} just before phase 0.2, although the position of velocity maximum is more ambiguous due to cycle-to-cycle variations in the velocities. Using the maximum velocity data point, the maximum occurs at 44 kms^{-1} at phase 0.95, while using the cluster of the next three highest velocity points, it occurs at 41 kms^{-1} a little after phase 0.85. Using the maximum velocity point to trace an upper limit, the upper limit of the amplitude of the velocity curve is 46 kms^{-1}, well above the Fe I and Na I amplitudes. Using the cluster of points, the lower limit to the amplitude is 43 kms^{-1}, which is also above those of the iron lines.

Based on the trends observed in the BL Her stars, it would be expected that the Hα velocities would produce a much higher amplitude velocity curve, which is shifted in phase such that it lags behind the metallic curves. The theory behind this is that the Hα line forming region is further out in the stellar photosphere. This means that the shock wave which propagates through the star and reverses the dominant velocity direction in the region, hits the middle of the region after moving through the middles of the metallic line forming regions.

As with κ Pav, this phase lag and heightened amplitude does occur at maximum velocity, where a velocity of 51 kms^{-1} is achieved a little before phase 0.1. However, like κ Pav, minimum velocity is much less clearly defined and is at a higher velocity than would be expected if the Hα line velocities behaved like those observed in VY Pyx (Figure 5.2), SW Tau (Figure 5.10) and V381 Cen (Figure 5.17). The minimum velocity

data point occurs at 19 kms^{-1} at a phase of 0.25, and the velocities stay around 20-25 kms^{-1} from phases 0.25 to 0.7. This is similar in shape to the κ Pav velocities which also stayed within a small range between phases 0.25 and 0.75 (Figure 6.2) and, to a lesser extent, TX Del (Figure 5.25). However, before interpreting this pulsationally, we need to examine the lines themselves.

Hα line

When the AL Vir Hα lines are stacked in order of phase (Figure 6.10), the resemblance is less to κ Pav (Figure 6.5), and more to SW Tau (Figure 5.13) with respect to the distinct line components observed. The Hα line in AL Vir is clearly split between phases 0.0 and 0.35, in a similar fashion to the SW Tau splitting observed between phases 0.0 and 0.3. However the relative depths of the line components is closer to that observed in κ Pav, in that the blue-ward component is never observed to be deeper than the red-ward component when it is present. In comparison to SW Tau, the blue-ward component takes a larger percentage of the pulsation cycle to become dominant. This can be seen in the way the double components of the Hα line are apparent around phase 0.08 in both stars, but have disappeared by phase 0.33 in SW Tau and phase 0.46 in AL Vir. This would appear to indicate that the shock wave is traveling though the Hα line forming region for longer in AL Vir, than for SW Tau. Physically, as AL Vir has a much longer period, and is therefore larger in radius, this is not surprising. However for the percentage of the pulsation cycle the shock is observable in the Hα line forming region to change, the relative sizes of the line forming regions or the relative speed/strength of the shock must change.

It may be possible that it is the shock which has changed in AL Vir as there is some possible emission observed in the blue wings of the Hα line in cycles 32, 36, 38,and 67, between phases 0.78 and 0.98. This would indicate that the shock (in certain pulsations) is becoming strong enough such that hydrogen is ionized by the shock and recombines in the shock wake to create the emission line. Certainly the emission appears to the blue, indicating the material which is de-exciting is moving out from the star's center. While such emission might be considered to be present in one of the κ Pav Hα spectra (spectrum 52.09), it is not observed in the remainder indicating either a weaker shock, or material in front of the shock/emission region of the appropriate material and velocity to absorb any light from it. The blue-ward component of the κ Pav Hα line may be strong enough to do that but the evidence here is inconclusive either way.

If we examine the Hα line velocities in more detail, by examining the 0.9 and 0.5 line level bisector velocities, the agreement with the historical κ Pav Hα velocities becomes apparent. When these bisector velocities are plotted as a function of phase (Figure 6.11), they show a marked similarity to the previously published plot of bisector velocities for κ Pav (Wallerstein et al., 1992, Figure 13,). Maximum line asymmetry occurs approximately 0.2 of a pulsational cycle after velocity maximum, with minimum asymmetry occurring for 0.6 of a pulsation cycle before this. This is in contrast to the Hα 0.5 and 0.9 level line bisector velocities presented here (Figure 6.7) where, as stated in Section 6.2.1, the same correlation of line asymmetry with phase is not observed and the lines are shock broadened to the red.

This marked difference is also observable when the same bisector velocities at depths 0.5 and 0.9 are plotted as a function of phase, while including the line widths (in velocity

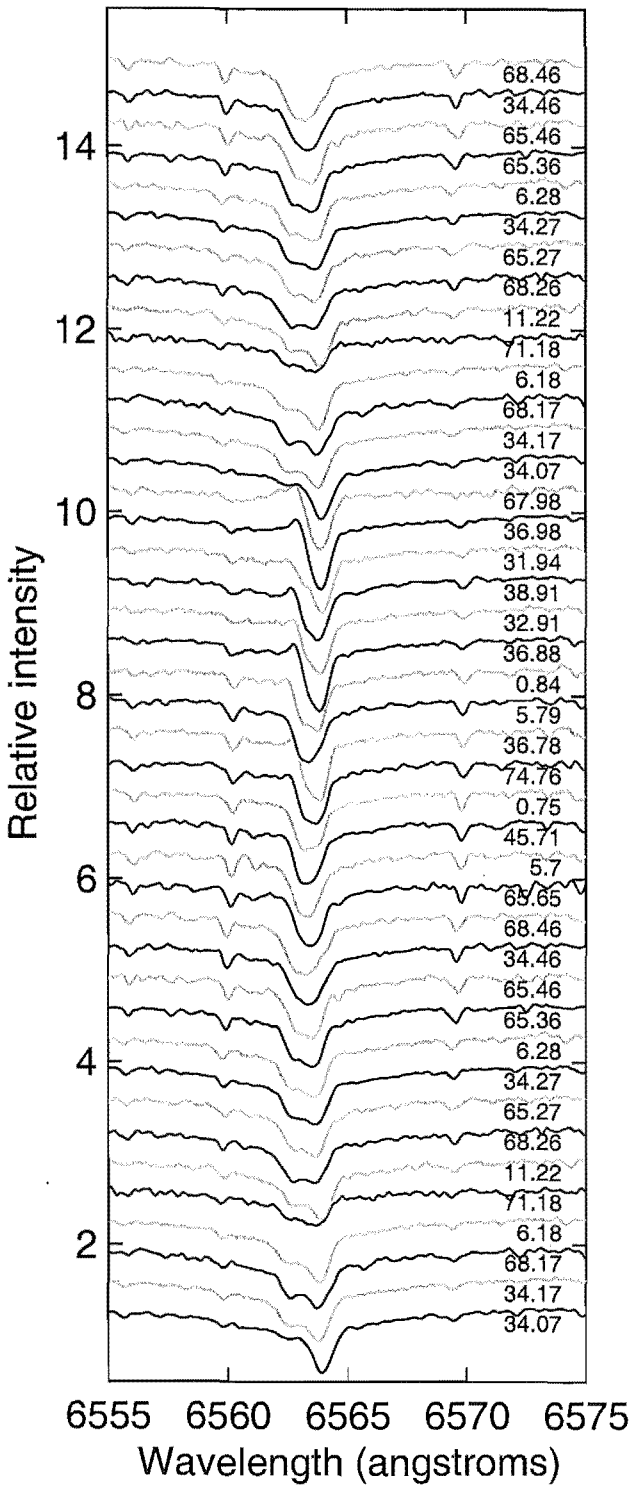

Figure 6.10: AL Vir stacked Hα lines.

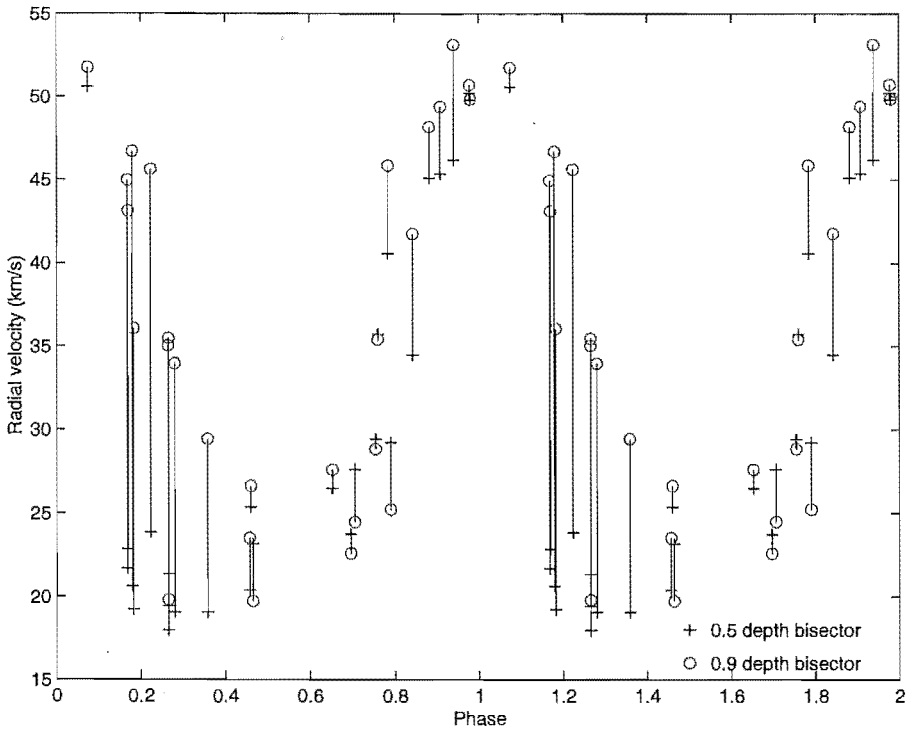

Figure 6.11: Radial velocity curves for AL Vir, measured from the Hα line using line bisector velocities at line depths 0.5 and 0.9.

space) at the specified line depths (Figure 6.12). A much smoother variation of line width at the 0.5 line depth is observed. This is far more comparable to that observed for V381 Cen (Figure 5.18) and SW Tau (Figure 5.11). The AL Vir Hα line widths share the smoothness of the V381 Cen variations with a comparable degree of narrowing down in width as observed in SW Tau. All of these variations were in clear contrast to the line width variability observed in the Hα lines in κ Pav (Figure 6.6). This is quite curious in that the metallic lines observed in AL Vir (Fe I and Fe II, Figure 6.9) are far less regular in their variation (showing a greater scatter from a mean velocity curve) than the same lines in κ Pav, whereas the Hα lines are far more regular in their variation. This may indicate that AL Vir's inner layers exhibit more cycle to cycle variations than its outer layers. This is unexpected as the accepted correlation appears to be that the longer the period of the star, the larger and less compact the star is, and the more likely perturbations occur in the outer layers of the star as they pulsate, leading to more cycle to cycle variations. As the period difference between these stars is so small[3], and estimates of the stellar radii so varying (Table 6.3), there is too little information to conclude anything at present.

Na I lines

In comparison to the discussion over Hα, for all its strange behaviour around minimum velocity (Figure 6.9), the Na I line velocity behaviour is more easily understood. Examining the Na D lines stacked in order of phase (Figure 6.13), a relatively stationary

[3] κ Pav: P=9.0741 days, AL Vir: P=10.295 days (Table 6.1)

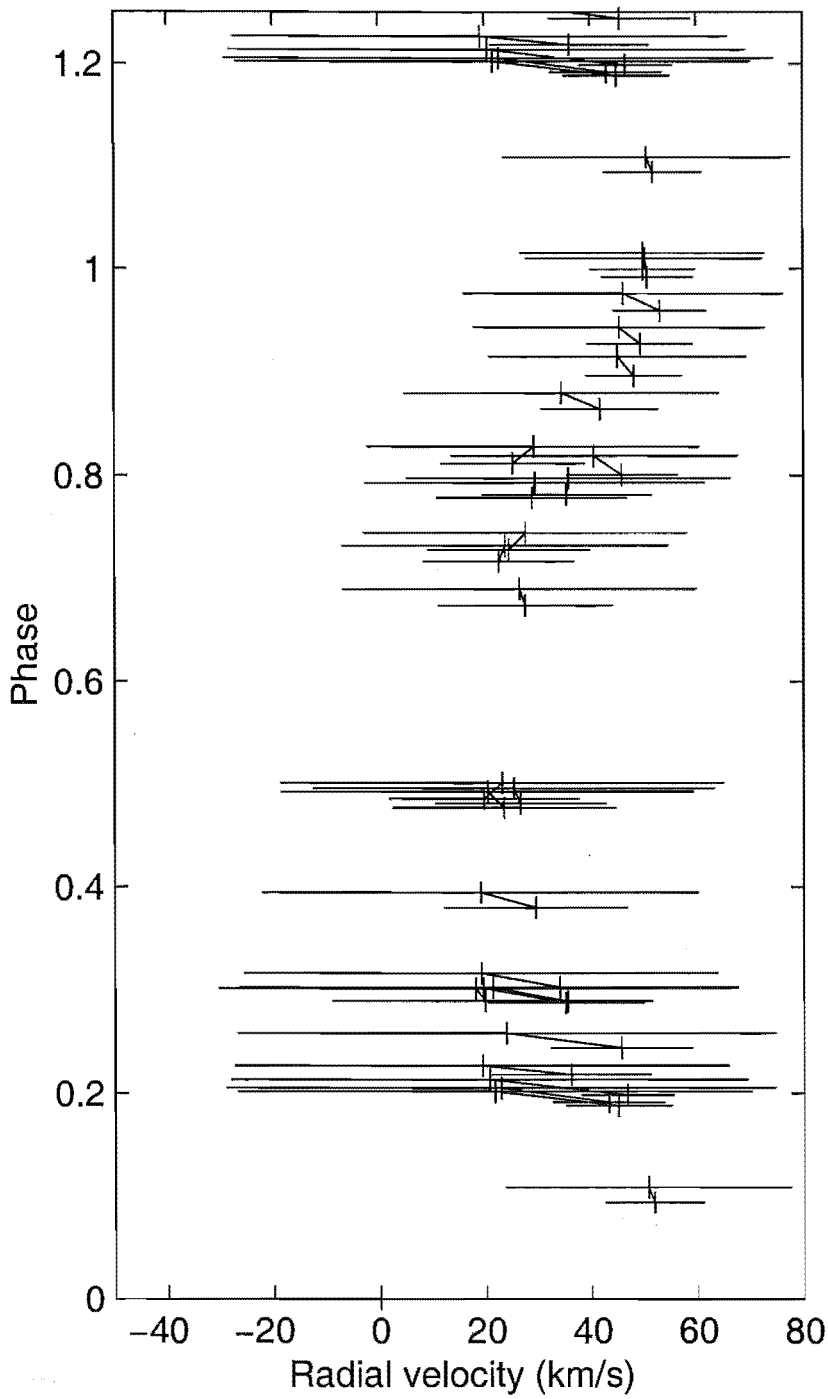

Figure 6.12: AL Vir phased Hα line bisector velocities for line depths 0.5 and 0.9, showing line widths (in velocity space) at these depths. Lines connect the 0.5 and 0.9 level bisector velocities for each observation.

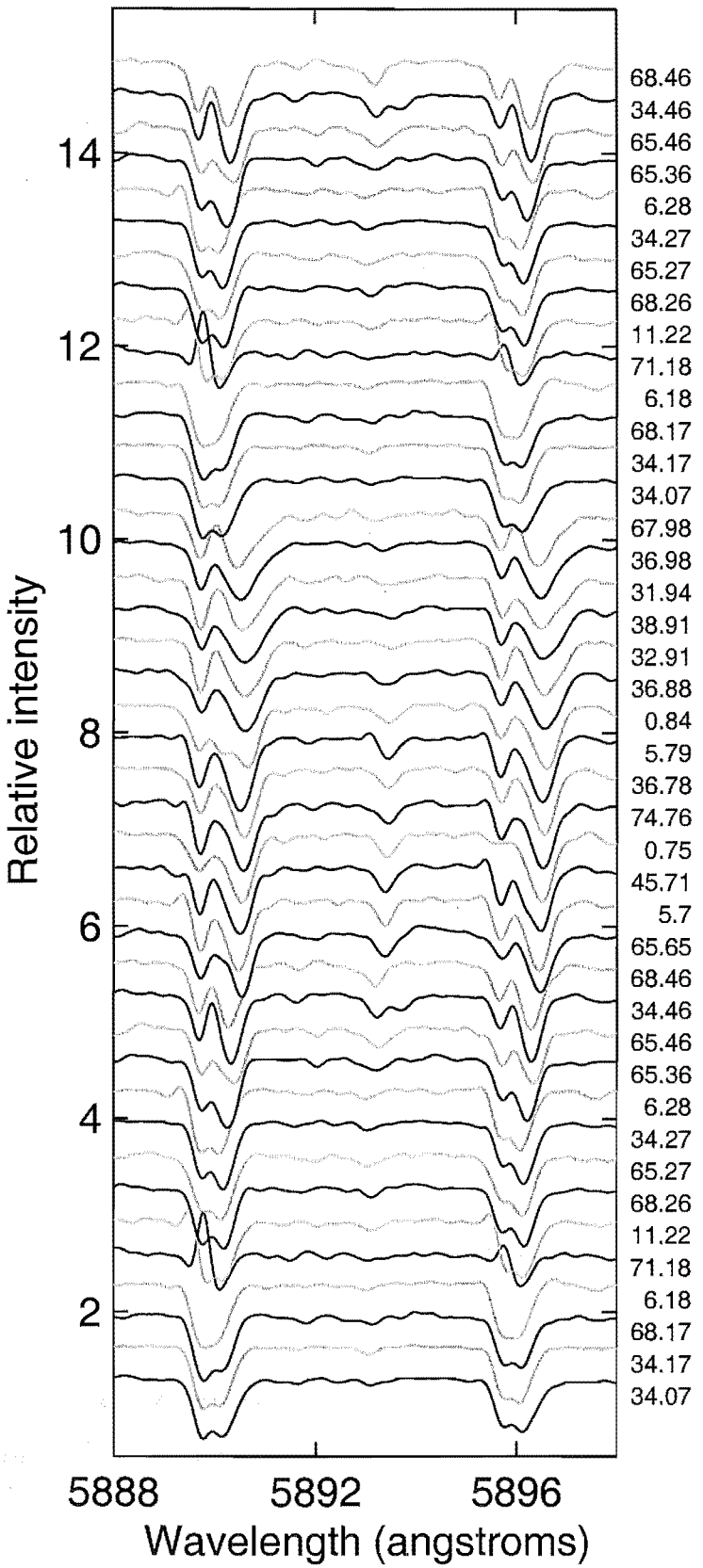

Figure 6.13: AL Vir stacked Na D lines.

secondary line component clearly observed to the blue. This line component is most likely interstellar in origin as it does not appear to shift as a function of pulsational phase. Due to its blue-ward placement, at most phases it does not affect the velocity derived from the bisector values as it is well separated above the 0.7 level of the line bisector. However, around minimum velocity the pulsational component of the line shifts such that the interstellar component is the deeper component and thus reduces the mean velocity obtained from the bisector. Unfortunately the line blending means that the pulsational component (and thus velocity) cannot be easily extracted without introducing too much uncertainty from the interstellar component removal. This means that it cannot be confirmed if the pulsational amplitude of the Na I line velocities is greater than that observed for the iron lines, as is observed in κ Pav (Figure 6.2). It also makes it difficult to tell if there is a consistent line level difference in the velocities measured around velocity minimum as opposed to velocity maximum, as is also observed in κ Pav (Figure 6.2).

Ca II lines

The Ca II lines (Figure 6.14) are also less complicated than the Hα line, with a small amount of splitting at phase 0.07 on the 8498 Å line, and phases 0.07 to 0.27 for the 8542 Å line. Thus it presents a much smoother curve than the Na D lines and shows similar behaviour to κ Pav's Ca II lines. Again the line behaviour difference is due to the relative strengths of the lines as stated in Section 6.2.1. The 8542 Å line has a lower log(gf) value and is thus formed more easily so it is able to be formed over a larger region. Hence the shock travels through the region for longer and a split line is observed for longer.

The pulsational behaviour of AL Vir is therefore very similar overall to that of κ Pav, with its Hα line behaviour conforming more closely to earlier observations of κ Pav than to more recent observations. This may mean that AL Vir is now in a similar evolutionary and pulsational state as κ Pav was in the late 1980s, however there are still many differences between the stars. Both do show smooth variations with minimal splitting of the metallic lines apart from the Ca II lines indicating that either the metal line forming regions are not being shocked (the transition between maximum and minimum velocity is not instantaneous) or the line-forming regions are small enough that we do not have the temporal resolution to catch when the splitting occurs easily. AL Vir is starting to exhibit more shock features than κ Pav in that more emission is present at certain phases. This progression of more or stronger shock features becomes more pronounced as we move to longer periods, with W Vir.

6.4 W Vir

The behaviour of W Vir is more complicated than both κ Pav and AL Vir. Curiously, it appears more similar to SW Tau than to any of the other stars examined so far. However, there are significant differences especially in terms of emission from Hα and He I 5876 Å.

As the prototype star of the W Virginis class, W Vir has been studied a great deal more than the preceding stars, despite it being fainter (V=9.6-10.8). Joy (1937) presented radial velocities and reported hydrogen emission lines as the star rose to maximum light. The next major discovery was the reporting of doubled absorption lines at certain phases (Sanford, 1952, 1954) and the suggestion of a shock wave causing the line doubling and emission lines (Schwarzschild, 1954). Abt (1954) explored this in more detail, collating

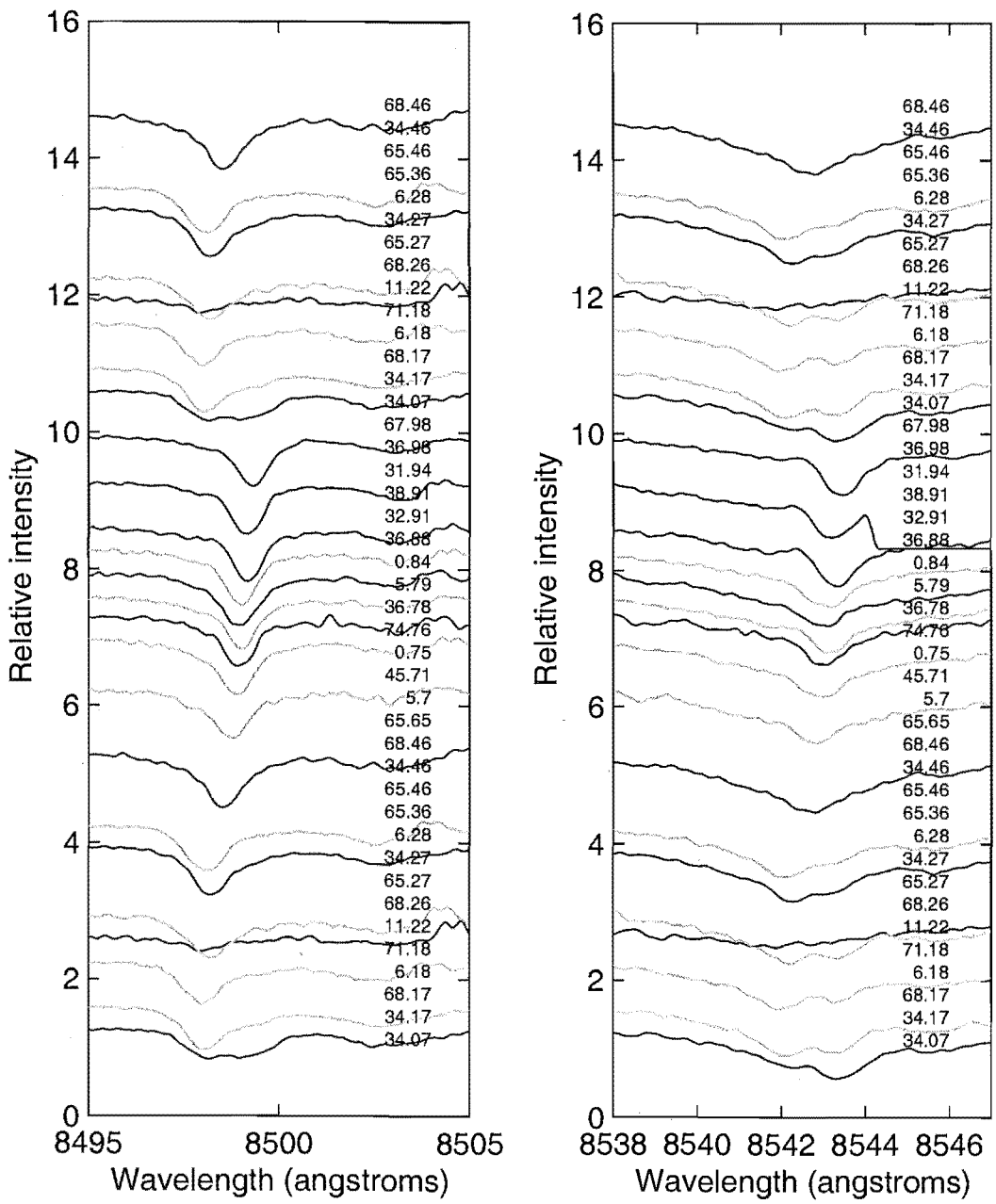

(a) 8498 Å. (b) 8542 Å.

Figure 6.14: AL Vir stacked Ca II lines. Gaps indicate observations for which wavelength coverage does not extend to 8000 Å due to filter problems (Section 2.2.3).

spectra and photometry from a variety of sources. He investigated the shock wave model of the line splitting but was unconvinced of its validity, whereas Wallerstein (1959b) found far more evidence, including observations of He I 5876 Å emission at certain phases which supported the shock wave idea. Raga et al. (1989) continued this work by examining emission from Hα, Hβ, and He I during rising light. The most detailed work has been by Lèbre and Gillet (1992), who used high resolution spectra covering Hα, He I and Na D, to investigate the atmospheric motion of W Vir. They used acceleration curves from Fe I lines to establish that there was one shock per pulsation cycle, as they found one photospheric acceleration peak per cycle (Figure 2, Lèbre and Gillet, 1992).

6.4.1 Spectroscopy

When an acceleration curve is derived from the MJUO Fe I radial velocities (Figure 6.15), it shows one clear acceleration minimum. As the acceleration curve presented here has not been corrected for projection factors or transformed into the rest frame of the star, it appears as a minimum, rather than the maximum of Lèbre and Gillet (1992). Midway along rising light occurs at the same phase as the acceleration minimum and thus the minimum photospheric radius of the star (as defined by the Fe I lines).

When the range of line species examined is increased, the sudden velocity transition between maximum and minimum radial velocity is still quite apparent. The average velocities of Fe I, Fe II and Na I all show the effect, although the phase at which it occurs varies between 0.00 and 0.15. For this star, the radial velocity of Hα has not been measured due to the line being in emission for much of the time.

In contrast to the BL Her stars and κ Pav and AL Vir, the Fe I and Fe II line velocities in W Vir do not agree at all times. The minimum Fe I velocity of -82 kms^{-1} occurs at phase 0.15, whereas the minimum Fe II velocity of -78 kms^{-1} occurs at phase 0.15. The next largest difference between the velocity curves occurs at phase 0.9, where Fe II reaches a maximum velocity of -30 kms^{-1}, while Fe I is still around -45 kms^{-1}. Fe I reaches a peak around phase 0.00 with a velocity of -33 kms^{-1}, which agrees with one of the measured Fe II velocities. Another Fe I velocity from around that same phase is, however, back at -78 kms^{-1}. Thus the Fe I velocity curve has a peak to peak amplitude of 49 kms^{-1}, whereas the Fe II velocity curve has an amplitude of 48 kms^{-1}, and is offset by approximately 5 kms^{-1}.

The Na I behaviour is a little less complicated. There is a slightly greater scatter in the velocities obtained and the velocity behaviour does not parallel any of the other species examined. It has a minimum velocity of -95 kms^{-1}, which it does not reach until phase 0.15 and its maximum velocity of -40 kms^{-1} is not reached until phase 0.05. This gives a peak to peak amplitude of 55 kms^{-1} and a systemic velocity much lower than that of the Fe lines.

In contrast to the other species, the Ca II radial velocity curve is far more sinusoidal, with minimum velocity occurring far later in the pulsation cycle of $\sim$ -64 kms^{-1} at phase 0.3[4]. Maximum velocity is closer in phase to the other species maximum velocities, occurring at -40 kms^{-1} at phase 0.9. This gives a much lower peak-to-peak velocity amplitude of 24 kms^{-1}.

[4]The point at -90 kms^{-1}, phase 0.45 is thought to be an outlying point

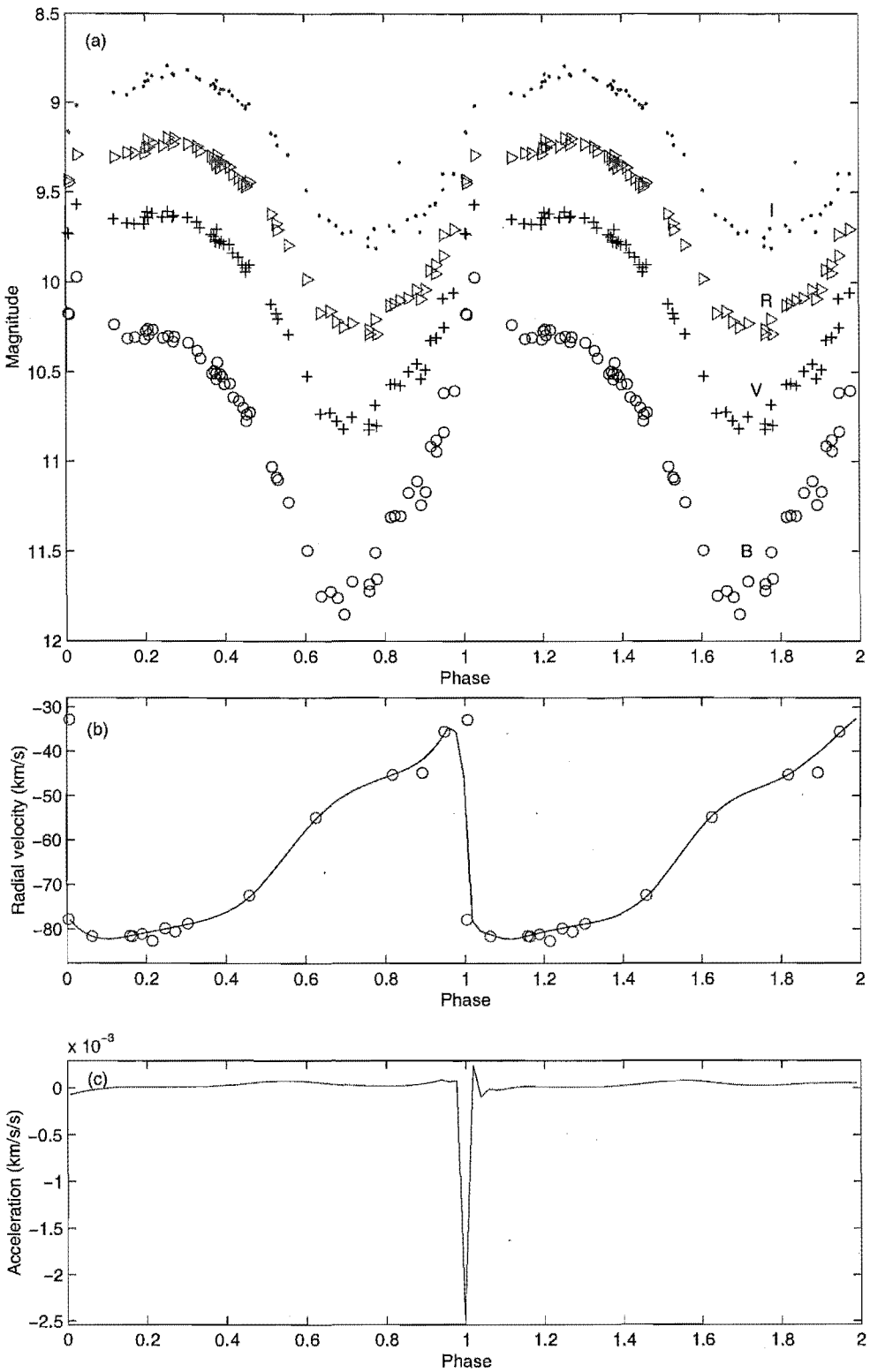

Figure 6.15: (a) *BVRI* magnitudes, (b) Fe I radial velocity and (c) acceleration curves for W Vir.

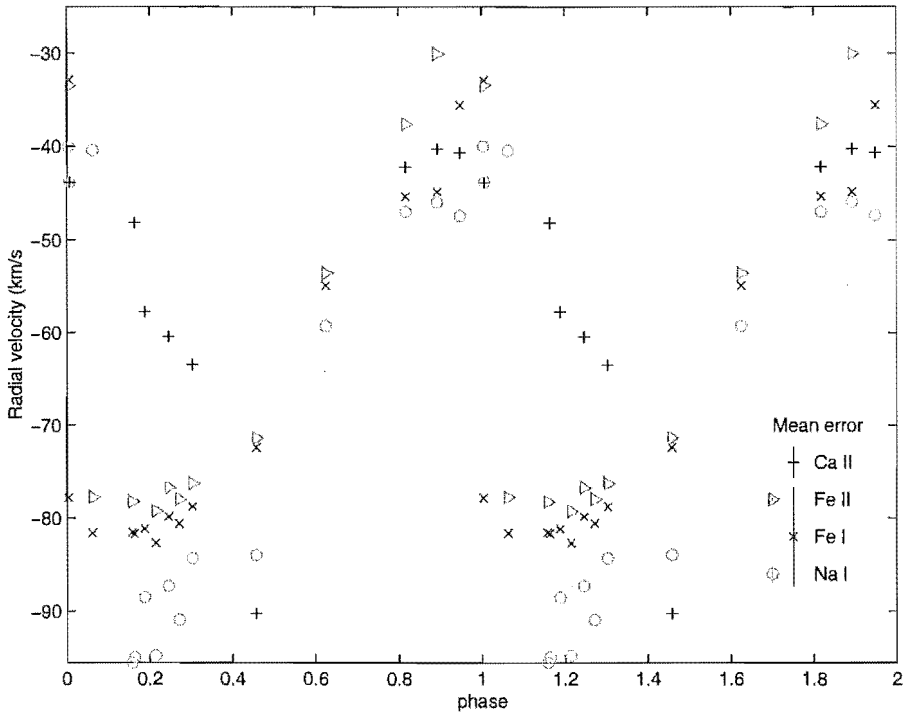

Figure 6.16: Radial velocity curves for W Vir, measured from averaged Fe I , Fe II, Ca II and Na I lines.

Ca II lines

A possible explanation of the quite different velocity behaviour of Ca II results when we examine the stacked Ca II lines at 8498 and 8542 Å. From Figure 6.17, it is quite clear that the lines are quite irregular, with multiple components, including possible emission between phases 0.89 and 0.16. Unfortunately, due to the small number of spectra available of these lines, it is difficult to confirm any definite trends. Hence it is not possible to separate out any pulsational behaviour.

Na D and He I lines

In contrast to the Ca II line behaviour, the more numerous stacked spectra in the region of the Na D lines (Figure 6.18) do show distinct variations as a function of phase. One of the most noticeable of these is the weakening and disappearance of many of the metallic absorption lines at phase 0.00 just before or around maximum light. Between 5850 and 5870 Å, a maximum of five lines are clearly observed. These are Ba II 5854 Å, Ca I 5857 Å, Fe I 5860 Å, Fe I 5862 Å and Ti I 5866 Å[5]. All five lines are most distinctly visible at phases 0.27 to 0.63, yet have disappeared almost completely at phase 0.00. Of these, Ca I 5857 is the only line detectable at all the phases, and it is very weak around phase 0.01. Ba II 5854 appears soon after, around phase 0.06, and the Fe I lines appear around phase 0.16. Ti I 5866 is the weakest line and appears last in the pulsation cycle around phase 0.27. Due to the gaps in phase coverage, it is unclear at what phase the lines first

[5]See Tables E.1, E.3, E.6 and E.18 for log(gf) and excitation potentials of these lines.

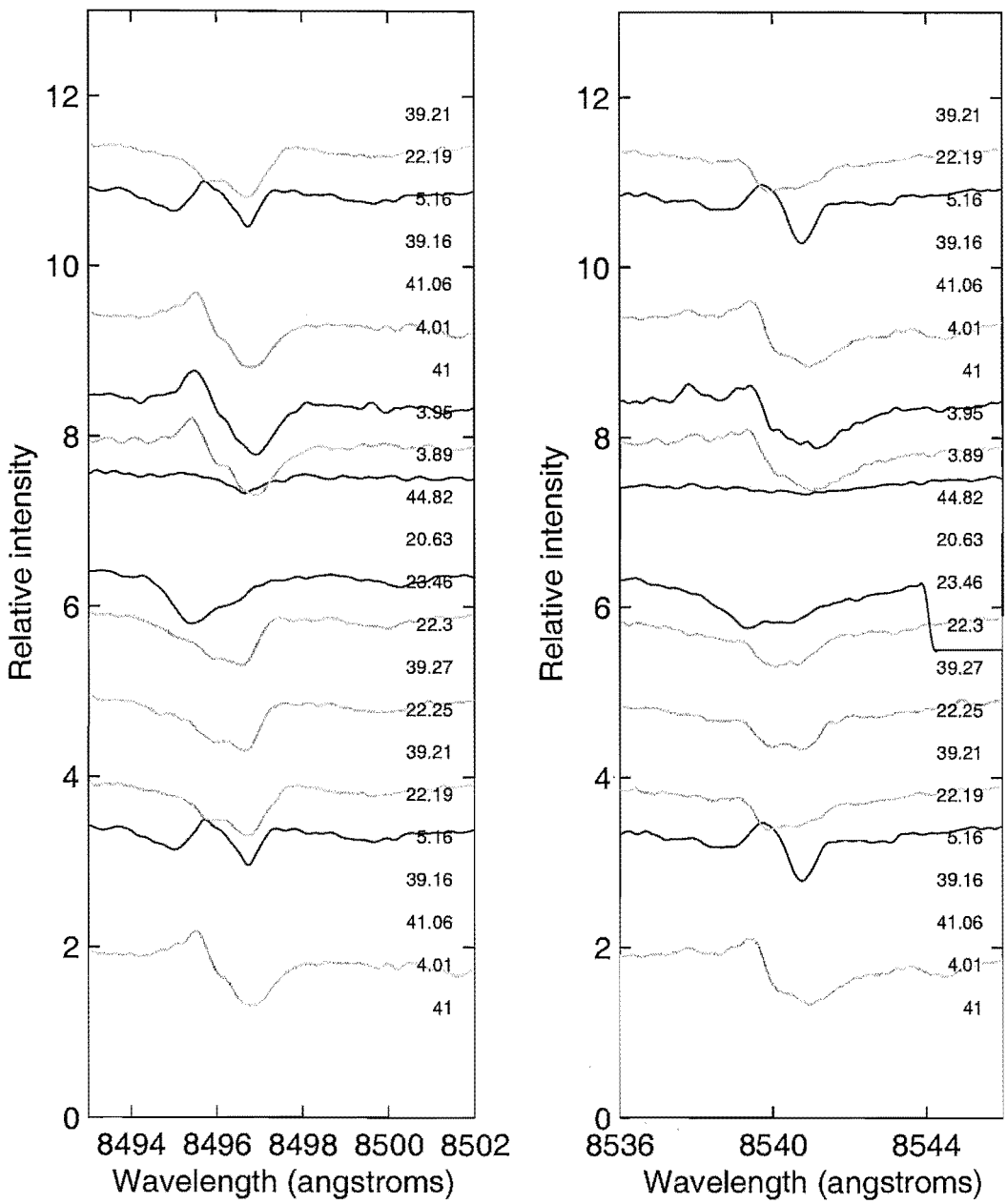

(a) 8498 Å. (b) 8542 Å.

Figure 6.17: W Vir stacked Ca II lines. Gaps indicate observations for which wavelength coverage does not extend to 8000 Å due to filter problems (Section 2.2.3).

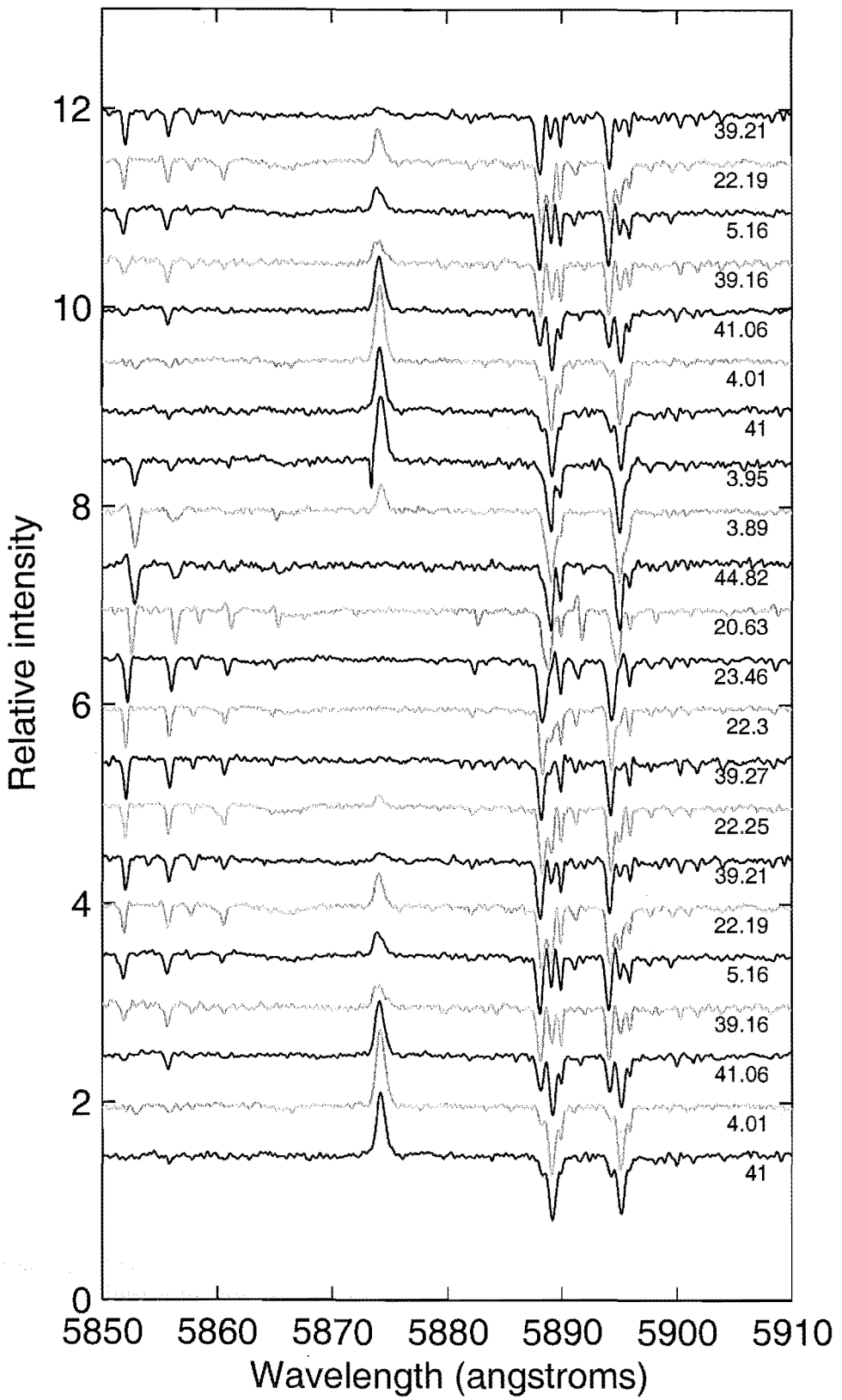

Figure 6.18: Stacked spectra of Na D and He I 5875 Å lines for W Vir.

start disappearing, but the two Fe I lines are far weaker than the Ti I line at phase 0.89, and by 0.95, only the Ba II line and the Ca I line are discernible above the noise.

At this same time, He I 5875 Å emission is at its peak. The emission strength correlates inversely with the five metallic line strengths as when the emission is strongest, the metallic absorption lines are weakest and vice versa. The He I emission is caused by de-excitation of ionized material behind the shock wave and as its peak appears to occur when the photospheric layers (as defined by Fe I) reach minimum acceleration and are forced outwards, that is when the shock wave hits the line forming regions and reverses the mean motion of the material in them. The Ba II line is just discernible as split at phase 0.01 (Figure 6.18). It may be that the metallic line forming regions of the star are so thin that when the shock passes through it disrupts the whole region such that one or more clear velocity regimes are not discernible. Another possibility is that the shock is strong enough to create emission in the line forming regions which fills in the absorption lines. It may be that the star is at its hottest then, as the lines are no longer visible due to the conditions no longer being optimal for them to form.

The other lines in this region which show evidence of a shock wave passing through are the Na D lines (5890 and 5895 Å). However their observed structure is more complicated than the previous metallic lines, with up to three line components visible at any one time. This is simplified when it is realized that the furthest red-ward line component is understood to be of interstellar origin (Wallerstein, 1959a; Raga et al., 1989; Lèbre and Gillet, 1992), a concept supported by its lack of motion (Figure 6.18). The remaining two bluer components appear to be associated with the pulsations of the star, as they change in position and depth in a reasonably consistent fashion through the pulsation cycle. If we consider these two components to make up the Na D "line" as formed by the star's pulsations, the line begins splitting around phase 0.00. The blue component is just starting to form at this phase, indicating that the shock is only now far enough through the line forming region to create two velocity regimes where material is moving inwards and outwards in the line forming region. As the blue-ward line component increases in strength, the red-ward component decreases, indicating a greater proportion of the material is now moving outwards, rather than falling inwards towards the stellar centre. The shock has almost completely passed by phase 0.46 and the material is around or just past maximum radius by phase 0.63. At many of the phases when the multiple pulsational components are present, the lines are quite distinct, indicating a strong shock to create such a large velocity difference. The one problem with this interpretation is that on at least two occasions (cycles 5.16 and 23.46), the bump between the two line components is higher than the continuum level. The source of this is unclear, but if this is shock related emission, it does not strictly correlate with the He I emission observed, indicating that it cannot be forming in the same region of the star. The fact that the Na D pulsational line components are equally split (that is, the shock is halfway through the line forming region) around phase 0.06–0.16, indicates that the Na D line forming regions are further out in the stellar photosphere than the metallic line forming regions, as exemplified by Ba II, Ca I, Fe I and Ti I.

Hα line

Where the Hα line is formed is less easily stated, as it shows a much more complicated structure than those lines previously examined (Figure 6.19). It shows multiple compo-

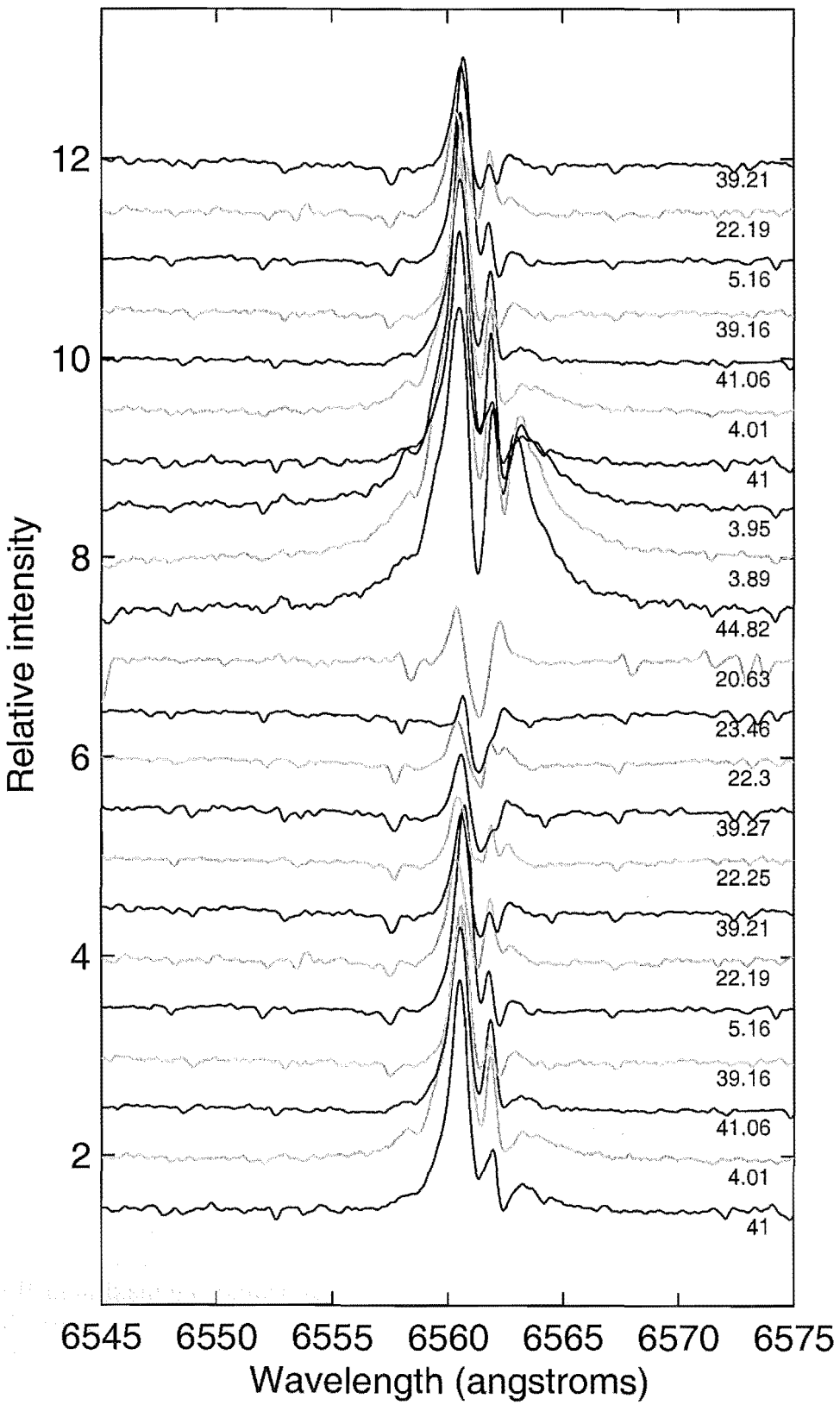

Figure 6.19: Stacked spectra of the Hα line for W Vir.

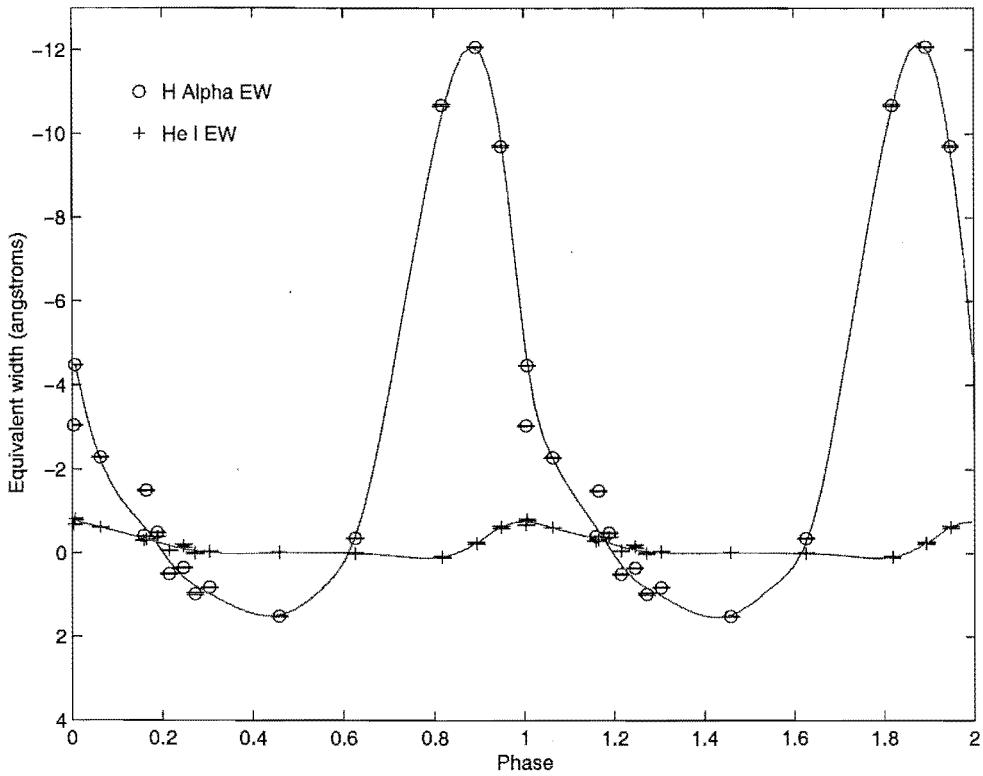

Figure 6.20: Phased Hα and He I equivalent widths for W Vir.

nents which vary in amplitude and position over a pulsational cycle. Overall amplitude is a minimum around phase 0.63, but has increased by phase 0.89 and reaches a peak soon after that. Unfortunately the overlapping structure makes it difficult to discern where in phase this occurs. Another curious line behaviour is that the central absorption component centered on 6561.5 Å does not appear to vary in position. It is unclear what the origin of this feature is. Unfortunately, fitting multiple Gaussian shaped components to the line to attempt to derive velocities for each is too ambiguous, as the large number of line components reduces the probability of attaining a unique solution. Instead the equivalent width of the line has been examined, and also compared to the other emission line of He I 5875 Å (Figure 6.20).

Hα emission peaks significantly between phases 0.8 and 0.00, with peak emission occurring at phase 0.9. This is 0.1 of a pulsational cycle ahead of when the maximum He I emission occurs, and when the shock wave hits the metallic line forming regions. This contradicts Lèbre and Gillet (1992), who stated that He emission appeared after new Hα emission [6] and was only present during the strongest Hα emission intensity phases. From Figure 6.20, it is clear that the He I emission lags behind the maximum Hα emission and is not occurring at the same time as the strongest Hα emission intensity. In the previous stars, the shock wave had been reaching the Hα line forming regions last, as evidenced by the large phase delay in velocity reversal in the line forming region as shown by the velocity curves, but it is unclear when the shock is reaching the Hα line forming region

[6]The new Hα emission appears at phase 0.537 by the Lèbre and Gillet (1992) phasing which is based on minimum radial velocity, placing it ~0.2 of a cycle ahead of the acceleration minimum phasing.

in W Vir. Also in the previous stars, the shock wave had only been exciting material detectably for a small percentage of the pulsation cycle, if at all, whereas for W Vir, emission is observable at all phases in the Hα line. This may be due to a larger star (as evidenced by the longer period) having a much larger Hα line forming region due to more diffuse outer layers. This does not explain how this emission is extended to all pulsational phases, as it should only affect the absolute time taken to cross the star, not the relative time, assuming similar relative structure of the various outer layers of the star.

Another point of note with respect to the shock wave is the peak associated with maximum light (Figure 6.15a). This peak is generally considered to be associated with the shock wave and Hα emission, as it decreases in magnitude to the redder wavelengths. This does not seem consistent with the results presented here since maximum light (in V) occurs between phases 0.00 and 0.1, which is well after maximum Hα emission and even just maximum He I emission. This may be due to the overall photometric flux from the star, resulting from further out in the star, with the increased light output being due to increased temperatures as the shock hit those outer layers, but the light origin being further out in the star seems counterintuitive.

Overall, W Vir shows more complicated motions than the previously examined stars in that the shock wave has a far greater effect on the star, as indicated by the line behaviour, than on the other stars. This is evident in the far more rapid transition between maximum and minimum velocity, and in the heightened Hα emission and He I emission indicating the presence of a very strong shock in the stellar photosphere.

6.5 ST Pup

ST Pup, the longest period (18.6 days) W Vir star examined here, is also well known for exhibiting the same emission features as W Vir. However, the understanding of its behaviour is greatly complicated by its orbital motion.

Gonzalez and Wallerstein (1996) derived an orbital period of 410.4 $\pm$ 2.9 days for ST Pup. They used a spectroscopic baseline of nearly 7 years. Unfortunately, there is a difficulty in using the historical data to give a long baseline in that in the first half of the 20th century, ST Pup underwent frequent period changes, with one clear period change between approximately 1950 and 1996 (Gonzalez and Wallerstein, 1996). From a comparison of the MJUO photometric observations (Section 4.3.4) with the SAAO photometry of Kilkenny et al. (1993), it is clear that a distinct period change has occurred since then, as the period increased from 18.4622 days (Gonzalez and Wallerstein, 1996) to 18.6204 days (Section 4.3.4). Due to the gaps in photometric coverage, it is unclear whether this was a gradual or sudden period change.

Orbital analysis

As stated earlier, Gonzalez and Wallerstein (1996) found an orbital period of 410 days for ST Pup. The rest of their orbital parameters are detailed in Table 6.2. Using these parameters and their velocities, the pulsational and orbital components of the motion can be clearly separated out (Figure 6.21). Unfortunately the usual test of adding the latest data to the historical data to improve the orbital solution is not possible in this case. The pulsational period changes mean that pulsational and orbital curves cannot be simultaneously fitted to the velocities. Also, the relatively small number of MJUO

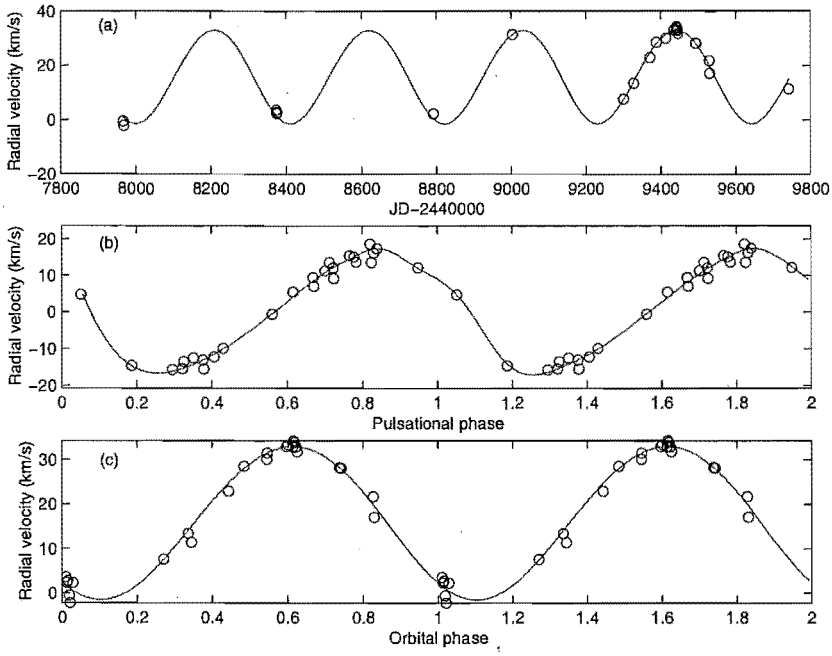

Figure 6.21: Velocity curves of ST Pup using Gonzalez and Wallerstein (1996) velocity data and orbital characteristics. (a) Orbital motion as a function of JD. (b) Pulsational motion as a function of pulsational phase. (c) Orbital motion as a function of orbital phase.

spectral observations of ST Pup means that fitting an orbital curve to only these data is unrealistic. It was decided to trial the acceleration phasing using the historical data and see how this compared to the MJUO radial velocities with the Gonzalez and Wallerstein (1996) orbital motion removed.

6.5.1 Spectroscopy

Acceleration minimum phased photometry and spectroscopy (Figure 6.22) are presented using Gonzalez and Wallerstein (1996) radial velocities and Kilkenny et al. (1993) *BVRI* photometry. The orbital motion has been removed from the velocities and a spline curve fitted to the metallic line radial velocities. This spline curve was then differentiated to find the acceleration curve and the minimum acceleration point was then used to rephase the data. As can be seen from the fitted curves (Figure 6.22), the velocity curve is quite similar that for Fe I for TX Del (Figure 5.24). Unfortunately, it is difficult to comment on line level effects, as Gonzalez and Wallerstein (1996) used mainly iron lines of average excitation potential with some extra Ca I and O I lines included.

In order to examine the MJUO velocities and see how their variability compared to the historical curves, it was first necessary to see if the velocities could be phased such that they at least overlay each other in phase space. Due to the disappearance of most Fe I lines at certain phases, the averages of the selection of Fe I lines used for the previous stars was not reliable. A survey of lines previously used demonstrated that most disappeared at certain phases, with a rare exception being the Fe II line at 6516 Å[7]. This line was

[7]Any possible offset between the Fe I and Fe II line velocity curves has been ignored in this case as

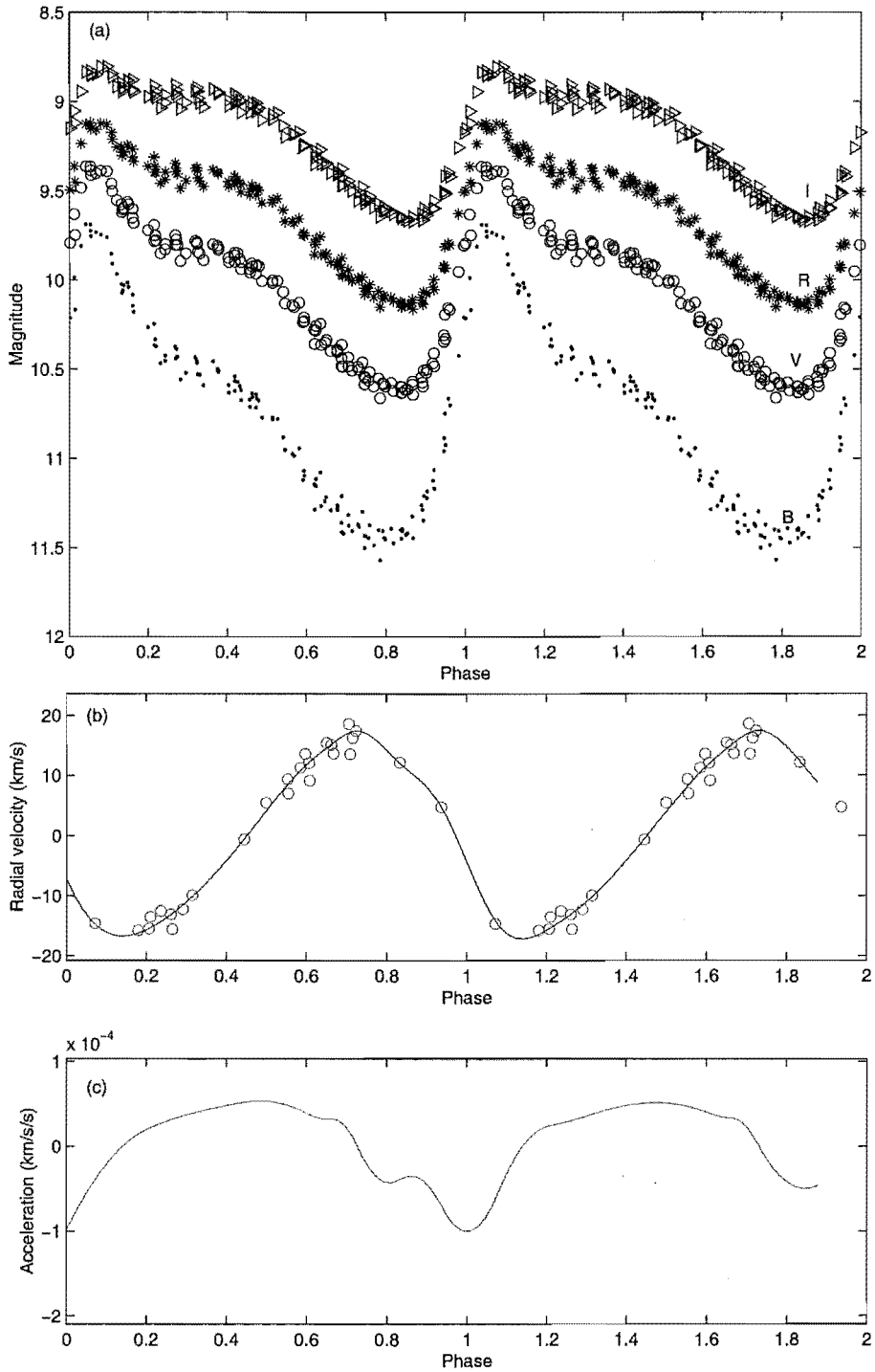

Figure 6.22: (a) *BVRI* magnitudes (Kilkenny et al., 1993), (b) metallic radial velocities (Gonzalez and Wallerstein, 1996) and (c) acceleration curves of ST Pup.

Table 6.2: Gonzalez and Wallerstein (1996) orbital parameters for ST Pup.

P	(days)	410.4 ± 2.9
γ	(kms^{-1})	16.1 ± 0.6
K_1	(kms^{-1})	17.2 ± 0.7
e		0.029 ± 0.024
ω	(^{o})	141 ± 47
T_0	(JD)	2448779.2 ± 5.2
σ	(kms^{-1})	0.81
$a \sin i$	(km)	$(9.7 \pm 0.4)\mathrm{x}10^7$
$f(m)$	(solar masses)	0.22 ± 0.03

re-measured using the bisector method and the velocity was taken to be the average of the velocities at depths 0.7, 0.8 and 0.9 of the line.

The velocity comparison was also complicated by the different pulsational periods. Initially, a common epoch was chosen, based on the minimum light phase from the MJUO photometry, and then the velocity curves were phased using this epoch and the appropriate period applying to each time span (Figure 6.23a). This appeared to work reasonably well for the four velocities between phases 0.6 and 0.9, but the remaining six velocities do not fit nearly as well. Examination of the lines themselves and the bisectors derived did not clarify why these velocities were different as the lines did not show atypical splitting or asymmetry which could have skewed the velocities obtained. Curiously, the best fitting velocities were from pulsation cycles 10, 14 and 23, whereas the more scattered velocities were from cycles 6, 8 and 31.

Taking the above fit as a preliminary fit, based on the four good velocities, the data was then rephased using the acceleration minimum derived from the Gonzalez and Wallerstein (1996) data (Figure 6.23b). This was more complicated as, while the phase shifts were the same, the different periods resulted in separate epochs for each data set. This resulted in an acceleration epoch of JD 2451390.248 for the Gonzalez and Wallerstein (1996) data and JD 2451390.141 for the MJUO data.

To test if the scatter in velocity for the six more-highly-scattered velocity points was possibly due to a poorly-defined orbital solution, the MJUO velocities were plotted as a function of JD, along with the Gonzalez and Wallerstein (1996) orbital motions (Figure 6.24). While there is some slight correlation of higher scatter at peak orbital velocity and a little after, the evidence is inconclusive and more observations are required.

For the rest of the ST Pup discussion, phasing is based on the MJUO period of 18.6204 days and the associated acceleration minimum epoch of JD 2451388.125.

Na D, He I and associated lines

While the individual velocities from the lines are difficult to interpret, the structure of those lines is more easily examined. Examining stacked spectra in the region of the Na D lines (Figure 6.25) reveals a number of features. The Na D lines themselves are quite prominent, and would have been perfect for velocity measurement, were it not for

the only interest here is in confirming the overall pulsational behaviour.

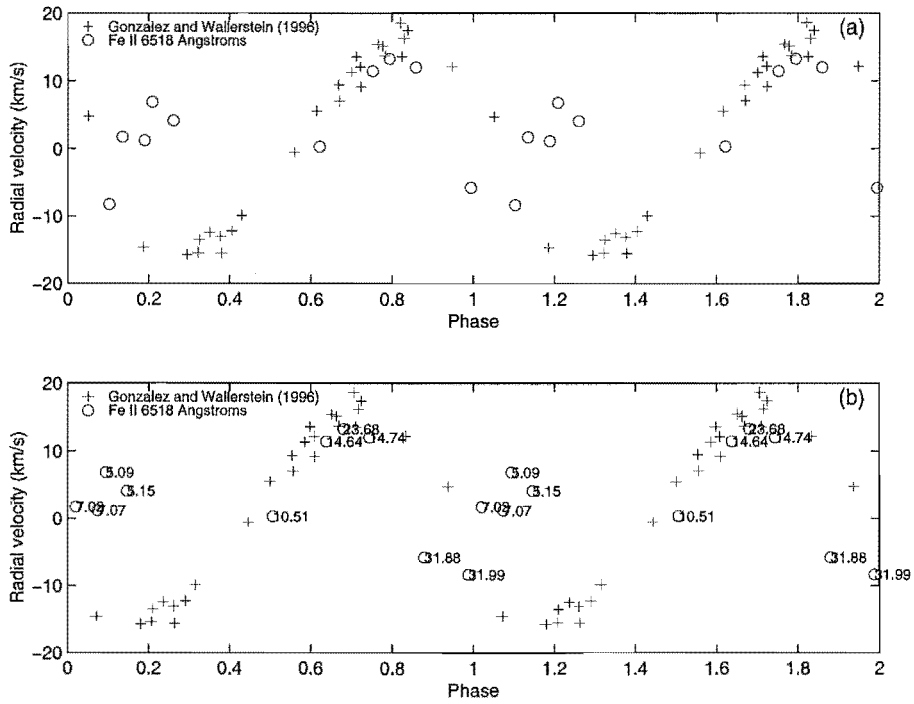

Figure 6.23: Radial velocity curves for ST Pup with Gonzalez and Wallerstein (1996) orbital motion removed.
(a): Gonzalez and Wallerstein (1996) radial velocities phased on 18.4622 day period. MJUO Fe II 6516 Å radial velocities phased on 18.6204 day period. Both use the MJUO photometric epoch of JD 245 1388.125.
(b): As above but epoch established using acceleration minimum (Figure 6.22). Gonzalez and Wallerstein (1996) radial velocities use epoch of JD 2451390.248. MJUO Fe II 6516 Å radial velocities use epoch of JD 2451390.141.

the unchanging blue-ward component of the lines. This line component appears to be interstellar in nature as it shows no evidence of the pulsational or binary motion of the star and is thus unlikely to be part of the stellar system.

The next line encountered moving towards the blue, is the He I 5876 Å emission line. It is present between phases 0 and 0.12 in cycles 7.03, 7.08, 5.1 (barely) and 6.12. It is unclear if any He I emission is observable at the earlier phase of 0.99, as the spectra at cycle 31.99 appears very noisy, as also for cycle 31.89. This is due to the star showing molecular bands (CH and CN) at minimum light (Gonzalez and Wallerstein, 1996), approximately around phase 0.0. These make the spectra appear more noisy than they actually are. While not a feature shared by the Cepheids examined so far, the presence of molecular band at minimum light is a feature of various RV Tauri stars such as U Mon and R Sct (Pollard et al., 1997).

The only other line to be clearly featured in Figure 6.25 is the Ba II line at 5854 Å. The extent of when it is cleanly visible makes it clear why it was difficult to find metallic lines for orbital and pulsational analysis. The line only appears during phases 0.51 to 0.75, over four spectra, which is not a large enough baseline from which to derive an orbit. Instead, the line used was the Fe II line at 6516 Å.

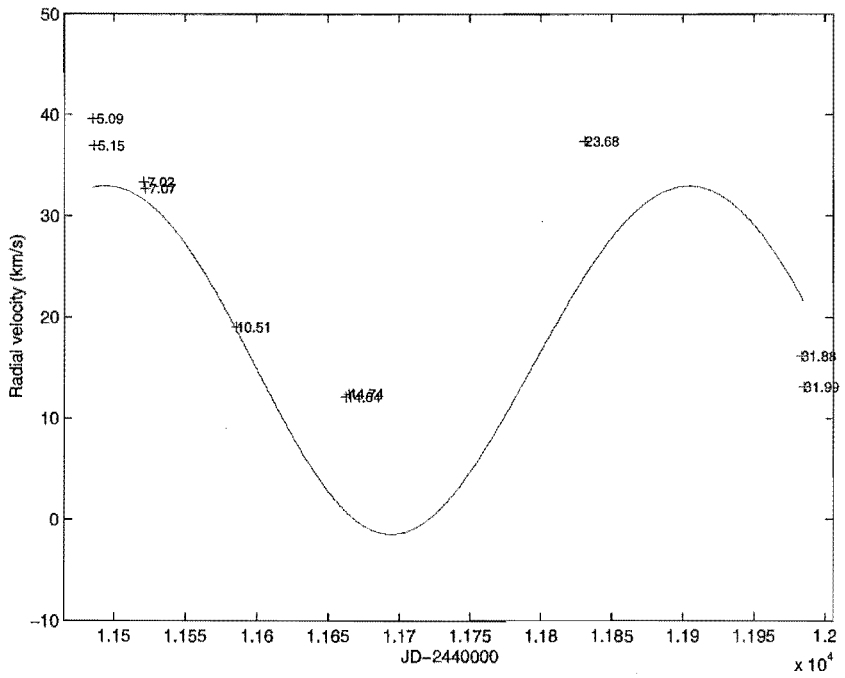

Figure 6.24: MJUO ST Pup Fe II velocities as a function of JD. Pulsational motion has not been removed, however the Gonzalez and Wallerstein (1996) orbital solution is indicated by the solid line. Pulsational cycle numbers and phases are based on the MJUO period and epoch of Figure 6.23b.

The metallic lines disappearing at certain phases is a characteristic previously noted in W Vir (Figure 6.18). Again the presence/strength of the Ba II absorption line correlates with the lack of He I 5876 emission. In addition, neither is present when the star is at its coolest, when the molecular bands are visible (as far as can be discerned amongst the molecular bands). Unfortunately the lack of phase coverage between phases 0.15 and 0.51 means that it cannot be established when in the pulsation cycle the Ba II line appears. It has, however, completely disappeared during phases 0.03–0.15, which is a greater percentage of the pulsation cycle that that seen in W Vir (0.00–0.06).

The lines shown in Figure 6.25 do not show signs of splitting, similar to W Vir. Allowing for the interstellar line component, the Na D lines show no sign of splitting and neither does the Ba II line. In fact, the only signs of passage of a shock wave is through the observed He I 5876 emission (which is weaker than observed in W Vir and observed at less phases) and through the Hα emission.

Hα and Fe II lines

The Hα line of ST Pup is similar to that observed in W Vir in that it shows a quite complicated emission structure (Figure 6.26). The line consists of multiple components which vary in height and position through the pulsational cycle. Peak Hα emission occurs at phase $\sim$ 0.0, as confirmed by examining the equivalent widths of the line (Figure 6.27). This is at a slightly later phase than observed in W Vir (peak emission phase 0.9), but this may be due to the problems of phasing the data set, rather than a physical difference

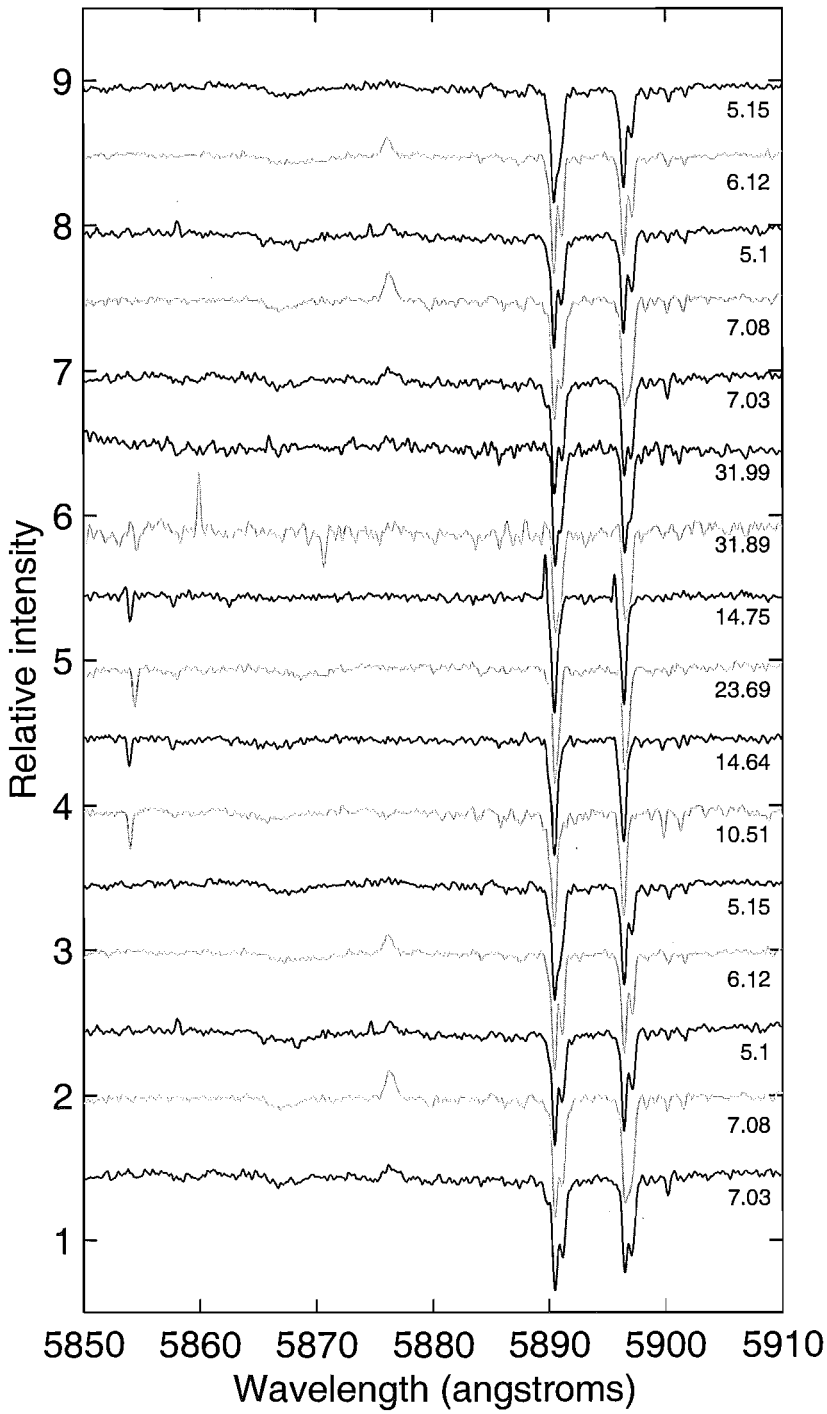

Figure 6.25: Stacked spectra for ST Pup in the spectral region of the Na D and He I 5875 Å lines.

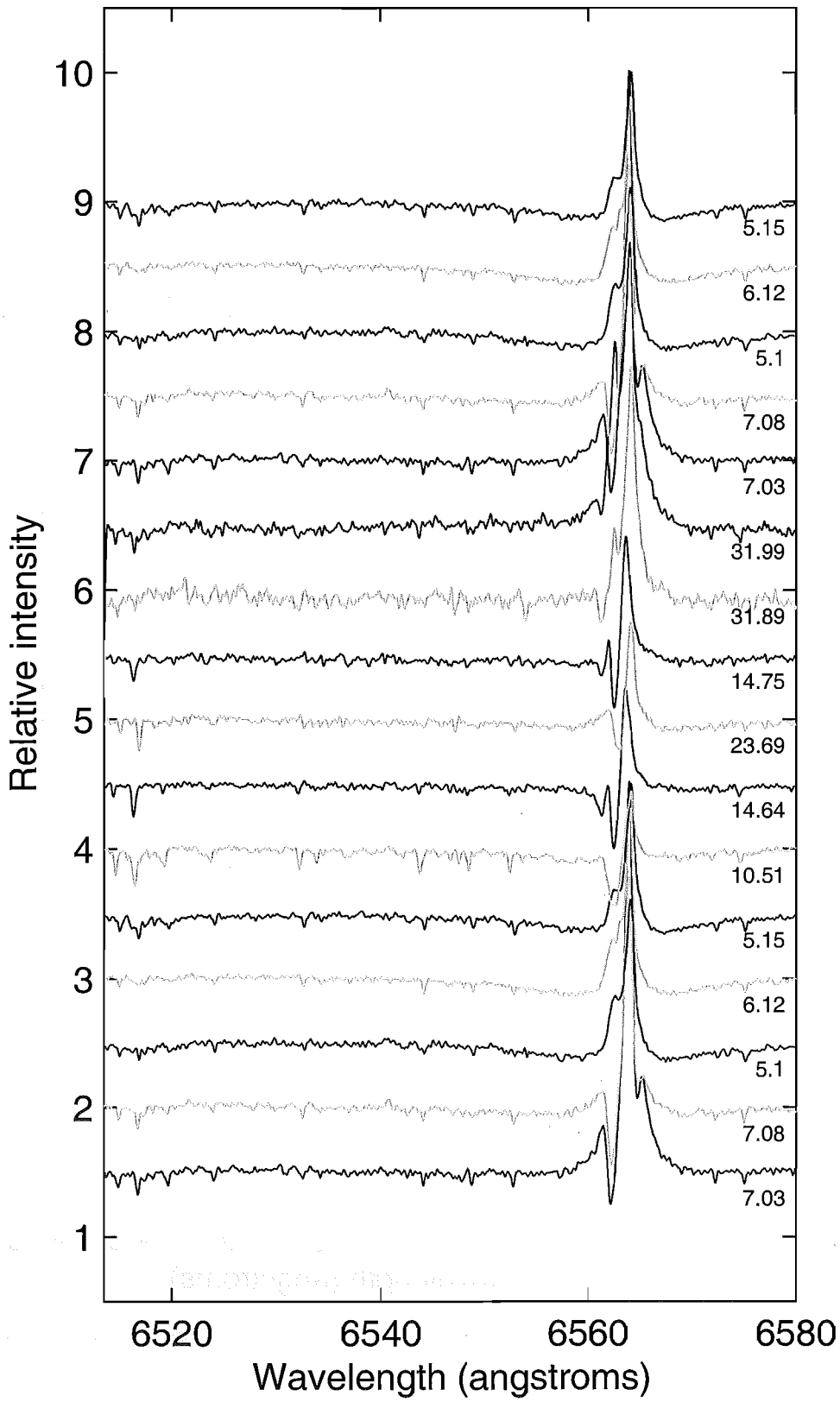

Figure 6.26: Stacked spectra of the Hα region for ST Pup.

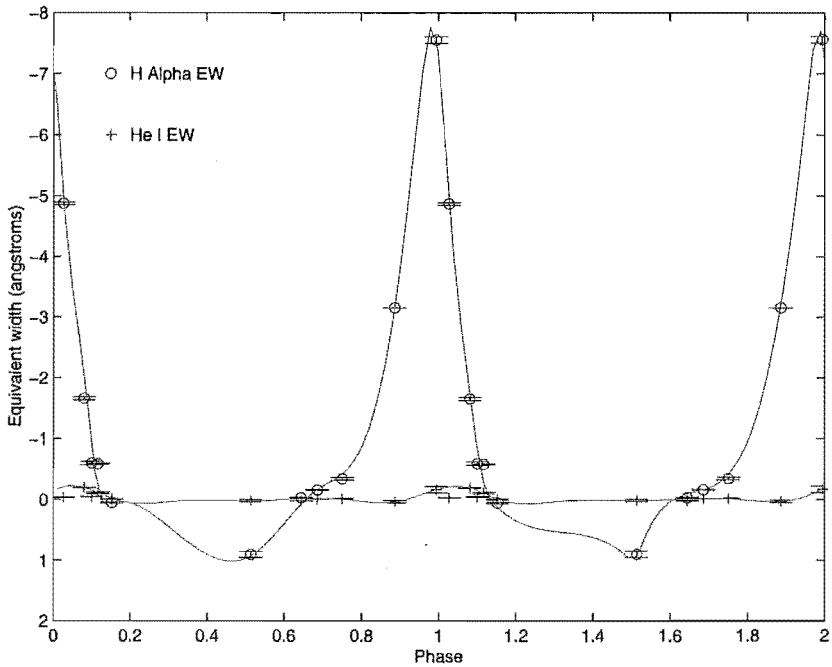

Figure 6.27: Phased Hα and He I (5876 Å) equivalent widths for ST Pup.

in when minimum photospheric radius (as defined by the acceleration minimum from Fe I lines) occurs compared to maximum Hα emission. The phase shifts between the peak emission positions for the Hα and He I 5876 equivalent widths are similar to that observed in W Vir, indicating similar processes are going on. The amplitude of the emission is much higher in W Vir for both lines and that, combined with the relative degrees of line splitting observed in each star, indicates a weaker shock in ST Pup compared to W Vir.

The pattern observed in the equivalent widths also confirms the phasing used as, based on what was observed in W Vir, it would be expected that peak emission would occur just before phase 0.00 for Hα and around phase 0.00 for He I 5876.

Figure 6.26 also shows the Fe II line at 6516 Å, which is far more prominent than the Ba II line previous examined and is present at a greater range of pulsational phases. This made it far more promising for analysis although, as seen from Figure 6.23 and in Section 6.5.1, only cycles 10.51, 14.64, 23.69 and 14.75 resulted in velocities which fitted in with the historical velocity curves.

Overall, what can be deciphered of the behaviour of ST Pup is similar to the previously-examined Cepheids. It shows similar trends in emission-line behaviour to W Vir, indicating that similar shock waves are present though less strong. Also, that similarity in shock wave behaviour confirms the acceleration phasing presented. Clearly while the period has changed in the star, the relative phases at which shock waves propagate through the star and affect the various layers of the star have not. Using the phasing from the two epochs, the He I 5976 emission associated with the shock wave (which reaches a maximum at phase 0.00 in W Vir) phases up with the change in the bulk motion of the photosphere, as defined by the acceleration curve minimum from the historical Wallerstein et al. (1992) velocities.

This effect has been observable throughout the stars examined as similar line be-

Table 6.3: W Vir star summary.

	κ Pav	AL Vir	W Vir	ST Pup
period (days)	9.0741	10.295	17.2768	18.6204
epoch[a]	11308.336	11310.281	11305.594	11390.141
radii (in solar radii)[b]	29.1±0.8[c]	26.2[d]	35±10[b]	—
	19±5[b]	34.0±2.0[c]		
		38±10[b]		
Hα velocity amplitude	38	32	—	—
phase max velocity	0.1	0.1	—	—
phase min velocity	0.2-0.8	0.25	—	—
Hα EW amplitude	—	—	13.5	8.5
phase max EW	—	—	0.89	0.00
phase min EW	—	—	0.47	0.50
Ca II velocity amplitude	36	43-46	24	—
phase max velocity	0-0.05	0.2	0.9	—
phase min velocity	0.3	0.85-0.95	0.3	—
Fe I velocity amplitude	28	25	49	—
phase max velocity	0.9	0.85	0.00	—
phase min velocity	0.15	0.20	0.15	—
Na I velocity amplitude	30	35	55	—
phase max velocity	0.9	0.9	0.05	—
phase min velocity	0.15	0.2	0.15	—
	Type II	Type II	Type II	Type II

[a]From acceleration phasing. Epoch = JD -2440000.
[b]Balog et al. (1997)
[c]Laney (1995)
[d]Balona (1977)

haviours have occurred at similar phases through all of these stars. What does appear to be dependent on the period is the occurrence of emission lines in the spectra.

Chapter 7

RV Tauri stars

RV Tauri stars are the longest period stars of the Type II Cepheids, with periods between successive deep minima of 30–150 days. As stated in Chapter 1, they are defined by the alternations in the depths of successive minima, period range and spectral type range of F-K, with a luminosity class of Ia–II.

RV Tauri stars are further sub-categorized in two ways: (1) photometrically based on a constant mean/maximum magnitude (RVa) or long-term variations in mean/maximum magnitude (RVb), and (2) spectroscopically based on particular line strengths (Preston et al., 1963). The spectral types are RVA, RVB and RVC, with RVA stars being G-K spectral type, while occasionally showing TiO bands (a feature normal in stars of as late a type as M5) at minimum light. RVB stars are classed as Fp(R) stars as they show weak metallic line absorption and CH and CN bands which vary in strength as a function of phase. The final class of RVC stars are the same as RVB stars (Fp) but they show little or no CH and CN bands at all phases (Pollard, 1994).

As the RV Tauri stars have recently been reviewed (Pollard et al., 1997; Maas et al., 2002; Wallerstein, 2002, and references therein), historical spectroscopy will not be reviewed in detail here. Major general spectroscopic reviews include Rosino (1951); Joy (1952); Preston et al. (1963); DuPuy (1973); Wahlgren (1992); Pollard et al. (1997), with individual stars such as R Sct (Howell et al., 1983; Gillet et al., 1989, 1990; Lèbre and Gillet, 1991a,b; Matsuura et al., 2002), U Mon (Preston, 1964; Bopp, 1984; Shenton et al., 1994b), RU Cen and SX Cen (Maas et al., 2002, both stars), (Shenton et al., 1994a, SX Cen only) all being studied in more detail.

Of primary interest in this work are the pulsational properties of the RV Tauri stars, as represented by the selection shown in Table 7.1. Of the pulsational properties, several areas are of interest. The first is the connection to the shorter period Type II Cepheids, examining the similarities in radial velocity curve and shock related features as we move to longer and less reliable periods. The second is related to the periods themselves and the alternations in deep and shallow minima which characterize the RV Tauri stars. Here we wish to examine the radial velocities and line profiles as a function of phase based on both the 'single' periods (between successive minima) and 'formal' periods (between successive deep minima), to see if the photometric changes are detectable on a spectroscopic level in the wavelength range examined. Thirdly, we wish to examine the spectroscopy in connection with the long-term photometric changes observed in the RVb stars, to see if there are links between these, and also to see if long-term spectroscopic variations occur in the RVa stars which do not show up in the photometry. These latter changes may in fact be orbital rather than pulsational, but they do need to be examined in case they affect the pulsations of the stars.

To this end, three stars have been singled out for quantitative review of the three areas of interest: TT Oph, RU Cen, and U Mon, with the remaining stars (SX Cen, AI Sco, AR Pup, AR Sgr, R Sct and IW Car) briefly qualitatively reviewed for evidence of similar

Table 7.1: Starting parameters for RV Tauri stars.

	period (days)	epoch[a]	Photometric type	Spectral type	Min. V	Max. V
TT Oph	60.97	11251.709	RVa	RVA	9.4	10.7
RU Cen	64.57	11295.618	RVa	RVB	8.5	9.8
U Mon	91.79	9326.507	RVb	RVA	5.5	7.8
SX Cen	32.82	11292.410	RVb	RVB	9.1	11.4
AI Sco	71.45	11263.092	RVb	RVA	8.8	11.2
AR Pup	76.47	11226.331	RVb	RVB	9.1	10.1
AR Sgr	87.13	11236.023	RVa	RVA	9.1	10.4
R Sct	134.87	11075.524	RVa	RVA	4.9	6.7
IW Car	142.73	11204.448	RVb	RVB	7.8	9.2

[a]From photometric phasing. Epoch = JD - 2440000.

features.

7.1 TT Oph

While not possessing the shortest period of the examined RV Tauri stars, TT Oph (P = 60.97 days) is one of the most regular of the shorter period RV Tauris, and is an RVA star. That is to say, by the Preston et al. (1963) spectral classification scheme the spectral features indicate spectral type G to K, though they may show molecular bands at light minimum. With respect to the analysis presented here, this means that the metallic lines are strong enough to be easily measured and there are a reasonable number present.

Historically, the spectra of TT Oph have been studied reasonably well, though not to as great a degree as the two brightest RV Tauri stars (R Sct and U Mon). Joy (1952) established it as varying between spectral types G2e and K0 based on atomic line behaviour, with no signs of TiO bands, a mean velocity of -50 kms^{-1} and a range of 45 kms^{-1}. Its regularity of behaviour was commented on even then and, as pointed out in Section 4.4.2, it had a regular light curve with a small difference in depth between deep and shallow minimum (now observed as V=10.4–10.7). Since 1952, spectroscopic studies have been done by Preston et al. (1963), Cardelli and Howell (1989) and Wahlgren (1992), with abundances derived by Giridhar et al. (2000). Not since those earlier observations has anyone examined the pulsational characteristics in detail.

As a continuation of the dynamical work, it was decided to test the acceleration phasing on one of the RV Tauri stars, to see if it was applicable at the longer periods, with the more complicated radial velocity curves. TT Oph has been chosen for this due to its regular period and abundant metallic lines. It also shows a phase lag in the colours, which leads to ambiguities in phasing with a photometric minimum. As with the previous stars, the Fe I line velocities have been selected as being representative of the mean photospheric motion. As a greater number of these lines show line splitting at various phases, it was decided to measure a smaller selection of Fe I lines of a range of excitation potentials and line strengths. These line velocities are shown in Figure 7.1 and their excitation potentials

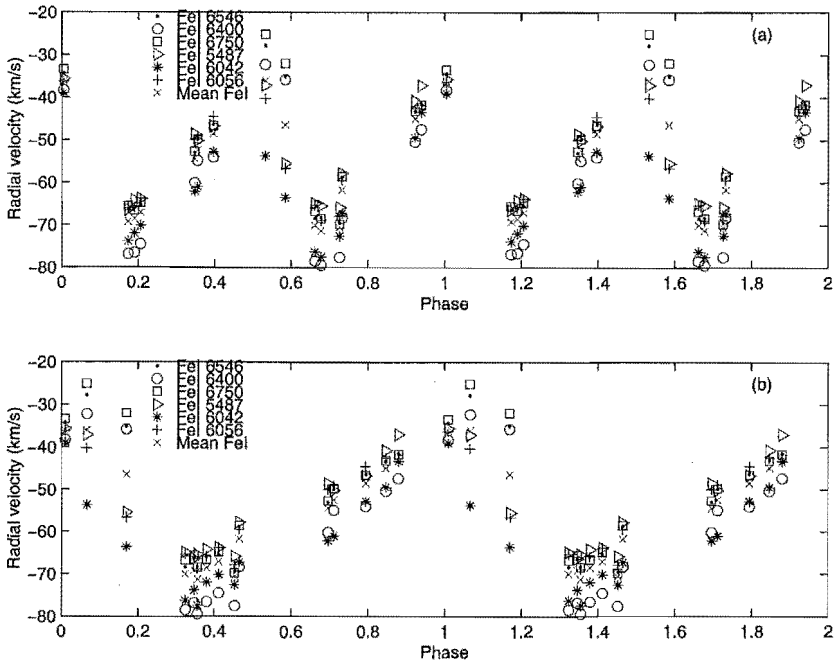

Figure 7.1: Selected Fe I radial velocities for TT Oph phased on photometric epoch.
(a) Phased on 60.97 day period.
(b) Phased on 30.485 day period.

and log(gf) values are given in Table E.6.

As can be seen from Figure 7.1, the Fe I line velocities are scattered over more than 10 kms^{-1} for the same phase for most of the pulsation cycle, with the greatest difference observed at phases 0.5–0.6 (Figure 7.1a), which is just after the shallow minimum. This is much larger than the scatter observed in even the longest period W Vir stars for Fe I, and reflects the effect of the longer period indicative of a larger star. The Fe I lines form at a physically wider range of depths such that different mean motions in the line forming regions may be detected depending on the excitation potential and intrinsic strength of the line. In the W Vir stars previously examined, this is mainly visible between species, with the effect getting larger for the longer period stars. W Vir shows this for iron, as the velocity differences becomes larger between Fe I and Fe II (Section 6.4).

Another area of investigation in comparing W Vir and RV Tauri stars is that of repeatability between deep and shallow minima, and if and how these may be different. For this reason radial velocity curves and equivalent widths have been phased on both a 60.97 day period between successive deep minima and a 30.865 day period between successive minima (see Figure 7.1a and b). The iron velocity curve phase well on both periods, producing smooth velocity curves in each. These curves have been averaged to form a mean Fe I velocity curve, and this curve has been spline fitted and differentiated to obtain an acceleration curve. As with the shorter period stars, projection factors have not been taken into account as phasing is based on the minimum phase position and not an absolute value. The results for each period are shown in Figures 7.2 and 7.3.

The velocity and acceleration curves derived are very similar in shape to those derived from AL Vir (Figure 6.8) and VY Pyx (Figure 5.1). The schematic shape of the accelera-

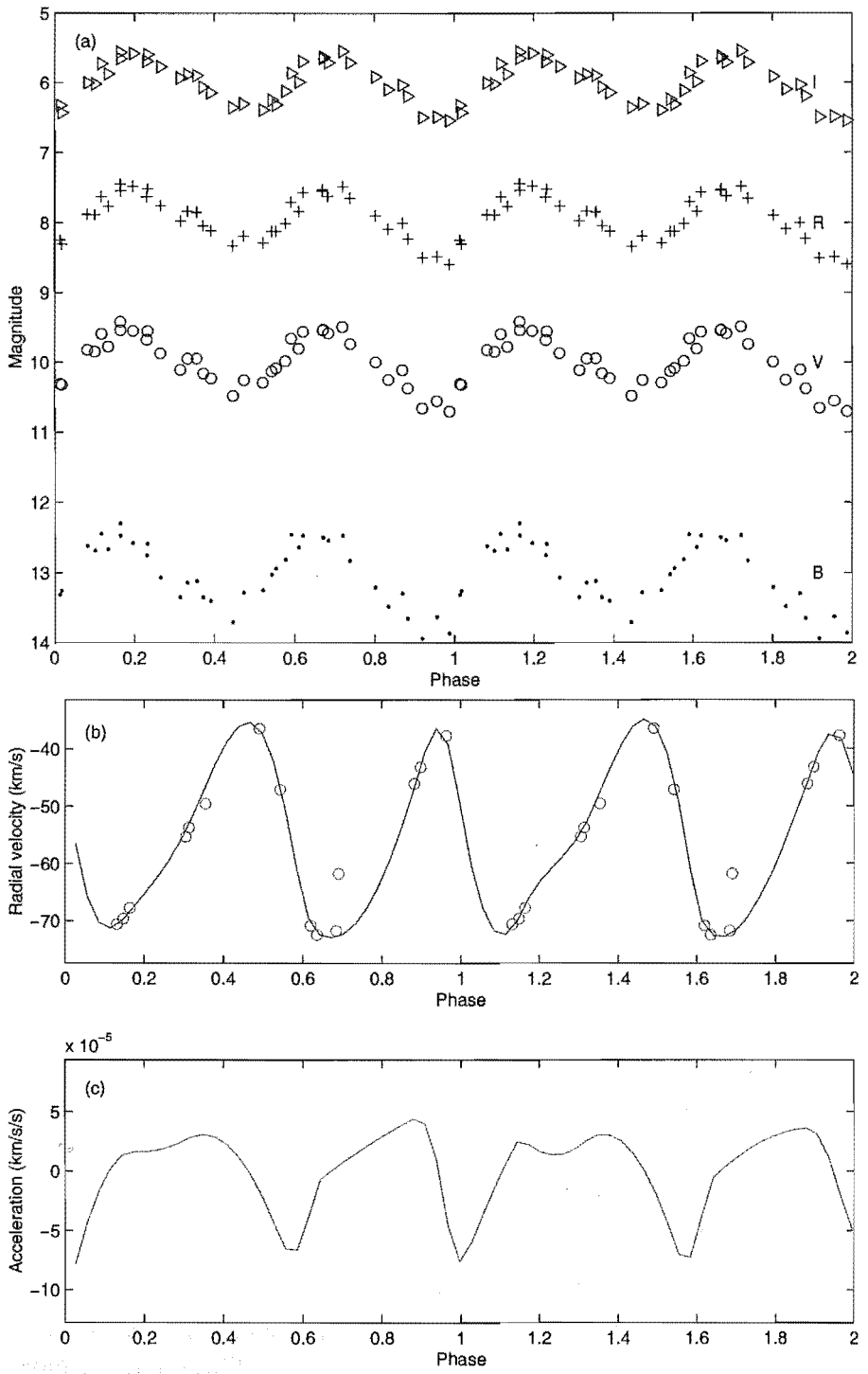

Figure 7.2: (a) *BVRI* magnitudes, (b) Fe I radial velocity and (c) acceleration curves of TT Oph phased on 60.97 day period. *B* photometry has been offset by 2 magnitudes, *R* by -1.5 and *I* by -3.

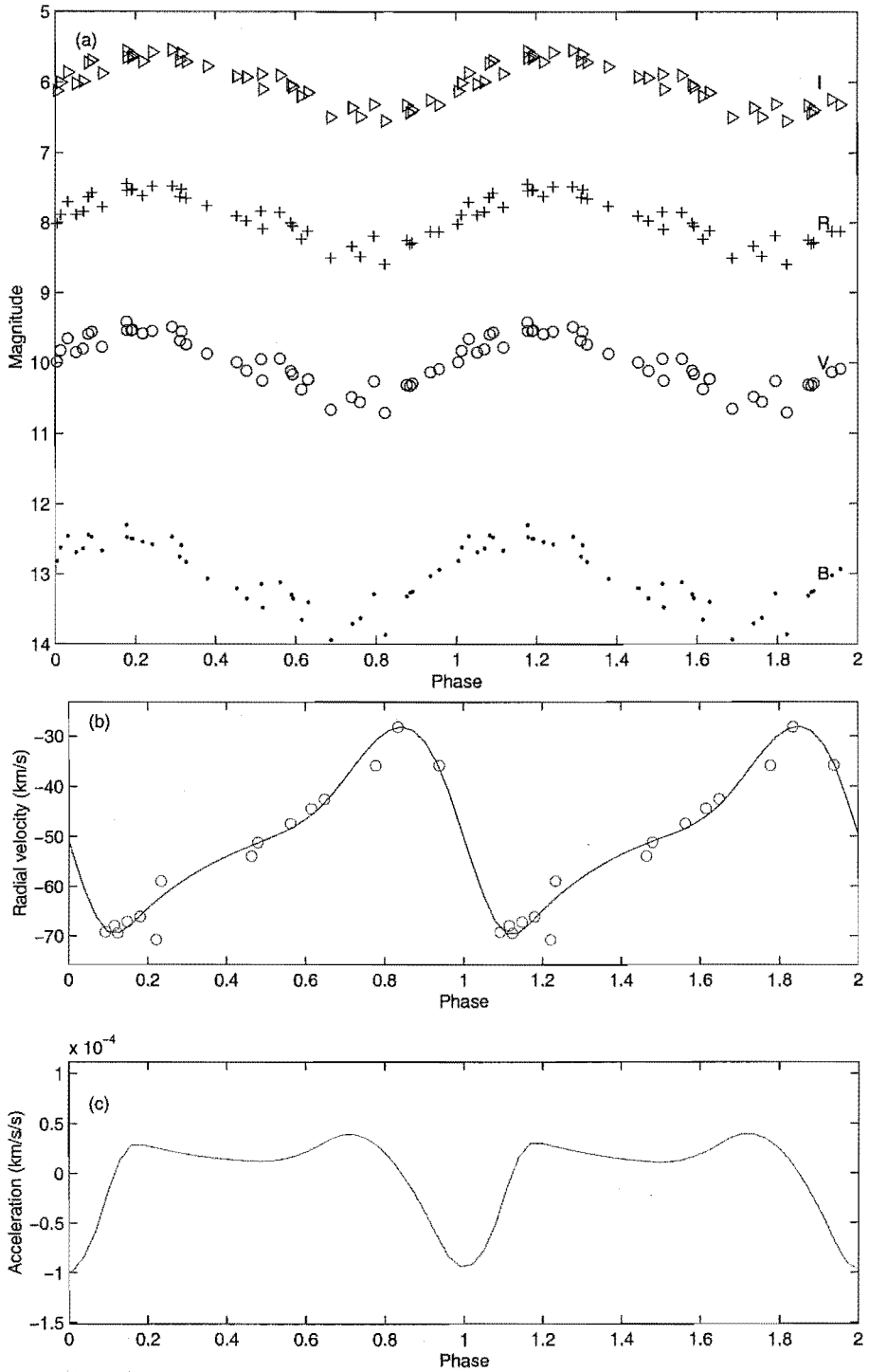

Figure 7.3: (a) *BVRI* magnitudes, (b) Fe I radial velocity and (c) acceleration curves of TT Oph phased on 30.485 day period. *B* photometry has been offset by 2 magnitudes, *R* by -1.5 and *I* by -3.

tion curve does not really change whether the star is phased on the 90 day or the 30 day period. There are however slight differences as to where the acceleration phasing places phase 0.0 on the light curve. Figure 7.2 phases maximum deceleration and minimum photospheric radius just after deep photometric minimum, whereas Figure 7.3 phases this more than halfway between maximum and minimum light. This difference is more likely due to the differences in phase coverage for each period rather than actual physical differences. Such phasing differences are also most likely responsible for the differences in velocity curve shape between phases 0.1–0.6 and 0.6–0.1. Confirmation of this would require further spectroscopic observations.

7.1.1 Spectroscopy

Due to the less regular line behaviour, stacked spectra will be displayed before examining radial velocity curves in detail. Also, rather than averaged velocities (except for Fe I) for a certain species, selected lines will be examined individually.

Na D and associated lines

Spectra around the Na D lines have been phased and stacked on a period of 60.97 days (Figure 7.4). The Na D lines show multiple components with the red-ward component not varying as a function of pulsational phase. This component is most likely interstellar in origin.

Another line of interest in this spectral region is the He I (emission) line at 5876 Å, as its presence clearly indicates the passage of a strong shock through the line forming regions, and in W Vir correlates with maximum deceleration and minimum photospheric radius. Slight emission is observable in cycles 7 and 13 at phases 0.13 and 0.54 respectively. However the emission is not large and the spectra are quite noisy. The spectrum at 7.13 is just prior to primary light maximum and around the start of minimum Fe I radial velocity, whereas cycle 13.54 is midway towards secondary light maximum and just before the shallower acceleration minimum. More observations are needed at these crucial phases (0.95–0.05) to determine if the He I emission is stronger at these phases or if there is a systematic difference in amplitude between the emission following deep minimum and the emission following the shallow minimum, indicating a difference in shock strength.

The other lines of interest in this region are the cluster of five lines between 5850 and 5868 Å. These consist of Ba II (5853 Å), Ca I (5857 Å), two Fe I lines at 5859 and 5862 Åand a Ti I line at 5866 Å (see Appendix E for exact rest wavelengths, excitation potentials and log(gf) values). These lines are of interest in terms of their changing profile as a function of pulsational phase, as this behaviour is a good indication of the presence of shock waves in the line forming region. This has already been seen in the case of W Vir (Section 6.4.1), when these same lines are most visible between phases 0.27-0.63 and disappear almost completely at phase 0.00 when the shock enters these line forming regions (Figure 6.18). While these lines do not disappear completely in TT Oph, indicating temperatures are not as high as for W Vir at the equivalent phase, the line strengths do vary as a function of pulsational cycle. This shows most clearly in the Ti I 5866 Å line, which is very temperature sensitive, and most easily affected by shocks. This line is weakest at phase 0.13, but gains in strength until phase 0.49, where it has disappeared in absorption, and now appears in emission. The next spectrum (in cycle 13 at phase 0.54)

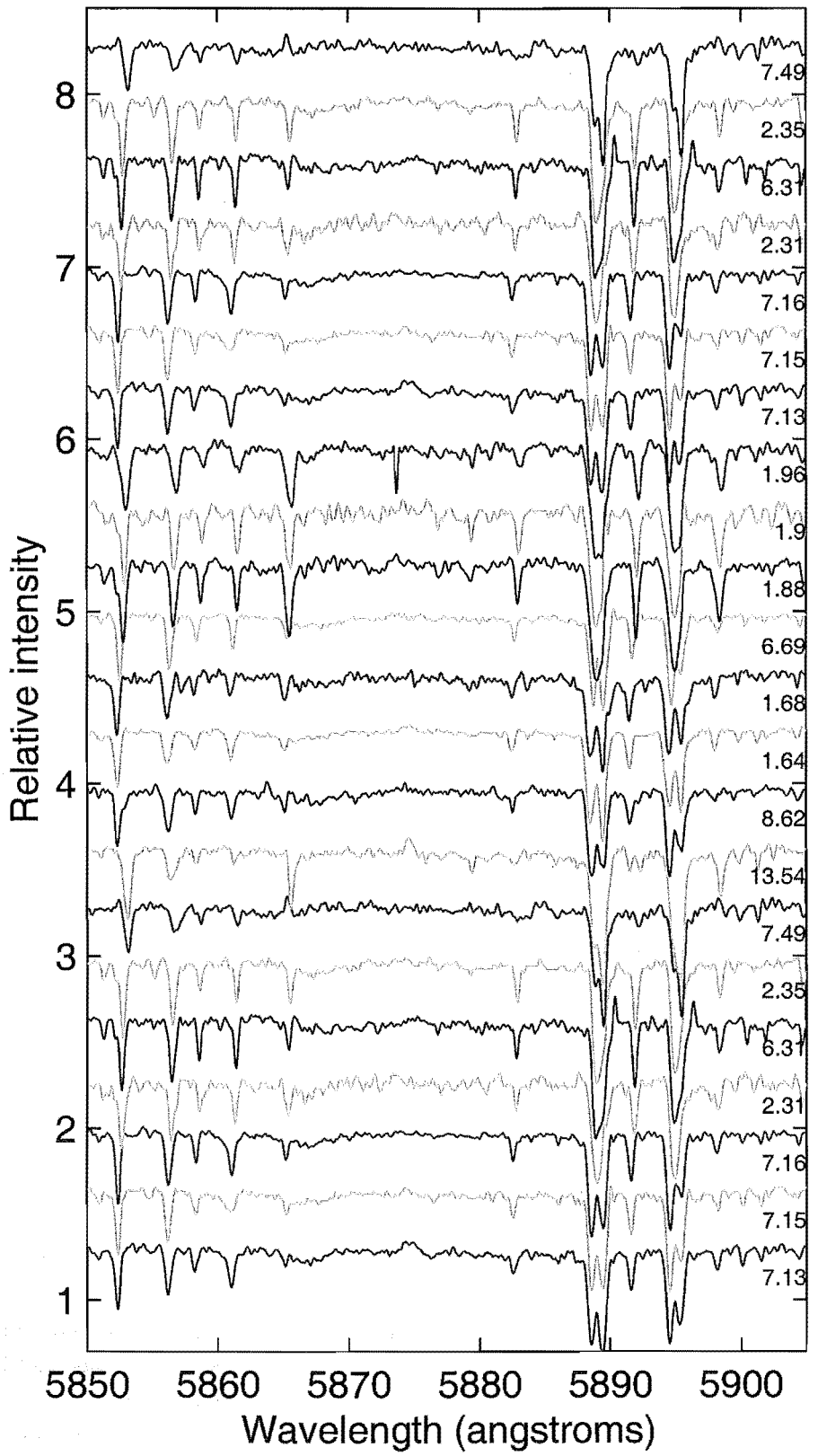

Figure 7.4: TT Oph stacked Na D and He I 5875 Å lines, phased on a period of 60.97 days.

shows it in strong absorption, but the other lines present are of similar strength to those observed in the previous spectrum (7.49). This may just be cycle to cycle variations, as by phase 0.62, the Ti I line is back to being weak. Then, it slowly strengthens to phases 0.88–0.96 where it is at its strongest, before nearly disappearing again by phase 0.13. This behaviour, combined with that of the He I 5876 Å emission, indicates shock waves in the line forming regions in the vicinity phases 0.13 and 0.54. Unfortunately gaps in the phase coverage in these regions mean that higher time resolution of the shock behaviour cannot be obtained without more observations. However more information can be obtained from examining the Hα profiles.

Hα and associated lines

As can be seen from Figure 7.5, the Hα line behaviour is similar to that observed in W Vir (Figure 6.19). In TT Oph it is always in emission, with two main emission peaks which vary in amplitude as a function of pulsational phase. Between these two emission peaks there is a strong absorption line which varies in depth, but not in position. The overall Hα profile is most likely to be composed of a single emission component created in the relaxation zone behind the shock, overlaid by an absorption component created further out, in a region unaffected or minimally affected by the star's pulsations.

Examining the Hα line behaviour quantitatively (equivalent widths, see Figure 7.6), there are clear variations as a function of pulsational phase. When phased on the 60.97 day period (Figure 7.6a), two distinct peaks are visible at phase 0.54 ($\sim$ 4.5 Å) and at phase 0.05 ($\sim$ 1.5 Å). However the amplitude and exact phase for the peak associated with deep minimum light are extrapolated from the fitted curve and are unreliable. When rephased on the 30.485 day period (Figure 7.6b), the peaks combine smoothly to produce a single peak of amplitude 4.5 Å at phase $\sim$0.95. The He I 5876 Å equivalent widths have also been plotted, but as their amplitude is lost amongst the noise of the individual spectra for most phases, there is little information there, except that as mentioned earlier from the stacked spectra (Figure 7.4), phases 0.13 and 0.54 (60 day cycle) showed the most definite emission. More observations at these phases are required to confirm these details.

Another line of interest in the stacked spectra of Figure 7.5 is the Fe I line at 6546 Å. As the Hα line structure is unsuited to line bisector analysis, this metallic line has been chosen instead as it shows slight signs of broadening, splitting and even possible emission as a function of pulsational period. Figure 7.7 shows the velocities of this line at line bisector depths of 0.5 and 0.9 for both periods. The line stays quite symmetrical at all phases, as both velocities agree well with each other, with the greatest velocity difference occurring at phase 0.54 (60.97 day period), just after shallow minimum, and phase 0.95 (30.485 day period), further after light minimum. This is also observed when the line velocities and widths for the different line bisector depths are plotted as a function of pulsational phase (Figure 7.8). Examining the vectors connecting the 0.5 and 0.9 depth velocities, the direction of the slope indicates that the line asymmetry is quite small and apparently randomly fluctuating, and the line widths are relatively constant at most phases. They reach a maximum line width around phase 0.5–0.6 (Figure 7.8a) and 0.9–0.0 (Figure 7.8b). It should be noted that this method of line analysis is not completely quantitative, as the depths 0.5 and 0.9 are relative and do not indicate the absolute line depths as observed by the shallowness of the Fe I 6546 Å line at phases 0.49 and 0.54 in

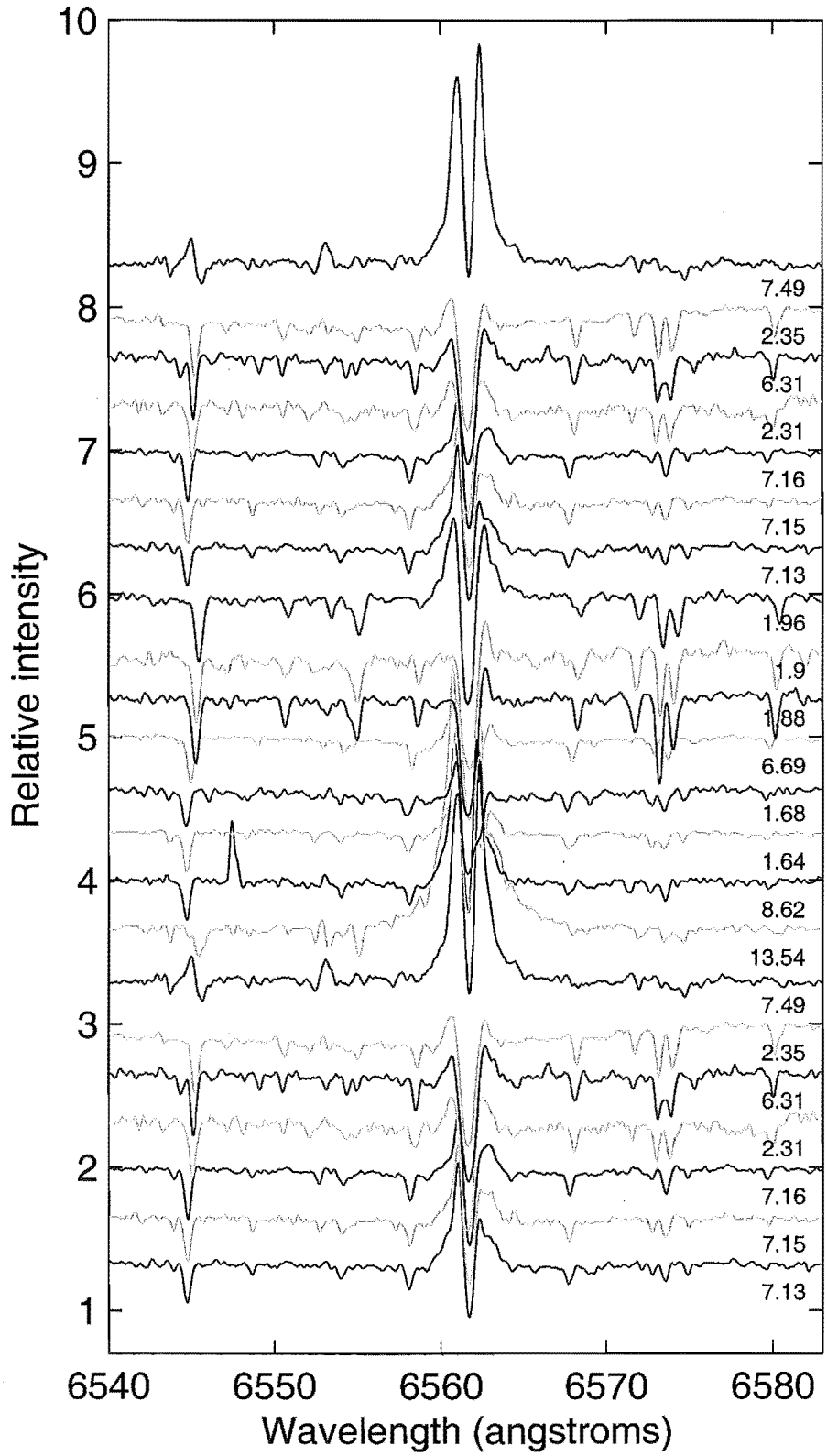

Figure 7.5: TT Oph stacked Hα lines and associated wavelengths, phased on a period of 60.97 days.

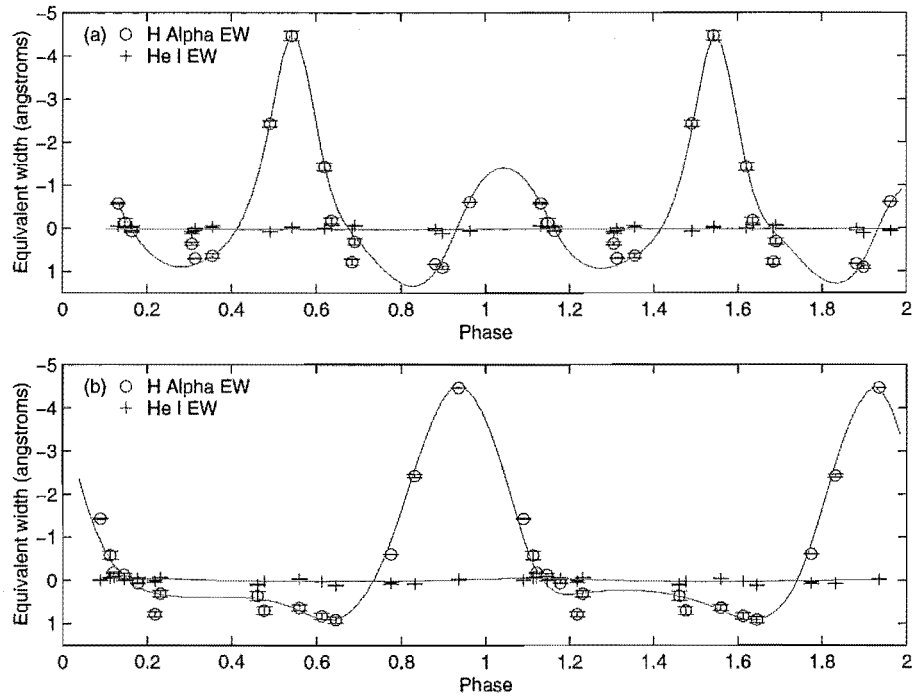

Figure 7.6: Hα and He I 5876 Å equivalent widths for TT Oph.
(a) Phased on 60.97 day period using acceleration phasing from Figure 7.2.
(b) Phased on 30.485 day period using acceleration phasing from Figure 7.3.

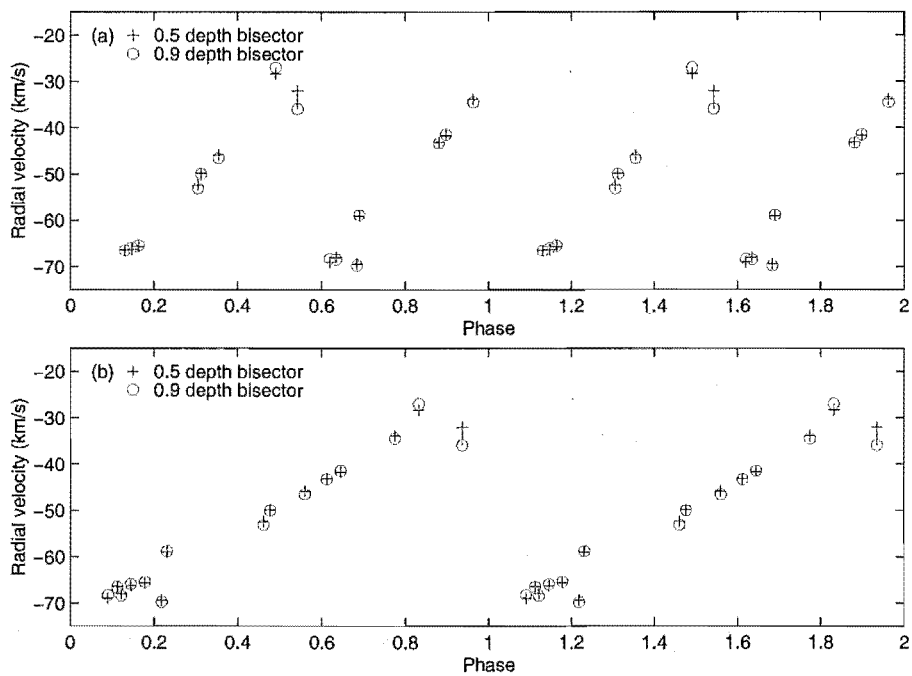

Figure 7.7: Radial velocity curves of TT Oph, measured from Fe I line (6546Å) using line bisector velocities at depths of 0.5 and 0.9.
(a) Phased on 60.97 day period using acceleration phasing from Figure 7.2.
(b) Phased on 30.485 day period using acceleration phasing from Figure 7.3.

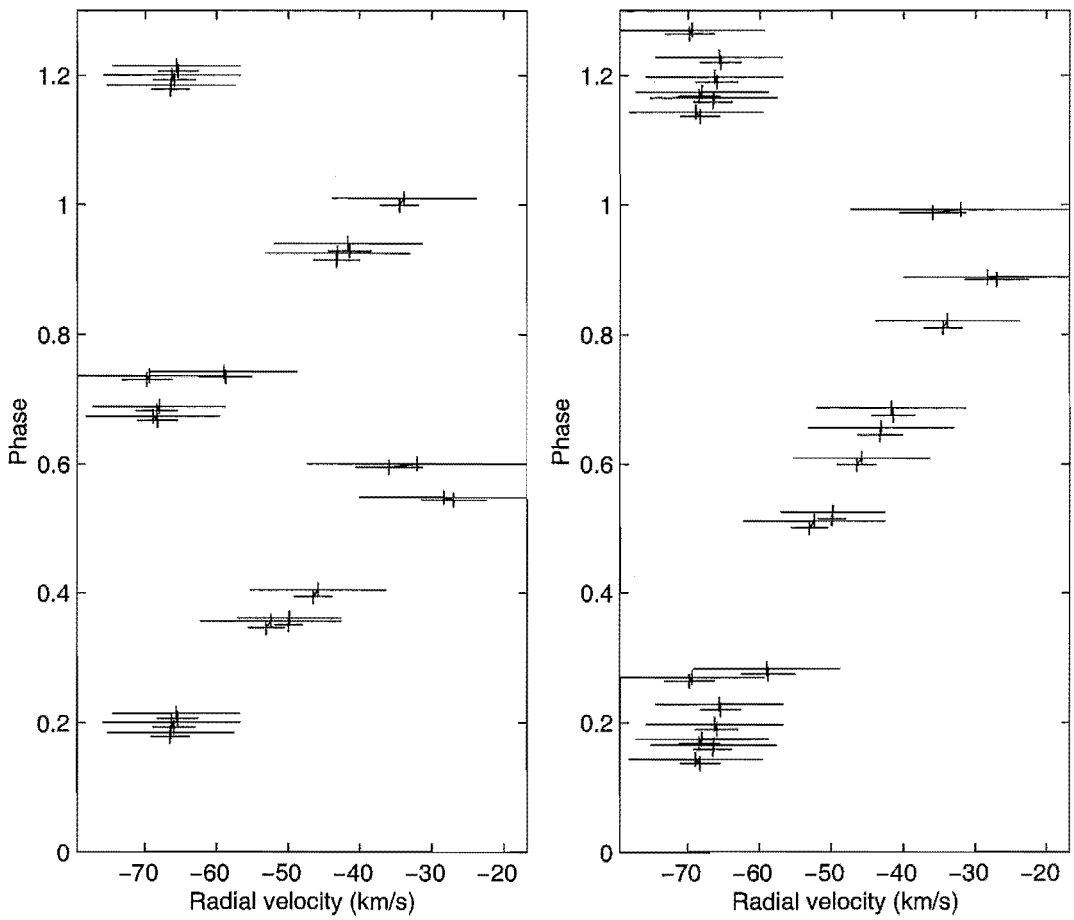

(a) Phased on 60.97 day period.

(b) Phased on 30.485 day period.

Figure 7.8: TT Oph stacked Fe I line (6546 Å) lines.

Figure 7.5.

Ca II lines

The final lines to be stacked are the Ca II lines at 8498 and 8542 Å (Figure 7.9). These show stronger evidence for shocks with multiple components as a function of pulsational phase, especially the stronger line at 8542 Å. This line shows two clear components at phases 0.49–0.62, and is distinctly broadened in the wings at phases 0.9-0.96, and 0.31-0.35, leading up to the 0.49 phase splitting. The 8498 Å line shows similar trends, with less prominent line splitting, which is mainly observed at phase 0.49. This line splitting, may also be interpreted as an emission line occurring in the middle, or to the blue edge of a single absorption line. There is definitely emission in the 8542 Å line in 13.54. However there is also line splitting observable there as well. Unfortunately, with many of the other spectra, it is difficult to quantify the differences between emission and line splitting.

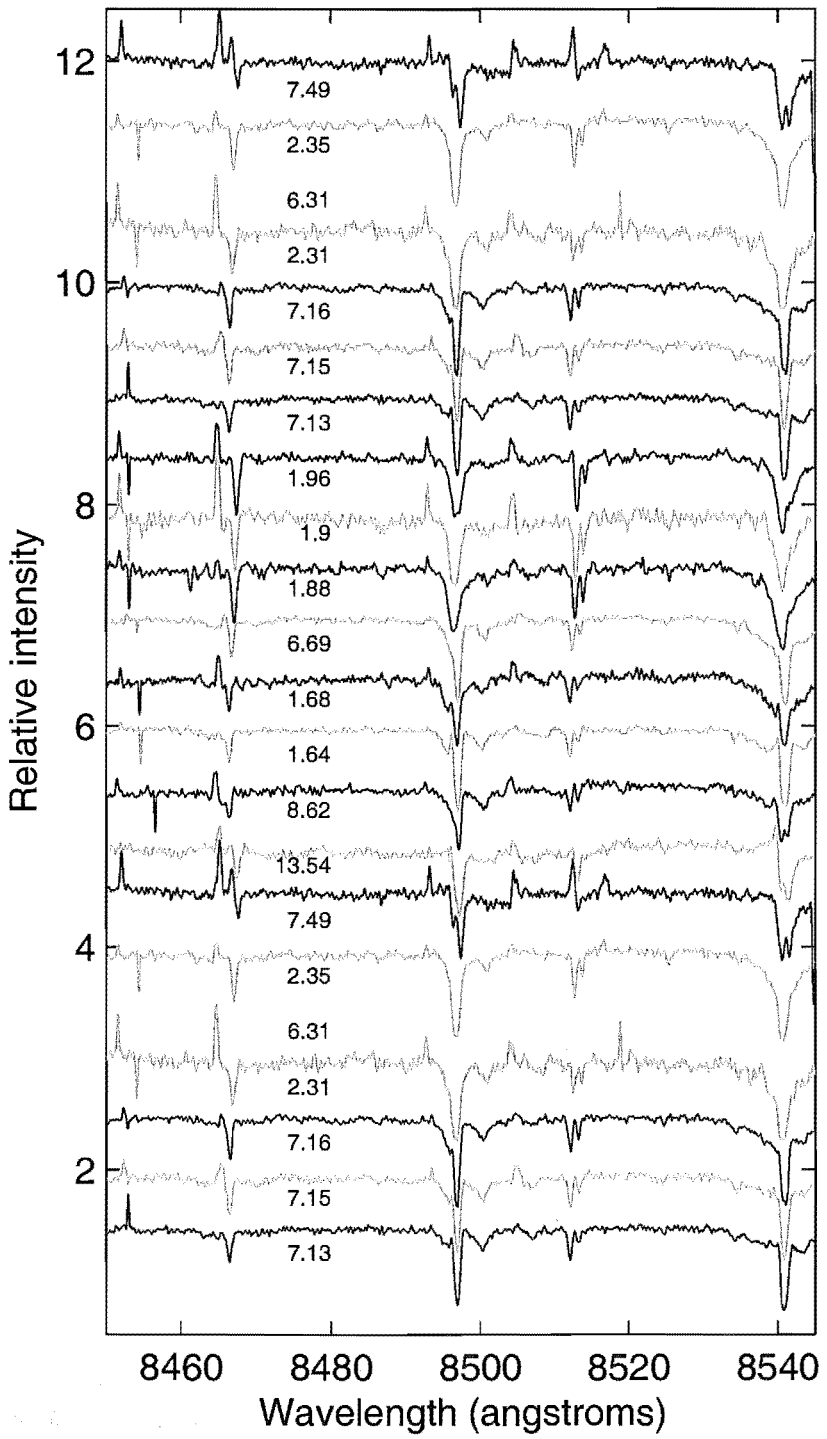

Figure 7.9: TT Oph stacked Ca II lines.

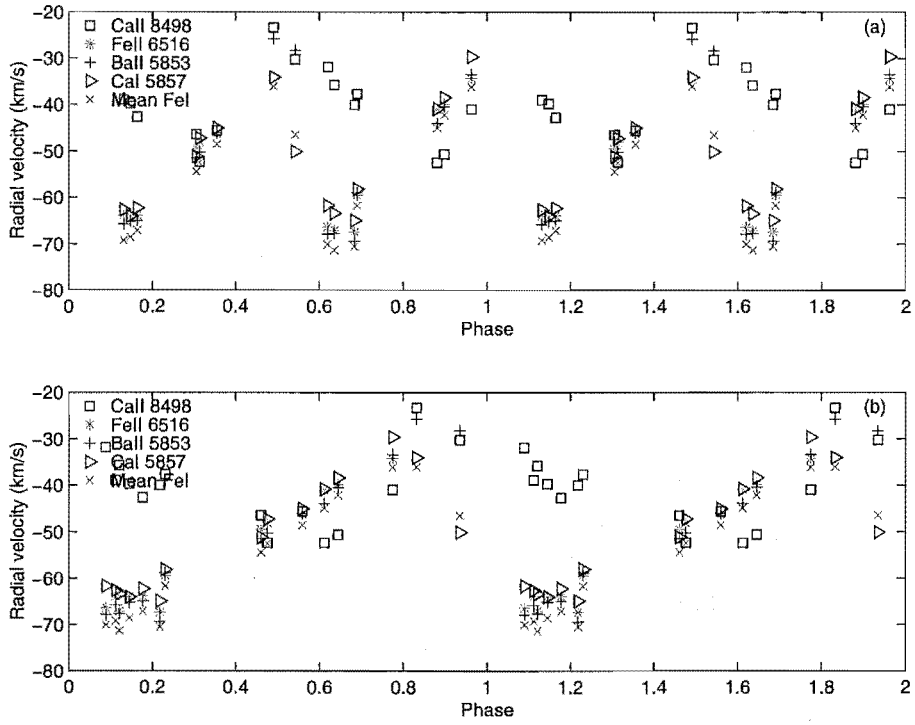

Figure 7.10: Radial velocity curves of TT Oph, measured from the mean Fe I velocities, Fe II (6516 Å), Ba II (5853 Å), Ca I (5957 Å) and Ca II (8498 Å).
(a) Phased on 60.97 day period.
(b) Phased on 30.485 day period.

Radial velocity curves

The velocities from the Ca II line at 8498 Å have been measured and, along with a selection of other lines from other species including the Fe I mean velocities, are displayed in Figure 7.10. The line amplitudes and phases of maximum and minimum are shown in Table 7.5.

The lines show quite similar behaviour apart from the Fe II line, which becomes unmeasurable around secondary maximum light, and the Ca II line. This line is most likely being red-shifted in velocity due to the possible emission component which appears at phases 0.1–0.2 and 0.6–0.7 (60.97 day period) and phases 0.1-0.25 (30.485 day period). The velocities show similar degrees of scatter at maximum and minimum velocity for both the formal and successive minima periods and during the primary and secondary minima.

For this and the emission results, it is clear that for TT Oph, there is little difference between primary and secondary light maximum which, given the lack of difference in depths between the light minima, is unsurprising. It may be that there are some slight differences between the two components of the pulsation cycle but to investigate that, more coverage of the star during rising light is required.

7.2 RU Cen

RU Cen (P = 64.57 days) is also an RVa star showing no signs of a long term variation in the mean photometric amplitude. However its classification based on its spectral variations is quite different to TT Oph. By the Preston et al. (1963) classification scheme, RU Cen is an RVB star as it has weak lines and shows enhanced carbon. As stated in Section 4.4.3, the most recent and comprehensive spectroscopic studies have been Pollard et al. (1997)and Maas et al. (2002), and these should be referred to for previous historical references.

Because of its weak lines, there is little radial velocity work on RU Cen. Pollard et al. (1997) and Maas et al. (2002) both include radial velocities for various pulsation cycles, with Maas et al. (2002) using the large variation in velocity between pulsational cycles to argue for RU Cen being a spectroscopic binary. Both authors also examined Hα equivalent widths, finding two emission peaks per 64 day pulsational cycles, associated with the passage of two shock waves per pulsation cycle. Maas et al. (2002) also found He I (5876 Å) emission, whose equivalent width also peaked twice per pulsational phase, but with a phase delay of 0.08-0.09 between the He I and Hα equivalent width peaks.

The weak lines of RU Cen have lead to practical difficulties in terms of finding metallic lines. The two previously cited papers used C I (6587 Å) (Pollard et al., 1997) and cross-correlation (Maas et al., 2002) to establish the velocities. To attempt to dynamically phase the data using the acceleration minimum, the mean photospheric motions could not be represented by the mean motions of the Fe I lines, as was done with TT Oph. The C I line proved too weak and scattered (see Figure 7.16 and subsequent discussions) and cross correlation would mask line level effects, so instead the velocities of the Ba II line at 5853 Å have been used. It should be noted that from the work on TT Oph (Figure 7.10), the Ba II radial velocities had a higher amplitude, and obtained peak amplitude shortly after the Fe I velocities. This means there may be a slight phasing difference, as both are phased based on the motions of slightly different regions of the star. However, since there are no Fe I lines observed in the wavelength range examined here, and the phase difference observed in TT Oph is only of the order of 0.05 of a pulsational cycle, the gains have been thought to outweigh the risks.

Spline curves have been fitted to the Ba II radial velocities for pulsational cycles 4 and 5 (Figures 7.11 and 7.12). Only these cycles have been used, to eliminate as much of the cycle to cycle variation as possible. These two consecutive cycles showed least difference in velocity variation. From these spline curves, acceleration curves have been derived and the resulting acceleration minimum used to rephase the data. As with the previous stars, projection effects have not been taken into account in calculating the acceleration, so the absolute acceleration amplitudes should not be relied upon, but the relative minima positions are accurate.

The RU Cen velocity and acceleration curves of Figure 7.11 and 7.12 are similar to those observed for TT Oph (Figures 7.2 and 7.3), although the acceleration curves more closely resembles that of W Vir (Figure 6.15). This is due to the rapid transition between maximum and minimum velocity, which is most marked in Figure 7.12. Here the shock rapidly moves through the line forming region, reversing the mean motion of the material. From Figure 7.11 the acceleration minimum following the photometric deep minimum is sharpest. However this may be due to the velocities selected in fitting the spline. Figure 7.12 indicates that there is very little velocity difference between the primary photometric

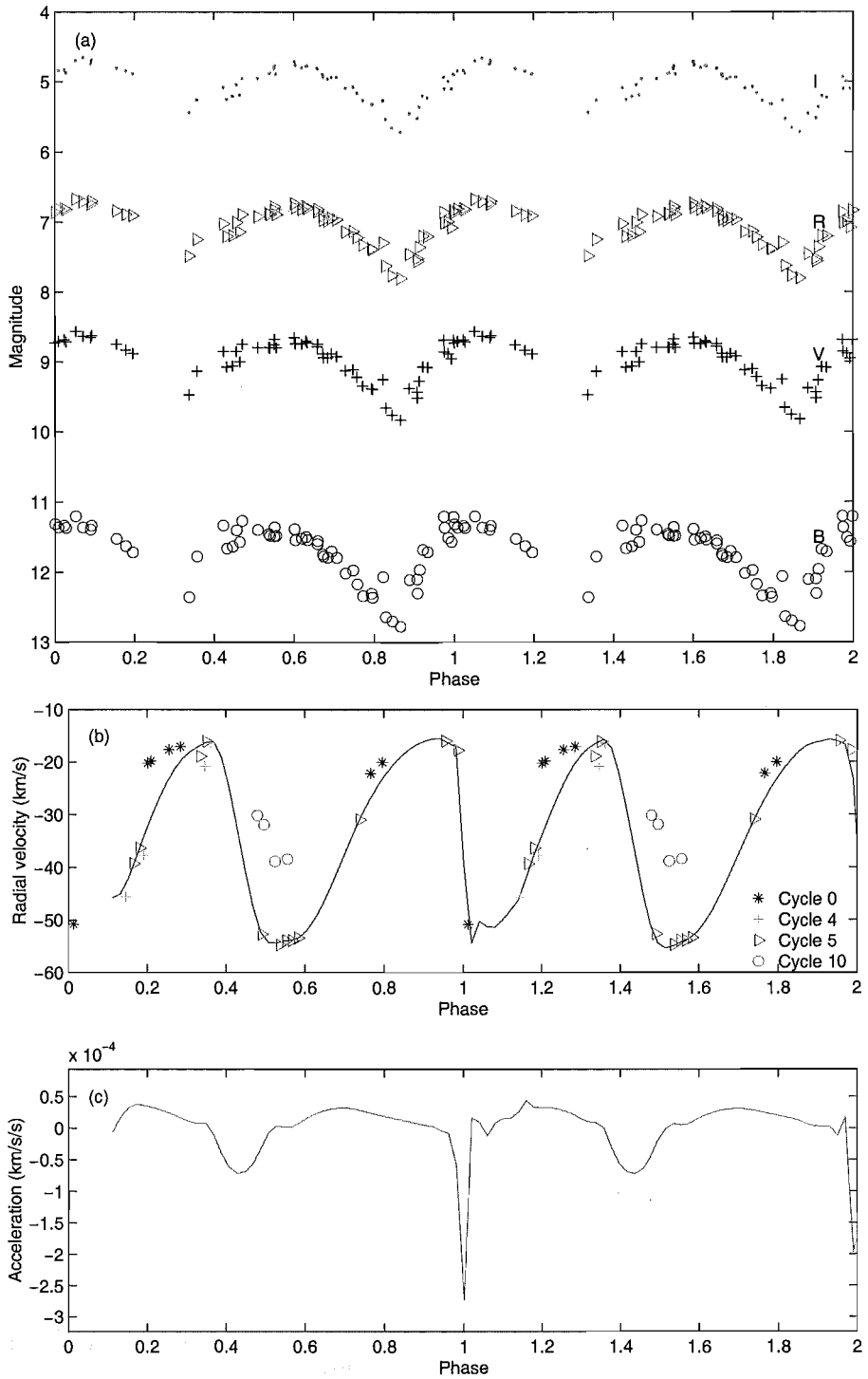

Figure 7.11: (a) *BVRI* magnitudes, (b) Ba II (5853 Å) radial velocity and (c) acceleration curves of RU Cen phased on the 64.57 day period. *B* photometry has been offset by 2 magnitudes, *R* by -1.5 and *I* by -3.

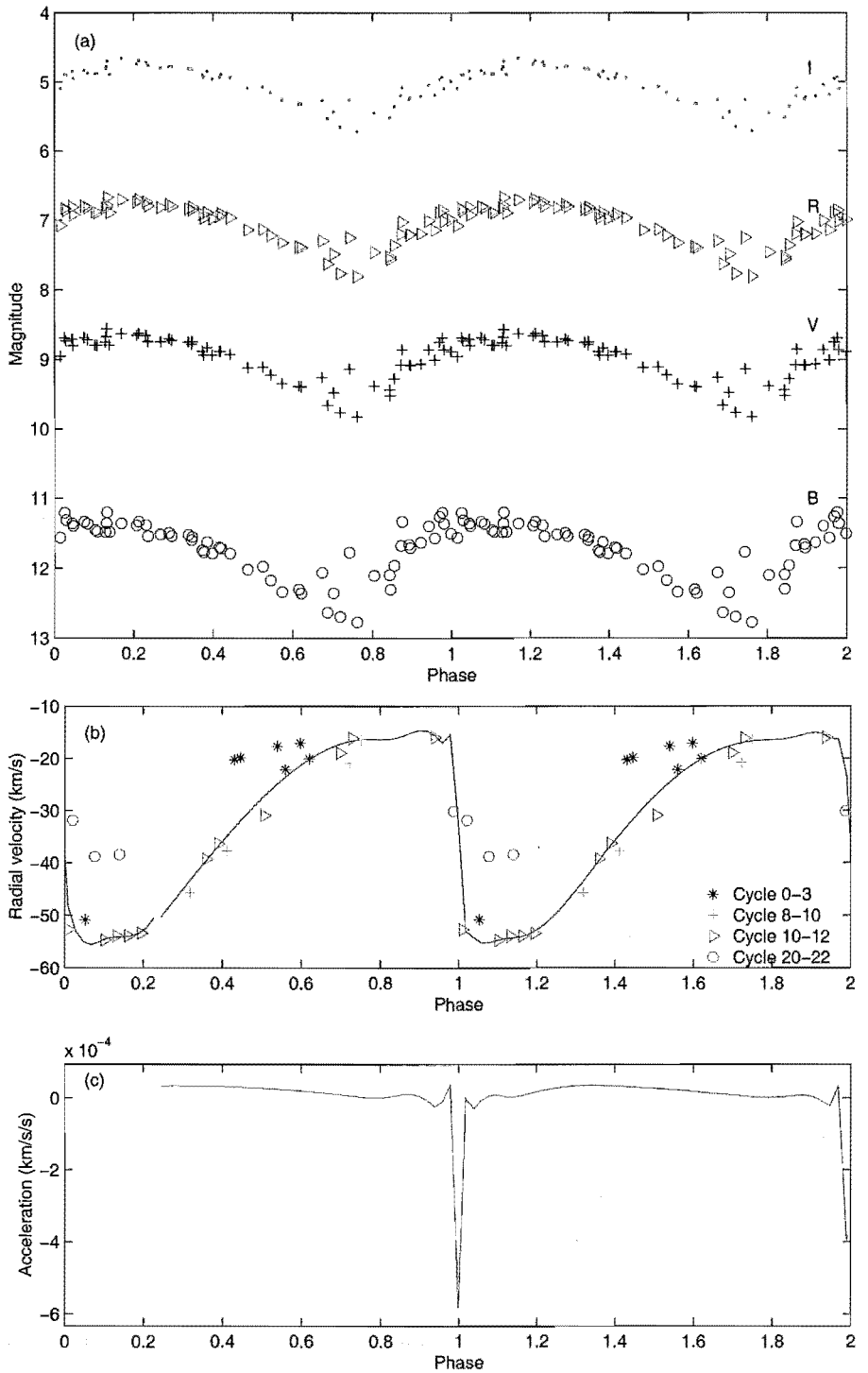

Figure 7.12: (a) *BVRI* magnitudes, (b) Ba II (5853 Å) radial velocity and (c) acceleration curves of RU Cen phased on the 32.285 day period. *B* photometry has been offset by 2 magnitudes, *R* by -1.5 and *I* by -3.

maximum and photometric secondary maximum, as both phase up well on the 32 day period, with a sharp acceleration minimum.

7.2.1 Spectroscopy

Due to the lack of absorption lines to measure stacked spectra will be examined first, before the detailed velocities are extracted.

Na D and associated lines

Spectra centered around the Na D lines have been stacked in order of phase (Figure 7.13). There are three main features: the Na D lines, the He I (5876 Å) emission line and the Ba II (5853 Å) line.

The Na D lines clearly consist of two components. The furthest red-ward component is constant in relative strength and position and is most likely interstellar in origin.

As with W Vir, ST Pup and TT Oph, the He I line at 5876 Å appears in emission at certain phases, and this inversely correlates with the line strength of the Ba II line at 5853 Å. The emission is stronger in RU Cen than with TT Oph, and is observed in more of the spectra (phases 0.44–0.55 and 0.96–0.01), indicating the passage of a shock wave at these phases. This confirms the observation of He I emission reported by Maas et al. (2002), which had not previously been reported for this star.

This emission being inversely correlated with the Ba II line strength has also been noticed in TT Oph (Figure 7.4), although not to as great an extent as the Ba II line is quite strong at most phases. This behaviour is very similar to that observed in W Vir (Figure 6.18), in which the Ba II line almost disappears at phase 0.00 when the shock produces the maximum He I emission.

Hα and associated lines

The other emission of note for RU Cen is that of the Hα line. This varies as a function of pulsational phase, but also shows cycle to cycle variations. In Figure 7.14, the spectra have been stacked both in order of Julian Date (Figure 7.14a) and in order of pulsational phase (Figure 7.14b). From the first of these figures, it is clear that RU Cen shows strong absorption to the blue in cycles 0 and 2. This strong blue-ward absorption does not appear again in any of the subsequent observations. It also does not phase well with the rest of the observations in order of phase. No blue-ward absorption was observed by Pollard et al. (1997) for the same spectral region. Unfortunately the exact same phases were not observed subsequently, and the remaining spectra all show a relatively strong blue-ward emission component. The other spectra in Figure 7.14a and the spectra observed by Pollard et al. (1997) show a constant pairing of two emission components with a central absorption component which all vary in amplitude as a function of pulsational phase (see Figures 8 and 9, Pollard et al., 1997). This is similar to the Hα profile observed in AI Sco (see Figure 21, Pollard et al., 1997) and in some spectra of R Sct (see Figure 2, cycles 3.22–3.24, Pollard et al., 1997). There is no atypical variation in the photometry over the corresponding time period. Thus, the origin of the blue-ward Hα absorption is unclear and more observations of when and if this occurs in RU Cen are required to further investigate this effect.

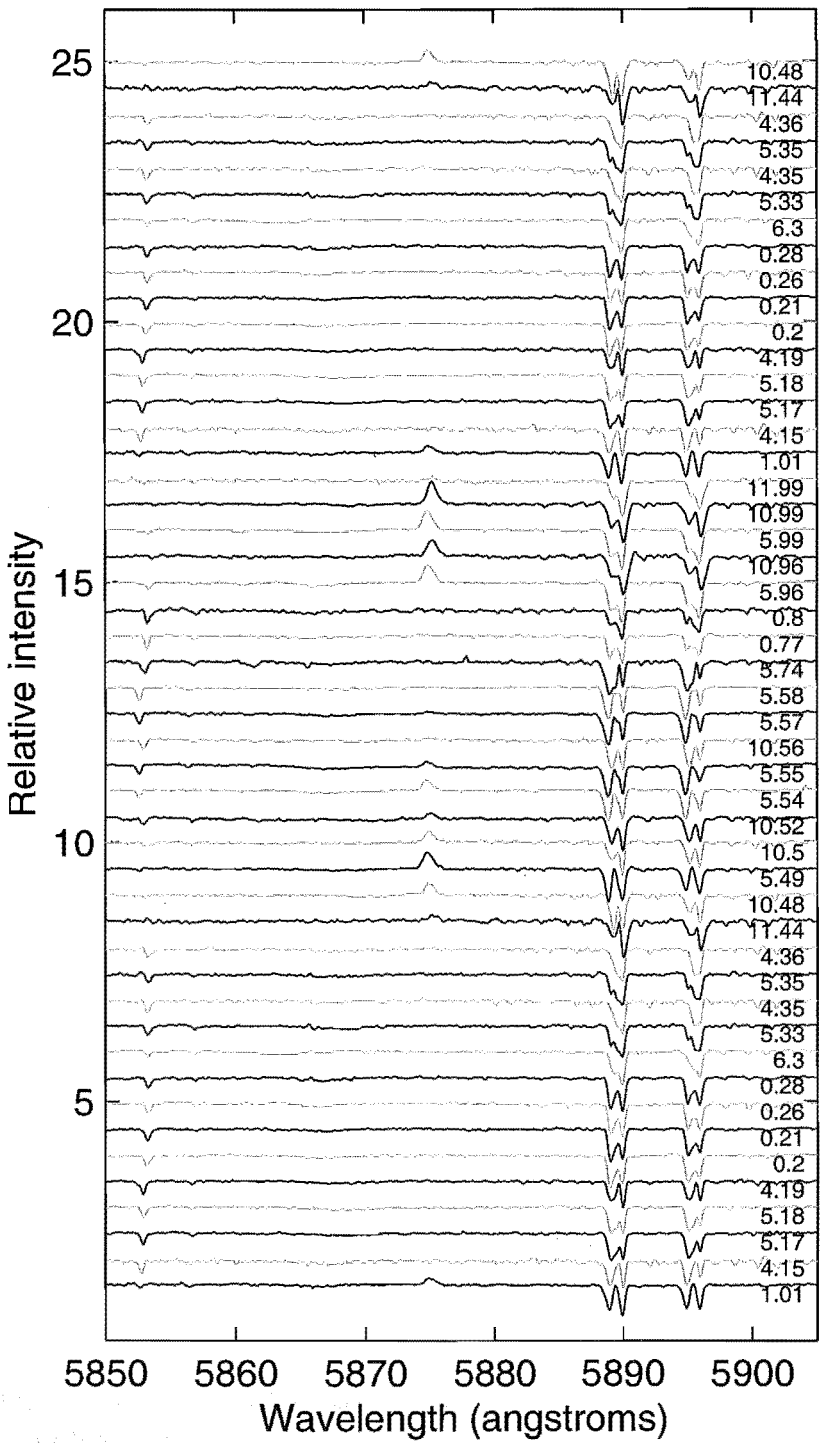

Figure 7.13: RU Cen stacked spectra of Na D lines and associated wavelengths, phased on a period of 64.57 days, using the acceleration phasing of Figure 7.11.

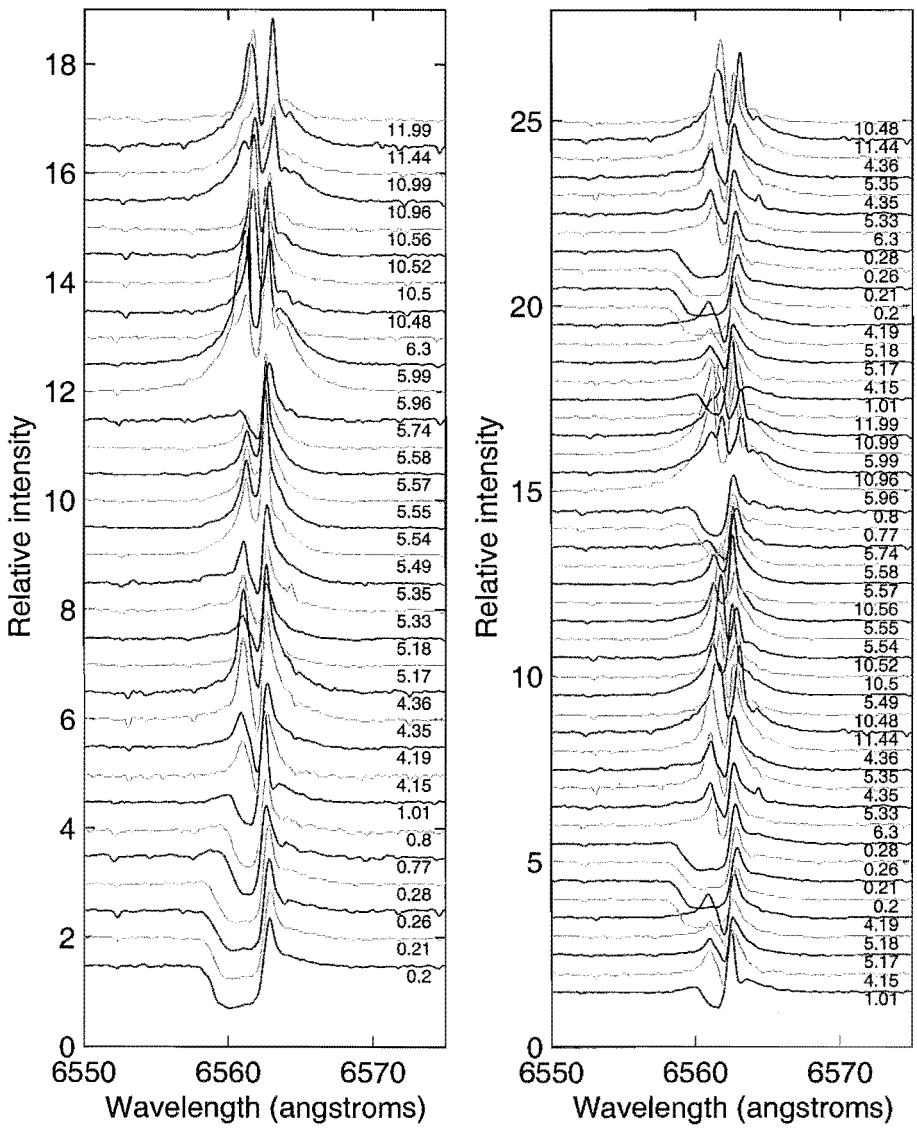

(a) Stacked as a function of Julian Date.

(b) Stacked as a function of phase and phased on a period of 64.57 days, using the acceleration phasing of Figure 7.11.

Figure 7.14: RU Cen stacked Hα lines.

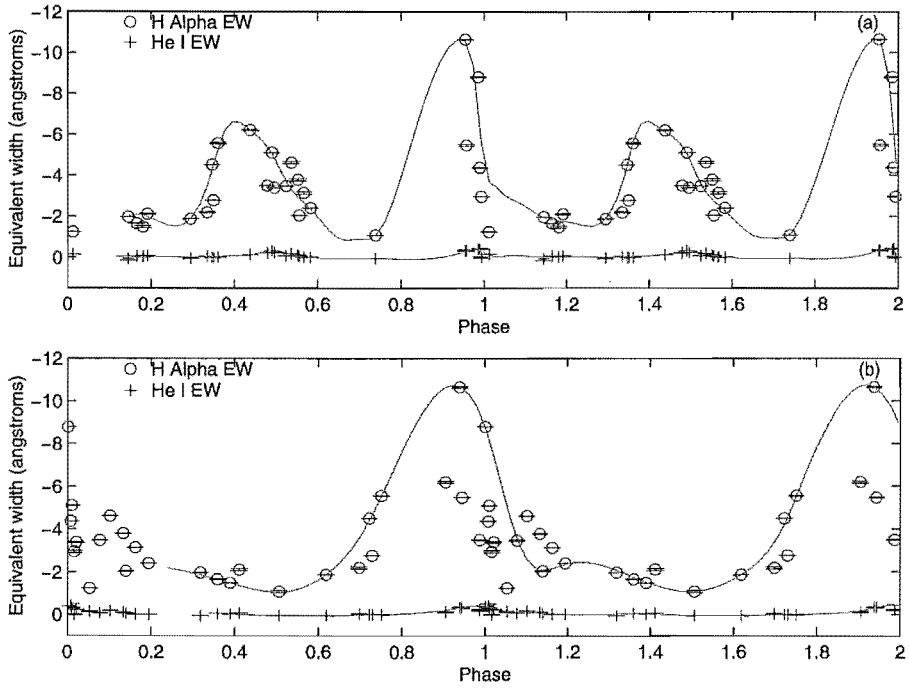

Figure 7.15: Phased Hα and He I equivalent widths of RU Cen.
(a) Phased on the 64.57 day period, using the acceleration phasing of Figure 7.11.
(b) Phased on the 32.285 day period using the acceleration phasing of Figure 7.12.
Equivalent widths for Hα for cycles 0 and 1 have not been included due to atypical absorption components.

If we quantitatively examine the non-atypical Hα emission lines by measuring equivalent widths as a function of phase (Figure 7.15), we see the same trends as were observed by Pollard et al. (1997) and Maas et al. (2002). These are two emission peaks separated by 0.5 pulsation cycles. Phased with respect to the photometric deep minimum (Pollard et al., 1996a), these both show maximum emission at primary maximum. Maas et al. (2002) also shows maximum He I emission around primary maximum, although ~0.1 of a phase after peak Hα emission. The same thing is observed in Figure 7.15a, with the additional acceleration phasing placing maximum He I emission closer to phase 0.0 than the peak Hα emission. This is as observed for W Vir and ST Pup (Figures 6.20 and 6.27 respectively). The He I emission is not exactly centered on phases 0.0 and 0.5, as observed in the alignment of W Vir's He I emission with its acceleration minimum. However this may be due to differences in atmospheric motion between the Ba II line forming regions and the Fe I line forming regions. The amplitude difference observed between the velocities in TT Oph would appear to indicate Ba II forms slightly further out in the stellar atmosphere, compared to Fe I. This is qualitatively what would be expected based on line formation theory.

The other line of interest in the vicinity of the Hα line is the C I line at 6587 Å. This line was measured by Pollard et al. (1997) and these velocities were plotted by Maas et al. (2002) along with their cross-correlation velocities. Observations of the line presented here have been stacked in order of phase separately from the Hα line. The line is very weak, as can be seen from Figure 7.16. At several phases (0.26, 0.28, 6.3, 0.77, 0.8, 5.96,

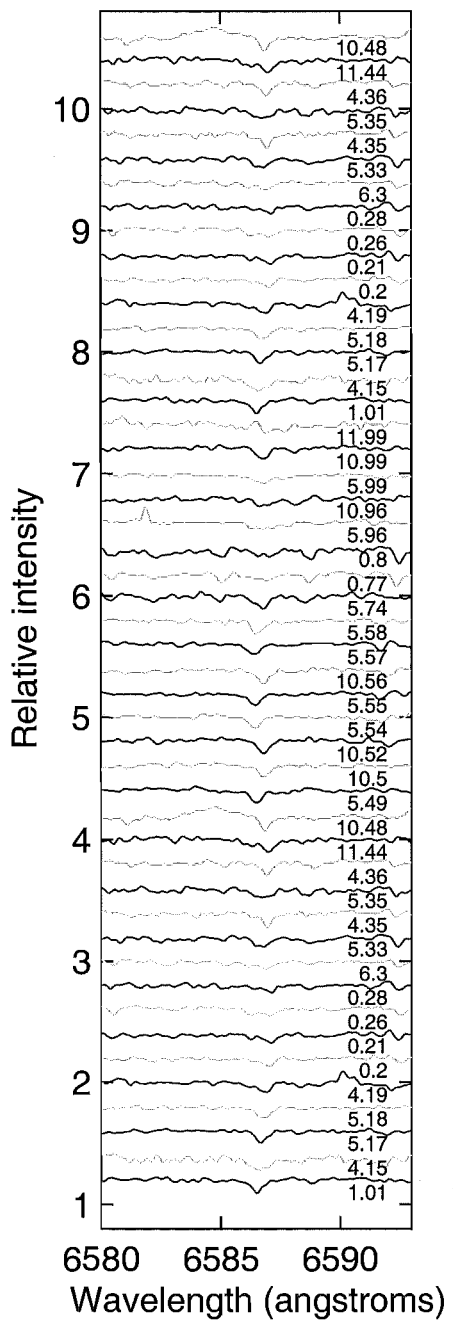

Figure 7.16: RU Cen stacked spectra of C I (6587 Å), phased on a period of 64.57 days, using the acceleration phasing of Figure 7.11.

and 10.96) it is barely discernible from the background noise level.

There is quite a difference between the velocities derived from the C I (6587 Å) line (Figure 7.17c and d) and the Ba II (5853 Å) line (Figure 7.17a and b). Using the 64.57 day period phasing, the primary photometric maximum shows very similar velocities apart from phases 0.3–0.4. Secondary photometric minimum, especially phases 0.8–0.0, is quite different, with the C I line constant around -40kms^{-1}. This lack of variation compared to that seen in the Ba II line is most likely due to the low signal noted previously, at least for spectra 5.96 and 10.96. However the cause of the variation for the other cycles and phases is unclear. The Ba II line phases up more cleanly on the 32 day period. However the curves are quite similar between phases 0.0 and 0.6, with the major differences occuring between phases 0.7 and 0.0. While such variation in velocity might be expected due to shocks splitting the line and reducing the line strength, so it is lost in the noise, the phases at which it occurs are much earlier than the observed known shock correlated effects such as He I emission. In order for these to be caused by the shock so early in the pulsation cycle, the C I line forming region would have to be very deep in the photosphere. Alternately, they could be considered to be formed much further out in the atmosphere, with the shock hitting much later, but the directions of motion do not support such a conclusion.

In addition, the motions of both lines are definitely complicated by cycle to cycle variations. For both the Ba II line and the C I line, cycle 0 is offset from cycles 4 and 5, which are both quite closely aligned. In contrast, cycle 10 is clearly offset. While this variation has been used as an argument for RU Cen being a binary (Maas et al., 2002), no orbital solution has been derived. A combination of the velocities from Pollard et al. (1997), Maas et al. (2002) and this work may be able to be used for this, especially if the Ba II line pulsations fitted in Figure 7.11 can be used. However, as seen from Figure 7.17, these velocities may not be consistent enough for a reliable orbit to be determined. As stated in Maas et al. (2002), a longer velocity monitoring program to establish an orbit is required, and from the results found here, any program needs to use a consistent set of lines.

Overall, RU Cen shows a different spectral composition to TT Oph in that it has much weaker metallic lines, but it does show a very similar radial velocity curve, with no difference between primary light maximum and secondary light maximum. It does however show marked differences in the equivalent width of Hα over the same maxima, with maximum emission and therefore maximum shock strength associated with primary light maximum. RU Cen also shows long-term variations in the Hα profile of an unknown origin, which are not reflected by long-term photometric variations.

7.3 U Mon

U Mon (P = 90.29 days) does show both long-term photometric variations (see Section 4.5) and long-term spectroscopic variations (Pollard, 1994; McSaveney et al., 2002). As the second brightest RV Tauri star, and the brightest RVb star it has been widely studied. The most recent spectroscopic review is Pollard et al. (1997), and this should be consulted for historical references, with a more comprehensive review in Pollard (1994). This also contains orbital work (see Table 4.25 and Table 7.2 for orbital solutions), as does a more recent unpublished study (McSaveney, 1998). Since then, abundances have also been derived for U Mon (Giridhar et al., 2000).

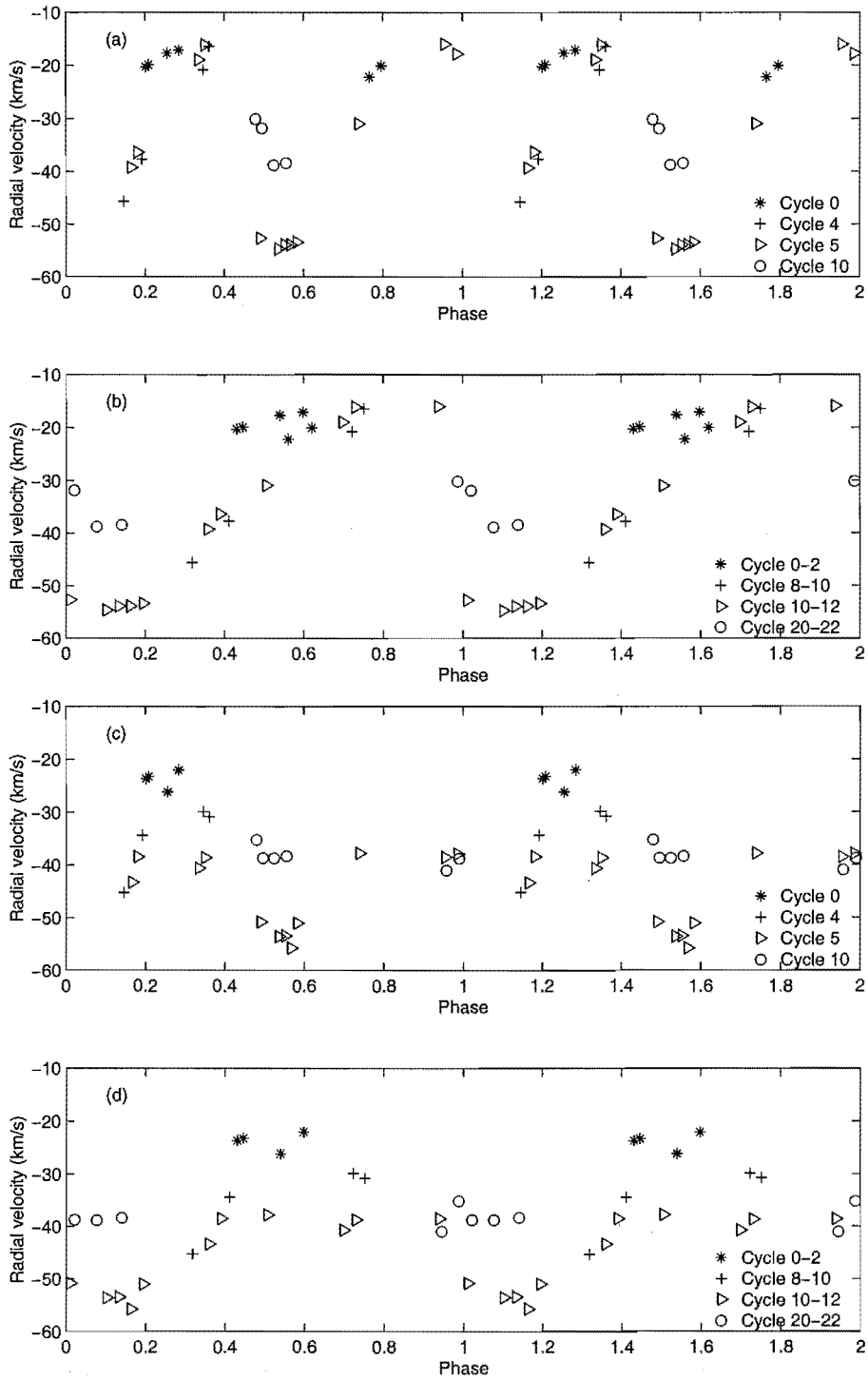

Figure 7.17: Phased RU Cen radial velocities for individual cycles.
(a) Ba II (5853 Å) phased on the 64.57 day period.
(b) Ba II (5853 Å) phased on the 32.285 day period.
(c) C I (6587 Å) phased on the 64.57 day period.
(d) C I (6587 Å) phased on the 32.285 day period.

Table 7.2: U Mon orbital data.

	Pollard (1994)	McSaveney (1998)
period (d)	2597±6	2595±5
centre-of-mass velocity (kms^{-1})	34.9±0.7	34.9±0.7
radial velocity semi-amplitude (kms^{-1})	17±1	16±1
eccentricity	0.43±0.05	0.44±0.06
longitude of periastron (^{o})	191±6	201±5
Julian Date of periastron - 2440000	558±58	610±59
$a \sin i$ (Gm)	537±38	520±38
mass function ($M_\odot$)	0.92±0.18	0.84±0.17

The aim is to look for similar spectral behaviour to that observed in TT Oph and RU Cen with respect to pulsations and shock waves. Stacked spectra, equivalent widths and radial velocities will be used to investigate this. Due to the changes in the observed pattern of deep and shallow minima, the stacked spectra have not been phased based on acceleration minima, but are instead examined as a function of Julian Date. The equivalent widths and radial velocities for various line species are then also examined as a function of Julian Date. This is to allow the cycle-to-cycle variations to be studied and to search for differences in the behaviour associated with the deep and shallow minima. The difficulty in phasing the data due to the changes in the pattern of deep and shallow minima has meant that only the Fe I velocities and Hα equivalent widths have been phased.

7.3.1 Spectroscopy

Na D lines and associated wavelengths

As an RVA star (Preston et al., 1963), U Mon has a greater number of stronger metallic lines than RU Cen (Figure 7.18). The Na D lines change shape over time but show little variation in position. This may be due to an interstellar component making up the bulk of the line and obscuring the pulsational component from the star.

In contrast to TT Oph and RU Cen U Mon shows very little sign of He I (5876 Å) emission. This is curious as both Preston (1964) and Bopp (1984) reported clear He I (5876 Å) emission on rising light. The emission is quite prominent in Bopp (1984, see Figure 4) as the star emerges from a deep minimum. The strength of the emission was commented upon by the author, in comparison to the slightly weaker emission reported by Preston (1964). Unfortunately there is not enough information to establish if the particularly high emission amplitude is atypical, although it is of a magnitude which would been noticed had it occurred over the course of the current work. Based on the previous stars, any He I emission would be expected to appear at or just prior to phase 0.0 by the acceleration phasing, which has occurred just after minimum light on the previous stars. This is in agreement with what was observed in Bopp (1984), although it should be noted that from the AAVSO photometry presented in that paper, this was a deep minimum both preceded and followed by a deep minimum. It should also be noted that

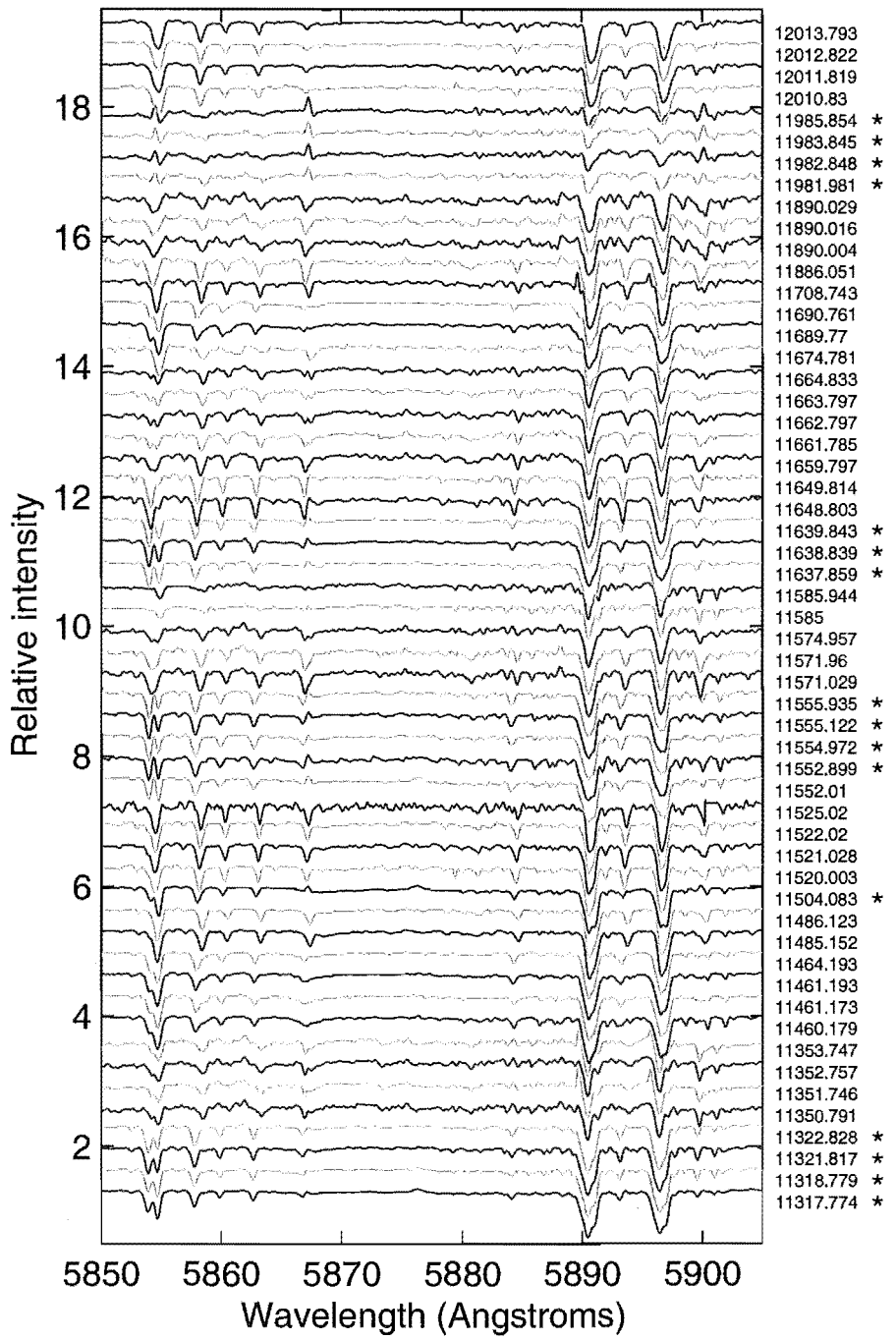

Figure 7.18: U Mon stacked Na D region spectra as a function of Julian Date. Julian Date - 2440000 of observations is labeled to the right, with * indicating observations in which the Ba II (5853 Å) and/or Ti I (5866 Å) lines are strongly split and/or show emission components.

U Mon has been observed to possess molecular bandheads of CN and TiO at deep and occasionally shallow minimum (Pollard et al., 1996a). This is when the outer layers of the star are at their coolest. It may be that the overlap of the time when such bandheads form in the outer atmosphere with when the shock propagates through the deeper line forming regions (indicated by the split metallic lines), means that the He I line is obscured by the molecular bands. However this does not explain why it has been observed previously.

The other lines of interest in Figure 7.18 are the Ba II line (5853 Å), Ca I line (5957 Å), Fe I lines (5859 and 5862 Å) and Ti I line (5866 Å). These all vary as a function of pulsational cycle and in the case of the Ba II and Ti I lines, show evidence of shock waves. The Ba II line shows this through line splitting. In several instances the line is completely split, with various other spectra showing less distinct double components. The Ba II line is also observed in emission from Julian Date 2451981 to 2451985. At these and a number of other times times, the Ti I line at 5866Å also appears in emission (starred spectra in Figure 7.18). This shows the same trends of line strength variation with phase as in TT Oph.

Hα line

As with TT Oph and RU Cen, U Mon shows constant Hα emission (Figure 7.19). The structure of the line itself is quite complicated, and while it generally has an emission feature either side of an absorption feature, the relative strengths and positions vary. On average, the blue-ward emission feature is strongest.

Previous work (Pollard, 1994; McSaveney, 1998; McSaveney et al., 2002) has established that U Mon's Hα profile varies as a function of the long-term photometric variations. This is confirmed by examining the Hα equivalent widths over the past two long-term minima (Figure 7.20). Outside of the long-term minima, Hα emission has an average maximum value of 3 Å, whereas during the first long-term minimum shown (Pollard, 1994), Hα emission peaks at 6.5 Å. The second long-term minimum is of a smaller amplitude ($\sim$0.5 V), but the minimum is still detectable through the heightened Hα emission reaching a peak of 4.5 Å. Hα emission as a function of pulsation is examined in Section 7.3.2 and 7.3.3.

Ca II lines

The final stacked spectra presented are those of the Ca II lines (Figure 7.21). Some of these show evidence of blue-ward emission (starred spectra in Figure 7.21). Not all these are correlated with when the Ti I line at 5866 Å appears in emission and the Ba II line at 5853 Å is completely split. This indicates that there may be a propagation delay as the shock moves through the outer layers of the star.

7.3.2 Spectral variations as a function of Julian Date

Because of the changes observed in the pattern of deep and shallow minima (Figure 4.72), phasing has initially not been performed on the spectra. To get an picture of the pulsational patterns the radial velocities for a selection of unsplit Fe I lines for one season of observations (1999–2000), have been plotted along with the photometry for the corresponding season (Figure 7.22). The scatter in radial velocity for the different lines is comparable to that observed for TT Oph (Figure 7.1). The greatest scatter ($\sim$10kms^{-1})

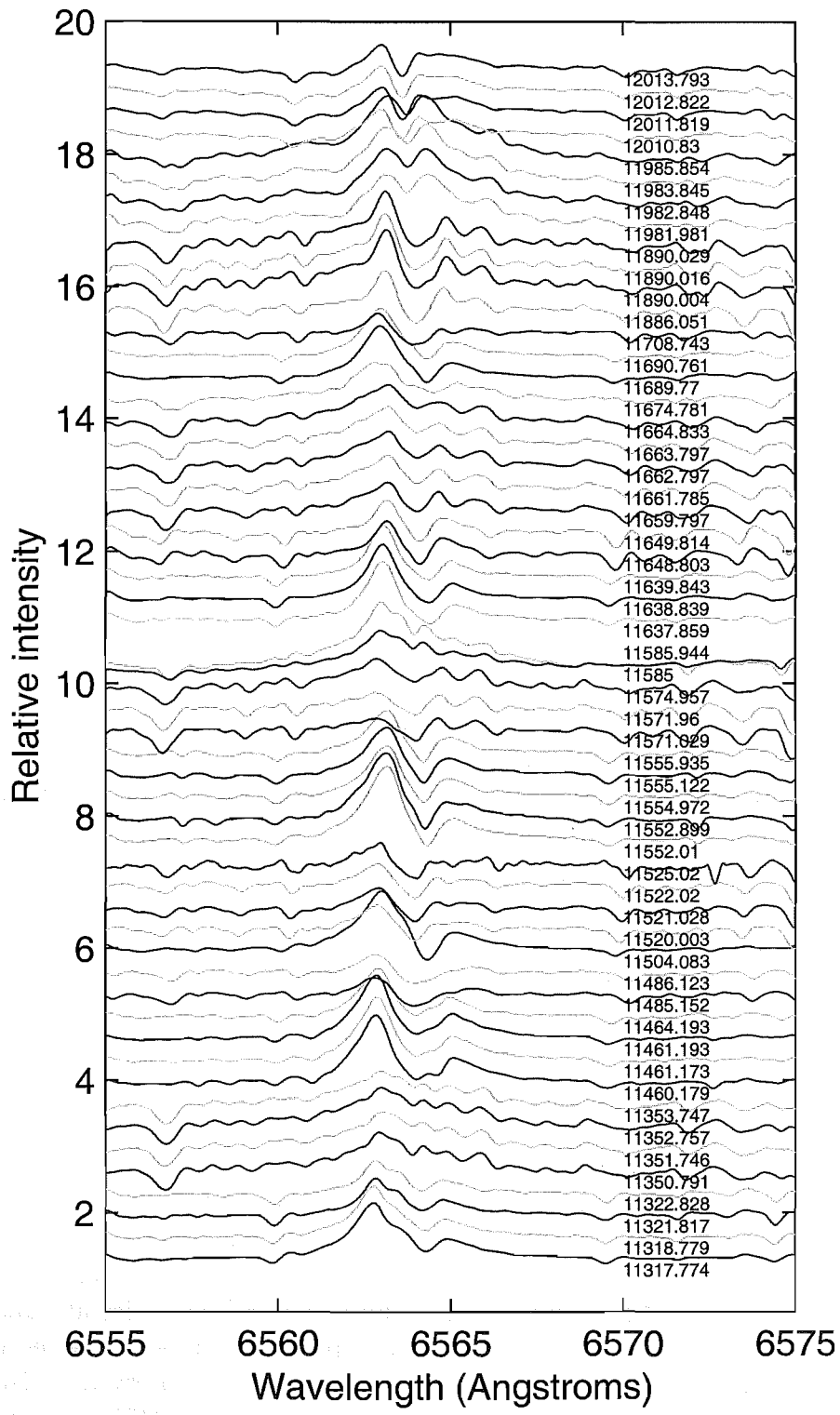

Figure 7.19: U Mon stacked Hα lines as a function of Julian Date.

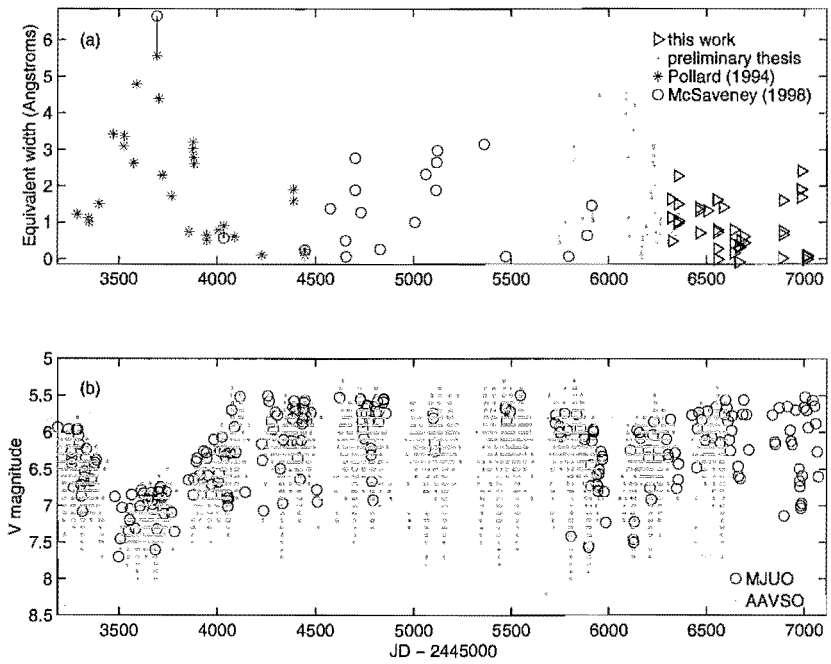

Figure 7.20: (a) Hα equivalent width variations and (b) photometry over two successive long-term minima.

is observed near maximum velocity (around Julian Date 2451570), which is approximately when the star is in a photometric deep minimum. However the same degree of scatter is not observed at the following deep minimum (Julian Date 2451670). The origin of this scatter is unknown as at maximum velocity the bulk of the material in each line forming region will be falling inwards, and from the pattern observed in the W Vir stars (Figure 6.2 for κ Pav and Figure 6.9 for AL Vir), the greatest difference in velocity usually occurs when the radial velocities are at a minimum. At this time the stellar photosphere is moving outward with maximum speed. It is also unclear why the pulsations should be different in the following deep minimum. A mean Fe I velocity can still be derived which represents the mean motion of the stellar photosphere.

In Figure 7.23, we compare the mean Fe I velocities to the velocities derived from a selection of individual lines: Fe II 6516 Å, Ca I 5857 Å, and Ca II 8490 Å for the 1999–2000 observing period, and also examine the Hα equivalent widths for the same time frame. The Fe I velocities agree well with the Ca I velocities, in that the maximum velocity difference observed at any one time is approximately 8 kms^{-1}, and neither species is observed to significantly lead or lag. The two lines from ionized species are a different matter. Fe II (6516 Å) is found to lag behind the Fe I velocities at Julian Date 2451460, as it is still at maximum velocity, but within one night both species were at the same velocity ($\sim$20 kms^{-1}). The following occasion when the observed Fe I-Fe II line velocity difference was greater than 30kms^{-1} was at Julian Date $\sim$2451580, immediately prior to a photometric deep minimum. Here the Fe I line is at a minimum velocity of $\sim$15kms^{-1}, while Fe II is at $\sim$48kms^{-1}. Such an extreme velocity difference between Fe I and Fe II is observed in W Vir (Figure 6.16, phase 0.0), when Fe I is observed at a minimum velocity while Fe II is still at maximum velocity. TT Oph also shows a similar velocity lag, where

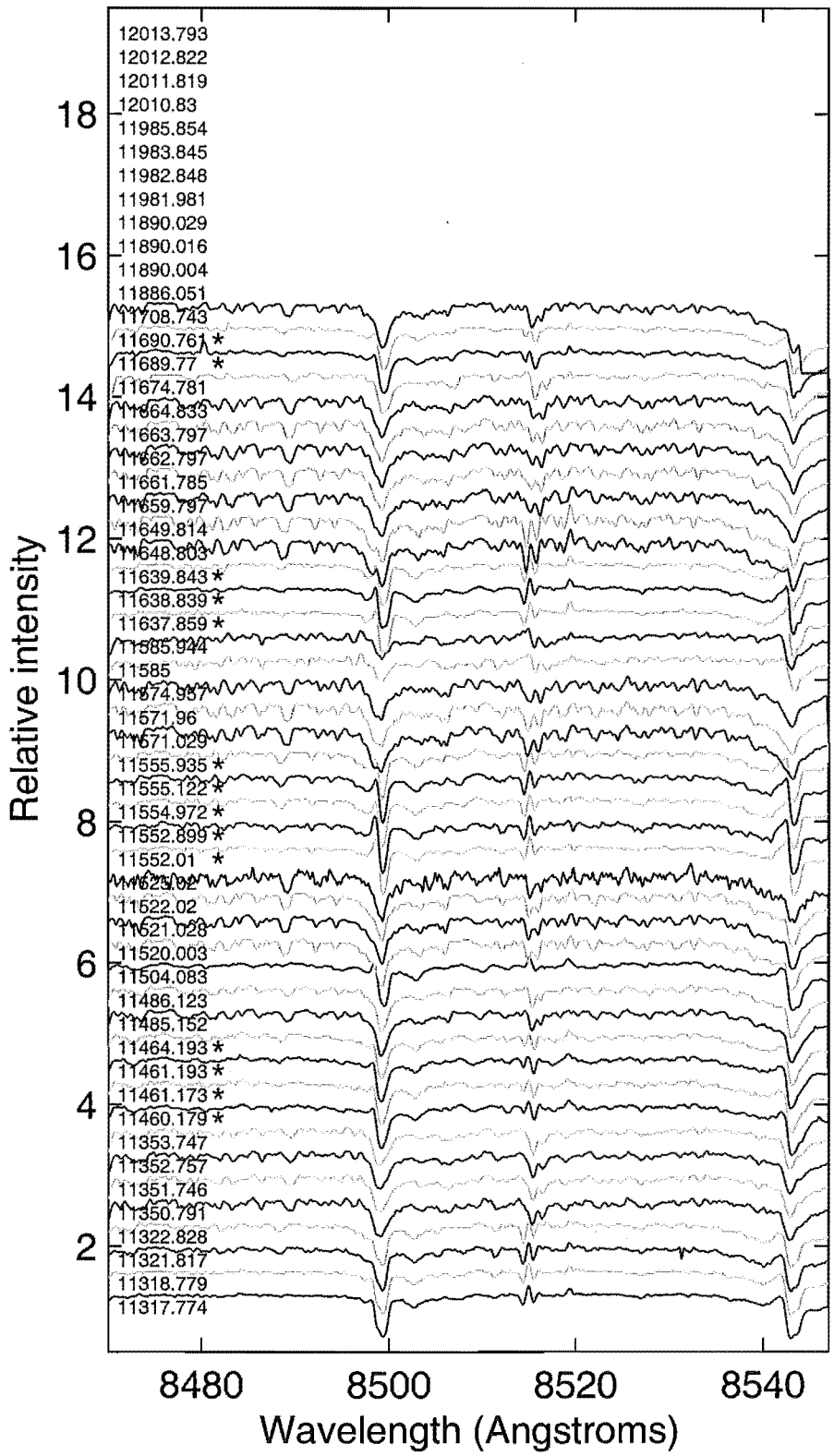

Figure 7.21: U Mon stacked Ca II lines as a function of Julian Date. Julian Date - 2440000 of observations is labeled to the left, with * indicating observations which show emission components in the Ca II lines. Gaps indicate observations for which wavelength coverage does not extend to 8000 Å due to filter problems (Section 2.2.3).

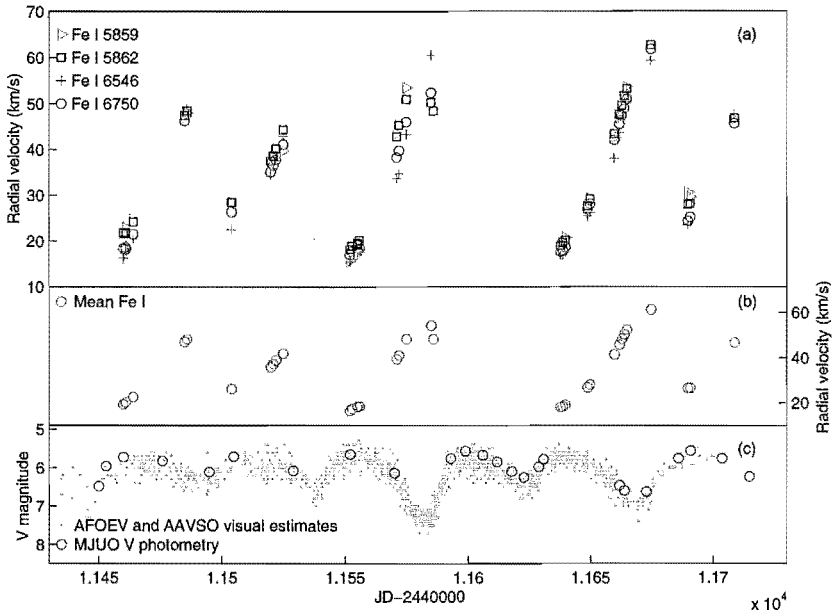

Figure 7.22: U Mon Fe I radial velocities as a function of Julian Date, with corresponding photometry for the 1999-2000 observing season.
(a) Fe I radial velocities.
(b) Mean Fe I radial velocities.
(c) V photometry.

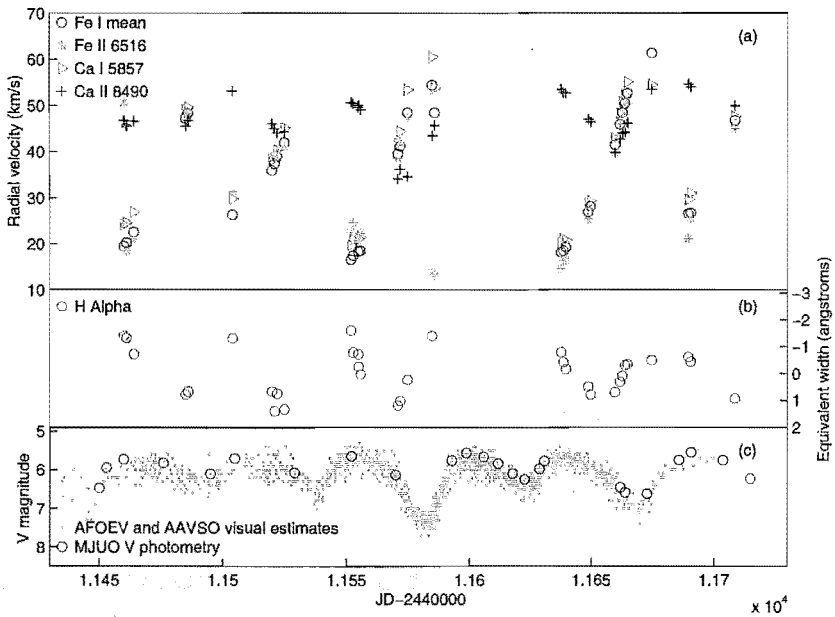

Figure 7.23: U Mon radial velocities as a function of Julian Date, with corresponding photometry for the 1999-2000 observing season.
(a) Fe I, Fe II, Ca I and Ca II radial velocities.
(b) Hα equivalent widths.
(c) V photometry.

the Fe I velocity is at -50kms^{-1} ($\sim$ mean velocity amplitude) while Fe II is near maximum, at -30kms^{-1} (Figure 7.10). The results from these stars would appear to indicate that Fe II forms further out in the stellar photosphere, due to the observed phase lag in W Vir and TT Oph, and this is supported by the initial Fe I-Fe II difference at Julian Date 2451460 observed in U Mon. The reason for the non-repeatability of this phase lag for the second deep minimum in U Mon at Julian Date $\sim$2451580 is unknown, and more observations would be required to establish if it is a repeated trend.

Ca II (8490 Å) is observed to agree with the Fe I lines far less often than the other lines. It varies between 35 and 55kms^{-1}, compared to the 15 to 60kms^{-1} observed for the other lines. While it does agree reasonably well with the Fe I velocities when they fall in the 35–55kms^{-1} range, at times when the other lines are around minimum velocity, Ca II is still around 48–50kms^{-1}. These correspond to those dates when blue-ward emission is observed in the Ca II line profiles (Figure 7.21), which will shift the measured velocity to a higher value.

Figure 7.23b also shows Hα equivalent widths over the 1999–2000 observing season. As this time period does not fall in a long-term minimum, the average pulsational Hα behaviour can be examined. Maximum Hα emission (2 Å) occurs just after light minimum and also just before light maximum, similar to W Vir and ST Pup. This coincides with velocity minimum for the Fe I, Ca I and often Fe II lines, and where a maximum velocity difference exists between the velocities of the majority of these lines and the Ca II line velocities.

7.3.3 Radial velocities as a function of phase

Part of the work of this thesis involves the investigation of the pulsational characteristics of the RV Tauri stars with respect to the deep and shallow minima, and whether these photometric variations have spectroscopic counterparts. With TT Oph and RU Cen the deep and shallow minima are regular and their velocity data can be phased using the period between successive deep minima and an appropriate epoch. The changes in the pattern of deep and shallow minima observed in U Mon, especially over the time examined spectroscopically (Figure 4.72), make phasing impossible. Instead, the star has been phased on a period between successive minima of 45.14 days from Fourier fitting to AAVSO observations of Julian Date 2451000–2452100. Initially the velocities were phased on the 45.895 day period found from Fourier analysis of the MJUO V photometry, but this resulted in a $\sim$10kms^{-1} greater scatter in velocities between cycles, so the period was amended to that resulting from an analysis of only the photometry of the three seasons of spectral observation.

Figure 7.24 shows the mean Fe I velocity data and AAVSO visual estimates as a function of Julian Date, with the different pulsation cycles represented by different symbols.

Before discussing the phased radial velocities with respect to pulsational differences, any residual non-pulsational motion needs to be removed. Orbital solutions for U Mon have been derived, with the most recent (McSaveney, 1998) being used in this work (see Table 7.2). Figure 7.24 shows the orbital motion as a function of Julian Date over the relevant time period, and shows the effect is not large. Figure 7.25 shows the effect of removing this orbital motion. From this figure the orbital motion does improve the velocity curve by reducing the scatter between cycles, especially the maximum velocity phases around 0.8. Since these are cycles 0 and 15 and are at the start and end of the

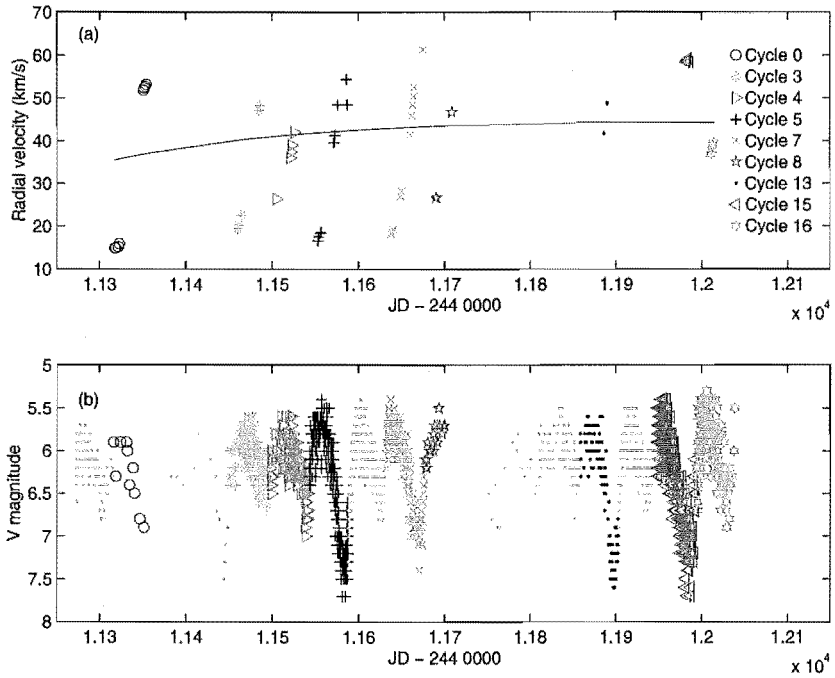

Figure 7.24: U Mon (a) mean Fe I radial velocities as a function of Julian Date identified by cycle number with the line showing the orbital solution from Table 7.2 (McSaveney, 1998) and (b) AAVSO visual estimates using the same cycle symbols at in (a).

spectral observations this confirms that this is a reasonable orbital solution with respect to these cycles. However there is still scatter of up to 10 kms^{-1} around velocity minimum and phase 0.2.

Once these orbital motions have been removed, the mean Fe I velocities have been phased on the 45.14 day period, a spline curve fitted and an acceleration curve derived (Figure 7.26). A similar acceleration curve to the previous stars is found, with the double peak at acceleration minimum being a residual of the spline curve fitted, rather than a real feature. Line projection effects have not been taken into account, so the absolute magnitude of the acceleration curve is not reliable, but the phase of acceleration minimum is relatively consistent. This results in an epoch of Julian Date 2451316.334 which is used in Figure 7.24 onwards.

Figure 7.26 also includes the Hα equivalent widths phased with respect to the acceleration minimum on the 45.14 day period. These show more scatter between cycles than the radial velocities. Maximum emission occurs at phase 0.8 for cycles 0 and 15, reaching a value of approximately 2.5 Å, but at phase 0.77, the equivalent width in cycle 3 is only 0.8 Å. Hence while there is little evidence of large cycle to cycle variations in the radial velocities, the Hα equivalent widths are less conclusive.

To investigate whether the equivalent width variations are connected to the photometric deep and shallow minima, the pulsation cycles have been classed in two ways. First they have been classified based on whether they follow a deep or shallow minimum, and secondly whether they precede or include a deep or shallow minimum. This is to investigate whether the spectroscopic features examined show a pattern associated with

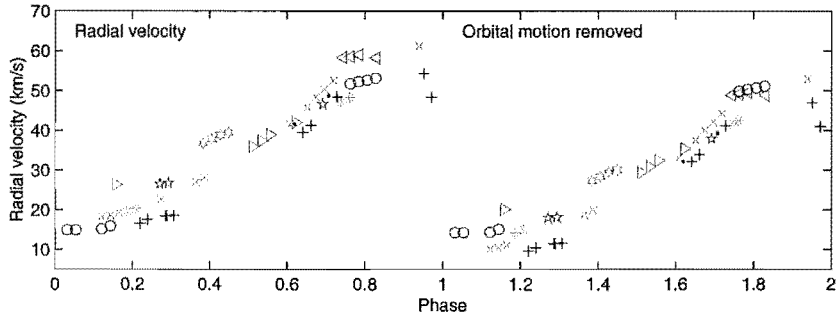

Figure 7.25: Fe I radial velocity curves of U Mon phased on 45.14 day period with and without orbital motion. Phase 0-1 shows radial velocities as measured. Phase 1-2 shows radial velocities with orbital motion removed using the McSaveney (1998) orbital solution. The symbol scheme for cycle identification is as in Figure 7.24.

the photometric minimum occuring beforehand or the minimum following. In the regularly pulsating RV Tauri stars, the two classifications would provide the same results as for these, a deep minimum always follows a shallow minimum and vice versa. Thus for the more regular stars, phasing purely on the formal period would automatically produce a deep minimum, followed by a shallow minimum around phase 0.5 leading to another deep minimum. However with the changes in the pattern of deep and shallow minima in U Mon, automatic phasing purely on calculation will mix deep minima over shallow minima at the same phase. Hence the manual sorting based on the depth of minimum preceding or following/falling inside the particular cycle. The results are shown in Table 7.3. To get the phased alternating minima pattern with the regular stars, we can either phase on the formal period or we can phase on the period between successive minima and plot all the odd numbered cycles between 0 and 1, and the even numbered cycles between 1 and 2. This will automatically produce the deep-shallow-deep pattern required, but phased between 0 and 2. The same can be done for U Mon, however rather than do it automatically, the cycles based on the 45 day period must be manually assigned to being phased either between 0 and 1 or 1 and 2, based on the minimum criteria mentioned earlier. The results of this are plotted in Figure 7.27, using the two possible classification schemes.

Figures 7.27a-c phase the radial velocities, equivalent widths and photometry such that cycles that follow a deep minimum are phased 0–1, and cycles that follow a shallow minimum are phased 1–2. Figures 7.27d-f phase these such that the cycles that precede or include a shallow minimum are phased 0–1, while those cycles which precede or include a deep minimum are phased 1–2. As can be seen from this and Table 7.3, only cycle 4 changes from being phased 1–2 in Figures 7.27a-c, to being phased 0–1 in Figure 7.27d-f. This is because a shallow minimum follows another shallow minimum. From the photometry this cycles fits better with those cycles preceding a shallow minimum, rather than those following a shallow minimum. The Fe I radial velocities and Hα equivalent widths are inconclusive with respect to this pulsation cycle as they form a smooth curve when phased between 0 and 1 and when phased between 1 and 2.

In terms of overall differences between phase 0–1 and 1–2, there seems little difference in the radial velocities and only a slight difference observed in the equivalent widths.

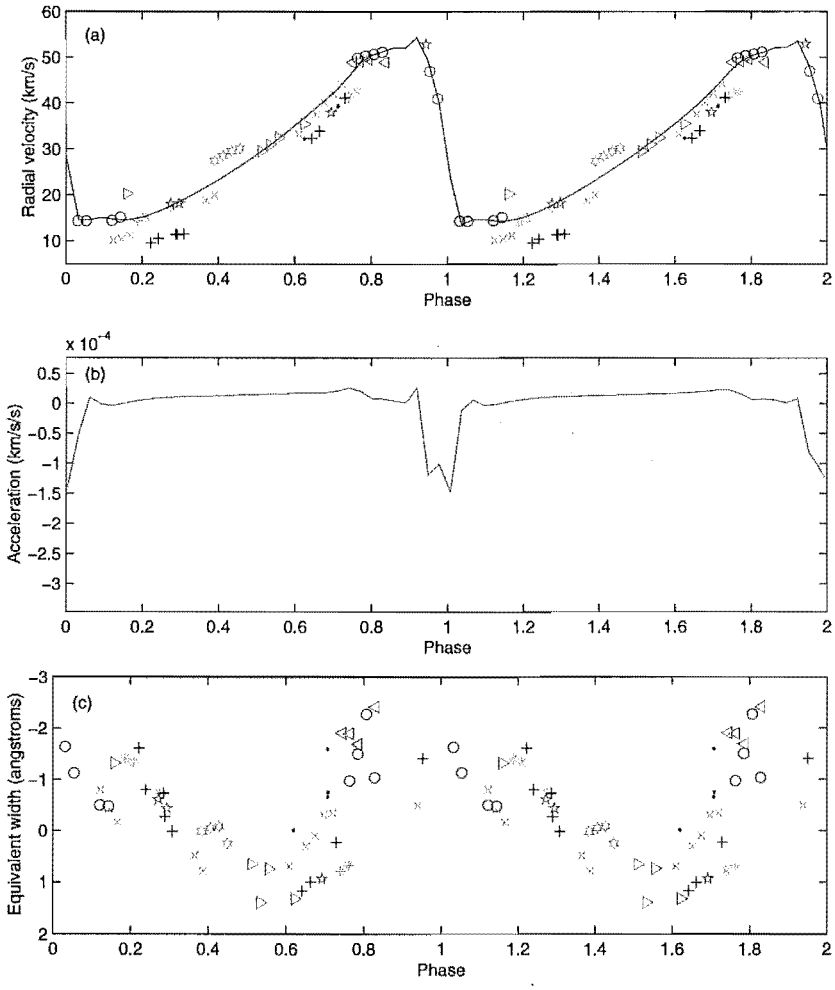

Figure 7.26: (a) Fe I radial velocity, (b) acceleration curves and (c) equivalent widths for U Mon phased on the 45.14 day period. The symbol scheme for cycle identification is as in Figure 7.24.

The reliability of these conclusions is limited by the gaps in phase coverage between 0.0 and 0.15 and 0.8 and 1.00. From the overlap observed in the velocity curves from the acceleration phasing (Figure 7.26) there is little or no difference in the different cycles depending on their association with the photometric deep or shallow minima. At this preliminary stage the radial velocities observed are not dependent on the photometry, at least for the levels of the photosphere associated with the lines investigated here. Further spectral observations of U Mon just after deep minimum and around shallow minimum would be required to confirm this, in case any velocity differences occur only at these phases. However, this lack of velocity difference associated with the photometry is the same as has been found for TT Oph and RU Cen.

The equivalent widths do show a possible difference in that those cycles phased between 0 and 1 form a much smoother curve as a function of phase, than those falling between phases 1 and 2. Minimum Hα equivalent width in the 0–1 interval falls at phase $\sim$0.7, whereas the minimum equivalent width in the 1–2 interval is at $\sim$1.5. There is a great deal more scatter observed between phases 1–2, as cycle 0 reaches an equivalent width of

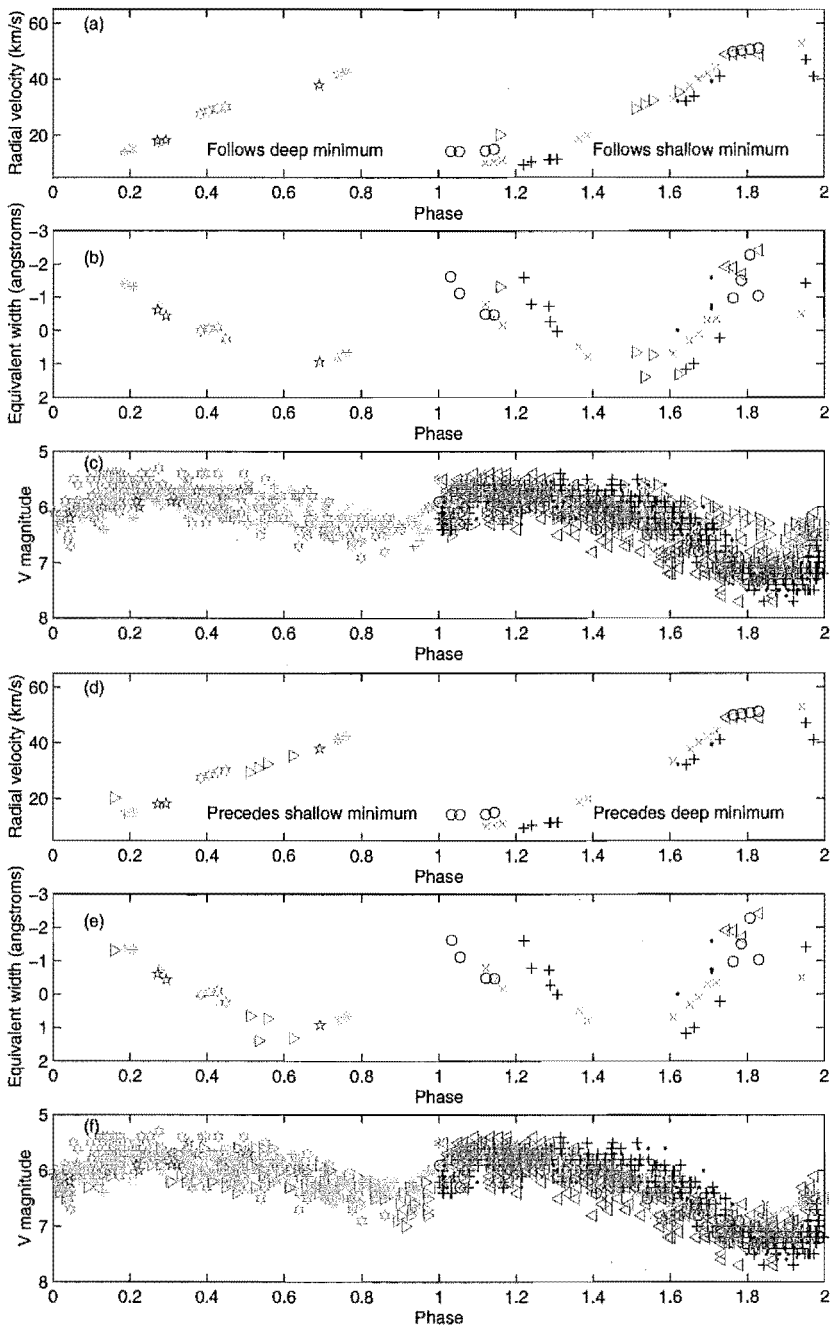

Figure 7.27: Fe I radial velocity, Hα equivalent widths and photometry curves of U Mon phased on the 45.14 day period.
(a)-(c) Phase 0–1 shows cycles classified as following deep minima. Phase 1–2 shows cycles classified as following shallow minima.
(d)-(f) Phase 0–1 shows cycles classified as preceding/including shallow minima. Phase 1–2 shows cycles classified as preceding/including deep minima.
The symbol scheme for cycle identification is as in Figure 7.24.

Table 7.3: U Mon pulsation cycle classification based on photometric minima.

Cycle	Minima preceding	Minima following/included
0	shallow	deep
3	deep	shallow
4	shallow	shallow
5	shallow	deep
7	shallow	deep
8	deep	shallow
13	shallow	deep
15	shallow	deep
16	deep	shallow

2 Å a little after phase ~1.0, whereas cycle 5 reaches the same equivalent width (2 Å) 0.2 of a cycle later. This would appear to give a preliminary indication that the strength of the shock producing the Hα emission is more variable when preceding or associated with a deep minimum, than when preceding or associated with a shallow minimum. However, more shallow minimum observations would be required to confirm this, as it is at this stage of the pulsation cycle where peak emission would be expected based on the pattern observed in W Vir, ST Pup, TT Oph and RU Cen (phases 0.0–0.2 and 0.8-1.0 especially). Also, from the photometry, the phase of deep minimum shifts slightly, and can be found anywhere between 1.75 and 1.9. The shallow minimum appears to vary less in phase space (although it is less clearly visible from the photometry), so cycle to cycle variations may be connected to the exact phasing between minima. Certainly, it is unclear whether, if the observations were to be rephased so that the deep minima lined up exactly, the radial velocities and the equivalent widths would line up. The effects of such re-phasing on the observations associated with the shallow minima are also unclear as these already line up well under the current phasing.

What is clear is that for U Mon, as with TT Oph and RU Cen, the radial velocity curves show little sign of the photometric variations associated with the generally alternating light curve pattern of deep and shallow minima upon which the RV Tauri classification was originally based. The velocity curves themselves are very similar to those seen in W Vir and ST Pup, with similar sorts of shock features (emission and line splitting). With U Mon, the shock related emission features are less strongly correlated with the depths of the minima, as maximum peak Hα emission is not positively associated with the deep minimum as it is with RU Cen. However there does appear to be a greater degree of variation in shock behaviour during the deep minima.

7.4 Other stars

Six other RV Tauri stars (SX Cen, AI Sco, AR Pup, AR Sgr, R Sct and IW Car) have been observed spectroscopically over the course of this thesis and these will be briefly presented and qualitatively examined in terms of their Hα variations and spectral behaviour in the Na D regions. The spectra stacked in order of Julian Date and are shown in Figures 7.28 and 7.29.

Hα line

SX Cen, AI Sco, AR Pup and IW Car all show long-term variations in the Hα profile (Figure 7.28). This is interesting, as all these stars are RVb stars so also show long-term variations in their maximum light output. SX Cen, AR Pup and IW Car show slight changes in the wavelength of Hα, which are most likely to be orbital in nature. Certainly Maas et al. (2002) reported that their radial velocities for SX Cen fitted a pulsational period of 32.8642 days and and they also fitted a sine wave of period 621±31 days to their minimum pulsational velocities, with a systemic velocity of 11.0±0.1 kms^{-1} and an amplitude of 20.6±0.1 kms^{-1}. A larger data set of velocities would be required to derive further orbital parameters for SX Cen and the other two stars to confirm if the long-term velocity variations correlate with the long-term photometric variations.

A clearer correlation of Hα line profile variation with the long-term photometric variations is observed in AI Sco (Figure 7.28b). U Mon shows enhanced Hα emission around long-term photometric minimum (Figure 7.20), and AI Sco shows this trend to an even greater extent. From Figure 4.41, the spectra can be roughly divided into three groups which fall either side of and inside the long-term photometric minimum.

Between Julian Date 2451317 and 2451425, when AI Sco is at long-term maximum light (13 spectra), the Hα profile shows strong broad blue-ward absorption, with a slight emission peak to the red. The blue-ward absorption appears quite complicated, with multiple components which vary in size and position.

Between Julian Date 2451711 and 2451829, as AI Sco is approximately mid-way through and coming out of its long-term photometric minimum, Hα is very sharply in emission, with two emission peaks either side of an absorption core. This is very similar to the Hα peaks observed in TT Oph (Figure 7.5), RU Cen (Figure 7.14), AR Sgr (Figure 7.28d) and U Mon (Figure 7.19). The similarity is most striking with RU Cen, as RU Cen shows a similar style blue-ward absorption feature with a stronger emission peak to the red during its first pulsation cycle (P = 64.57 days) between Julian Date 2451317 and 2451369. There is no accompanying change in *V* observed in RU Cen (Figure 4.35), although the *(B-V)*, *(V-R)* and *(V-I)* colours appear slightly redder during these dates. Gaps in the photometric coverage prevent any firm conclusions about colour changes.

The final set of observations cover Julian Date 2452014 to 2452042, when AI Sco is at its long-term photometric maximum. Here the Hα emission has decreased to lower levels, and is of a similar magnitude to that observed in SX Cen and R Sct. It still does not show the extreme blue-ward absorption observed earlier.

The origin of this Hα variation is unclear. With respect to the long-term variation observed in U Mon, possible theories include interaction between U Mon and its binary companion at closest approach leading to the enhanced Hα emission (Pollard, 1994). This is as yet unconfirmed, and does not explain the large blue-ward absorption observed in RU Cen and AI Sco. Pollard et al. (1997) observed similar broad blue-ward absorption features in AI Sco at long-term photometric maximum (Julian Date 2448402–2448470) and around the pulsational shallow minimum. They also saw narrower blue-ward absorption with a slight red emission peak at long-term light maximum (Julian Date 2458470–24585070), while the star was at a pulsational secondary light maximum and descending towards deep minimum, implying a possible connection between the absorption line widths and the phase.

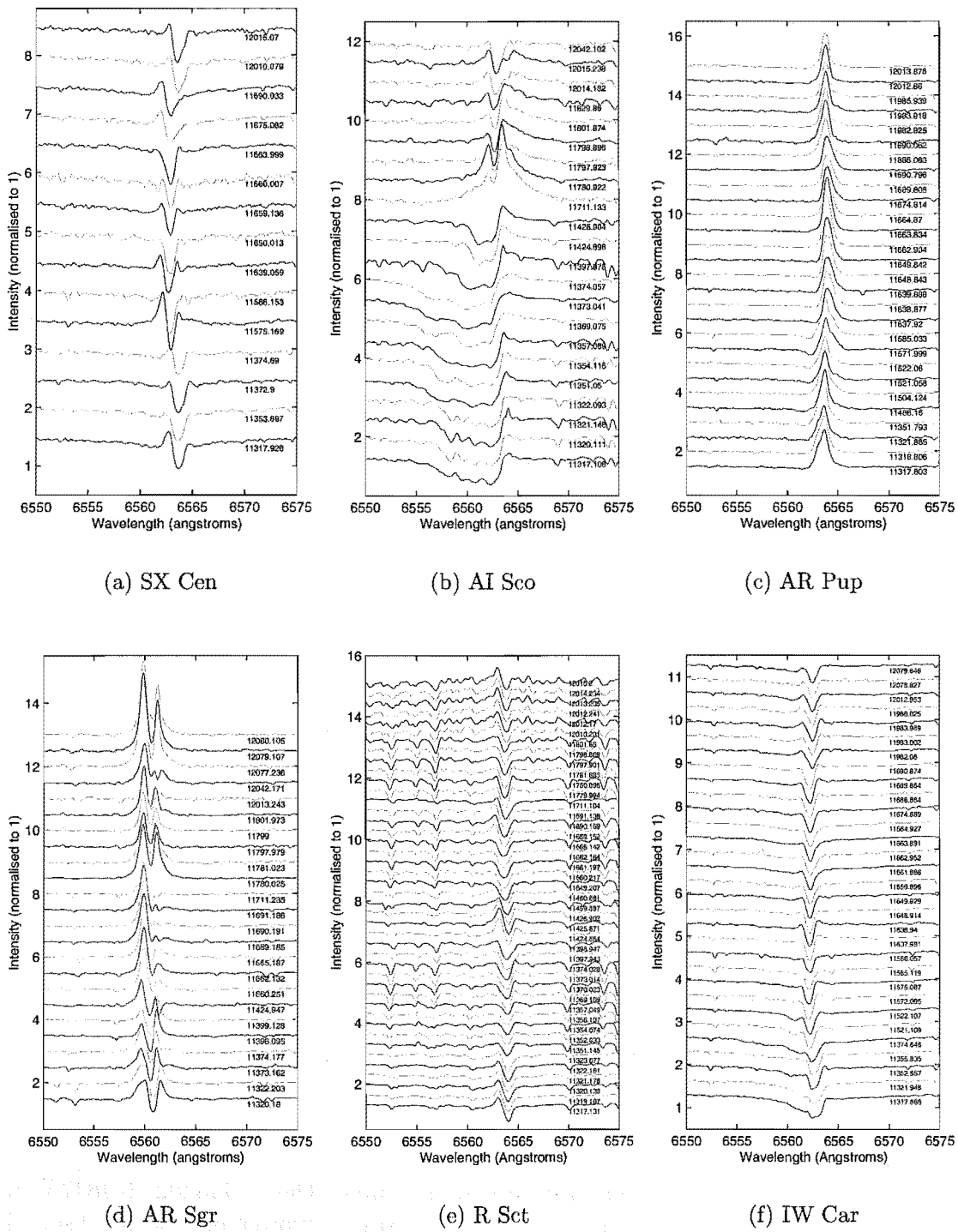

(a) SX Cen (b) AI Sco (c) AR Pup

(d) AR Sgr (e) R Sct (f) IW Car

Figure 7.28: RV Tauri Hα line spectra stacked as a function of Julian Date.

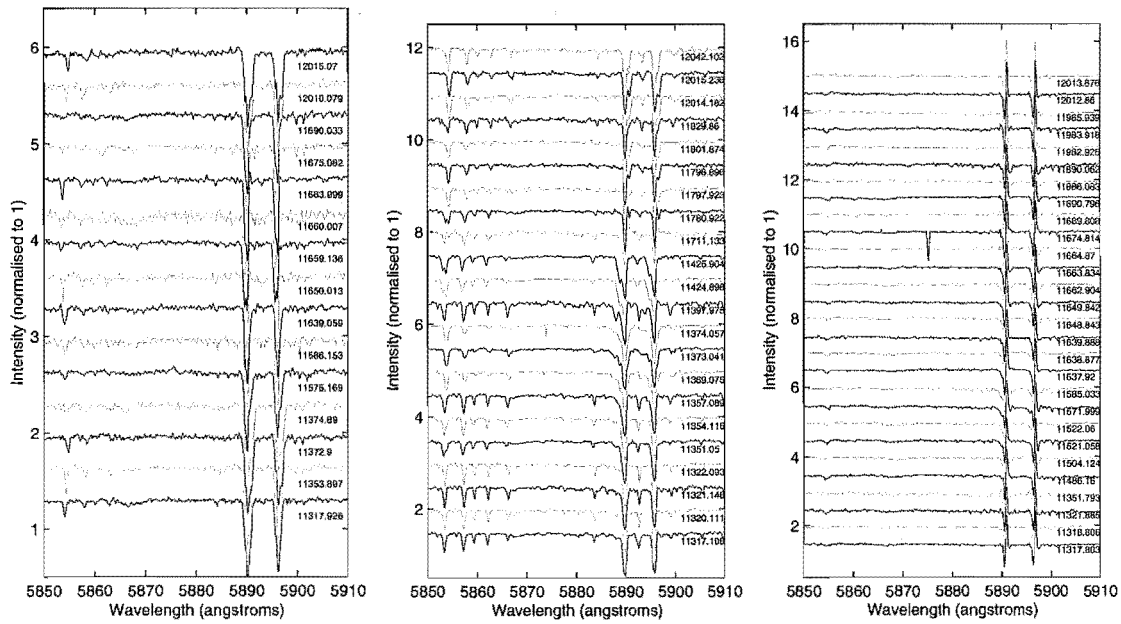

(a) SX Cen (b) AI Sco (c) AR Pup

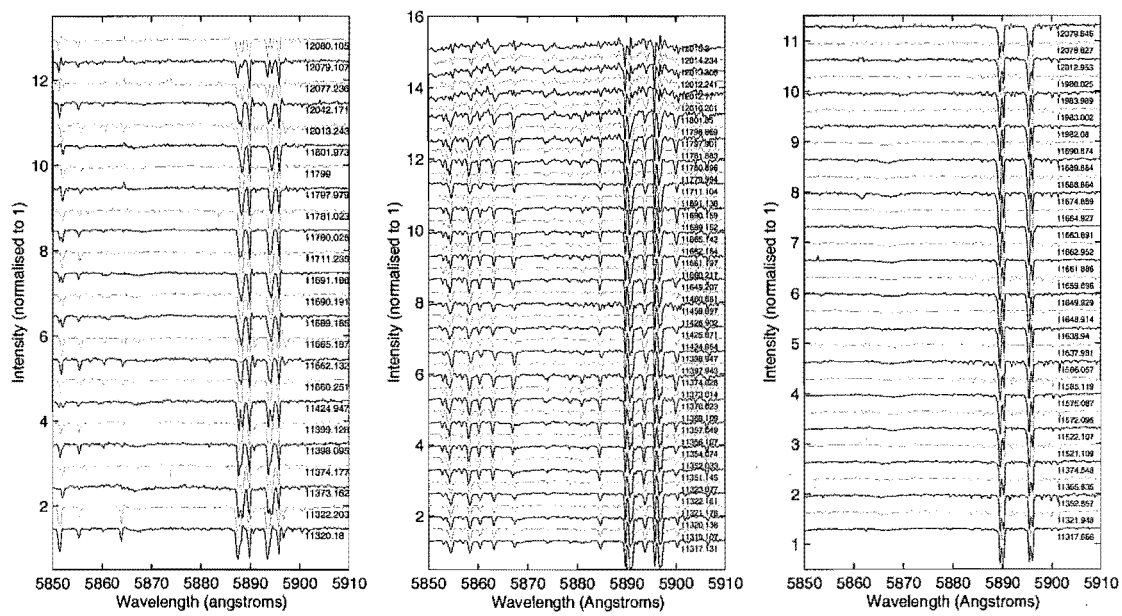

(d) AR Sgr (e) R Sct (f) IW Car

Figure 7.29: RV Tauri Na D line region spectra stacked as a function of Julian Date.

This same pattern is not observed in the spectra presented here, as the broad blue-ward absorption exists for cycles 0.76–0.83 and 1.23–1.89, over approximately primary maximum, shallow minimum and the approach to deep minimum. It is not observed around shallow minimum or at the approach to deep minimum over the second photometric long-term maximum. Thus it does not repeat at the same phases which implies that the broad blue-ward absorption in Hα is not related to the 71.45 day pulsations of AI Sco.

All the RV Tauri stars apart from AR Pup show quite complicated Hα emission and absorption components which vary over time. While AR Pup shows only the main single emission peak, this does vary in amplitude and asymmetry over time.

Na D lines and associated wavelengths

As seen in Figure 7.29, the Na D lines of all six RV Tauri stars show multiple components. All appear to show a narrow non-moving absorption component which is most likely interstellar in origin. AR Pup is unusual in that it shows a red-ward emission peak in all the observations. The origin of this emission is unknown.

Of the six RV Tauri stars shown here, only AR Sgr shows any indication of He I (5876 Å) emission. this occurs at Julian Date 2452077 and 2452079, but is very weak. R Sct has been observed to have He I emission at 6678 Å by Gillet et al. (1989) but that was observed halfway towards maximum light, as it emerged from a deep minimum, and there are no such observations of an equivalent pulsational phase in this work (Figure 4.61). This implies weaker shocks than observed in those stars for which He I emission is clearly observed (W Vir, ST Pup, TT Oph and RU Cen). AR Sgr also shows emission for the same dates in the Ti I 5866 Å line, and at Julian Date 2451797–2451801 and 2452080.

Overall the three RVA stars (AI Sco, AR Sgr and R Sct) somewhat unsurprisingly show the strongest metallic lines, as evidenced from Ba II (5853 Å), Ca I (5857 Å), Fe I (5859 and 5862 Å) and the aforementioned Ti I 5866 Å line. All three of these stars show evidence of the strengths of these lines varying as a function of pulsational phase (TT Oph and U Mon). As with all these stars, the Ba II line shows evidence of shock effects, as it is split at certain phases, often when the Ti I line is at its weakest. AR Sgr shows most variation in the Ti I line strength, then AI Sco and finally R Sct. However R Sct is on average a later type star, and cools enough during deep minima that molecular bandheads are visible. These are particularly prominent in the spectra from Julian Date 2451779 onwards. They gain in strength from Julian Date 2451779–2451801 as R Sct approaches a true deep minimum, and are well developed in the deep minimum of Julian Date 2452010–2452015.

The only one of the five metallic lines from the RVA stars to appear in some of the RVB stars is the Ba II 5853 Å line. As seen in Section 7.2, and Figures 7.11, 7.12 and 7.13, the Ba II line in RU Cen is strong enough to derive clear radial velocities, and this also appears to be the case with SX Cen and to a lesser extent AR Pup. This is not however the case for IW Car which shows very few lines other that the Na D lines over the spectral range shown and definitely no evidence of a Ba II line.

Table 7.4: Qualitative summary of selected RV Tauri stars.

	Type		Period	Description/features
	Photometric	Spectral		
SX Cen	RVb	RVB	32.82	Ba II line. Hα absorption. Possible orbital variations.
AI Sco	RVb	RVA	71.45	Metallic lines varying as a function of pulsational phase. Ba II line splitting. No metallic line variations similar to Hα long-term variations. Broad blue-ward absorption before long-term minimum, strong emission during and weak emission after.
AR Pup	RVb	RVB	76.47	Weak Ba II lines. Small long-term Hα velocity variation. Na D red-ward emission.
AR Sgr	RVa	RVA	87.13	Metallic lines varying as a function of pulsational phase. Ba II line splitting, Ti I emission, He I emission. Hα variations appear linked to pulsational characteristics rather than any long-term effect.
R Sct	RVa	RVA	134.87	Molecular bandheads at deep minimum. Hα mainly absorption.
IW Car	~RVb	RVB	142.73	Hα mainly absorption with long-term motion.

Table 7.5: Quantitative summary of selected RV Tauri stars.

		TT Oph	RU Cen	U Mon
period (days)		60.97	64.57	90.29
(between successive minima)		30.485	—	45.14
epoch[1]		11254.288	11304.478	—
(between successive minima)		11258.867	11303.564	11316.334
Hα equivalent width amplitude		5.5	10	4.0
	Primary maximum	5.5	9	2.5
	Secondary maximum	5.5	5	4.0
ϕ_{max}	(successive minima)	0.94	0.94	∼>0.8
	Primary maximum	0.05	0.96	0.2
	Secondary maximum	0.54	0.44	0.8
ϕ_{min}	(successive minima)	0.65	0.5	∼0.6
	Primary maximum	0.3	0.2	0.7
	Secondary maximum	0.8	0.75	∼0.5
Ba II velocity amplitude		44	40	—
	Primary maximum	30	25	—
	Secondary maximum	44	40	—
ϕ_{max}	(successive minima)	0.85	0.95	—
	Primary maximum	0.96	0.35	—
	Secondary maximum	0.49	0.95	—
ϕ_{min}	(successive minima)	∼0.1		—
	Primary maximum	0.31	<0.15	—
	Secondary maximum	0.68	0.55	—
Ca I velocity amplitude		31	—	—
	Primary maximum	31	—	—
	Secondary maximum	31	—	—
ϕ_{max}	(successive minima)	∼0.75	—	—
	Primary maximum	0.96	—	—
	Secondary maximum	0.49	—	—
ϕ_{min}	(successive minima)	∼0.15	—	—
	Primary maximum	0.31	—	—
	Secondary maximum	0.68	—	—
Ca II velocity amplitude		30	—	—
	Primary maximum	14	—	—
	Secondary maximum	30	—	—
ϕ_{max}	(successive minima)	0.85	—	—
	Primary maximum	0.13	—	—
	Secondary maximum	0.49	—	—
ϕ_{min}	(successive minima)	0.6	—	—
	Primary maximum	0.31	—	—
	Secondary maximum	0.88	—	—
Fe I velocity amplitude		35	—	44
	Primary maximum	33	—	44
	Secondary maximum	35	—	42
ϕ_{max}	(successive minima)	∼0.75	—	0.95
	Primary maximum	0.96	—	0.95
	Secondary maximum	0.49	—	0.8
ϕ_{min}	(successive minima)	∼0.1	—	0.02
	Primary maximum	0.31	—	0.2
	Secondary maximum	0.64	—	0.02
Fe II velocity amplitude		33	—	—
	Primary maximum	33	—	—
	Secondary maximum	28	—	—
ϕ_{max}	(successive minima)	∼0.75	—	—
	Primary maximum	0.96	—	—
	Secondary maximum	∼0.9	—	—
ϕ_{min}	(successive minima)	∼0.1	—	—
	Primary maximum	0.31	—	—
	Secondary maximum	0.68	—	—
Photometric type		RVa	RVa	RVb
Spectroscopic type		RVA	RVB	RVA

[1]From acceleration phasing. Epoch = Julian Date -2440000.

Chapter 8

Summary and discussion

Over the past four chapters, photometry and spectroscopy of a selection of Type II Cepheids has been presented and discussed in the context of the three star types examined: BL Her, W Vir and RV Tauri. These results will now be summarized and discussed in a more general context, focusing on common behavioural characteristics and distinctions among them. To this end, the photometric characteristics of the Type II Cepheids will be reviewed, followed by the spectral characteristics. These will then be combined to examine the overall pulsational characteristics and the longer-term variations that are observed and their possible causes.

8.1 Photometric characteristics of Type II Cepheids

One of the main motivations in gathering photometric observations concurrently with the spectroscopic observations was to enable the spectroscopy to be phased accurately based on actual measurements at the time, rather than ephemerides from earlier times. This has proved necessary as several of the stars have changed period since they were last studied (eg. ST Pup and U Mon), while others have been less than regular in their pulsation patterns (eg. R Sct and U Mon).

Period changes play an important role in the analysis of these stars, especially with respect to the evolutionary models and their predicted behaviour, and constant monitoring is required to keep track of these changes. The lack of detailed photometric studies over long time spans has meant that previous researchers have tended to take the closest historical period source (often various editions of the GCVS) which can mask various behavioural changes and lead to misunderstandings of the star's behaviour.

U Mon is an example of the need for constant monitoring. Over the last 11 years the period has changed by 2 days, from 92.32 days (Pollard et al., 1996a) to 91.75 days (Fourier analysis of MJUO V photometry 1990–2001) to 90.29 days (Fourier analysis of AAVSO visual estimates of 1998–2001). Using the 91.75 day period to phase the radial velocity curves, compared with the period derived from the analysis of photometry from the same time frame as the spectral observations, was enough to initially lead to inaccurate conclusions about the cycle to cycle variation of the star. While it is often difficult to get simultaneous photometry and spectroscopy, efforts should be made to at least have some idea of the star's photometric variations when it is examined spectroscopically. Here the amateur star observers can prove invaluable. For the brighter stars, such as U Mon and R Sct, large databases of visual estimates exist with the AAVSO, AFOEV, Variable Star Section of RASNZ and other such organizations, and these can be used to precisely determine what pulsational phase and period are appropriate for the spectroscopic observations.

Table 8.1: Type II Cepheids photometric characteristics.

Star	Type	Period[a] (days)	V range	Pulsational amplitude in V[b]	ϕ_{min} shifts between B and I
VY Pyx	BL Her	1.239938	7.15–7.4	0.25	0.024
SW Tau	BL Her	1.583560	9.4–10.2	0.8	0.122
V381 Cen	Classical Cepheid	5.07878	7.2–8.0	0.8	0.03
TX Del	BL Her?	6.1634	8.9–9.6	0.7	0.039
κ Pav	W Vir	9.0741	4.0–4.8	0.8	0.049
AL Vir	W Vir	10.2950	9.2–10.0	0.8	0.194
W Vir	W Vir	17.2768	9.6–10.8	1.2	0.028
ST Pup	W Vir	18.6204	9.6–10.8	1.2	0.063
SX Cen	RVb Tauri	32.82	9.1–11.4	0.8	0.475
TT Oph	RVa Tauri	60.97	9.4–10.7	1.5	0.036
RU Cen	RVa Tauri	64.57	8.5–9.8	1.3	0.419
CT Ori	RVa Tauri	67.42	10.3–11.2	0.9	0.014
AI Sco	RVb Tauri	71.45	8.8–11.2	1.4	0.043
AR Pup	RVb Tauri	76.47	9.1–10.1	0.55	0.553
AR Sgr	RVa Tauri	87.13	9.1–10.4	1.3	0.017
UZ Oph	RVa Tauri	88.90	10.2–12.5	2.3	0.027
U Mon	RVb Tauri	90.29	5.5–7.8	2.0	0.053
R Sct	RVa Tauri	134.87	4.9–6.7	1.8	0.019
TX Oph	RVa Tauri	135.81	9.7–10.7	1.0	0.418
IW Car	RVb Tauri?	142.73	7.8–9.2	0.35	0.473

[a]Between successive deep minima for RV Tauri stars and successive minima for the other stars.

[b]Long-term variations removed.

8.1.1 General characteristics

As can be seen from Table 8.1, the periods for the shorter period BL Her and W Vir stars could be determined to a far greater precision than those for the RV Tauri stars. Overall trends showed a greater scatter between the photometry as the period of the star increased. This contributed to the accuracy of the period found, especially when it was defined by the lowest residuals of a Fourier fit (see Tables 4.1, 4.6, 4.11 and 4.12). This also contributed to difficulties in defining the phase of minimum light, especially since these were dependent on how good a Fourier fit had been obtained in the first place. Hence the phase shifts in the last column of Table 8.1 should be examined in context with the photometry. In several cases (SX Cen, RU Cen, AR Pup, TX Oph and IW Car), the large shifts are due to the minimum fit to B or I falling on the shallow minimum with respect to the V photometry, rather than the deep minimum. On average, there is a tendency for the light minimum to occur earlier in the pulsation cycle as we move to the bluer wavelengths.

The phase shift of minimum light at redder wavelengths is unsurprising when the temperature changes observed in the stars are taken into account. The phase lag implies that the *(B-V)* or *(V-I)* colours are changing over a pulsation cycle as the star changes

effective temperature.

The maximum light brightness dependence on photometric bandpass is especially interesting for the stars of periods greater than 17 days (W Vir onwards). In the Type II Cepheids of shorter period, the extreme variations in the light maximum with photometric bandpass are not observed as the light is mainly governed by the effective temperature changes which produces the phase lag. For the longer period stars this is no longer the case as the symmetry of the light curves (as observed in W Vir and ST Pup) is upset by an initial peak which is strongest in the bluer wavelengths. To understand this feature we need to examine the spectroscopy. In the longer period range, we pass into the region where the shock-waves are strong enough that Hα emission is present at all phases but is strongest around, or just before, minimum mean photospheric radius. This has been examined quantitatively in W Vir, ST Pup, TT Oph, RU Cen and U Mon, all of which show heightened Hα emission at this phase (see Figures 6.20, 6.27, 7.6, 7.15 and 7.26). Of these, W Vir, ST Pup and RU Cen also show the separate bluer peak. Photometrically this peak appears just after phase 0.0, as defined by the acceleration in W Vir and ST Pup and at phase 0.0 in RU Cen. Peak Hα emission occurs just before phase 0.0 in all three of these stars and it is unclear why this phase difference occurs. This will be further discussed in association with the spectral features in Section 8.3.

Table 8.2: BL Her star summary.

	VY Pyx	SW Tau	V381 Cen	TX Del
period (days)	1.2399	1.5836	5.0788	6.1634
epoch[a]	11310.396	11394.589	11310.913	11314.228
radii (in solar radii)[b]	—	8.3±0.8[c]	—	38.8[d]
		12.3±3[b]		47.6±5.4[c]
				43±7[b]
Hα velocity amplitude	30	55[e]	49	>40[e]
phase max	0.0	>0.9	0.95	0.9
phase min	0.4	0.15	0.05	<0.1
Ca II velocity amplitude	27	32	41	>40
phase max	0.9	>0.9	0.95	0.9
phase min	0.2	0.15	0.15	<0.1
Fe I velocity amplitude	17	35	35	>30
phase max	0.8	>0.9	0.9	0.8
phase min	0.2	0.1	0.1	<0.1
Na I velocity amplitude	11	—	—	—
phase max	0.85	—	—	—
phase min	0.2	—	—	—
	Type II	Type II	Type I	Type ?

[a]From acceleration phasing. Epoch = JD -2440000.
[b]Balog et al. (1997)
[c]Laney (1995)
[d]Balona (1977)
[e]From 0.9 level bisector.

Table 8.3: W Vir star summary.

	κ Pav	AL Vir	W Vir	ST Pup
period (days)	9.0741	10.295	17.2768	18.6204
epoch[a]	11308.336	11310.281	11305.594	11390.141
radii (in solar radii)[b]	29.1±0.8[c]	26.2[d]	35±10[b]	—
	19±5[b]	34.0±2.0[c]		
		38±10[b]		
Hα velocity amplitude	38	32	—	—
phase max velocity	0.1	0.1	—	—
phase min velocity	0.2-0.8	0.25	—	—
Hα EW amplitude	—	—	13.5	8.5
phase max EW	—	—	0.89	0.00
phase min EW	—	—	0.47	0.50
Ca II velocity amplitude	36	43-46	24	—
phase max velocity	0-0.05	0.2	0.9	—
phase min velocity	0.3	0.85-0.95	0.3	—
Fe I velocity amplitude	28	25	49	—
phase max velocity	0.9	0.85	0.00	—
phase min velocity	0.15	0.20	0.15	—
Na I velocity amplitude	30	35	55	—
phase max velocity	0.9	0.9	0.05	—
phase min velocity	0.15	0.2	0.15	—
	Type II	Type II	Type II	Type II

[a]From acceleration phasing. Epoch = JD -2440000.
[b]Balog et al. (1997)
[c]Laney (1995)
[d]Balona (1977)

8.2 Spectroscopic characteristics of Type II Cepheids

The Type II Cepheids cover the spectral range of late A to K. Hence for all the stars, other than the RVB and RVC stars (Preston et al., 1963), metallic lines are strong and generally easily measured, but the line strengths can vary as a function of phase. Those stars strongly affected by shocks show very weak, if any lines when the shock is most evident (W Vir, TT Oph, U Mon). At the other extreme in line behaviour, the molecular bandheads occur in the longer period stars when the atmosphere is at its most extended and cool (R Sct and U Mon).

The properties of the radial velocity curves are summarized in Tables 8.2, 8.3 and 8.4, while Table 8.5 gives a general description of the spectroscopic features observed in the remaining RV Tauri stars which did not have radial velocities measured.

As can be seen from Tables 8.2, 8.3 and 8.4, the velocity amplitudes do not strongly correlate with period for the Type II Cepheids for the same line species. For two stars with very similar periods, VY Pyx (P = 1.2399 days) and SW Tau (P = 1.5836 days), the amplitudes can be quite different (Hα and Fe I), or agree quite closely (Ca II).

Table 8.4: Quantitative summary of selected RV Tauri stars.

	TT Oph	RU Cen	U Mon
period (days)	60.97	64.57	90.29
(between successive minima)	30.485	—	45.14
epoch[a]	11254.288	11304.478	—
(between successive minima)	11258.867	11303.564	11316.334
Hα equivalent width amplitude	5.5	10	4.0
Primary maximum	5.5	9	2.5
Secondary maximum	5.5	5	4.0
ϕ_{max} (successive minima)	0.94	0.94	$\sim>0.8$
Primary maximum	0.05	0.96	0.2
Secondary maximum	0.54	0.44	0.8
ϕ_{min} (successive minima)	0.65	0.5	~0.6
Primary maximum	0.3	0.2	0.7
Secondary maximum	0.8	0.75	~0.5
Ba II velocity amplitude	44	40	—
Primary maximum	30	25	—
Secondary maximum	44	40	—
ϕ_{max} (successive minima)	0.85	0.95	—
Primary maximum	0.96	0.35	—
Secondary maximum	0.49	0.95	—
ϕ_{min} (successive minima)	~0.1	0.00–0.2	—
Primary maximum	0.31	<0.15	—
Secondary maximum	0.68	0.55	—
Fe I velocity amplitude	35	—	44
Primary maximum	33	—	44
Secondary maximum	35	—	42
ϕ_{max} (successive minima)	~0.84	—	0.95
Primary maximum	0.96	—	0.95
Secondary maximum	0.49	—	0.8
ϕ_{min} (successive minima)	~0.1	—	0.02
Primary maximum	0.31	—	0.2
Secondary maximum	0.64	—	0.02
Photometric type	RVa	RVa	RVb
Spectroscopic type	RVA	RVB	RVA

[a]From acceleration phasing. Epoch = JD -2440000.

Table 8.5: Qualitative summary of selected RV Tauri stars.

	Type		Period	Description/features
	Photometric	Spectral		
SX Cen	RVb	RVB	32.82	Ba II line. Hα absorption. Possible orbital variations.
AI Sco	RVb	RVA	71.45	Metallic lines varying as a function of pulsational phase. Ba II line splitting. No metallic line variations similar to Hα long-term variations. Hα shows broad blue-ward absorption before long-term minimum, strong emission during and weak emission after.
AR Pup	RVb	RVB	76.47	Weak Ba II lines. Small long-term Hα velocity variation. Na D red-ward emission.
AR Sgr	RVa	RVA	87.13	Metallic lines varying as a function of pulsational phase. Ba II line splitting, Ti I emission, He I emission. Hα variations appear linked to pulsational characteristics rather than any long-term effect.
R Sct	RVa	RVA	134.87	Molecular bandheads at deep minimum. Hα mainly absorption.
IW Car	~RVb	RVB	142.73	Hα mainly absorption with long-term motion.

In contrast, the amplitude of the Fe I curve in TT Oph (P = 60.97 days) is similar to that of SW Tau and V381 Cen (P = 5.0788 days). Also the Fe I amplitude observed in U Mon (P = 90.29 days) is similar to that observed in W Vir (P = 17.2768 days).

The phases at which the various velocities peak also shows no correlation with period for the same line species. For instance, the Fe I curves peak between phases $\sim$ 0.8 (VY Pyx) and 0.0 (W Vir), with the majority of stars falling between phases 0.8–0.9. This is not the case when the range of other line species is examined, as the differences in velocities observed between line species increases as the period increases. This is most easily examined by comparing the BL Her and W Vir stars (excluding ST Pup) and to a lesser extent TT Oph and U Mon as these share a great many of the same lines (Hα, Ca I, Ca II, Fe I, Fe II, Ba II, and Na I).

Of the lines examined in the majority of stars, Fe I and Fe II agree most closely in the BL Her stars, but show a 2–3 kms^{-1} difference at minimum velocity in κ Pav and by W Vir, a difference of up to 10 kms^{-1} at maximum velocity. In TT Oph and U Mon, a difference of up to 5 kms^{-1} may be observed. Na I shows large variations but is contaminated by interstellar lines in most, if not all, cases so has not been pursued further here. Also not to be discussed here are Ba II and Ca I as these were only examined for the RV Tauri stars, but follow up work on these lines in the BL Her and W Vir stars is recommended at a future date, especially since the Ba II line at 5853 Å is also found in some of the RVB stars and allows comparison of a greater range of stars.

Of the remaining lines, the Hα behaviour is most complicated. When in absorption, it shows an increased velocity amplitude compared to the metallic lines and peaks in velocity later in phase. This is most clearly evident in VY Pyx, V381 Cen and κ Pav. VY Pyx and V381 Cen also show definite Hα line broadening, whereas in SW Tau and κ Pav, the behaviour has become more complicated with line splitting at certain phases, indicating a shock wave traversing the line forming region. This splitting reaches a peak in κ Pav where the line splits at two different phases, implying a second shock which appears to be propagating back into the star. By AL Vir, we see blue-ward emission in the Hα wings, and by the longer periods of W Vir and ST Pup, the emission is very strong with multiple components. This strong Hα emission behaviour persists in TT Oph and RU Cen, but has become much weaker in U Mon.

The Ca II behaviour is approximately midway between that observed in the metallic lines and the Hα line. Again, VY Pyx, V381 Cen and κ Pav all show this most clearly. Their velocity variations in Ca II are larger than the Fe I velocities but smaller than the Hα variations, but with a smaller phase lag in the peak velocity position. Splitting associated with shock related effects does not appear until κ Pav and longer periods, although V381 Cen and TX Del both show broadening of the Ca II lines. VY Pyx and SW Tau also show secondary components in some observations of the Ca II 8542 Å line, but these do not correlate with phase and their origin is unknown. For AL Vir and longer period stars, the Ca II velocities become less of a smooth curve and decrease in amplitude. This is due to possible emission in the line's blue wing, which is most clearly seen in W Vir and U Mon.

8.2.1 Line level effects

Line level effects have been observed in all of the stars examined in this work. As seen in Tables 8.2, 8.3 and 8.4 and discussed in the previous section, the different metallic lines reach maximum and minimum velocity at different phases and with different amplitudes. This has been reported in the literature for Type I Cepheids (Petterson, 2002), and for the shorter period BL Her and W Vir stars (Wallerstein et al., 1992; Vinkó et al., 1998), especially with respect to the difference between the metallic and Hα absorption line velocities. It is clear that such effects are visible for all the stars observed for this thesis. The degree of difference in velocity is correlated with the period. The longer period stars show much larger velocity differences than the shorter period stars. This is unsurprising when the relationship between the period of the star and the size of the star is taken into account. The longer period stars are larger and hence the photosphere and line-forming regions are larger and more extended. There is thus the potential for far greater ranges of pulsational velocities than the more compact, shorter period stars.

Current work already exists in attempting to trace line splitting and shock wave behaviour as a function of depth and pulsational phase for Long-Period-Variables (Alvarez et al., 2000) using the different line-level effects. With the LPV work, typical effects for a particular temperature and pressure range are created by cross-correlating the observed spectrum with a model spectrum of lines formed under those particular conditions. Different model spectra are created for a range of conditions and thus a range of depths. This allows a snapshot into different depths of the star at one time. Examination of other spectra at successive pulsational phases allows the shock behaviour to be tracked. The technique is model dependent and gives relative rather that absolute depths.

The different line level effects presented here are an initial investigation of this phenomenon and have the advantage that they are not model dependent, and can thus be compared directly.

The line level effects also mean that Baade-Wesselink radii for Type II Cepheids should be counted as indicative only and used with caution, as it cannot be assumed that the velocities of the lines traced are derived from the same levels in the star as those examined through the photometry. More specifically the velocities measured will depend on the lines measured. Several authors have warned of this previously with respect to the Type I Cepheids (Sasselov and Lester, 1990; Sasselov, 1997). The results of this work confirm that the method is not recommended for the Type II Cepheids unless extreme care is taken. In any case, the radii obtained from such surveys (Tables 8.2 and 8.3) vary quite widely.

8.2.2 Phasing dynamically

Both the spectroscopic and photometric features cannot be compared in a realistic way if they are not phased up consistently. Traditionally, the approach has been to phase the data based on either the maxima or the minima of the light curve such that one of the extrema defines phase 0.0. As seen from the photometric curves presented here (Chapter 4), while light minimum has been generally viable, the exact zero-point phase depends on the photometric bandpass used and may be affected by the fit to the curve used and the regularity of the minimum. As an alternative approach, a spline curve has been fitted to the mean Fe I velocity curve and its derivative found to give an acceleration curve. The well defined minimum of this acceleration curve has then been used as phase 0.0, and then all the data has been rephased.

Astrophysically, this shifts the phasing to a dynamical zero-point, as the acceleration minimum (in the observer's rest-frame) is when the photosphere of the star is at its maximum inward displacement, and marks the boundary between deceleration inwards as material fall towards the centre of the star, and acceleration outwards, away from the centre. This gives a clear reference point with respect to all the stars. The velocity curves show similar features at similar phases. It also means that the phases of shock features, such as line splitting and line emission, can be compared in a standardized way. This has established that peak emission is associated with minimum photospheric radius for all the stars in which it is observed.

It should be noted that, due to the line level effects, different zero-points will occur depending on the line species used, just as different zero-points result from the *BVRI* filters due to the different bandpasses examined. It could be argued that the acceleration phasing just results in a different version of the same problem as the line species still has to be chosen and the "most representative" line species for the photospheric layer decided. However, preliminary line level work on Type I Cepheids (Petterson, 2002) has shown that the mean Fe I velocities best represent the mean velocities of all the lines examined (a selection similar to that listed in Appendix E). More importantly, a single line can more accurately have its line forming region defined, compared to the broader photometric bandpasses.

8.3 Pulsational characteristics of Type II Cepheids

Examined purely on the mean Fe I radial velocity curves observed, the pulsational behaviour of the Type II Cepheids examined here is remarkably similar. The main difference in overall shape is due to shock waves splitting the lines such that maximum and minimum velocity can be measured simultaneously. Those stars for which the shocks are not strong enough to create a measurable discontinuity show a more gradual velocity slope with a greater phase difference between minimum and maximum velocity. This can be seen both in those stars which appear to have no shock and those for which the shock only broadens the lines due to the velocity difference across the shock not being large enough to create two distinct peaks. This behaviour is shared by both RV Tauri and W Vir type stars. Figure 8.1 demonstrates this with velocity curves representative of the three main star types examined here: BL Her, W Vir and RV Tauri. There is little sign of a shock in the velocities of VY Pyx, but shock waves are clearly evident from the discontinuous velocities in W Vir and TT Oph. Table 8.6 summarizes the shock-related features observed in the Type II Cepheids examined here, typified by the pulsational and shock affected behaviour observed in W Vir (see Figure 8.2). These provide examples of the photometric and spectroscopic features associated with shocks which are tabulated in Table 8.6.

The features associated with shocks are (1) the strong Hα and He I 5875 Å emission (Figure 8.2a), (2) the rapid transition from maximum to minimum mean Fe I radial velocity (Figure 8.2b) which correlates with the line splitting and broadening listed in Table 8.6 and (3) (derived from (2)), the acceleration minimum at which the mean photospheric layer is at its lowest radial displacement from the centre of the star (Figure 8.2c). Figure 8.2d shows the *B* magnitude peak which occurs slightly ahead of a more rounded peak in the *BVRI* photometry and which decreases in magnitude towards redder wavelengths. Figure 8.2e shows the blue peak in the *(B-V)* colour occuring before the *V* magnitude light minimum. All of these features occur around phase 0.0. This is unsurprising as the acceleration phasing was an attempt to phase based on minimum photospheric radius and in those stars with shock waves propagating through, it is this shock which reverses the mean direction of motion in the line forming region. The velocity curve phase shifts for different line species are evident, representing the lines with different excitation levels forming in different regions of the photosphere and the velocity structure changing in these line forming regions. The shock hits different layers at slightly different phases as it propagates out through the star. Hence Fe I and Fe II form further into the star than Ca II and Hα since Ca II and Hα show mean velocity reversal for the greater part of their line forming regions at a later phase than Fe I and Fe II.

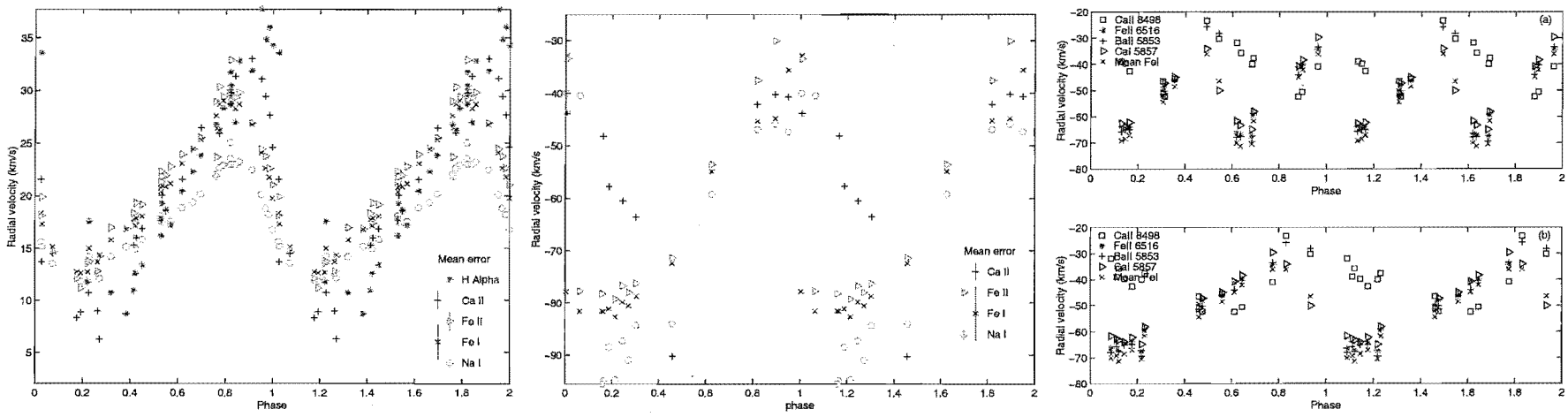

(a) VY Pyx

(b) W Vir

(c) TT Oph: (a) Phased on 60.97 day period and (b) phased on 30.485 day period.

Figure 8.1: Representative radial velocity curves for the BL Her, W Vir and RV Tauri stars.

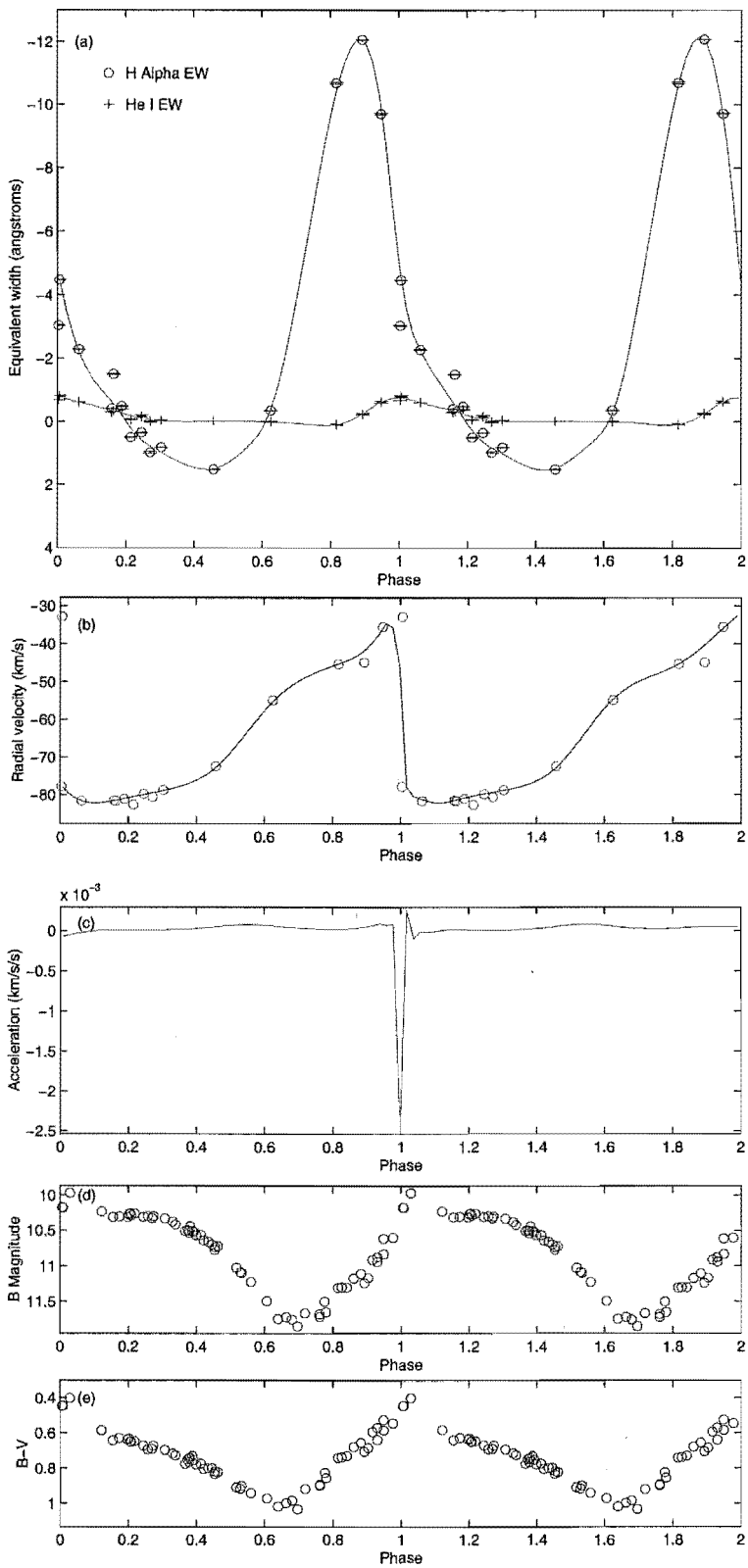

Figure 8.2: A summary of W Vir features, all phased using the minimum of the acceleration curve in (c).
(a) Equivalent widths of Hα and He I 5875 Å.
(b) Mean Fe I velocity curve with spline fit.
(c) Acceleration derived from spline fitted Fe I velocity curve.
(d) *B* magnitude curve.
(e) *(B-V)* colour curve.

Table 8.6: Shock characteristics present in Cepheids.

Star	Type	Period (days)	Separate blue peak indicating shock	Colour phase lag	Line broadening/splitting	Emission
VY Pyx	BL Her	1.239938	No	Yes (slight)	Slight Hα broadening. Ca II 8542 Å splitting (not phase related)	No
SW Tau	BL Her	1.583560	No	No	Hα splitting. Ca II 8542 Å splitting (not phase related)	No
V381 Cen	Classical Cepheid	5.07878	No	No	Hα broadening. Ca II broadening.	No
TX Del	BL Her?	6.1634	Maybe	Yes (slight)	Hα broadening. Ca II broadening.	No
κ Pav	W Vir	9.0741	Maybe	Yes	Hα broadening and splitting. Ca II splitting.	No
AL Vir	W Vir	10.2950	Maybe	Yes	Hα splitting. Ca II splitting.	Slight blue wing emission Hα.
W Vir	W Vir	17.2768	Yes	Yes	Ca II splitting. Na D splitting. Metal lines weakening/possible splitting.	Strong multiple component Hα. Strong He I 5875Å. Possible Ca II blue wing emission.
ST Pup	W Vir	18.6204	Yes	Yes	Metal lines weakening/possible splitting.	Strong multiple component Hα. He I 5875 Å.
SX Cen	RVb Tauri	32.82	Yes — Larger on primary maximum.	Yes/no — on shallow/deep minimum.	—	Blue-ward wing emission on Hα.
TT Oph	RVa Tauri	60.97	Maybe	Yes	Ti I 5866 Å splitting.	Ti I 5866 Å. Slight He I 5875 Å. Strong multiple component Hα.
RU Cen	RVa Tauri	64.57	Yes	Yes	Few lines.	Strong multiple component Hα with strong blue-ward absorption on certain dates. He I 5875 Å.
CT Ori	RVa Tauri	67.42	Yes	No? — Bad data coverage around deep minimum.	—	—
AI Sco	RVb Tauri	71.45	Yes — Only on secondary maximum.	Yes — But only *(B-V)* and *(V-R)*. No phase lag in *(V-I)*.	Metallic line splitting.	Strong multiple component Hα with strong blue-ward absorption prior to long-term minimum.

continued on next page

Table 8.6: *continued*

Star	Type	Period (days)	Separate blue peak indicating shock	Colour phase lag	Line broadening/splitting	Emission
AR Pup	RVb Tauri	76.47	Yes — Strongest on primary maximum.	Yes/no — on shallow/deep minimum.	Few lines	Single component Hα. Red-ward Na D.
AR Sgr	RVa Tauri	87.13	Yes — Both maxima.	Yes/no — on shallow/deep minimum.	Metallic line splitting.	Strong multiple component Hα.
UZ Oph	RVa Tauri	88.90	Yes — Both maxima.	Yes — But only *(B-V)* and *(V-R)*. No phase lag in *(V-I)*.	—	—
U Mon	RVb Tauri	90.29	Can't tell	Yes — But only *(B-V)* and *(V-R)*. No phase lag in *(V-I)*.	Ba II (and other metals) line splitting.	Multiple component Hα. Ti I 5866 Å. Ca II.
R Sct	RVa Tauri	134.87	Can't tell	Can't tell	Metallic line splitting.	Slight blue-ward wing Hα emission.
TX Oph	RVa Tauri	135.81	Yes — slightly on primary maximum only.	Yes — Only on shallow minimum. Can't tell on deep minimum.	—	—
IW Car	~RVb Tauri	142.73	No	No	Few lines	Very slight Hα emission on wings.

It should be noted that while all the shock related features do occur around phase 0.0, they only fall exactly on it for the acceleration minimum and Fe I splitting (by definition) and the He I emission. The Hα emission peaks around phase 0.9, whereas the *B* and *(B-V)* curves peak just a little after, at around phase 0.05. The photometric phase lag is interesting given that the *BVRI* light characterizes a sum over all the different regions, from the continuum outwards and it is unclear why this phase lag exists. The He I emission is less surprising given that it is originating in the photosphere in the recombination and relaxation zone behind the shock wave, and not out in the stellar chromosphere (Wallerstein and Elgar, 1992). The Hα emission peak is a little more puzzling in that it peaks well before the shock hits the middle of the mean Fe I line forming regions. This is curious as the velocities from the Hα absorption profiles in the shorter period stars peak well after the Fe I line velocities, indicating a mean radius of the formation region further out than that of the Fe I, although the regions quite possibly overlap due to the large region of Hα line contribution. If the Hα emission line is also formed in the same regions, and maximum emission is associated with the transition through the mean Hα line forming region, then it would be expected that peak Hα emission would be associated with phase 0.0–0.1. This is not the case in W Vir, ST Pup, TT Oph and RU Cen, as Hα emission peaks between phases 0.9 and 0.0. A definitive answer is not possible from the information here, but possible options can be suggested. It may be that peak emission is associated with the start of the shock entering the line-forming region, and that as the shock gets further though the region, the emission is reduced by the effects of the absorption on either side. This suggestion is highly speculative. Certainly the Hα line structure is quite complicated in W Vir, ST Pup, TT Oph, RU Cen, AR Sgr and U Mon, with multiple emission and absorption components, which may contribute various amounts at various phases and from a range of regions within the photosphere.

The RV Tauri stars examined show similar shock features, with similar colour changes, line splitting and emission (Table 8.6). These are however less correlated with the period between successive minima, and appear to show variations which repeat on the period between successive deep minima. Also particular features are more pronounced during particular minima depths. However whether these features precede the deep or the shallow minimum varies between stars. This indicates the shock strength may affect how deep minimum light is. It should be noted that the continuum from the photometry and the Hα line emission varies in this way. This indicates that stronger shocks, or at least very high temperatures, are associated with them, varying with the continuum light levels or at least on the same time-scale as these. Another way of characterizing shock strength is to examine the velocity difference across the shock, as a stronger shock will show a greater velocity difference. This is observed as a greater separation between line components for a given line species. This is not observed in the RV Tauri stars examined here, as the Fe I (and Ba II) velocities measured did not show amplitude changes between primary maximum and secondary maximum, indicating that the shocks were of similar, if not identical, strength. This may be a selection effect, as the lines examined are generally picked to show as little line splitting as possible so as to measure the velocities more accurately. Examination of a wider variety of lines formed at a greater range of optical depths may show more variation at certain depths which may correlate with the depths of the light minima. More observations are needed to confirm this.

8.3.1 Similarities and differences

BL Her/W Vir/RV Tauri and Type I/Type II

The radial velocity curves are very similar for all three of the BL Her, W Vir and RV Tauri classes examined here. The main difference appears to relate to the strength of the shock, which is a function of period (up until somewhere in the RV Tauri stars), rather than dividing clearly into the three types. This is unsurprising when it is considered that the same pulsation mechanism (κ) is thought to be responsible. Compared to the Type I Cepheid observed (V381 Cen), there is little difference in the velocity curves, such that TX Del, being alternately classed as Type I or Type II by various authors, could not be classified based on the radial velocity curves presented.

8.3.2 Stability of periods and period changes

The initial hypothesis was that the longer-period Type II Cepheids had less reliable periods and would show greater cycle to cycle variations. Generally this hypothesis has been upheld. The BL Her stars show a greater degree of repeatability in their light curves and velocity patterns than the longer period stars, with the degree of scatter observed in the light and velocity curves increasing at longer wavelengths. It is certainly the case that κ Pav (P = 9.0741 days) shows less scatter than AL Vir (P = 10.295 days), which in turn shows less scatter than W Vir (P = 17.2768 days) and ST Pup (P = 18.6204 days). This trend become less reliable when we move to the RV Tauri stars. Of the RV Tauri stars for which velocities have been derived, TT Oph (P = 60.97 days) appears to show the least scatter in the radial velocity curves. However U Mon (P = 90.29 days used for the radial velocities) shows less scatter than RU Cen (P = 64.57 days). The greater degree of repeatability of the U Mon curve is most likely due to the removal of the orbital motion, however this cannot be confirmed in comparison to RU Cen without defining an orbital solution for RU Cen and removing its orbital motion, which is beyond the scope of this work. Also the velocity curves for U Mon were only 9 cycles in duration, compared to the 12 cycles monitored for RU Cen.

The remaining RV Tauri stars can only be evaluated based on the light curves at this time. But our hypothesis still holds, as the longer period stars such as R Sct (P = 134.87 days) and TX Oph (P = 135.81 days) have greater RMS residuals from the Fourier fitting than TT Oph and RU Cen (see Section 8.1.1). However, of far greater effect on the photometric residuals is the long-term variations, since the accuracy of the spline fit to try to remove the long-term variations dictates the size of the RMS value for the RVb stars. Generally, once the long-term variations are removed, the RMS values are of the same order as the other RV Tauri stars. U Mon is a notable exception to this trend as the RMS residuals value remains high. This is mainly due to the longer baseline of observations and the range of periods observed over the eight year long baseline (See also Section 8.1).

The period changes examined in most detail here have been those for ST Pup and U Mon, with ST Pup showing an increase in period from 18.462 days (Kilkenny et al., 1993) to 18.6204 days (this work) (a 0.9% increase), and U Mon changing from 92.32 days (Pollard et al., 1996a) to 91.75 days (from Fourier analysis of MJUO V photometry 1990-2001) to 90.29 days (from Fourier analysis of AAVSO visual estimates of 1998-2001) (a 1.7% decrease). Unfortunately it is rare to find photometry of sufficient time resolution over a long enough baseline to be able to determine large and/or systematic period changes

for the majority of the stars and also to determine if such changes are abrupt, gradual or whether or not they follow a consistent slope or random variation about a constant mean. The method of period analysis may also affect the conclusions reached. Percy et al. (1991) found U Mon and R Sct to be decreasing in period using O-C techniques whereas Matsuura et al. (2002) found the period of R Sct to be varying between 130 to 150 days in an irregular fashion via wavelet analysis. Wavelet analysis of U Mon (McSaveney et al., 2002) found the period varied but found no specific trend in evolution (Figure 4.67).

Overall, there appears to be insufficient evidence at present to be able to confidently comment on the period changes observed in the Type II Cepheids and how this relates to their evolutionary status. The uncertainty in the accuracy of the historically reported periods, the lack of consistent observed trends and the paucity of methodical long-term observations for the majority of the stars are problems which will need to be overcome before that can be resolved.

8.3.3 RV Tauri periods and the alternating minima

The definition of an RV Tauri star involves a pattern of alternating deep and shallow minima in the light curve with qualifications limiting the spectral type. Hence there has always been the question of whether the most physically relevant period is that between successive minima or successive deep minima. Observations of variations in the pattern of minima, such that deep minima may occasionally or quite regularly be followed by deep minima, or shallow minima may be followed by shallow minima ("flips"), have only complicated matters. As such, the fundamental definition of the period for the RV Tauri stars has always been an interesting question. This is especially so with respect to establishing a Period-Luminosity (P-L) relationship for the Type II Cepheids. The most recent work on this did establish a P-L relationship (Alcock et al., 1998) but raised issues as to the fundamental period observed (Pollard et al., 1997). The work here does not solve this dilemma, but suggests that it is greatly dependent on the regions of the star being examined and suggests regions of the star which might be examined in future to test this.

All three of the RV Tauri stars examined in detail showed no radial velocity differences in the pulsations following the deep minima or the shallow minima. All phased cleanly on the period between successive minima as well as between successive deep minima, implying that in the regions being traced by those particular metallic lines (Ba II, Ca I, Ca II, Fe I, Fe II) the fundamental period of pulsation is that between successive minima. This is in contrast to the infrared spectra work by Mozurkewich et al. (1987); Hinkle et al. (1996); Pollard et al. (1996b) who found that the infrared atomic lines they examined in R Sct varied purely on the formal period between successive deep minima and showed no signs of variation on the shorter period time-scales. However the infrared lines examined are probing far deeper into the stellar photosphere, taking advantage of the decrease in H^- opacity in that wavelength range.

This infrared variation combined with the differences in photometric and Hα equivalent width behaviour preceding shallow minima and deep minima implies quite different behaviour as a function of depth in the stellar photosphere of the Type II Cepheids. Clearly in the layers where the metallic lines are formed, the pulsation mechanisms are causing those particular layers to move in similar ways in all of the Type II Cepheids. The differences are introduced as the stars become large enough that the density, temperature

and velocity differences become too great to return to the same starting point over the cycle between successive minima, and require approximately two or more cycles to return to approximately the same conditions (same light depths in the minima). R Sct appears to represent the extreme of this condition as chaotic behaviour leads to extreme variations on long time-spans (Buchler et al., 1996; Buchler and Kolláth, 2001, 2003), where several years may pass before the star is back in a quasi-stable pattern of deep/shallow alternating minima.

8.3.4 RV Tauri long-term variations

The chaotic behaviour of the light curve of R Sct has lead some to argue that it should be classed as an RVb star (Howell et al., 1983; Cardelli, 1985; Cardelli and Howell, 1989) in that its light curve shows variations, especially with respect to the depths of its minima, on a time-scale greater than that of the pulsation cycle. Examining the spectra of R Sct and the variations observed in the observed RVb stars (SX Cen, AI Sco, AR Pup, U Mon and IW Car), R Sct does not fall in the long-term variation patterns observed, or more specifically, perhaps the defining characteristics of the RVb stars should be clarified.

The variations R Sct show in the depths of its minima where the "deep" minima (see the AFOEV photometry, Figure 4.61) can be as shallow as the shallow minima, or as observed by Howell et al. (1983), an especially deep minimum can occur. In contrast, based on the photometry from Section 4.4, the RVb stars can be most easily characterized by their variation in maximum light level. AAVSO visual estimates show that the depths of the minima vary during the long-term minima, as the amplitude of the pulsations decreases at this time (McSaveney et al., 2002, Figure 4.67 and Figure F.4.1 in Appendix F), so the depths of the minima can vary as part of the long-term variation. But this is not in as irregular a fashion as observed in R Sct. Also in U Mon, the pattern of "flips", where a deep minimum may be followed by a deep minimum or a shallow minimum by a shallow minimum, is not correlated with the long-term minima. Both the 46 day and 92 day periods can be equally found or not found inside and outside of the long-term minima (McSaveney et al., 2002, and Figure 4.67 and Appendix F). If flips correlated with the long-term minima, the 45 day period would be found during the minima, but not the 90 day period.

Also generally associated with the RVb long-term behaviour are colour changes. The stars become redder during the long-term minima. This is observed in the photometry (Section 4.4) for SX Cen, AI Sco, U Mon and IW Car, but curiously not in AR Pup. SX Cen shows one complete long-term minimum, and half of the next one, with the *(B-V)*, *(V-R)* and *(V-I)* colours all becoming redder during the long-term minima. A lack of observations over the deepest part of the long-term minima means it cannot be established if there is a phase lag observable in the colours but the transitions into and out of the long-term minima do not appear to show one. AI Sco also shows reddening during the long-term minimum, but it is less distinct than in SX Cen. It appears to show a slight time lag as the colours redden after the V minimum of the long-term minimum. This is not well defined, due to the gaps in the observing season where the deepest part of the long-term minimum was not observed. Pollard et al. (1996a) observed AI Sco for the deepest part of a previous long-term minimum, which also showed reddening, but it cannot be assumed that one long-term minimum will repeat exactly like another, as seen in the AAVSO visual estimates of U Mon (Figure 4.66) and the MJUO photometry (Figure 4.69). As stated

earlier, AR Pup shows no signs of reddening over a long-term maximum but maintains this behaviour over the long-term minimum observed by Pollard et al. (1996a). IW Car shows definite reddening as it entered its long-term minimum but, as only part of the minimum has been observed, it is difficult to establish if a time lag between V and the colours exists. Based on the decline into the long-term minimum it does not appear so. The final star, U Mon, shows definite reddening. It is more pronounced in the first of the long-term minima shown (Figure 4.69 and Pollard et al., 1996a), than the more recent long-term minimum. U Mon also shows a time lag with the colours becoming redder well after the V long-term minimum.

R Sct show completely different colour variations during individual minima, where the colours getting bluer during the deeper minima (Figure 4.58 and Pollard et al., 1996a). Spectroscopically there are also variations associated with this as R Sct shows molecular bandheads during the bluer minimum (Lèbre and Gillet, 1991a; Pollard, 1994, and Figure 7.29e)). This same association of molecular bandheads with deep minima is also observed in RY Ara (Pollard et al., 1996a, 1997). In fact it was even suggested by Lèbre and Gillet (1991a) that the great depths of the minima observed in R Sct could be due to the large opacity due to TiO absorption in the visual spectral region. Certainly this ties in with the bluer *(B-V)* and *(V-R)* colours during the deep minima, as these would be bluer if the V light were reduced in comparison to the B and R. Relative to the long-term variations of the RVb stars, these are completely different colour variations as the only one of the RVb stars studied here to show evidence of molecular bandheads is U Mon, and these are associated with its pulsational deep minima as opposed to the long-term minima. Also U Mon does not become bluer during those deep minima. The spectroscopic changes which do correlate with the long-term variations in the RVb stars are quite different.

U Mon shows greatly enhanced Hα emission over the long-term minima (Figure 7.20). The strength of the emission also appears to correlate with the depth of the long-term minimum in that the emission is stronger during the first, deeper, long-term minimum and weaker during the second, less deep, long-term minimum. The only other RVb star which shows variations of such a scale is AI Sco (Figure 7.28b), which shows strong blue-ward absorption prior to the long-term minimum and very strong multicomponent emission similar to that seen in AR Sgr, TT Oph and RU Cen, in the long-term minimum. As AI Sco exits the long-term minimum, the amplitude of the Hα emission decreases such that it resembles U Mon and then evolves to look more like SX Cen and R Sct. This degree of Hα variation is not observed in any of the other stars. The closest such behaviour is that shown by RU Cen, with strong blue-ward absorption at all phases of the first pulsation cycle observed for this thesis (Figure 7.14a). However, RU Cen shows no accompanying long-term photometric variations and is thus not classed as an RVb star.

Any explanation of the RVb phenomenon must explain long-term photometric variations in the light curve maxima, colour variations and lack of colour variations, enhancement of Hα emission in some cases and not in others, and the decrease of light curve amplitudes in some cases and not in others.

Several possible scenarios to explain this behaviour have been raised by various authors, including a single star which is periodically eclipsed by dust in an R Coronae Borealis type outburst (Shenton et al., 1994b; Zsoldos, 1996), a binary star system (Percy, 1993) with such an outburst (Fokin, 1994) and a binary system in which the pulsating star is periodically eclipsed at certain phases in its orbit by a circumbinary dust torus (Waelkens and Waters, 1993; Pollard et al., 1996a; Van Winckel et al., 1999; Fokin, 2001;

Table 8.7: Orbits and suggested binarity for Type II Cepheids.

Star	Type	Orbit suggested	Orbital solution derived
TX Del	BL Her?		Harris and Welch (1989)
ST Pup	W Vir		Gonzalez and Wallerstein (1996)
SX Cen	RVb Tauri	Maas et al. (2002), this work	
RU Cen	RVa Tauri	Maas et al. (2002), this work	
AR Pup	RVb Tauri	this work	
U Mon	RVb Tauri		Pollard (1994), this work
IW Car	RVb Tauri	this work	
AC Her	RVa Tauri		Van Winckel et al. (1998)
EN TrA	RV Tauri		Van Winckel et al. (1998)

Maas et al., 2002).

In this latter hypothesis, the RVb long-term light variation is a geometric effect as the light variations are a function of the intersection of the stellar orbit, dusty torus and the line of sight. The dust reduces the V magnitude and reddens the colours. The spectral and amplitude variations are more complicated, but a possible explanation using the circumbinary dust hypothesis is that the stars interact at their closest approach, which may not necessarily coincide with the dust obscuration. The exact mechanism by which this may enhance Hα emission (possibly mass loss) and dampen photometric pulsational amplitude is unclear. If it is tidal influences which distort the star and/or cause interaction between the stars then it is plausible that the outer layers (as seen with the $BVRI$ photometry) are distorted and may produce the damped photometric variations. This may in turn affect the regions over which the Hα line forms, which include a greater extent of the star in comparison to the other spectral lines. Damping of the pulsations as indicated by the velocities of such metallic lines as Fe I, typifying the mean photospheric motions, have not been observed, but also do not appear to have been investigated. However, the Fe I velocities for TT Oph and U Mon did not show any indication of the short-term pulsational photometric variations between deep minima, and thus may not show any further interaction on a longer term basis. Future observations at various wavelengths would be needed to confirm this, to examine various depths into the star and if and how the line behaviour changes at the projected interaction times.

It has been hypothesized that all RV Tauri stars, both RVa and RVb, are binary, and that this is one of their major evolutionary influences, producing the observed chemical composition. Their pulsations are a function of their temperature and luminosity and differ little in the photospheric regions from the shorter period W Vir stars. Table 8.7 lists the Type II Cepheids examined here which show evidence for orbital behaviour, as well as a few other binary RV Tauri stars. As can be seen, a number have been suggested binary stars, but few have confirmed derived orbital solutions. This is another area where further observations are needed over many years.

Chapter 9

Conclusions

The aim of this thesis was to examine the Type II Cepheids in terms of their dynamics and investigate the similarities and differences in behaviour between the short period W Virginis stars and the long period RV Tauri stars. To this end, a selection of twenty Type II Cepheids (periods 1 to 150 days) were studied photometrically and spectroscopically. To conclude this work, the photometric (Chapter 4) and spectroscopic (Chapters 5, 6 and 7) results are summarized, especially with respect to the dynamical phasing and line level effects observed. The pulsational characteristics are reviewed, followed by the RV Tauri variations. Future work suggested by this research is then discussed.

9.1 Photometry

BVRI photometry of 20 Type II Cepheids was obtained from April 1999 to May 2002. Periods were found for these stars using Fourier analysis techniques. This revealed that the periods of the shorter period BL Her stars could be determined to a greater accuracy and the scatter on the photometry was less than that for the longer period W Vir stars. These in turn were more accurate in period and less scattered in photometry than those for the RV Tauri stars.

Of the stars studied, significant period changes were detected in ST Pup and U Mon. When the later *BVRI* photometry for U Mon was combined with the earlier *BVRI* photometry, the period was found to have changed from 92.32 (Pollard et al., 1996a) to 91.75 days. Fourier analysis of AAVSO visual estimates over the period of spectral observation gave a revised period of 90.29 days. Wavelet analysis of AAVSO visual estimates over a longer baseline (1961–2000) established that the period varied between approximately 90 and 95 days but showed no evolutionary trends in a particular direction. Overall, there was insufficient evidence to comment on period changes observed as related to their evolutionary status, for the Type II Cepheids. However, the importance of concurrent high density photometry with spectroscopy was emphasized, especially in the use of visual estimates to supplement photometric coverage.

With respect to the light curves, all the stars showed a phase shift as a function of bandpass, with minimum light occurring later at redder wavelengths. For the stars with periods greater than 17 days (W Vir onwards), maximum light also showed a general bandpass dependence with an initial peak which was stronger in the bluer wavelengths. The strength of this peak varied in the RV Tauri stars depending on whether it was the primary or secondary maximum, but no consistent trend was found between the stars.

9.2 Dynamical phasing

As the phase of minimum light varied as a function of bandpass, an alternative method of phasing the data was trialled. Mean Fe I radial velocity curves were phased on the photometric period found and a spline curve fitted. This curve was then differentiated to find an acceleration curve. The minimum of this acceleration curve, which corresponded to the minimum photospheric radius of the star, was then used to rephase the data. This shifted the phasing basis from a relatively arbitrary observational one to one more firmly astrophysically based. While still dependent on the lines used for the radial velocities, the acceleration phasing made use of a much more narrowly defined region of the star than the photometric bandpasses. This provided a more consistent-zero point in phase between the stars and was found to work for the BL Her, W Vir, and RV Tauri stars, and the stray Type I Cepheid observed.

9.3 Spectroscopy

Apart from the RVB stars, the Type II Cepheids were found to have similar strong metallic lines, which varied in position and, in some cases, strength as a function of phase. Those stars most strongly affected by shocks showed very weak, if any, absorption lines when the shock was most evident. Also, molecular bandheads were observed in several of the longer period stars when they were at their most extended and coolest. The metallic lines in the Cepheids were on average unsplit, apart from those stars which were strongly affected by shocks (such as U Mon), and even then only those lines with a greater potential line forming region showed this around phase 0.0.

The most complicated lines examined were those of Hα and Ca II. Hα broadened for the shorter period stars, split and occasionally showed emission in the wings for the slightly longer period stars, and showed strong emission in those stars with periods of approximately 17 days onwards, with certain exceptions at the longest period examined. This emission in the longer period stars was in most places complicated with multiple components. The Ca II line behaviour was approximately midway between that of the metallic lines and Hα. It started to show line splitting at shorter periods than that observed for the metallic lines such as Fe I, but only showed slight emission in the wings with strong absorption in the core in the longer period stars where Hα was strongly in emission.

With respect to the velocity curve behaviour, the shape of the velocity curve is most affected by the strength of any shock propagating through the line forming region which, while it does correlate with period to a certain extent, is not specific to the particular star types. The amplitudes of the velocity curves also did not correlate strongly with period for the same line species, but showed a greater variation between species than between stars.

9.3.1 Line level effects

Line level effects were found in all the stars on the observing program, as different line species showed different velocities for the same phases. The amplitude of these differences increased in the longer period stars, as the shorter period stars were more compact and thus less of a velocity difference was obtainable in their line-forming regions. The greatest

differences were found between Hα, Ca II and Fe I, with the Hα line in absorption showing the highest amplitude and peaking the latest in phase. Next was Ca II, followed by Fe I, with the Ca II behaviour falling midway between that of Hα and Fe I. Fe I and Fe II were the most similar among the shortest period stars, but were beginning to show noticeable velocity differences by κ Pav (9 day period). These different line behaviours could be used to indicate the passage of the shock wave through different regions of the stars as the different lines reached peak velocity at different phases. Care had to be taken with the line measurement technique, as the line bisector depth and the phase at which line splitting and asymmetry occurred had a large effect on the velocity derived.

9.4 Pulsational characteristics

As stated earlier, it is the shock behaviour which has the greatest effect on the line shape. In all the stars examined, the shock-associated effects of line broadening, splitting, emission and the B magnitude peak occurred around phase 0.0, associated with minimum photospheric radius. In the W Vir stars these all repeated, with the same pattern between successive minima, but this was not the case for the RV Tauri stars.

As traced by the photospheric velocity curves, the RV Tauri stars examined showed the same pulsational behaviour as the W Vir stars, especially W Vir. The velocities repeated on the period between successive minima, and there was no observed differences in velocity curve behaviour between deep and shallow minima. The light emitting features, such as the Hα and He I emission and the blue peak in *(B-V)* colours, were found to vary in strength depending on whether they were associated with a deep or shallow minimum. However, the depth of minimum associated with the stronger shock varied between the stars.

9.5 RV Tauri long-term variations

The long-term photometric minima observed in the RVb stars were variations not shared by the W Vir stars. Colour reddening at long-term minimum was confirmed for SX Cen, AI Sco, U Mon and IW Car, but was not observed in AR Pup. By wavelet analysis, U Mon also showed a decrease in pulsational photometric amplitude, but this did not appear to affect the stability of the patterns of deep and shallow minima. U Mon also showed variation in the depths of the long-term minima, as the most recent was much shallower in terms of how much the maximum light level decreased. It still was as faint as its deepest as the previously observed long-term minimum.

Spectroscopically, both U Mon and AI Sco showed long-term variations associated with the long-term minima. Both showed enhanced Hα emission during the long-term minima. The AI Sco Hα behaviour was the more extreme, as it showed strong blue-ward absorption and little emission prior to long-term minimum, but had strong multiple component emission during the long-term minimum. This emission weakened as the star emerged from the long-term minimum. Hence, over the course of the long-term variations, AI Sco showed Hα variations similar to a wide variety of RV Tauri stars at different times. This included RU Cen, which showed similar strong blue-ward absorption for a single cycle, before returning to the strong multiple component emission usually observed. However, this was not associated with any long-term photometric variations.

The orbital variations observed in many of the RVb stars support the idea that the long-term photometric variations are a result of eclipse by a circumbinary dust torus as the star orbits its companion, with the spectral emission variation being a result of interaction between the stars in the system. The extension of this hypothesis to include the RVa stars is also plausible when combined with the orbital motion and long-term spectroscopic variations of RU Cen. However, a great deal more observation is required before this can be confirmed or denied with respect to the RV Tauri class as a whole.

9.6 Future work

The overall conclusion with respect to future work is that more observations are required at a greater range of wavelengths. Examination of a greater range of wavelengths allows a greater range of optical depths to be probed, thus giving spatial as well as temporal resolution of the shock behaviour. More observations also allow higher temporal resolution of features and mean a larger probability of confirming the existence of more transient features in the observing pattern maintained here. It is understood how rare it is to have constant access to telescopes in order to maintain on-going long-term monitoring as is presented here, but the patterns observed show such an observing rate, if not higher, is necessary.

As this work follows on in part from the RV Tauri work of Pollard (1994), so it would be useful to have a similar study undertaken of at least the RV Tauri stars observed here in approximately 5–10 years time or at 5–10 year intervals. This would capture more long-term variations and make further orbital study for a larger number of the stars possible. Orbital solutions for RU Cen and SX Cen could be derived, as opposed to conjectured from the size of the cycle-to-cycle variations. This would in turn allow testing of the interacting binary hypothesis if the orbital elements and the stars closest approach to each other were known. A point brought up by both this thesis and Pollard (1994) is the question of whether the velocity variations themselves are damped during the long-term minima, and this too would require further observation during the long-term minima of several of the RVb stars. This would however require more frequent observations of the stars at a fainter phase. Follow-up photometric observations would also establish a greater photometric baseline from which to track evolutionary changes in the periods of the stars.

There is also more work that could be done with the data currently available. Only three of the RV Tauri stars observed spectroscopically were studied in detail, so there is a great deal of velocity work remains, which could be done with the SX Cen, AI Sco, AR Pup, AR Sgr, R Sct and IW Car spectra. While three of these stars do not show strong metallic lines, AI Sco, AR Sgr and R Sct do show clean lines which should be investigated for pulsational and possibly binary motion. Both AR Sgr and, to a lesser extent, AI Sco are prime candidates for examining radial velocity and equivalent width curves to see if the trends observed in W Vir, ST Pup, TT Oph, RU Cen and U Mon are also present. In addition, the spectra of AI Sco during the long-term minimum need to be examined to see if the large variations in the Hα line are reflected by metallic line variations. Based on the behaviour of U Mon, this is not expected to be the case, but it does need to be followed up, and further observations of the same wavelengths during a future long-term minimum will confirm the behaviour observed.

Photometrically, there is also more work that can be done with the existing data. Further information can be obtained from the *BVRI* photometry by plotting colour-colour

and colour-magnitude curves for the Type II Cepheids and examining the patterns which occur in these loops. Some preliminary work on this has been done but not presented here. Any trends observed in these curves could be extended further by using the equivalent colour photometry from the MACHO database of Type II Cepheids in the LMC in the same fashion.

Important future work which requires equipment outside what is currently available at MJUO is a survey of the behaviour of the Type II Cepheids at infrared as well as optical wavelengths as a function of time. While there has been some work in examining infrared photometry, which established the presence of a dusty environment around many of the RV Tauri stars, there is little work giving time resolution of the infrared behaviour. This is very important in probing the deeper layers of the Cepheids to see what periods are dominant and if there is a fundamental difference in the motions of the deeper layers of the W Vir stars and the RV Tauri stars.

A further area of work with respect to dominant periods is the stability of the pattern of deep and shallow minima observed in the RV Tauri stars. Already some work has been done in attempting to quantify the stability as reflected by the regularity of deep and shallow minima (Percy et al., 2003), but this has not been extended to the pulsational motions of the stars. It would be very useful in terms of an overall picture of how these stars pulsate to establish the regularity of the pulsations for as wide a range of optical depths as possible. This includes the shorter as well as the longer period Type II Cepheids, to attempt to establish the boundaries between the star types and to see if the origin of the deep and shallow minima can be traced.

Acknowledgments

Thank you to my supervisors Karen Pollard and Peter Cottrell for general levels of encouragement, enthusiasm and persuasion that there is, in fact, a way around that particular brick wall.

Thank you also to:

- Alan Gilmore and Pam Kilmartin for their photometric observations, answering of strange questions at odd hours of the night about the frailties of telescopes and operating systems and Tom Lehrer collection.
- Albert Jones for his visual estimates, which very usefully filled in some gaps in the MJUO photometry and meant that some of the stars didn't escape completely on occasion.
- David Kilkenny for historical data on ST Pup.
- John Percy for RV Tauri discussions and U Mon photometry.
- Andre Fokin for VY Pyx discussions.
- Orlon Petterson and my other fellow astronomy students for long discussions both on and off topic.

In this research, I have used, and acknowledge with thanks, data from the AAVSO International Database, based on observations submitted to the AAVSO by variable star observers worldwide, and the AFOEV database, operated at CDS, France.

This research has also used the SIMBAD data base operated at CDS, Strasbourg, France, the McMasters Cepheid Photometry and Radial Velocity Data Archive, the Vienna Atomic Line Database, and the NASA Astrophysics Data System database.

I was financially supported in this work through a Department of Physics and Astronomy teaching scholarship (1999), W.G. Wybourne scholarship (1999), Dennis Moore scholarship (2001), and Amelia Earhart Fellowship (2001) from the Zonta organization.

Attendance at the 2001 Brussels workshop on pulsational aspects of A & B stars, and IAU Colloquium 185 in 2001 in Leuven was financially enabled through a range of sources: Frank Bradshaw and Elizabeth Pepper Wood fund, Royal Society of New Zealand (Canterbury branch), New Zealand Federation of University Women (Canterbury branch), International Astronomical Union, and the Department of Physics and Astronomy.

Finally, very special thanks to my parents, sister and Zane Bruce. For wandering out and enjoying the stars with me and everything.

References

The Astronomical Almanac. Washington: US government printing office, London: the stationary office, 2002.

H. Abt. Studies of RV Tauri stars. I. U Monocerotis. *ApJ*, 122:72, 1955.

H.A. Abt. An analysis of W Virginis. *ApJSS*, 1:63, 1954.

European Space Agency, editor. *The Hipparcos and Tycho Catalogues.* ESA Publications division, Noordwijk, the Netherlands, 1997.

S. Albrecht. A Spectroscopic Study of the Fourth-class Variable Stars Y Ophiuchi and T Vulpeculae. *ApJ*, 25(5), 1907.

M.D. Albrow and P.L. Cottrell. Line profiles of Cepheid variables: projection factors and metallic line asymetries. *MNRAS*, 267:548–56, 1994.

C. Alcock, R.A. Allsman, D.R. Alves, T.S Axelrod, A. Becker, D.P. Bennet, K.H. Cook, K.C. Freeman, K. Griest, W.A. Lawson, M.J. Lehner, S.L. Marshall, D. Minniti, B.A. Peterson, K.R. Pollard, M.R. Pratt, P.J. Quinn, A.W. Rogers, W. Sutherland, A. Tomaney, and D.L. Welch. The MACHO project LMC variable star inventory. VII The discovery of RV Tauri stars and new Type II Cepheids in the Large Magellanic Cloud. *AJ*, 115:1921–1933, 1998.

J. Alcolea and V. Bujarrabal. The post-AGB evolution of low-mass stars. *A&A*, 245: 499–512, 1991.

R. Alvarez, A. Jorissen, B. Plez, D. Gillet, and A. Fokin. Envelope tomography of long-period variable stars I. The Schwarzschild mechanism and the Balmer emission lines. *A&A*, 362:655–665, 2000.

A. Arellano Ferro, E. Rojo Arellanno, S. González-Bedolla, and P. Rosenzweig. *uvbyβ* photometric data and fourier coefficients for Galactic Population I and Population II cepheids. *ApJSS*, 117:167–208, 1998.

H.C. Arp. Cepheids of period greater than one day in globular clusters. *A.J.*, 60(1):1, January 1955.

W. Baade. The Period-Luminosity relation of the Cepheids. *PASP*, 68(400):5–16, February 1956.

Z. Balog and J. Vinkó. Is TX Delphini a Population I (classical) Cepheid. *Commissions 27 and 42 of the IAU information bullitin on variable stars*, (4150):1–3, January 1995.

Z. Balog, J. Vinkó, and G. Kaszás. Baade-Wesselink radius determination of Type II Cepheids. *AJ*, 113(5):1833–1840, May 1997.

L.A. Balona. Application of the method of maximum likelihood to the determination of Cepheid radii. *MNRAS*, 178:231, 1977.

S.I. Barnes, M. Clark, P.L. Cottrell, J.B. Hearnshaw, O.K.L Petterson, K.R. Pollard, J.D. Pritchard, A. Richards, and W. Tobin. Characteristics of the Mt John Series 200 CCD system. *Southern Stars*, 39(1):1–8, September 2000.

T.G. Barnes, J.A. Fernley, M.L. Frueh, J.G. Navas, T.J. Moffett, and I. Skillen. *BVRIJHK* Photometry of Cepheid Variables. *PASP*, 109:645, 1997.

T.G. Barnes, T.J. Moffett, and M.H. Slovak. Observational studies of cepheids. VII – Radial velocities of faint cepheids. *ApJSS*, 66:43, 1988.

T.R. Bedding, Albert A. Zijlstra, A. Jones, and G. Foster. Mode switching in the nearby Mira-like variable R Doradus. *MNRAS*, 301:1073–1082, 1998.

R.A. Bell and A.W. Rogers. The atmosphere of Kappa Pavonis II. Line profiles. *MNRAS*, 127:15–20, 1953.

D. Bersier, G. Burki, M. Mayor, and A. Duquennoy. Fundamental parameters of Cepheids. II. Radial velocity data. *A&ASS*, 108:25, 1994.

Erika Böhm-Vitense. *Introduction to stellar astrophysics*, volume I: Basic stellar observations and data. Cambridge University Press, 1989.

B. Bopp. Emission lines in the spectra of the RV Tauri stars U Monocerotis and AC Herculis. *PASP*, 96:432–436, 1984.

J.R. Buchler and Z. Kolláth. Nonlinear analysis of irregular variables. In M. Takeuti and D.D. Sasselov, editors, *Stellar pulsation - nonlinear studies*, volume 257 of *Astrophysics and Space Science Library*, pages 185–213. Kluwer academic publishers, Dordrecht, The Netherlands, 2001.

J.R. Buchler and Z. Kolláth. Nonlinear properties of the semiregular variable stars. In Y. Nakada and M. Homma, editors, *Mass-Losing pulsating stars and their circumstellar matter*, volume 283 of *ASSL Ser.*, pages 59–66, 2003. (in press) http:/www.lanl/gov/abs/astro-ph/0303046.

J.R. Buchler, Z. Kolláth, T. Serre, and J. Mattei. Nonlinear analysis of the light curve of the variable star R Scuti. *ApJ*, 462:489–501, May 1996.

J.R. Buchler and G. Kovacs. Period doubling bifurcations and chaos in W Virginis models. *ApJ*, 320:L57–62, September 1987.

J.R. Buchler and P. Moskalik. Pulsational study of BL Herculis models.I. Radial velocities. *ApJ*, 391:736–749, 1992.

J.R. Buchler, T. Serre, Z. Kolláth, and J. Mattei. A chaotic pulsating star: the case of R Scuti. *Physical Review Letters*, 74(6):842–845, February 1995.

R.P. Butler. Cepheid velocity curves from lines of different excitation and ionization. I. Observations. *ApJ*, 415:323–334, September 1993.

R.P. Butler, R.A. Bell, and R.B. Hindsley. The effect of velocity gradients on Cepheid spectra: models. *ApJ*, 461:362–371, April 1996.

C. Cacciara. Star clusters, Globular, Variable stars. *The Astronomy and Astrophysics Encyclopaedia*, Cambridge University Press:Cambridge, 1992.

J.A.R. Caldwell and I.M. Coulson. Milky Way rotation and the distance to the galactic center from Cepheid variables. *AJ*, 93:1090–1105, May 1987.

J. Cardelli and S. Howell. The nature of RV Tauri variables. I Spectrophotometric atlas of selected field stars. *AJ*, 98(1):311–323, 1989.

J.A. Cardelli. Observations of RV Tauri variables: light curves and circumstellar reddening. *AJ*, 90(8):1494–1502, 1985.

R. Carsons and R. Stothers. BL Herculis stars: theoretical models for field variables. *ApJ*, 259:740–748, August 1982.

R. Carsons, R. Stothers, and S. Vemury. Type II Cepheids: A comparison of theory with observations. *ApJ*, 244:230–241, 1981.

J.P. Cox. *Theory of Stellar Pulsations.* Princeton University, Princeton, 1980.

D. Dawson. A photometric investigation of RV Tauri and yellow semiregular variables. *ApJSS*, 41:97–117, 1979.

D. DuPuy. New observations of RV Tauri stars. *ApJ*, 185:597, 1973.

M. Feast and P. Whitelock. Galactic kinematics of Cepheids from HIPPARCOS proper motions. *MNRAS*, 291:683, 1997.

M.W. Feast and A.R. Walker. Cepheids as distance indicators. *Annual Review of Astonomy and Astrophysics*, 25:345, 1987.

J.D. Fernie. Classical Cepheids and Galactic structure. *AJ*, 73:995, 1968.

J.D. Fernie, B. Beattie, N.R. Evans, and S. Seager. A database of Galactic Classical Cepheids. *IBVS*, (4148), 1995.

J.D. Fernie and P. Ehlers. Using BV photometry to distinguish between Type I and Type II Cepheids. *AJ*, 117:1563–1567, 1999.

A.B. Fokin. Investigation of resonances in models of Population-II Cepheids. *Astrophysics*, 24:66, 1986.

A.B. Fokin. Nonlinear pulsations of the RV Tauri stars. *A&A*, 292:133, 1994.

A.B. Fokin. RV Tauri stars. In M. Takeuti and D.D. Sasselov, editors, *Stellar pulsation - nonlinear studies*, volume 257 of *Astrophysics and Space Science Library*, chapter 4, pages 103–136. Kluwer Accademic Publishers, Dordrecht, The Netherlands, 2001.

A.B. Fokin and D. Gillet. The shock wave propagation effects in BL Herculis II. Nonlinear model and theoretical profile of Hα. *A&A*, 290:875–884, 1994.

G. Foster. Wavelets for period analysis of unevenly sampled time series. *AJ*, 112(4): 1709–1729, 1996.

G.A. Galazutdinov. Spectroscopic study of a pulsating star TX Del. *Astronomy Letters*, 21(5):691–694, 1995. Translated from Pis'ma V Astronomischkii Zhurnal, Vol 21, No 10, 1995, pg 772-775.

R.D. Gehrz and E. Ney. Infrared observations of southern RV Tauri stars. *PASP*, 84: 768–771, 1972.

R.D. Gehrz and N.J. Woolf. RV Tauri stars: a new class of infrared object. *ApJ*, 161: L213–217, September 1970.

B. Gerasimovič. A general study of RV Tauri variables. *Harv. Coll. Obs. Circ.*, 341:1, 1929.

D. Gillet, G. Burki, A. Chatel, A. Duquennoy, and A. Lèbre. The shock wave propagation effects in BL Herculis I. The Hα profile. *A&A*, 286:508–514, 1994.

D. Gillet, G. Burki, and A. Duquennoy. The pulsations of the photosphere of the RV Tauri stars – AC Herculis and R Scuti. *A&A*, 237(1):159–168, October 1990.

D. Gillet, A. Duquennoy, P. Bouchet, and C. Gouiffes. Shock phenomina in the atmosphere of the RV Tauri star, R Scuti. *A&A*, 215(2):316–330, May 1989.

D. Gillet and J.-P.J. Lafon. On radiative shocks in atomic and mollecular stellar atmospheres. 1. Dominant physical phenomena. *A&A*, 128:53–63, 1983.

R. Gingold. The evolutionary status of Population II Cepheids. *ApJ*, 204:116–130, 1976.

S. Giridhar, D. Lambert, and G. Gonzalez. Abundance analysys of field RV Tauri stars. V. DS Aquarii, UY Arae, TW Camelopardalis, BT Librae, U Monocerotis, TT Ophiuchi, R Scuti, and RV Tauri. *ApJ*, 531:521–536, March 2000.

M.J. Goldsmith, A. Evans, J.S. Albinson, and M.F. Bode. Optical and infrared observations of RV Tauri stars. *MNRAS*, 227:143–159, 1987.

G. Gonzalez, D. Lambert, and S. Giridhar. Abundance analyses of the field RV Tauri variables: EP Lyrae, DY Orionis, AR Puppis, R Sagittae. *ApJ*, 479:427–440, 1997.

G. Gonzalez and G. Wallerstein. ST Pup: a binary Type II Cepheid with a peculiar chemical composition. *MNRAS*, 280:525–536, 1996.

David Gray. *The observation and analysis of stellar photospheres.* Cambridge University Press, 2nd edition, 1992.

J.G. Hagan. Minor Contributions and Notes: The problem of the δ Cephei variables. *ApJ*, 51:62, 1920.

H.C. Harris. *Photometric abundences of Cepheid variables in the Galaxy and the Small Magellanic Cloud.* PhD thesis, University of Washington, 1980.

H.C. Harris. Photometric abundences of Type II Cepheid variables. *AJ*, 86(5):719–729, 1981.

H.C. Harris. A catalogue of field Type II Cepheids. *AJ*, 90(5):756–760, 1985.

H.C. Harris and D.L. Welch. The binary Type II Cepheids IX Cas and TX Del. *AJ*, 98 (3):981–986, 1989.

J.B. Hearnshaw. The Cassegrain Échelle Spectrograph at Mt John Observatory. *Proc. Astron. Soc. Australia*, 3:102, 1977.

J.B. Hearnshaw. An échelle spectrograph. *Sky & Telescope*, 56:6, 1978.

A.A. Henden. A search for northern hemisphere Double-Mode Cepheids.II New *UBV* Cepheid photometry. *MNRAS*, 192:621, 1980.

R. Hindsley and R.A. Bell. An investigation of photoelectric radial-velocity spectrometers as used in the analysis of Cepheid variables. *PASP*, 98:881–888, September 1986.

K.H. Hinkle, K.R. Pollard, and G.M. Wahlgren. Infrared spectroscopy of the RV Tauri star R Scuti. In H. Morrison and A. Sarajedini, editors, *Formation of the Galactic Halo ... Inside and Out*, volume 92 of *ASP Conference series*, pages 204–207, 1996.

S.W. Hodson, A.N. Cox, and D.S. King. Opacity and nonlinear effects on theoretical BL Herculis models. *ApJ*, 253:260–267, 1982.

D.J. Hollenbach and C.F. McKee. Shock wave, Astrophysical. In *The Astronomy and Astrophysics Encyclopedia*. Cambridge University Press, Cambridge, 1992.

D.H. Horowitz. Revised period of CT Orionis. *JAAVSO*, 15(2):223, 1986.

D.H. Horowitz. Graphical characterization of RV Tauri light curves. *JAAVSO*, 16:71, 1987.

S.B. Howell, B.W. Bopp, and P.V. Noah. The remarkable spectrum of the RV Tauri star R Scuti at deep minimum. *PASP*, 95:762–767, October 1983.

A. Joy. The semi-regular variable stars of the RV Tauri and related classes. *ApJ*, 115:25, 1952.

A.H. Joy. Radial velocities of Cepheid variable stars. *ApJ*, 86:363, 1937.

M. Jura. RV Tauri stars as post-asymptotic giant branch objects. *ApJ*, 309:732–736, October 1986.

P.N. Kholopov, N.N. Sanus, O.V. Durlevich, E.V. Kazarovets, N.N. Kireeva, and T.M. Tsvetkova. *General Catalogue of Variable Stars*, volume IV. Nauka, 4th edition, 1990.

B.V. Khopolov, N.N. Sanus, M.S. Frolov, V.P. Gorasnkij, N.A. Gorynya, N.N. Kireeva, N.P. Kukarnina, N.E. Kurochkin, G.I Medvedeva, N.B. Perova, and S.Y. Shugarov. *General Catalogue of Variable Stars*, volume I. Nauka Publishing House, Moscow, 4th edition, 1985.

D. Kilkenny, F. van Wyk, F. Marang, G. Roberts, J.D. Laing, H. Winkler, and J.E. Westerhuys. *UBVRI* photometry of the Type II Cepheid, ST Pup. *SAAO Circulars*, (23):85–89, 1993.

D. King, A. Cox, and S.W. Hodson. Linear and nonlinear studies of BL Herculis variables. *ApJ*, 244:242–251, February 1981.

L.L. Kiss. A photometric and spectroscopic study of the brightest northern Cepheids- I. Observations. *MNRAS*, 297:825–838, 1998.

L.L. Kiss and J Vinkó. A photometric and spectroscopic study of the brightest northern Cepheids- III. A high-resolution view of Cepheid atmospheres. *MNRAS*, 314:420–432, 2000.

G. Kovács and J.R. Buchler. Regular and irregular nonlinear pulsations in population II Cepheid models. *ApJ*, 334:971–994, 1988.

B.V. Kukarkin, P.P. Parenago, Y.I. Efremov, and P.N. Kholopov. *General Catalogue of Variable Stars*. Publishing House of the Academy of Sciences of USSR, Moscow, 2nd edition, 1958.

F.G. Kupka, T.A. Ryabchikova, N.E. Piskunov, H.C. Stempels, and W.W. Weiss. VALD-2 – the new Vienna Atomic Line Database. *Baltic Astronomy*, 9:590–594, 2000.

C.D. Laney. Type II? Cepheid radii and TX Del. In R.S. Stobie and P.A. Whitelock, editors, *Astrophysical Applications of Stellar Pulsation*, volume 83 of *A.S.P Conference series*, page 367, 1995.

A. Lèbre and D. Gillet. The bright RV Tauri star R Scuti during an exceptional irregular light phase. *A&A*, 246(2):490–502, 1991a.

A. Lèbre and D. Gillet. The multicomponent motion of the very high atmosphere of the RV Tauri star - R Scuti. *A&A*, 251(2):549–559, 1991b.

A. Lèbre and D. Gillet. Atmospheric motions in the Population II Cepheid W Virginis. *A&A*, 255(1-2):221–232, 1992.

T. Lloyd Evans. Circumstellar material and the light variations of RV Tauri stars. *MNRAS*, 217:493–506, 1985.

E. Loreta. Etoiles variables semi-régulières avec deux périodes superposées. *AN*, 267:399, 1939.

T. Maas, H. Van Winckel, and C. Waelkens. RU Cen and SX Cen: two strongly depleted RV Tauri stars in binary systems. The RV Tauri photometric b phenomenon and binarity. *A&A*, 386:504–516, 2002.

L. Mantegazza. Near infrared spectra of RV Tauri stars. *A&ASS*, 88:255–263, 1991.

M. Matsuura, I. Yamamura, A.A. Zijlstra, and T.R. Bedding. The extended atmosphere and evolution of the RV Tau star, R Scuti. *A&A*, 387:1022–1031, 2002.

J.A. McSaveney. RV Tauri stars: U Monocerotis. 400 level Undergraduate Project Report, University of Canterbury, 1998.

J.A. McSaveney, P.L. Cottrell, K.R. Pollard, and J.A. Mattei. Wavelet analysis of the RV Tauri star U Mon. In C. Aerts, T.R. Bedding, and J. Christensen-Dalsgaard, editors, *Radial and nonradial pulsations as probes of stellar physics*, volume 259 of *ASP Conference series*, pages 576–577. Astronomical Society of the Pacific, 2002.

M. Meakes, Wallerstein G, and J.F. Opalko. Strömgren photometry of short period Population II Cepheids. *AJ*, 101(5):1795, 1991.

T.J. Moffett and T.G Barnes. Observational studies of Cepheids. II *BVRI* photometry of 112 Cepheids. *ApJSS*, 55:389–432, 1984.

T.J. Moffett and T.G Barnes. Observational studies of Cepheids. III Catalog of light curve parameters. *ApJSS*, 58:843–872, 1985.

D. Mozurkewich, R. Gehrz, K. Hinkle, and D. Lambert. Velocity structure of stellar atmospheres: R Scuti. *ApJ*, 314:242–251, 1987.

G.R. Nankivell and N.J. Rumsey. The optical system of the Mt John one metre telescope. In J.B. Hearnshaw and P.L. Cottrell, editors, *Proc. IAU Symp. 118, Instrumentation and research programmes for small telescopes*, page 101, Dordrecht, 1986. Reidel.

A. Opotaki. Observational determination of pulsation modes and photometric masses of Cepheid variables. *AcA*, 34(2):2250, 1984.

C. Payne-Gaposchkin. The connection of motion with intrinsic variability. *AJ*, 53:193–194, 1948.

C. Payne-Gaposchkin. –. *Harvard Annals*, 115(18):210, 1950.

J. Percy. Long-term changes in RV Tauri stars. *ASP Conference Series*, 45:295–299, 1993.

J.R. Percy, M. Bezuhly, M. Milanowski, and E. Zsoldos. The nature of the period changes in RV Tauri stars. *PASP*, 109:264–269, 1997.

J.R. Percy, J. Hosick, and N.W.C. Leigh. Self-correlation analysis of RV Tauri stars and related objects. *PASP*, 115:59–66, 2003.

J.R. Percy, D.D. Sasselov, A. Alfred, and G. Scott. Period changes and evolution in RV Tauri stars. *ApJ*, 375:691, 1991.

J.O. Petersen. v553 Centauri and a progression of bumps in BL Herculis light curves. *A&A*, 96:146–150, 1981.

Orlon Petterson. *A spectroscopic and dynamical study of binary and other Cepheids.* PhD thesis, University of Canterbury, 2002.

N.E. Piskunov, F. Kupka, T.A. Ryabchikova, W.W. Weiss, and C.S. Jeffery. VALD: The Vienna Atomic Line Data Base. *A&ASS*, 112:525–535, 1995.

K.R. Pollard. *The nature of the low mass supergiants: RV Tauri and R Coronae Borealis variables.* PhD thesis, University of Canterbury, 1994.

K.R. Pollard, P.L. Cottrell, P. Kilmartin, and A. Gilmore. RV Tauri stars -I. A long-term photometric survey. *Mon. Not. R. Astron. Soc.*, 279:949–977, 1996a.

K.R. Pollard, P.L. Cottrell, W. Lawson, M. Albrow, and W. Tobin. RV Tauri stars -II. A spectroscopic study. *Mon. Not. R. Astron. Soc.*, 286:1, 1997.

K.R. Pollard, K.H. Hinkle, W.A. Lawson, P.L. Cottrell, and G.M. Wahlgren. High-resolution optical and infrared spectroscopy of the RV Tauri star R Sct. In R. Pallavicini and A.K. Dupree, editors, *Cool Stars, Stellar Systems, and the Sun, 9th Cambridge Workshop*, volume 109 of *ASP Conference series*, pages 719–720, 1996b.

F. Pont, M. Mayor, and G. Burki. New radial velocities for Classical Cepheids. Local galactic rotation revisited. *A&A*, 285:415–439, 1994.

G. Preston. Metallic emission and other spectroscopic peculiarities of U Monocerotis. *ApJ*, 140:173, 1964.

G.W. Preston, W. Krzeminski, J. Smak, and J.A. Williams. A spectroscopic and photoelectric survey of the RV Tauri stars. *ApJ*, 137:401–430, 1963.

A. Raga, G. Wallerstein, and J.B. Oke. The helium abundance in the Population II Cepheid, W Virginis. *ApJ*, 347:1107–1113, 1989.

A. Raveendran. Dust envelopes around RV Tauri stars. *MNRAS*, 238:945–953, 1989.

A.V. Raveendran. Linear polarization in the RV Tauri star AR Puppis. *MNRAS*, 303: 595–602, 1999.

A.W. Roberts. Southern variable stars. *AJ*, 21:81, February 1901.

A.W. Roberts. An inquiry into the variation of the spectroscopic binary κ Pavonis. *ApJ*, 34:164, 1911.

A.W. Rogers. Radius variation and population type of Cepheid variables. *MNRAS*, 117: 85–94, 1957.

A.W. Rogers and R.A. Bell. The atmosphere of Kappa Pavonis I. A coarse analysis. *MNRAS*, 125:487, 1963.

A.W. Rogers and R.A. Bell. The temperature, metal abundance and mass of the Disc Cepheid κ Pavonis. *MNRAS*, 139:175–187, 1968.

L. Rosino. The spectra of the variables of the RV Tauri and yellow semi-regular types. *ApJ*, 113:60, 1951.

C.N. Sabbey, D.D. Sasselov, M.S. Fieldus, J.B. Lester, K.A. Venn, and R.P. Butler. On spectral line formation and measurement in Cepheids: Implications to distance determination. *ApJ*, 446:250–260, June 1995.

M. Saladyga. The "pre-embryonic" state of the AAVSO: Amateur observersion in the United States from 1875 to 1911. *JAAVSO*, 27:126?, 1999.

R.F. Sanford. On the spectrum and radial velocity of U Monocerotis. *ApJ*, 77:120, 1933.

R.F. Sanford. The spectrum and radial velocities of W Virginis. *ApJ*, 116:331–336, 1952.

R.F. Sanford. The widening or doubling of lines in the spectra of variable stars. In P. Th. Oosterhoff, editor, *Trans I.A.U.*, volume VIII, pages 809–811, Cambridge, 1954. University Press. Often refered to as either Sanford (1952) or (1954) in the literature due to the IAU General Assembly it is from being in 1952, and it's being published in 1954. Have also seen it refered to as Sanford (1953).

N.B. Sarnwal and M.B.K. Sarma. BV 680, a new bright type II cepheid. *JApA*, 12:119, 1991.

D. D. Sasselov. Pulsating stellar atmospheres. In T.R. Bedding, A.J. Booth, and J. Davis, editors, *Fundimental stellar properties: the interaction between observation and theory*, page 253, Dordrecht, 1997. Kluwer. IAU Symposium 189, Sydney, Australia, held 1997.

D. D. Sasselov and J.B. Lester. Infrared spectroscopy of Cepheids. II. Line profiles from different atmosperic layers. *ApJ*, 360:333–345, October 1990.

R. Schaltenbrand and G.A. Tammann. The light curve parameters of photoelectrically observed Galactic Cepheids. *A&AS*, 4:265–314, 1971.

M. Schwarzschild. Shock waves in the atmospheres of pulsating stars. In P. Th. Oosterhoff, editor, *Trans I.A.U.*, volume VIII, pages 811–812, Cambridge, 1954. University Press. Often refered to as either Schwarzschild (1952) or (1954) in the literature due to the IAU General Assembly it is from being in 1952, and it's being published in 1954. Have also seen it refered to as Schwarzschild (1953).

K. Serkowski. Polarimetric observations of the RV Tauri stars U Monocerotis and R Scuti. *ApJ*, 160:1107–1116, June 1970.

H. Shapley. On the nature and cause of Cepheid variation. *ApJ*, 40:448–465, 1914.

H. Shapley. Studies based on the colors and magnitudes in stellar clusters: Paper 6 on the determination of the distances of globular clusters. *ApJ*, 48:89–124, 1918.

H. Shapley. Studies based on the colors and magnitudes in stellar clusters: Paper 9 three notes on Cepheid variation. *ApJ*, 49:24–41, 1919.

M. Shenton, A. Evans, J.S. Albinson, P. Barrett, J.K. Davies, M.J. Goldsmith, M.G. Hutchinson, D. Laney, and R.C. Maddison. Multi-wavelength observations of RV Tauri stars IV SX Centauri. *A&A*, 292:102–114, 1994a.

M. Shenton, A. Evans, J. Cardelli, F. Marung, F. van Wyk, and A. Weight. Multi-wavelength observations of RV Tauri stars II. U Monocerotis. *A&A*, 287:852, 1994b.

M. Shenton, R. Monier, A. Evans, B. Carter, T. Lloyd Evans, F. Marung, Q.A. Parker, J.M.C Rawlings, A.D. Scott, and F. van Wyk. Multi-wavelength observations of RV Tauri stars III. R Scuti. *A&A*, 287:866–880, 1994c.

R. R. Shobbrook. *UBV(RI)$_c$* observations for 13 bright Cepheids. *MNRAS*, 255:486–494, 1992.

H.A. Smith. *RR Lyrae stars.* Cambridge University Press, 1995.

W.N. Stibbs. Radial velocities of Cepheid variable stars in the Southern Hemisphere. *MNRAS*, 115(4):363–390, 1955.

R.S. Stobie and L.A. Balona. Observations of short period Cepheids. *MNRAS*, 189: 641–648, 1979.

L. Szabados. Photoelectric UBV photometry of Northern Cepheids.II. *Commun. Konkoly Obs. Hung Acad. Sci.*, (76), 1980.

K Szatmáry. Pulsating variable stars in binary systems. *JAVSO*, 19:52, 1990.

M. Takeuti and O. Petersen. The resonance hypothesis applied to RV Tauri stars. *A&A*, 117:352, 1983.

W. Tobin. *The Mount John Photometrics CCD System: Use and Perfomance Note Number 1, Use of system.* MJUO, 1990.

W. Tobin. Gain, Noise and Related Characteristics of the Mt John Photometrics CCD System. *Southern Stars*, 34:421, 1992.

W. Tobin, J.B. Hearnshaw, G.M. Kershaw, G.R. Nankivell, S. Persson, N.J. Rumsey, and R. Thirkettle. A Focal Reducer for the Mt John Échelle Spectrograph. *Southern Stars*, 37(7):197–205, March 1998.

H. Van Winckel, C. Waelkens, J.D. Fearnie, and L.B.F.M Waters. The RV Tauri phenomenon and binarity. *A&A*, 343:202–212, March 1999.

H. Van Winckel, C. Waelkens, L.B.F.M. Waters, F.J. Molster, S. Udry, and E.J. Bakker. The binary RV Tauri star AC Her and evidence for a long–lived dust–disc. *A&A*, 336: L17–L20, 1998.

J. Vinkó and Z. Balzog. Baade–Wesselink analysis of Type II Cepheids. In R.S. Stobie and P.A. Whitelock, editors, *Astrophysical Applications of Stellar Pulsation*, volume 83 of *A.S.P. Conference Series*, page 369, 1995.

J. Vinkó, N. Evans, L. Kiss, and L Szabados. Spectroscopic survey of field Type II Cepheids. *MNRAS*, 296:824–838, 1998.

C. Waelkens and L.B.F.M Waters. Binarity of high-latitude supergiants: observational evidence. In D.D. Sasselov, editor, *Luminous High-Latitude Stars*, volume 45 of *ASP Conference Series*, page 219, 1993.

G.M. Wahlgren. The metallicity and luminosity of RV Tauri variables from medium-resolution spectra. *AJ*, 104(3):1174–1192, September 1992.

G.M. Wahlgren. The RV Tauri and SRd variables. *ASP Conference Series*, 45:270–284, 1993.

G. Wallerstein. Effective temperatures, radii, masses, and pulsation properties of the Population II Cepheids M5 no. 42 and W Virginis. *ApJ*, 129:356, 1959a.

G. Wallerstein. The shock-wave model for the Population II Cepheids. *ApJ*, 130:560, 1959b.

G. Wallerstein. The Cepheids of Population II and Related stars. *PASP*, 114:689–699, July 2002.

G. Wallerstein and A. Cox. The Population II Cepheids. *PASP*, 96:677–691, 1984.

G. Wallerstein and S. Elgar. Shock waves in stellar atmospheres and breaking waves on an ocean beach. *Science*, 256:1531, June 1992.

G. Wallerstein, T.S. Jacobsen, P.L. Cottrell, M. Clark, and M. Albrow. Metallic-line and Hα radial velocities of seven southern Cepheids: a comparitive analysis. *MNRAS*, 259: 474–488, 1992.

P.N.J. Wisse and M. Wisse. Photoelectric observations of the bright RV Tauri stars R Scuti and U Monoceotis. *A&A*, 23:463–466, 1973.

W.H. Wright. On some results obtained by the D.O. Mills expedition to the Southern Hemisphere. *ApJ*, 20:140, 1904.

E. Zsoldos. RV Tauri and the RVB phenomenon. 1. Photometry of RV Tauri. *A&ASS*, 119:431–437, 1996.

Appendix A

Stellar details

Table A.1: Observing program Cepheids.

Star	Type	Period[1] (days)	V range	Spectral Type [2]
VY Pyx	BL Her	1.239938	7.15–7.4	F3/F5III
SW Tau	BL Her	1.583560	9.4–10.2	A7
V381 Cen	Classical Cepheid	5.07878	7.2–8.0	F8Ib/II
TX Del	BL Her?	6.1634	8.9–9.6	F8
κ Pav	W Vir	9.0741	4.0–4.8	F5Ib/II
AL Vir	W Vir	10.2950	9.2–10.0	F3/F5III
W Vir	W Vir	17.2768	9.6–10.8	F0Ib
ST Pup	W Vir	18.6204	9.6–10.8	G2Iab
SX Cen	RVb Tauri	32.82	9.1–11.4	G3/G5Vp
TT Oph	RVa Tauri	60.97	9.4–10.7	F5pe
RU Cen	RVa Tauri	64.57	8.5–9.8	G2w
CT Ori	RVa Tauri	67.42	10.3–11.2	F9
AI Sco	RVb Tauri	71.45	8.8–11.2	G4
AR Pup	RVb Tauri	76.47	9.1–10.1	F0Iab
AR Sgr	RVa Tauri	87.13	9.1–10.4	G4
UZ Oph	RVa Tauri	88.90	10.2–12.5	G2
U Mon	RVb Tauri	91.79	5.5–7.8	K0Ibpvar
R Sct	RVa Tauri	134.87	4.9–6.7	K0Ibpvar
TX Oph	RVa Tauri	135.81	9.7–10.7	G0
IW Car	RVb Tauri?	142.73	7.8–9.2	A4Ib/II

Appendix B

Photometric data

B.1 W Vir stars

B.1.1 VY Pyx

Table B.1: MJUO VY Pyx photometry.

JD-2440000	V	B-V	V-I	V-R
11315.909	7.213	0.569	0.335	0.649
11326.890	7.159	0.532	0.327	0.513
11333.878	7.349	0.593	0.364	0.671
11339.812	7.372	0.615	0.370	0.694
11347.834	7.146	0.521	0.316	0.597
11355.819	7.322	0.608	0.370	0.700
11357.805	7.149	0.522	0.323	0.603
11364.826	7.381	0.599	0.355	0.683
11368.789	7.204	0.531	0.319	0.617
11372.810	7.179	0.527	0.348	0.639
11373.791	7.183	0.520	0.324	0.600
11383.819	7.120	0.501	0.326	0.597
11390.785	7.404	0.632	0.369	0.696
11476.166	7.349	0.631	0.361	0.690
11496.128	7.397	0.619	0.365	0.715
11505.096	7.279	0.562	0.339	0.646
11557.069	7.343	0.597	0.353	0.669
11575.092	7.228	0.585	0.339	0.656
11593.049	7.331	0.591	0.352	0.663
11596.986	7.182	0.528	0.324	0.608
11606.074	7.223	0.581	0.345	0.667
11611.055	7.239	0.585	0.341	0.665
11613.949	7.392	0.625	0.364	0.692
11619.971	7.339	0.618	0.365	0.698
11622.966	7.214	0.552	0.324	0.619
11630.969	7.267	0.601	0.354	0.675
11661.911	7.244	0.591	0.352	0.668
11664.944	7.346	0.589	0.362	0.675
11667.918	7.173	0.548	0.322	0.633
11673.840	7.190	0.535	0.321	0.614
11690.875	7.396	0.619	0.373	0.691
11714.870	7.143	0.518	0.315	0.607
11720.844	7.253	0.553	0.337	0.609
11721.827	7.390	0.631	0.352	0.692
11725.836	7.250	0.554	0.344	0.622
11853.102	7.343	0.627	0.367	0.694
11854.053	7.223	0.552	0.354	0.667
11931.015	7.250	0.590	0.346	0.665
11933.068	7.152	0.472	0.341	0.599
11959.039	7.166	0.537	0.315	0.603
12012.976	7.307	0.609	0.368	0.686
12013.957	7.210	0.560	0.354	0.649
12015.898	7.313	0.571	0.346	0.655
12018.022	7.354	0.599	0.358	0.698
12021.020	7.197	0.528	0.298	0.595
12021.916	7.401	0.622	0.360	0.687
12022.938	7.333	0.621	0.360	0.686
12023.873	7.191	0.572	0.328	0.641
12043.949	7.281	0.606	0.362	0.677
12067.850	7.384	0.611	0.359	0.681

B.1.2 SW Tau

Table B.2: MJUO SW Tau photometry.

JD-2440000	V	B-V	V-I	V-R
11400.211	9.787	0.682	0.425	0.722
11426.118	10.133	0.744	0.497	0.804
11445.129	10.111	0.758	0.469	0.724
11450.058	9.895	0.637	0.446	0.709
11460.074	9.483	0.516	0.348	0.593
11476.043	9.699	0.605	0.407	0.663
11484.984	9.485	0.483	0.319	0.524

continued on next page

Table B.2: *continued*

JD-2440000	V	B-V	V-I	V-R
11494.993	9.601	0.577	0.368	0.602
11496.018	9.680	0.528	0.371	0.611
11504.980	9.996	0.744	0.483	0.770
11528.939	10.141	0.781	0.499	0.778
11603.907	9.418	0.478	0.320	0.486
11839.061	9.950	0.756	0.457	0.754
11852.019	10.133	0.790	0.469	0.786
11853.017	9.770	0.643	0.440	0.698
11853.954	9.483	0.482	0.327	0.488
11861.950	9.434	0.474	0.311	0.463
11873.959	9.999	0.761	0.468	0.760
11878.972	10.128	0.759	0.487	0.791
11895.997	9.872	0.726	0.462	0.718
11928.961	9.700	0.643	0.424	0.629
11978.847	10.136	0.770	0.488	0.764
11982.878	9.747	0.671	0.449	0.704
11988.868	9.370	0.504	0.331	0.500
12149.194	9.793	0.674	0.440	0.730
12163.128	9.441	0.510	0.346	0.543
12171.146	9.587	0.552	0.404	0.637
12177.147	9.445	0.440	0.343	0.504
12181.155	10.005	0.734	0.496	0.768
12221.019	10.139	0.764	0.478	0.783
12228.985	10.127	0.734	0.479	0.776
12255.931	10.113	0.752	0.483	0.781
12306.896	9.458	0.464	0.331	0.476
12320.894	10.119	0.729	0.465	0.761
12321.882	9.841	0.706	0.453	0.723

B.1.3 V381 Cen

Table B.3: MJUO V381 Cen photometry.

JD-2440000	V	B-V	V-I	V-R
11316.053	7.549	0.733	0.417	0.814
11317.068	7.401	0.684	0.405	0.796
11318.023	7.635	0.841	0.477	0.917
11327.097	7.354	0.683	0.390	0.762
11334.038	7.796	0.925	0.503	0.968
11336.034	7.820	0.855	0.475	0.927
11339.070	7.790	0.917	0.506	0.974
11348.077	7.533	0.784	0.446	0.861
11356.004	7.974	0.944	0.520	0.993
11357.958	7.463	0.742	0.424	0.826
11364.043	7.703	0.878	0.487	0.935
11368.081	7.452	0.736	0.422	0.821
11368.992	7.674	0.866	0.480	0.931
11373.045	7.418	0.711	0.412	0.807
11374.032	7.669	0.863	0.480	0.939
11380.077	7.847	0.945	0.514	0.987
11384.028	7.629	0.839	0.471	0.910
11397.070	7.752	0.810	0.467	0.893
11398.968	7.569	0.788	0.500	0.892
11413.807	7.460	0.737	0.430	0.832
11415.971	7.920	0.946	0.522	1.018
11597.066	7.565	0.802	0.450	0.927
11607.154	7.547	0.792	0.448	0.869
11614.914	7.988	0.952	0.530	1.022
11620.206	7.946	0.919	0.514	0.990
11623.133	7.710	0.897	0.481	0.943
11629.897	7.982	0.983	0.522	1.003
11663.939	7.755	0.901	0.502	0.956
11673.084	7.528	0.776	0.447	0.866
11726.964	7.904	0.904	0.502	0.950
11730.995	7.929	0.968	0.522	1.010
11742.001	7.958	0.946	0.518	0.985
11754.973	7.666	0.862	0.480	0.923
11770.015	7.623	0.835	0.471	0.912
11979.130	7.809	0.940	0.489	0.974
11316.053	7.549	0.733	0.417	0.814
11317.068	7.401	0.684	0.405	0.796
11318.023	7.635	0.841	0.477	0.917
11327.097	7.354	0.683	0.390	0.762
11334.038	7.796	0.925	0.503	0.968
11336.034	7.820	0.855	0.475	0.927
11339.070	7.790	0.917	0.506	0.974
11348.077	7.533	0.784	0.446	0.861
11356.004	7.974	0.944	0.520	0.993
11357.958	7.463	0.742	0.424	0.826
11364.043	7.703	0.878	0.487	0.935
11368.081	7.452	0.736	0.422	0.821
11368.992	7.674	0.866	0.480	0.931
11373.045	7.418	0.711	0.412	0.807
11374.032	7.669	0.863	0.480	0.939
11380.077	7.847	0.945	0.514	0.987
11384.028	7.629	0.839	0.471	0.910
11397.070	7.752	0.810	0.467	0.893
11398.968	7.569	0.788	0.500	0.892
11413.807	7.460	0.737	0.430	0.832

continued on next page

Table B.3: *continued*

JD-2440000	V	B-V	V-I	V-R
11415.971	7.920	0.946	0.522	1.018
11597.066	7.565	0.802	0.450	0.927
11607.154	7.547	0.792	0.448	0.869
11614.914	7.988	0.952	0.530	1.022
11620.206	7.946	0.919	0.514	0.990
11623.133	7.710	0.897	0.481	0.943
11629.897	7.982	0.983	0.522	1.003
11663.939	7.755	0.901	0.502	0.956
11673.084	7.528	0.776	0.447	0.866
11726.964	7.904	0.904	0.502	0.950
11730.995	7.929	0.968	0.522	1.010
11742.001	7.958	0.946	0.518	0.985
11754.973	7.666	0.862	0.480	0.923
11770.015	7.623	0.835	0.471	0.912
11979.130	7.809	0.940	0.489	0.974

B.1.4 TX Del

Table B.4: MJUO TX Del photometry.

JD-2440000	V	B-V	V-I	V-R
11327.204	8.931	0.559	0.332	0.593
11334.255	9.047	0.679	0.388	0.719
11339.229	8.922	0.564	0.311	0.591
11357.163	9.002	0.595	0.353	0.617
11364.242	8.942	0.575	0.334	0.628
11368.231	9.521	0.895	0.475	0.891
11369.145	9.136	0.656	0.389	0.706
11373.132	9.413	0.910	0.483	0.875
11374.213	9.540	0.935	0.486	0.889
11398.101	9.493	0.948	0.483	0.889
11400.114	9.064	0.633	0.374	0.677
11414.083	9.027	0.641	0.350	0.665
11416.137	9.443	0.894	0.480	0.861
11452.972	9.389	0.901	0.469	0.850
11459.943	9.521	0.968	0.483	0.911
11721.157	8.942	0.581	0.324	0.605
11727.183	8.970	0.599	0.327	0.621
11730.214	9.369	0.882	0.459	0.853
11731.180	9.511	0.989	0.476	0.897
11742.166	9.286	0.847	0.438	0.826
11749.072	9.447	0.917	0.502	0.899
11802.001	8.962	0.575	0.347	0.633
12013.209	9.247	0.817	0.439	0.796
12055.193	9.037	0.647	0.369	0.681
12060.204	8.936	0.579	0.328	0.597
12066.211	8.979	0.593	0.338	0.643
12080.108	9.055	0.694	0.389	0.710
12115.115	9.052	0.629	0.348	0.648
12116.049	8.940	0.559	0.328	0.598
12117.033	9.059	0.674	0.369	0.694
12163.074	9.549	0.923	0.502	0.900

B.1.5 κ Pav

Table B.5: MJUO κ Pav photometry.

JD-2440000	V	B-V	V-I	V-R
11316.155	4.661	0.760	0.403	0.766
11317.280	4.518	0.659	0.326	0.654
11327.158	4.150	0.536	0.263	0.538
11334.219	4.671	0.778	0.400	0.777
11336.160	4.170	0.544	0.262	0.536
11339.191	4.242	0.736	0.369	0.712
11357.207	4.215	0.716	0.362	0.705
11364.168	3.966	0.509	0.245	0.500
11368.169	4.603	0.927	0.441	0.845
11369.157	4.732	0.934	0.468	0.878
11373.174	3.970	0.522	0.242	0.497
11374.197	3.979	0.579	0.273	0.562
11380.222	4.597	0.718	0.366	0.716
11397.233	4.721	0.857	0.436	0.829
11398.983	4.515	0.656	0.340	0.656
11414.155	4.657	0.927	0.457	0.861
11416.152	4.641	0.764	0.390	0.757
11426.060	4.559	0.677	0.341	0.671
11439.123	4.248	0.746	0.368	0.720
11445.082	4.192	0.554	0.263	0.538
11449.096	4.450	0.869	0.411	0.794
11453.064	4.567	0.708	0.344	0.690
11476.013	4.380	0.829	0.404	0.774
11484.934	4.348	0.800	0.398	0.764
11621.132	4.343	0.794	0.392	0.760
11631.180	4.530	0.871	0.441	0.829
11665.070	4.024	0.617	0.293	0.595

continued on next page

Table B.5: *continued*

JD-2440000	*V*	*B-V*	*V-I*	*V-R*
11688.261	4.653	0.775	0.396	0.764
11715.189	4.704	0.813	0.423	0.808
11721.194	4.404	0.821	0.412	0.790
11730.162	4.383	0.810	0.405	0.774
11731.129	4.562	0.893	0.449	0.842
11742.217	4.717	0.845	0.425	0.823
11754.167	4.060	0.526	0.257	0.525
11770.939	4.537	0.668	0.333	0.659
11799.076	4.213	0.567	0.268	0.549
11839.040	4.393	0.829	0.398	0.783
11850.923	4.725	0.846	0.417	0.815
11852.948	4.431	0.609	0.311	0.621
11857.963	4.553	0.889	0.433	0.831
11873.927	4.065	0.651	0.307	0.621
11896.915	4.692	0.782	0.389	0.770
12001.206	4.153	0.684	0.352	0.680
12013.186	4.725	0.915	0.458	0.862
12014.260	4.750	0.836	0.417	0.814
12023.185	4.776	0.853	0.437	0.827
12042.226	4.653	0.729	0.382	0.738
12055.224	4.059	0.627	0.310	0.618
12060.253	4.682	0.763	0.377	0.736
12066.268	4.518	0.854	0.436	0.827
12113.281	4.752	0.909	0.454	0.857
12115.243	4.592	0.692	0.357	0.694
12116.082	4.365	0.605	0.308	0.609
12117.045	3.984	0.513	0.240	0.499
12149.161	4.710	0.930	0.465	0.873
12153.150	4.056	0.528	0.257	0.520
12154.897	4.029	0.626	0.290	0.600
12163.058	3.964	0.542	0.253	0.525
12164.066	4.066	0.611	0.325	0.627
12171.049	4.135	0.543	0.260	0.538
12177.098	4.751	0.892	0.451	0.855
12181.075	3.963	0.526	0.262	0.536
12218.948	4.129	0.673	0.322	0.661
12220.967	4.575	0.913	0.443	0.837
12228.960	4.351	0.801	0.391	0.768
12255.904	4.267	0.746	0.374	0.740
12410.225	4.289	0.772	0.378	0.732

B.1.6 AL Vir

Table B.6: MJUO AL Vir photometry.

JD-2440000	*V*	*B-V*	*V-I*	*V-R*
11316.070	9.828	0.774	0.607	1.052
11317.052	9.923	0.804	0.605	1.035
11333.924	9.292	0.477	0.475	0.796
11336.003	9.724	0.734	0.587	0.986
11338.969	9.955	0.765	0.594	1.026
11347.953	9.918	0.817	0.629	1.093
11355.990	9.593	0.679	0.557	0.967
11357.943	9.863	0.814	0.607	0.956
11363.975	9.192	0.406	0.423	0.708
11368.948	9.915	0.799	0.623	1.048
11372.905	9.403	0.415	0.425	0.693
11373.886	9.231	0.405	0.428	0.706
11383.922	9.246	0.395	0.412	0.682
11397.912	9.683	0.718	0.585	0.994
11398.881	9.806	0.788	0.597	1.027
11399.915	9.907	0.796	0.607	1.055
11408.892	9.755	0.778	0.584	1.022
11412.917	9.793	0.571	0.510	0.871
11415.867	9.226	0.443	0.447	0.744
11620.191	9.326	0.400	0.413	0.710
11623.122	9.482	0.623	0.522	0.899
11629.998	9.504	0.445	0.444	0.726
11673.074	9.207	0.450	0.436	0.736
11691.018	9.748	0.535	0.506	0.827
11715.004	9.331	0.516	0.477	0.816
11726.951	9.671	0.700	0.569	0.977
11729.958	9.956	0.742	0.599	1.026
11743.881	9.245	0.391	0.428	0.698
11754.955	9.178	0.416	0.390	0.685
11768.884	9.800	0.751	0.595	1.036
11931.129	9.309	0.482	0.478	0.792
11979.118	9.749	0.544	0.497	0.906
11983.177	9.482	0.581	0.522	0.878
11984.129	9.643	0.702	0.556	0.962
11985.110	9.790	0.762	0.604	1.030
11986.184	9.890	0.794	0.595	1.034
11991.147	9.220	0.396	0.428	0.700
12000.097	9.615	0.499	0.475	0.798
12006.110	9.829	0.780	0.605	1.026
12013.068	9.268	0.487	0.459	0.782
12014.053	9.479	0.603	0.586	0.897
12021.085	9.383	0.416	0.442	0.706
12023.098	9.252	0.470	0.461	0.768

continued on next page

Table B.6: *continued*

JD-2440000	*V*	*B-V*	*V-I*	*V-R*
12042.056	9.265	0.393	0.423	0.679
12051.984	9.375	0.411	0.438	0.720
12052.955	9.184	0.397	0.428	0.698
12054.964	9.416	0.583	0.509	0.861
12056.025	9.630	0.693	0.561	0.954
12058.982	9.931	0.758	0.599	1.009
12059.960	9.921	0.689	0.577	0.956
12065.931	9.561	0.669	0.548	0.924
12079.913	9.938	0.751	0.585	0.984
12115.943	9.245	0.467	0.454	0.762
12116.972	9.439	0.579	0.522	0.859
12121.833	9.933	0.692	0.577	0.984
12124.892	9.238	0.397	0.402	0.680
12133.869	9.759	0.526	0.488	0.823
12143.837	9.809	0.580	0.503	0.881
12152.851	9.945	0.701	0.584	1.000
12322.175	9.238	0.451	0.463	0.765
12339.200	9.877	0.622	0.532	0.911
12345.211	9.671	0.720	0.581	0.996
12408.911	9.901	0.776	0.610	1.039

B.1.7 W Vir

Table B.7: MJUO W Vir photometry.

JD-2440000	*V*	*B-V*	*V-I*	*V-R*
11318.007	10.750	0.919	0.523	1.031
11333.909	10.732	1.018	0.561	1.105
11336.019	10.791	0.893	0.528	1.038
11338.947	10.305	0.640	0.403	0.745
11347.851	9.901	0.798	0.450	0.889
11355.974	10.322	0.594	0.390	0.745
11357.918	9.570	0.402	0.276	0.552
11363.958	9.774	0.766	0.431	0.865
11372.827	10.537	0.706	0.444	0.816
11373.823	10.250	0.585	0.398	0.766
11383.905	10.201	0.901	0.492	0.962
11389.928	10.454	0.656	0.413	0.824
11397.826	9.697	0.726	0.426	0.827
11398.866	9.788	0.779	0.438	0.861
11399.832	9.918	0.819	0.465	0.899
11408.850	10.058	0.546	0.351	0.661
11415.844	9.705	0.740	0.410	0.829
11607.137	9.941	0.833	0.473	0.909
11620.172	9.643	0.649	0.391	0.767
11623.108	9.763	0.745	0.429	0.840
11629.984	10.683	0.825	0.478	0.980
11673.062	9.639	0.691	0.407	0.799
11691.001	9.641	0.695	0.409	0.824
11714.989	10.819	1.034	0.569	1.090
11726.938	9.781	0.730	0.418	0.832
11729.903	10.288	0.940	0.495	0.995
11743.862	9.733	0.775	0.433	0.831
11756.897	9.651	0.584	0.344	0.706
11768.870	10.569	0.742	0.440	0.883
11770.854	10.310	0.571	0.360	0.744
11931.117	9.611	0.649	0.400	0.772
11983.163	9.618	0.646	0.391	0.767
11984.111	9.631	0.672	0.429	0.786
11985.098	9.665	0.716	0.418	0.806
11986.171	9.771	0.754	0.440	0.846
11991.136	10.774	0.984	0.556	1.087
12000.086	9.678	0.638	0.392	0.768
12013.057	10.090	0.526	0.354	0.692
12014.041	9.727	0.447	0.294	0.564
12021.072	9.790	0.774	0.430	0.856
12021.941	9.902	0.823	0.458	0.895
12023.085	10.172	0.917	0.498	0.986
12051.970	9.640	0.631	0.385	0.758
12052.941	9.607	0.693	0.408	0.814
12054.951	9.744	0.750	0.433	0.851
12056.013	9.861	0.800	0.440	0.873
12058.968	10.524	0.972	0.542	1.035
12059.947	10.726	0.998	0.565	1.073
12065.916	9.733	0.446	0.284	0.564
12078.922	10.823	0.899	0.536	1.022
12115.930	10.486	0.685	0.446	0.864
12121.818	9.639	0.671	0.397	0.780
12124.878	9.837	0.804	0.436	0.875
12143.823	10.120	0.909	0.499	0.948
12154.834	9.673	0.641	0.391	0.714
12321.120	10.800	0.855	0.512	0.988
12322.162	10.575	0.730	0.476	1.241
12339.187	10.565	0.738	0.444	0.849
12345.193	9.677	0.629	0.393	0.754
12408.892	10.497	0.679	0.409	0.845

B.1.8 ST Pup

Table B.8: MJUO ST Pup photometry.

JD-2440000	V	B-V	V-I	V-R
11398.215	9.944	0.728	0.412	0.831
11400.231	10.044	0.770	0.444	0.877
11408.190	10.609	0.776	0.464	0.894
11414.168	9.799	0.623	0.375	0.762
11416.166	9.879	0.741	0.409	0.887
11426.131	10.726	0.825	0.480	0.931
11445.099	10.559	0.711	0.444	0.859
11450.069	9.783	0.551	0.351	0.699
11476.062	10.195	0.847	0.470	0.938
11495.003	10.295	0.866	0.510	0.976
11496.030	10.418	0.917	0.504	0.976
11505.040	9.602	0.405	0.305	0.602
11528.994	9.931	0.702	0.439	0.875
11552.096	10.473	0.940	0.522	0.992
11600.939	9.841	0.691	0.405	0.786
11605.923	10.157	0.810	0.473	0.916
11611.943	10.784	0.873	0.493	0.982
11613.934	10.297	0.561	0.383	0.785
11617.880	9.782	0.560	0.360	0.740
11628.890	10.610	0.843	0.485	0.952
11661.862	10.096	0.770	0.455	0.909
11673.824	9.934	0.605	0.384	0.780
11714.833	9.989	0.769	0.410	0.519
11850.957	10.666	0.940	0.518	1.011
11852.029	10.751	0.934	0.526	0.999
11853.028	10.773	0.887	0.491	1.538
11854.011	10.744	0.802	0.483	0.957
11873.973	10.343	0.594	0.379	0.768
11879.014	9.844	0.606	0.379	0.780
11896.036	9.675	0.470	0.313	0.645
11915.967	9.782	0.553	0.370	0.738
11932.980	9.668	0.457	0.313	0.625
11938.984	10.051	0.776	0.455	0.924
11958.999	10.069	0.776	0.460	0.904
11975.859	10.014	0.763	0.446	0.891
11978.897	10.308	0.860	0.501	0.960
11983.932	10.668	0.810	0.473	0.952
11985.968	10.244	0.581	0.382	0.768
12013.887	9.999	0.734	0.453	0.898
12020.960	10.704	0.818	0.492	0.943
12021.874	10.642	0.766	0.455	0.901
12043.856	9.542	0.388	0.274	0.551
12071.801	10.277	0.894	0.502	0.974
12149.174	10.491	0.852	0.492	0.956
12163.141	10.053	0.792	0.456	0.907
12171.176	10.822	0.847	0.502	0.979
12177.175	9.802	0.552	0.375	0.744
12181.181	9.968	0.716	0.419	0.859
12219.014	9.969	0.738	0.450	0.890
12221.029	10.136	0.819	0.475	0.946
12256.096	10.011	0.758	0.438	0.873
12298.021	10.527	0.927	0.521	1.004
12320.005	10.514	0.716	0.441	0.877
12321.956	10.213	0.525	0.350	0.717
12325.969	9.933	0.594	0.381	0.766
12338.942	10.719	0.805	0.485	0.953
12406.840	10.070	0.782	0.446	0.885
12410.872	10.522	0.890	0.490	0.962

B.2 RV Tauri stars

B.2.1 SX Cen

Table B.9: MJUO SX Cen photometry.

JD-2440000	V	B-V	V-I	V-R
11294.946	9.908	0.774	0.451	0.912
11305.005	9.783	0.966	0.535	1.051
11308.936	9.997	0.913	0.510	0.985
11316.039	9.412	0.684	0.434	0.858
11317.988	9.440	0.756	0.456	0.871
11339.003	9.750	0.927	0.506	0.960
11347.989	9.308	0.641	0.407	0.796
11364.002	9.317	0.636	0.392	0.794
11367.997	9.430	0.812	0.457	0.867
11373.032	9.720	0.868	0.504	0.958
11380.031	9.308	0.621	0.393	0.773
11388.854	9.745	0.911	0.499	0.939
11397.900	9.261	0.663	0.413	0.804
11399.928	9.310	0.750	0.464	0.853
11407.899	9.822	0.810	0.483	0.909
11413.852	9.287	0.681	0.429	0.830

continued on next page

Table B.9: *continued*

JD-2440000	*V*	*B-V*	*V-I*	*V-R*
11558.020	9.319	0.526	0.338	0.691
11593.157	9.165	0.554	0.363	0.728
11606.177	9.841	0.788	0.453	0.881
11614.015	9.224	0.718	0.428	0.825
11620.114	9.771	0.895	0.502	0.956
11623.043	9.561	0.661	0.464	0.800
11629.128	9.346	0.765	0.459	0.877
11631.134	9.417	0.858	0.482	0.927
11662.032	9.401	0.774	0.451	0.893
11668.037	9.694	0.882	0.486	1.075
11672.993	9.489	0.597	0.380	0.756
11685.974	9.873	0.905	0.504	0.970
11690.954	9.490	0.621	0.389	0.766
11714.974	9.729	0.931	0.513	0.980
11721.913	9.893	0.803	0.459	0.901
11730.947	9.790	0.955	0.526	1.009
11741.944	9.646	0.780	0.473	0.907
11754.940	10.018	0.831	0.490	0.946
11769.943	10.184	0.980	0.551	1.071
11780.960	10.088	1.099	0.612	1.168
11931.066	10.521	1.205	0.663	1.289
11978.097	9.619	0.889	0.509	0.998
11983.086	9.931	0.871	0.505	0.990
11991.085	9.528	0.829	0.477	0.935
12000.070	9.911	0.877	0.460	0.958
12006.133	9.348	0.655	0.416	0.819
12018.140	9.713	0.753	0.434	0.879
12021.035	9.348	0.639	0.403	0.784
12052.030	9.557	0.605	0.396	0.803
12054.937	9.253	0.633	0.400	0.812
12058.994	9.402	0.810	0.465	0.893
12067.894	9.530	0.629	0.393	0.788
12114.940	9.910	0.911	0.490	0.938
12121.912	9.159	0.621	0.398	0.800
12124.859	9.282	0.763	0.448	0.879
12133.909	9.383	0.597	0.349	0.735
12137.923	9.255	0.668	0.422	0.839
12143.936	9.509	0.848	0.472	0.959
12149.844	9.581	0.659	0.396	0.768
12149.950	9.580	0.646	0.400	0.780
12153.890	9.143	0.604	0.393	0.760
12221.101	9.328	0.750	0.447	0.864
12320.117	10.396	1.115	0.651	1.292
12322.111	10.505	1.156	0.680	1.327
12339.125	10.849	1.154	0.706	1.405
12345.147	11.285	1.107	0.663	1.359

Table B.10: Albert Jones SX Cen visual estimates.

JD	V
2451661.9667	9.60
2451669.9160	9.50
2451680.8264	9.40
2451688.8326	9.30
2451703.8507	9.90
2451708.8035	9.30
2451725.8903	9.60
2451729.9535	9.50
2451733.9250	9.60
2451748.8944	10.10
2451754.8729	10.20
2451760.8972	10.10
2451764.8944	10.20
2451779.8319	10.30
2451791.8292	10.20
2451804.8639	10.30
2451813.8334	10.80
2451836.1736	11.30
2451851.1438	11.10
2451865.1556	11.30
2451878.1292	10.80
2451879.1215	10.70
2451888.1125	10.70
2451901.1042	10.90
2451913.1069	10.70
2451940.9806	9.90
2451949.9160	10.60
2451960.8903	10.30
2451963.8972	10.10
2451973.8792	9.80
2451984.9243	9.90
2451991.8944	9.50
2451995.9326	9.40
2452002.8917	9.60
2452022.8264	9.30
2452026.8438	9.60
2452044.7910	9.60
2452052.9479	9.40
2452057.8576	9.30
2452070.9174	9.40

continued on next page

Table B.10: *continued*

JD	V
2452081.9215	9.50
2452086.8979	9.40
2452099.9049	9.80
2452112.8222	10.20
2452115.8701	10.30
2452133.8792	9.60
2452137.8139	9.40
2452149.8451	9.40
2452152.8319	9.40
2452152.8319	9.50
2452163.8264	9.90
2452168.8306	9.10
2452197.1819	10.10
2452220.1563	9.20
2452256.1146	9.60
2452289.9958	10.20
2452300.1174	10.20
2452308.9951	10.50
2452324.0792	10.50
2452329.9229	10.90
2452336.8764	10.60
2452340.9500	10.80
2452344.9528	11.30
2452357.8479	11.30
2452360.9076	11.40
2452366.8938	11.40
2452372.8257	11.70
2452380.9194	11.50
2452393.8583	11.60
2452402.8194	11.40
2452411.8167	11.50
2452425.9194	11.50
2452429.9118	11.60
2452436.8924	11.50
2452446.8944	11.60

B.2.2 TT Oph

Table B.11: MJUO TT Oph photometry.

JD-2440000	*V*	*B-V*	*V-I*	*V-R*
11316.091	10.312	1.004	0.568	0.985
11339.084	10.230	1.173	0.615	1.083
11349.017	10.088	0.851	0.465	0.773
11356.109	9.543	0.955	0.504	0.890
11369.071	10.375	1.279	0.643	1.180
11397.927	9.945	1.177	0.598	1.046
11407.962	10.293	0.958	0.511	0.899
11417.932	9.586	0.957	0.470	0.875
11459.854	10.160	1.189	0.615	1.094
11621.185	10.322	0.942	0.521	0.891
11630.114	9.418	0.881	0.474	0.860
11664.052	9.488	0.982	0.506	0.942
11673.113	10.111	1.186	0.609	1.075
11686.064	9.823	0.798	0.440	0.817
11691.116	9.539	0.936	0.501	0.889
11722.014	9.533	0.964	0.508	0.905
11729.974	9.991	1.218	0.593	1.071
11754.002	9.549	1.029	0.569	0.970
11770.874	10.256	1.027	0.569	0.948
11779.890	9.562	0.912	0.491	0.869
11792.892	10.254	1.227	0.665	1.155
11985.121	10.705	1.159	0.617	1.159
11992.092	9.849	0.838	0.462	0.825
12000.109	9.556	1.034	0.536	0.954
12006.199	9.947	1.198	0.613	1.063
12013.102	10.482	1.228	0.649	1.123
12021.135	9.986	0.826	0.472	0.862
12023.113	9.802	0.835	0.463	0.812
12055.042	9.774	0.893	0.504	0.896
12063.060	9.873	1.195	0.615	1.098
12066.070	10.113	1.239	0.639	1.182
12079.999	10.132	0.895	0.509	0.888
12114.968	9.592	0.855	0.462	0.863
12121.926	9.680	1.073	0.548	0.982
12143.886	9.655	0.803	0.452	0.794
12152.889	9.738	1.092	0.587	1.024
12163.896	10.659	1.282	0.659	1.161
12410.037	10.554	1.077	0.572	1.064

Table B.12: Albert Jones TT Oph visual estimates.

JD-2440000	V
2451681.2257	10.60
2451689.9799	9.40
2451702.9688	10.80
2451704.9236	10.80
2451718.8889	9.90
2451725.8979	9.80
2451729.9444	10.10
2451732.9208	10.60
2451748.9216	9.40
2451755.8861	9.50
2451761.8729	10.60
2451779.8910	9.80
2451792.8403	10.60
2451803.8215	10.10
2451813.8722	9.90
2451960.1694	10.60
2451975.1528	10.20
2451985.1861	11.00
2451994.2257	10.00
2451998.1278	9.80
2452004.1674	9.90
2452021.1903	9.80
2452044.9326	10.80
2452053.1979	9.80
2452061.1236	9.60
2452071.9160	10.80
2452080.9444	10.50
2452086.9229	11.00
2452088.9382	10.50
2452100.8833	11.10
2452112.8285	9.90
2452115.8826	9.40
2452129.9375	10.60
2452136.9049	10.60
2452146.8708	9.60
2452163.8139	10.90
2452170.8403	10.70
2452312.1514	10.70
2452320.1556	10.80
2452330.1569	10.40
2452345.2007	11.20
2452356.1326	10.90
2452368.1847	10.00
2452373.2056	10.90
2452381.1813	10.80
2452399.2104	10.20
2452407.9715	10.80
2452427.9361	10.50
2452436.9028	11.10

B.2.3 RU Cen

Table B.13: MJUO RU Cen photometry.

JD-2440000	*V*	*B-V*	*V-I*	*V-R*
11305.021	8.704	0.655	0.394	0.860
11309.024	8.634	0.728	0.427	0.978
11315.978	8.833	0.795	0.442	0.986
11333.971	8.856	0.542	0.350	0.811
11347.999	8.939	0.833	0.469	1.014
11355.896	9.395	0.965	0.504	1.077
11363.988	9.077	0.601	0.380	0.876
11368.960	8.685	0.524	0.353	0.793
11390.823	9.474	0.882	0.490	1.035
11397.890	9.065	0.569	0.372	0.855
11407.883	8.653	0.732	0.416	0.940
11413.837	8.886	0.816	0.443	0.950
11557.157	9.274	0.688	0.418	0.917
11593.145	8.747	0.516	0.354	0.790
11606.159	8.883	0.862	0.469	0.986
11614.004	9.386	0.919	0.508	1.067
11620.099	9.381	0.724	0.424	0.928
11623.030	9.085	0.625	0.381	0.859
11629.115	8.712	0.654	0.394	0.837
11662.018	8.794	0.662	0.414	0.911
11668.023	8.702	0.794	0.427	0.928
11672.983	8.923	0.869	0.460	0.988
11685.963	9.523	0.780	0.464	1.005
11690.941	8.883	0.623	0.391	0.895
11714.960	9.136	0.639	0.389	0.875
11721.898	9.005	0.565	0.363	0.814
11730.883	8.741	0.802	0.447	0.980
11754.926	8.856	0.506	0.345	0.758
11921.127	8.756	0.729	0.431	0.948
11928.150	8.782	0.815	0.433	0.972
11939.168	9.656	0.982	0.532	1.125
11978.086	9.079	0.583	0.373	0.827
11983.074	8.797	0.599	0.374	0.845

continued on next page

Table B.13: *continued*

JD-2440000	*V*	*B-V*	*V-I*	*V-R*
11985.038	8.798	0.680	0.403	0.919
11986.041	8.798	0.682	0.405	0.907
11991.075	8.726	0.815	0.426	0.952
11999.139	9.220	0.953	0.502	1.058
12000.057	9.348	0.990	0.525	1.082
12006.122	9.826	0.948	0.523	1.110
12013.079	8.687	0.517	0.331	0.756
12018.120	8.567	0.635	0.395	0.870
12042.069	8.854	0.485	0.329	0.769
12058.954	8.940	0.849	0.461	0.980
12063.043	9.105	0.869	0.475	1.034
12067.878	9.254	0.809	0.461	0.988
12078.881	8.953	0.611	0.375	0.855
12114.929	8.677	0.682	0.395	0.902
12121.900	8.744	0.809	0.430	0.929
12133.896	9.761	0.936	0.498	1.105
12137.911	9.436	0.660	0.414	0.916
12143.925	8.731	0.582	0.371	0.835
12149.834	8.623	0.712	0.419	0.933
12153.878	8.751	0.772	0.412	0.943
12221.088	8.883	0.835	0.475	0.996
12313.030	8.750	0.770	0.432	0.950
12313.030	8.750	0.770	0.432	0.950
12320.105	9.118	0.900	0.479	1.026
12339.114	8.684	0.652	0.378	0.849
12407.939	8.654	0.738	0.412	0.915

Table B.14: Albert Jones RU Cen visual estimates.

JD	V
2451688.8403	8.90
2451703.8465	8.70
2451708.8132	8.70
2451725.8944	8.50
2451729.9563	8.40
2451733.9271	8.50
2451748.8972	9.10
2451754.8722	8.70
2451760.9007	8.70
2451764.8951	8.80
2451779.8340	9.20
2451791.8319	8.40
2451804.8653	9.40
2451813.8389	9.50
2451836.1771	9.50
2451851.1458	9.20
2451865.1569	9.20
2451878.1333	9.50
2451879.1222	9.50
2451888.1146	9.10
2451901.1069	8.60
2451913.1076	9.00
2451940.9833	9.20
2451949.9174	9.20
2451960.8910	9.00
2451963.9007	8.90
2451973.8806	9.20
2451984.9264	8.50
2451991.8951	8.70
2451995.9340	8.90
2452002.9111	9.50
2452022.8278	9.10
2452026.8451	8.90
2452044.7931	8.70
2452052.9493	8.90
2452057.8972	9.20
2452070.9188	9.10
2452081.9229	8.70
2452086.8993	8.70
2452099.9069	8.70
2452112.8243	9.00
2452115.8743	8.50
2452133.8826	9.00
2452137.8146	8.90
2452149.8500	8.40
2452152.8354	8.40
2452163.8285	8.80
2452168.8319	8.70
2452168.8334	11.00
2452197.1847	9.00
2452220.1583	8.40
2452256.1194	9.10
2452289.9972	9.20
2452300.1201	8.40
2452308.9972	8.90
2452324.0826	8.70
2452329.9271	10.10
2452336.8792	8.80
2452340.9521	8.70
2452344.9549	9.30

continued on next page

Table B.14: *continued*

JD	V
2452357.8542	9.60
2452360.9125	10.10
2452366.8979	9.50
2452372.8361	8.30
2452380.9257	8.90
2452393.8743	9.80
2452402.8278	9.10
2452411.8201	8.60
2452425.9250	8.70
2452429.9160	8.70
2452436.9000	8.80
2452446.8979	8.90

B.2.4 CT Ori

Table B.15: MJUO CT Ori photometry.

JD-2440000	*V*	*B-V*	*V-I*	*V-R*
11426.212	10.671	1.050	0.636	1.251
11450.151	10.406	0.875	0.554	1.127
11460.103	10.512	0.983	0.606	1.230
11476.106	10.529	0.812	0.527	1.089
11495.128	10.660	1.066	0.622	1.284
11505.026	11.099	1.103	0.684	1.334
11528.980	10.613	1.000	0.619	1.251
11552.085	10.588	0.978	0.599	1.280
11570.006	11.079	1.217	0.676	1.352
11611.881	10.496	0.796	0.552	1.105
11619.856	10.597	1.019	0.617	1.255
11628.869	10.689	1.059	0.641	1.280
11852.047	10.457	0.869	0.550	1.136
11873.993	10.742	0.942	0.575	1.183
11879.001	10.657	0.845	0.546	1.127
11896.012	10.563	1.038	0.567	1.196
11915.955	10.575	0.881	0.550	1.111
11927.982	10.470	0.978	0.599	1.223
11932.967	10.533	0.979	0.634	1.236
11978.866	11.165	1.112	0.660	1.333
11982.912	10.738	0.938	0.578	1.216
11991.884	10.418	0.909	0.581	1.190
12003.834	10.587	0.901	0.573	1.203
12012.872	10.652	0.897	0.522	1.105
12015.863	10.535	0.805	0.530	1.103
12021.840	10.607	0.988	0.585	1.212
12163.162	10.625	1.062	0.596	1.204
12181.166	11.178	1.139	0.685	1.333
12229.048	10.585	1.002	0.617	1.260
12255.966	10.502	0.859	0.531	1.102
12319.930	10.636	0.909	0.549	1.151
12321.914	10.345	0.748	0.507	1.050
12325.954	10.404	0.812	0.532	1.103
12333.890	10.527	0.944	0.597	1.210

Table B.16: Albert Jones CT Ori visual estimates.

JD	V
2451755.2583	11.00
2451760.2618	10.90
2451765.2528	10.80
2451769.2465	10.70
2451776.2451	10.90
2451780.2403	10.70
2451791.2458	10.20
2451798.2361	10.30
2451809.2056	10.70
2451838.1396	11.10
2451842.1479	11.10
2451849.1486	11.10
2451851.1229	11.00
2451870.1410	11.00
2451880.0924	10.70
2451885.1410	10.70
2451896.9229	10.50
2451901.0729	10.70
2451904.9584	10.80
2451912.9167	11.10
2451920.8917	11.00
2451925.9507	10.90
2451940.8903	11.10
2451949.8868	10.70
2451954.8965	11.00
2451959.9167	10.90
2451966.9278	10.80
2451972.8903	12.50
2451982.8507	10.80
2451984.8792	10.90

continued on next page

Table B.16: *continued*

JD	V
2451988.8500	10.70
2451990.8403	10.70
2451998.8417	10.70
2452010.8153	10.80
2452025.7910	10.70
2452113.2604	11.10
2452117.2646	11.10
2452137.2486	10.90
2452140.2507	11.00
2452147.2132	11.00
2452153.2292	10.90
2452161.2049	11.00
2452166.1972	10.90
2452169.2208	10.90
2452181.1826	11.30
2452200.1500	10.90
2452205.1194	10.80
2452220.0972	10.70
2452255.9958	10.70
2452289.9611	10.70
2452297.9472	10.80
2452305.9111	11.00
2452308.9521	11.20
2452310.8750	11.20
2452322.9242	11.00
2452326.9535	10.80
2452335.9090	10.80
2452340.8576	10.90
2452343.8708	10.90
2452352.8590	10.80
2452356.8438	10.60
2452365.8861	10.80
2452367.8653	10.60
2452378.8160	11.20
2452380.8181	11.20
2452382.8125	11.10
2452393.7951	10.60
2452396.7903	10.70
2452401.7972	10.60

B.2.5 AI Sco

Table B.17: MJUO AI Sco photometry.

JD-2440000	*V*	*B-V*	*V-I*	*V-R*
11295.120	9.308	1.380	0.736	1.306
11303.137	9.402	1.175	0.645	1.151
11306.150	8.995	0.968	0.549	1.008
11316.124	8.902	1.335	0.667	1.222
11334.161	9.920	1.540	0.788	1.470
11339.164	9.291	1.169	0.641	1.152
11349.062	8.873	1.235	0.647	1.163
11357.129	9.087	1.429	0.706	1.273
11368.099	9.740	1.295	0.694	1.367
11373.163	9.311	1.159	0.619	1.159
11398.113	9.480	1.543	0.748	1.383
11408.128	0.224	1.310	0.697	1.591
11413.903	9.050	1.148	0.621	1.124
11425.990	8.933	1.293	0.718	1.217
11452.980	9.308	1.208	0.665	1.222
11459.904	9.336	1.400	0.752	1.349
11475.909	0.285	1.707	0.847	1.516
11621.028	1.454	0.599	0.310	0.611
11630.078	0.617	1.240	0.744	1.383
11664.094	0.713	1.178	0.679	1.290
11688.096	0.992	1.543	0.826	1.518
11720.934	0.825	1.518	0.778	1.479
11721.996	0.877	1.529	0.764	1.473
11730.080	1.218	1.474	0.808	1.522
11731.105	1.231	1.473	0.792	1.505
11733.996	1.114	1.417	0.787	1.446
11742.130	0.416	1.272	0.727	1.368
11742.849	0.367	1.282	0.745	1.389
11748.986	0.315	1.454	0.796	1.490
11754.086	0.520	1.526	0.847	1.543
11755.010	0.564	1.556	0.823	1.526
11779.970	0.177	1.368	0.758	1.452
11798.951	0.515	1.516	0.837	1.556
11801.926	0.479	1.434	0.799	1.492
11838.883	0.453	1.454	0.797	1.519
11851.890	9.425	1.269	0.718	1.316
11853.885	9.396	1.329	0.720	1.348
11856.894	9.431	1.422	0.738	1.375
11985.168	9.393	1.163	0.642	1.179
11992.059	9.122	1.303	0.684	1.253
12001.192	9.372	1.498	0.746	1.362
12006.239	9.701	1.522	0.772	1.415
12013.148	9.970	1.407	0.754	1.403
12023.157	9.118	1.185	0.659	1.216

continued on next page

Table B.17: *continued*

JD-2440000	*V*	*B-V*	*V-I*	*V-R*
12042.169	9.616	1.562	0.784	1.414
12063.181	9.083	1.313	0.691	1.250
12066.116	9.143	1.402	0.726	1.300
12113.198	9.450	1.459	0.760	1.343
12116.994	9.575	1.443	0.740	1.337
12124.914	9.017	1.032	0.579	1.042
12130.016	8.984	1.201	0.633	1.181
12144.001	9.334	1.542	0.754	1.347
12150.868	9.826	1.549	0.781	1.420
12162.936	9.058	1.132	0.619	1.127
12171.003	8.793	1.256	0.664	1.222
12176.926	8.867	1.322	0.675	1.245
12180.963	9.053	1.366	0.702	1.284
12220.906	9.762	1.552	0.775	1.508
12230.898	9.413	1.250	0.661	1.265
12410.092	9.874	1.284	0.711	1.332

Table B.18: Albert Jones AI Sco visual estimates.

JD	V
2451661.0021	11.30
2451679.2549	11.10
2451687.9146	11.30
2451702.9556	11.10
2451704.9028	10.90
2451708.8889	10.90
2451718.2028	11.10
2451725.9778	11.10
2451732.9042	11.30
2451742.0972	10.80
2451748.8500	10.80
2451754.8424	10.80
2451761.8840	11.30
2451779.9444	10.60
2451792.8972	10.70
2451803.8847	10.90
2451810.9681	10.70
2451814.8701	10.50
2451817.9681	10.60
2451834.9049	10.90
2451844.9222	10.40
2451850.8972	10.10
2451936.1542	10.40
2451948.1563	9.70
2451960.1639	9.60
2451975.1944	10.70
2451985.1951	9.60
2451996.1771	9.40
2452004.2090	9.70
2452021.2194	9.30
2452026.2549	9.10
2452037.2597	8.80
2452043.9632	9.40
2452046.9208	10.00
2452052.2604	10.00
2452053.2146	9.00
2452055.2549	9.10
2452058.2292	8.80
2452062.2278	9.20
2452086.9410	10.10
2452089.2167	10.00
2452090.8326	9.50
2452093.2431	9.10
2452100.9083	9.10
2452112.1938	10.00
2452126.8014	9.30
2452129.9319	9.10
2452135.9556	9.00
2452143.9438	9.10
2452146.9653	10.20
2452164.8396	9.30
2452168.9840	9.10
2452173.9188	9.00
2452179.9007	8.90
2452182.9458	9.30
2452193.9285	9.50
2452204.9181	9.00
2452296.1500	9.30
2452299.1597	9.90
2452303.1618	9.50
2452312.1438	9.00
2452313.1729	9.10
2452319.1847	9.40
2452324.1660	9.30
2452326.1944	9.60
2452329.1146	10.00
2452338.1590	9.90
2452349.1729	9.40
2452352.1764	9.40
2452357.2014	9.60

continued on next page

Table B.18: *continued*

JD	V
2452360.1528	9.40
2452372.9660	10.00
2452379.2403	9.90
2452385.2410	9.50
2452395.9083	10.00
2452399.2347	10.70
2452408.2319	10.80
2452419.2084	9.90
2452424.8639	9.10
2452427.9556	9.90
2452430.2313	9.40
2452432.2431	9.90
2452436.8521	10.00
2452447.2639	9.90

B.2.6 AR Pup

Table B.19: MJUO AR Pup photometry.

JD-2440000	*V*	*B-V*	*V-I*	*V-R*
11294.914	9.810	0.912	0.492	1.010
11301.866	10.059	0.882	0.478	1.015
11306.892	9.697	0.647	0.395	0.841
11315.895	9.585	0.728	0.409	0.892
11339.802	9.926	0.842	0.485	1.019
11347.818	9.695	0.704	0.405	0.885
11355.807	9.596	0.760	0.434	0.944
11364.815	9.535	0.819	0.450	0.947
11368.802	9.663	0.845	0.467	1.001
11383.807	9.688	0.785	0.377	0.858
11450.083	9.736	0.868	0.499	1.018
11476.080	9.438	0.835	0.465	0.984
11496.046	9.619	0.752	0.440	0.913
11505.007	9.472	0.705	0.414	0.881
11555.999	9.309	0.823	0.466	1.026
11570.105	9.620	0.843	0.473	0.999
11575.070	9.561	0.692	0.423	0.907
11593.025	9.171	0.780	0.451	0.947
11606.017	9.489	0.899	0.501	1.037
11611.041	9.620	0.869	0.491	1.030
11613.916	9.620	0.825	0.474	0.993
11619.890	9.468	0.715	0.413	0.883
11622.936	9.383	0.721	0.418	0.895
11628.975	9.209	0.765	0.441	0.939
11661.896	9.197	0.641	0.393	0.855
11672.901	9.147	0.823	0.467	0.984
11685.880	9.491	0.938	0.500	1.051
11690.862	9.494	0.853	0.478	1.002
11714.856	9.091	0.782	0.432	0.935
11721.815	9.253	0.837	0.451	0.946
11729.854	9.371	0.772	0.442	0.941
11741.815	9.207	0.728	0.451	0.919
11852.140	9.085	0.582	0.352	0.776
11854.023	9.089	0.606	0.379	0.807
11916.049	9.537	0.879	0.487	1.010
11928.065	9.204	0.611	0.397	0.823
11933.056	9.227	0.706	0.407	0.897
11939.076	9.193	0.783	0.440	0.937
11957.999	9.562	0.782	0.446	0.926
11975.944	9.187	0.708	0.424	0.899
11978.949	9.253	0.768	0.432	0.922
11983.984	9.367	0.830	0.461	0.962
11988.030	9.444	0.861	0.459	0.992
11991.934	9.538	0.845	0.463	0.980
11998.993	9.536	0.734	0.585	0.895
12005.989	9.308	0.650	0.397	0.849
12012.949	9.293	0.758	0.445	0.925
12020.982	9.408	0.846	0.476	0.993
12052.890	9.320	0.773	0.447	0.931
12058.921	9.459	0.868	0.465	0.971
12065.881	9.692	0.905	0.484	1.018
12071.826	9.703	0.804	0.443	0.943
12079.865	9.500	0.693	0.394	0.863
12163.175	9.361	0.726	0.409	0.875
12219.026	9.913	0.901	0.504	1.010
12256.082	9.793	0.801	0.466	0.980
12298.093	10.002	0.856	0.483	0.996
12312.965	9.582	0.705	0.416	0.887
12320.020	9.536	0.772	0.443	0.945
12321.998	9.564	0.797	0.449	0.946
12339.038	9.879	0.749	0.438	0.936
12406.872	9.800	0.853	0.478	0.972
12410.896	9.909	0.884	0.487	0.998

Table B.20: Albert Jones AR Pup visual estimates.

JD	V
2451661.9444	9.10
2451669.8993	9.10
2451674.8347	9.00
2451688.8167	9.50
2451700.8097	10.10
2451708.8306	9.40
2451725.7785	10.00
2451730.8014	9.80
2451751.2542	9.60
2451754.2479	9.60
2451758.2451	9.60
2451761.2507	9.70
2451765.2472	9.60
2451770.2514	9.80
2451779.2236	9.60
2451791.2333	9.60
2451804.2250	9.80
2451814.1750	9.60
2451820.1188	9.50
2451827.1965	9.50
2451837.1196	9.70
2451853.0271	9.60
2451869.9465	9.60
2451882.9431	9.80
2451888.1035	9.60
2451896.9493	9.50
2451904.9694	9.60
2451913.9549	9.60
2451935.9576	9.70
2451949.9125	9.80
2451961.1417	9.80
2451973.8757	9.70
2451984.8334	9.70
2451995.9132	9.50
2452000.8993	9.40
2452017.8938	9.50
2452025.8556	9.80
2452043.8146	9.00
2452052.8250	9.00
2452057.8361	8.90
2452062.8111	9.70
2452080.8042	9.50
2452086.8201	9.70
2452100.7951	10.00
2452112.2514	9.90
2452117.2688	9.50
2452122.2354	9.60
2452133.2542	9.40
2452136.2403	9.60
2452140.2521	9.70
2452150.2076	9.70
2452153.2424	9.60
2452166.1951	9.50
2452172.2146	9.70
2452181.1444	9.80
2452194.1736	9.60
2452201.1646	9.50
2452220.1646	9.90
2452256.0049	9.90
2452308.9396	9.80
2452321.1083	9.60
2452330.0819	10.00
2452336.8653	9.90
2452345.8604	9.80
2452352.8785	9.70
2452357.9569	9.60
2452366.9451	9.80
2452372.9264	10.30
2452380.8639	9.90
2452393.8181	9.60
2452400.8347	9.80
2452407.9333	9.90
2452423.8514	9.80
2452427.8021	9.60
2452436.8250	9.40
2452449.7931	9.80

B.2.7 AR Sgr

Table B.21: MJUO AR Sgr photometry.

JD-2440000	*V*	*B-V*	*V-I*	*V-R*
11316.175	9.259	0.968	0.533	1.002
11339.204	9.587	0.815	0.484	0.873
11357.179	9.431	0.964	0.577	1.030
11364.183	9.661	1.030	0.579	1.084
11368.195	9.745	0.994	0.567	1.028
11373.187	9.354	0.756	0.440	0.794

continued on next page

Table B.21: *continued*

JD-2440000	*V*	*B-V*	*V-I*	*V-R*
11398.163	9.550	1.022	0.577	1.071
11408.144	9.970	1.091	0.580	1.127
11414.098	9.991	1.032	0.574	1.082
11426.033	9.128	0.697	0.420	0.778
11445.026	9.427	0.974	0.557	1.026
11449.050	9.700	1.043	0.606	1.115
11452.996	0.023	1.117	0.625	1.143
11459.951	0.390	0.982	0.593	1.063
11630.201	9.638	0.768	0.471	0.841
11665.116	9.980	1.131	0.603	1.162
11688.159	9.223	0.843	0.501	0.941
11721.100	9.912	0.839	0.522	0.966
11727.099	9.206	0.669	0.435	0.809
11730.180	9.186	0.792	0.479	0.903
11731.164	9.154	0.879	0.489	0.915
11749.085	9.533	1.041	0.567	1.052
11770.084	9.198	0.716	0.430	0.785
11799.091	9.564	0.836	0.504	0.885
11838.971	9.808	1.087	0.607	1.139
11851.949	9.537	0.729	0.470	0.860
11853.917	9.412	0.707	0.431	0.782
11856.921	9.413	0.746	0.430	0.833
11992.199	9.439	0.856	0.508	0.948
12001.220	9.359	0.995	0.582	1.054
12013.199	9.755	1.136	0.656	1.183
12023.199	0.367	1.127	0.648	1.232
12042.211	9.189	0.864	0.514	0.944
12055.114	9.631	0.998	0.571	1.052
12059.183	9.803	1.498	0.579	1.047
12066.241	9.601	0.743	0.460	0.839
12113.225	9.761	0.897	0.532	0.986
12117.007	9.415	0.772	0.458	0.867
12130.000	9.208	0.857	0.502	0.958
12153.105	0.199	1.075	0.610	1.093
12162.997	9.206	0.645	0.399	0.754
12176.976	9.220	0.916	0.509	0.944
12181.017	9.394	0.976	0.524	0.990
12220.921	9.382	0.881	0.499	0.970
12410.265	9.636	0.816	0.498	0.911

Table B.22: Albert Jones AR Sgr visual estimates.

JD	V
2451679.2611	9.70
2451690.2271	9.10
2451761.8938	10.60
2451764.9118	10.10
2451779.9493	9.20
2451788.9535	9.50
2451803.8993	9.20
2451814.9243	9.20
2451819.9160	9.10
2451833.9326	9.10
2451837.9111	9.10
2451844.9118	9.10
2451961.1861	9.10
2451973.2035	9.20
2451994.2194	9.70
2451996.1806	9.60
2452001.2118	9.60
2452004.2063	10.00
2452018.1868	10.20
2452023.2354	10.40
2452043.9674	9.20
2452053.2188	9.70
2452060.2014	10.00
2452073.2764	9.00
2452081.9424	9.60
2452089.2382	9.10
2452093.2326	9.00
2452100.8979	10.00
2452112.8326	9.70
2452117.9403	9.60
2452129.9083	9.60
2452136.9146	9.70
2452146.9569	10.10
2452163.9750	9.10
2452168.9417	9.10
2452173.9306	9.40
2452180.8751	9.40
2452204.8576	9.20
2452221.8688	9.10
2452320.1785	9.70
2452323.1806	10.10
2452330.1903	9.40
2452352.1958	9.60
2452357.2000	10.10
2452371.2174	9.70
2452373.2250	9.80
2452381.2076	9.50

continued on next page

Table B.22: *continued*

JD	V
2452399.2389	9.60
2452407.9889	9.70
2452427.9549	9.20
2452432.2597	8.90
2452443.2472	9.50

B.2.8 UZ Oph

Table B.23: MJUO UZ Oph photometry.

JD-2440000	*V*	*B-V*	*V-I*	*V-R*
11316.106	10.776	1.214	0.667	1.239
11334.125	10.631	0.951	0.573	1.015
11339.108	10.485	1.002	0.569	1.031
11348.990	10.538	1.157	0.607	1.151
11356.145	10.865	1.244	0.661	1.292
11364.936	11.363	1.257	0.669	1.459
11369.086	11.541	1.180	0.653	1.487
11373.102	11.241	1.075	0.617	1.285
11383.973	10.418	0.901	0.528	0.979
11397.951	10.647	1.183	0.631	1.196
11407.993	11.085	1.247	0.677	1.329
11412.985	11.355	1.176	0.660	1.422
11425.931	10.528	0.949	0.520	1.034
11449.859	10.941	1.345	0.697	1.311
11621.209	10.750	1.296	0.661	1.303
11630.148	11.962	1.346	0.649	1.746
11673.139	11.082	1.226	0.656	1.333
11686.093	10.328	0.798	0.515	0.922
11691.149	10.320	0.976	0.556	1.016
11722.077	11.583	1.135	0.628	1.492
11727.063	11.236	1.137	0.635	1.299
11729.998	11.091	1.128	0.623	1.183
11754.038	10.528	1.152	0.616	1.163
11770.901	10.997	1.079	0.621	1.103
11779.948	10.619	0.921	0.537	1.028
11792.916	10.523	1.203	0.640	1.179
11992.119	11.630	1.248	0.677	1.290
12000.134	10.807	1.020	0.589	1.089
12006.226	10.282	0.970	0.555	1.058
12013.126	10.195	0.998	0.561	1.074
12023.142	10.512	1.155	0.641	1.144
12063.084	10.587	1.263	0.646	1.200
12066.099	10.858	1.309	0.691	1.308
12080.023	12.509	1.014	0.593	1.956
12114.992	10.698	1.198	0.661	1.138
12121.951	10.992	1.185	0.694	1.164
12137.903	10.285	0.967	0.544	1.038
12143.914	10.288	1.117	0.587	1.103
12152.916	10.679	1.313	0.666	1.224
12163.923	12.177	1.421	0.718	1.813
12410.070	10.571	1.284	0.638	1.176

Table B.24: Albert Jones UZ Oph visual estimates.

JD	V
2451689.9938	10.20
2451702.9785	10.90
2451704.9285	10.40
2451725.9056	11.30
2451729.9493	11.00
2451732.9257	10.80
2451748.9326	10.20
2451755.9069	10.80
2451761.8771	11.00
2451779.8958	10.50
2451792.8431	10.70
2451803.8729	11.60
2451813.8792	12.00
2451960.1778	10.50
2451975.1576	10.80
2451985.1917	11.50
2451994.2292	11.00
2451998.1299	11.00
2452004.1729	10.80
2452021.1979	10.70
2452044.9389	10.70
2452053.2056	10.10
2452061.1326	10.80
2452071.9236	11.30
2452080.9493	12.50
2452086.9306	11.20
2452088.9465	11.10
2452100.8882	9.50
2452112.8313	10.60

continued on next page

Table B.24: *continued*

JD	V
2452115.8861	10.90
2452129.9458	10.10
2452136.9097	10.50
2452146.8764	10.00
2452163.8208	12.10
2452170.8500	12.30
2452320.1576	10.10
2452330.1611	10.80
2452345.2056	12.10
2452356.1368	9.70
2452368.1910	10.10
2452373.2104	10.20
2452381.1847	10.70
2452399.2153	10.20
2452407.9743	10.10
2452427.9417	11.70
2452436.9063	10.10

B.2.9 U Mon

Table B.25: MJUO U Mon photometry.

JD-2440000	*V*	*B-V*	*V-I*	*V-R*
9421.865	6.638	0.992	0.509	1.145
9427.926	6.111	0.905	0.517	0.932
9431.877	5.885	0.944	0.504	0.875
9432.931	5.851	0.968	0.504	0.872
9433.862	5.811	0.971	0.495	0.853
9439.931	5.681	0.954	0.523	0.922
9441.853	5.593	0.976	0.514	0.865
9445.855	5.567	1.035	0.513	0.871
9451.879	5.780	1.110	0.543	0.959
9453.860	5.844	1.115	0.569	0.984
9476.908	5.731	0.794	0.442	0.769
9506.836	6.781	1.131	0.539	1.366
9508.829	6.946	1.113	0.522	1.390
9623.164	5.525	0.945	0.494	0.887
9729.017	5.545	1.007	0.526	0.900
9729.955	5.562	1.034	0.533	0.907
9734.907	5.734	1.058	0.549	0.938
9737.961	5.854	1.077	0.571	0.952
9741.034	5.958	1.087	0.570	0.948
9745.960	6.080	1.052	0.561	0.938
9746.937	6.083	1.039	0.555	0.927
9757.974	5.744	0.959	0.444	0.828
9761.003	5.641	0.994	0.502	0.871
9761.965	5.625	1.016	0.503	0.883
9763.943	5.628	1.062	0.525	0.905
9764.923	5.631	1.087	0.537	0.913
9776.867	5.840	1.259	0.593	1.015
9782.959	6.216	1.278	0.581	1.121
9783.873	6.307	1.268	0.591	1.153
9787.907	6.664	1.227	0.594	1.261
9793.903	6.919	1.087	0.543	1.280
9802.925	5.648	0.839	0.466	0.795
9815.897	5.583	1.067	0.535	0.935
9819.829	5.721	1.125	0.543	0.956
9822.854	5.851	1.176	0.567	0.994
9844.816	5.588	0.780	0.425	0.730
9846.853	5.556	0.835	0.450	0.782
9847.860	5.545	0.861	0.459	0.798
9859.860	5.740	1.140	0.551	0.941
10099.048	5.742	1.101	0.563	0.994
10101.072	5.808	1.132	0.573	1.003
10108.067	6.147	1.202	0.595	1.039
10110.106	6.261	1.196	0.624	1.066
10471.001	5.651	1.016	0.557	0.979
10472.002	5.682	1.035	0.571	0.978
10475.963	5.837	1.047	0.597	1.010
10494.941	5.715	0.904	0.511	0.889
10546.959	5.499	0.917	0.488	0.972
10726.128	5.875	1.015	0.549	1.004
10729.095	5.760	0.972	0.537	1.035
10748.081	5.917	1.050	0.581	1.037
10751.113	6.002	1.026	0.606	1.054
10756.070	6.060	1.018	0.562	1.010
10775.132	5.742	1.012	0.544	0.990
10789.098	5.975	1.312	0.608	1.097
10808.044	7.417	0.994	0.560	1.415
10835.103	5.757	1.047	0.595	1.053
10855.066	5.949	0.854	0.513	0.881
10875.970	6.054	1.244	0.597	1.061
10877.025	6.095	1.240	0.618	1.088
10896.943	7.570	0.978	0.545	1.344
10897.895	7.551	0.847	0.523	1.295
10907.930	6.730	0.947	0.523	1.216
10909.979	6.444	1.034	0.561	1.155
10913.921	6.119	1.101	0.577	1.098
10919.897	5.962	1.074	0.577	1.082

continued on next page

Table B.25: *continued*

JD-2440000	*V*	*B-V*	*V-I*	*V-R*
10921.858	5.973	1.087	0.577	1.084
10922.931	5.995	1.046	0.587	1.106
10938.889	6.575	1.176	0.645	1.154
10941.844	6.712	1.158	0.636	1.153
10944.829	6.799	1.121	0.632	1.127
10947.861	6.738	1.019	0.585	1.056
10950.875	6.565	0.900	0.526	0.991
10951.831	6.510	0.879	0.504	0.980
10960.828	6.263	1.062	0.581	1.103
10961.820	6.261	1.078	0.604	1.103
10967.860	6.328	1.197	0.602	1.156
10968.829	6.368	1.197	0.622	1.159
10978.818	6.808	1.228	0.650	1.301
10984.773	7.228	1.175	0.605	1.371
11110.113	6.244	1.258	0.626	1.169
11125.159	7.456	1.033	0.568	1.503
11128.070	7.501	0.936	0.560	1.472
11131.159	7.220	0.911	0.519	1.382
11145.043	5.972	1.165	0.628	1.170
11158.096	6.002	1.197	0.638	1.141
11163.134	6.082	1.156	0.627	1.103
11203.078	6.237	1.292	0.643	1.173
11205.052	6.334	1.293	0.632	1.210
11211.069	6.753	1.206	0.607	1.336
11218.016	6.914	1.051	0.545	1.273
11227.044	6.033	0.974	0.544	0.982
11230.947	5.856	1.047	0.555	1.000
11294.898	6.095	1.242	0.630	1.139
11301.853	6.303	1.228	0.623	1.147
11305.844	6.345	1.173	0.617	1.115
11315.881	5.825	0.954	0.512	0.913
11339.783	6.277	1.224	0.599	1.196
11347.797	6.763	1.111	0.562	1.339
11355.788	6.644	1.003	0.532	1.219
11357.787	6.431	1.019	0.522	1.112
11426.231	5.766	1.228	0.581	1.016
11450.126	6.479	1.011	0.486	1.127
11453.139	5.954	0.958	0.507	0.923
11460.136	5.729	1.050	0.583	0.972
11476.129	5.825	1.179	0.575	1.006
11495.031	6.107	1.020	0.542	0.955
11504.994	5.712	0.946	0.489	0.885
11529.085	6.076	1.232	0.617	1.100
11552.128	5.647	0.914	0.486	0.856
11570.039	6.133	1.234	0.573	1.131
11592.985	5.758	0.921	0.491	0.878
11598.937	5.562	1.027	0.518	0.899
11605.992	5.670	1.119	0.556	0.989
11611.983	5.846	1.196	0.575	0.996
11617.913	6.101	1.214	0.609	1.051
11622.859	6.251	1.174	0.601	1.067
11628.939	5.977	0.929	0.504	0.887
11630.938	5.776	0.837	0.470	0.807
11661.842	6.463	1.128	0.554	1.171
11663.838	6.594	1.091	0.544	1.204
11672.884	6.628	0.976	0.514	1.138
11685.849	5.752	0.980	0.532	0.914
11690.842	5.558	1.002	0.504	0.905
11703.803	5.761	1.180	0.552	0.986
11714.814	6.239	1.228	0.603	1.068
11839.129	5.765	1.086	0.536	0.968
11852.058	6.130	1.067	0.545	0.960
11854.040	6.161	1.024	0.522	0.926
11874.039	5.667	1.106	0.525	0.905
11896.941	7.140	1.065	0.542	1.432
11916.022	5.650	1.000	0.529	0.941
11928.017	5.971	1.180	0.594	1.024
11933.021	6.122	1.187	0.599	1.039
11939.066	6.166	1.109	0.577	1.008
11957.971	5.698	0.973	0.537	0.921
11975.915	6.497	1.136	0.545	1.151
11977.942	6.661	1.099	0.538	1.194
11978.916	6.738	1.063	0.534	1.226
11982.966	6.999	0.979	0.514	1.288
11983.968	7.034	0.970	0.506	1.290
11987.971	6.968	0.883	0.471	1.250
11990.955	6.591	0.878	0.453	1.110
11998.976	5.667	0.941	0.502	0.873
12005.959	5.521	1.035	0.510	0.885
12012.933	5.700	1.107	0.544	0.975
12020.946	5.936	1.163	0.568	0.980
12043.836	5.566	0.909	0.476	0.858
12052.858	5.644	1.102	0.552	0.955
12058.835	5.883	1.196	0.581	1.018
12065.835	6.263	1.270	0.581	1.126
12071.812	6.603	1.148	0.588	1.232
12163.191	6.386	1.257	0.627	1.106
12177.189	5.663	0.756	0.417	0.760
12219.049	6.021	0.925	0.484	0.907
12229.077	5.644	1.030	0.528	0.914
12256.049	5.978	0.999	0.524	0.938
12298.060	6.382	1.202	0.602	1.176
12312.980	6.003	0.925	0.502	0.895

continued on next page

Table B.25: *continued*

JD-2440000	*V*	*B-V*	*V-I*	*V-R*
12319.994	5.631	0.882	0.487	0.871
12321.986	5.604	0.941	0.480	0.877
12338.995	6.075	1.200	0.580	1.116
12406.856	5.798	0.865	0.461	0.827
12410.858	5.771	0.986	0.490	0.890

Table B.26: Albert Jones U Mon visual estimates.

JD	V
2451662.8174	6.70
2451666.8632	6.60
2451673.8306	7.10
2451674.8236	6.60
2451687.8063	6.40
2451700.7958	6.30
2451751.2590	6.50
2451755.2660	6.80
2451760.2576	6.40
2451762.2611	6.90
2451765.2569	6.90
2451770.2542	6.20
2451779.2299	5.90
2451784.2118	6.00
2451789.2306	6.20
2451794.2042	6.30
2451798.2201	6.20
2451810.2035	6.40
2451821.1306	6.20
2451822.1701	6.10
2451827.1785	6.20
2451834.1576	6.10
2451838.1417	6.10
2451840.1597	6.00
2451845.1326	6.20
2451851.1278	6.40
2451865.1458	5.90
2451870.1528	6.10
2451874.1132	6.20
2451883.1194	6.20
2451886.1389	6.40
2451891.1389	6.80
2451896.9458	7.20
2451901.0972	6.90
2451910.0139	6.30
2451912.9201	6.10
2451915.9146	6.00
2451925.9403	6.00
2451934.1069	6.50
2451935.9694	6.50
2451948.8792	5.90
2451954.9014	5.80
2451960.8751	5.90
2451965.9194	6.20
2452009.8236	6.30
2452017.8486	6.50
2452025.8389	6.50
2452043.8000	6.10
2452045.8049	6.20
2452052.8118	6.30
2452059.8001	6.50
2452068.7771	6.60
2452153.2313	6.10
2452161.2007	6.30
2452166.1986	6.50
2452173.2007	6.30
2452181.1854	5.80
2452194.1569	6.00
2452201.1542	6.70
2452205.1264	6.60
2452220.1021	6.30
2452239.1125	6.30
2452255.9993	6.30
2452279.9014	6.20
2452290.9451	6.30
2452297.9417	6.40
2452300.9250	6.60
2452335.8993	5.90
2452340.8931	6.30
2452342.8618	6.50
2452348.8792	6.70
2452356.8486	6.80
2452365.8924	6.40
2452367.8632	6.50
2452370.8340	6.10
2452378.8389	6.30
2452382.8194	6.40
2452393.8139	6.40
2452395.8097	6.30
2452402.8118	6.20
2452410.8229	6.00

continued on next page

Table B.26: *continued*

JD	V
2452424.7840	6.40
2452427.7868	6.50
2452435.7861	6.90

B.2.10 R Sct

Table B.27: MJUO R Sct photometry.

JD-2440000	*V*	*B-V*	*V-I*	*V-R*
11295.192	5.114	1.373	0.724	1.339
11303.171	4.964	1.284	0.710	1.297
11309.182	4.960	1.259	0.689	1.304
11316.139	4.973	1.290	0.700	1.295
11327.141	4.981	1.280	0.692	1.262
11334.178	5.172	1.317	0.712	1.308
11357.146	5.422	1.386	0.744	1.369
11368.147	5.513	1.471	0.761	1.462
11373.120	5.604	1.490	0.756	1.522
11398.073	5.505	1.363	0.734	1.495
11408.096	5.373	1.313	0.722	1.401
11413.883	5.248	1.269	0.685	1.341
11425.952	5.232	1.383	0.760	1.367
11448.922	5.462	1.322	0.704	1.427
11459.925	5.538	1.296	0.730	1.450
11630.183	4.982	1.307	0.724	1.309
11688.112	5.403	1.422	0.752	1.481
11721.077	4.934	1.224	0.698	1.220
11727.084	5.048	1.257	0.710	1.238
11731.088	5.132	1.283	0.711	1.298
11749.041	5.437	1.381	0.736	1.387
11770.069	5.534	1.428	0.734	1.446
11799.002	5.965	1.482	0.764	1.715
11851.877	4.962	1.310	0.712	1.293
11852.867	4.967	1.316	0.725	1.306
11992.228	5.277	1.485	0.745	1.422
12000.235	5.628	1.476	0.754	1.615
12013.171	6.649	1.228	0.697	2.080
12023.170	6.624	0.972	0.564	1.927
12042.186	5.267	1.311	0.694	1.445
12055.099	5.098	1.401	0.742	1.391
12066.166	5.185	1.355	0.756	1.353
12115.069	5.235	1.254	0.700	1.276
12129.983	5.181	1.433	0.749	1.411
12137.985	5.169	1.528	0.778	1.417
12143.973	5.290	1.563	0.817	1.508
12150.902	5.556	1.575	0.768	1.591
12154.878	5.761	1.568	0.770	1.661
12176.944	5.308	1.220	0.678	1.251
12180.934	5.194	1.218	0.671	1.256
12410.209	5.409	1.524	0.782	1.478

Table B.28: Albert Jones R Sct visual estimates.

JD	V
2451665.1701	6.30
2451681.2625	6.30
2451690.2292	6.00
2451704.2063	5.90
2451707.2188	5.40
2451718.1889	5.20
2451725.9681	5.80
2451731.9347	6.00
2451748.9715	6.30
2451754.9465	6.30
2451757.9313	6.30
2451761.8889	6.30
2451779.9507	6.30
2451788.8993	6.30
2451803.9007	6.40
2451807.9375	6.40
2451814.9264	6.40
2451821.8993	5.80
2451834.8965	5.50
2451837.8694	5.40
2451848.8694	5.40
2451958.1903	5.80
2451960.1847	5.40
2451972.1938	5.60
2451985.2056	6.00
2451988.1861	5.80
2451996.1813	6.20
2451999.1896	6.30
2452004.2118	6.30
2452022.2271	6.60
2452044.2299	5.50
2452053.2118	5.70

continued on next page

Table B.28: *continued*

JD	V
2452060.1896	6.20
2452063.2632	6.20
2452072.2146	5.60
2452080.2104	5.50
2452086.2035	5.50
2452093.2097	5.70
2452100.8924	5.80
2452112.8403	5.80
2452117.8813	5.80
2452129.8278	5.80
2452136.9111	6.20
2452146.9451	6.30
2452168.9014	6.40
2452173.9125	6.30
2452180.8757	6.20
2452200.9181	5.80
2452221.8611	6.30
2452330.1854	5.40
2452349.2028	6.30
2452356.1972	6.30
2452360.2264	6.10
2452371.2306	6.20
2452379.2132	6.00
2452399.2403	5.70
2452404.2035	5.80
2452409.2208	6.00
2452419.2396	6.30
2452427.9569	6.50
2452430.2104	6.40

B.2.11 TX Oph

Table B.29: MJUO TX Oph photometry.

JD-2440000	*V*	*B-V*	*V-I*	*V-R*
11339.095	10.293	0.993	0.577	1.123
11349.002	10.190	0.984	0.563	1.091
11356.126	10.098	0.929	0.555	1.060
11373.091	9.995	0.952	0.525	1.071
11383.959	10.084	1.011	0.562	1.112
11397.939	10.123	1.104	0.619	1.192
11407.978	10.205	1.122	0.601	1.185
11412.966	10.289	1.112	0.603	1.198
11417.948	10.392	1.080	0.607	1.168
11630.131	10.203	0.987	0.583	1.122
11691.133	10.347	0.974	0.555	1.057
11722.062	10.090	1.046	0.585	1.138
11729.986	10.267	1.132	0.621	1.204
11754.020	10.678	1.079	0.605	1.233
11770.889	9.953	0.986	0.558	1.102
11779.903	9.875	0.984	0.560	1.101
11792.904	10.005	0.960	0.581	1.122
11985.136	10.444	1.090	0.599	1.186
11992.108	10.323	1.086	0.602	1.175
12000.122	10.249	1.090	0.626	1.203
12006.212	10.252	1.091	0.609	1.223
12023.128	10.360	1.091	0.581	1.143
12042.138	9.881	0.907	0.461	0.962
12055.055	9.774	0.968	0.535	1.069
12063.074	9.907	1.038	0.567	1.126
12080.012	10.526	1.218	0.660	1.284
12114.980	10.044	1.022	0.591	1.164
12121.939	9.939	0.990	0.560	1.111
12143.899	9.916	0.946	0.549	1.062
12152.899	10.190	1.054	0.587	1.120
12163.908	10.407	1.042	0.615	1.129
12410.052	10.002	1.081	0.603	1.167

Table B.30: Albert Jones TX Oph visual estimates.

JD	V
2451689.9868	10.40
2451702.9736	10.10
2451704.9264	9.80
2451725.9021	10.10
2451729.9458	10.30
2451732.9229	10.40
2451748.9250	10.90
2451755.9028	10.80
2451761.8751	10.60
2451779.8938	10.00
2451792.8417	10.50
2451803.8375	9.90
2451813.8757	10.30
2451960.1736	10.00

continued on next page

Table B.30: *continued*

JD	V
2451975.1556	10.40
2451985.1882	10.50
2451994.2271	10.30
2451998.1292	10.30
2452004.1694	10.60
2452021.1951	10.50
2452044.9368	9.20
2452053.2021	9.90
2452061.1292	9.70
2452071.9181	10.40
2452079.9382	10.40
2452080.9458	10.60
2452086.9257	10.90
2452088.9424	10.90
2452100.8854	10.40
2452112.8306	9.90
2452115.8847	10.00
2452129.9417	9.70
2452136.9035	9.80
2452146.8736	10.10
2452163.8160	10.50
2452170.8451	10.40
2452312.1549	10.10
2452320.1597	10.00
2452330.1597	9.70
2452345.2021	9.90
2452356.1347	9.90
2452368.1875	10.10
2452373.2084	10.40
2452381.1826	10.10
2452399.2132	10.10
2452407.9729	10.00
2452427.9382	10.80
2452436.9049	10.50

B.2.12 IW Car

Table B.31: MJUO IW Car photometry.

JD-2440000	*V*	*B-V*	*V-I*	*V-R*
11276.972	8.092	0.899	0.536	1.191
11294.928	7.963	0.812	0.508	1.129
11301.930	7.913	0.811	0.494	1.097
11305.999	7.875	0.806	0.486	1.089
11308.897	7.850	0.813	0.486	1.086
11315.927	7.845	0.823	0.495	1.111
11326.990	7.931	0.867	0.504	1.127
11333.892	8.064	0.909	0.528	1.166
11339.839	8.143	0.933	0.548	1.182
11347.923	8.111	0.942	0.564	1.219
11364.873	7.818	0.809	0.495	1.093
11367.961	7.814	0.787	0.492	1.078
11372.890	7.809	0.790	0.470	1.051
11383.836	7.843	0.807	0.486	1.084
11394.838	7.935	0.875	0.515	1.124
11398.821	7.944	0.849	0.502	1.121
11408.867	8.018	0.907	0.521	1.143
11411.830	8.056	0.907	0.528	1.157
11496.139	8.021	0.884	0.510	1.136
11505.105	7.929	0.835	0.488	1.085
11557.102	8.142	0.944	0.545	1.167
11575.101	7.931	0.836	0.495	1.105
11593.057	7.879	0.796	0.484	1.071
11600.998	7.902	0.815	0.478	1.086
11611.065	7.952	0.833	0.498	1.123
11619.991	8.072	0.853	0.512	1.131
11661.939	8.092	0.802	0.490	1.094
11667.934	8.099	0.797	0.488	1.102
11672.928	8.174	0.835	0.502	1.127
11685.895	8.358	0.915	0.536	1.200
11720.860	8.379	0.903	0.538	1.203
11729.868	8.207	0.837	0.516	1.144
11741.844	8.154	0.808	0.514	1.131
11753.865	8.331	0.884	0.536	1.190
11780.889	8.396	0.919	0.565	1.231
11850.937	8.546	1.003	0.591	1.268
11853.037	8.538	1.000	0.588	1.288
11921.060	8.797	0.972	0.601	1.325
11928.094	8.819	0.968	0.594	1.302
11939.100	8.772	0.939	0.581	1.288
11960.998	8.695	0.934	0.571	1.276
11978.010	8.927	1.008	0.607	1.344
11984.026	8.939	1.022	0.609	1.349
11988.068	8.923	1.014	0.606	1.348
11991.970	8.887	1.002	0.611	1.333
11999.069	8.822	0.980	0.599	1.324
12006.019	8.810	0.960	0.605	1.327
12011.926	8.770	0.972	0.596	1.332
12012.985	8.769	0.950	0.603	1.304

continued on next page

Table B.31: *continued*

JD-2440000	*V*	*B-V*	*V-I*	*V-R*
12022.991	8.697	0.948	0.575	1.278
12042.005	8.780	0.954	0.617	1.330
12052.908	8.939	1.030	0.608	1.356
12055.973	8.982	1.030	0.625	1.377
12059.880	9.023	1.039	0.633	1.397
12062.933	9.029	1.043	0.644	1.392
12067.864	8.993	1.050	0.633	1.376
12079.881	8.839	0.976	0.601	1.338
12114.877	8.918	0.957	0.623	1.380
12121.846	8.979	0.986	0.631	1.381
12133.842	9.135	1.027	0.640	1.405
12137.878	9.140	1.039	0.635	1.407
12143.854	9.084	1.035	0.643	1.401
12153.824	8.979	0.948	0.627	1.381
12171.128	8.873	0.949	0.597	1.319
12177.156	8.970	0.955	0.609	1.346
12218.996	9.135	0.995	0.639	1.400
12258.051	9.091	0.994	0.636	1.409
12312.948	8.867	0.937	0.585	1.328
12322.057	8.940	0.962	0.623	1.381
12339.063	9.111	1.023	0.656	1.442
12410.958	8.994	1.050	0.683	1.441

Table B.32: Albert Jones IW Car visual estimates.

JD	V
2451661.9632	7.90
2451669.9021	8.10
2451688.8313	8.10
2451700.8167	8.30
2451708.8403	8.40
2451718.8743	8.60
2451725.8340	8.40
2451730.8229	8.30
2451748.7986	8.30
2451754.8743	8.10
2451760.8681	8.30
2451764.7972	8.30
2451779.2501	8.40
2451791.2389	8.40
2451804.2292	8.60
2451814.2028	8.80
2451820.1215	8.30
2451827.1938	8.60
2451840.1438	8.80
2451855.0972	8.80
2451865.1583	8.60
2451876.9611	8.60
2451882.9444	8.60
2451888.1083	8.70
2451899.9000	8.60
2451904.9701	8.80
2451913.9569	8.80
2451920.9090	8.90
2451941.9549	8.80
2451949.9139	8.60
2451961.1438	8.40
2451973.8771	8.60
2451984.9188	8.60
2451992.9479	8.60
2451992.9493	8.60
2452002.9201	8.60
2452017.9396	8.40
2452025.9236	8.60
2452044.8799	8.60
2452052.8611	9.20
2452057.8715	8.80
2452070.8243	8.90
2452081.8049	8.60
2452089.9042	8.60
2452100.8188	8.60
2452112.8194	8.60
2452115.8028	8.40
2452129.8063	8.60
2452135.2229	8.90
2452140.2535	8.90
2452150.2438	9.10
2452161.1667	8.90
2452169.1924	8.90
2452181.1479	9.20
2452194.1972	9.20
2452201.1688	9.60
2452220.1604	9.30
2452257.9028	9.20
2452279.8993	9.30
2452291.1271	8.90
2452295.1389	8.90
2452301.1708	8.80
2452308.9389	8.80
2452321.1097	8.80

continued on next page

Table B.32: *continued*

JD	V
2452327.1458	8.90
2452338.1243	8.90
2452345.8639	8.60
2452352.8743	8.80
2452359.1278	8.80
2452366.9528	8.60
2452372.8222	8.80
2452380.9090	8.60
2452393.8785	8.80
2452400.8361	8.80
2452407.9361	8.80
2452424.9042	8.60
2452427.8806	8.70
2452436.8299	8.60
2452446.8701	8.60

Appendix C

Fourier fitting data from photometry

Definitions are as follows:

p = period between sucessive deep minima in days. The periods listed for BRI will be the fitted periods (if fitted) however subsequent phasing is done using the V period value.

ϕ_0 = zero point phase offset for phasing with 0 = faintest magnitude.

ϕ_{max} = raw phase of maximum brightness - needs $\phi_o(V)$ subtracted for absolute phase of maximum brightness.

fit = rms(fit - observed magnitude).

C.1 W Virginis stars

C.1.1 VY Pyx

Table C.1: Historical phasing and fourier parameters for VY Pyx.

	V_1	V_2	V_3	V_4
p	1.2399380	1.239963272 [1]	1.239948 [2]	1.2400 [3]
ϕ_0	0.575	0.3850	0.4990	0.1100
ϕ_{max}	0.962	0.7730	0.8860	0.5030
c_0	7.2652	7.2653	7.2653	7.2655
c_1	-0.1182	-0.0613	-0.1147	0.1137
c_2	-0.0218	0.1038	0.0364	0.0412
c_3	-0.0007455	0.0153	0.0177	-0.0097
c_4	0.0221	-0.0157	0.0131	0.0193
c_5	-0.0013	0.00053733	0.00057653	0.00057446
c_6	0.00067747	-0.0011	0.0013	-0.00034175
c_7	-0.027702	-0.0016	0.0018	-0.0029
c_8	0.0018	-0.0012	0.000057953	-0.0016
c_9	0.00053081	-0.00013349	0.0015	0.0010
c_{10}	0.0030	0.0026	-0.0025	-0.00078655
RMS fit	0.0065	0.0067	0.0065	0.0081

Table C.2: *BVRI* phasing and fourier parameters for VY Pyx.

	B	*V*	*R*	*I*
p	1.2399010	1.2399380	1.2399830	1.2400300
ϕ_0	0.5720	0.575	0.5820	0.5960
ϕ_{max}	0.9520	0.9620	0.9660	0.9810
c_0	7.8396	7.2652	6.9196	6.6106
c_1	-0.1711	-0.1182	-0.0965	-0.0727
c_2	-0.0121	-0.0218	-0.0268	-0.0356
c_3	-0.0049	-0.0007455	0.000051524	-0.00061776
c_4	0.0296	0.0221	0.0181	0.0125
c_5	-0.0017	-0.0013	-0.0045	-0.0015
c_6	0.00097207	0.00067747	-0.0013	-0.00032841
c_7	-0.00064930	-0.027702	0.00024469	0.000088769
c_8	0.0054	0.0018	0.0028	0.0020
c_9	0.0028	0.00053081	0.0011	0.0022
c_{10}	0.0053	0.0030	0.0052	0.0022
RMS fit	0.0109	0.0065	0.0084	0.0066

[1] least squares fourier fitting
[2] Hipparcos 1997
[3] Sarnwal and Sarma (1991)

C.1.2 SW Tau

Table C.3: Historical phasing and fourier parameters for SW Tau.

	V_1	V_2	V_3	V_4	V_5	V_6
p	1.5836	1.58361754 [4]	1.58368 [5]	1.583584 [6]	1.583584 [7]	1.583560 [8]
ϕ_0	0.1600	0.0830	0.7900	0.2410	0.4370	0.4820
ϕ_{max}	0.6540	0.5790	0.1320	0.7330	0.7860	0.8330
c_0	9.7832	9.7848	9.7874	9.7813	9.7388	9.7536
c_1	0.2221	0.3318	0.0649	0.0535	-0.0920	-0.1879
c_2	0.2915	0.1574	-0.3611	0.3617	0.3447	0.3102
c_3	-0.1060	-0.0933	0.0516	-0.0236	0.0730	0.1124
c_4	-0.0389	0.0640	-0.1010	-0.1103	-0.0830	-0.0325
c_5	0.0127	-0.0099	0.0089	0.0144	-0.0116	-0.0181
c_6	-0.0128	-0.0155	-0.0202	0.0107	0.0222	0.0039
c_7	-0.0347	0.0472	0.0455	-0.0195	0.0337	0.0368
c_8	0.0370	0.0224	-0.0285	-0.0452	-0.0237	0.0233
c_9	0.0075	-0.0347	0.0381	0.0180	-0.0291	-0.0095
c_{10}	-0.0411	0.0250	-0.0137	0.0365	0.0094	-0.0286
RMS fit	0.0228	0.0251	0.0374	0.0210	0.0177	0.0281

Table C.4: *BVRI* phasing and fourier parameters for SW Tau.

	B	V	R	I
p	1.583560	1.583560	1.583560	1.583560
ϕ_0	0.3540	0.4820	0.3620	0.4760
ϕ_{max}	0.6880	0.8330	0.8400	0.8560
c_0	10.4155	9.7536	9.3596	9.1124
c_1	-0.2372	-0.1879	-0.1651	-0.1472
c_2	0.4586	0.3102	0.2304	0.1645
c_3	0.1384	0.1124	0.0825	0.0572
c_4	-0.0596	-0.0325	-0.0316	-0.0221
c_5	-0.0335	-0.0181	-0.0107	-0.0063
c_6	0.0167	0.0039	0.0064	0.0106
c_7	0.0461	0.0368	0.0235	0.0284
c_8	0.0469	0.0233	0.0193	0.0097
c_9	-0.0011	-0.0095	-0.0056	0.000064325
c_{10}	-0.0499	-0.0286	-0.0289	-0.0200
RMS fit	0.0269	0.0281	0.0144	0.0178

C.1.3 V381 Cen

Table C.5: Hisorical phasing and fourier parameters for V381 Cen.

	V_1	V_2	V_3	V_4	V_5
p	5.0848	5.0805 [9]	5.0787 [10]	5.07878 [11]	5.0816 [12]
ϕ_0	0.1580	0.0960	0.9670	0.9300	0.6090
ϕ_{max}	0.5720	0.4440	0.2470	0.2130	0.9930
c_0	7.7006	7.6925	6.7783	7.6859	7.6969
c_1	0.1892	0.2930	0.1244	0.1028	-0.2712
c_2	0.2232	0.0468	-0.1335	-0.2805	-0.1137
c_3	-0.0838	-0.0618	0.0620	0.0892	-0.0890
c_4	-0.0603	0.0792	-0.0012	-0.0550	0.0391
c_5	0.0186	-0.0087	0.0199	0.0387	-0.0120
c_6	0.0336	-0.0263	0.0171	0.0044	0.0188
c_7	-0.0145	0.0084	-0.0051	0.0094	-0.0044
c_8	-0.0095	0.0081	0.0088	0.0097	0.0133
c_9	-0.0073	0.00086829	-0.0029	0.0022	0.0089
c_{10}	-0.0040	0.0084	0.00099075	0.0041	-0.0098
RMS fit	0.0382	0.0110	0.0044	0.0042	0.0168

[4] least squares fourier fitting to MJUO dataset.

[5] period from Hipparcos 1997, MJUO dataset.

[6] period from Moffett and Barnes (1984), MJUO dataset.

[7] period from Moffett and Barnes (1984) used on Moffett and Barnes (1984) dataset

[8] period from stepping through MJUO and Moffett and Barnes (1984) data, as applied to the MJUO data set

[9] least squares fourier fitting

[10] Hipparcos 1997

[11] Schaltenbrand and Tammann (1971)

[12] Opotaki (1984)

Table C.6: *BVRI* phasing and fourier parameters for V381 Cen.

	B	*V*	*R*	*I*
p	5.0848	5.07878	5.0838	5.0836
ϕ_0	0.9120	0.9300	0.9280	0.9420
ϕ_{max}	0.2100	0.2130	0.2140	0.2190
c_0	8.5249	7.6859	7.2171	6.7785
c_1	0.1202	0.1028	0.0961	0.0919
c_2	-0.4324	-0.2805	-0.2161	-0.1576
c_3	0.1275	0.0892	0.0689	0.0554
c_4	-0.0836	-0.0550	-0.0402	-0.0276
c_5	0.0545	0.0387	0.0318	0.0258
c_6	0.00039329	0.0044	0.0032	0.0011
c_7	0.0109	0.0094	0.006	0.0034
c_8	0.0109	0.0097	0.0105	0.0095
c_9	0.0019	0.0022	-0.00097958	-0.00041928
c_{10}	0.0050	0.0041	0.0035	0.0031
RMS fit	0.0047	0.0042	0.0072	0.0084

C.1.4 TX Del

Table C.7: Hisorical phasing and fourier parameters for TX Del.

	V_1	V_2	V_4	V_5	V_6	V_7	V_8	V_9
p	6.1634	6.1628 [13]	6.1657 [14]	6.1660 [15]	6.165907 [16]	6.165981 [17]	6.165981 [18]	6.165806 [19]
ϕ_0	0.4290	0.6220	0.7310	0.6400	0.6680	0.6460	0.5780	0.5960
ϕ_{max}	0.7870	0.9840	0.0790	0.9870	0.0150	0.9930	0.9790	0.0020
c_0	9.2255	9.2226	9.2272	9.2267	9.2268	9.2267	9.1669	9.1672
c_1	-0.1762	-0.2848	-0.1891	-0.2840	-0.2637	-0.2806	-0.2956	-0.2900
c_2	0.2398	-0.0842	-0.2281	-0.0856	-0.1353	-0.0960	-0.0202	-0.0594
c_3	0.0484	-0.0088	-0.0641	-0.0271	-0.0461	-0.0314	-0.00040300	-0.0187
c_4	-0.0348	0.0583	-0.0020	0.0590	0.0454	0.0568	0.0695	0.0678
c_5	-0.0262	0.0178	-0.0173	0.0255	0.0150	0.0239	0.0186	0.0179
c_6	-0.0072	0.0178	0.0209	0.0116	0.0232	0.0144	-0.0030	0.0057
c_7	0.0031	-0.0100	0.0129	-0.0159	-0.0076	-0.0147	-0.0057	-0.0010
c_8	-0.0080	-0.0060	-0.0063	-0.0060	-0.0142	-0.0082	-0.0087	-0.0102
c_9	-0.0059	-0.0070	0.0103	-0.0127	-0.0103	-0.0132	-0.0092	-0.0039
c_{10}	-0.0046	-0.0025	-0.0047	0.0039	-0.0075	0.0015	-0.0049	-0.0113
RMS fit	0.0090	0.0101	0.0200	0.0220	0.0214	0.0219	0.0109	0.0112

Table C.8: *BVRI* phasing and fourier parameters for TX Del.

	B	*V*	*R*	*I*
p	6.1614	6.1634	6.1637	6.1640
ϕ_0	0.3930	0.4290	0.4230	0.4320
ϕ_{max}	0.7960	0.7870	0.8050	0.7910
c_0	9.9857	9.2255	8.8099	8.4606
c_1	-0.2525	-0.1762	-0.1491	-0.1098
c_2	0.4183	0.2398	0.1648	0.1083
c_3	0.0663	0.0484	0.0313	0.0177
c_4	-0.0576	-0.0348	-0.0314	-0.0252
c_5	-0.0282	-0.0262	-0.0273	-0.0165
c_6	-0.00021191	-0.0072	-0.0092	-0.0002009
c_7	0.0006067	0.0031	-0.00059574	-0.00039333
c_8	-0.0169	-0.0080	-0.0106	-0.0090
c_9	-0.0056	-0.0059	-0.0043	-0.0019
c_{10}	-0.0135	-0.0046	-0.0136	0.0003566
RMS fit	0.0109	0.0090	0.0099	0.0118

[13] least squares fourier fitting
[14] Hipparcos 1997
[15] Harris (1980)
[16] Szabados (1980)
[17] Moffett and Barnes (1985)
[18] Moffett and Barnes (1985) using Moffett and Barnes (1984) data
[19] Moffett and Barnes (1984) using Moffett and Barnes (1984) data

C.1.5 κ Pav

Table C.9: historical phasing and fourier parameters for κ Pav.

	V_1	V_2	V_3	V_4	V_5
p	9.0720	9.0726 [20]	9.0741 [21]	9.0694 [22]	9.0944 [23]
ϕ_0	0.2690	0.1850	0.9750	0.6450	0.0020
ϕ_{max}	0.7230	0.6340	0.4140	0.1250	0.5720
c_0	4.3861	4.3869	4.3889	4.3826	4.4176
c_1	-0.0226	0.1756	0.3810	-0.2574	0.2810
c_2	0.3907	0.3495	-0.0839	-0.2937	0.1378
c_3	0.0419	-0.0104	-0.0169	-0.0334	-0.0199
c_4	-0.0360	-0.0548	0.0541	-0.0395	0.0099
c_5	-0.0241	-0.0065	-0.0159	-0.0083	0.0269
c_6	-0.0066	0.0250	-0.0227	-0.0187	0.0093
c_7	0.0177	-0.0094	0.0101	-0.0128	0.0301
c_8	-0.0010	-0.0160	-0.0174	0.0067	-0.0179
c_9	-0.0117	0.0105	0.0107	-0.0083	0.0128
c_{10}	0.0018	0.0045	0.0021	0.0116	-0.0201
RMS fit	0.0246	0.0226	0.0214	0.0386	0.1479

Table C.10: *BVRI* phasing and fourier parameters for κ Pav.

	B	*V*	*R*	*I*
p	9.0747	9.0741	9.0700	9.0685
ϕ_0	0.9510	0.9750	0.9900	0.00
ϕ_{max}	0.3910	0.4140	0.4390	0.4700
c_0	5.1185	4.3889	4.0275	3.6834
c_1	0.5189	0.3810	0.3050	0.2536
c_2	-0.2208	-0.0839	-0.0167	0.0290
c_3	-0.0167	-0.0169	-0.0184	-0.0212
c_4	0.0599	0.0541	0.0458	0.0364
c_5	-0.0225	-0.0159	-0.0124	-0.0108
c_6	-0.0287	-0.0227	-0.0187	-0.0172
c_7	0.0116	0.0101	0.0104	0.0088
c_8	-0.0239	-0.0174	-0.0143	-0.0119
c_9	0.0138	0.0107	0.0085	0.0069
c_{10}	0.0039	0.0021	0.00099711	-0.00073611
RMS fit	0.0280	0.0214	0.0194	0.0182

C.1.6 AL Vir

Table C.11: Historical phasing and fourier parameters for AL Vir.

	V_1	V_2	V_3	V_4	V_5	V_6
p	10.3048	10.2950 [24]	10.3113 [25]	10.30 [26]	10.299971 [27]	10.302323 [28]
ϕ_0	0.2920	0.4980	0.5910	0.8250	0.8280	0.5670
ϕ_{max}	0.7640	0.8280	0.0310	0.2880	0.2910	0.0360
c_0	9.6230	9.6330	9.6160	9.6282	9.6282	9.6256
c_1	-0.0083	-0.2311	-0.3331	0.0941	0.1011	-0.3478
c_2	0.3496	0.2872	-0.0589	-0.3474	-0.3455	-0.0703
c_3	0.0543	0.0846	-0.0609	0.0855	0.0868	-0.0766
c_4	-0.0639	0.0486	0.0417	-0.0326	-0.0291	0.0424
c_5	-0.0085	-0.0028	0.0073	0.0174	0.0171	-0.0013
c_6	0.0046	-0.0259	-0.00052385	0.0047	0.0058	0.0137
c_7	0.0088	0.0038	0.0098	0.0216	0.0220	0.0205
c_8	-0.0215	0.0224	-0.0111	-0.0060	-0.0042	-0.0107
c_9	-0.0236	0.0095	0.0074	0.0152	0.0137	0.0119
c_{10}	0.0060	-0.0036	-0.0097	0.0136	0.0150	-0.0208
RMS fit	0.0642	0.0348	0.0895	0.0467	0.0466	0.0547

[20] least squares fourier fit
[21] Schaltenbrand and Tammann (1971)
[22] Shobbrook (1992)
[23] Hipparcos 1997
[24] least squares fourier fit
[25] Hipparcos 1997
[26] Joy (1937)
[27] Schaltenbrand and Tammann (1971)
[28] Moffett and Barnes (1984)

Table C.12: *BVRI* phasing and fourier parameters for AL Vir.

	B	*V*	*R*	*I*
p	10.2950	10.2950	10.2949	10.2940
ϕ_0	0.3210	0.4980	0.5160	0.5150
ϕ_{max}	0.7850	0.8280	0.8580	0.8770
c_0	10.2484	9.6330	9.1043	8.7372
c_1	-0.2627	-0.2311	-0.2135	-0.1949
c_2	0.4820	0.2872	0.1943	0.1192
c_3	0.1086	0.0846	0.0646	0.0457
c_4	0.0549	0.0486	0.0448	0.0384
c_5	-0.0043	-0.0028	-0.0039	0.0061
c_6	-0.0348	-0.0259	-0.0211	-0.0151
c_7	0.0107	0.0038	0.00026455	0.00080055
c_8	0.0366	0.0224	0.0203	0.0097
c_9	0.0134	0.0095	0.0086	0.0085
c_{10}	-0.0017	-0.0036	-0.00043962	0.0053
RMS fit	0.0453	0.0348	0.0326	0.0330

C.1.7 W Vir

Table C.13: Historical phasing and fourier parameters for W Vir.

	V_1	V_2	V_3	V_4	V_5	V_6	V_7
p	17.2666	17.2787 [29]	17.267 [30]	17.27 [31]	17.2768 [32]	17.273 [33]	17.242 [34]
ϕ_0	0.5000	0.0170	0.4830	0.3640	0.0940	0.2460	0.4700
ϕ_{max}	0.8550	0.3730	0.8370	0.7190	0.4500	0.6010	0.8310
c_0	10.0912	10.0913	10.0911	10.0907	10.0909	10.0906	10.0978
c_1	-0.6077	0.6038	-0.6070	-0.4181	0.4907	-0.0108	-0.5736
c_2	-0.0232	0.0979	0.0427	0.4444	0.3653	0.6111	0.0596
c_3	0.1250	0.0999	0.1366	0.0511	-0.0194	-0.1247	0.1277
c_4	0.0681	0.0930	0.0397	-0.1317	0.1364	-0.0634	0.0132
c_5	0.0420	-0.0336	0.0427	-0.0301	0.0254	-0.0103	0.0306
c_6	0.0081	-0.0314	-0.0055	-0.0325	-0.0381	0.0441	0.0029
c_7	0.0133	0.0552	-0.0106	-0.0029	0.0187	0.0187	-0.0300
c_8	-0.0553	-0.0388	-0.0562	0.0595	0.0631	-0.0594	-0.0447
c_9	-0.0164	0.0124	-0.0235	0.0258	-0.0306	-0.0180	-0.0244
c_{10}	-0.0175	0.0354	-0.0066	-0.0096	-0.0176	0.0251	-0.00086332
RMS fit	0.0494	0.0379	0.0485	0.0429	0.0372	0.0392	0.1214

Table C.14: *BVRI* phasing and fourier parameters for W Vir.

	B	*V*	*R*	*I*
p	17.2767	17.2768	17.2795	17.2750
ϕ_0	0.0810	0.0940	0.1040	0.1090
ϕ_{max}	0.4380	0.4500	0.6490	0.6530
c_0	10.8292	10.0909	9.6576	9.2381
c_1	0.7123	0.4907	0.3884	0.2920
c_2	0.3234	0.3653	0.3715	0.3674
c_3	0.0087	-0.0194	-0.0252	-0.0222
c_4	0.1968	0.1364	0.0997	0.0640
c_5	0.0299	0.0254	0.0204	0.0264
c_6	-0.0533	-0.0381	-0.0278	-0.0112
c_7	0.0273	0.0187	0.0161	0.0011
c_8	0.0856	0.0631	0.0485	0.0510
c_9	-0.0482	-0.0306	-0.0209	-0.0258
c_{10}	-0.0204	-0.0176	-0.0164	-0.0229
RMS fit	0.0538	0.0372	0.0287	0.0500

[29] least squares fourier fitting
[30] Hipparcos 1997
[31] Joy (1937)
[32] Schaltenbrand and Tammann (1971)
[33] Meakes et al. (1991)
[34] Fernie and Ehlers (1999)

C.1.8 ST Pup

Table C.15: Historical phasing and fourier parameters for ST Pup.

	V_1	V_2	V_3	V_4	V_5	V_6
p	18.6359	18.6204 [35]	18.559[36]	17.4 [37]	18.462 [38]	
ϕ_0	0.0730	0.5940	0.2090	0.5240	0.9310	
ϕ_{max}	0.3030	0.8390	0.3560	0.0120	0.4040	
c_0	10.1416	10.1491	10.1955	10.2366	10.2113	
c_1	0.4517	-0.4631	0.1618	-0.0819	0.2672	
c_2	-0.0923	0.0053	0.0711	0.0131	-0.0092	
c_3	0.1562	0.1033	-0.0189	0.0136	0.0653	
c_4	0.1073	0.1417	0.1403	-0.0057	0.0704	
c_5	-0.0434	0.0761	-0.0621	-0.0286	0.0518	
c_6	0.0772	-0.0319	-0.0792	-0.0463	-0.0374	
c_7	-0.0557	-0.0246	-0.0523	-0.0288	0.0187	
c_8	-0.0377	-0.0606	0.0080	0.0248	-0.0266	
c_9	0.0170	-0.0032	0.0488	-0.1012	-0.1322	
c_{10}	-0.0111	-0.0201	0.1176	-0.0427	-0.0120	
RMS fit	0.0771	0.0723	0.1454	0.03395	0.2664	

Table C.16: *BVRI* phasing and fourier parameters for ST Pup.

	B	*V*	*R*	*I*
p	18.6207	18.6204	18.6220	18.6252
ϕ_0	0.5800	0.5940	0.5990	0.6430
ϕ_{max}	0.8310	0.8390	0.8450	0.8370
c_0	10.8622	10.1491	9.7255	9.3042
c_1	-0.6145	-0.4631	-0.3919	-0.3087
c_2	0.1479	0.0053	-0.0494	-0.0757
c_3	0.1788	0.1033	0.0773	0.0483
c_4	0.1849	0.1417	0.1237	0.1009
c_5	0.1055	0.0761	0.0599	0.0566
c_6	-0.0342	-0.0319	-0.0232	0.0082
c_7	-0.0427	-0.0246	-0.0183	-0.0317
c_8	-0.0741	-0.0606	-0.0491	-0.0582
c_9	-0.0052	-0.0032	-0.0039	-0.0165
c_{10}	-0.0141	-0.0201	-0.0196	0.0028
RMS fit	0.1024	0.0723	0.0605	0.0892

C.2 RV Tauri stars

C.2.1 SX Cen

Table C.17: Phasing and Fourier parameters for SX Cen with long-term spline curve removed. To obtain modelled long-term maximum value, add offset of 9.0418.

	B	*V*	*R*	*I*
p	32.82188	32.82188	32.82188	32.82188
ϕ_0	0.5460	0.0710	0.0710	0.0710
ϕ_{max}	0.2530	0.7700	0.7760	0.9070
c_0	1.1460	0.3381	-0.1356	-0.5895
c_1	-0.0027	0.0026	0.0016	0.0061
c_2	0.0217	0.0260	0.0284	0.0321
c_3	0.3789	0.2033	0.1281	0.0619
c_4	0.1282	0.1730	0.1994	0.2180
c_5	-0.0038	0.0018	0.0085	0.0156
c_6	0.0161	0.0110	0.0086	0.0093
c_7	-0.0543	-0.0351	-0.0260	-0.0200
c_8	0.0443	0.0418	0.0410	0.0485
c_9	-0.0060	0.0045	0.0120	0.0220
c_{10}	-0.0278	0.0048	0.0244	0.0389
RMS fit	0.1480	0.0914	0.1024	0.1383

[35] least squares fourier fitting
[36] Schaltenbrand and Tammann (1971)
[37] Harris (1980)
[38] Kilkenny et al. (1993)

C.2.2 TT Oph

Table C.18: Phasing and fourier parameters for TT Oph.

	B	V	R	I
p	60.9682	60.9682	60.9682	60.9682
ϕ_0	0.5270	0.5450	0.5520	0.5630
ϕ_{max}	0.7430	0.2590	0.7790	0.7880
c_0	11.0575	10.0042	9.4467	9.0143
c_1	-0.0921	-0.0794	-0.0745	-0.0548
c_2	-0.0166	-0.0111	-0.0059	0.0045
c_3	0.5777	0.4222	0.3489	0.2984
c_4	0.0726	0.1894	0.2300	0.2675
c_5	-0.0512	-0.0385	-0.0337	-0.0274
c_6	-0.0187	-0.0129	-0.0138	-0.0022
c_7	-0.0398	-0.0512	-0.0539	-0.0581
c_8	0.0754	0.0494	0.0366	0.0288
c_9	-0.0140	-0.0141	-0.0193	-0.0136
c_{10}	3.2779e-04	-0.0096	-0.0130	-0.0100
RMS fit	0.1265	0.0963	0.0835	0.0737

C.2.3 RU Cen

Table C.19: Phasing and fourier parameters for RU Cen.

	B	V	R	I
p	64.566	64.566	64.566	64.566
ϕ_0	0.3660	0.9360	0.9420	0.94701
ϕ_{max}	0.0940	0.2020	0.1990	0.2020
c_0	9.7915	9.0293	8.5918	8.0766
c_1	0.0606	0.0370	0.0305	0.0201
c_2	-0.0182	-0.0118	-0.0145	-0.0112
c_3	0.0785	0.1783	0.2095	0.2330
c_4	-0.5302	-0.3780	-0.3135	-0.2777
c_5	0.1508	0.1081	0.0849	0.0751
c_6	-0.0479	-0.0376	-0.0323	-0.0197
c_7	-0.1279	-0.0657	-0.0352	-0.0220
c_8	-0.0450	-0.0266	-0.0233	-0.0069
c_9	0.0236	0.0208	0.0180	0.0141
c_{10}	-0.1112	-0.0757	-0.0571	-0.0517
RMS fit	0.1286	0.0936	0.0803	0.0701

C.2.4 CT Ori

Table C.20: Phasing and fourier parameters for CT Ori.

	B	V	R	I
p	67.41728	67.41728	67.41728	67.41728
ϕ_0	0.6390	0.6470	0.6520	0.6530
ϕ_{max}	0.8140	0.8190	0.8280	0.8430
c_0	11.6395	10.6637	10.0659	9.4477
c_1	-0.2183	-0.1297	-0.0979	-0.0812
c_2	-0.1085	-0.0679	-0.0478	-0.0445
c_3	0.0827	0.0070	-0.0246	-0.0421
c_4	0.2553	0.2079	0.1875	0.1792
c_5	0.1348	0.0877	0.0581	0.0354
c_6	-0.0235	-0.0102	0.0043	0.0020
c_7	-0.1153	-0.0729	-0.0598	-0.0446
c_8	-0.0568	-0.0416	-0.0406	-0.0391
c_9	-0.0315	-0.0274	-0.0208	-0.0104
c_{10}	0.0059	0.0114	0.0091	0.0097
RMS fit	0.0789	0.0522	0.0437	0.0402

C.2.5 AI Sco

Table C.21: Phasing and fourier parameters for AI Sco with long-term spline curve removed. To obtain modelled long-term maximum value, add offset of 8.8017.

	B	V	R	I
p	71.45	71.45	71.45	71.45
ϕ_0	0.6060	0.6360	0.6460	0.6490
ϕ_{max}	0.3160	0.3500	0.3580	0.3650
c_0	1.7893	0.4364	-0.2819	-0.8924
c_1	0.0351	0.0188	0.0147	0.0123
c_2	-0.0068	-0.0102	-0.0199	-0.0319
c_3	0.2055	0.0484	-0.0035	-0.0385
c_4	0.4578	0.4138	0.3987	0.3681

continued on next page

Table C.21: *continued*

	B	V	R	I
c_5	0.0116	0.0313	0.0494	0.0554
c_6	-0.0091	-0.0061	-0.0064	-0.0171
c_7	-0.0749	-0.0648	-0.0572	-0.0422
c_8	-0.0038	-0.0338	-0.0465	-0.0483
c_9	0.0299	-0.0082	-0.0128	-0.0091
c_{10}	0.0034	0.0294	0.0467	0.0476
RMS fit	0.2749	0.1916	0.1785	0.1777

C.2.6 AR Pup

Table C.22: Phasing and fourier parameters for AR Pup with long-term spline curve removed. To obtain modelled long-term maximum value, add offset of 9.0812.

	B	V	R	I
p	76.47	76.47	76.47	76.47
ϕ_0	0.7920	0.8070	0.8150	0.3450
ϕ_{max}	0.0220	0.6170	0.6220	0.6280
c_0	0.9574	0.1795	-0.2669	-0.7591
c_1	0.0132	0.0105	0.0085	0.0139
c_2	-0.0530	-0.0338	-0.0237	-0.0241
c_3	-0.1759	-0.0878	-0.0562	-0.0278
c_4	-0.1311	-0.1422	-0.1440	-0.1533
c_5	-0.0142	-0.0013	0.0043	0.0114
c_6	0.0184	0.0089	0.0129	0.0008605
c_7	-0.0048	-0.0039	-0.0011	-0.0022
c_8	0.0432	0.0314	0.0266	0.0173
c_9	-0.0242	-0.0139	-0.0037	-0.0057
c_{10}	-0.0231	-0.0252	-0.0174	-0.0225
RMS fit	0.1054	0.0775	0.0664	0.0616

C.2.7 AR Sgr

Table C.23: Phasing and fourier parameters for AR Sgr.

	B	V	R	I
p	87.1282	87.1282	87.1282	87.1282
ϕ_0	0.9510	0.9570	0.9610	0.9680
ϕ_{max}	0.6420	0.6560	0.6650	0.6730
c_0	10.4443	9.5254	8.9962	8.5427
c_1	0.0903	0.0597	0.0476	0.0242
c_2	-0.0774	-0.0366	-0.0192	-0.0035
c_3	0.3100	0.3031	0.2980	0.2978
c_4	-0.3395	-0.1931	-0.1319	-0.0809
c_5	0.0236	0.0034	-0.0082	-0.0246
c_6	-0.0618	-0.0617	-0.0540	-0.0354
c_7	0.1071	0.0990	0.0868	0.0758
c_8	-0.1428	-0.0710	-0.0429	-0.0154
c_9	0.0184	0.0049	0.0053	0.0049
c_{10}	-0.0986	-0.0765	-0.0641	-0.0566
RMS fit	0.2789	0.1959	0.1645	0.1413

C.2.8 UZ Oph

Table C.24: Phasing and fourier parameters for UZ Oph.

	B	V	R	I
p	88.9027	88.9027	88.9027	88.9027
ϕ_0	0.8420	0.8550	0.8580	0.8690
ϕ_{max}	0.0720	0.0760	0.1460	0.1220
c_0	11.9140	10.7919	10.1762	9.5897
c_1	0.1060	0.1100	0.1115	0.0610
c_2	-0.3158	-0.2355	-0.2169	-0.1256
c_3	-0.3234	-0.1682	-0.1130	-0.0278
c_4	-0.5337	-0.5032	-0.4742	-0.3781
c_5	-0.0360	-0.0652	-0.0807	-0.0215
c_6	-0.0944	-0.0645	-0.0560	-0.0441
c_7	-0.1424	-0.1337	-0.1293	-0.0663
c_8	0.0873	0.0602	0.0554	0.0083
c_9	0.0326	0.0020	-0.0057	0.0023
c_{10}	-0.0306	0.0057	0.0196	0.0060
RMS fit	0.2304	0.2186	0.2203	0.1316

C.2.9 U Mon

Table C.25: Phasing and fourier parameters for U Mon with long-term spline curves removed. To obtain modelled long-term maximum value, add offset of 5.4384.

	B	*V*	*R*	*I*
p	91.79	91.79	91.79	91.79
ϕ_0	0.5960	0.6070	0.6260	0.6490
ϕ_{max}	0.2840	0.8810	0.3930	0.3650
c_0	1.1690	0.3820	-0.0620	-0.8924
c_1	-0.2419	-0.1301	-0.0916	0.0123
c_2	-0.1692	-0.1020	-0.1357	-0.0319
c_3	0.1005	0.0430	0.0256	-0.0385
c_4	0.1989	0.2783	0.2883	0.3681
c_5	0.0032	0.0160	0.0464	0.0554
c_6	-0.0504	-0.0210	-0.0578	-0.0171
c_7	-0.0501	-0.0279	-0.0593	-0.0422
c_8	-0.0391	-0.0127	0.0077	-0.0483
c_9	0.0629	0.0542	-0.0237	-0.0091
c_{10}	-0.0435	-0.0197	0.0032	0.0476
RMS fit	0.5113	0.3359	0.3462	0.4031

C.2.10 R Sct

Table C.26: Phasing and fourier parameters for R Sct.

	B	*V*	*R*	*I*
p	134.87	134.87	134.87	
ϕ_0	0.1090	0.1200	0.1240	0.1280
ϕ_{max}	0.8280	0.8300	0.8300	0.8350
c_0	6.7202	5.3692	4.6444	3.9374
c_1	-0.0019	0.0025	0.0071	-0.0070
c_2	0.1857	0.1761	0.1782	0.1059
c_3	0.1178	0.0859	0.0731	0.0294
c_4	0.2345	0.2340	0.2370	0.1422
c_5	-0.0452	-0.0827	-0.0952	-0.0549
c_6	0.0865	0.0460	0.0298	-0.0056
c_7	0.0028	-0.0176	-0.0297	-0.0028
c_8	0.0320	0.0404	0.0472	0.0337
c_9	-0.1283	-0.1009	-0.0942	-0.0537
c_{10}	-0.0634	-0.0863	-0.1003	-0.0684
RMS fit	0.2770	0.2805	0.2930	0.1677

C.2.11 TX Oph

Table C.27: Phasing and fourier parameters for TX Oph.

	B	*V*	*R*	*I*
p	135.81426	135.81426	135.81426	135.81426
ϕ_0	0.9580	0.5420	0.5400	0.5400
ϕ_{max}	0.7020	0.7310	0.7600	0.7660
c_0	11.2112	10.1735	9.5897	9.0332
c_1	0.0678	0.0348	0.0194	0.0081
c_2	0.1265	0.0997	0.0814	0.0712
c_3	0.1870	0.1460	0.1271	0.1180
c_4	-0.0016	0.0374	0.0525	0.0686
c_5	0.0109	-0.0108	-0.0112	-0.0182
c_6	-0.0995	-0.0751	-0.0598	-0.0503
c_7	-0.00060138	-0.0136	-0.0085	-0.0197
c_8	0.0651	0.0618	0.0591	0.0616
c_9	-0.0368	-0.0394	-0.0431	-0.0513
c_{10}	-0.0722	-0.0481	-0.0340	-0.0247
RMS fit	0.1569	0.1289	0.1177	0.1034

C.2.12 IW Car

Table C.28: Phasing and fourier parameters for IW Car with long-term spline curves removed. To obtain modelled long-term maximum value, add offset of 7.7993 to V, 8.5722 to B, 7.3045 to R and 6.7031 to I.

	B	*V*	*R*	*I*
p	142.73	142.73	142.73	142.73
ϕ_0	0.4980	0.5010	0.5010	0.9710
ϕ_{max}	0.2530	0.2560	0.2600	0.2750

continued on next page

Table C.28: *continued*

	B	V	R	I
c_0	0.2001	0.1459	0.1237	0.1039
c_1	0.0114	0.0100	0.0076	0.0042
c_2	-0.0305	-0.0243	-0.0271	-0.0265
c_3	0.1572	0.1083	0.0815	0.0638
c_4	-0.0391	-0.0228	-0.0160	-0.0095
c_5	-0.0243	-0.0194	-0.0165	-0.0125
c_6	0.0109	0.0086	0.0093	0.0068
c_7	0.0101	0.0049	0.0051	0.0063
c_8	0.0023	-0.00081022	-0.0012	-0.0067
c_9	0.0039	0.0001814	0.0014	0.0058
c_{10}	-0.0122	-0.0113	-0.0083	-0.0071
RMS fit	0.0672	0.0531	0.0503	0.0447

Appendix D

Spectral observations list

Velocities listed for W Vir and BL Her stars are splecline velocities and have already had the telluric line correction applied.

D.1 BL Her stars

D.1.1 VY Pyx

Table D.1: VY Pyx spectral observations

JD - 2400000	telluric line correction	Hα	Ca II	Fe I	Fe II	Na I
51317.835	-1.64 ± 0.89	34.28 ± 0.00	24.60 ± 2.60	19.76 ± 1.89	21.04 ± 0.95	16.76 ± 0.64
51318.853	-1.49 ± 0.71	30.04 ± 0.00	29.71 ± 1.03	28.83 ± 1.42	29.45 ± 0.07	23.54 ± 0.42
51319.842	-1.24 ± 0.89	20.42 ± 0.00	21.55 ± 0.02	23.05 ± 1.36	23.93 ± 1.05	18.88 ± 0.68
51321.838	-1.46 ± 0.86	17.59 ± 0.00	10.72 ± 0.20	14.99 ± 1.25	13.77 ± 1.21	14.22 ± 0.41
51351.829	-0.97 ± 0.91	10.93 ± 0.00	15.30 ± 0.32	17.77 ± 1.33	18.34 ± 0.38	15.30 ± 0.42
51352.795	-1.35 ± 0.85	-	8.89 ± 0.33	12.63 ± 1.85	11.18 ± 1.48	11.83 ± 0.37
51460.206	-2.13 ± 0.64	31.76 ± 0.00	28.72 ± 0.00	29.41 ± 1.39	32.90 ± 3.41	25.04 ± 1.78
51504.163	-1.90 ± 0.92	-	6.30 ± 1.67	14.34 ± 1.91	14.24 ± 0.70	12.12 ± 0.11
51521.147	-1.39 ± 0.86	34.83 ± 0.00	29.42 ± 3.86	22.62 ± 1.67	23.75 ± 0.43	18.82 ± 0.41
51522.145	-1.15 ± 0.92	26.20 ± 0.00	25.93 ± 0.22	28.71 ± 1.91	30.35 ± 1.32	22.64 ± 0.72
51572.059	-1.27 ± 1.00	-	13.71 ± 0.00	17.33 ± 1.93	19.91 ± 3.95	15.18 ± 0.52
51575.031	-0.62 ± 0.86	-	15.99 ± 0.00	17.89 ± 1.55	19.34 ± 1.15	16.00 ± 0.44
51585.079	-1.48 ± 0.94	16.19 ± 0.00	17.66 ± 0.00	20.37 ± 1.39	22.31 ± 1.72	17.83 ± 0.69
51637.959	-0.40 ± 0.80	-	8.33 ± 0.00	12.76 ± 1.38	12.13 ± 0.53	11.92 ± 0.39
51638.920	-1.14 ± 0.63	37.71 ± 0.00	31.12 ± 1.83	24.08 ± 1.85	24.43 ± 0.27	20.12 ± 0.53
51639.926	-1.12 ± 1.87	-	-	26.43 ± 1.97	23.67 ± 0.69	21.83 ± 0.38
51648.880	-1.14 ± 0.78	36.00 ± 0.00	27.67 ± 2.45	21.78 ± 1.93	22.61 ± 0.29	18.21 ± 0.21
51649.879	-0.96 ± 0.93	28.34 ± 0.00	28.31 ± 0.66	29.03 ± 1.82	29.41 ± 0.52	22.90 ± 0.54
51659.861	-0.39 ± 0.50	26.96 ± 0.00	31.33 ± 0.49	28.27 ± 1.68	29.32 ± 0.64	22.96 ± 0.18
51661.857	-0.17 ± 0.88	13.40 ± 0.00	16.85 ± 0.04	18.06 ± 1.56	19.18 ± 0.66	15.83 ± 0.33
51662.866	-0.32 ± 0.77	-	8.96 ± 0.52	13.70 ± 1.59	12.82 ± 1.01	12.58 ± 0.38
51663.871	-0.52 ± 1.11	-	14.50 ± 1.70	15.13 ± 1.49	14.67 ± 0.54	13.56 ± 0.35
51664.908	-0.21 ± 0.98	31.89 ± 0.00	33.02 ± 1.30	26.74 ± 1.73	26.90 ± 0.32	22.48 ± 0.43
51689.849	-0.94 ± 0.75	33.58 ± 0.00	21.58 ± 2.73	18.37 ± 1.58	18.16 ± 0.27	15.63 ± 0.35
51690.837	-0.90 ± 0.86	30.46 ± 0.00	29.77 ± 0.89	28.70 ± 1.28	29.10 ± 0.08	22.99 ± 0.45
51886.125	-0.77 ± 1.25	10.73 ± 0.00	-	15.79 ± 1.74	16.98 ± 0.00	14.19 ± 0.17
51890.102	-1.60 ± 1.09	17.87 ± 0.00	-	20.77 ± 1.91	21.37 ± 0.00	18.07 ± 0.60
51890.129	-2.13 ± 1.09	18.68 ± 0.00	18.61 ± 0.00	20.86 ± 1.69	21.92 ± 0.00	18.59 ± 0.62
51982.025	-0.96 ± 1.10	22.30 ± 0.00	-	24.43 ± 1.85	24.44 ± 0.00	19.37 ± 0.66
51982.966	0.05 ± 1.15	12.61 ± 0.00	-	17.15 ± 2.15	17.40 ± 0.40	14.94 ± 0.64
51983.958	0.49 ± 1.15	11.77 ± 0.00	-	12.72 ± 1.99	13.56 ± 0.88	11.90 ± 0.57
51985.985	0.67 ± 1.17	32.81 ± 0.00	-	28.68 ± 1.62	29.80 ± 0.84	23.24 ± 0.67
52011.902	0.02 ± 1.12	26.78 ± 0.00	-	27.61 ± 1.84	28.95 ± 0.70	22.02 ± 0.61
52012.907	-0.31 ± 1.73	17.20 ± 0.00	-	21.15 ± 1.74	22.78 ± 1.53	17.56 ± 0.56
52013.918	-0.42 ± 1.20	8.73 ± 0.00	-	16.83 ± 1.67	16.86 ± 0.51	15.14 ± 0.56
52078.781	0.20 ± 1.08	23.84 ± 0.00	26.43 ± 0.00	25.31 ± 1.51	25.50 ± 0.30	20.17 ± 0.49
52079.819	-1.26 ± 1.07	19.26 ± 0.00	20.04 ± 0.04	20.95 ± 1.80	21.83 ± 0.93	17.50 ± 0.53

D.1.2 SW Tau

Table D.2: SW Tau spectral observations

JD - 2400000	telluric line correction	Hα	Ca II	Fe I	Fe II	Na I
51398.269	-1.12 ± 1.05	-7.98 ± 0.00	-4.92 ± 2.05	2.02 ± 1.62	2.54 ± 0.28	10.11 ± 0.64
51425.210	-0.66 ± 1.06	-4.50 ± 0.00	-1.99 ± 3.25	5.91 ± 1.62	6.85 ± 0.01	12.29 ± 0.86
51460.131	-0.78 ± 7.03	-2.46 ± 0.00	1.07 ± 1.79	7.33 ± 1.63	8.98 ± 0.00	12.73 ± 1.04
51485.059	-2.08 ± 0.90	2.76 ± 0.00	-14.83 ± 1.54	-2.92 ± 1.90	-1.80 ± 0.00	17.31 ± 2.03
51486.027	-1.40 ± 1.15	15.13 ± 0.00	10.83 ± 0.25	20.38 ± 1.61	23.58 ± 1.66	21.30 ± 0.71
51503.988	-1.44 ± 0.89	-	-11.87 ± 0.00	-3.55 ± 2.08	-3.77 ± 0.00	18.50 ± 0.57
51519.965	-1.45 ± 0.85	-	-12.00 ± 0.77	-2.12 ± 1.65	0.62 ± 0.00	17.05 ± 0.93
51520.933	-1.24 ± 1.03	19.86 ± 0.00	16.02 ± 0.07	23.81 ± 2.08	22.70 ± 0.65	21.10 ± 0.15
51521.933	-1.31 ± 0.96	3.48 ± 0.00	1.48 ± 2.75	7.71 ± 1.95	10.80 ± 1.89	15.65 ± 0.46
51524.939	-0.60 ± 1.04	-6.54 ± 0.00	-3.06 ± 1.77	4.87 ± 1.93	6.49 ± 1.50	14.60 ± 0.83
51779.259	-0.66 ± 2.02	30.10 ± 0.00	16.81 ± 0.00	28.45 ± 2.07	30.83 ± 0.99	12.11 ± 0.80
51780.247	-1.32 ± 1.61	10.17 ± 0.00	10.37 ± 0.22	6.05 ± 1.74	6.65 ± 0.35	12.01 ± 1.67
51799.223	-0.74 ± 1.29	8.66 ± 0.00	9.87 ± 1.30	5.57 ± 1.50	5.80 ± 0.09	12.50 ± 0.88
51802.230	-1.15 ± 1.19	0.25 ± 0.00	4.59 ± 2.08	7.54 ± 1.98	8.51 ± 0.15	13.68 ± 0.85

continued on next page

Table D.2: *continued*

JD - 2400000	telluric line correction	Hα	Ca II	Fe I	Fe II	Na I
51830.169	-0.75 ± 1.05	-	- ± -	-2.26 ± 2.06	-2.17 ± 0.00	13.64 ± 1.29
51831.127	-0.53 ± 1.22	12.92 ± 0.00	9.83 ± 0.04	14.69 ± 1.53	15.12 ± 0.52	17.38 ± 0.34
51885.970	0.91 ± 1.74	-6.90 ± 0.00	-	3.32 ± 2.01	4.25 ± 0.00	14.76 ± 0.37

D.1.3 V381 Cen

Table D.3: V381 Cen spectral observations

JD - 2400000	telluric line correction	Hα	Ca II	Fe I	Fe II	Na I
51318.000	-1.18 ± 1.98	-49.30 ± 0.00	-50.03 ± 0.57	-45.59 ± 1.64	-45.49 ± 0.00	-8.75 ± 3.14
51318.914	-1.38 ± 1.32	-37.71 ± 0.00	-38.86 ± 0.67	-36.08 ± 1.96	-33.76 ± 0.00	-15.20 ± 2.69
51319.960	-0.68 ± 2.21	-26.85 ± 0.00	-28.49 ± 0.31	-26.82 ± 1.86	-25.48 ± 1.11	-11.16 ± 3.08
51322.008	-1.23 ± 1.71	-12.65 ± 0.00	-17.62 ± 0.82	-17.48 ± 2.00	-16.19 ± 0.66	-10.67 ± 0.54
51352.909	-1.10 ± 0.91	-16.16 ± 0.00	-29.94 ± 2.63	-32.40 ± 1.36	-30.56 ± 0.00	-17.29 ± 1.38
51354.047	-0.99 ± 0.92	-50.31 ± 0.00	-50.29 ± 0.94	-45.97 ± 1.69	-44.56 ± 0.00	-7.32 ± 2.25
51355.979	-1.42 ± 0.82	-40.72 ± 0.00	-40.52 ± 0.99	-37.94 ± 1.81	-37.66 ± 0.00	-17.36 ± 4.49
51356.925	-1.37 ± 0.85	-48.55 ± 0.00	-50.88 ± 0.71	-44.83 ± 1.38	-45.35 ± 0.00	-11.81 ± 0.17
51369.029	-1.38 ± 1.06	-45.47 ± 0.00	-45.19 ± 0.65	-42.39 ± 1.85	-40.01 ± 0.00	-
51372.945	-0.95 ± 0.86	-32.27 ± 0.00	-32.79 ± 0.42	-31.45 ± 1.65	-30.44 ± 0.82	-19.01 ± 0.28
51373.991	-1.12 ± 0.74	-8.10 ± 0.00	-13.20 ± 0.75	-14.02 ± 1.88	-13.22 ± 0.16	-9.37 ± 0.60
51374.987	-0.84 ± 0.77	-47.45 ± 0.00	-49.36 ± 0.35	-43.71 ± 1.63	-43.69 ± 0.00	-
51398.918	-1.11 ± 1.04	-35.63 ± 0.00	-35.90 ± 0.51	-33.71 ± 1.38	-30.51 ± 0.00	-18.04 ± 1.99
51424.826	-1.01 ± 0.66	-48.52 ± 0.00	-48.31 ± 0.74	-45.19 ± 1.92	-44.65 ± 0.00	-5.96 ± 0.00
51426.848	-1.17 ± 0.70	-37.28 ± 0.00	-37.64 ± 0.00	-35.46 ± 1.66	-34.66 ± 0.00	-
51586.190	-1.02 ± 1.04	-23.12 ± 0.00	-24.79 ± 0.34	-25.34 ± 1.99	-24.78 ± 0.43	-12.60 ± 1.59
51638.064	-0.91 ± 1.30	-42.78 ± 0.00	-42.75 ± 0.87	-39.44 ± 2.00	-38.37 ± 0.00	-
51639.144	-0.85 ± 1.05	-36.33 ± 0.00	-36.76 ± 0.34	-34.29 ± 1.71	-33.44 ± 0.00	-
51649.113	-0.79 ± 0.96	-10.56 ± 0.00	-15.56 ± 0.55	-15.37 ± 1.65	-13.78 ± 0.34	-7.70 ± 0.04
51650.100	-0.54 ± 0.99	-50.06 ± 0.00	-49.33 ± 1.57	-45.00 ± 2.00	-42.43 ± 0.00	-
51655.096	-0.32 ± 0.88	-37.76 ± 0.00	-38.05 ± 0.75	-34.71 ± 1.46	-33.78 ± 0.00	-20.22 ± 0.00
51659.078	-0.56 ± 0.91	-23.17 ± 0.00	-24.25 ± 0.36	-24.26 ± 1.61	-23.57 ± 0.01	-14.24 ± 1.09
51661.166	-0.78 ± 0.97	-25.16 ± 0.00	-27.56 ± 1.08	-25.99 ± 1.79	-25.38 ± 0.54	-14.79 ± 1.36
51662.084	-0.52 ± 1.60	-12.52 ± 0.00	-17.15 ± 0.48	-17.04 ± 1.74	-16.56 ± 0.68	-10.87 ± 0.41
51663.141	-0.59 ± 1.11	-13.09 ± 0.00	-18.33 ± 0.61	-18.05 ± 1.29	-16.86 ± 0.50	-10.67 ± 0.31
51664.083	-0.36 ± 1.30	-28.12 ± 0.00	-28.75 ± 0.21	-27.97 ± 1.40	-27.74 ± 0.07	-15.83 ± 1.30
51665.110	-0.35 ± 1.42	-3.18 ± 0.00	-11.08 ± 2.05	-20.61 ± 1.52	-19.14 ± 0.00	-11.39 ± 0.44
51675.130	-0.91 ± 0.79	-51.12 ± 0.00	-51.20 ± 0.58	-47.11 ± 1.85	-47.19 ± 0.61	-7.64 ± 1.92
51689.112	-1.14 ± 0.72	-40.72 ± 0.00	-40.73 ± 0.36	-38.60 ± 1.49	-38.09 ± 0.00	-
51690.119	-0.58 ± 0.80	-28.62 ± 0.00	-30.00 ± 0.21	-28.72 ± 1.40	-28.36 ± 0.12	-16.97 ± 0.45
51691.100	-0.86 ± 0.67	-15.55 ± 0.00	-18.33 ± 0.70	-19.38 ± 1.29	-19.03 ± 0.00	-11.91 ± 0.53
51711.052	-0.88 ± 0.73	-16.22 ± 0.00	-19.49 ± 1.03	-20.38 ± 1.89	-19.33 ± 0.11	-11.34 ± 0.40
51779.876	-0.48 ± 0.92	-33.83 ± 0.00	-34.23 ± 0.12	-32.34 ± 1.42	-31.65 ± 0.09	-19.35 ± 0.43
51780.867	-1.10 ± 1.74	-19.32 ± 0.00	-21.93 ± 0.53	-22.52 ± 1.50	-21.90 ± 0.14	-13.98 ± 0.28
51797.839	-0.41 ± 0.65	-8.87 ± 0.00	-13.81 ± 0.91	-13.89 ± 1.52	-13.89 ± 0.11	-9.44 ± 0.62
51798.836	0.06 ± 0.72	-12.47 ± 0.00	-17.44 ± 0.00	-17.43 ± 1.94	-17.12 ± 0.31	-11.89 ± 0.77
51984.200	1.37 ± 1.63	-41.60 ± 0.00	-41.82 ± 0.98	-39.27 ± 1.38	-38.36 ± 0.00	-
51986.115	1.32 ± 1.36	-29.56 ± 0.00	-29.90 ± 0.13	-29.23 ± 1.31	-28.83 ± 0.10	-16.85 ± 1.57
51986.214	1.35 ± 1.37	-8.69 ± 0.00	-13.75 ± 0.87	-14.29 ± 1.54	-11.92 ± 0.00	-9.84 ± 0.52
52010.171	0.71 ± 2.37	-49.26 ± 0.00	-50.53 ± 1.02	-44.83 ± 1.87	-45.56 ± 0.00	-
52012.132	1.52 ± 1.64	-	-	-27.51 ± 1.66	-22.70 ± 0.00	-16.71 ± 0.40
52013.112	1.10 ± 1.87	-4.45 ± 0.00	-	-17.06 ± 1.62	-12.27 ± 0.00	-10.79 ± 0.52
52014.138	0.95 ± 1.95	-4.82 ± 0.00	-	-21.25 ± 1.86	-18.40 ± 0.00	-12.17 ± 0.45
52015.168	1.60 ± 1.30	-19.11 ± 0.00	-	-22.44 ± 1.77	-21.19 ± 1.95	-13.18 ± 0.48
52042.059	-0.10 ± 0.72	-51.47 ± 0.00	-	-45.52 ± 1.73	-44.32 ± 0.00	-13.10 ± 1.18
52077.046	-0.72 ± 0.81	-45.95 ± 0.00	-	-43.23 ± 1.97	-41.79 ± 0.00	-14.98 ± 3.24
52079.043	-0.28 ± 0.92	-35.27 ± 0.00	-	-33.23 ± 1.89	-31.40 ± 1.86	-18.05 ± 2.21
52080.031	-0.33 ± 0.71	-20.62 ± 0.00	-	-22.99 ± 1.83	-21.79 ± 1.09	-13.16 ± 0.17
51317.016	-1.00 ± 2.30	-4.75 ± 0.00	-11.16 ± 2.19	-20.16 ± 1.51	-17.42 ± 0.00	-11.11 ± 0.49
51321.104	-1.33 ± 1.42	-9.73 ± 0.00	-14.97 ± 0.98	-14.81 ± 1.88	-13.83 ± 0.18	-9.49 ± 0.78
51322.911	-1.10 ± 1.76	-47.05 ± 0.00	-47.89 ± 0.83	-43.98 ± 1.68	-43.34 ± 0.00	-
51351.883	-0.93 ± 1.71	-34.65 ± 0.00	-36.60 ± 0.42	-34.20 ± 1.89	-32.73 ± 0.00	-20.10 ± 0.08

D.1.4 TX Del

Orbital motion has not beem removed.

Table D.4: TX Del spectral observations

JD - 2400000	telluric line correction	Hα	Ca II	Fe I	Fe II	Na I
51318.208	-0.85 ± 1.88	-2.36 ± 0.00	2.24 ± 0.00	6.44 ± 1.50	6.83 ± 0.01	3.35 ± 0.55
51319.258	-1.38 ± 1.22	6.99 ± 0.00	10.17 ± 1.02	13.02 ± 1.46	13.55 ± 0.83	4.88 ± 1.00
51320.216	-1.16 ± 1.62	20.22 ± 0.00	19.43 ± 0.29	19.42 ± 1.49	19.65 ± 0.50	8.65 ± 2.60
51322.252	-1.31 ± 1.95	22.27 ± 0.00	20.13 ± 0.18	15.57 ± 1.74	16.77 ± 0.58	6.65 ± 0.77
51352.166	-0.57 ± 2.11	-7.78 ± 0.00	-14.44 ± 1.77	-6.37 ± 1.53	-5.93 ± 0.00	-7.55 ± 0.01
51353.214	-1.31 ± 0.70	-7.06 ± 0.00	-9.38 ± 2.18	0.89 ± 1.79	2.17 ± 1.10	-1.52 ± 0.31
51354.161	-0.53 ± 2.12	38.91 ± 0.00	36.88 ± 0.75	28.27 ± 1.91	30.50 ± 0.80	24.42 ± 2.61
51357.139	-1.62 ± 1.07	11.94 ± 0.00	5.31 ± 1.55	11.76 ± 1.95	11.73 ± 0.10	4.06 ± 1.08
51369.143	-1.57 ± 0.99	13.59 ± 0.00	12.61 ± 2.24	20.13 ± 1.61	20.47 ± 0.13	12.90 ± 4.30
51373.117	-1.32 ± 2.17	20.58 ± 0.00	23.66 ± 1.34	27.67 ± 1.73	29.10 ± 1.50	23.11 ± 3.58
51374.135	-1.31 ± 0.95	42.38 ± 0.00	41.15 ± 0.33	35.19 ± 1.43	35.39 ± 0.26	32.40 ± 0.70

continued on next page

Table D.4: *continued*

JD - 2400000	telluric line correction	Hα	Ca II	Fe I	Fe II	Na I
51398.047	-0.78 ± 1.32	47.02 ± 0.00	44.46 ± 0.67	39.04 ± 1.59	39.99 ± 0.04	38.09 ± 0.00
51399.064	-1.50 ± 1.12	29.16 ± 0.00	30.39 ± 0.02	31.83 ± 1.85	34.62 ± 2.15	34.76 ± 0.21
51424.997	-0.89 ± 0.73	38.85 ± 0.00	36.26 ± 0.39	36.34 ± 1.66	36.00 ± 0.13	33.74 ± 0.63
51425.957	-1.00 ± 0.99	19.68 ± 0.00	20.03 ± 0.00	19.74 ± 1.53	18.76 ± 1.01	13.71 ± 2.92
51485.867	-1.45 ± 0.96	27.69 ± 0.00	27.81 ± 3.83	25.84 ± 1.30	25.97 ± 0.05	23.66 ± 0.00
51662.247	-0.60 ± 1.32	18.30 ± 0.00	14.85 ± 0.79	8.47 ± 1.60	9.23 ± 0.14	4.74 ± 0.31
51665.227	-0.76 ± 1.49	-14.99 ± 0.00	-	-13.99 ± 1.96	-14.28 ± 0.00	-11.48 ± 0.53
51689.224	-1.62 ± 0.87	42.62 ± 0.00	38.97 ± 1.44	38.65 ± 1.85	40.18 ± 0.52	35.52 ± 0.12
51690.231	-1.03 ± 0.93	11.14 ± 0.00	11.53 ± 1.85	16.43 ± 1.52	16.55 ± 0.14	7.68 ± 2.08
51691.226	-0.91 ± 1.33	31.10 ± 0.00	-	23.27 ± 2.01	23.13 ± 0.15	5.59 ± 2.72
51711.181	-0.82 ± 0.99	19.73 ± 0.00	16.29 ± 0.18	15.39 ± 1.76	15.48 ± 0.35	4.70 ± 1.07
51780.970	-1.24 ± 1.33	14.22 ± 0.00	11.23 ± 2.13	-2.39 ± 1.81	0.90 ± 0.00	-1.16 ± 0.14
51798.944	-0.88 ± 1.46	-11.52 ± 0.00	-17.68 ± 1.12	-12.24 ± 1.70	-13.08 ± 0.00	-10.62 ± 0.06
51801.926	-0.29 ± 1.04	-3.25 ± 0.00	-2.83 ± 1.29	0.85 ± 1.83	1.03 ± 0.30	-1.73 ± 0.50
51830.851	-0.32 ± 0.97	35.93 ± 0.00	33.25 ± 0.87	35.43 ± 1.83	36.10 ± 0.12	32.01 ± 0.69
52042.236	-0.18 ± 0.99	21.53 ± 0.00	21.98 ± 0.01	21.90 ± 1.84	21.59 ± 0.57	16.01 ± 1.81
52077.124	-0.88 ± 1.00	-5.73 ± 0.00	-11.35 ± 0.87	-2.13 ± 1.34	-1.74 ± 0.00	-4.14 ± 0.26
52080.145	-0.94 ± 1.19	16.43 ± 0.00	13.30 ± 0.06	13.69 ± 1.70	13.54 ± 0.82	6.60 ± 0.68
51317.245	-1.24 ± 1.02	10.59 ± 0.00	-14.04 ± 0.00	12.00 ± 1.95	12.18 ± 0.47	2.69 ± 0.75
51321.257	-1.29 ± 1.40	17.82 ± 0.00	17.07 ± 0.40	20.12 ± 1.60	19.70 ± 0.17	9.52 ± 0.46
51351.183	-0.84 ± 2.01	-9.57 ± 0.00	-9.12 ± 0.94	-3.88 ± 1.53	-3.27 ± 0.00	-5.01 ± 0.17

D.2 W Vir stars

D.2.1 κ Pav

Table D.5: κ Pav spectral observations

JD - 2400000	telluric line correction	Hα	Ca II	Fe I	Fe II	Na I
51317.184	-1.61 ± 0.78	58.83 ± 0.00	58.39 ± 0.99	45.52 ± 1.78	45.92 ± 0.56	48.11 ± 0.40
51318.089	-1.48 ± 0.83	62.01 ± 0.00	51.30 ± 0.57	30.12 ± 1.53	31.20 ± 1.47	27.83 ± 0.88
51319.123	-0.53 ± 1.94	33.46 ± 0.00	25.69 ± 0.00	26.89 ± 1.98	28.93 ± 4.46	24.10 ± 0.98
51320.154	-1.16 ± 0.63	32.10 ± 0.00	23.06 ± 1.36	31.18 ± 1.69	31.27 ± 0.60	28.67 ± 0.82
51321.190	-1.41 ± 0.81	33.03 ± 0.00	27.15 ± 0.78	35.43 ± 1.46	36.22 ± 0.50	33.46 ± 0.88
51322.174	-1.42 ± 0.99	33.58 ± 0.00	31.92 ± 2.10	39.69 ± 1.52	40.49 ± 0.36	38.30 ± 0.66
51323.057	-1.50 ± 1.11	34.34 ± 0.00	37.23 ± 2.61	43.74 ± 1.48	44.57 ± 0.29	43.10 ± 0.56
51351.084	-1.64 ± 1.37	35.29 ± 0.00	43.61 ± 1.86	47.73 ± 1.88	48.93 ± 0.87	46.88 ± 0.44
51352.016	-1.06 ± 0.89	37.88 ± 0.00	49.32 ± 1.89	51.80 ± 1.79	52.49 ± 0.17	51.68 ± 0.29
51354.196	-1.07 ± 0.69	67.08 ± 0.00	55.71 ± 1.08	29.80 ± 1.69	29.19 ± 0.77	28.28 ± 0.65
51369.187	-1.96 ± 1.19	35.08 ± 0.00	27.51 ± 0.12	33.55 ± 1.57	33.03 ± 0.76	31.89 ± 0.50
51357.168	-0.97 ± 0.82	36.98 ± 0.00	43.75 ± 2.06	48.22 ± 1.24	49.39 ± 0.32	47.60 ± 0.45
51370.168	-1.25 ± 0.77	38.32 ± 0.00	50.19 ± 1.50	52.55 ± 1.66	53.09 ± 0.47	52.31 ± 0.28
51372.172	-1.02 ± 0.57	-	58.34 ± 0.99	32.33 ± 1.69	31.73 ± 0.56	31.69 ± 0.46
51373.188	-1.35 ± 0.51	40.80 ± 0.00	33.51 ± 0.00	26.90 ± 1.96	25.21 ± 1.13	24.07 ± 0.63
51374.205	-1.27 ± 0.56	33.44 ± 0.00	23.43 ± 2.35	29.26 ± 1.83	27.71 ± 0.82	26.19 ± 0.60
51375.156	-1.63 ± 0.59	34.65 ± 0.00	26.37 ± 0.13	33.42 ± 1.98	32.79 ± 0.60	31.38 ± 0.49
51394.126	-0.79 ± 0.70	37.15 ± 0.00	29.90 ± 0.66	36.16 ± 1.97	36.39 ± 0.32	35.10 ± 0.43
51398.124	-1.09 ± 0.69	47.75 ± 0.00	55.03 ± 0.90	52.75 ± 1.73	53.89 ± 0.66	53.79 ± 0.25
51399.156	-0.91 ± 0.65	-	57.88 ± 0.87	36.01 ± 1.60	37.03 ± 0.50	39.27 ± 0.05
51424.035	-1.15 ± 0.67	34.34 ± 0.00	44.53 ± 1.49	49.49 ± 1.46	50.31 ± 0.11	48.75 ± 0.12
51425.025	-0.99 ± 0.71	-	50.96 ± 2.19	52.89 ± 1.38	53.76 ± 0.28	52.57 ± 0.25
51425.987	-0.94 ± 0.49	-	56.53 ± 1.48	46.00 ± 1.89	46.57 ± 0.15	49.12 ± 0.08
51426.935	-0.86 ± 1.46	-	47.81 ± 0.00	29.13 ± 1.90	30.26 ± 2.23	27.50 ± 0.55
51459.923	-2.32 ± 0.82	39.12 ± 0.00	42.56 ± 0.40	46.83 ± 1.69	47.68 ± 0.00	46.27 ± 0.25
51460.902	-1.99 ± 0.90	41.05 ± 0.00	48.94 ± 0.47	52.00 ± 1.44	53.21 ± 0.41	51.97 ± 0.21
51462.909	-1.30 ± 0.81	-	56.98 ± 0.00	33.56 ± 1.60	33.75 ± 0.08	34.73 ± 0.01
51484.893	-2.44 ± 0.73	37.02 ± 0.00	32.83 ± 2.83	36.61 ± 1.88	36.91 ± 0.11	35.36 ± 0.42
51485.901	-1.80 ± 0.73	37.38 ± 0.00	35.46 ± 0.81	40.88 ± 1.93	41.50 ± 0.01	39.98 ± 0.40
51639.180	-0.93 ± 0.57	35.33 ± 0.00	29.78 ± 1.45	36.56 ± 1.56	37.52 ± 0.64	35.27 ± 0.54
51644.192	-0.72 ± 0.76	-	57.88 ± 0.09	40.78 ± 1.82	42.08 ± 1.66	44.36 ± 0.76
51649.131	-0.69 ± 0.83	38.05 ± 0.00	35.03 ± 1.28	40.28 ± 1.75	41.18 ± 0.39	39.54 ± 0.54
51660.278	-0.61 ± 0.88	39.44 ± 0.00	49.01 ± 1.07	50.45 ± 1.60	50.41 ± 0.94	50.83 ± 0.34
51661.217	-1.20 ± 0.66	-	57.23 ± 0.05	52.79 ± 1.42	53.07 ± 0.30	54.05 ± 0.23
51661.237	-1.02 ± 0.70	-	56.84 ± 0.50	52.70 ± 1.36	52.95 ± 0.01	54.06 ± 0.08
51661.243	-0.89 ± 0.92	-	56.49 ± 0.44	52.49 ± 1.45	53.08 ± 0.12	53.71 ± 0.14
51662.103	-1.04 ± 0.82	-	59.31 ± 0.15	45.63 ± 1.83	46.33 ± 0.57	47.62 ± 0.36
51663.218	-0.46 ± 0.68	64.08 ± 0.00	-	28.12 ± 1.69	28.27 ± 0.20	25.60 ± 0.68
51664.133	-0.81 ± 0.82	40.92 ± 0.00	30.12 ± 0.00	28.03 ± 1.72	27.43 ± 0.20	25.16 ± 0.56
51665.157	-0.49 ± 0.79	36.94 ± 0.00	25.64 ± 1.09	31.37 ± 1.71	31.04 ± 0.17	29.19 ± 0.57
51675.160	-0.95 ± 0.67	37.32 ± 0.00	28.55 ± 0.45	35.36 ± 1.43	36.32 ± 0.08	33.76 ± 0.65
51689.259	-0.97 ± 0.57	56.53 ± 0.00	58.05 ± 0.19	46.66 ± 1.70	45.57 ± 0.94	47.94 ± 0.70
51690.266	-0.68 ± 0.63	67.12 ± 0.00	58.84 ± 0.74	28.46 ± 1.71	28.58 ± 0.84	26.16 ± 0.85
51691.261	-0.68 ± 0.54	43.97 ± 0.00	29.94 ± 0.00	27.85 ± 1.84	27.26 ± 0.08	24.73 ± 0.66
51711.262	-1.03 ± 0.84	37.71 ± 0.00	27.36 ± 0.00	34.62 ± 1.70	33.86 ± 0.86	32.89 ± 0.57
51748.126	-0.59 ± 0.59	39.17 ± 0.00	30.72 ± 0.61	36.65 ± 1.54	36.84 ± 0.24	35.28 ± 0.43
51748.138	-0.62 ± 0.59	38.94 ± 0.00	31.26 ± 0.66	36.57 ± 1.52	36.73 ± 0.22	35.24 ± 0.40
51748.144	-0.39 ± 0.50	38.87 ± 0.00	31.39 ± 0.71	36.64 ± 1.51	36.83 ± 0.26	35.25 ± 0.36
51779.076	-0.86 ± 0.92	54.53 ± 0.00	54.96 ± 0.25	52.08 ± 1.68	53.34 ± 0.27	52.87 ± 0.26
51780.054	-1.13 ± 0.77	61.26 ± 0.00	58.56 ± 0.01	45.24 ± 1.99	46.04 ± 0.25	47.55 ± 0.05
51781.051	-0.84 ± 0.92	66.82 ± 0.00	57.60 ± 0.24	28.90 ± 1.68	28.45 ± 0.21	26.82 ± 0.37
51798.008	-0.63 ± 0.45	59.39 ± 0.00	59.20 ± 0.53	47.49 ± 1.94	47.68 ± 0.41	49.00 ± 0.17
51799.027	-0.63 ± 0.64	70.17 ± 0.00	58.02 ± 0.04	29.09 ± 1.61	28.75 ± 0.27	27.69 ± 0.46
51802.001	-0.29 ± 0.95	40.71 ± 0.00	30.43 ± 0.22	34.04 ± 1.57	33.88 ± 0.30	32.62 ± 0.42
51829.898	-0.34 ± 0.75	38.39 ± 0.00	31.83 ± 0.75	37.35 ± 1.52	37.63 ± 0.41	36.35 ± 0.36

continued on next page

Table D.5: *continued*

JD - 2400000	telluric line correction	Hα	Ca II	Fe I	Fe II	Na I
51830.890	-0.73 ± 0.69	39.25 ± 0.00	37.09 ± 1.24	41.94 ± 1.43	42.25 ± 0.36	41.44 ± 0.30
52010.222	0.39 ± 0.97	39.27 ± 0.00	-	32.79 ± 1.95	32.32 ± 0.00	31.29 ± 0.60
52010.242	1.20 ± 1.49	38.78 ± 0.00	-	32.95 ± 1.94	32.25 ± 0.00	31.36 ± 0.61
52012.206	1.40 ± 1.36	41.68 ± 0.00	-	41.40 ± 1.86	41.99 ± 0.00	40.68 ± 0.74
52012.216	1.55 ± 1.36	41.75 ± 0.00	-	41.75 ± 1.94	41.99 ± 0.00	41.15 ± 0.79
52014.264	1.85 ± 1.34	48.14 ± 0.00	-	51.05 ± 1.60	51.93 ± 0.00	50.87 ± 0.52
52016.253	1.42 ± 1.50	58.42 ± 0.00	-	35.63 ± 1.99	34.80 ± 0.00	36.09 ± 0.68
52042.204	-0.21 ± 0.83	52.41 ± 0.00	53.50 ± 0.56	51.96 ± 1.48	52.12 ± 0.62	52.31 ± 0.25
52043.224	-0.53 ± 0.72	57.13 ± 0.00	54.74 ± 0.84	43.30 ± 1.84	42.85 ± 1.31	45.00 ± 0.75
52077.267	-0.76 ± 0.96	39.75 ± 0.00	47.97 ± 0.00	48.88 ± 1.79	49.92 ± 0.70	49.21 ± 0.22
52079.189	-0.49 ± 0.73	53.35 ± 0.00	56.42 ± 1.07	49.58 ± 1.57	49.71 ± 0.50	49.53 ± 0.26
52080.230	-0.43 ± 1.03	61.55 ± 0.00	53.83 ± 0.48	28.39 ± 1.82	28.37 ± 0.09	26.58 ± 0.93

D.2.2 AL Vir

Table D.6: AL Vir spectral observations

JD - 2400000	telluric line correction	Hα	Ca II	Fe I	Fe II	Na I
51318.051	-1.30 ± 1.07	28.40 ± 0.00	28.32 ± 1.05	29.70 ± 1.53	30.56 ± 1.14	28.88 ± 0.34
51318.958	-1.22 ± 1.40	35.25 ± 0.00	32.88 ± 0.58	32.79 ± 1.73	32.78 ± 0.80	31.55 ± 1.96
51368.927	-0.90 ± 2.03	22.00 ± 0.00	23.48 ± 0.36	25.84 ± 1.76	25.84 ± 0.74	25.34 ± 0.37
51369.893	-0.95 ± 2.12	26.11 ± 0.00	30.04 ± 1.47	29.35 ± 1.53	29.58 ± 0.09	28.21 ± 1.17
51373.899	-1.28 ± 0.99	-	-2.09 ± 0.00	7.95 ± 1.68	3.40 ± 0.00	-2.42 ± 1.45
51374.938	-1.57 ± 0.96	-	2.69 ± 0.71	8.99 ± 1.48	7.32 ± 1.63	0.92 ± 2.62
51425.824	3.20 ± 1.07	-	1.18 ± 0.00	7.85 ± 1.67	6.36 ± 0.93	-0.04 ± 1.45
51639.104	-0.98 ± 1.02	51.62 ± 0.00	35.71 ± 0.00	28.14 ± 1.97	32.22 ± 0.31	29.91 ± 0.86
51649.071	-1.20 ± 1.01	46.13 ± 0.00	21.11 ± 0.00	30.51 ± 1.77	30.33 ± 0.16	32.23 ± 0.06
51661.076	0.09 ± 0.93	50.92 ± 0.00	20.29 ± 0.00	10.24 ± 1.90	13.65 ± 0.00	-0.15 ± 3.60
51662.037	-0.57 ± 1.25	-	-0.03 ± 0.00	9.03 ± 1.80	7.97 ± 0.11	-0.90 ± 0.87
51663.045	-0.02 ± 0.77	22.40 ± 0.00	4.92 ± 0.00	10.65 ± 1.71	11.52 ± 0.29	7.31 ± 1.79
51665.044	-0.71 ± 1.82	24.15 ± 0.00	17.90 ± 1.05	18.50 ± 1.98	18.85 ± 0.26	17.93 ± 0.47
51688.973	-1.14 ± 0.82	41.88 ± 0.00	34.30 ± 0.88	30.24 ± 1.46	30.98 ± 0.13	31.08 ± 0.33
51689.978	-0.97 ± 1.25	45.39 ± 0.00	40.73 ± 0.00	31.04 ± 1.54	31.96 ± 0.09	32.28 ± 0.16
51690.965	-0.68 ± 1.01	49.24 ± 0.00	44.03 ± 0.52	25.97 ± 1.99	26.82 ± 0.72	27.40 ± 0.21
51710.910	-0.73 ± 1.05	41.44 ± 0.00	38.29 ± 0.00	30.66 ± 1.76	30.66 ± 1.44	31.64 ± 0.05
51780.822	-1.11 ± 1.80	24.67 ± 0.00	0.00 ± 0.00	27.21 ± 1.55	28.13 ± 0.46	26.51 ± 0.09
51982.185	0.07 ± 1.81	24.47 ± 0.00	0.00 ± 0.00	10.29 ± 1.70	11.31 ± 0.00	3.31 ± 1.96
51983.145	0.82 ± 1.80	21.79 ± 0.00	0.00 ± 0.00	14.47 ± 2.01	13.36 ± 0.00	12.04 ± 0.40
51984.160	1.22 ± 1.88	21.37 ± 0.00	0.00 ± 0.00	17.84 ± 1.57	20.53 ± 0.00	17.00 ± 0.71
51986.173	1.51 ± 1.87	26.09 ± 0.00	0.00 ± 0.00	24.14 ± 2.85	24.19 ± 0.00	25.56 ± 0.52
52010.129	-0.64 ± 2.49	48.81 ± 0.00	0.00 ± 0.00	21.59 ± 1.93	19.42 ± 0.00	25.22 ± 0.44
52012.086	0.29 ± 1.44	34.18 ± 0.00	0.00 ± 0.00	8.08 ± 1.71	9.74 ± 0.00	-2.51 ± 2.38
52013.069	-0.78 ± 1.51	18.60 ± 0.00	0.00 ± 0.00	10.98 ± 1.45	10.02 ± 0.00	5.32 ± 2.42
52015.122	-1.52 ± 1.21	19.55 ± 0.00	0.00 ± 0.00	17.79 ± 1.42	18.52 ± 0.00	17.64 ± 1.30
52043.105	-0.84 ± 1.73	-	-0.17 ± 0.00	8.19 ± 2.13	9.11 ± 0.08	8.22 ± 0.79
52079.938	-0.76 ± 0.98	34.72 ± 0.00	30.62 ± 0.71	30.00 ± 1.76	29.29 ± 0.23	29.80 ± 0.09

D.2.3 W Vir

Table D.7: W Vir spectral observations

JD - 2400000	telluric line correction	Hα EW	He I EW	Ca II	Fe I	Fe II	Na I
51372.852	-1.41 ± 0.95	12.07±0.02	0.24±0.00	-40.25 ± 2.16	-44.84 ± 5.026	-30.06 ± 0	-45.92 ± 0.96
51373.805	-1.05 ± 1.71	9.71±0.00	0.63±0.02	-40.65 ± 1.49	-35.58 ± 6.329	-	-47.35 ± 1.50
51374.806	-1.11 ± 1.12	4.47±0.01	0.81±0.00	-43.86 ± 0.54	-32.88 ± 7.123	-33.46 ± 0	-43.83 ± 1.30
51394.810	-0.97 ± 0.90	1.50±0.01	0.33±0.00	-48.15 ± 0.76	-81.65 ± 5.524	-	-94.96 ± 0.34
51661.934	-0.72 ± 1.95	0.36±0.01	-	-	-54.90 ± 2.434	-53.56 ± 0.72	-59.23 ± 2.13
51688.933	-1.39 ± 1.02	0.49±0.01	0.39±0.00	-57.73 ± 5.68	-81.14 ± 6.161	-	-88.49 ± 0.08
51689.931	-0.78 ± 1.02	-0.35±0.02	0.17±0.01	-60.44 ± 1.60	-79.84 ± 6.272	-76.72 ± 0	-87.28 ± 0.11
51690.924	-1.13 ± 0.70	-0.82±0.01	0.04±0.04	-63.47 ± 2.21	-78.76 ± 5.177	-76.27 ± 0	-84.33 ± 0.61
51710.872	-0.60 ± 1.23	-1.51±0.03	0.02±0.02	-90.24 ± 0.00	-72.41 ± 3.776	-71.39 ± 0.13	-83.96 ± 1.47
51982.124	0.49 ± 1.75	0.41±0.01	0.30±0.01	-	-81.54 ± 5.691	-78.25 ± 0	-95.54 ± 0.19
51983.096	1.57 ± 1.73	-0.50±0.01	0.06±0.00	-	-82.66 ± 5.819	-79.25 ± 0	-94.76 ± 1.14
51984.085	0.36 ± 1.87	-0.98±0.01	0.00±0.02	-	-80.56 ± 5.010	-77.98 ± 0	-90.93 ± 1.35
52014.004	-1.08 ± 1.63	3.04±0.03	0.68±0.02	-	-77.82 ± 4.452	-	-40.00 ± 1.18
52015.023	-0.24 ± 1.83	2.28±0.01	0.61±0.02	-	-81.62 ± 6.266	-77.76 ± 0	-40.45 ± 0.90
52079.896	-1.00 ± 1.50	10.69±0.02	-0.09±0.03	-42.16 ± 0.00	-45.31 ± 3.619	-37.59 ± 0	-46.95 ± 0.71

D.2.4 ST Pup

Table D.8: ST Pup spectral observations

JD - 2400000	telluric line correction	Hα EW	He I EW	Fe II (6515 Å)
51485.117	-1.71 ± 1.05	0.596 ± 0.021	0.046 ± 0.004	39.60 ± 0.02
51486.084	-1.40 ± 1.15	-0.053 ± 0.024	0.005 ± 0.004	36.90 ± 0.15
51504.046	-0.79 ± 1.29	0.584 ± 0.029	0.110 ± 0.006	-47.19 ± 0.36
51520.990	-0.95 ± 0.99	4.873 ± 0.008	0.034 ± 0.013	33.29 ± 0.07
51521.988	-1.17 ± 0.86	1.658 ± 0.010	0.196 ± 0.005	32.65 ± 0.04
51585.908	-0.94 ± 1.51	-0.903 ± 0.049	-0.017 ± 0.019	19.05 ± 0.22
51662.827	-0.06 ± 0.91	0.031 ± 0.008	-0.018 ± 0.001	12.15 ± 0.14
51664.804	-0.39 ± 1.89	0.346 ± 0.007	0.015 ± 0.007	12.45 ± 0.05
51831.189	-0.86 ± 1.41	0.161 ± 0.021	0.017 ± 0.004	37.36 ± 0.1
51983.876	1.72 ± 1.75	3.157 ± 0.002	-0.029 ± 0.021	16.16 ± 0.06
51985.892	2.11 ± 1.72	7.556 ± 0.055	0.169 ± 0.054	13.12 ± 0.1

D.3 RV Tauri stars

D.3.1 SX Cen

Table D.9: SX Cen spectral observations

JD - 2400000	telluric line correction	standard deviation
51317.926	-1.64	1.00
51353.897	-1.11	0.91
51372.900	-1.33	0.87
51374.890	-0.79	1.09
51575.169	-0.72	0.98
51586.153	-1.41	1.09
51639.059	-0.94	0.89
51650.013	-1.08	1.68
51659.136	-2.69	0.85
51660.007	-1.29	1.65
51663.999	-0.23	1.52
51675.082	-0.90	1.11
51690.033	-1.03	0.88
52010.079	0.09	2.46
52015.070	-1.08	1.82

D.3.2 TT Oph

Table D.10: TT Oph spectral observations

JD - 2400000	telluric line correction	Fe I	Fe II (6515 Å)	Ba II (5853 Å)	Ca I (5957 Å)	Hα (EW) (Å)	He I (EW) (Å)
51354.002	-1.12 ± 1.02	-72.47 ± 5.69	-67.10 ± 0.73	-67.68 ± 0.16	-63.38 ± 1.48	0.177 ± 0.016	0.069 ± 0.006
51356.970	-1.21 ± 1.39	-71.78 ± 4.11	-67.36 ± 0.76	-69.41 ± 0.03	-64.91 ± 0.85	-0.783 ± 0.094	-0.024 ± 0.013
51368.986	-1.19 ± 1.43	-46.24 ± 4.00	-40.99 ± 0.2	-43.92 ± 0.02	-40.82 ± 0.6	-0.829 ± 0.016	-0.025 ± 0.018
51369.988	-1.08 ± 1.97	-43.27 ± 3.35	-39.83 ± 0.51	-40.43 ± 0.03	-38.40 ± 0.63	-0.912 ± 0.034	-0.117 ± 0.024
51373.950	-1.55 ± 1.08	-37.75 ± 2.17	-34.29 ± 0.47	-33.44 ± 0.04	-29.63 ± 0.82	0.607 ± 0.008	-0.061 ± 0.026
51394.864	-0.92 ± 1.50	-55.48 ± 5.50	-49.46 ± 0.33	-51.50 ± 0.3	-51.17 ± 0.29	-0.360 ± 0.055	-0.101 ± 0.025
51397.866	-1.09 ± 1.11	-49.71 ± 3.92	-46.20 ± 0.04	-45.97 ± 0.04	-44.99 ± 0.41	-0.637 ± 0.073	0.034 ± 0.005
51639.216	-1.31 ± 1.16	-53.90 ± 4.70	-48.09 ± 0.22	-50.23 ± 0.05	-47.23 ± 0.38	-0.701 ± 0.109	-0.025 ± 0.016
51662.200	-0.10 ± 1.33	-61.83 ± 4.77	-59.39 ± 0.18	-58.87 ± 0.01	-58.08 ± 0.15	-0.309 ± 0.087	0.062 ± 0.002
51689.072	-1.38 ± 0.92	-70.61 ± 4.85	-63.89 ± 0.34	-65.77 ± 0.21	-62.62 ± 0.31	0.579 ± 0.066	0.051 ± 0.004
51690.074	-1.09 ± 0.92	-69.65 ± 4.73	-63.99 ± 0.16	-65.16 ± 0.17	-64.02 ± 0.23	0.126 ± 0.072	0.017 ± 0.002
51691.061	-0.66 ± 0.85	-67.85 ± 4.33	-63.90 ± 0.08	-64.98 ± 0.11	-62.25 ± 0.21	-0.067 ± 0.072	0.040 ± 0.009
51711.009	-0.40 ± 1.38	-36.50 ± 10.34	–	-25.78 ± 0.29	-34.06 ± 0.42	2.430 ± 0.005	-0.077 ± 0.025
51779.827	-0.77 ± 1.42	-71.39 ± 5.87	-66.41 ± 0.53	-67.91 ± 0.33	-61.69 ± 0.29	1.428 ± 0.036	0.001 ± 0.003
52079.986	-0.70 ± 1.13	-47.26 ± 13.66	–	-28.27 ± 0.63	-50.09 ± 2.05	4.465 ± 0.006	0.020 ± 0.012

D.3.3 RU Cen

Table D.11: RU Cen spectral observations

JD - 2400000	telluric line correction	C I (6587.622 Å)	Ba II (5853 Å)	Hα (EW)	He I (EW)
51317.486	-3.65 ± 1.43	-23.60 ± 0.08	-20.23 ± 0.29	-1.586 ± 0.011	0.022 ± 0.003
51317.966	-1.41 ± 1.33	-23.28 ± 0.47	-19.83 ± 0.22	-1.345 ± 0.009	0.006 ± 0.005
51320.975	-0.86 ± 1.22	-26.20 ± 0.13	-17.66 ± 0.38	-1.168 ± 0.018	0.000 ± 0.002
51322.866	-1.52 ± 1.10	-22.02 ± 0.49	-17.07 ± 0.21	-0.747 ± 0.014	0.025 ± 0.005
51353.937	-0.85 ± 1.24	50.15 ± 0.23	-22.16 ± 0.08	-0.014 ± 0.023	0.069 ± 0.024
51355.873	-0.17 ± 1.66	51.67 ± 1.09	-20.02 ± 0.22	-0.187 ± 0.050	0.008 ± 0.019
51369.845	-0.75 ± 1.39	-50.15 ± 0.03	-50.82 ± 0.29	1.239 ± 0.002	0.147 ± 0.003
51572.133	-1.26 ± 1.07	-45.25 ± 1.38	-45.66 ± 0.13	1.961 ± 0.003	-0.061 ± 0.092
51575.132	-1.22 ± 0.99	-34.38 ± 0.59	-37.69 ± 0.01	2.107 ± 0.005	0.072 ± 0.014

continued on next page

Table D.11: *continued*

JD - 2400000	telluric line correction	C I (6587.622 Å)	Ba II (5853 Å)	Hα (EW)	He I (EW)
51585.159	-1.06 ± 0.89	-29.85 ± 0.07	-20.79 ± 0.19	4.497 ± 0.052	-0.003 ± 0.016
51586.093	-1.13 ± 0.82	-30.80 ± 0.06	-16.44 ± 0.25	5.554 ± 0.031	0.005 ± 0.006
51638.020	-0.65 ± 1.25	-43.33 ± 0.06	-39.30 ± 0.02	1.646 ± 0.011	0.052 ± 0.022
51639.003	-0.97 ± 1.00	-38.47 ± 0.22	-36.34 ± 0.07	1.481 ± 0.029	0.025 ± 0.003
51648.959	-0.99 ± 0.90	-40.69 ± 2.29	-18.94 ± 0.54	2.184 ± 0.004	0.037 ± 0.001
51649.965	-0.67 ± 1.17	-38.66 ± 0.56	-16.12 ± 0.1	2.764 ± 0.007	-0.005 ± 0.006
51659.035	-0.39 ± 0.74	-50.81 ± 0.01	-52.71 ± 0.38	5.100 ± 0.031	0.319 ± 0.004
51661.989	-0.42 ± 1.33	-53.58 ± 0.26	-54.73 ± 0.13	4.617 ± 0.019	0.185 ± 0.002
51662.999	-0.45 ± 0.88	-53.45 ± 0.28	-53.93 ± 0.08	3.775 ± 0.005	0.103 ± 0.001
51663.943	0.31 ± 1.47	-55.78 ± 0.07	-53.94 ± 0.09	3.133 ± 0.002	0.013 ± 0.005
51664.976	0.00 ± 2.00	-51.02 ± 0.95	-53.44 ± 0.17	2.398 ± 0.010	0.010 ± 0.002
51675.043	-0.62 ± 0.94	-37.81 ± 0.21	-30.95 ± 0.87	1.075 ± 0.001	-0.049 ± 0.008
51689.020	-1.08 ± 0.69	-38.55 ± 0.05	-15.97 ± 0.09	10.649 ± 0.052	0.336 ± 0.000
51691.010	-0.54 ± 0.93	-37.93 ± 1.27	-17.74 ± 0.04	8.793 ± 0.054	0.397 ± 0.015
51710.958	-0.97 ± 0.90	-32.71 ± 0.16	-18.95 ± 0.12	1.867 ± 0.003	-0.045 ± 0.019
51981.138	-0.32 ± 1.03	-35.22 ± 0.07	-30.14 ± 2.79	3.489 ± 0.051	0.214 ± 0.010
51982.233	0.79 ± 1.33	-38.70 ± 0.46	-31.87 ± 0.64	3.382 ± 0.005	0.237 ± 0.012
51984.043	1.11 ± 1.51	-38.75 ± 0.15	-38.84 ± 0.14	3.467 ± 0.001	0.077 ± 0.005
51986.069	0.98 ± 1.33	-38.36 ± 0.28	-38.45 ± 0.13	2.036 ± 0.006	0.063 ± 0.018
52012.033	0.97 ± 1.61	-40.99 ± 3.04	-2.12 ± 0.02	5.466 ± 0.048	0.335 ± 0.034
52014.094	0.77 ± 1.47	-38.80 ± 0.19	9.59 ± 0.01	4.365 ± 0.031	0.420 ± 0.006
52043.047	-0.72 ± 0.89	-28.28 ± 0.06	2.27 ± 0.74	6.195 ± 0.020	0.124 ± 0.021
52078.928	0.86 ± 2.45	-32.76 ± 0.44	-32.02 ± 0.14	2.945 ± 0.021	0.000 ± 0.036

D.3.4 CT Ori

No spectral observations made.

D.3.5 AI Sco

Table D.12: AI Sco spectral observations

JD - 2400000	telluric line correction	standard deviation
51317.108	-1.23	1.06
51320.111	-1.31	1.34
51321.148	-1.11	1.17
51322.093	-0.81	1.20
51351.050	-0.87	1.21
51354.115	-0.94	1.34
51357.089	-1.22	1.64
51369.075	-1.17	1.25
51373.041	-0.90	0.65
51374.057	-1.06	0.90
51397.975	-0.34	2.19
51424.898	-1.35	0.85
51425.904	-1.03	0.97
51711.133	-0.80	1.23
51780.922	-0.45	2.08
51797.923	-0.66	1.69
51798.896	-0.50	1.61
51801.874	0.11	1.63
51829.860	-0.15	1.75
52014.182	0.40	1.44
52015.238	1.28	1.89
52042.102	0.40	1.26

D.3.6 AR Pup

Table D.13: AR Pup spectral observations

JD - 2400000	telluric line correction	standard deviation
51317.803	-1.28	1.18
51318.806	-1.04	0.88
51321.885	-0.94	1.20
51351.793	-1.06	1.87
51486.160	-0.82	1.03
51504.124	-0.82	1.21
51521.058	-0.83	1.01
51522.060	-1.40	0.77
51571.999	0.05	0.93
51585.033	-2.27	1.84
51637.920	-0.68	0.85
51638.877	-0.76	1.21
51639.888	-1.06	1.08
51648.843	-0.46	0.74
51649.842	-1.13	1.03
51661.821	-0.15	1.13
51662.904	-0.93	0.83
51663.834	-0.39	1.34
51664.870	-0.76	1.50
51674.814	-1.00	0.88
51689.808	-0.80	0.96
51690.796	-0.76	1.05

continued on next page

Table D.13: *continued*

JD - 2400000	telluric line correction	standard deviation
51886.083	0.14	1.79
51890.062	-0.41	1.38
51982.925	0.37	1.11
51983.918	1.08	0.97
51985.939	1.22	1.20
52012.860	1.44	2.03
52013.876	0.03	1.58

D.3.7 AR Sgr

Table D.14: AR Sgr spectral observations

JD - 2400000	telluric line correction	standard deviation
51320.180	-1.13	1.10
51322.203	-0.76	0.96
51373.162	-1.12	1.01
51374.177	-1.54	1.31
51398.095	-1.00	1.32
51399.128	-0.94	1.00
51424.947	-0.94	1.15
51660.251	-2.02	1.30
51662.132	-0.92	1.61
51665.187	-0.33	2.06
51689.185	-0.88	0.88
51690.191	-0.48	1.12
51691.186	-0.43	1.32
51711.235	-1.21	1.10
51780.025	-0.72	1.05
51781.023	-0.76	1.92
51797.979	-0.63	1.32
51799.000	-0.32	1.11
51801.973	0.00	1.34
52013.243	0.66	2.21
52042.171	0.95	0.86
52077.236	-1.04	0.97
52079.107	-0.78	1.57
52080.105	-0.41	1.34

D.3.8 UZ Oph

No spectral observations made.

D.3.9 U Mon

See Pollard et al. (1997) for spectra.

Table D.15: MJUO spectra of U Mon (McSaveney, 1998).

JD [1] JD - 2440000	region	observer[2]	phase (ϕ)	W_λ(Hα) (Å)	rv(Fe)[3] (kms^{-1})
8694.884	Hα	MDA	4.12	<6.64	+48.78[7]
9446.852	Hα	PLC	12.26	0.24	+37.67[d]
9576.274	Hα	MDA	13.66	1.38	+38.08
9654.143	Hα	PLC	14.51	0.50	+52.60
9655.154	Hα	PLC	14.52	0.06	+49.53
9701.978	Hα	PLC	15.02	1.89	+49.60
9703.097	Hα	PLC	15.04	2.77	+49.96
9731.000	Hα	PLC	15.34	1.27	–
9828.828	Hα	PCDP	16.40	0.26	+39.54
10007.197	Hα	PLC	18.33	1.01	+22.74
10061.098	Hα	MDA	18.91	2.32	–
10115.961	Hα	MTPC	19.51	1.88	+26.48
10117.933	Hα	MTPC	19.53	2.65	+29.01
10122.893	Hα	MTPC	19.58	2.98	–
10358.172	Hα	PLC	22.13	3.15	+38.12
10360.207	Hα	PCOP	22.15	3.34	+37.51
10470.923	Hα	PLC	23.35	0.07	+19.76
10471.900	Hα	PLC	23.36	0.07	+19.34
10795.568	Hα	OKP	26.87	0.07	+21.87
10887.456	Hα	OKP	27.86	0.65	+26.57
10911.887	Hα	OKP	28.13	1.46	+46.34

[7] A spectrum already included in Pollard (1994) but reanalysed to enable comparisons with this project

Table D.16: MJUO spectra of U Mon (Intermediate analysis). Data reduced in same way as detailed in Chapter 2, but no 2 dimentional wavelength callibration or telluric line correction measured. For this reason only Hα equivalent widths have been used from these measurements. Some overlap with main spectral observaitons. Observer code MDA: Albrow; DP: Pooley; OKP: Petterson; KRP: Pollard; KPJM Pollard & McSaveney; OPJM: Petterson & McSaveney.

JD [8] 2440000+	region	observer	W_λ(Hα) (Å)
10746.111	Hα	KRP	0.60
10746.128	Hα	KRP	0.63
10746.147	Hα	KRP	0.63
10748.119	Hα	KRP	0.47
10749.176	Hα	KRP	0.43
10777.132	Hα	DP	1.00
10781.138	Hα	DP	–
10795.568	Hα	OKP	–
10821.070	Hα	DP	3.09
10822.060	Hα	DP	2.71
10864.921	Hα	DP	1.10
10888.000	Hα	OKP	–
10911.887	Hα	OKP	–
10913.817	Hα	KPJM	1.28
10914.844	Hα	KPJM	1.03
10914.864	Hα	KPJM	1.19
10915.874	Hα	KRP	1.10
10915.901	Hα	KRP	1.11
10918.816	Hα	KRP	1.07
10951.849	Hα	KRP	4.48
10952.818	Hα	KRP	–
11085.208	Hα	MDA	3.98
11086.205	Hα	MDA	4.55
11087.213	Hα	MDA	4.37
11095.143	Hα	OKP	2.79
11096.170	Hα	OKP	–
11100.186	Hα	KRP	1.14
11103.184	Hα	KRP	0.62
11125.129	Hα	OKP	3.52
11128.171	Hα	OKP	–
11133.144	Hα	DP	4.22
11161.129	Hα	OKP	0.05
11163.030	Hα	OKP	0.19
11167.015	Hα	KRP	0.08
11167.158	Hα	KRP	0.11
11169.953	Hα	KRP	0.03
11170.984	Hα	KRP	0.00
11172.119	Hα	DP	0.33
11173.139	Hα	DP	0.52
11174.059	Hα	DP	0.61
11190.058	Hα	DP	0.89
11194.135	Hα	MDA	0.66
11214.938	Hα	OKP	1.75
11215.947	Hα	OKP	1.83
11219.954	Hα	DP	1.65
11224.924	Hα	KRP	2.65
11225.902	Hα	KRP	2.83
11226.939	Hα	KRP	3.10
11229.043	Hα	KRP	3.04
11229.962	Hα	KRP	2.81
11230.944	Hα	KRP	2.55
11232.895	Hα	MDA	2.01
11236.959	Hα	MDA	1.24
11240.908	Hα	OPJM	0.73
11244.912	Hα	OPJM	0.45
11261.907	Hα	OKP	0.97
11262.908	Hα	OKP	0.68
11263.904	Hα	OKP	1.10
11317.774	Hα	KPJM	1.78
11318.779	Hα	KPJM	1.48
11321.817	Hα	KPJM	0.75
11330.780	Hα	OKP	0.41
11338.756	Hα	MDA	0.63
11350.791	Hα	JAM	1.49
11351.746	Hα	JAM	1.34
11352.757	Hα	JAM	1.39
11353.747	Hα	JAM	1.21
11355.747	Hα	JAM	1.21

Table D.17: U Mon spectral observations

JD - 2400000	telluric line correction	Fe I	Fe II (6516 Å)	Ba II (5853 Å)	Ca I (5957 Å)	Ca II (8498 Å)	Hα (EW) (Å)
51317.774	-1.61 ± 0.51	14.92 ± 1.68	8.73 ± 0.15	54.17 ± 0.16	17.19 ± 0.07	47.03 ± 1.68	1.632 ± 0.027
51318.779	-1.68 ± 0.81	14.92 ± 1.44	7.58 ± 0.83	53.93 ± 0.17	17.18 ± 0.09	46.58 ± 1.86	1.124 ± 0.002
51321.817	-1.13 ± 0.83	15.16 ± 0.82	8.88 ± 1.1	14.39 ± 0.17	17.38 ± 0.22	44.85 ± 1.6	0.497 ± 0.034
51322.828	-1.22 ± 0.99	15.91 ± 0.98	11.69 ± 0.49	15.16 ± 0.03	17.64 ± 0.24	44.10 ± 2.47	0.479 ± 0.033
51350.791	-1.76 ± 0.81	51.81 ± 3.87	14.38 ± 0.08	56.81 ± 0.43	53.89 ± 0.24	38.50 ± 1.67	0.972 ± 0.034
51351.746	-1.06 ± 1.02	52.32 ± 5.10	51.89 ± 3.22	56.24 ± 0.97	53.77 ± 0.66	38.72 ± 1.61	1.502 ± 0.022
51352.757	-1.22 ± 0.62	52.72 ± 5.04	12.57 ± 0.07	53.67 ± 4.54	52.32 ± 0.72	39.31 ± 1.89	2.272 ± 0.004
51353.747	-1.02 ± 0.62	53.20 ± 5.80	13.39 ± 0.03	53.69 ± 4.78	49.77 ± 0.38	38.75 ± 2.33	1.035 ± 0.029
51460.179	-2.00 ± 0.79	19.51 ± 2.69	50.66 ± 0.21	54.26 ± 0.24	24.18 ± 0.7	46.73 ± 0.95	1.405 ± 0.023
51461.173	-1.28 ± 0.82	20.22 ± 2.54	18.65 ± 0.02	53.31 ± 0.16	24.63 ± 0.22	45.83 ± 0.91	1.328 ± 0.014
51461.193	-2.52 ± 0.80	20.31 ± 1.80	18.51 ± 0.07	53.40 ± 0.22	24.56 ± 0.33	45.47 ± 0.66	1.324 ± 0.036
51464.193	-1.88 ± 0.67	22.64 ± 2.03	21.04 ± 0.15	52.42 ± 0.57	26.91 ± 0.51	46.60 ± 0.95	0.724 ± 0.027
51485.152	-1.33 ± 0.69	47.16 ± 0.66	48.25 ± 0.06	52.09 ± 0.05	49.06 ± 0.25	45.56 ± 0.96	-0.783 ± 0.004
51486.123	-1.38 ± 0.81	48.30 ± 0.59	48.77 ± 0.08	52.84 ± 0.14	49.58 ± 0.29	46.72 ± 0.87	-0.663 ± 0.041
51504.083	-1.38 ± 0.67	26.38 ± 2.81	31.39 ± 1.02	57.79 ± 0.08	29.83 ± 0.23	53.17 ± 0.16	1.315 ± 0.013
51520.003	-2.33 ± 1.01	35.98 ± 1.53	39.14 ± 0.14	42.77 ± 0.16	38.14 ± 0.13	46.05 ± 0.77	-0.650 ± 0.063
51521.028	-1.66 ± 1.03	37.42 ± 1.32	39.20 ± 0.1	42.61 ± 0.04	38.54 ± 0.26	45.02 ± 0.93	-1.389 ± 0.041
51522.020	-1.53 ± 1.10	38.97 ± 1.45	40.36 ± 0.08	43.69 ± 0.07	40.41 ± 0.28	44.13 ± 1.08	-0.733 ± 0.051
51525.020	-1.61 ± 1.62	42.02 ± 2.01	41.18 ± 0.04	44.53 ± 0.17	45.17 ± 0.3	44.40 ± 1.53	-1.316 ± 0.036
51552.010	-0.20 ± 0.66	16.61 ± 1.25	22.62 ± 0.83	56.54 ± 0.12	19.79 ± 0.26	50.69 ± 0.53	1.614 ± 0.002
51552.899	-1.30 ± 0.66	17.54 ± 1.16	24.70 ± 0.39	16.25 ± 0.19	20.99 ± 0.13	50.49 ± 0.45	0.795 ± 0.049
51554.972	-0.70 ± 0.71	18.43 ± 1.20	20.91 ± 0.67	16.39 ± 0.13	21.04 ± 0.12	49.63 ± 0.27	0.728 ± 0.014
51555.122	-0.85 ± 0.68	18.40 ± 1.03	21.47 ± 0.54	16.31 ± 0.14	21.26 ± 0.15	50.09 ± 0.38	0.273 ± 0.042
51555.935	-0.71 ± 0.76	18.59 ± 1.08	22.38 ± 0.47	17.19 ± 0.21	21.52 ± 0.03	49.13 ± 0.28	-0.017 ± 0.040
51571.029	-0.74 ± 1.15	39.58 ± 4.57	38.63 ± 4.3	31.52 ± 0.61	41.81 ± 0.28	34.19 ± 3.32	-1.169 ± 0.057
51571.960	-0.84 ± 1.07	41.26 ± 5.12	42.19 ± 0.62	32.46 ± 1.29	44.48 ± 0.13	36.21 ± 4.43	-1.000 ± 0.064
51574.957	-1.43 ± 1.28	48.47 ± 4.63	47.35 ± 0.39	45.47 ± 5.51	53.44 ± 0.05	34.61 ± 1.22	-0.221 ± 0.008
51585.000	-1.47 ± 1.83	54.42 ± 5.42	13.86 ± 0.03	61.23 ± 1.38	60.53 ± 3.63	43.50 ± 1.19	1.411 ± 0.022
51585.944	-1.59 ± 0.88	48.46 ± NaN	13.05 ± 0.01	61.76 ± 1.25	53.74 ± 4.63	45.63 ± 1.8	—
51637.859	-0.40 ± 0.59	18.20 ± 1.08	14.56 ± 1.87	16.49 ± 0.14	20.28 ± 0.19	53.43 ± 0.47	0.794 ± 0.031
51638.839	-0.79 ± 0.68	18.55 ± 1.36	16.52 ± 0.54	17.31 ± 0.2	21.05 ± 0.17	52.74 ± 0.22	0.419 ± 0.031
51639.843	-0.78 ± 0.55	19.26 ± 1.42	16.39 ± 1.69	17.42 ± 0.23	20.86 ± 0.19	52.59 ± 0.45	0.165 ± 0.024
51648.803	-0.86 ± 0.97	26.96 ± 1.11	25.38 ± 0.3	24.75 ± 0.28	28.73 ± 0.04	47.04 ± 0.1	-0.481 ± 0.094
51649.814	-0.66 ± 1.05	28.17 ± 1.42	27.12 ± 0.31	25.10 ± 0.32	29.34 ± 0.08	46.47 ± 0.24	-0.783 ± 0.027
51659.797	0.21 ± 1.26	41.47 ± 2.38	39.76 ± 0.69	34.48 ± 0.75	42.88 ± 0.23	39.86 ± 2.8	-0.690 ± 0.028
51661.785	-0.38 ± 1.69	45.91 ± 1.75	43.71 ± 0.24	45.63 ± 6.23	48.18 ± 0.34	42.64 ± 2.66	-0.303 ± 0.016
51662.797	-0.21 ± 1.04	48.42 ± 1.27	45.98 ± 0.11	52.95 ± 0.02	50.73 ± 0.31	43.99 ± 1.95	-0.093 ± 0.015
51663.797	-0.55 ± 1.57	50.42 ± 1.12	47.89 ± 0.21	54.06 ± 0.15	52.21 ± 0.32	44.14 ± 1.5	0.305 ± 0.016
51664.833	-0.61 ± 1.95	52.57 ± 1.14	50.57 ± 0.05	55.51 ± 0.41	55.10 ± 0.06	46.14 ± 0.78	0.345 ± 0.031
51674.781	-0.83 ± 0.50	60.58 ± 1.75	-0.69 ± 0.04	58.51 ± 1.52	54.43 ± 0.12	53.44 ± 0.71	0.492 ± 0.023
51689.770	-1.11 ± 0.65	26.55 ± 3.32	21.15 ± 4.23	58.20 ± 0.64	29.64 ± 0.8	54.58 ± 0.47	0.609 ± 0.011
51690.761	-0.44 ± 0.82	26.69 ± 2.59	25.53 ± 0.19	57.37 ± 0.63	31.08 ± 0.78	53.95 ± 0.54	0.435 ± 0.016
51708.743	-0.96 ± 0.91	46.68 ± 0.83	44.85 ± 0.25	49.80 ± 0.02	47.56 ± 0.25	49.87 ± 0.3	-0.931 ± 0.005
51886.051	-0.83 ± 1.29	41.65 ± 4.44	-34.49 ± 1.14	33.09 ± 0.35	42.75 ± 0.14	—	0.015 ± 0.013
51890.004	-0.74 ± 1.07	48.71 ± 6.95	-33.27 ± 2.15	37.93 ± 0.94	50.57 ± 0.59	—	1.594 ± 0.020
51890.016	-1.06 ± 1.16	48.66 ± 7.78	-31.75 ± 0.8	37.64 ± 2.03	52.99 ± 0.78	—	0.660 ± 0.019
51890.029	-0.92 ± 1.08	48.84 ± 7.13	-36.11 ± 3.01	38.86 ± 1.42	50.57 ± 0.81	—	0.749 ± 0.030
51981.981	-0.27 ± 1.23	58.34 ± 1.89	3.35 ± 0.16	62.16 ± 0.65	58.23 ± 0.16	—	1.909 ± 0.014
51982.848	0.20 ± 0.93	59.23 ± 1.26	3.26 ± 0.21	61.94 ± 0.73	57.65 ± 2.72	—	1.896 ± 0.021
51983.845	0.25 ± 0.91	59.95 ± 2.16	2.44 ± 0.15	62.37 ± 0.77	56.88 ± 6.22	—	1.689 ± 0.008
51985.854	0.08 ± 1.01	61.56 ± 5.94	2.88 ± 0.2	62.46 ± 0.7	46.62 ± 7.89	—	2.414 ± 0.023
52010.830	0.40 ± 1.10	36.79 ± 1.27	38.32 ± 0.31	54.60 ± 3.23	40.17 ± 0.28	—	-0.014 ± 0.013
52011.819	0.77 ± 0.88	37.86 ± 0.72	39.46 ± 0.51	53.11 ± 2.21	40.07 ± 0.2	—	0.053 ± 0.031
52012.822	0.16 ± 1.02	38.88 ± 0.91	40.41 ± 0.17	53.26 ± 1.77	41.18 ± 0.27	—	0.090 ± 0.306
52013.793	0.74 ± 1.01	39.47 ± 0.71	41.79 ± 0.21	52.27 ± 1.3	41.87 ± 0.28	—	-0.253 ± 0.027

D.3.10 R Sct

Table D.18: R Sct spectral observations

JD - 2400000	telluric line correction	standard deviation
51317.131	-1.64	0.76
51319.107	-1.38	0.92
51320.138	-1.47	0.78
51321.178	-1.80	0.91
51322.161	-1.38	0.77
51323.077	-1.92	1.25
51351.145	-1.02	1.17
51352.033	-1.03	1.18
51354.074	-0.68	1.25
51356.107	-0.79	1.34
51357.049	-1.66	0.88
51369.109	-1.81	1.07
51370.023	-1.43	1.06
51373.014	-1.15	1.12
51374.028	-1.22	1.19
51397.943	-0.76	0.84
51398.947	-0.59	1.37
51424.864	-0.93	0.69
51425.871	-0.97	0.79
51426.902	-0.71	0.51
51459.897	-2.13	0.85
51460.881	-2.00	0.86
51649.207	-0.94	1.02
51660.217	-0.79	0.93
51661.197	-0.18	1.30
51662.164	-0.58	1.68

continued on next page

Table D.18: *continued*

JD - 2400000	telluric line correction	standard deviation
51665.142	-1.14	2.20
51689.152	-1.62	0.98
51690.159	-1.10	0.85
51691.136	-1.37	0.96
51711.104	-0.93	0.81
51779.994	-1.15	1.63
51780.896	-1.22	2.05
51781.883	-0.70	1.06
51797.901	-0.45	1.16
51798.869	0.11	1.39
51801.850	-0.66	1.31
52010.201	-0.46	1.47
52012.170	-0.45	1.31
52012.241	-0.68	1.20
52013.205	-0.37	1.32
52014.234	0.27	1.76
52015.200	0.62	1.67

D.3.11 TX Oph

No spectral observations made.

D.3.12 IW Car

Table D.19: IW Car spectral observations

JD - 2400000	telluric line correction	standard deviation
51317.866	-1.46	1.08
51321.948	-1.12	0.73
51352.857	-0.41	0.68
51355.835	-1.86	0.63
51374.848	-1.32	0.81
51521.109	-0.31	0.63
51522.107	-0.80	0.85
51572.095	-0.72	0.74
51575.087	-1.61	0.82
51585.119	-2.01	0.76
51586.057	-0.99	0.89
51637.981	-0.92	0.76
51638.940	-0.97	0.71
51648.914	-0.98	0.64
51649.929	-0.98	0.86
51659.896	-0.87	0.51
51661.886	-0.18	0.93
51662.952	-0.70	0.91
51663.891	-0.55	1.04
51664.927	-0.57	1.35
51674.889	-0.99	0.65
51688.884	-1.15	0.71
51689.884	-1.37	0.70
51690.874	-0.82	0.72
51982.080	0.38	1.02
51983.002	1.14	0.85
51983.989	1.43	1.00
51986.025	1.48	0.88
52012.953	1.30	1.42
52078.827	-0.48	1.37
52079.846	-0.66	0.81

D.4 Radial velocity standard stars

D.4.1 β Lep

Table D.20: β Lep spectral observations

JD - 2400000	telluric line correction	mean radial velocity
51485.159	-0.91±0.71	-14.01±1.55
51521.075	-1.07±0.88	-13.88±1.32
51522.077	-1.41±0.97	-13.94±1.38
51524.999	-1.55±0.89	-13.69±1.49
51553.016	-0.13±0.71	-14.21±1.10
51554.873	-0.93±0.79	-13.77±1.18
51555.890	-1.03±0.69	-13.98±1.24
51571.950	-1.11±0.78	-14.00±1.47
51585.877	-0.95±0.88	-13.84±1.56
51889.982	-0.31±1.05	-13.54±1.53
51982.826	1.16±1.06	-14.61±1.66
51983.833	1.48±1.10	-14.62±1.75
51985.848	0.75±0.99	-14.05±1.78

D.4.2 β Cet

Table D.21: β Cet spectral observations

JD - 2400000	telluric line correction	mean radial velocity
51399.207	-0.77±1.73	13.06±1.05
51425.145	-0.76±1.52	13.13±1.16
51426.093	-0.35±1.66	13.30±1.58
51460.049	-1.46±0.76	13.70±1.18
51461.066	-2.28±0.96	13.71±1.20
51464.090	-1.63±0.86	13.55±1.12
51484.996	-1.44±0.94	13.36±1.43
51485.997	-2.71±0.96	13.18±1.37
51503.925	-1.86±1.01	13.44±1.23
51519.928	-1.21±0.88	13.27±1.20
51520.900	-1.05±1.05	13.52±1.41
51521.912	-1.33±0.86	13.43±1.12
51524.920	-0.76±1.01	13.25±1.31
51798.195	-0.26±1.45	13.30±1.10
51799.177	-0.27±1.66	13.36±1.10
51802.116	-0.17±2.06	13.09±1.09
51830.017	-0.35±1.23	13.75±1.06
51831.110	-0.41±1.22	13.56±1.16

D.4.3 β Crv

Table D.22: β Crv spectral observations

JD - 2400000	telluric line correction	mean radial velocity
51317.893	-1.62±1.58	-7.04±1.35
51318.878	-1.47±0.77	-6.96±1.32
51319.898	-1.43±0.72	-7.09±1.35
51321.086	-0.67±1.86	-8.86±1.22
51321.984	-1.53±0.85	-7.03±1.43
51322.928	-1.54±1.04	-7.18±1.35
51351.851	-1.16±1.35	-7.05±1.24
51369.817	-1.12±0.89	-7.25±1.14
51393.794	-0.74±0.71	-7.51±1.02
51394.776	-1.04±0.79	-7.33±1.11
51397.790	-0.71±0.80	-7.45±1.12
51398.777	-0.93±0.90	-7.48±1.07
51648.986	-0.80±0.91	-6.67±1.19
51650.040	-1.10±1.15	-6.80±1.25
51655.032	-1.04±0.76	-6.75±1.20
51659.017	-0.23±0.88	-7.19±1.07
51659.924	-1.09±0.68	-7.00±0.96
51661.058	-0.25±0.61	-7.30±1.05
51661.909	0.50±1.49	-7.43±1.14
51674.951	0.13±0.89	-7.59±1.06
51708.824	-0.10±0.91	-7.49±1.20
51710.846	-0.78±0.95	-7.21±1.15
51981.167	-0.94±1.22	-7.33±1.67
51983.230	1.00±0.93	-7.36±1.74
51984.123	1.51±1.15	-8.03±1.62
51986.129	1.27±1.18	-7.75±1.55
52010.043	0.27±1.92	-6.93±1.61
52012.984	-0.82±1.59	-7.07±1.58
52043.029	-0.16±0.82	-7.29±1.16

D.4.4 β Aqr

Table D.23: β Aqr spectral observations

JD - 2400000	telluric line correction	mean radial velocity
51317.270	-1.00±0.62	6.59 ±1.31
51320.240	-1.16±0.64	6.62 ±1.31
51321.280	-1.07±0.82	6.83 ±1.51
51323.172	-1.33±0.54	6.66 ±1.38
51353.240	-0.94±0.68	6.77 ±1.19
51354.230	-0.95±0.85	6.59 ±1.26
51424.024	-0.99±0.60	6.61 ±1.14
51662.270	0.19±1.06	6.12 ±1.15
51675.224	-0.72±0.68	6.91 ±1.28
51690.275	-0.97±0.62	6.95 ±1.05
51691.268	-0.47±0.80	6.50 ±1.09
51711.270	-0.60±0.79	6.80 ±1.15
51779.061	-0.63±0.76	7.03 ±1.12

continued on next page

Table D.23: *continued*

JD - 2400000	telluric line correction	mean radial velocity
51780.063	-0.55±0.69	7.10 ±1.13
51798.014	0.01±0.62	6.73 ±1.09
51799.036	-0.18±1.00	6.82 ±1.06
51802.006	-0.46±1.00	6.92 ±1.14
51829.903	-0.32±0.95	6.70 ±1.20
51830.922	-0.78±0.82	7.16 ±1.26
52042.263	-0.27±0.77	6.40 ±1.33
52077.209	-0.15±0.95	6.30 ±1.25
52079.210	-0.21±1.21	6.15 ±1.26
52080.234	-0.75±0.67	6.47 ±1.13

D.4.5 α Hya

Table D.24: α Hya spectral observations

JD - 2400000	telluric line correction	mean radial velocity
1353.811	-1.12±1.11	-4.17±1.20
51571.063	-1.41±1.25	-3.98±1.21
51585.071	-1.45±1.21	-4.11±1.23
51638.897	-0.79±1.56	-4.18±1.16
51688.860	-1.56±1.08	-4.40±1.24
51689.861	-0.79±1.15	-4.66±1.12
51690.847	-0.96±1.20	-4.45±1.16
51886.137	-0.64±1.66	-4.15±1.46
51981.013	0.88±1.59	-4.70±1.77
51982.013	-0.28±2.47	-4.44±1.49
52078.767	-0.04±1.75	-4.29±1.24
52079.743	-1.00±1.13	-4.21±1.30

D.4.6 α TrA

Table D.25: α TrA spectral observations

JD - 2400000	telluric line correction	mean radial velocity
51371.011	-1.31±1.40	-4.55±1.24
51372.096	-0.69±1.94	-4.35±1.23
51372.987	-1.33±1.65	-4.72±1.23
51374.014	-0.71±2.01	-4.78±1.30
51375.019	-0.89±1.89	-4.71±1.26
51424.849	-0.64±1.73	-3.83±1.23
51425.854	-0.64±1.90	-3.85±1.30
51426.877	-0.70±1.67	-3.90±1.24
51460.857	-2.07±1.33	-4.82±1.51
51639.188	-0.52±1.46	-3.61±1.32
51644.135	-0.42±1.44	-3.46±1.32
51663.173	-0.16±1.72	-3.35±1.10
51664.111	-0.29±2.04	-3.37±1.25
51665.088	-0.83±2.36	-3.51±1.27

D.4.7 δ Sgr

Table D.26: δ Sgr spectral observations

JD - 2400000	telluric line correction	mean radial velocity
51319.089	-1.50±1.77	-13.56±1.73
51357.116	-1.07±2.11	-21.18±1.80
51748.109	-0.74±1.40	-20.29±1.78
51781.064	0.08±1.57	-20.40±1.83
52012.194	0.19±1.80	-19.65±1.75
52014.210	0.06±1.66	-19.51±1.59
52015.264	0.77±1.77	-18.94±1.57
52016.165	-0.14±2.24	-19.50±1.88

Appendix E

Atomic line data

The following parameters were obtained from the Vienna Atomic Line Database (VALD) on 26-29.4.02 and as such represent a weighted mean of the data available at that time. These have been sorted according to species.

E.1 Ba II

Table E.1: Ba II lines used

wavelength (Å)	excitation potential (eV)	log(gf)
5853.6680	0.6040	-1.000

E.2 C I

Table E.2: C I lines used

wavelength (Å)	excitation potential (eV)	log(gf)
6587.6100	8.5370	-1.596

E.3 Ca I

Table E.3: Ca I lines used

wavelength (Å)	excitation potential (eV)	log(gf)
6572.7790	0.0000	-4.104
6162.1730	1.8990	-0.167
5581.9650	2.5230	-0.569
5588.7490	2.5260	0.313
5590.1140	2.5210	-0.596
5594.4620	2.5230	0.051
5598.4800	2.5210	-0.134
5601.2770	2.5260	-0.552
6166.4390	2.5210	-1.156
6717.6810	2.7090	-0.596
7148.1500	2.7090	0.208
7202.2000	2.7090	-0.807
5857.4510	2.9330	0.257

E.4 Ca II

Table E.4: Ca II lines used

wavelength (Å)	excitation potential (eV)	log(gf)
8498.0230	1.6920	-1.416
8542.0910	1.7000	-0.463

E.5 Cr I

Table E.5: Cr I lines used

wavelength (Å)	excitation potential (eV)	log(gf)
7400.2260	2.9000	-0.111
6748.3350	4.4400	-3.286

E.6 Fe I

Table E.6: Fe I lines used

wavelength (Å)	excitation potential (eV)	log(gf)
6358.6976	0.8590	-4.468
6400.3180	0.9150	-4.318
5446.9168	0.9900	-1.914
6574.2284	0.9900	-5.023
5434.5238	1.0110	-2.122
5455.6095	1.0110	-2.091
5497.5161	1.0110	-2.849
6710.3195	1.4850	-4.880
6219.2810	2.1980	-2.433
6335.3308	2.1980	-2.177
8514.0721	2.1980	-2.229
6173.3356	2.2230	-2.880
6213.4303	2.2230	-2.482
8468.4074	2.2230	-2.072
6750.1525	2.4240	-2.621
6945.2052	2.4240	-2.482
6191.5584	2.4330	-1.417
6393.6013	2.4330	-1.432
6593.8705	2.4330	-2.422
5916.2474	2.4530	-2.994
6978.8516	2.4840	-2.500
5701.5446	2.5590	-2.216
6230.7230	2.5590	-1.281
6575.0158	2.5880	-2.710
5567.3911	2.6080	-2.564
6065.4822	2.6080	-1.530
6200.3129	2.6080	-2.437
6180.2042	2.7270	-2.586
6592.9138	2.7270	-1.473
6546.2395	2.7580	-1.536
6703.5674	2.7580	-3.160
6518.3671	2.8310	-2.460
6229.2283	2.8450	-2.805
6355.0290	2.8450	-2.350
8515.1084	3.0180	-2.073
5909.9736	3.2110	-2.587
5848.0640	3.2660	-3.442
5615.6439	3.3320	0.050
5586.7559	3.3680	-0.120
5572.8424	3.3960	-0.275
5569.6181	3.4170	-0.486
5712.1316	3.4170	-1.990
5576.0888	3.4300	-1.000
6232.6412	3.6540	-1.223
6411.6493	3.6540	-0.595
6336.8243	3.6860	-0.856
6408.0184	3.6860	-1.018
6003.0123	3.8810	-1.120
6008.5540	3.8840	-1.078
6187.9904	3.9430	-1.720
5466.3962	4.3710	-0.630
6027.0509	4.0760	-1.089
7132.9863	4.0760	-1.628
5487.7400	4.1430	-0.710
5587.5740	4.1430	-1.850
6165.3603	4.1430	-1.474
7418.6674	4.1430	-1.376
5620.4924	4.1540	-1.790
6916.6815	4.1540	-1.450
7207.3810	4.1540	-0.352
5563.6002	4.1910	-0.990
6215.1438	4.1860	-1.320
6380.7433	4.1860	-1.376
6786.8604	4.1910	-2.070
7401.6849	4.1860	-1.599
5618.6327	4.2090	-1.276
5762.9922	4.2090	-0.450
7130.9221	4.2170	-0.790
5731.7623	4.2560	-1.300
7445.7460	4.2560	-0.237
5717.8329	4.2840	-1.130
7411.1540	4.2830	-0.428
7937.1310	4.3120	0.152
8220.3790	4.3200	0.275
5445.0424	4.3860	-0.020
7945.8440	4.3860	0.154
5562.7060	4.4350	-0.659
5432.9479	4.4450	-1.040
8207.7450	4.4460	-0.987
5752.0230	4.5490	-1.267
5852.2187	4.5480	-1.330
5859.5780	4.5490	-0.398
5862.3530	4.5490	-0.058
6024.0580	4.5480	-0.120
8439.5630	4.5490	-0.698
6737.9870	4.5580	-1.750
5565.7040	4.6080	-0.285
5705.9922	4.6070	-0.530

continued on next page

Table E.6: *continued*

wavelength (Å)	excitation potential (eV)	log(gf)
6020.1692	4.6070	-0.270
6705.1010	4.6070	-1.496
6726.6610	4.6070	-0.829
7145.3160	4.6070	-1.532
6733.1513	4.6380	-1.580
6752.7071	4.6380	-1.204
5905.6720	4.6520	-0.730
6007.9600	4.6520	-0.966
6042.2290	4.6520	-2.438
6056.0047	4.7330	-0.460
6569.2155	4.7330	-0.420
7353.5300	4.7330	-1.570
7386.3870	4.9130	-0.402
7389.3350	4.9130	-0.665
7440.9520	4.9130	-0.682
8526.6690	4.9130	-0.760
7142.5030	4.9560	-0.931
7363.9100	4.9560	-0.891
8471.7390	4.9560	-0.863
7155.6220	5.0100	-0.806

E.7 Fe II

Table E.7: Fe II lines used

wavelength (Å)	excitation potential (eV)	log(gf)
6369.4620	2.8910	-4.160
6516.0800	2.8910	-3.320

E.8 H I

Table E.8: H I lines used

wavelength (Å)	excitation potential (eV)	log(gf)
6562.7970	10.1990	0.710

E.9 He I

Table E.9: He I lines used

wavelength (Å)	excitation potential (eV)	log(gf)
5875.5990	20.9640	-1.511
5875.6140	20.9640	-0.341
5875.6150	20.9640	0.409
5875.6250	20.9640	-0.341
5875.6400	20.9640	0.139
5875.9660	20.9640	-0.211

E.10 Mg I

Table E.10: Mg I lines used

wavelength (Å)	excitation potential (eV)	log(gf)
7657.6030	5.1080	-1.120
7930.8140	5.9460	-1.610

E.11 Mn I

Table E.11: Mn I lines used

wavelength (Å)	excitation potential (eV)	log(gf)
6013.5130	3.0720	-0.251

continued on next page

Table E.11: *continued*

wavelength (Å)	excitation potential (eV)	log(gf)
6021.8190	3.0750	0.034

E.12 Na I

Table E.12: Na I lines used

wavelength (Å)	excitation potential (eV)	log(gf)
5889.9510	0.0000	0.117
5895.9240	0.0000	-0.184

E.13 Ni I

Table E.13: Ni I lines used

wavelength (Å)	excitation potential (eV)	log(gf)
5846.9860	1.6760	-3.210
5578.7110	1.6760	-2.640
6767.7680	1.8260	-2.170
5754.6550	1.9350	-2.330
5592.2590	1.9510	-2.570
6586.3080	1.9510	-2.810
5892.8680	1.9860	-2.350
7414.5000	1.9860	-2.570
8183.2550	2.1020	0.230
8194.8240	2.1040	0.490
7385.2360	2.7400	-1.970
7122.1910	3.5420	0.040
7393.6000	3.6060	-0.825
7422.2770	3.6350	-0.140
6772.3130	3.6580	-0.980
7917.4300	3.7400	-0.995
5600.0100	4.0890	-0.609
6175.3600	4.0890	-0.559
6176.8070	4.0880	-0.260
6053.6790	4.2360	-1.070

E.14 O I

Table E.14: O I lines used

wavelength (Å)	excitation potential (eV)	log(gf)
8446.3591	9.5210	0.236

E.15 S I

Table E.15: S I lines used

wavelength (Å)	excitation potential (eV)	log(gf)
6052.6740	7.8700	-0.740
6757.1710	7.8700	-0.310

E.16 Si I

Table E.16: Si I lines used

wavelength (Å)	excitation potential (eV)	log(gf)
5708.4000	4.9540	-1.470
5772.1460	5.0820	-1.750
5747.6670	5.6140	-0.780
6237.3190	5.6140	-0.530
7405.7720	5.6140	-0.820
7415.9480	5.6160	-0.500

continued on next page

Table E.16: *continued*

wavelength (Å)	excitation potential (eV)	log(gf)
7423.4960	5.6190	-0.314
6721.8480	5.8630	-1.490
7680.2660	5.8630	-0.690
6527.2020	5.8710	-1.500
7165.5450	5.8710	-0.600
8443.9700	5.8710	-1.400
8502.2190	5.8710	-1.260
6976.5130	5.9540	-1.170
7918.3840	5.9540	-0.610
7932.3480	5.9640	-0.470
6555.4630	5.9840	-1.000
7373.0040	5.9840	-1.340
7944.0010	5.9840	-0.310
8536.1640	6.1810	-0.910

E.17 Si II

Table E.17: Si II lines used

wavelength (Å)	excitation potential (eV)	log(gf)
6371.3710	8.1210	-0.003
6347.1090	8.1210	0.297

E.18 Ti I

Table E.18: Ti I lines used

wavelength (Å)	excitation potential (eV)	log(gf)
5866.4510	1.0670	-0.840
5490.1480	1.4600	-0.933

E.19 Ti II

Table E.19: Ti II lines used

wavelength (Å)	excitation potential (eV)	log(gf)
6559.5880	2.0480	-2.019

E.20 V I

Table E.20: V I lines used

wavelength (Å)	excitation potential (eV)	log(gf)
5627.6330	1.0810	-0.363
5727.0480	1.0810	-0.012

E.21 Positions of lines used

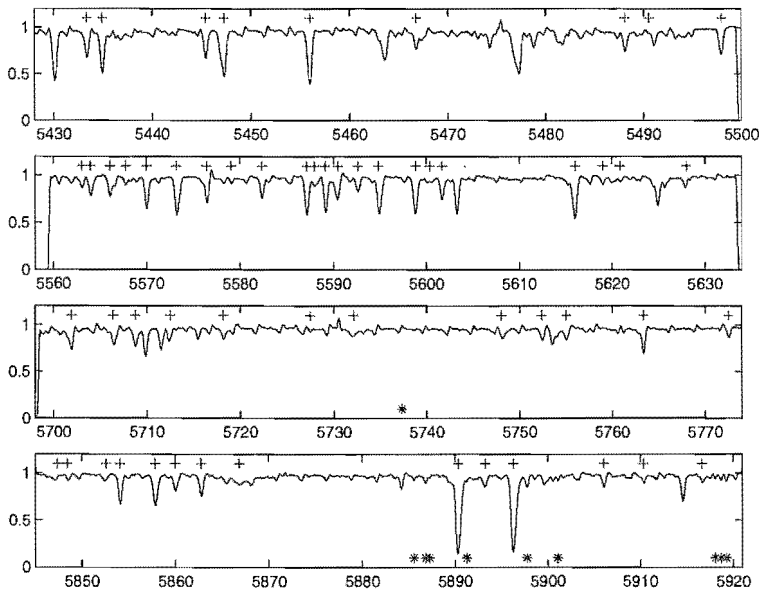

(a) Positioning of lines used on spectra for orders 1–4.

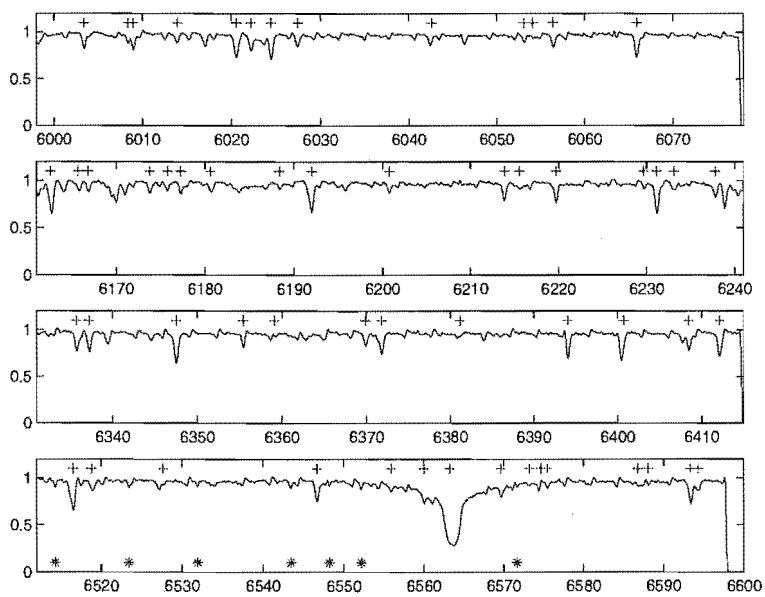

(b) Positioning of lines used on spectra for orders 5–8.

Figure E.1: Positioning of lines used on spectra. (+) show stellar line rest wavelengths offset by 20 kms^{-1} to account for the velocity of VY Pyx. (*) show telluric line rest wavelengths offset by -20 kms^{-1} to account for the heliocentric correction applied to the star.

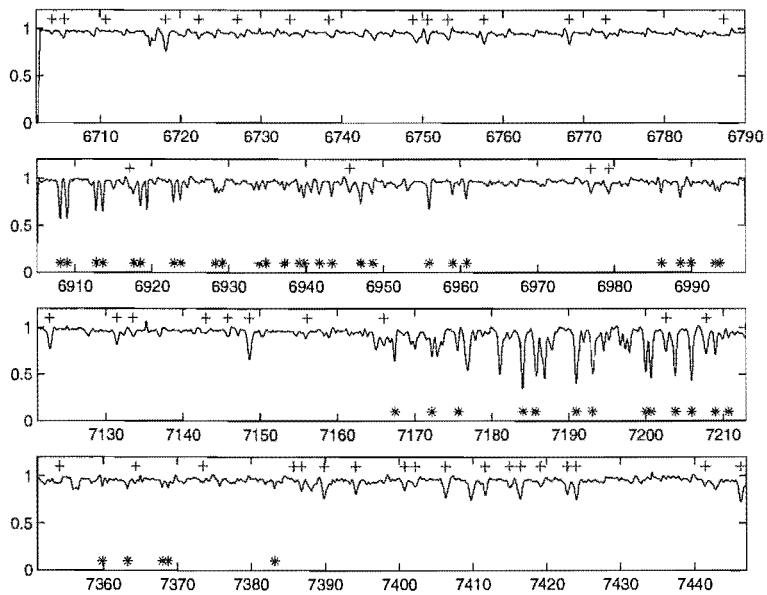

(a) Positioning of lines used on spectra for orders 9–12.

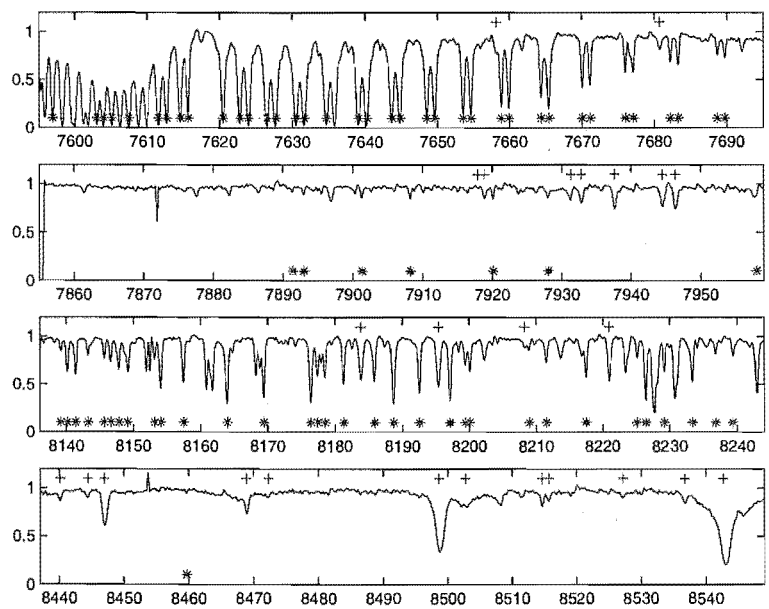

(b) Positioning of lines used on spectra for orders 13–16.

Figure E.2: Positioning of lines used on spectra. (+) show stellar line rest wavelengths offset by 20 kms^{-1} to account for the velocity of VY Pyx. (*) show telluric line rest wavelengths offset by -20 kms^{-1} to account for the heliocentric correction applied to the star.

Appendix F

Wavelet analysis work presented at Leuven conference

The following is the text and figures of a poster presented at the IAU Colloquium 185: Radial and nonradial pulsations as probes of stellar physics, Leuven, 2001. While a condensed version of this was published in the conference procedings (McSaveney et al., 2002) and some of the material covered elsewhere in the thesis, it was decided to include the full details here.

Wavelet analysis of the RV Tauri star U Mon

J.A. McSaveney[1], P.L. Cottrell[1], K.R. Pollard[1], J.A. Mattei[2]

The RV Tauri star U Monocerotis (U Mon) is the second brightest RV Tauri star and the brightest RVb star and as a consequence has been observed for many years. It is considered to be one of the more stable of the RV Tauri stars with clear alternations in deep and shallow minima and generally distinct long-term fluctuations in mean magnitude of the order of $\sim$ 2500 days. At present it has a formal period between successive deep minima of 93.32 days (Pollard, Cottrell, Kilmartin, and Gilmore, 1996a). Historically though, the period has been known to change, with Percy, Sasselov, Alfred, and Scott (1991) finding a period between successive deep and shallow minima of 46.117 $\pm$ 0.003 days prior to 1957 and 45.814 $\pm$ 0.005 days after this time.

U Mon is amongst a collection of RV Tauri stars that have been studied by successive students at Mount John University Observatory since 1990. It has been monitored both spectroscopically and photometrically for over two successive long-term minima and several trends have begun to emerge, especially concerning the long term behaviour (McSaveney et al (in preparation)). Currently efforts are being focused on these long-term variations, with the pulsational variations and shock-wave behaviour to be followed up at a later date. As a part of the study of this star, data has been gathered from a variety of sources including historical visual estimates such as those detailed below.

Wavelet analysis has been performed on American Association of Variable Star Observers (AAVSO) visual estimates of the RV Tauri star U Mon from 1961 - 2000 using the AAVSO wavelet analysis program (WWZ). Periods of 46.07, 92.40, and 2498 days have been found to be present with the 92 day period not always being detectable. A constant ratio between the amplitudes of the 46 and 92 day periods has been found, even during a single long-term deep minimum. The period of the long term variations has been found to be reasonably constant but has changed in amplitude significantly with the most recent deep minimum showing atypical shallowness.

[1]Mount John University Observatory, Department of Physics and Astronomy, University of Canterbury, Christchurch, New Zealand

[2]AAVSO, 25 Birch St, Cambridge, MA 02138, USA

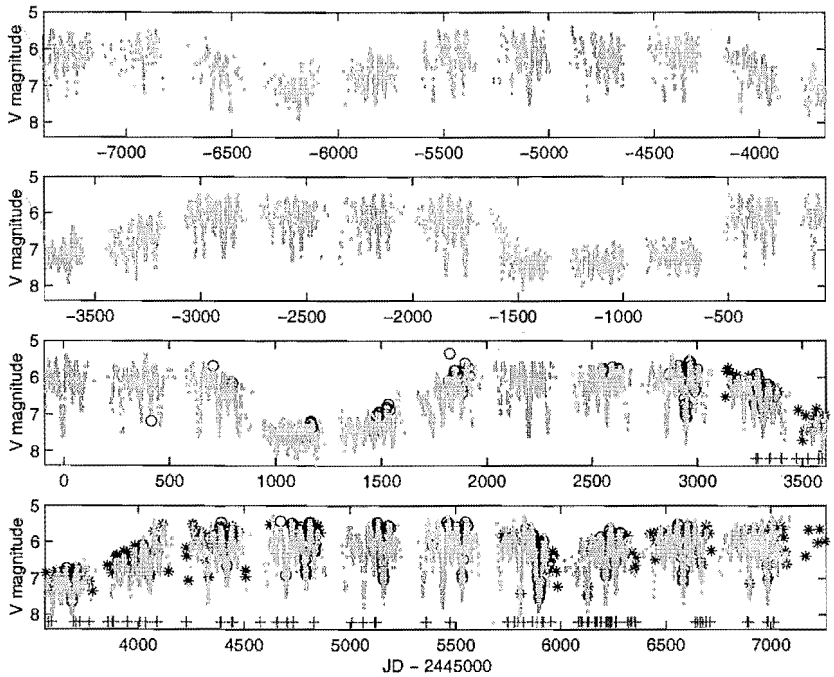

Figure F.1: Photometry of the RV Tauri star U Mon. (.) are AAVSO visual estimates, (o) are AAVSO photoelectric photometry, (*) are MJUO photoelectric photometry. (+) indicate times of spectral observation. While AAVSO observations date back from 1961, intensive monitoring at MJUO has been going on since 1990, covering the two most recent deep minima. Both long-term and short-term variations are visible in this figure. Also visible is the changeable nature of the long-term minima with a range of depths and strengths observable.

F.1 Introduction

RV Tauri stars are luminous low-mass supergiants which pulsate with a distinctive light curve of alternating deep and shallow minima and semi-regular periods between successive deep minima of 50 to 150 days. They are restricted to between F to K spectral type and luminosity class Ia-II. Chronologically, they are thought to be on their final blue loop or post-Asymptotic-Giant-Branch (AGB) transition through the Type II Cepheid instability strip. Photometrically they can be subdivided into two categories: RVa with constant mean magnitude, and RVb which show an additional long-term variation in magnitude of the order of 600 to 2600 days.

F.2 Observations

The RV Tauri star U Mon has been monitored at MJUO both spectroscopically and photometrically since 1990. The spectroscopic observations from 1990 to 1993 were analysed by Karen Pollard as part of her PhD thesis with subsequent observations being analysed by Jennifer McSaveney more recently in the course of various postgraduate work. In both cases the observations have been obtained using an echelle spectrograph mounted on the 1m McLellan telescope at MJUO[3]. U Mon has been observed photometrically at MJUO in

[3]Small number of KRP observations obtained using MSO 74" telescope and spectrograph

the *BVRI* band-passes. Only the *V* photometry is presented here (Figure F), but to gain a better understanding of the long-term variations and stability of pulsational behaviour, visual estimates and photoelectric data have been obtained from the AAVSO's extensive data collection. These observations date back from the early 1960s onward and the visual estimates are what makes up the bulk of the data analysed for this paper.

For wavelet analysis (see below for technique), the AAVSO visual data was binned into daily averages and then divided into 2 subsets. These subsets were used due to limitations in the size of data set that the WWZ program could handle. They also were selected to overlap significantly so that end effects could be selected out and discarded.

F.3 Periods

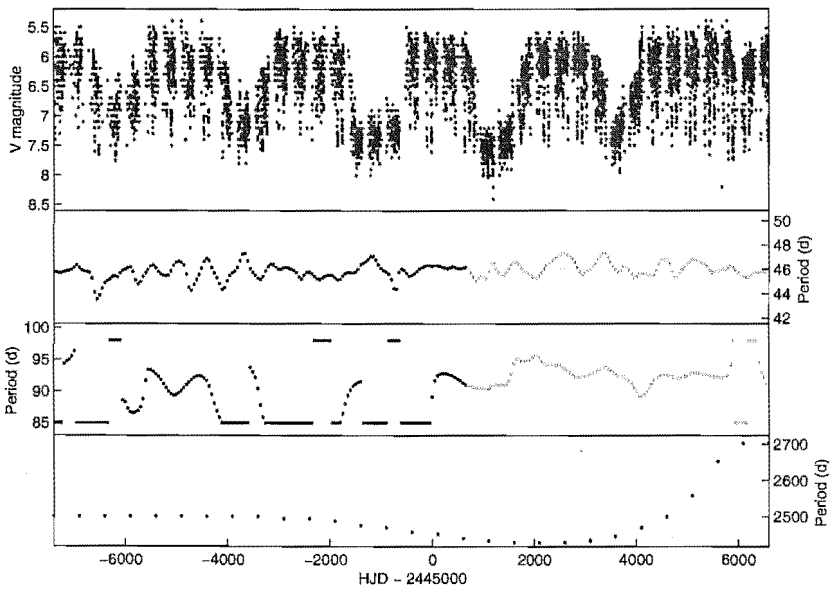

Figure F.2: Dominant periods derived from wavelet analysis of AAVSO visual estimates. While the 46 day period is constantly present, the 92 day period is far less distinct. It was only detected sporadically in the initial half of the data set but is clearly present for much of the later half, only to be lost again during parts of the most recent long term minimum. The presence of the 92 day period shows less correlation with long-term minima than with the stability of the deep shallow alternation pattern in the pulsations. On the occasions when flips occur in the alternation pattern, the 92 day period is lost or at least becomes difficult to find. This can be seen figureF where several flips are present during the latest minimum and the 92 day period is lost.

As can been seen from Figure F.3, there are distinct differences in the periods obtained from the two halves of the data set. At all times, the 46 day period is present, however the 92 day period was not detected for much of the first half.

This is supported in the values for the periods obtained for each half of the data set. The periods obtained are shown in the table below.

This lack of detection at certain times is understandable when one looks closely at the actual observations. The pattern of deep-shallow alternations in minima is quite upset with a great deal of flips where a deep minimum follows a deep minimum or a shallow

minimum follows a shallow one. This may indicate that during this earlier time period, the star's pulsations were less stable.

F.4 Long-term variations

As an RVb star, U Mon has been observed to vary over the long-term in 3 ways over an approximately 8 year cycle. Photometrically it goes into a long-term minimum with decreased amplitude pulsations (see Figure F) and a general reddening of colour (Pollard, 1994) and McSaveney et al in preparation). Spectroscopically it shows two variations: it shows radial velocity variations above that of the pulsational ones (Pollard, 1994) and McSaveney 1998), and it shows heightened Hα emission during long-term minima (see Figure F.4.2)

F.4.1 Amplitudes

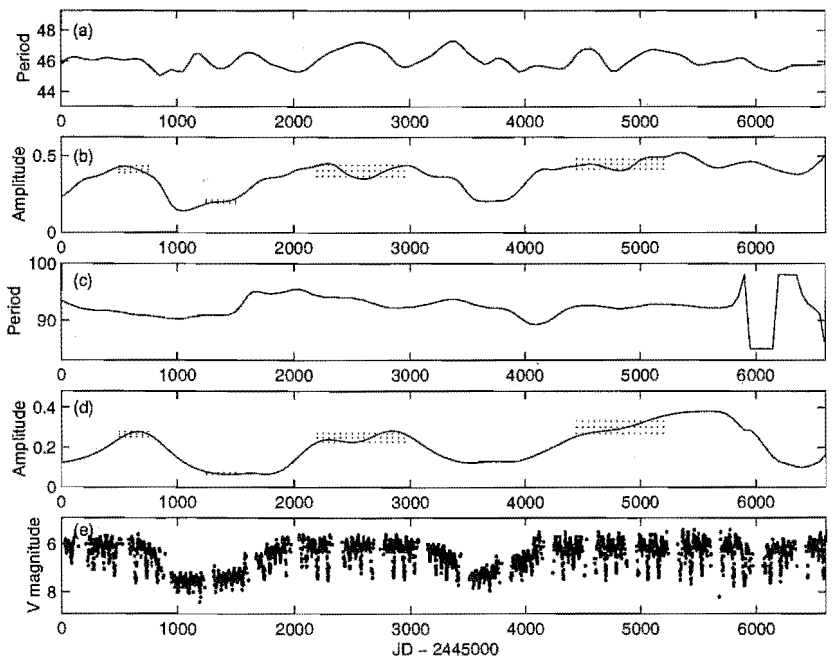

Figure F.3: Different amplitudes for various pulsational components. Long-term minima are clearly detectable in a decrease in the pulsational amplitudes in both the periods however when the amplitudes change is somewhat variable. Ratios of the 92 day to 46 day periods are approximately 0.6 in most cases except for the initial long-term minimum shown, where it is 0.3 (see table in amplitudes section for further values). This particular minimum is also the deepest minimum in the time period examined.

Long-term variations are observable in the amplitudes of the various components of the pulsations (see Figure F.4.1).

Overall variations are also observable in the amplitude of the long-term variations themselves (see Figure F.4.2). Peak amplitude is found in the fourth long-term minima shown with the most recent minimum having the smallest amplitude. This is also reflected in the Hα equivalent widths (see Figure F.4.2), where the average equivalent width is

Table F.1: Periods and amplitudes derived.

	45 day	92 day	Ratio (long/short)
initial long-term max	0.41	0.27	0.64 ± 0.06
long-term min 1	0.20	0.07	0.34 ± 0.04
middle long-term max	0.40	0.25	0.62 ± 0.11
long-term min 2	0.21	0.13	0.63 ± 0.02
final long-term max	0.45	0.30	0.67 ± 0.12

increased in the most recent long-term minimum but not nearly as much as the previous minimum.

F.4.2 Theory behind long-term variations

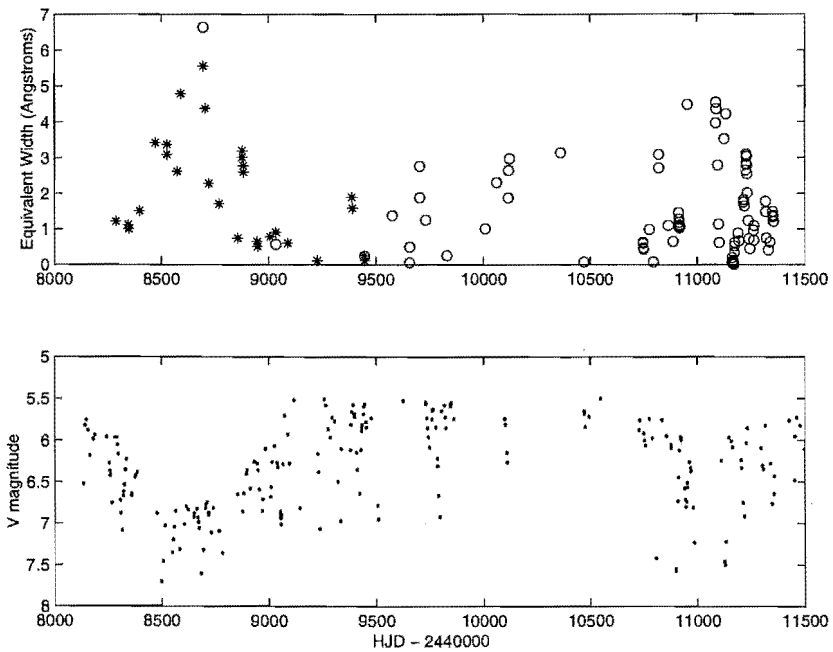

Figure F.4: Hα equivalent width variations. A clear correlation with long-term minima is observable with increased emission during these times. The relatively shallow nature of the most recent minimum is reflected in a corresponding decrease in the Hα equivalent width, however it is still increased in relation to the average long-term maximum value. For the equivalent widths (*) are taken from Pollard (1994), (o) are from McSaveney (1998) and more recent observations with lines link points re-measured to check consistency. For the photometry, (.) are AAVSO visual estimates and (o) are MJUO photometric points.

The mechanism behind the long-term variations by RVb stars has long been debated. Possible interpretations include the idea of the stars being in a binary system (Pollard, 1994) or the stars being isolated but periodically emitting material in a similar manner to R Coronae Borealis stars and becoming pulsationally unstable during the minima, decreasing the amplitude of the pulsations (Shenton et al., 1994b).

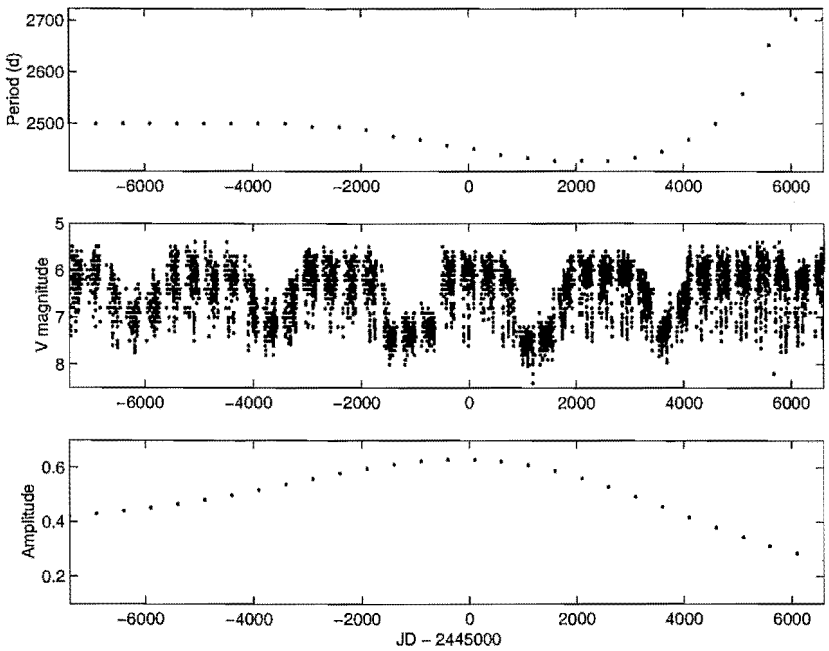

Figure F.5: Period and amplitude of long-term variations from AAVSO visual estimates. The shallow nature of the most recent minimum makes it difficult to detect, and thus increases the period found. The amplitude obtained is also clearly variable with the greatest amplitude ie the deepest minimum being found in the middle.

F.5 Conclusions and future work

The work presented above supports the idea of the star being in an interacting binary system more than it being isolated as there is not clear correlation between pulsational stability and long-term deep minima. Data from amplitude ratios is inconclusive as while amplitude ratios are reasonably constant for inside and out of one long-term minimum, they were not for another. Analysis of further visual estimates from during and after the most recent deep minimum may be able to shed more light on the situation, however the shallowness of the minimum may only complicate the issue. Orbital characteristics can be derived from the radial velocity variations, making the star highly likely to be a binary, however increased Hα emission n relation to the long-term minima mean that some form of interaction is mostly likely present.

In conclusion, more work is needed on the stars as many questions still remain to be answered.

F.6 Wavelet analysis techniques

Wavelet analysis was performed on the AAVSO visual estimate data by the AAVSO WWZ program[4]. In the wavelet analysis, basically a Morelet wavelet is fitted to the data in a series of time steps for a range of frequencies with the best fit in the frequency range producing the maximum WWZ value. Thus, there are 3 free parameters, the frequency

[4]for more information on the program see http://www.aavso.org/cdata/software.stm and Foster (1996)

Table F.2: Historical periods for U Mon

Author	single period (d)	formal period [a] (d)	long-term period (d)
Gerasimovič (1929)	–	92.26	–
Sanford (1933)	–	92.26	2300 [b]
Loreta (1939)	–	–	2320 [c]
Abt (1955)	46	–	1980/2640 [b]
Preston (1964)	46.1	–	1560 [b]
Percy et al. (1991)	46.117 ± 0.003 (pre1957) 45.814 ± 0.005 (post1957)	–	2475 [c]
Pollard (1994)	46.16	92.32 ± 0.04	2597 ± 6 [b]
McSaveney (1998)	–	–	2595 ± 5 [b]
This work	45.81 ± 1.9	90.70 ± 2.0	2498 ± 72 [c]
(Wavelet)	46.07 ± 0.7	92.40 ± 1.4	

[a]The formal period is taken to be the time between successive deep minima.
[b]Long-term period determined from spectroscopic measurements.
[c]Long-term period determined from photometric measurements.

Table F.3: Periods derived from model data using various c values

Inputted data	c value	p (av)	p (med)	p (1sd)
90 d model	0.1125	91.7318	92.1744	5.9711
	0.0125	90.5573	90.5469	1.2108
	0.0025	90.1230	90.0576	0.1871

being looked at, the time of observation being centred on, and the rate of decay of the wavelet which is a function of the frequency being looked at and the c value. The process is made more complicated by the fact that the data needs to be projected and weighted to get around the uneven sampling. A full mathematical description along with discussion of the pros and cons of the method is detailed in Foster (1996). For the purposes of this study, 3 c values were looked at using model data to select the c value to apply to the visual data. While the lowest c value gave the most accurate data, it also was the longest to run with running times of up to 5 hours over one half of the AAVSO visual estimate data set.

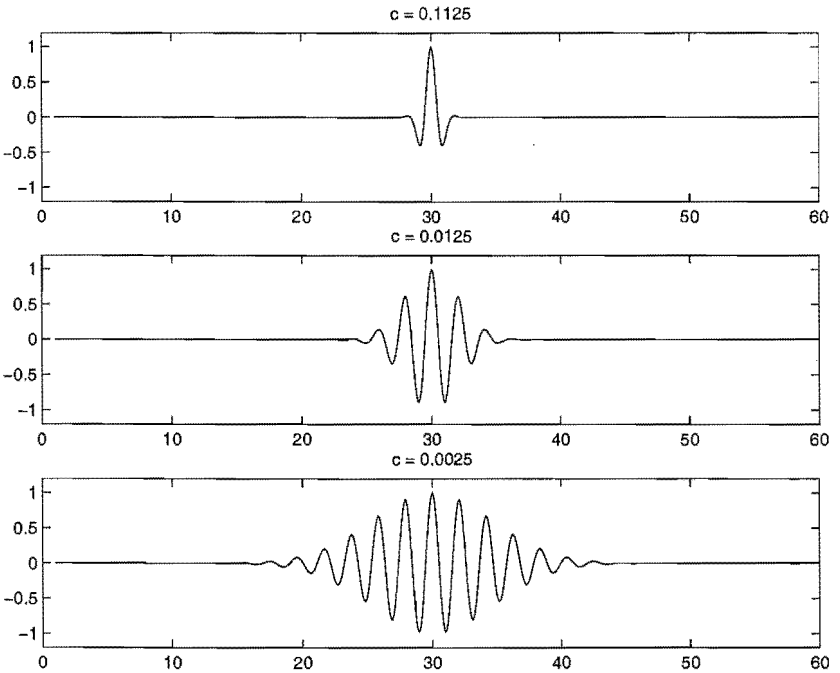

Figure F.6: Schematic shape of wavelet produced by various c values, and model RV Tauri light curve created by addition of 2 sine waves of periods 45 and 90 days. Data sampling is based on AAVSO visual estimate sampling rate to reflect seasonal gaps and irregular spacing of data.

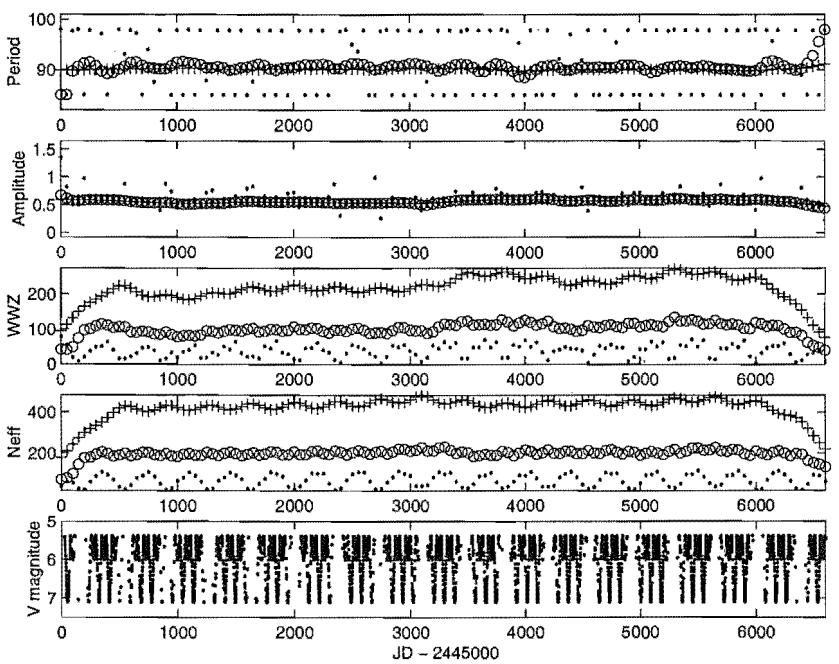

Figure F.7: Wavelet responses obtained using various c values for the wavelet. (.) c = 0.1125, (o) c = 0.0125, (+) c = 0.0025. Decreasing the c value increases the accuracy of the results obtained, as illustrated by less scatter in the period obtained and a higher WWZ value and N_{eff}.